Universidade de Brasília
Instituto de Geociências
Programa de Pós-graduação em Geologia

# Evidências de oceanos Paleo- a Mesoarqueanos e siderianos do Domínio Rio Grande do Norte, Província Borborema

## Evidence for Paleo- to Mesoarchean and Siderian Oceans in the Rio Grande do Norte Domain, Borborema Province

**PAULA FREIRE TRINDADE ALVIM**

**Tese de Doutorado Nº 227**

**Orientador:** Prof. Dr. Elton Luiz Dantas

**Brasília, 27/03/2026**

Universidade de Brasília
Instituto de Geociências
Programa de Pós-graduação em Geologia

# Evidências de oceanos Paleo- a Mesoarqueanos e siderianos do Domínio Rio Grande do Norte, Província Borborema

## Evidence for Paleo- to Mesoarchean and Siderian Oceans in the Rio Grande do Norte Domain, Borborema Province

**PAULA FREIRE TRINDADE ALVIM**

Tese apresentada ao Programa de Pós-Graduação em Geologia – Instituto de Geociências – IG da Universidade de Brasília – UnB como requisito parcial obrigatório para a obtenção do título de Doutor em Geologia.

**Área de concentração:** Geologia regional

**Orientador:** Prof. Dr. Elton Luiz Dantas

**Comissão Examinadora:**

Prof. Dr. Claudinei Gouveia de Oliveira (IG/UnB);
Prof. Dr. Frederico Castro Jobim Vilalva (DG/UFRN);
Prof. Dr. Vitor Garcia (University of Otawwa);
Prof. Dr. Tiago Luis Reis Jalowitzki (Suplente IG/UnB).

Ficha catalográfica elaborada automaticamente,
com os dados fornecidos pelo(a) autor(a)

Fe

Freire Trindade Alvim, Paula
Evidências de oceanos Paleo- a Mesoarqueanos e siderianos do Domínio Rio Grande do Norte, Província Borborema / Paula Freire Trindade Alvim; orientador Elton Luiz Dantas. Brasília, 2026.
263 p.

Tese(Doutorado em Geologia) Universidade de Brasília, 2026.

1. associações máfica-ultramáficas. 2. geodinâmica arqueana. 3. ofiolitos. 4. crosta oceânica juvenil. 5. crosta oceânica juvenil. I. Luiz Dantas, Elton, orient. II. Título.

## AGRADECIMENTOS

Agradeço ao meu Deus pela graça, pela força, pelas orações atendidas, pelos “nãos” recebidos, por me capacitar ao longo de todo este processo e, principalmente, por alinhar as minhas escolhas à Sua vontade para a minha vida. Agradeço ao meu esposo, André Mateus, pelo amor, pelo ombro amigo, pelo suporte e por sempre dizer: “Você só precisa se preocupar com a sua tese; deixe o resto comigo”. Estendo este muito obrigado à minha sogra, Márcia Cristina, pelo amparo durante a minha estadia em Brasília, pelo incentivo e pelo cuidado. Aos meus pais, Oziê e Iêda, na falta de palavras melhores, fica aqui registrado o meu respeito, a minha gratidão e o meu desejo de continuar honrando cada sacrifício, cada princípio e cada ensinamento, feitos ou repassados. Ao meu irmão Paulo Gabriel, por colocar sua fé em mim e tornar tudo mais leve. À Igreja Presbiteriana da Alvorada, por me adotar em seu seio e ser minha família no Planalto Central.

Poderia agradecer ao meu orientador, Prof. Dr. Elton L. Dantas, pela ajuda em campo, na interpretação dos resultados, na confecção dos mapas, na elaboração dos artigos, na revisão da tese e nas discussões geológicas. Todavia, seria muito. Elton se preocupa em tornar a Borborema conhecida ao redor do mundo, presenteou-me com as regiões de Lajes e Bonfim, acredita em mim muito mais do que, de fato, eu mesma acredito, e o que ele me ensinou vai muito além dessas duzentas e tantas páginas. E, mesmo sendo pouco, muito obrigada, professor.

Agradeço a toda a equipe do Laboratório de Estudos Geodinâmicos, Geocronológicos e Ambientais (LEGGA) — o dia a dia e o partilhar de experiências com cada um de vocês tornaram o peso do doutorado mais suave. Em especial, meu muito obrigada ao Prof. Dr. Reinhardt A. Fuck, pelas contribuições acadêmicas; ao Prof. Dr. Roberto V. Santos, pelo aprendizado e pelas oportunidades profissionais; e ao Prof. Dr. Guilherme de O. Gonçalves, pela paciência e generosidade em compartilhar conhecimento.

Por fim, agradeço à Universidade de Brasília (UnB), ao Instituto de Geociências (IG), ao Programa de Pós-Graduação em Geologia (PPGG) e ao Conselho Nacional de Desenvolvimento Científico e Tecnológico (CNPq).

Obrigada por me abrirem as portas da pesquisa e por me fornecerem os recursos necessários. O presente trabalho foi realizado com apoio da Coordenação de Aperfeiçoamento de Pessoal de Nível Superior-Brasil (CAPES) – Código de Financiamento 001.

## RESUMO

O Domínio Rio Grande do Norte (DRGN) constitui uma das principais compartimentações geotectônicas da Província Borborema. Esse situa-se na porção setentrional da província, abrangendo principalmente o Rio Grande do Norte e, secundariamente, áreas do Ceará e da Paraíba. Trata-se de um segmento crustal complexo, cuja evolução está vinculada à amalgamação do Gondwana Ocidental no Neoproterozoico. É formado por núcleos arqueanos preservados, terrenos paleoproterozoicos retrabalhados e magmatismo neoproterozoico. Dentre essas unidades litoestratigráficas, destacam-se duas associações litológicas pela relevância científica e rara ocorrência global. A primeira é o Complexo Máfico-Ultramáfico do Bonfim, localizado na porção leste do DRGN. Ele é composto por: serpentinito, clinopiroxenito, anfibolito, tremolititos, cloritito, antofilitos-cloritito, talco-xisto e camadas de óxido de Fe-Ti. O complexo ganhou destaque por ser interpretado como a unidade mais antiga da Plataforma Sul-Americana, derivada de fontes mantélicas enriquecidas desde o Éon Hadeano. Análises U-Pb em zircão realizadas na presente tese indicam idades de cristalização entre ~3,57 ± 0,62 e 3,48 ± 0,57 Ga, com o intercepto mais antigo associado a harzburgitos residuais, interpretados como remanescentes de fontes mantélicas previamente depletadas. Três outras amostras apresentam idades com valores entre 3,13 ± 30 Ga e 3,09 ± 34 Ga. Essas unidades representam um segundo evento máfico-ultramáfico, marcado também por um componente de subducção em toleítos de arco insular. Juntos, esses dois episódios representam uma sequência pseudoestratigráfica ofiolítica cíclica no tempo e parcialmente preservada no espaço. A segunda associação, a sequência Santa Luzia, insere-se no Bloco Lajes, no centro-norte do DRGN. Essa é composta por anfibolitos, rochas calssilicáticas e hornblenditos com idades siderianas (2,48–2,31 Ga; U-Pb em zircão), associadas a um período de relativa quiescência tectônica global. Seus padrões geoquímicos em rocha total exibem anomalias negativas de Nb, Ta e Ti, típicas de magmatismo oceânico relacionado a arcos insulares. Os dados Sm–Nd reforçam essa interpretação: litotipos juvenis apresentam $\varepsilon_{Nd(t)}$ positivo e idades Nd $T_{DM}$ de 2,36–2,12 Ga, enquanto parte dos anfibolitos registra $T_{DM}$ mais antigas (3,97–2,62 Ga), indicando contribuição de crosta arqueana prévia à formação do arco. Em

conjunto, esses resultados indicam que o magmatismo associado à subducção persistiu localmente na Província Borborema, em contraposição aos modelos de paralisação tectônica durante o Sideriano.

***Palavras-chave***: associações máfica-ultramáficas, ofiolitos, geodinâmica arqueana, crosta oceânica juvenil, quiescência tectônica.

## ABSTRACT

The Rio Grande do Norte Domain (RGND) constitutes one of the main geotectonic compartments of the Borborema Province. It is located in the northern part of the province, primarily encompassing Rio Grande do Norte, and secondarily, areas of Ceará and Paraíba. It is a complex crustal segment whose evolution is linked to the Neoproterozoic amalgamation of Western Gondwana. It consists of preserved Archean cores, reworked Paleoproterozoic terrains, and Neoproterozoic magmatism. Among these units, two lithological associations stand out for their scientific significance and rarity worldwide. The first is the Bonfim Mafic-Ultramafic Complex, located in the eastern portion of the RGND. It is composed of: serpentinite, clinopyroxenite, amphibolite, tremolite, chloritite, anthophyllite-chloritite, talc-schist and Fe-Ti oxide layers. The complex gained prominence after being interpreted as the oldest unit of the South American Platform, derived from mantle sources enriched since the Hadean Eon. U-Pb analyses on zircon indicate crystallization ages between ~3.57 ± 0.62 and 3.48 ± 0.57 Ga, with the oldest intercept associated with residual harzburgites, interpreted as remnants of previously depleted mantle sources. Three other samples have ages ranging from 3.13 ± 30 Ga to 3.09 ± 34 Ga. These units represent a second mafic–ultramafic event, also characterized by a subduction-related component recorded in island arc tholeiites. Together, these two episodes define a pseudostratigraphic ophiolitic succession, cyclic in time and only partially preserved in space. The second association, the Santa Luzia sequence, is located in the Lajes Block, in the north-central part of the RGND. It includes amphibolites, calc-silicate rocks, and hornblendites with Siderian ages (2.48–2.31 Ga; U-Pb in zircon), associated with a period of relative global tectonic quiescence. Its geochemical patterns in whole rock exhibit negative Nb, Ta, and Ti anomalies, typical of oceanic magmatism related to island arcs. The Sm–Nd data further support this interpretation: juvenile lithotypes display positive $\varepsilon_{Nd(t)}$ values and Nd $T_{DM}$ model ages of 2.36–2.12 Ga, whereas some amphibolites yield older $T_{DM}$ ages (3.97–2.62 Ga), indicating an Archean crustal contribution prior to arc formation. Collectively, these results suggest that subduction-related

magmatism persisted locally within the Borborema Province, challenging models that invoke tectonic quiescence.

***Keywords***: Mafic–ultramafic associations; Ophiolites; Archean geodynamics; Juvenile oceanic crust; Tectonic quiescence.

# LISTA DE ILUSTRAÇÕES


**Figura 1** Mapa de localização e vias de acesso das áreas de estudo. a. Delimitação da América do Sul. b. Mapa apresentando as principais rodovias e cidades do Estado do Rio Grande do Norte, além das duas áreas de estudo descritas no texto. **27**

**Figura 2** Mapas geológicos e relações litológico-estruturais. a) Localização do Domínio Rio Grande do Norte (DRGN) no contexto do Gondwana Ocidental. b) Mapa esquemático simplificado do DRGN, destacando o tectonismo regional e o arcabouço geológico (modificado de JARDIM DE SÁ, 1994; MEDEIROS et al., 2017). As idades U–Pb em zircão do embasamento de cada bloco são apresentadas na figura (ANGELIM, 2006 e referências ali citadas; SOUZA et al., 2007; COSTA et al., 2018). DCC – Domínio Ceará Central; LTB – Lineamento transbrasiliano. **32**

**Figura 3** Modelo esquemático mostrando a hipótese da Terra se formar por acreção de gases e partículas há aproximadamente 4,58 Ga. O núcleo metálico formou-se rapidamente (>4,54 Ga) e separou-se dos silicatos. A comparação com condritos sugere que a Terra evoluiu, desde o início da história do Sistema Solar (ou algumas poucas dezenas de milhões de anos depois), com uma alta razão Sm/Nd. Assim, o manto primitivo da Terra pode ter passado por uma diferenciação Sm/Nd há >4,53 Ga, levando à formação de um reservatório primitivo empobrecido (*Early Depleted Reservoir*–EDR) e de um reservatório enriquecido complementar (*Early Enriched Reservoir*–EER). Adaptado de Rizo et al. (2013). **36**

**Figura 4** Modelo de diferenciação terrestre a partir da cristalização de um oceano de magma. Espera-se que a cristalização do oceano de magma tenha se iniciado sob pressões do manto inferior e progredido para níveis mais rasos à medida que a temperatura diminuía. Conforme a cristalização avançava, o fundido residual era expelido para profundidades progressivamente menores, até que uma pequena fração de fundido se segregasse do mush cristalino, formando uma protocrosta na superfície da Terra. As proporções de fases correspondem a composição do manto primitivo, e os intervalos de pressão refletem as pressões das transições de fase ao longo do solidus do manto. f representa a fração em massa (wt.%) de fundido residual. Ol, olivina; Wad, wadsleyita; Ring, ringwoodita; Gt, granada; Cpx, clinopiroxênio; Maj, granada majorítica; CaPv, perovskita de cálcio; MgPv, perovskita de magnésio; FP, ferropericlásio. Os coeficientes de partição cristal/fundido para Sm, Nd, Lu e Hf são considerados desprezíveis em olivina, wadsleyita, ringwoodita e ferropericlásio. Fonte: Caro et al., (2005). **37**

**Figura 5** Distribuição geográfica das províncias arqueanas. (1) Escudo Báltico, (2) Escudo Ucraniano, (3) Escudo Escocês, (4) Escudo Siberiano, (5) Cráton Indiano, (6) Cráton Sino-Coreano, (7) Cráton de Pilbara, (8) Cráton de Yilgarn, (9) Cráton do Norte da Austrália, (10) Complexo de Napier, (11) Cráton de Kaapvaal, (12) Cráton do Zimbábue, (13) Cráton de Madagascar, (14) Cráton da África Central, (15) Cráton da África Ocidental, (16) Crátons de São Francisco e Amazônico, (17) Escudo das Guianas, (18) Província de Wyoming, (19) Província Superior, (20) Província dos Escravos, (21) Escudo do Labrador e (22) Escudo da Groenlândia. As áreas pontilhadas representam terrenos arqueanos expostos, enquanto as áreas listradas indicam regiões subjacentes a rochas arqueanas. Fonte: Condie, 1994. **40**

**Figura 6** Seção colunar mostrando os componentes do manto superior e da crosta de um ofiolito típico de zona de suprassubducção, ilustrados por fotografias de campo. (a) e (b): Harzburgito bandado e dobrado (olivina + ortopiroxênio); (c): Cumulatos acamadados de dunito e wehrlito (olivina + clinopiroxênio); (d): Gabro acamadado e dobrado; (e): Gabro de textura variada; (f): Gabro cortado por intrusões basálticas e félsicas; (g): Enxame de diques; (h): Brecha vulcânica inserida; (i): Pillow lava; (j): Fluxo de lava andesítica maciça; (k): Camadas de chert dobradas. Fotografias: (a–c, i) Ofiolito de Leka (Noruega); (d) Ofiolito de Karmøy (Noruega); (e–h) Ofiolito de Solund–Stavfjord (Noruega); (j, k) Ofiolito de Mirdita (Albânia). Legenda das abreviações: Chpyr – calcopirita; H/D – harzburgito/dunito; H – harzburgito; L – lherzolito; Opx-veins – veios de ortopiroxenito; Pyr – pirita. Fonte: Furnes e Dilek (2022). **43**

**Figura 7** Distribuições globais de idade de zircão detrítico plotadas em janelas de idade deposicional de 300 milhões de anos. As probabilidades são para caixas de 25 Ma e incluem apenas idades superiores à idade máxima de deposição para cada grupo. As porcentagens são diminuições médias na probabilidade de frequência de 2.700 Ma a 2.350 Ma. TML, Calmaria Tectono-Magmática; n, número de idades do zircão. Fonte: Condie et al., 2022. **47**

**Figura 8** Distribuição temporal das rochas magmáticas no início do Paleoproterozoico, discriminada por continente. Fonte: Spencer et al., 2018. **48**

**Figura 9** Compilação de idades magmáticas para o intervalo de tempo <2,45 a >2,22 Ga. Círculos e quadrados numerados representam rochas ígneas (TTGs, rochas intrusivas félsicas e máficas e rochas extrusivas félsicas), enquanto estrelas identificadas por letras indicam sucessões sedimentares contendo **50**

zircões detríticos dessa idade. Fonte e detalhes da legenda: Partin et al. (2014).

**Figura 10** Mapa geológico do Núcleo Arqueano Bonfim com a localização dos pontos amostrados. **57**

**Figura 11** Mapa geológico da Sequência Santa Luzia com a localização dos pontos amostrados. **58**

**Figura 1 (Artigo I)** Localization map of the Rio Grande do Norte Domain (RGND) in the Borborema Province context (Modified after Van Schmus et al., 2008, 2003). b. Schematic and simplified map of the eastern RGND, showing its regional tectonics and geological framework (modified from Jardim de Sá, 1994). TBL – Transbrasiliano Lineament Belt; CC – Ceará Central Domain. **67**

**Figura 2 (Artigo I)** Geological map and lithological-structural relations of the Bonfim Complex. **71**

**Figura 3 (Artigo I)** a. Field photograph illustrating lithological characteristics and field relationships of the PFE-29 outcrop, Bonfim Mafic–Ultramafic Complex, Borborema Province. b. Distinct petrographic facies were identified and systematically characterized, revealing compositionally and texturally distinct protolith-derived assemblages and reflecting variable degrees of progressive metasomatic alteration. I – chlorite schist; II – Anthophyllite-chlorite schist; III-IV – tremolitite; V – serpentinite. **76**

**Figura 4 (Artigo I)** Field photographs illustrating lithological characteristics and field relationships of the Bonfim Mafic–Ultramafic Complex, Borborema Province. a. Serpentinite outcrop displaying a greenish coloration, with a well-developed network of serpentine veins. b-c. Serpentinite outcrop characterized by a massive to weakly foliated structure, greenish coloration. d. Tremolitite intruded by pegmatite. e. Amphibolite fragment showing macroscopic textural features. f. Amphibolite outcrop crosscut by granodioritic to tonalitic leucosome. g. Chloritite outcrop dominantly composed of chlorite, displaying a massive structure and a characteristic greenish coloration. h. Chloritite outcrop composed dominantly of chlorite, with well-developed schistosity. **78**

**Figura 5 (Artigo I)** Photomicrographs showing the representative mineralogy of typical rocks from the Bonfim Mafic–Ultramafic Complex. a. Serpentinite displaying relict olivine pseudomorphs replaced by serpentine, along with the formation of iron hydroxides derived from the destabilization of opaque phases, under plane-polarized light (PPL). b. Serpentinite showing opaque grains associated with the reticular network of serpentine veinlets or occurring within **79**

serpentine pseudomorphs (PPL). c. Chromite partially replaced by spinel (SEM backscatter electron - BSE). d. Serpentine veinlets under cross-polarized light (XPL). e. BSE image illustrating the textural relationships among amphibole crystals, serpentine-replaced olivine pseudomorphs, and associated serpentine veins. f. Tremolitite showing grains aligned along two distinct foliation directions (XPL). g. Subhedral magnetite grains enclosed within tremolite crystals (PPL). h. Aggregate of rutile included within a tremolite crystal (PPL). Amp – amphibole; Chr – chromite; FeOx-OH - iron hydroxides; Ol – olivine; Opq – opaque mineral; Spl – spinel; Rt – rutile; Srp – serpentine; and Tr – Tremolite.

**Figura 6 (Artigo I)** Photomicrographs showing the representative mineralogy of typical rocks from the Bonfim Mafic–Ultramafic Complex. a. Amphibolite dominantly composed of large hornblende grains, with plagioclase and minor opaque minerals, PPL. b. BSE image illustrating zircon grain enclosed within hornblende. c. Chlorite schist displaying subhedral, isolated magnetite crystals within a randomly oriented chlorite matrix (PPL). d. Chlorite schist showing aligned submillimeter chlorite grains (XPL). e. Anthophyllite crystals in a chlorite matrix. Euhedral to subhedral magnetite grains and iron hydroxide formation in the lower part of the image (PPL). f. Zircon enclosed within a chromite crystal (BSE). g. Talc schist displaying a micro-aggregate texture characterized by randomly oriented talc grains, accompanied by the alteration of primary opaque mineral phases to iron oxides. This oxidative transformation imparts a pervasive brownish coloration to the talc-rich matrix (XPL). e. Very fine-grained aggregates of talc contrasting with larger talc crystals (XPL). Ath – anthophyllite; Chl – chlorite; Chr – chromite; Hbl – hornblende; Opq – opaque mineral; Pl – plagioclase; Tlc – talc; and Zr – Zircon. **82**

**Figura 7 (Artigo I)** Cathodoluminescence images of representative zircon grains. Scale bar = 100 μm. **84**

**Figura 8 (Artigo I)** U–Pb in zircon concordia diagrams. **85**

**Figura 9 (Artigo I)** Chondrite- and primitive mantle-normalized diagrams for Paleoarchean ultramafic intrusions. Normalization values from Anders and Grevesse (1989) and Sun and McDonough (1989), respectively. **88**

**Figura 10 (Artigo I)** Chondrite- and primitive mantle-normalized diagrams for Mesoarchean mafic–ultramafic intrusions. Normalization values from Anders and Grevesse (1989) and Sun and McDonough (1989), respectively. **90**

| | | |
|---|---|---|
| **Figura 11 (Artigo I)** | Samples from the Bonfim Mafic–Ultramafic Complex defining a 4.20 Ga isochron (red circles) and a 3.61 Ga isochron (blue circles). | **92** |
| **Figura 12 (Artigo I)** | Harker diagrams for Yb (ppm) and relevant trace elements (ppm). | **95** |
| **Figura 13 (Artigo I)** | Figure 13 – a. MgO (wt%) versus TiO2 (wt%) (after Deschamps et al., 2013). b. Plots of Yb versus La/Yb (after Deschamps et al., 2013). c-d. Yb (ppm) versus U (ppm) and Yb (ppm) versus Sr (ppm) after Deschamps et al., (2013). e. Gd/Yb versus Th (ppm) plot from (Zuo et al., 2022). f. Th (ppm) versus U (ppm) from Niu (2004). Paleoarchean samples – pink diamond. Mesoarchean samples – blue diamond. | **97** |
| **Figura 14 (Artigo I)** | Block diagram illustrating the mixing of enriched melts into a depleted mantle reservoir; and stratigraphic columns showing Paleo- and Mesoarchean ophiolite sequences preserved in the Bonfim area. | **104** |
| **Figura S1 (Artigo I)** | TAS (Na2O+K2O–SiO2) diagram (Le Bas et al., 1986) showing the amphibolites (blue diamond). | **123** |
| **Figura S2 (Artigo I)** | AFM (Na2O+K2O–MgO–FeOt) diagram (Irvine and Baragar, 1971) showing the amphibolites (blue diamond). | **123** |
| **Figura 1 (Artigo II)** | Geological maps and lithological-structural relations. a. Localization of the Rio Grande do Norte domain (RGDN) in West Gondwana setting. b. Schematic and simplified map of RGND, showing its regional tectonism and geological framework (modified from Jardim de Sá, 1994; Medeiros et al., 2017). U–Pb zircon ages for the basement of each block are presented in the figure (Angelim, 2006 and references therein; Souza et al., 2007; Costa et al., 2018). | **130** |
| **Figura 2 (Artigo II)** | Geological framework of the Lajes Block in the central part of the Rio Grande do Norte Domain. a. Study area delimited by a black rectangle and U-Pb sample localization in the Lajes Block setting. b. The Th map (modified from Danta et al., 2003) of the Lajes Block region showing the distribution of $T_{DM}$ and ℇNd values. Geochronological data for the Caicó and Pedro Avelino complexes are provided Souza et al. (2007) and Costa et al. (2018). | **131** |
| **Figura 3 (Artigo II)** | Geological sketch of the Santa Luzia Sequence, in the Lajes Block region, showing the location of the U-Pb (purple square) studied samples and Sm-Nd TDM modal ages (red square). | **136** |
| **Figura 4 (Artigo II)** | Field photographs illustrating lithological characteristics and field relationships in the Santa Luzia Sequence, Lajes Block, Borborema Province. a. Amphibolite outcrop (2.48 Ga) intersected by 2.21 Ga | **137** |

granodioritic to tonalitic leucosome. b. Outcrop dated in this article, with granodioritic to tonalitic leucosome (2.21 Ga) with amphibolite xenoliths (2.48 Ga). c. Amphibolite fragments found as xenoliths within granodioritic and granitic orthogneisses. d. Banded amphibolite. e. Intense migmatization affecting the rocks of the Santa Luzia Sequence causes the amphibolites to be boudinaged and stretched along the main foliation of the rock, and aligned with the intrusive orthogneisses. f. Intense deformation orienting enclaves and xenoliths of amphibolites, diorites and tonalites. g. Granodioritic orthogneisses of the Caicó Complex with incipient migmatization. h-i. Intense Brasiliano deformation paralleling the layers and orienting boudins of amphibolites and more primitive rocks. SLS – Santa Luzia Sequence. The zircon U–Pb dated samples are shown in the photographs.

**Figura 5** **(Artigo II)** Field photographs illustrating lithological characteristics and field relationships in the Santa Luzia Sequence, Lajes Block, Borborema Province. a. Dated outcrop of calc-silicate rocks in contact with amphibolite. b. Different facies analyzed from the progressive transition from amphibolite to calc-silicate rock. c. Calc-silicate rock with layers richer in garnets and layers richer in epidote. d. Banded calc-silicate rock with outlined facies domains, displaying green epidote–hornblende layers alternating with white plagioclase-rich bands with minor quartz and opaques. e. Transitional amphibolite to calc-silicate rock. f. Garnet-bearing calc-silicate rock with extensive epidotization. g. Banded calc-silicate rock, with green bands composed mainly of epidote and hornblende, and white bands consisting primarily of plagioclase, minor quartz and opaque minerals. h. Aplite dike cutting the hornblende. Granodioritic orthogneisses of the Caicó Complex with incipient migmatization. i. Dated coarse-grained hornblendite. The zircon U–Pb dated samples are shown in the photographs. **139**

**Figura 6** **(Artigo II)** Photomicrographs showing representative mineralogy of typical rocks of the Santa Luzia Sequence. a. Amphibolite dominantly composed of large grains of hornblende with minor andesine and titanite under plane-polarized light (PPL). b. Augite relict crystal in contact with hornblende under PPL. c. SEM backscatter electron (BSE) image illustrating the petrographic characteristics of amphibolite. Hornblende contains hematite inclusions. d. Photomicrograph of garnet-bearing calc-silicate rock composed of diopside, andradite, andesine, quartz, K-feldspart, and zoisite under PPL. e. Hornblende replaced by epidote in garnet-bearing calc-silicate gneiss under PPL. f. BSE image illustrating epidotization in garnet-bearing calc-silicate rock; hornblende contains small hematite inclusions. g. Hornblende replaced by epidote in epidote-rich calc-silicate rock under PPL. h. Epidote corona around allanite **141**

crystal in epidote-rich calc-silicate rock under cross-polarized light (XPL). i. BSE image illustrating epidote corona around allanite crystal in epidote-bearing calc-silicate rock. Grt garnet, Aln allanite, Aug augite, Ep epidote, Hbl hornblende, Hem hematite, Kfs K-feldspar, Pl plagioclase, Qtz quartz and Ttn titanite.

**Figura 7** **(Artigo II)** Photomicrographs showing representative mineralogy of typical rocks of the Santa Luzia Sequence. a. Zoisite in epidote-rich calc-silicate rock under cross-polarized light (XPL). b. Titanite in in epidote-rich calc-silicate rock under XPL. c. BSE (backscatter electron) image illustrates an intergrowth of symplectitic hematite and epidote in epidote-rich calc-silicate rock. d. Hornblende in hornblendite from the Santa Luzia Sequence under plane-polarized light (PPL). e. Grains of hornblende enclosing diopside crystals in hornblendite under PPL. f. BSE image illustrates diopside grain containing numerous oriented hematite inclusions. g. Relicts of hornblende in diopside and olivine crystals in hornblendite under PPL. h. Cracks in olivine are partly filled with serpentine under PPL. i. BSE image illustrating cracks in olivine are partly filled with serpentine. Di diopside, Ep epidote, Hbl hornblende, Hem hematite, Kfs K-feldspar, Oli olivine, Pl plagioclase, Qtz quartz, Ser serpentine, Ttn titanite and Zo zoisite. **143**

**Figura 8** **(Artigo II)** Cathodoluminescence images of representative zircon grains and U-Pb Concordia diagrams. Scale bar = 100 μm. **146**

**Figura 9** **(Artigo II)** a. AFM (Na2O+K2O–MgO–FeOt) diagram (Irvine and Baragar, 1971) showing that the amphibolites (blue diamond) and hornblendite (gray diamond) plot along the tholeiite trend. b. Zr/Ti vs. Nb/Y diagram (Pearce, 1996). c. Harker diagrams for MgO (wt%) vs. Al2O3 (wt%). d. Harker diagrams for MgO (wt%) vs. CaO. **149**

**Figura 10** **(Artigo II)** Harker diagrams for Zr (ppm) and relevant trace elements (ppm). **150**

**Figura 11** **(Artigo II)** Chondrite- and primitive mantle-normalized diagrams for hornblendite, amphibolites and calc-silicate gneisses. Normalization values from Sun and McDonough (1989). a-b. The blue lines represent amphibolites from the Santa Luzia Sequence. c-d. Garnet-bearing calc-silicate rock. e-f. Epidote-rich calc-silicate rocks. g-h Hornblendite. The blue shade is REEs and trace elements normalized contents of low-K tholeiitic rocks overlapped to garnet-bearing calc-silicate and epidote-rich calc-silicate. Gray bands highlight the Eu, Nb, and Ti anomalies. **151**

**Figura 12 (Artigo II)** a. Sm-Nd isotopes diagrams. – blue diamond, garnet-bearing calc-silicate rock – red diamond, epidote-rich calc-silicate rock – green diamond, hornblendite – gray diamond. b. Samples from the Santa Luzia Sequence defining a 2.47 Ga isochron (blue circles), a 2.35 Ga isochron (red circles), and outlier samples (gray circles). **154**

**Figura 13 (Artigo II)** a. Variation diagram of Th/Yb vs Nb/Yb after Pearce (2008). b. Zr/Nb vs. Nb/Th plot reflecting mantle hydration (after Condie, 2015). c. (Hf/Sm)N vs (Ta/La)N (after La Flèche et al., 1998) diagram for identification of subduction-related characteristics. d. Nb/Y vs. La/Yb (after Hoffer et al., 2008). Amphibolite – blue diamond, garnet-bearing calc-silicate rock – red diamond, epidote-rich calc-silicate rock – green diamond, hornblendite – gray diamond. **157**

**Figura 14 (Artigo II)** a. Variation diagram of Nb (ppm) vs La (ppm). b. Yb (ppm) vs. Ce (ppm). c. Y (ppm) vs. Sr (ppm). Amphibolite – blue diamond, garnet-bearing calc-silicate rock – red diamond, epidote-rich calc-silicate rock – green diamond, hornblendite – gray diamond. **163**

**Figura 15 (Artigo II)** a. Compilation of magmatic ages for the Siderian time interval in the MCD (Médio Coreaú Domain), CCD (Ceará Central Domains), RGND (Rio Grande do Norte Domain), and TZD (Traversal Zone Domain) settings. Yellow stars denote: 1-2. granodiorite gneiss of the Ceará Central Domain related to an island arc setting (Fetter et al., 2000; Santos et al., 2008); 3. this study; 4. supracrustal sequences interpreted as a period of magmatic insertion (Hollanda et al., 2011); 5. orthogneisses and migmatites related to subduction settings in the Alto Moxotó Terrane (Santos et al., 2015); and 6-8. tonalite-granodiorite gneiss links with the Neoarchean Granjeiro Complex (Pitarello et al., 2019; Archanjo et al., 2021). b. Histogram of Proterozoic U-Pb zircon ages of igneous and metaigneous rocks from the Borborema Province. Data have been filtered and from Neve et al (2021). **166**

# LISTA DE TABELAS

**Tabela 1** (**Artigo I**) Modal concentration and mineralogical composition of samples from the Santa Luzia sequence. Higher modal concentrations are shown with a continuous line, while minor or trace phases are shown with a dashed line. **144**

## SUMÁRIO


| | | |
|---|---|---|
| | **CAPÍTULO I - INTRODUÇÃO** | |
| **1** | **APRESENTAÇÃO GERAL E ESTRUTURA DA TESE** | **23** |
| 1.2 | Contextualização do tema e áreas de estudo | 24 |
| *1.2.1* | *Localização das áreas de estudo* | 27 |
| 1.3 | Contextualização geológica das áreas de estudo | 27 |
| *1.3.1* | *Núcleo Arqueano Bonfim* | 29 |
| *1.3.2* | *Bloco Lajes* | 30 |
| 1.4 | Objetivos | 33 |
| | **CAPÍTULO II – FUNDAMENTAÇÃO TEÓRICA** | |
| **2** | **FUNDAMENTAÇÃO TEÓRICA** | **35** |
| 2.1 | O manto inicial | 35 |
| 2.2 | Éon Arqueano | 38 |
| 2.2.1 | *Ofiolitos arqueanos* | 41 |
| 2.3 | Transição Neoarqueano–Sideriano e o estabelecimento do 'estilo tectônico moderno' | 44 |
| 2.4 | Calmaria tectono-magmática | 45 |
| 2.5 | Registro Paleoproterozoico | 51 |
| *2.5.1* | *Produção crustal juvenil e orógenos acrescionários* | 51 |
| *2.5.2* | *Magmatismo máfico associado a arcos de ilhas* | 52 |
| *2.5.3* | *Metamorfismo* | 53 |
| | **CAPÍTULO III – METODOLOGIAS** | |
| **3** | **AQUISIÇÃO DE DADOS** | **56** |
| 3.1 | Análise geoquímica em rocha total | 58 |
| 3.2 | Análises isotópicas de Nd em rocha total | 59 |
| 3.3 | Datação U-Pb em zircão por LA-ICP-MS | 60 |
| | **CAPÍTULO IV – ARTIGO I** | |
| **4** | **REMNANTS OF THE EARLY EARTH: PRESERVED PALEO- TO MESOARCHEAN OCEANIC CRUST IN SOUTH AMERICA** | 63 |
| | **CAPÍTULO V – ARTIGO II** | |

| | | |
|---|---|---|
| 5 | A LOST FRAGMENT OF SIDERIAN OCEANIC AND JUVENILE ARC CRUST PRESERVED IN THE BORBOREMA PROVINCE, NORTHEAST BRAZIL | 126 |
| | CAPÍTULO VI – CONSIDERAÇÕES FINAIS | 191 |
| | REFERÊNCIAS | 194 |
| | APÊNDICE A | 219 |
| | APÊNDICE B | 244 |

# CAPÍTULO 1
# INTRODUÇÃO

# 1 APRESENTAÇÃO GERAL E ESTRUTURA DA TESE

Esta tese apresenta um estudo articulado, ancorado em distintas abordagens metodológicas, de dois grupos litológicos, diferenciados com base em características petrográficas, geoquímicas, geotectônicas e geocronológicas. Os grupos localizam-se nas porções leste e centro-norte do Domínio Rio Grande do Norte, inserido na província Borborema, no nordeste do Brasil. O primeiro deles, aqui denominado Complexo Máfico-Ultramáfico de Bonfim, localiza-se dentro do Núcleo Arqueano Bonfim e é constituído por litotipos paleo- a mesoarqueanos, incluindo serpentinitos, anfibolitos, tremolitos, cloritítos, antofilita–cloritítos e talco-xistos. O segundo diz respeito à Sequência Santa Luzia, a qual está situada dentro do Bloco Lajes. Essa é composta por anfibolitos, rochas calcossilicáticas e hornblenditos siderianos, associados a arcos de ilhas.

O texto está ordenado em seis capítulos centrais. O Capítulo I contempla uma breve introdução e contextualização do tema, além da caracterização das áreas de estudo e a pormenorização dos principais objetivos norteadores da pesquisa. Em seguida, na segunda seção, estão descritos os aspectos geológicos, petrotectônicos e geoquímicos do manto inicial, do éon Arqueano, da transição Arqueano–Proterozoico, além de uma apresentação sucinta do registro sideriano global. Na terceira parte encontra-se o detalhamento dos materiais e métodos adotados para viabilização dos alvos pretendidos. O quarto segmento compreende o manuscrito: *'Remnants of the early Earth: preserved Paleo- to Mesoarchean oceanic crust in South America'*, no qual são expostos e discutidos antigos fragmentos máfico-ultramáficos, paleo- a mesoarqueanos, em termos petrogenéticos e tectônicos. Os resultados deste capítulo foram submetidos à revista *Geochemistry, Geophysics, Geosystems* e encontram-se em processo de avaliação. Depois, é apresentado o artigo: *'A lost fragment of Siderian oceanic and juvenile arc crust preserved in the Borborema province, northeast Brazil'*. Os resultados apresentados neste capítulo foram publicados na revista *Precambrian Research*, volume 433, 107979, 2026 (doi.org/10.1016/j.precamres.2025.107979). Nesse artigo, o registro rochoso sideriano é descrito como uma evidência concreta da atividade tectônica ininterrupta durante um período de teórica calmaria geodinâmica, instaurado pouco após a transição Neoarqueano–Proterozoico. O capítulo VI, contém uma

síntese conclusiva a partir dos resultados discutidos nos dois artigos. Por fim, os anexos A e B reúnem, na forma de tabelas, todos os resultados analíticos obtidos durante este trabalho.

## 1.1 Contextualização do tema e áreas de estudo

A diferenciação terrestre é irreversível. Não importa qual tenha sido a composição mineralógica ou estruturação planetária logo após sua colisão com a lua. Hoje, a Terra silicatada é, indiscutivelmente, mais complexa em termos químicos, petrográficos e estruturais que esse planeta primitivo. Todavia, dos 4.567 milhões de anos de história (COHEN et al., 2013), pelo menos 2.300 Ma, ou cerca de 50%, da cronologia geológica terrestre decorreu entre o éon Hadeano (4.567–4.000 Ma) e o começo do Paleoproterozoico (*i.e.,* Sideriano; 2.500–2.300 Ma). Questões como o início da tectônica de placas, a formação do primeiro supercontinente, o resfriamento mantélico e o desenvolvimento da crosta oceânica, entre outras, só podem ser compreendidas a partir de uma análise minuciosa desses dois momentos distintos. Entretanto, para muitos, estudar o Arqueano e o Sideriano é lidar, inevitavelmente, com um passado preservado apenas em fragmentos rochosos desmembrados, metamorfizados e reciclados.

Dentre todas as camadas que formam o planeta Terra, o manto é sem dúvidas o segmento mais relevante para compreensão da litoquímica e reconstrução da geodinâmica arqueana. Na verdade, a investigação de um se condiciona à compreensão do outro. Isso porque rochas com idades superiores a 3.5 Ga são extremamente raras globalmente e as assinaturas mantélicas dos reservatórios iniciais são, em geral, inferidas indiretamente a partir de remanescentes arqueanos ricos em MgO (RIZO et al., 2013; GARCIA et al., 2024). Atualmente, os principais modelos propostos para o sistema mantélico o descrevem como um reservatório primordial que já apresentava heterogeneidades químicas desde o éon Hadeano (CARO et al., 2006; DEBAILLE et al., 2013). Essa heterogeneidade é interpretada como resultado da coexistência entre domínios empobrecidos e enriquecidos (MURPHY et al., 2010). No registro geológico, resquícios de crosta oceânica primitiva têm sido utilizados nessas investigações. Muitos desses fragmentos estão preservados

em *geenstone belts*, como na Groenlândia, no Canadá e na Austrália (RIZO et al., 2013; ROTH et al., 2013; MURPHY et al., 2021).

Isso ocorre porque a crosta oceânica preserva tanto a composição do manto quanto seus gradientes de diferenciação. Em seções ofiolíticas, por exemplo, essa variação composicional se manifesta em um empilhamento litoestratigráfico: peridotitos residuais na base e magmatismo máfico no topo (KUSKY, 2004). Durante o Arqueano, ofiolitos ainda funcionam como marcadores da expansão da crosta oceânica e de subducções incipientes, pelo menos até o pleno estabelecimento de um estilo tectônico moderno (CAWOOD et al., 2018; BROWN et al., 2020). Os motores geotectônicos do Arqueano atuaram sob altas temperaturas, provavelmente gerando regimes tectônicos híbridos e transicionais. Um esquema conciliatório propõe protoplacas móveis, com deformação intensa, coexistindo com litosfera estática de mínima mobilidade (CAPITANIO et al., 2019). Só que, neste contexto, o foco deixa de ser o 'como' e passa a ser 'até quando' essas forças impulsionadoras permaneceram ativas.

Logo após o Neoarqueano, o período Sideriano é marcado por uma consistente diminuição no histórico rochoso global (CONDIE, 1998; CONDIE et al., 2009; SPENCER et al., 2018). A faixa de idades U-Pb em grãos de zircão entre ~ 2,36 e 2,23 Ga representa um *gap* considerável na adição crustal do Proterozoico (CONDIE et al., 2009). Tanto no que diz respeito ao registro magmático, quanto à abundância de grãos de zircão detríticos. Os mínimos na distribuição de idades U-Pb em zircão são tão significativos que esse período ficou conhecido como *Siderian Quiet Interval* (SQI) ou Calmaria tectono-magmática (*Tectono-Magmatic-Lull*-TML; SPENCER et al., 2018; CONDIE et al., 2022). Por muito tempo, foi interpretado como o produto de um *shutdown* tectônico (CONDIE et al., 2009; CONDIE E O'NELL, 2010). Ou seja, uma estagnação litosférica generalizada em resposta a prolongada quiescência das placas tectônicas. Mais tarde, à medida que novos fragmentos siderianos surgiram, a ideia de um total desligamento tectônico passou a ser amplamente questionada (PEHRSSON et al., 2014; PARTIN et al., 2014; YANG E SANTOSH, 2015). Novas abordagens geodinâmicas menos abruptas — como desaceleração (*slowdown*) tectônica, orogêneses periféricas ou preservação

crustal preferencial — tornaram-se mais consideradas (PEHRSSON et al., 2014; SPENCER et al., 2018).

Diante de todo esse quadro, a Província Borborema, especificamente o Domínio Rio Grande do Norte, emerge como uma seção crustal promissora. Em uma área de pouco mais de 6.500 km², a cerca de 110 km de Natal – Rio Grande do Norte (RN), tipos máficos e ultramáficos preservam registros de antigos ambientes geotectônicos, do Paleo- ao Mesoarqueano e do Sideriano. Sobre o primeiro caso, o Complexo Máfico-Ultramáfico de Bonfim é interpretado como a associação litológica mais antiga da Plataforma Sul-Americana (~3,526 ± 0,5 Ga e 3,75 ± 0,12 Ga; SANTOS et al., 2020), derivada de fontes mantélicas hadeanas enriquecidas (GARCIA et al., 2024). Embora avanços significativos já tenham sido alcançados, os estudos na região de Bonfim ainda se concentram majoritariamente na compreensão das mineralizações e dos corpos ultramáficos aflorantes nas proximidades das minas de Oiticica, São Tomé e Bonfim. Neste trabalho, no entanto, o escopo é ampliado, abrangendo também áreas situadas ao norte e ao sul dessas mineradoras. Tanto do ponto de vista geocronológico quanto petrográfico e químico, busca-se integrar diferentes conjuntos de dados. O objetivo é estabelecer correlações mais robustas entre as unidades estudadas, bem como refinar a interpretação da evolução magmática e dos processos de modificação do manto reconhecidos na região. Sob a ótica geotectônica, ainda que de forma preliminar, o alvo é caracterizar o ambiente em que essas rochas foram geradas.

Já a sequência Sideriana Santa Luzia (DANTAS et al., 2008), localizada na região NW do Bloco Lajes, é tida como arco insular que, contraintuitivamente, evoluiu e amadureceu durante o SQI. Por décadas, essas rochas foram pouco ou quase nada estudadas. Muitas vezes, indissociadas do ambasamento Riaciano local ou associadas a metassedimentos neoprotorezoicos. No entanto, elas não representam apenas novas unidades geológicas na literatura regional, mas também marcam importantes fronteiras para a compreensão da evolução crustal e da dinâmica tectônica pré-cambriana. Juntas, as regiões de Lajes e Bonfim registram um intervalo de intenso dinamismo mantélico e tectônico, parcialmente preservado no DRGN e geneticamente associado a ambientes oceânicos. Do Paleoarqueano ao Sideriano, essas associações constituem uma

janela quase contínua para a compreensão dos eventos e transformações que afetaram a Borborema, raramente preservados ou documentados em escala global.

### *1.2.1 Localização das áreas de estudo*

A primeira área de estudo, associada ao Núcleo Arqueano Bonfim, está localizada no extremo nordeste do Brasil, englobando os municípios de São Tomé, Caiçara do Rio do Vento, Lajes e Jardim de Angicos, no estado do Rio Grande do Norte. A segunda região de pesquisas, relacionada ao Bloco Lajes, compreende os municípios de Lajes, Angicos e Pedro Avelino, também no RN. As áreas distam cerca de 32 km entre si. O principal acesso, a partir de Natal, dá-se pela BR-304. Como vias secundárias de acesso à Área I, destacam-se as rodovias RN-023, RN-203 e BR-104. Para a Área II, as rotas alternativas incluem as rodovias RN-041, RN-263 e BR-104.

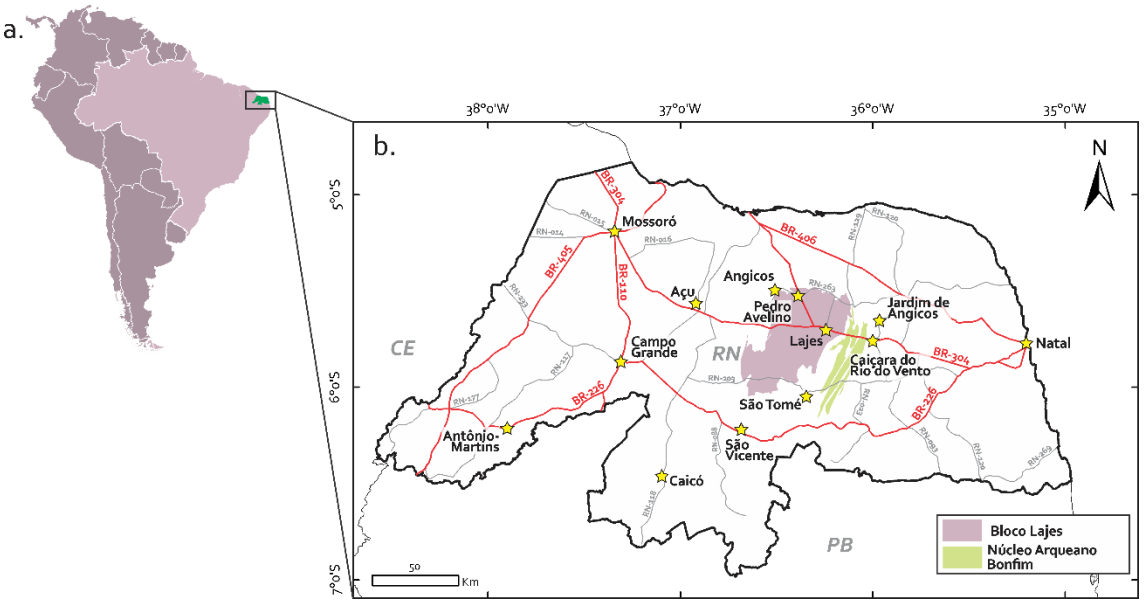



**Figura 1 -** Mapa de localização e vias de acesso das áreas de estudo. a. Delimitação da América do Sul. b. Mapa apresentando as principais rodovias e cidades do Estado do Rio Grande do Norte, além das duas áreas de estudo descritas no texto.

## 1.2 Contextualização geológica das áreas de estudo

A Província Borborema (PB) ocupa uma área de aproximadamente 450.000 Km$^2$, no extremo nordeste do Brasil. É uma grande região pré-cambriana resultante da convergência entre os crátons África-São Luiz,

Amazonas e São Francisco-Congo (ALMEIDA et al., 1977; TROMPETTE,1994; JARDIM DE SÁ, 1994). Ao longo da sua história evolutiva, a sobreposição de distintos episódios deformacionais, metamórficos e magmáticos ligados a uma ampla complexidade estrutural tornou a Borborema um intricado e polifásico sistema. No entanto, em sentido lato, o arcabouço litológico da PB pode ser descritos em termos dos seus grandes complexos gnáissicos-migmatíticos paleoproterozoicos (BRITO NEVES et al., 2000, FETTER et al., 2000; SOUZA et al., 2007, 2016; DANTAS et al., 2008; VAN SCHMUS et al., 2008; SANTOS et al., 2009; SANTOS et al., 2015, 2017) e núcleos arqueanos menores (DANTAS et al., 2004; ARTHAUD et al., 2008; FERREIRA et al., 2020, 2021; RIBEIRO et al., 2024) unidos durante o Meso- e o Neoproterozoico por assembleias rochosas metassedimentares e metavulcânicas (VAN SCHMUS et al., 2003; HOLLANDA et al., 2015).

A Orogenia Brasiliana (~570–540 Ma) foi responsável pelo retrabalhamento de todo o embasamento sob condições de baixo grau metamórfico, além da gênese de inúmeros plútons graníticos e do desenvolvimento de extensas zonas de cisalhamento (BRITO NEVES, 1975, 1981; BRITO NEVES et al., 2000). Hoje em dia, muitos pesquisadores utilizam essas importantes estruturas para subdividir a PB em sub-províncias menores (Norte, Central ou Transversal e Sul) ou em domínios geotectônicos informais (VAN SCHMUS et al., 2003, 2008, 2011). Localizado nos limites da Subprovíncia Norte, o Domínio Rio Grande do Norte (DRGN) constitui um desses segmentos informais (Fig. 2a). Esse domínio encontra-se limitado pelas zonas de cisalhamento de Portalegre, a oeste; Picuí–João Câmara, a leste; e Patos, ao sul, sendo recoberto, ao norte, pelos sedimentos *onshore* da Bacia Potiguar. Com base em dados de campo, geoquímica, isótopos Sm–Nd, idades U–Pb em zircão, descrições petrogenéticas e espectrometria gama, o embasamento do DRGN foi subdividido em três maciços arqueanos (São José do Campestre, Bonfim e Campo Grande) e três blocos crustais paleoproterozoicos. Os blocos Antônio Martins, Caicó-São Vicente e Lajes são formados por complexos migmatito-gnáissicos de alto grau, cortados por zonas de cisalhamento (DANTAS et al., 2003).

### *1.3.1 Núcleo Arqueano Bonfim*

O Núcleo Arqueano Bonfim é um alto do embasamento e cobre uma área de ~4.600 km$^2$. Está situado na porção leste do DRGN (Fig. 2b), próximo aos municípios de Lajes e São Tomé – RN. Compreende rochas metaplutônicas e vulcanossedimentares, com destaque para formações ferríferas bandadas, quartzitos e intrusões máficas e ultramáficas. As intrusões, foco desta pesquisa, configuram um conjunto de fragmentos rochosos desmembrados (VELÁSQUEZ RUIZ et al., 2019), cujas dimensões variam entre 100 e 2000 m de comprimento e cerca de 100 m de largura. A segmentação e a elongação desses corpos são interpretadas como resultado dos esforços tectônicos Neoproterozoicos, comumente registrados na PB. As intrusões estão alinhadas conforme o trend regional NNE-SSW e se estendem por mais de 35 km. Afloram em associação com os granada-biotita xistos da Formação Seridó e os biotita-anfibólios paragnaisses da Formação Jucurutu, formando pequenos montes que contrastam com a morfologia arrasada dos metassedimentos. Dois pulsos magmáticos arqueanos cálcio-alcalino e de tonalito-trondhjemito-granodiorito formam o embasamento da área.

A associação *in situ* entre metassedimentos e intrusões levou inicialmente à interpretação de contemporaneidade, sendo ambas atribuídas à Formação Jucurutu neoproterozoica (EBERT, 1969; SALIM, 1979; VAN SCHMUS et al., 2008, 2011). Posteriormente, Carvalho (1990) separou as unidades, interpretando a sucessão metassedimentar como arqueana (Sequência Amarante). Neste trabalho, as intrusões são redefinidas como Complexo Máfico-Ultramáfico de Bonfim, mantendo-se a designação Sequência Amarante. Velásquez Ruiz et al. (2019) descrevem a intrusão São Tomé como olivina-websteritos e clinopiroxenitos com lentes de ilmenita–magnetita, metamorfizados em fácies anfibolito. Contudo, o retrabalhamento metamórfico e hidrotermal resultou em anfibolitos, piroxenitos, tremolititos, hornblenditos, serpentinitos e xistos variados. Idades U–Pb em zircão indicam formação Eo- a Paleoarqueana (3,74–3,50 Ga; VELÁSQUEZ RUIZ et al., 2019; SANTOS et al., 2020), representando o registro crustal mais antigo da América do Sul, enquanto os sistemas Sm–Nd sugerem diferenciação mantélica em ~4,44 Ga e manto inicial enriquecido (GARCIA et al., 2024).

### *1.3.2 Bloco Lajes*

O Bloco Lajes (BL), situado na porção norte do DRGN compreende uma área de aproximadamente 2.270 km$^2$ (Fig. 2b). É limitado ao norte pelas coberturas fanerozoicas da Bacia Potiguar, enquanto zonas de cisalhamento dextrais definem a interface do embasamento do bloco com as rochas supracrustais neoproterozoicas do Grupo Seridó, ao sul e a leste (VAN SCHMUS et al., 2008, 2011), e com intrusões graníticas brasilianas a oeste. Em termos litológicos, o embasamento do BL é definido por três importantes segmentos Paleoproterozoicos. O primeiro deles compreende ortognaisses granodioríticos a tonalíticos, migmatitos e grabros de idade sideriana (2,45 ± 0,042 e 2,31 ± 0,37 Ga; DANTAS et al., 2008; COSTA et al., 2021); além de litotipos vulcanossedimentares associados à Sequência Santa Luzia (SSL; NEGRÃO et al., 2005; DANTAS et al., 2008), foco deste estudo.

A SSL aflora predominantemente na porção centro-oeste do bloco, sendo representada por formações ferríferas bandadas e anfibolitos toleíticos de baixo-K, associados a rochas calcissilicáticas e, localmente, a skarns e depósitos scheelitíferos (LIMA et al., 1980; SALIM, 1982; CORRÊA et al., 2020, 2021). Em contraste com a interpretação comumente adotada no DRGN, os litotipos calcissilicáticos são aqui atribuídos a processos metassomáticos, especificamente à epidotização de anfibolitos (LIMA et al., 1980), e não à sua inclusão no Grupo Seridó. Na verdade, conforme Souza Neto (2008), Hollanda et al. (2017) e Lucas et al. (2024), o processo metassomático é relacionado ao Neoproterozoico, mais especificamente à Orogenia Brasiliana (570–540 Ma); os protólitos, por sua vez, não.

O segundo segmento paleoproterozoico é representado por ortognaisses granodioríticos a graníticos e raras fácies gabroicas do Complexo Caicó, a leste (HACKSPACHER et al., 1990; JARDIM DE SÁ, 1994; SOUZA et al., 2007, 2016; HOLLANDA et al., 2011), ou por migmatitos quartzo-feldspáticos do Complexo Pedro Avelino, a oeste. O Complexo Caicó de idade riaciana entre 2.23-2.11 Ga (U-Pb em zircão) foi por muito tempo interpretado como sendo o único embasamento do Bloco Lajes (SOUZA et al., 2007, 2016; HOLLANDA et al., 2011). No entanto, com a descoberta dos fragmentos siderianos, ele passou a ser restrito apenas à porção leste da área. Hoje, a partir do trabalho de Padilha

et al. (2021), acredita-se que uma grande zona de sutura riaciana separa a Sequência Santa Luzia e as demais rochas siderianas dos ortognaisses e migamatítos do Complexo Caicó.

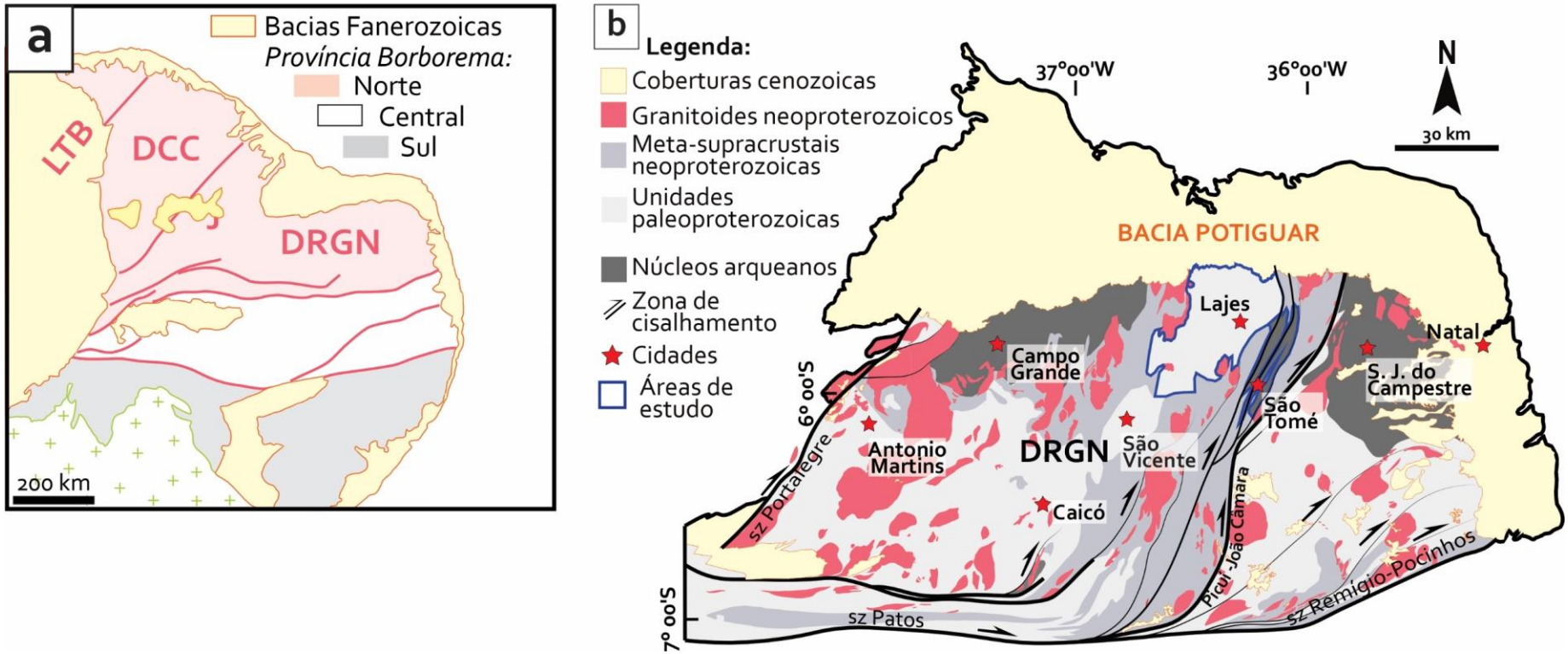



**Figura 2 -** Mapas geológicos e relações litológico-estruturais. a) Localização do Domínio Rio Grande do Norte (DRGN) no contexto do Gondwana Ocidental. b) Mapa esquemático simplificado do DRGN, destacando o tectonismo regional e o arcabouço geológico (modificado de JARDIM DE SÁ, 1994; MEDEIROS et al., 2017). As idades U–Pb em zircão do embasamento de cada bloco são apresentadas na figura (ANGELIM, 2006 e referências ali citadas; SOUZA et al., 2007; COSTA et al., 2018). DCC – Domínio Ceará Central; LTB – Lineamento transbrasiliano.

Intrusões máficas e ultramáficas, datadas em 2,19 ± 0,10 Ga (U–Pb em zircão) e alojadas nos ortognaisses e migmatitos do Complexo Caicó, complementam as unidades de embasamento da área. Toda essa configuração litológica é caracterizada por feições estruturais sutis e retilíneas, com orientação NNE–SSW, compatíveis com zonas de cisalhamento dextrais de grande escala da Orogenia Brasiliana. Elas apresentam mergulhos entre 55° e 80° para oeste ou leste (FERREIRA et al., 2019). Essas rochas foram intrudidas por granitos neoproterozoicos (Souza et al., 2016) e, posteriormente, cortadas por diques basálticos mesozoicos E–W do enxame de diques Rio Ceará-Mirim (Ar/Ar: 145–110 Ma; platô de 132,2 ± 1 Ma; Souza et al., 2003). O evento mais recente é o vulcanismo de Macau (24,06 ± 0,8 Ma; Ar/Ar), representado pelo Pico do Cabugi, a SE da área.

## 1.3 Objetivos

Independentemente do período geológico, inferências petrogenéticas e projeções evolutivas requerem a obtenção de dados petrográficos, mineralógicos, geoquímicos e isotópicos robustos, coerentes e devidamente concatenados. Dessa forma, este projeto tem como objetivo central a compreensão do regime geodinâmico e das assinaturas geoquímicas do Complexo Máfico-Ultramáfico do Bonfim e da Sequência Santa Luzia, bem como a inserção de ambos no contexto pré-cambriano global. Dessa forma, o estudo propõe-se a contribuir para:

a. Aprofundamento do conhecimento acerca dos processos geradores de crosta oceânica durante o Arqueano e o Proterozoico;
b. Ampliação da compreensão da dinâmica mantélica, de sua evolução ao longo desses dois éons e de suas interações com a crosta;
c. Estudo do comportamento dos sistemas isotópicos U–Pb e Sm–Nd e das respostas petrográficas à superposição de eventos (ciclos) magmáticos, metassomáticos e deformacionais;
d. Reconstrução dos ambientes geodinâmicos em escala regional (Província Borborema).

# CAPÍTULO 2
# FUNDAMENTAÇÃO TEÓRICA

# 2 FUNDAMENTAÇÃO TEÓRICA

O principal desafio deste trabalho é caracterizar duas unidades rochosas complexas e distintas, utilizando-as como peças-chave para compreender o cenário pré-cambriano em escala global. Em conjunto, essas unidades registram uma história que se estende desde o Hadeano, marcado pela diferenciação mantélica inicial, até o início do Neoproterozoico. As principais características de cada período ou sistema associado são detalhadas a seguir, servindo como base para as discussões sobre os regimes tectônicos e as assinaturas geoquímicas de cada litotipo.

## 2.1 O manto inicial

O manto hadeano é descrito como um reservatório globalmente heterogêneo, no qual domínios empobrecidos em elementos incompatíveis, coexistem com reservatórios enriquecidos (*e.g.,* BENNET et al., 2007; DEBAILLE et al., 2013; MALTESE et al., 2022). Esse manto primitivo teria se desenvolvido logo após os primeiros 50 Ma de evolução planetária (Fig. 3) e sobrevivido localmente até ~3.6 Ga (BENNET et al., 2007), estando preservado em tipos crustais juvenis, como no sudoeste da Groelândia (RIZO et al., 2013). Já em outros contextos, esses domínios depletados apresentam evidências de mistura parcial com componentes mais enriquecidos (TOUBOUL et al., 2012; GARCIA et al., 2023). Tais membros teriam ocorrido como um manto complementar ou indiferenciado. Muitas vezes interpretado como uma espécie de reservatório oculto (MURPHY et al., 2010).

Partindo desse pressuposto, modelagens isotópicas de Caro et al. (2006) estimaram que o pico da heterogeneidade mantélica ocorreu entre 4,2 e 4,0 Ga, seguido por um rápido intervalo de mistura de aproximadamente 100 a 250 Ma. Todavia, com o avanço na compreensão do sistema de radioisótopos de curta duração $^{146}Sm–^{142}Nd$, reconhece-se que o manto paleoarqueano preservou heterogeneidades em larga escala, associadas a um período de intensificação da diferenciação magmática ocorrido várias centenas de milhões de anos após a cristalização do oceano de magma terrestre (Fig. 4; MALTESE et al., 2022; CARO et al., 2005). O modelo proposto por Debaille et al. (2013), por exemplo,

sugere que uma ampla re-homogeneização do manto terrestre teria ocorrido apenas cerca de 1,8 Ga após sua diferenciação inicial. Embora o manto arqueano fosse mais quente e vigorosamente convectivo, a ausência de um regime de tectônica do tipo *'mobile lid'* teria limitado a eficiência da mistura entre os diferentes reservatórios, sem impedir completamente sua interação. Nesse contexto, infere-se que os episódios de crescimento crustal durante o Hadeano e o início do Arqueano podem não ter sido suficientemente extensos para promover uma homogeneização mantélica generalizada em estágios mais precoces (MACGREGOR, 1951; LENARDIC, 2018; LIU et al., 2022).

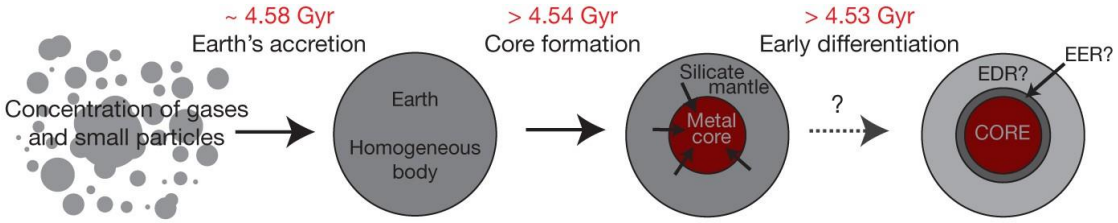



Figura 3 – Modelo esquemático mostrando a hipótese da Terra se formar por acreção de gases e partículas há aproximadamente 4,58 Ga. O núcleo metálico formou-se rapidamente (>4,54 Ga) e separou-se dos silicatos. A comparação com condritos sugere que a Terra evoluiu, desde o início da história do Sistema Solar (ou algumas poucas dezenas de milhões de anos depois), com uma alta razão Sm/Nd. Assim, o manto primitivo da Terra pode ter passado por uma diferenciação Sm/Nd há >4,53 Ga, levando à formação de um reservatório primitivo empobrecido (*Early Depleted Reservoir*–EDR) e de um reservatório enriquecido complementar (*Early Enriched Reservoir*–EER). Adaptado de Rizo et al. (2013).

Mas o aspecto central é que, no registro litológico, anomalias de $^{142}Nd$ são incomuns, e a maioria das rochas apresenta valores próximos de zero em relação ao manto moderno (CARO et al., 2005; BENNETT et al., 2007). De modo geral, rochas mais antigas tendem a registrar desvios mais pronunciados, enquanto amostras mais jovens convergem para valores próximos de zero, refletindo um manto progressivamente mais homogenizado. Esse padrão indica que, embora parte do manto tenha preservado heterogeneidades primordiais, a maior fração evoluiu para um estado isotopicamente homogêneo ao longo do tempo. Tal comportamento reflete a coexistência de domínios mantélicos que foram diferenciados e posteriormente homogenizados, enquanto outros preservaram assinaturas isotópicas de reservatórios antigos, sejam eles enriquecidos ou empobrecidos. Além das assinaturas isotópicas distintivas, a

ocorrência de rochas paleoarqueanas ricas em ferro (metaferropicritos e metaferrobasaltos) e enriquecidas em ETR também já está sendo utilizada como marcador de fontes primitivas enriquecidas (*cf.,* WANG et al., 2019). Isso porque a fusão parcial de um peridotito típico, por si só, não é suficiente para explicar os elevados teores de ferro observados nessas litologias ao longo de um intervalo temporal prolongado (GIBSON, 2000, 2002; WANG et al., 2019).

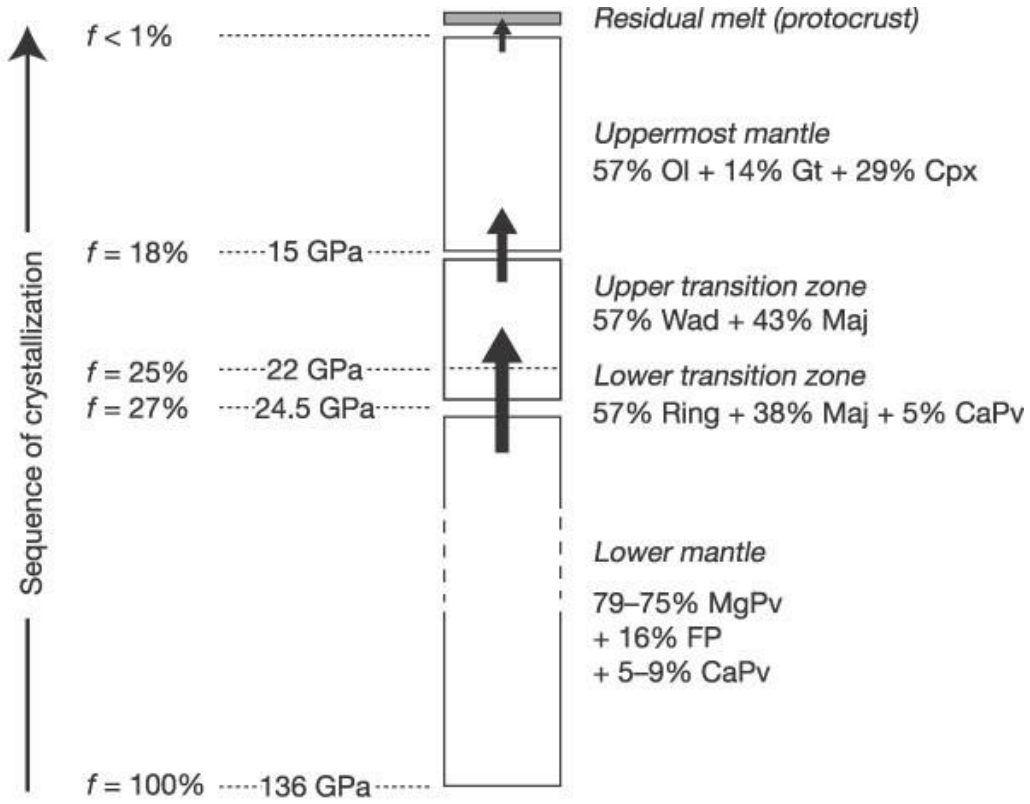



Figura 4 – Modelo de diferenciação terrestre a partir da cristalização de um oceano de magma. Espera-se que a cristalização do oceano de magma tenha se iniciado sob pressões do manto inferior e progredido para níveis mais rasos à medida que a temperatura diminuía. Conforme a cristalização avançava, o fundido residual era expelido para profundidades progressivamente menores, até que uma pequena fração de fundido se segregasse do mush cristalino, formando uma protocrosta na superfície da Terra. As proporções de fases correspondem a composição do manto primitivo, e os intervalos de pressão refletem as pressões das transições de fase ao longo do solidus do manto. f representa a fração em massa (wt.%) de fundido residual. Ol, olivina; Wad, wadsleyita; Ring, ringwoodita; Gt, granada; Cpx, clinopiroxênio; Maj, granada majorítica; CaPv, perovskita de cálcio; MgPv, perovskita de magnésio; FP, ferropericlásio. Os coeficientes de partição cristal/fundido para Sm, Nd, Lu e Hf são considerados desprezíveis em olivina, wadsleyita, ringwoodita e ferropericlásio. Fonte: Caro et al., (2005).

Uma vez reconhecida a presença de reservatórios enriquecidos e depletados, o foco passa a recair sobre sua possível interdependência. Nem sempre são observáveis rochas *in situ* com ambas as assinaturas preservadas. Pelo contrário, poucos sítios geológicos ao redor do mundo dispõem desse nível de conservação (O'NEIL et al., 2012). Uma hipótese menos provável seria a de um único reservatório mantélico empobrecido diferenciado precocemente no Hadeano-Arqueano (BOYET E CARLSON, 2005; CARO et al., 2006). Outra tese baseia-se na ideia de diferentes taxas de re-homogenização e preservação limitada ou preferencial, em um contexto de múltiplos reservatórios mantélicos (BENNET et al., 2007). Tanto os reservatórios quanto a sua diferenciação teriam se desencadeado a partir da extração diferencial e episódica da crosta inicial (WASILEWSKI et al., 2022) ou seriam o resultado da diferenciação de silicatos durante a cristalização do oceano de magma (CARO et al., 2006; BENNETT et al., 2007; RIZO et al., 2011; MORINO et al., 2017). Em síntese, além de apresentar porções pouco diferenciadas, o manto primitivo pode ser descrito como um sistema composto por domínios depletados e enriquecidos, mesmo que esses estejam associados a regimes de misturas restritos.

## 2.2 Éon Arqueano

No grego antigo, a palavra arqueano deriva do termo *ἀρχαῖος* (*arkhaîos*), que, em tradução literal, significa "antigo", "primitivo" ou "originário" e foi usado inicialmente pelo geólogo americano J. D. Dana em 1872. No contexto das Ciências da Terra, o vocábulo é empregado para designar o intervalo compreendido entre os éons Hadeano (4556 a 4000 Ma) e Proterozoico (2500 a 538,8 ± 0,2 Ma; COHEN et al., 2013). Enquanto o Hadeano registra as primeiras acreções terrestres e a diferenciação interna do planeta (núcleo, manto e crosta primitiva), o Proterozoico documenta a transição de uma atmosfera anóxica para oxidante, além de importantes episódios de acréscimo e estabilização crustal. Entre ambos, o Arqueano corresponde ao intervalo que sustentou e preparou o cenário para todas essas transformações. Cronoestratigraficamente, é subdividido em quatro eras distintas: Eoarqueano (4000 a 3600 Ma), Paleoarqueano (3600 a 3200 Ma), Mesoarqueano (3200 a 2800 Ma) e Neoarqueano (2800 a 2500 Ma; COHEN et al., 2013). Estudar cada um desses

momentos implica esbarrar no problema do registro rochoso preservado, que é escasso (especialmente para idades > 3,6 Ga), ambíguo e complexo.

Estudos estimam que, ao final do Éon Arqueano, mais de 75% da crosta continental já havia se formado a partir da extração de material mantélico e da subsequente diferenciação de grandes volumes crustais (CONDIE, 1994; BELOUSOVA et al., 2010; CAWOOD et al., 2013). Essas porções de crosta arquena estão preservadas em todos os continentes (Fig. 5). O gnaisse Acasta, no Canadá, por exemplo, apresenta idades até 4.03 Ga, sendo reconhecido como a rocha continental mais antiga já datada (BOWRING et al. 1990; BOWRING E HOUSH, 1995). Na Groenlândia, o *Greenland Shield* abriga não apenas alguns dos fragmentos mais antigos da crosta continental, mas também um dos registros arqueanos mais completos e bem preservados conhecidos. Suas idades se estendem aproximadamente de 3,8 a 2,6 Ga (MOORBATH et al., 1973; ASHWAL, 1993; POLAT et al., 2010).

Litologicamente, fragmentos arqueanos são formados por terrenos gnáissico-graníticos, de coloração acizentada e elevados graus metamórficos, *greenstone belts* de graus metamórficos mais baixos e granitoides tardios (CONDIE, 1981; HEILIMO et al., 2010, 2011; LAURENT et al., 2014). Os gnaisse-graníticos, também denominados de TTGs (tonalito-trondhjemito-granodioritos) perfazem mais de 80% da crosta arqueana (JAHN et al., 1981; MARTIN E MOYEN, 2002; MARTIN E PITIN, 2011). São rochas ricas em sílica, com altos níveis de $Al_2O_3$ e $Na_2O$, e baixas razões de $K_2O/Na_2O$ (MOYEN, 2011; LAURENT et al., 2014). Apresentam granulação grossa, com bandamento bem desenvolvido, caracterizado pela alternância de camadas quartzo-feldspáticas e feixas ricas em biotita e anfibólio. Os *greenstone*, por sua vez, representam de 5 a 10% da totalidade crustal arqueana preservada (MARTIN E PITIN, 2011). São formados por metabasaltos, rochas ultramáficas, félsicas subordinadas e sedimentares diversas (KING et al., 1998; HENDERSON et al., 2000).

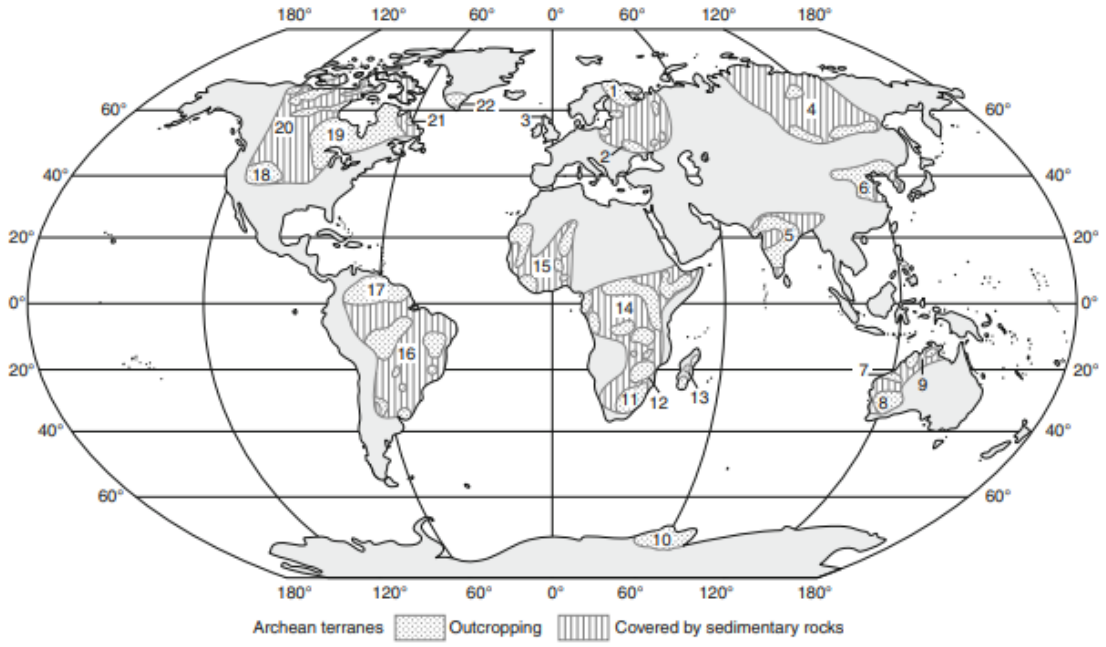



Figura 5 - Distribuição geográfica das províncias arqueanas. (1) Escudo Báltico, (2) Escudo Ucraniano, (3) Escudo Escocês, (4) Escudo Siberiano, (5) Cráton Indiano, (6) Cráton Sino-Coreano, (7) Cráton de Pilbara, (8) Cráton de Yilgarn, (9) Cráton do Norte da Austrália, (10) Complexo de Napier, (11) Cráton de Kaapvaal, (12) Cráton do Zimbábue, (13) Cráton de Madagascar, (14) Cráton da África Central, (15) Cráton da África Ocidental, (16) Crátons de São Francisco e Amazônico, (17) Escudo das Guianas, (18) Província de Wyoming, (19) Província Superior, (20) Província dos Escravos, (21) Escudo do Labrador e (22) Escudo da Groenlândia. As áreas pontilhadas representam terrenos arqueanos expostos, enquanto as áreas listradas indicam regiões subjacentes a rochas arqueanas. Fonte: Condie, 1994.

Destaca-se também a ocorrência de komatiitos, lavas ultramáficas ricas em MgO (>18%), cuja formação é geralmente atribuída às elevadas temperaturas do manto no Arqueano (JAHN et al., 1982; TOFT E PUCHTEL, 2010). São pouco frequentes no registro geológico pós-arqueano. Tanto o embasamento TTG quanto os greenstone belts foram posteriormente intrudidos por granitoides ricos em magnésio ou sanukitoides (HEILIMO et al., 2010, 2011). Esses granitos calco-alcalinos são enriquecidos em feldspato potássico e magnésio, podendo se originar da fusão de peridotitos mantélicos previamente modificados pela assimilação de material TTG (HALLA, 2005; LOBACH-ZHUCHENKO et al., 2008; HEILIMO et al., 2010).

Diferentemente do regime tectônico moderno, os motores geotectônicos do Arqueano se desenvolveram sob condições térmicas mais elevadas (HERZBERG et al., 2012; KELLER E SCHOENE, 2012). É provável que essas

altas temperaturas tenham condicionado estilos tectônicos híbridos ou transicionais. Sabe-se hoje que as placas tectônicas operam induzidas por forças horizontais que provocam empurrões durante processos orogenéticos. Certos autores reconhecem padrões semelhantes na maioria dos terrenos arqueanos, indicando que um conjunto de mecanismos análogos já atuava há pelo menos 4.0 Ga (HARRISON, 2009, 2020; TURNER et al., 2020; WINDLEY et al., 2021). Entretanto, alguns desses domínios também exibem grandes evidências de deformações proponderantemente verticais, gerando estruturas de domo e bacias (ROBIN E BAILEY, 2009; THÉBAUD E REY, 2013; FRANÇOIS et al., 2014). Nesse caso, a gravidade atua como a principal força impulsionadora, em um processo conhecido como sagducção.

Um modelo conciliatório se baseia na tese de proto-placas móveis, onde a deformação e a compressão eram mais intensas, coexistindo com uma litosférica estática, com mínima deformação. Enquanto a primeira podia se mover lateralmente, a outra teria permanecido estagnada (CAPITANIO et al., 2019). Todavia, mesmo que a tectônica de placas no Arqueano fosse diferente da atual, seu registro é evidenciado por dorsais oceânicas, falhas transformantes e fossas de subducção. Embora nem sempre facilmente reconhecíveis, fragmentos de litosfera oceânica incorporados durante a subducção e preservados como ofiolitos constituem evidências consistentes de processos tectônicos em terrenos arqueanos.

### *2.2.1 Ofiolitos arqueanos*

Ofiolitos são remanescentes da litosfera oceânica preservada que, sob circunstâncias geodinâmicas particulares, foram obduzidos sobre o continente (COLEMAN, 1971). Essas associações rochosas podem estar relacionadas a diversos ambientes geotectônicos, como: centros de expansão oceânica, bacias de retroarco, antearcos, arcos, plumas mantélicas, dentre outras configurações magmáticas extensionais (KUSKY, 2004). Quando bem caracterizados, tornam-se importantes veículos para a compreensão da estrutura, petrologia e geoquímica de domínios oceânicos desaparecidos. No Arqueano, essas unidades ajudam a reconstruir a litotectônica primitiva e frequentemente

constituem as únicas evidências disponíveis para estudar a antiga litosfera oceânica (*e.g.,* FURNES et al., 2007).

Seções ofiolíticas clássicas (*Penrose-type;* ANONYMOUS, 1972) são compostas, da base para o topo, por: tectonitos ultramáficos, seguidos de cumulatos ultramáficos e máficos, gabros maciços, enxames de diques máficos, *pillow* lavas e sedimentos pelágicos. Sob tudo isso, são descritos grandes sistemas de falhas delimitando o contato com as litologias subjacentes. No registro Arqueano, poucos ou quase nenhum remanescente ofiolítico conserva esse tipo de estratigrafia em sua totalidade. Ao contrário, geralmente se observam apenas porções parciais, desmembradas ou metamorfizadas, muitas vezes preservadas em antigos *greenstone belts*. De acordo com Kusky (2004) e Furnes e Dilek (2022), os basaltos são os principais componentes de ofiolitos arqueanos, muitas vezes descritos como *pillow* lavas não vesiculares expelidos em águas profundasEsses basaltos derivam de fusão parcial do manto superior, refletindo heterogeneidades preservadas no manto primitivo, incluindo domínios depletados. Depois desses, os mais abundantes são os komatiitos e basaltos komatiíticos de alto-Mg, seguidos por vulcanismo félsico, gabros, peridotitos e enxames de diques.

Comparados aos ofiolitos Paleoproterozoicos ou Fanerozoicos, os arqueanos apresentam teores de $TiO_2$ e $Al_2O_3$ ligeiramente menores e MgO, Cr e Ni maiores (FURNES E DILEK, 2022). Tecnicamente, são mais frequentemente ligados a contextos de subducção do que os ofiolitos mais jovens (Fig. 6). Ainda assim, em muitos casos, observa-se um caráter híbrido ou misto. Estudos indicam que peridotitos de dorsais meso-oceânicas (*MOR-type*) podem ser significativamente modificados ao entrar em uma zona de subducção (PEARCE et al., 1984; HODEL, 2017). Nesse cenário, a fusão parcial de peridotitos residuais ao longo de dorsais depletadas empobrece o manto, que posteriormente é refertilizado durante a subducção, dando origem a magmas boniníticos e andesíticos típicos de ambientes de subducção (ULRICH et al., 2010; UYSAL et al., 2015). Tais processos sustentam a diferenciação entre ofiolitos associados a MOR e aqueles formados em ambientes subductivos (DILEK E FURNES, 2011).

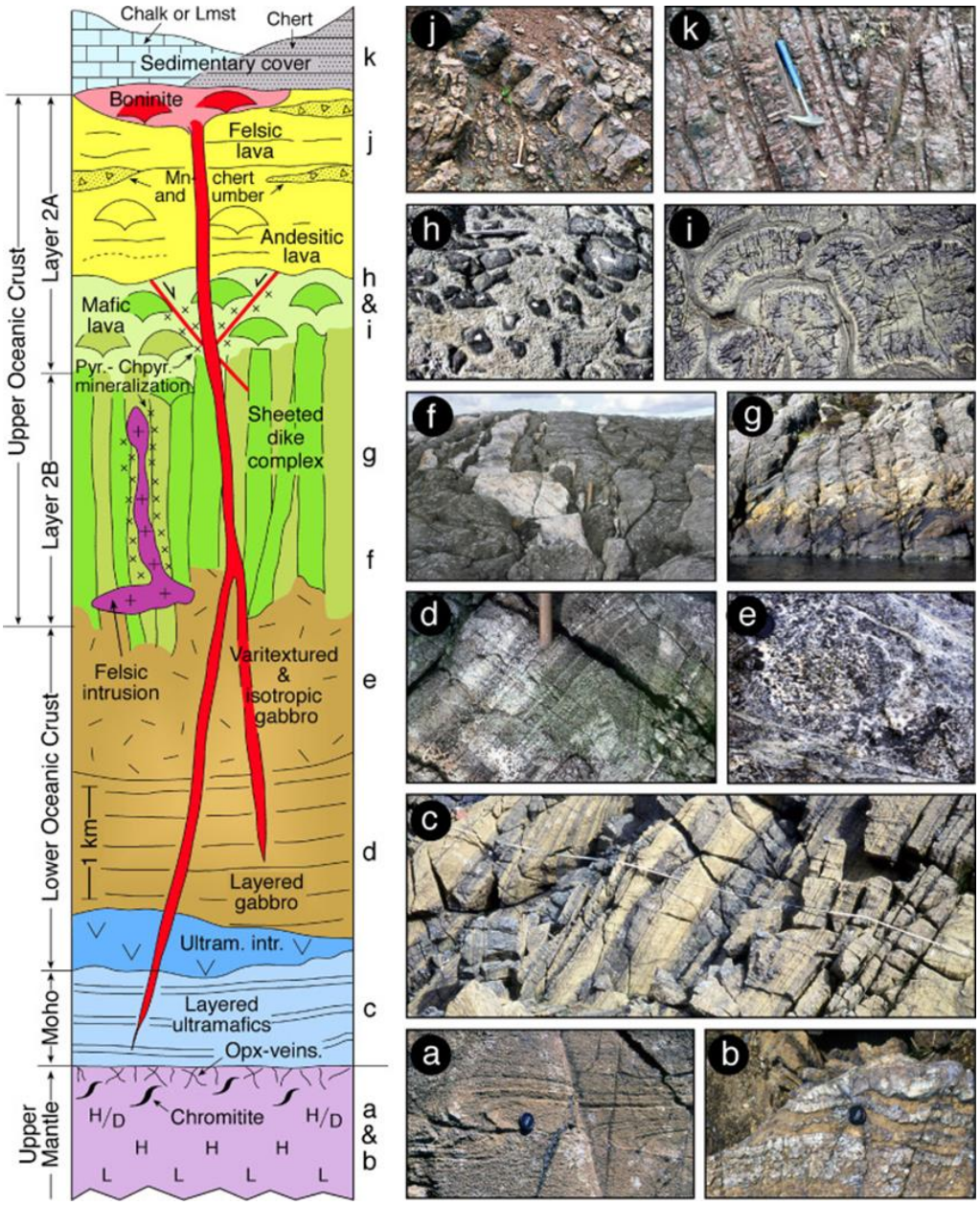



Figura 6 - Seção colunar mostrando os componentes do manto superior e da crosta de um ofiolito típico de zona de suprassubducção, ilustrados por fotografias de campo. (a) e (b): Harzburgito bandado e dobrado (olivina + ortopiroxênio); (c): Cumulatos acamadados de dunito e wehrlito (olivina + clinopiroxênio); (d): Gabro acamadado e dobrado; (e): Gabro de textura variada; (f): Gabro cortado por intrusões basálticas e félsicas; (g): Enxame de diques; (h): Brecha vulcânica inserida; (i): Pillow lava; (j): Fluxo de lava andesítica maciça; (k): Camadas de chert dobradas. Fotografias: (a–c, i) Ofiolito de Leka (Noruega); (d) Ofiolito de Karmøy (Noruega); (e–h) Ofiolito de Solund–Stavfjord (Noruega); (j, k) Ofiolito de Mirdita (Albânia). Legenda das abreviações: Chpyr – calcopirita; H/D – harzburgito/dunito; H – harzburgito; L – lherzolito; Opx-veins – veios de ortopiroxenito; Pyr – pirita. Fonte: Furnes e Dilek (2022).

## 2.3 Transição Neoarqueano–Sideriano e o estabelecimento do 'estilo tectônico moderno'

Estudos indicam um rápido aumento na taxa de retrabalhamento crustal por volta de ~3 Ga (KRAMERS E TOLSTIKHIN, 1997; DHUIME et al., 2012), acompanhado de intensificação do magmatismo juvenil, frequentemente associado a períodos de formação de supercontinentes. No Arqueano, quando as massas continentais se tornaram grandes o suficiente, elas foram soldadas entre si, formando os primeiros protocontinentes ou supercratons (*Kenorland* ou múltiplos supercratons; WILLIAMS et al., 1991; BLEEKER, 2003; LAURENT et al., 2014). Isso ocorreu aproximadamente entre 2,7 e 2,5 Ga (BLEEKER, 2003; SMITHIES et al., 2007; PERCIVAL et al., 2012; CAWOOD et al., 2018, FRIEND E NUTMAN, 2019). Paralelamente, o desenvolvimento de cinturões colisionais e a diferenciação interna são marcados pela transição de magmatismos TTG para a produção de grandes quantidades de granitos ricos em K e/ou peraluminosos (LAURENT et al., 2014; CAWOOD et al., 2018).

Segundo Laurent et al. (2014), esse plutonismo potássico e peraluminoso pode ser entendido como o último evento arqueano reconhecido nos crátons em escala global. Isso ocorre porque essas rochas são compatíveis com ambientes colisionais semelhantes aos tectônicos modernos e pouco preservados em unidades com idades superiores a 3,0 Ga (SMITHIES, 2000; LAURENT et al., 2014). Por um lado, as assinaturas geoquímicas dos pulsos tardios de TTGs indicam ambientes dominantemente subductivos, incluindo a presença de sanukitóides. Do outro, a evolução de TTGs para plutonismos potássicos e peraluminosos anuncia o início dos ciclos de subducção-colisão (Ciclo de Wilson) em escala planetária. Desse modo estabelece-se um 'estilo tectônico moderno' (LAURENT et al., 2014; BROWN et al., 2020).

Possivelmente, essa mudança na geodinâmica da Terra não aconteceu de forma sincrônica em todos os cratons (HICKMAN, 2004; SMITHIES et al., 2005, 2007; VAN KRANENDONK et al., 2010), e o seu intervalo exato ainda não está definido. No entanto, até meados do Arqueano, o cenário não era propício para que ela ocorresse. Primeiro, não é incorreto afirmar que nada disso teria acontecido se não tivesse sido desencadeado pelo resfriamento mantélico

(HERZBERG et al., 2012; KELLER E SCHOENE, 2012). As altas temperaturas do manto arqueano (~1500 °C, HERZBERG et al., 2012; KELLER E SCHOENE, 2012) teriam elevado significativamente suas taxas de fusão parcial. O resultado foi uma crosta primitiva extremamente espessa (~13-23 km de espessura; VAN THIENEN et al., 2004), mais flutuante e menos acoplada ao manto convectivo subjacente (MOYEN E VAN HUNEN, 2012). Fato que provavelmente resultou em subducções menos eficazes e de menor escala (O'NEILL et al., 2007b; MOYEN E VAN HUNEN, 2012; LAURENT et al., 2014). Outros parâmetros, como a reologia e a composição crustal, bem como o volume líquido do material continental, também teriam influenciado o estabelecimento de uma configuração moderna de placas (LAURENT et al., 2014; CAWOOD et al., 2018; BROWN et al., 2020). Não basta considerar apenas o volume: a crosta precisa ainda ser capaz de espessar e manter esse espessamento por um intervalo razoavelmente longo, para que os mecanismos de reciclagem possam se iniciar e se desenvolver (LAURENT et al., 2014).

Uma vez plenamente estabelecido, o Ciclo de Wilson, que inicialmente agregou os espessos fragmentos da crosta arqueana em protocontinentes, continua seu trabalho. Todavia, de forma totalmente oposta. Após a aglutinação, as massas continentais foram novamente dispersas (BLEEKER, 2003; PEHRSSON et al., 2013). Aparentemente, essa ruptura é evidenciada apenas por enxames de diques máficos associados a plumas (BLEEKER E ERNST, 2006; ERNST et al., 2013) e grandes deslocamentos horizontais suportados pela abundância de margens passivas, entre 2,2 e 1,8 Ga (BRADLEY, 2008). Isso ocorre porque o início do éon Proterozoico está associado ao maior *gap* de evidências no registro geológico já documentado (CONDIE et al., 2009; 2022).

## 2.4 Calmaria tectono-magmática

Há cerca de três décadas, Condie (1998) lançou luz sobre a possível episodicidade no registro geológico global. O autor compilou dados isotópicos de U-Pb em grãos de zircão e conseguiu relacionar os máximos na distribuição desses valores aos períodos de formação dos supercontinentes (2,7, 1,9 e 1,2 Ga, aproximadamente). Paralelamente, os intervalos entre uma aglutinação continental e outra estariam ligados a significativos decréscimos nas taxas de

crescimento crustal. O maior desses mínimos foi documento logo após o início do Paleoproterozoico (CONDIE, 1998; CONDIE et al., 2009; SPENCER et al., 2018). Inicialmente, como um intervalo de ~ 250 Ma, entre ~2.45 a 2.2 Ga (CONDIE et al., 2009; CONDIE E O'NELL, 2010). Mais tarde, novos estudos refinaram esse recorte ao espaço de tempo de ~2365 a 2235 Ma (Fig. 7; SPENCER et al., 2018; CONDIE et al., 2022).

A aparente lacuna de evidências foi tão significativa que essa época ficou conhecida como *Siderian Quiet Interval* (CONDIE et al., 2009; PEHRSSON et al., 2014), sendo mais tarde denominada Calmaria tectono-magmática (*Tectono-Magmatic-Lull*-TML; SPENCER et al., 2018; CONDIE et al., 2022). A princípio, o TML foi descrito como evento global, durante o qual a atividade orogênica e a produção magmática em todo o planeta teriam permanecido estagnadas (Fig. 8). Isso como resposta a um suposto *shutdown* tectônico (CONDIE et al., 2009; CONDIE E O'NELL, 2010) ou, pelo menos, desacelerado significativamente (*slowdown,* SPENCER et al., 2018; CONDIE et al., 2022).

Em essência, a hipótese de um *shutdown* atrela modelos teóricos de tectônica episódica (*e.g.,* O'NELL et al., 2007) a dados globais sobre magmatismo e metamorfismo, sugerindo uma quiescência prolongada nas placas tectônicas (CONDIE et al., 2009; CONDIE E O'NELL, 2010). Na realidade, O'Neill et al. (2007) correlacionaram dados paleomagnéticos e excursões positivas na velocidade de deslocamento das placas tectônicas aos picos de maior produção crustal. Eles utilizaram um sistema de subducção ininterrupta e inversões mantélicas para postular que a litosfera pré-cambriana pode não só ter aumentado sua rapidez, como também, ter permanecido estática em determinados momentos. Isso caracterizaria um estilo 'pré-moderno', antes das placas começarem a atuar de forma vigorosa e incessante (O'NELL et al., 2007). Mais tarde, essa teoria foi aplicada à compreensão do TML (CONDIE et al., 2009; CONDIE E O'NELL, 2010), na qual maior produção crustal implica em maior velocidade de deslocamento das placas tectônicas, enquanto menor produção crustal sugere um possível *shutdown* tectônico.

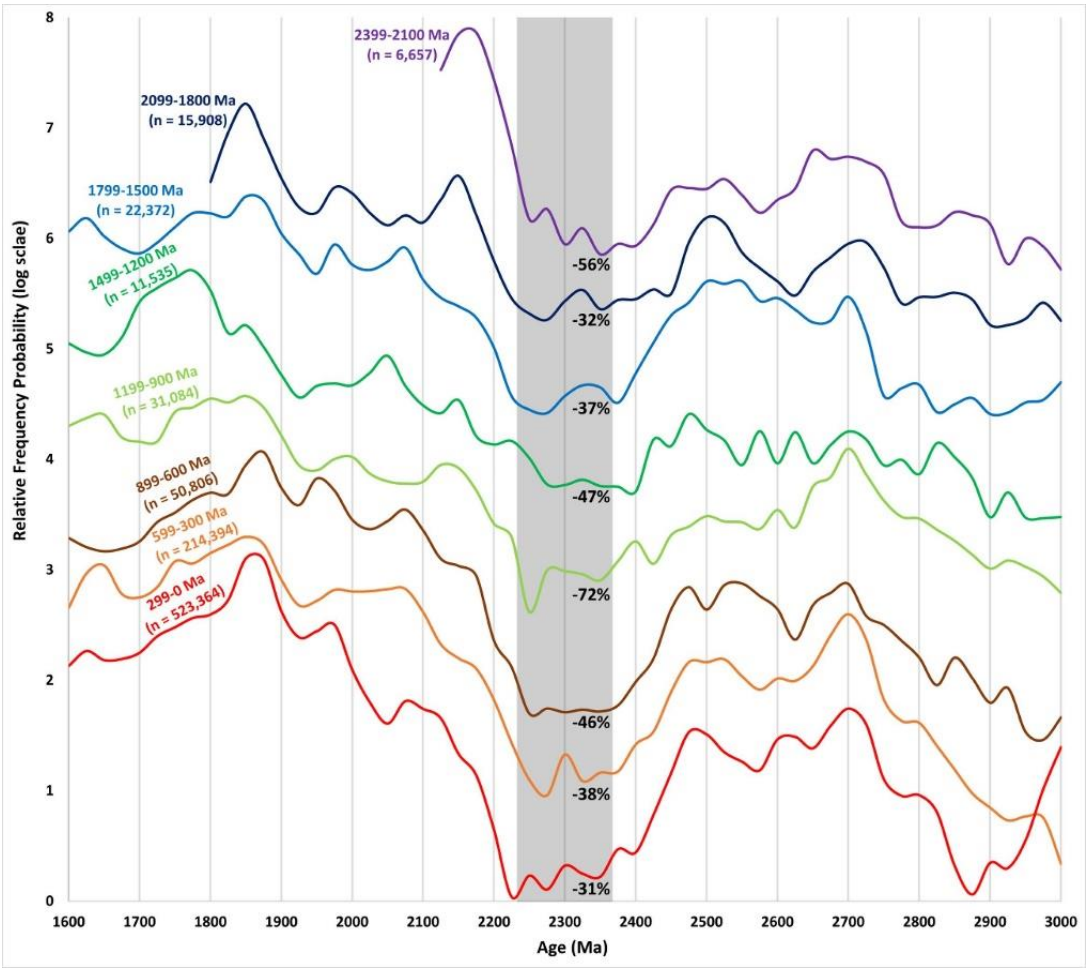



Figura 7 - Distribuições globais de idade de zircão detrítico plotadas em janelas de idade deposicional de 300 milhões de anos. As probabilidades são para caixas de 25 Ma e incluem apenas idades superiores à idade máxima de deposição para cada grupo. As porcentagens são diminuições médias na probabilidade de frequência de 2.700 Ma a 2.350 Ma. TML, Calmaria Tectono-Magmática; n, número de idades do zircão. Fonte: Condie et al., 2022.

Dada a escassez de dados paleomagnéticos siderianos, a ideia de um desligamento tectônico total enfrentou sérios entraves para ser aceita. Principalmente, entre os defensores de produção crustal progressiva, linear e contínua ao longo de todo o tempo geológico (PEHRSSON et al., 2014; PARTIN et al., 2014; YANG E SANTOSH, 2015). Para esse grupo, a atenuação do registro geotectônico poderia resultar da destruição litosférica por subducção, reciclagem e retrabalhamento metamórfico, além de vieses na amostragem de dados geocronológicos (PARTIN et al., 2014; YANG E SANTOSH, 2015). Ou ainda, ser o resultado de estágio de orogenias periféricas posterior à montagem dos primeiros super-crátons (PEHRSSON et al., 2014).

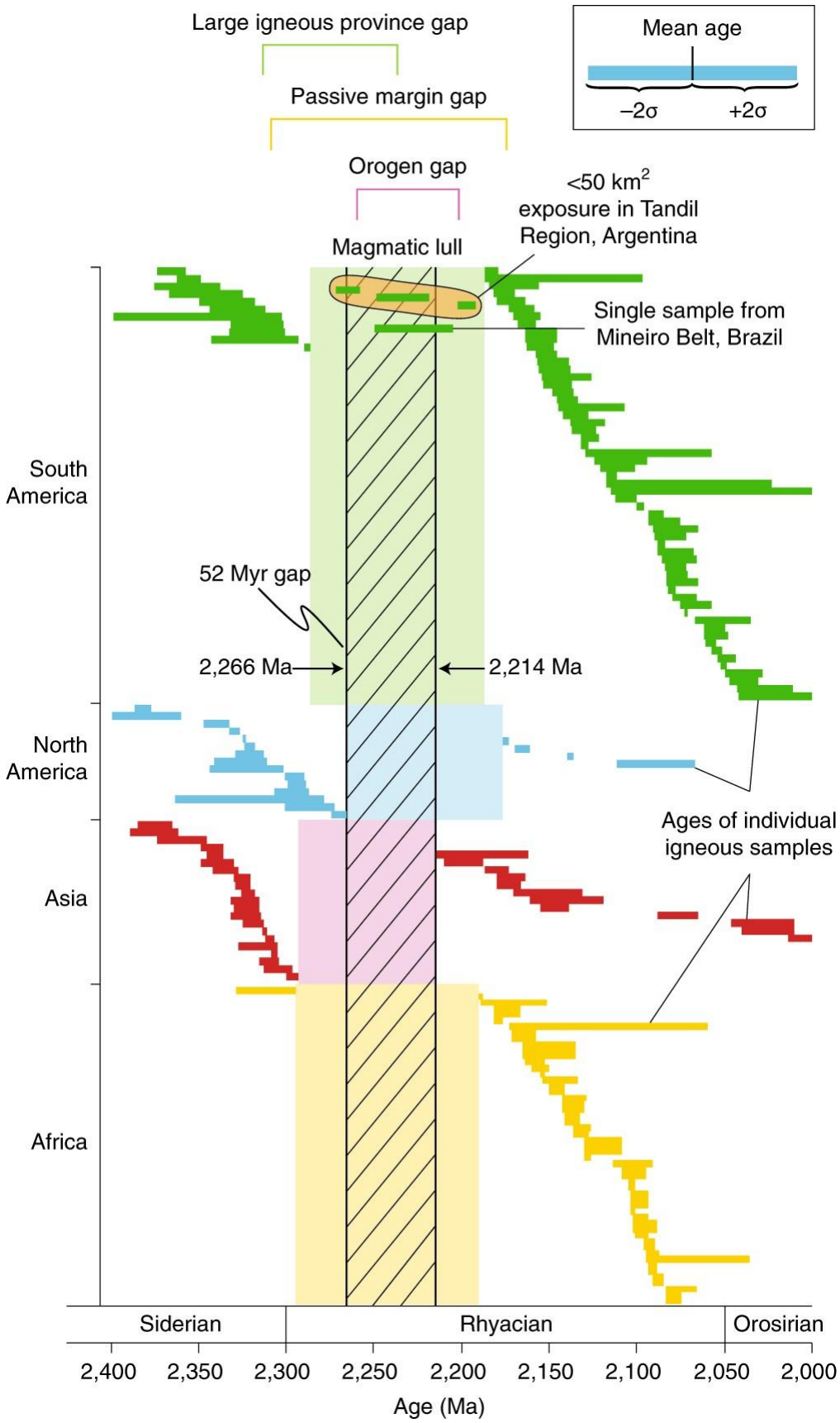



Figura 8 - Distribuição temporal das rochas magmáticas no início do Paleoproterozoico, discriminada por continente. *Fonte:* Spencer et al., 2018.

Todas essas suposições se baseiam no fato de que segmentos de rochas datadas do início do Paleoproterozoico, embora quantitativamente pouco expressivos, podem ser encontrados em todos os continentes (Fig. 9). No modelo alternativo de Pehrsson et al. (2014), os regimes subductivos não teriam cessado completamente, mas sim permanecido restritos às margens periféricas dos grandes aglomerados de massas. De forma clara, após a formação dos primeiros supercontinentes ou supercrátons, o interior cratônico pode ter permanecido relativamente estável, mas isso não impediu que o magmatismo de arco se concentrasse em suas bordas externas (PEHRSSON et al., 2014).

No entanto, estudos mais recentes apoiam a tese de uma desaceleração tectônica (SPENCER et al., 2018; CONDIE et al., 2022). Ocorre que os intervalos anterior e posterior ao TML são caracterizados por velocidades de deriva continentais bimodais, descritas como semelhantes ao observado para o campo de velocidades das placas tectônicas atuais (SPENCER et al., 2018). Em contraste, as velocidades de deriva durante o estágio de calmaria tectono-magmática são unimodais e relativamente mais lentas, algo similar às regiões de *lowtrench-effective plates* (FORSYTH E UYEDA, 1975; SPENCER et al., 2018). Atrelados a isso, os dados paleomagnéticos são consistentes com um distúrbio tectônico e indicam que o TML envolveu também o desacoplamento temporário entre as placas continentais e as placas oceânicas de movimento mais rápido (SPENCER et al., 2018).

Nesse esquema, a subducção ocorreria de forma continental planar (amagmática) ou via arcos oceânicos externos, mais difíceis de serem preservados, mas cessado genuinamente o magmatismo de arcos continentais (SPENCER et al., 2018). A ideia de um regime de subducção generalizada em 2,7 Ga endossa essa argumentação (CONDIE et al., 2022). Nesse período, as placas subduzidas teriam alcançado o limite núcleo-manto, diminuindo as taxas de convecção mantélica, de modo que a velocidade de consumo da litosfera oceânica passou a ser maior que a de sua produção. Esse fato levou a desaceleração da velocidade das placas durante o TML, com consequente diminuição na produção de magma, geração de pluma e atividade orogênica (CONDIE et al., 2022).

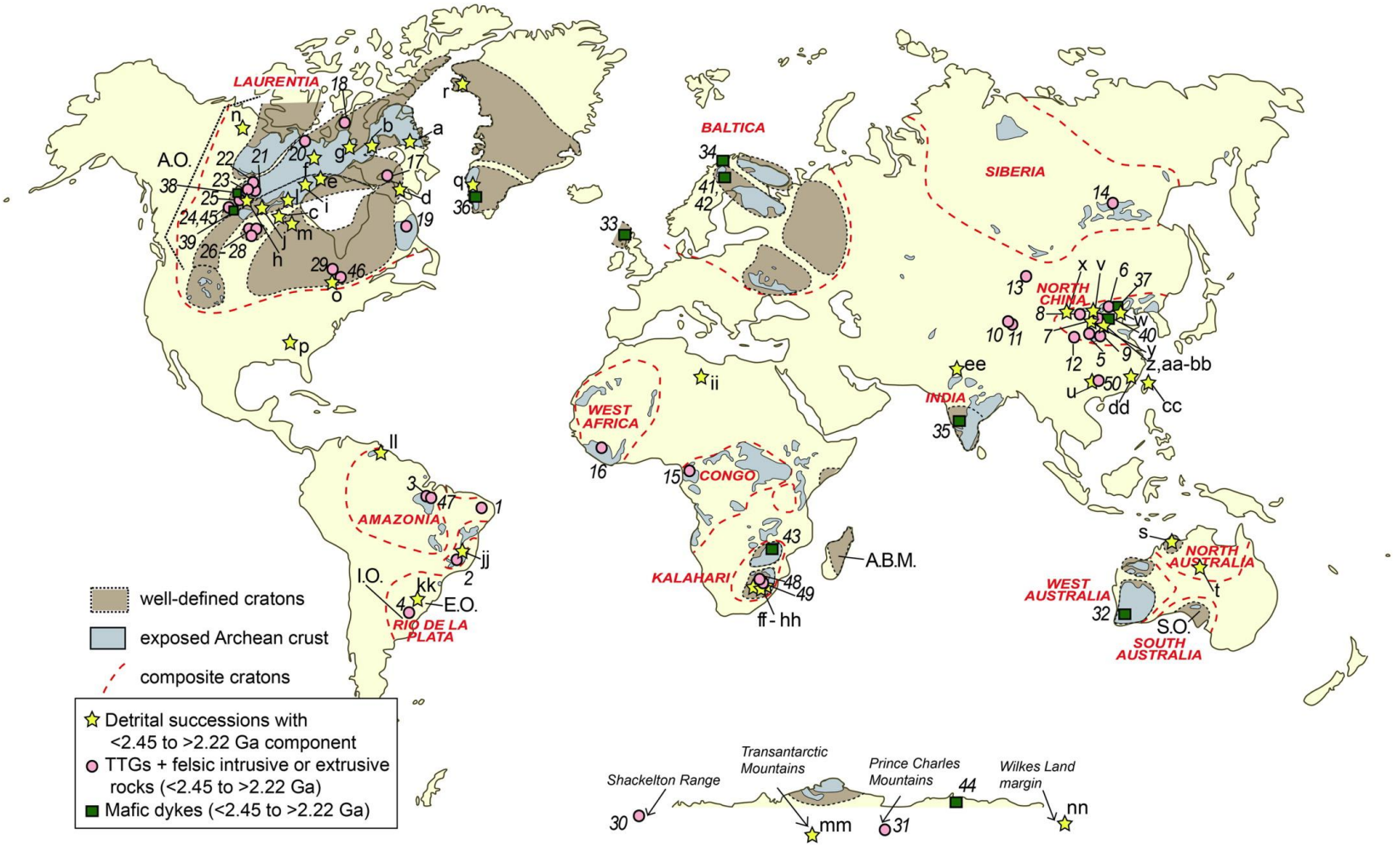



Figura 9 - Compilação de idades magmáticas para o intervalo de tempo <2,45 a >2,22 Ga. Círculos e quadrados numerados representam rochas ígneas (TTGs, rochas intrusivas félsicas e máficas e rochas extrusivas félsicas), enquanto estrelas identificadas por letras indicam sucessões sedimentares contendo zircões detríticos dessa idade. Fonte e detalhes da legenda: Partin et al. (2014).

## 2.5 Registro Paleoproterozoico

Como mencionado anteriormente, durante o TML, observam-se decréscimos significativos na frequência de idades U-Pb de grãos de zircão em todo o mundo. (CONDIE, 1998; CONDIE et al., 2009, 2022; CONDIE E O'NEILL, 2010). Esses vales na distribuição não refletem apenas descontinuidades no magmatismo continental, mas também se estendem à atividade orogênica e aos índices de metamorfismo. Contudo, não se observa correlação significativa entre o TML e a produção de crosta continental juvenil, conforme indicado por idades modelo $T_{DM}^{c}Hf$ (PEHRSSON et al., 2014).

### *2.5.1 Produção crustal juvenil e orógenos acrescionários*

Quando se analisam os mínimos e máximos na distribuição dos grãos de zircão, é quase impossível diferenciar se os picos são realmente um reflexo de maior adição crustal ou representam apenas períodos de máxima preservação (PARTIN et al., 2014). Embora os altos valores sejam diretamente proporcionais a maiores adições de crosta juvenil, o mais natural é esperar que essa geração crustal esteja relacionada a períodos de assembleias continentais ou a eventos orogenéticos (PERHSSON et al., 2014). Atualmente, ~85% da produção crustal juvenil está associada a sistemas convergentes, enquanto só 15% é adicionada em ambientes de rifts, *hotspots* ou rifts ao longo de margens continentais (STERN E SCHOLL, 2010). Se a ideia de *shutdown* (CONDIE et al., 2009) estivesse mesmo correta, qualquer vestígio de subducção durante o início do Proterozoico seria insustentável, incluindo adições crustais ou retrabalhamento em sistemas orogênicos. Contudo, se a tese de uma desaceleração tectônica (SPENCER et al., 2018) for verdadeira, a subducção não deixou de existir, mas ficou restrita a ambientes externos e arcos de ilhas. Isso não impede a adição de material jovem, mas também não corrobora a existência de retrabalhamento em orógenos continentais.

Segundo Cawood et al. (2009), o modelo clássico de orógenos está intimamente relacionado à dinâmica do Ciclo de Wilson. Nesse contexto, a convergência continental e o término da subducção em orógenos colisionais são geralmente precedidos por uma fase acrescionária associada à subducção. Em

contraste, em orógenos intracontinentais, a deformação e o magmatismo são dominados pelo retrabalhamento crustal e pela reativação de estruturas pré-existentes (DEWEY et al., 1986). Nesse sentido, estudos indicam que, durante o TML, a distribuição de valores de $\varepsilon_{Hf}$ em grãos de zircão (entre +5 e −20) apresenta um espalhamento que se estende a valores mais positivos do que aqueles descritos para o supercontinente Columbia (PEHRSSON et al., 2014). Assim, a diminuição observada na abundância de grãos de zircão não se reflete em dados globais de $\varepsilon_{Hf}$. A proporção relativamente elevada de componentes juvenis durante o TML pode estar relacionada a processos de rifteamento associados à fragmentação do primeiro supercontinente. Nesse caso, a escassez de registros pode resultar da baixa abundância de zircão em rochas máficas e/ou refletir a reciclagem preferencial da crosta juvenil (BELOUSOVA et al., 2010).

No Brasil, os principais exemplos incluem: granitoides juvenis do tipo TTG de ~2,35 Ga, relacionados a ambientes de arco acrescionário nas margens do Cráton do São Francisco (SEIXAS et al., 2012); pulsos juvenis discretos (εNd positivo) de ~2,36–2,29 Ga na Província Borborema (SANTOS et al., 2009); e greenstones e TTGs de ~2,34 Ga ligados a arcos de ilhas no domínio Bacajá, Cráton Amazônico (VASQUEZ et al., 2008; MACAMBIRA et al., 2009).

### *2.5.2 Magmatismo máfico associado a arcos de ilhas*

A atividade magmática associada a arcos em ambientes acrescionários é a principal responsável pela adição de material juvenil à crosta (STERN E SCHOLL, 2010). Isso não exclui a incorporação de material jovem via processos intraplaca, mas também não abarca todo o registro magmático máfico do início do Paleoproteroizoco. Embora as LIPS (*Large Igneous Provinces*) sejam as principais representantes do período, exemplos no leste da Índia já têm comprovado a existência de litotipos típicos de ambientes subductivos (MANIKYAMBA et al., 2015). A composição química de magmas de zonas de subducção é uma ferramenta-chave para compreender os processos subductivos, a ciclagem elementar e a variabilidade química controlada por pulsos tectônicos (SINGH et al., 2017).

Isso acontece porque durante o progresso da subducção, desde seu início até sua consequente maturação, a cunha mantélica é quimicamente modificada/enriquecida pelo influxo de fluidos hidratados (VAN KEKEN et al., 2011; MULLEN E MCCULLUM, 2014). Esses fluidos são o produto da desidratação da crosta oceânica descendente. Eles atuam em conjunto com *input* de sedimentos subductados, auxiliando a transferência de diferentes elementos da placa para a cunha mantélica, desencadeando fusão parcial e metassomatismo. Além de gerarem distintos pulsos de magmatismo em regimes de antearco, arco e retroarco.

BADRs (basaltos-andesitos-dacitos-riolitos) toleíticos a cálcio-alcalinos, lavas alcalinas, boninitos, LOTI (*Low-Ti Basalts*), picritos, adakitos, HMA (*High-Mg Andesites*) e NEB (Nb *Enriched Basalts*) são os principais exemplos associados a arcos insulares (POLAT E KERRICH, 2006). Os seis últimos são interpretados como produtos da subducção de litosfera oceânica jovem e quente, pertencendo ao grupo das *hot subduction volcanic rocks* (POLAT E KERRICH, 2006). Nuances e associações entre alguns desses (*e.g.,* boninitos e adakitos-HMA-NEBs) são encontrados desde o Arqueano até o Fanerozoico. No início do Paleoproterozoico, rochas como essa são descritas no Cráton Singhbhum, no leste da Índia (~2,25 Ga; SINGH et al., 2017).

### *2.5.3 Metamorfismo*

O TML também se reflete de forma significativa no registro metamórfico global. Apenas duas ocorrências bem caracterizadas são reconhecidas para o intervalo (BROWN E JOHNSON, 2019; HOLDER et al., 2019; BROWN et al., 2022; CONDIE et al., 2022). A primeira delas é localizada na Península de Boothia do Sul (~700°C e 5-6 kbar; rochas metassedimentares), a norte do Cráton Rae. A segunda está situada no lago McCann (~800 °C e 7 kbar), em rochas metassedimentares e ortognaisses ao sul do Cráton Rae, no Canadá (BERMAN et al., 2013). Conforme Holder et al. (2019), até pouco antes do TML, os vetores de pressão (P) e temperatura (T) costumavam expressar razões termobarométricas (T/P) elevadas e padrão quase gaussiano de distribuição. Estatisticamente, o que se observa é uma certa bimodalidade no caráter do metamorfismo a partir do Neoarqueano. Regimes semelhantes aos modernos já

se manifestavam gradualmente, tornando-se mais bem definidos no Paleoproterozoico (HOLDER et al., 2019; BROWN et al., 2020). Isso se deve ao fato de que no Riaciano os índices T e P decaem de forma significativa (BROWN E JOHNSON, 2019; HOLDER et al., 2019).

Condie et al. (2022) indicam que os primeiros eventos metamórficos de baixa T/P ocorrem em ~2150–2130 Ma, documentados na África Ocidental (domínio Bole-Bulenga, Gana; BLOCK et al., 2015; região de Fada N'Gourma, Burkina Faso; GANNE et al., 2012; área de Tidjenouine, Argélia; BENDAOUD et al., 2008) e no Cráton Rio de la Plata (sudeste do cinturão de Tandilia, Argentina; MARTINEZ et al., 2017) após o TML. Como o arranjo termobarométrico global reflete a evolução secular da tectônica terrestre, o surgimento do metamorfismo de baixa T/P provavelmente resultou de uma leve transição nas condições térmicas do manto (BROWN E JOHNSON, 2019; HOLDER et al., 2019) e da evolução dos estilos de subducção e orogêneses colisionais.

# CAPÍTULO 3
# METODOLOGIAS

# 3 AQUISIÇÃO DE DADOS

A definição de setores representativos para a reconstituição da geodinâmica pré-cambriana e a interpretação das assinaturas litogeoquímicas nas porções leste e centro-norte do DRGN baseou-se na literatura previamente publicada sobre as áreas de Bonfim e Lajes. O Núcleo Arqueano de Bonfim é considerado o fragmento rochoso mais antigo da Plataforma Sul-Americana, cuja diferenciação mantélica teria ocorrido no éon Hadeano (SANTOS et al., 2020; GARCIA et al., 2024). No Bloco Lajes, a Sequência Santa Luzia é interpretada como um raro e bem preservado remanescente crustal de idade Sideriana (DANTAS et al., 2005; NEGRÃO et al., 2008; COSTA et al., 2022). Apesar de estarem separadas por apenas 32 km, essas rochas registram mais de dois bilhões de anos de história geológica. Por representarem períodos tectônicos críticos, sua compreensão também possui relevância global.

No que concerne aos dados adquiridos *in situ,* quatro atividades de campo foram realizadas entre janeiro de 2022 e janeiro de 2025. Descrições petrográficas e medições estruturais foram integradas em dois mapas geológicos distintos, com escalas 1:100.000. Foram também consultados os trabalhos de Salim (1979), Carvalho et al. (1980), Dantas et al. (2005), Negrão et al. (2008) e a folha geológica Lajes SB. 24-X-D-VI (COSTA e DANTAS, 2018), cujas informações foram agregadas aos mapas. Na região de Bonfim, visitaram-se 32 afloramentos, dos quais 17 foram amostrados (Fig. 10). Na região de Lajes, a coleta concentrou-se no setor NW do bloco, especificamente nas unidades siderianas que compõem a Sequência Santa Luzia. Os pontos amostrados estão expressos na Fig. 11. A coleta de amostras abrangeu os diferentes tipos litológicos aflorantes, buscando representar de forma sistemática a geologia de cada setor. As principais técnicas abordadas estão pormenorizadas em seguida.

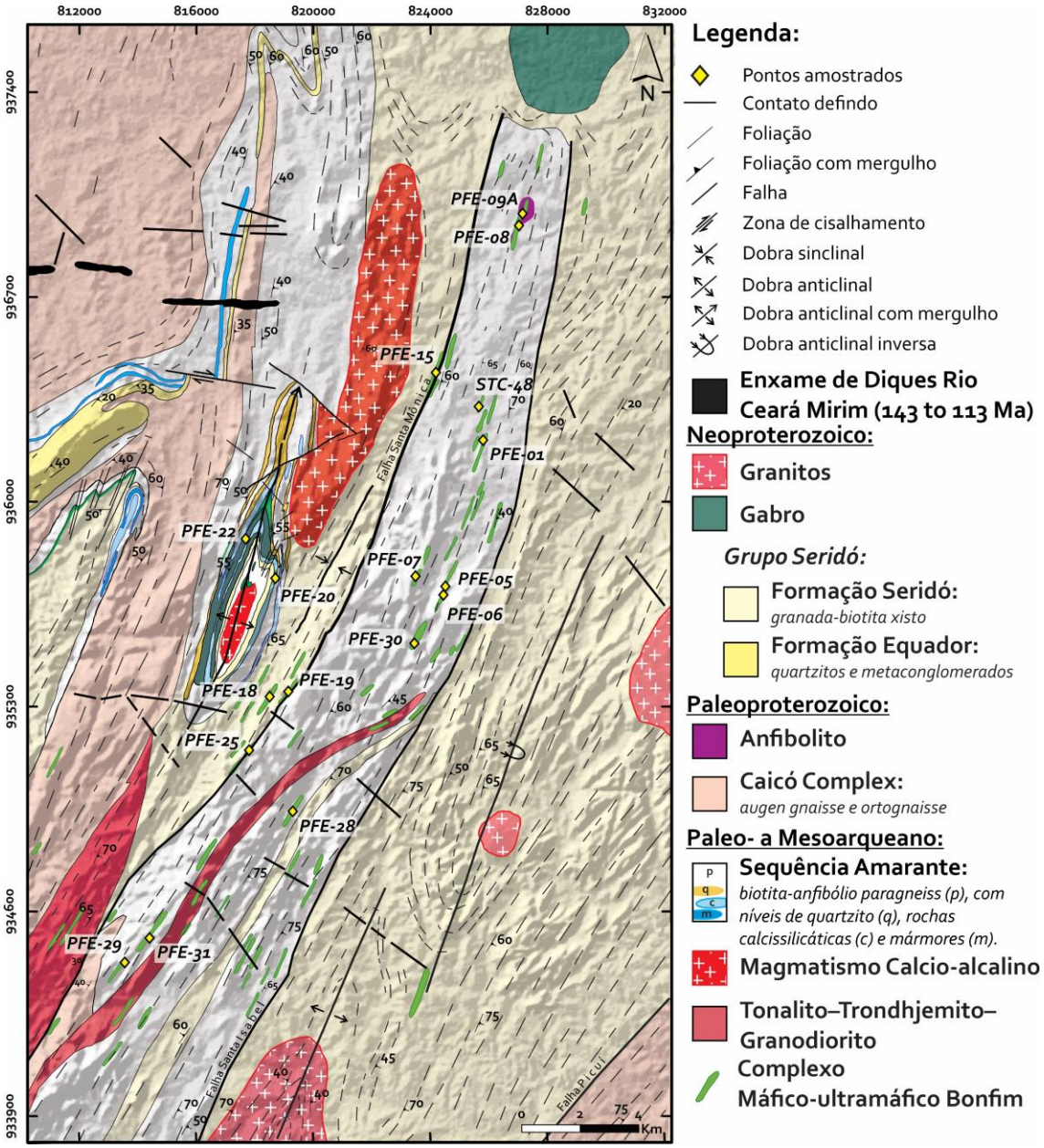



Figura 10 – Mapa geológico do Núcleo Arqueano Bonfim com a localização dos pontos amostrados.

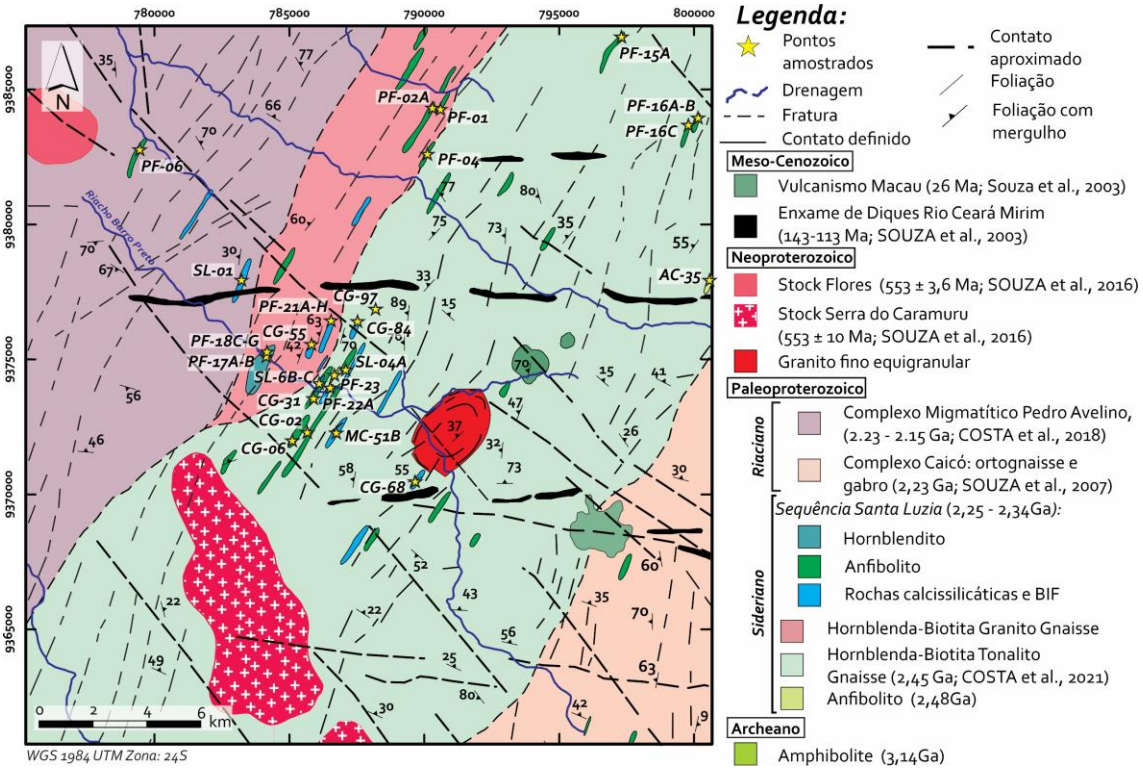



Figura 11 – Mapa geológico da Sequência Santa Luzia com a localização dos pontos amostrados.

## 3.1 Análise geoquímica em rocha total

Dados geoquímicos, incluindo elementos maiores, menores e traços, em rocha total de amostras representativas das principais variedades máficas e ultramáficas das regiões de Lajes e Bonfim, foram obtidos no laboratório *Acme Analytical Laboratories Limited*, em Vancouver, Canadá. As amostras foram previamente preparadas no Laboratório de Estudos Geodinâmicos, Geocronológicos e Ambientais (LEGGA) da Universidade de Brasília. Nesse laboratório, seguiram-se as etapas usuais de fragmentação com auxílio de ferramentas de impacto (marreta ou martelo), britagem em britador primário de mandíbulas de aço e moagem em moinho de panela Herzog (ciclos de 5 minutos, ou até que as rochas atingissem granulometria inferior a 200 mesh).

As concentrações de óxidos de elementos maiores foram determinadas pela técnica de espectrometria de fluorescência de raios X em discos de fusão. Os discos foram preparados por meio da fusão da mistura de subamostras de 0,2 g e fundente de metaborato/tetraborato de lítio. A perda percentual ao fogo (*loss on ignition*–LOI) foi calculada pela diferença de peso após o aquecimento

da amostra a 1000 °C por aproximadamente 150 minutos. Os valores obtidos na perda ao fogo são descontados no cálculo final dos óxidos. A precisão analítica foi monitorada utilizando os padrões OREAS 24b, SY-4, SY-5, OREAS 146 e NCSDC71301.

Já as abundâncias de elementos menores e traços e a quantificação de metais base e preciosos foram estimadas pela técnica de ICP-MS (*Inductively Coupled Plasma Mass Spectrometry*). No caso dos elementos menores e traços, subamostras de 0,5 g foram submetidas à digestão de $HNO_3$ e HF concentrados em micro-ondas e, posteriormente, rediluídas em $HNO_3$ diluído (2% v/v) antes da análise. No caso dos elementos metálicos, subamostras de 0,5 g foram submetidas à digestão em água régia (75% HCl + 25% $HNO_3$ concentrados) antes da análise. A precisão analítica foi monitorada utilizando os padrões geológicos STD SO-18, STD SO-19, OREAS 24b, SY-4, SY-5, OREAS 460 e OREAS 146. As análises do branco produziram valores abaixo dos limites de detecção.

## 3.2 Análises isotópicas de Nd em rocha total

Após a pulverização (*cf.* tópico 3.1), as análises isotópicas de Sm–Nd em rocha total foram processadas no LEGGA, seguindo as técnicas analíticas descritas por Gioia e Pimentel (2000). Inicialmente, foram pesados cerca de 50–100 mg de cada amostra, aos quais foram adicionados entre 20–40 µL de spike O spike é uma solução enriquecida nos isópotos de $^{149}Sm$ (97.58%) e de $^{150}Nd$ (97.80%; WASSERBURG et al. 1981; GIOIA E PIMENTEL; 2000). Em seguida, as amostras foram submetidas a uma nova etapa de digestão com $HNO_3$ e HF destilados e HCl 6N. Duas colunas de teflon para separação cromatográfica iônica foram empregadas nas etapas de separação isotópica. Na primeira, de troca iônica, foram separados os elementos terras raras (ETR). Já a segunda coluna é carregada com pó de politetrafluoretileno (PTFE), impregnado com ácido fosfórico di-(2-etilexil) (HDEHP) e resina catiônica comercial LN-Spec, destinada à separação específica dos íons Sm e Nd. A eluição das amostras em ambas as colunas foi realizada com $HNO_3$ 6N. As frações de Sm e Nd obtidas foram depositadas em filamentos de evaporação de rênio, e as análises foram processadas em um espectrômetro de massas TIMS (*Thermal Ionization Mass*

*Spectrometry*) TRITON multicoletor, operando em modo estático. Os resultados indicam incertezas para Sm/Nd e para as razões $^{143}Nd/^{144}Nd$ melhores que 0.1% (erro padrão de 2σ) e 0.0015% (1σ), respectivamente, consistentes com análises repetidas do padrão internacional de rocha BHVO-1 (Basalt Hawaiian-USGS; Nd=24.83 ppm and Sm=6.2 ppm; GLADNEY E ROELANDTS, 1987). A constante de decaimento utilizada foi $\lambda = 6.54 \times 10^{-12}$, com normalização para $^{146}Nd/^{144}Nd = 0.7219$. Os valores das razões $^{143}Nd/^{144}Nd$ foram estimados utilizando o modelo de DePaolo (1981).

### 3.3 Datação U-Pb em zircão por LA-ICP-MS

A separação dos grãos de zircão foi realizada por meio de metodologias gravimétricas, com o bateamento das amostras para a concentração das fases minerais mais pesadas, e de métodos magnéticos, utilizando o Separador Magnético Isodinâmico de Frantz, para a exclusão de minerais ferromagnéticos. Em seguida, os cristais de zircão foram selecionados manualmente com o auxílio de um microscópio binocular e embutidos em resina epóxi. Uma vez completamente seca, a resina é polida até que as formas minerais se tornem aparentes. Após, os grãos são metalizados, e imagens de catodoluminescência (CL) e de elétrons secundários (SE) são obtidas com o auxílio do Microscópio Eletrônico de Varredura (MEV).

As massas isotópicas foram medidas utilizando um espectrômetro de massas com plasma indutivamente acoplado Thermo Finnigan Element XR de alta resolução com coletor único e setor magnético, acoplado a um sistema de ablação a laser de excímero Iridia (*Argon Fluoride*–ArF) de 193 nm do LEGGA. O sistema a laser está equipado com uma câmara de cobalto de duplo volume. O espectrômetro de massas foi ajustado para melhorar a sensibilidade ao U e ao Pb, minimizando a produção de óxidos antes de cada sessão analítica. Cada aquisição consistiu em 10 s de medição de *background* seguidos por 20 s de ablação. As massas de $^{202}Hg$, $^{204}Pb$, $^{206\text{-}208}Pb$, $^{232}Th$ e $^{238}U$ foram medidas e estimadas utilizando o modo de detecção tripla (MEV + Faraday) por meio da varredura do setor eletrostático em cada massa. Cada varredura durou 82 ms, resultando em mais de 800 varreduras para ablação. Os parâmetros do laser

incluíram um tamanho de spot de 25 µm, frequência de 20 Hz e fluência de 2.0 J/cm².

Os dados brutos foram processados utilizando o *Iolite 4.0* (PATON et al., 2011) para análise do sinal com resolução temporal, e a inspeção individual dos sinais foi realizada utilizando o *VizualAge* (PETRUS E KAMBER, 2012). A correção dos dados incluiu a subtração do branco, a correção LIEF usando um modelo exponencial mais linear e a normalização pelo grão de zircão GJ-1 (JACKSON et al., 2004). Os grãos de zircão Plešovice (SLÁMA et al., 2008) e 91.500 (WIEDENBECK et al., 2007) foram utilizados para o controle de qualidade. A variância excessiva no calibrador primário foi propagada para cada ponto analítico. Uma incerteza sistemática de aproximadamente 1% foi propagada em cada idade final. A correção de chumbo comum não foi aplicada. As idades são apresentadas com dois sigma (2σ).

# CAPÍTULO 4
# ARTIGO I

# 4 REMNANTS OF THE EARLY EARTH: PRESERVED PALEO- TO MESOARCHEAN OCEANIC CRUST IN SOUTH AMERICA

Paula F. T. Alvim[1], Elton L. Dantas[1], Reinhardt A. Fuck[1]
[1]Instituto de Geociências, Universidade de Brasília, Brasília - DF, Brazil.

## ABSTRACT

Ophiolites are remnants of ancient oceanic crust formed by mantle–crust interaction, and Archean examples are typically fragmented, reflecting a heterogeneous, superheated mantle and early proto-tectonic dynamics. The Bonfim mafic–ultramafic complex is a basement high in the central-eastern Rio Grande do Norte Domain, Borborema Province, northeastern Brazil. Petrographically, it is composed of serpentinites, clinopyroxenites, amphibolites, tremolites, chloritites, anthophyllite chloritites, talc schists, and Fe-Ti oxide layers. The region hosts the oldest rocks of the South American Platform, derived from enriched Hadean mantle sources. Here, our data confirm Paleoarchean rocks derived from enriched mantle sources at ~3.53 ± 0.28 Ga (U–Pb zircon), as well as older fragments at ~3.57 ± 0.62 Ga (U–Pb zircon) that resemble a depleted MORB-type mantle source. Additionally, three samples yield Mesoarchean U–Pb zircon ages (3.13 ± 30 Ga, 3.10 ± 0.15 Ga, and 3.09 ± 0.34 Ga), interpreted as recording a second mafic–ultramafic pulse with a subduction component well expressed through island arc tholeiitic basalts. Sm-Nd isochron ages for the episodes indicate linear regressions of 4.20 ± 0.382 Ga and 3.61 ± 0.316 Ga, confirming that differentiation had been occurring since the Hadean eon. These two episodes may represent a dismembered ophiolitic sequence, possibly formed in an oceanic mid-ocean ridge setting. Its repetition in time and space attests to the cyclical nature of magmatism.

**Keywords:** ophiolites, mafic and ultramafic intrusions, depleted mantle, enriched mantle.

# 1 INTRODUCTION

Theories of mantle chemistry and isotopic composition suggest that this primordial reservoir already exhibited heterogeneities in the Hadean eon (Bennet et al., 2007; Debaille et al., 2013; Maltese et al., 2022). These heterogeneities reflect the coexistence of chemically enriched and depleted sources, now recorded in some of the oldest Archean cratonic rocks (e.g., Roth et al., 2013; Liou et al., 2024). The progressive mechanisms and mantle dynamics involved in the evolution of these systems remain poorly understood. However, most models attribute these complexities to the tectonic regime operating at that time. In other words, they would be a reflection of a relatively stable maturation of the Earth after the magma ocean (Caro et al., 2005; Corgne et al. 2005), or the extraction of large volumes of crust followed by rapid recycling and crustal rejuvenation (Harrison et al., 2005, 2008; Kemp et al., 2010).

Chemically, this differentiation is expressed by the extraction of incompatible-trace-element–enriched residues, leaving a convective mantle depleted in these elements (Caro et al., 2003; Debaille et al., 2013). Early depleted reservoirs have been identified in amphibolites from the western portion of the Isua Supracrustal Belt (ISB, southwestern Greenland; Rizo et al., 2011), as well as in mafic and ultramafic rocks in the Saglek Block region (northern Labrador, Canada; Morino et al., 2017), and more recently in Mesoarchean amphibolites from the Eastern Hebei region of the North China Craton (Liou et al., 2024). Instead, enriched counterparts have been found in mantle amphibolites from the Ancient Gneissic Complex (Swaziland), in ancient metavolcanic units of the Barberton greenstone belt (South Africa), in 3.4 Ga old amphibolites from the São José do Campestre Massif, and in Eo- to Paleoarchean ultramafic intrusions from the Bonfim region, both in the Borborema Province (BP; Schneider et al., 2018; Garcia et al., 2023, 2024).

The Bonfim Archean core is a basement high located in the central–eastern Rio Grande do Norte Domain, BP, NE Brazil. The lithologic association comprises metaplutonic and volcanosedimentary rocks (including banded iron formations, biotite–amphibole paragneiss, calc-silicate rocks, marbles, and quartzites), as well as mafic and ultramafic intrusions. The intrusions, the focus

of this study, occur as fragmented bodies extending for more than 35 km along the regional SW–NE trend. To the south of the study area, Velásquez Ruiz et al. (2019) identified a correlated ultramafic body dominantly composed of olivine websterites and clinopyroxenites, which host massive to stratiform Fe–Ti oxide (ilmenite–magnetite) lenses. Beyond oxides, gold, scheelite, and bismuth have also been commercially mined in the region. U–Pb zircon ages ranging from 3.74 ± 12 to 3.50 ± 5 Ga (Santos et al., 2020) establish these rocks as the oldest known segment of the South American Platform and a unique archive of early crust–mantle differentiation processes.

In this last sense, the work of Garcia et al. (2024) was fundamental. This is because the authors can trace the isotopic signature of these intrusions and correlate them with previously enriched mantle reservoirs, as mentioned. However, links to a potentially depleted mantle component remain tentative and ill-defined. Here we present new U–Pb zircon ages, Sm–Nd isotopic data, and whole-rock geochemistry that provide revised geotectonic and petrogenetic constraints, including a new evolutionary sequence inferred from depleted mantle–related sources. Moreover, we document a previously unrecognized Mesoarchean mafic–ultramafic event in the study area. In general, these rocks are interpreted as pseudostratigraphic sections of an ancient, partially preserved, and cyclic ophiolite that is repeated in space and time.

## GEOLOGICAL BACKGROUND

The Borborema Province (Almeida et al., 1981) is a crustal domain formed during the Brasiliano/Pan-African orogeny. This province results from the convergence and subsequent collision of the São Luis-West Africa and São Francisco-Congo cratons within the context of West Gondwana amalgamation at *c.* 600 Ma (Fetter et al. 2003; Ganade de Araujo et al., 2014; Santos et al., 2015). Its pre-drift reconstruction reaches further south into the Brasília Belt and extends into West Africa via the Trans-Sahara Belt (Caby, 1989; Van Schmus et al., 2008). The current structural frame results from diachronic Neoproterozoic events involving tectonic collage along lithospheric or crustal-scale shear zones (Archanjo et al., 2008; Caxito et al., 2016; Oliveira and Medeiros, 2018). A

complex mosaic of independent domains or terrains is arranged along these large shear zones in a continent-wide montage. Borborema domains typically consist of Medio Coreaú, Ceará Central, Rio Grande do Norte, Central or Transversal, and Southern (Brito Neves et al., 2000; Van Schmus et al., 2011; Neves, 2015).

The Rio Grande do Norte Domain (RGND), the study's main focus, is in the northeastern Borborema Province (Fig. 1a). To the west, it is bordered by the NE-trending rectilinear Portalegre dextral strike-slip shear zone, while to the south, it is adjacent to the discontinuous Patos EW-trending shear zone (Brito Neves et al., 2000). RGND displays Neoproterozoic supracrustal sequences (Jardim de Sá, 1994; Van Schmus et al., 2003; Hollanda et al., 2015) over Paleoarchean (3.5 Ga) to Neoarchean (2.7 Ga) nuclei (Dantas et al., 2004; Arthaud et al., 2008) and Paleoproterozoic gneissic-migmatitic basements, with Brasiliano-age granitoids intrusions (Nascimento et al., 2015). The central eastern area features Siderian (2.4 to 2.3 Ga) supracrustal (Dantas et al., 2008; Alvim et al., 2026) units and Rhyacian (2.25 to 2.15 Ga) high-K calc-alkaline metamorphic rocks (Souza et al., 2007; Hollanda et al., 2011). In this section, the Archean cores include the São José do Campestre massif, along with trondhjemite to granitic gray gneisses dating from 3.5 to 2.7 Ga (Dantas et al., 2004; Ribeiro et al., 2024, and references therein), as well as the Bonfim nucleus (Santos et al., 2020).

## 2.1 Local geology

The Bonfim Archean fragment is a basement high, covering an area of approximately 4,600 km$^2$ and located in the central-eastern portion of the RGND (Fig. 1b), near the municipalities of Lajes and São Tomé – RN. It consists of a metaplutonic and volcano-sedimentary sequence, including banded iron formation, biotite–amphibole paragneiss, calc-silicate rocks, marbles, and quartzites. The frequent in situ association between metasedimentary rocks and intrusions initially suggested contemporaneity between the two in early lithostratigraphic reconstructions of the area (Ebert, 1969; Salim, 1979). These formations were all attributed to the Neoproterozoic Jucurutu Formation (Van Schmus et al., 2008, 2011). However, Carvalho (1990) later distinguished the

metasedimentary units from the basic magmatism, interpreting the metasedimentary succession as an Archean basal unit, which he informally designated as the Amarante Sequence. Here, the intrusions are redefined as the Bonfim Mafic–Ultramafic Complex, while the name Amarante Sequence is retained.

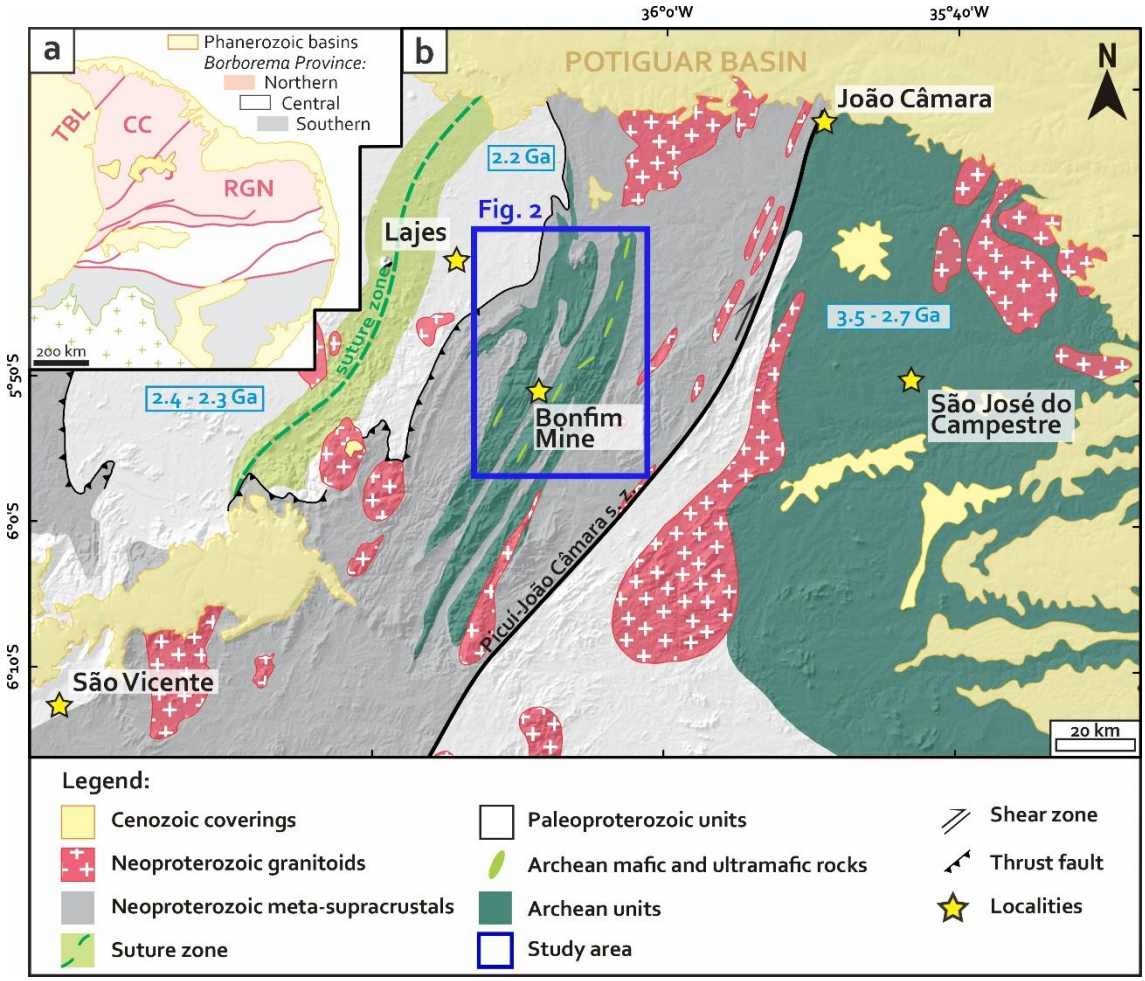



Figura 1 – a. Localization map of the Rio Grande do Norte Domain (RGND) in the Borborema Province context (Modified after Van Schmus et al., 2008, 2003). b. Schematic and simplified map of the eastern RGND, showing its regional tectonics and geological framework (modified from Jardim de Sá, 1994). TBL – Transbrasiliano Lineament Belt; CC – Ceará Central Domain.

The intrusions consist of fragmented rocks that range from 100 to 2000 meters in length and about 100 meters in width. They extend for more than 35 km, following a regional NNE-SSW trend. In total, at least 70 bodies have been described, which vary between pyroxenite, serpentinite, tremolitite, amphibole schists, talc schists, chloritites, and anthophyllite chloritite. They crop out in

association with the garnet-biotite schists of the Seridó Formation and the biotite-amphibole paragneisses of the Amarante Sequence, forming small mounds that contrast with the eroded morphology of the metasedimentary rocks. It is common to observe these intrusions associated with longitudinal faults or fault systems that run parallel to the main foliation. Two Archean magmatic pulses form the basement of the area: one is calc-alkaline, and the other consists of tonalite-trondhjemite-granodiorite (TTG).

Velásquez Ruiz et al. (2019) describe the protolith of the São Tomé layered intrusion as olivine websterites and clinopyroxenites, intercalated with ilmenite-magnetite lenses. It has undergone amphibolite-facies metamorphism, for which precise geochronological constraints are still lacking. However, U-Pb ages in zircon grains indicate complex ages ranging from 3.74 ± 0.12 to 3.50 ± 0.05 Ga (Velásquez Ruiz et al., 2019; Santos et al., 2020). This represents the oldest record of crust formation in South America. Furthermore, the intrusions maintain a relatively unaltered long-lived $^{147}Sm–^{143}Nd$ system, which, in conjunction with the short-lived $^{146}Sm–^{142}Nd$ system, provides a differentiation age of approximately 4.44 Ga and suggests an initially enriched Hadean mantle source (Garcia et al., 2024).

The Archean paragneisses of Amarante sequence constitute a laterally continuous, elongated lithostratigraphic unit approximately 4–6 km in width and exceeding 24 km in length. They occur interlayered with other metasedimentary units and are locally spatially associated with magmatic intrusions. Marbles form 15 to 20m layers in the Seridó schist. Medium- to coarse-grained quartzite appears as elongated white to light gray lenses in marble and schist up to 100m wide (Souza Neto et al., 2008), with minor calc-silicate rocks in association. This lithological framework is closely associated with NE-trending, kilometer-scale shear zones. The shear movement also relates to the folding of preexisting planar surfaces. The most prominent Bonfim structure is a 3-km-wide antiform, featuring a granite core (Souza Neto et al., 2008). High-angle faults show dominant sinistral movement and are associated with quartz veins, calcite, amphibole, and ore deposits (Fig. 2).

In the northwestern sector of study area, orthogneissic rocks crop out, including hornblende-bearing granodioritic gneisses of the Caicó Complex, which

yield U–Pb zircon ages between 2.23 and 2.11 Ga (Hackspacher et al., 1990; Jardim de Sá, 1994; Souza et al., 2007, 2016; Hollanda et al., 2011). The Seridó supracrustal sequence comprises, from base to top, quartzites of the Equador Formation, and mica schists of the Seridó Formation (Hollanda et al., 2015; Van Schmus et al., 2003). This sequence was deposited over the metaplutonic and migmatitic units of the Caicó Complex (Souza et al., 2007) and was subsequently metamorphosed under amphibolite facies conditions during the Brasiliano Orogeny. Numerous granitoids intruded these rocks between 630 and 520 Ma (Nascimento et al., 2015). In the NW sector, mafic dikes related to the Rio Ceará Mirim volcanism have been described, with Ar/Ar ages ranging from 145 to 110 Ma and a plateau age of 132.2 ± 1 Ma (Souza et al., 2003).

Four late hydrothermal events have been identified, which are responsible for the gold mineralization in quartz veins and tungsten-molybdenum (W–Mo) mineralization in skarns (Hollanda et al., 2017). The plateau ages determined by $^{40}Ar/^{39}Ar$ dating of phlogopite show values of 597 ± 5 Ma, 553 ± 4 Ma, and 517 ± 6 Ma (Velásquez Ruiz et al., 2019; Santiago et al., 2019). Additionally, Re-Os dating of molybdenite crystals estimates an age of 524 ± 2 Ma for another of these hydrothermal episodes (Hollanda et al., 2017). Souza Neto et al. (2008) and Mesquita et al. (2019) propose that there was at least one progressive phase associated with pressures ranging from 2.0 to 4.0 kbar and temperatures between 500 and 580°C, followed by a regressive stage with temperatures between 400 and 500°C. The age ranges indicate the emplacement of various local granites (Nascimento et al., 2015), which have a significant impact on the source of hydrothermal fluids. According to Domingos et al. (2020), certain granitic plutons, along with Neoproterozoic migmatitic rocks, are found as structural domes in the Seridó Belt. These features resulted from the partial melting of the middle to lower crust and were likely exhumed during the continental collisions that led to the amalgamation of Western Gondwana in the Ediacaran period.

The paragneisses constitute a laterally continuous, elongated lithostratigraphic unit approximately 4–6 km in width and exceeding 24 km in length. They occur interlayered with other metasedimentary units and are locally spatially associated with magmatic intrusions. Marbles form 15 to 20m layers in

the Seridó schist. Medium- to coarse-grained quartzite appears as elongated white to light gray lenses in marble and schist up to 100m wide (Souza Neto et al., 2008), with minor calc-silicate rocks in association. This lithological framework is closely associated with NE-trending, kilometer-scale shear zones. The shear movement also relates to the folding of preexisting planar surfaces. The most prominent Bonfim structure is a 3-km-wide antiform, featuring a granite core (Souza Neto et al., 2008). High-angle faults show dominant sinistral movement and are associated with quartz veins, calcite, amphibole, and ore deposits (Fig. 2).

Four late hydrothermal events have been identified, which are responsible for the gold mineralization in quartz veins and tungsten-molybdenum (W–Mo) mineralization in skarns (Hollanda et al., 2017). The plateau ages determined by $^{40}Ar/^{39}Ar$ dating of phlogopite show values of 597 ± 5 Ma, 553 ± 4 Ma, and 517 ± 6 Ma (Velásquez Ruiz et al., 2019; Santiago et al., 2019). Additionally, Re-Os dating of molybdenite crystals estimates an age of 524 ± 2 Ma for another of these hydrothermal episodes (Hollanda et al., 2017). Souza Neto et al. (2008) and Mesquita et al. (2019) propose that there was at least one progressive phase associated with pressures ranging from 2.0 to 4.0 kbar and temperatures between 500 and 580°C, followed by a regressive stage with temperatures between 400 and 500°C. The age ranges indicate the emplacement of various local granites (Nascimento et al., 2015), which have a significant impact on the source of hydrothermal fluids. According to Domingos et al. (2020), certain granitic plutons, along with Neoproterozoic migmatitic rocks, are found as structural domes in the Seridó Belt. These features resulted from the partial melting of the middle to lower crust and were likely exhumed during the continental collisions that led to the amalgamation of Western Gondwana in the Ediacaran period.

Based on our recent fieldwork and laboratory analysis, we provide a detailed description of seventeen different intrusions within the Bonfim mafic and ultramafic rock complex. This includes whole-rock geochemistry and, where applicable, geochronological data, such as U-Pb dating on zircon and rutile grains, as well as Sm-Nd isotopic analyses.

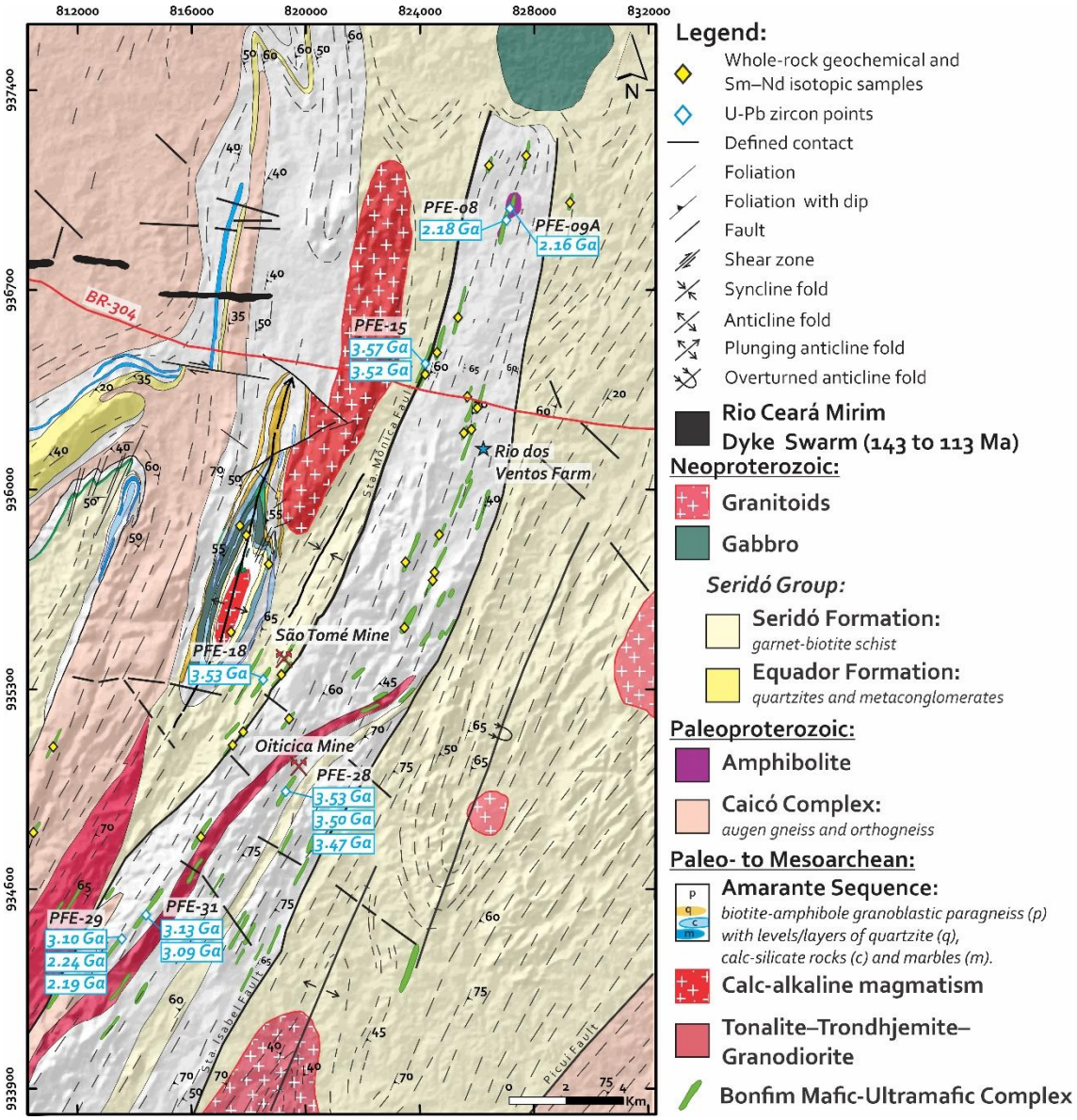



Figura 2 – Geological map and lithological-structural relations of the Bonfim Complex. (Modified from Salim 1979, Carvalho et al. 1980, Costa and Dantas, 2018).

## 2 ANALYTICAL TECHNIQUES

The fieldwork primarily focused on sampling mafic and ultramafic rocks exposed in the Bonfim nucleus for detailed petrographic and geochemical studies, as well as U-Pb and Sm-Nd isotopic analyses. These rocks occur as lenses or xenoliths, separated from one another by approximately 0.3 to 2.0 km, which corresponds to our sampling intervals, along a 35 km stretch following the regional NE trend. During the geological mapping, 17 ultramafic bodies were sampled. The most representative petrographic occurrences, along with those

with the best exposure conditions, are shown in Figure 2. Notable bodies include: (i) Body PFE-29, close to the Rio dos Ventos Farm (Fig. 3); (ii) Body PFE-15 (Fig. 4a), located about 250 m north of BR-304; (iii) Body PFE-28, within the boundaries of the Oiticica mine (Fig. 4b-c); and (iv) Body PFE-18, near the São Tomé mine (Fig. 4d). Additionally, smaller occurrences are also depicted in Figure 2.

### 3.1 LA-ICP-MS Zircon U-Pb dating

Twelve large samples (approximately 15 kg to 20 kg) were collected for zircon U-Pb dating. Gravimetric and magnetic methods were employed to separate zircon grains. The finest mineral grains were then meticulously selected using a binocular microscope, mounted in epoxy resin, and polished to reveal nearly all zircon shapes. U-Pb data were collected at the Laboratório de Estudos Geodinâmicos, Geocronológicos e Ambientais at the Universidade de Brasília, in Brazil. The isotope masses of interest were analyzed using a Thermo Finningan Element XR high-resolution single-collector sector field ICP-MS, paired with a 193 nm Iridia Excimer (ArF) laser ablation system. This laser system features a cobalt dual-volume chamber. Before each analytical session, the mass spectrometer was optimized to enhance the sensitivity of U and Pb while reducing oxide production. Each acquisition comprised 10 seconds of background measurement followed by 20 seconds of ablation. The masses $^{202}$Pb, $^{204}$Pb, $^{206-208}$Pb, $^{232}$Th, and $^{238}$U were measured using the triple detection mode (SEM+Faraday) while sweeping the electrostatic sector for each mass. One sweep lasted 82 ms, resulting in over 800 scans for ablation.

The laser settings featured a spot size of 25 µm, a frequency of 20 Hz, and a fluence of 2.0 J/cm². Raw data were processed using Iolite 4.0 (Paton et al., 2011), while time-resolved signal analysis and individual signal inspection were performed with the assistance of VizualAge (Petrus and Kamber, 2012). Data correction involved subtracting blanks, applying LIEF (Lead Isotope Evolution/Filtering) correction through an exponential plus linear model, and normalizing with GJ-1 zircon grain (Jackson et al., 2004). Quality control utilized Plešovice zircon (Sláma et al., 2008) and 91500 zircon (Widenbeck et al., 1995).

Excess variance in the primary calibrant was propagated across each analytical point. Each final age carries a systematic uncertainty of approximately 1%. No universal lead correction was utilized. Ages are reported at 2 sigma.

### 3.2 Whole-rock major and trace element analyses

Twenty-six whole-rock samples were analyzed for major and trace elements using X-ray fluorescence (XRF) spectrometry and inductively coupled plasma-mass spectrometry (ICP-MS) at ACME Analytical Laboratories in Vancouver, Canada. Before analysis, samples were crushed and ground to 200-mesh using a vibratory grind mill at the Laboratório de Estudos Geodinâmicos, Geocronológicos e Ambientais, Universidade de Brasília (Brazil). X-ray fluorescence was used to determine the concentrations of major oxides and minor elements in fusion disks made from lithium tetraborate. The abundances of trace elements were determined by melting a 0.2 g subsample with lithium metaborate/tetraborate, followed by digestion in diluted nitric acid and subsequent ICP-MS analysis. The quantities of base and precious metals were assessed by digesting a 0.5 g subsample in Aqua Regia and analyzing it with ICP-MS. The loss on ignition (LOI) percentage is determined by measuring the weight difference after the sample is heated to 1000°C.

### 3.3 Whole-rock nd isotope analyses

Sm-Nd isotope analyses of whole rock were conducted at the Laboratório de Estudos Geodinâmicos, Geocronológicos e Ambientais, Universidade de Brasília (Brazil), following techniques by Gioia and Pimentel (2000). The rock samples were pulverized to a 200-mesh powder using a vibratory grind mill. A 50 mg whole-rock subsample was mixed with a $^{149}$Sm-$^{150}$Nd spike (isotopic abundance for $^{149}$Sm 97.58% and isotopic abundance for $^{150}$Nd = 97.80%; Wasserburg et al. 1981; Gioia and Pimentel, 2000) solution and dissolved in Savillex beakers. The extractions of Sm and Nd employed standard cation exchange chromatography methods using Teflon columns filled with LN-Spec resin, which is diethylhexyl phosphoric acid supported on PTFE powder. Sm and Nd fractions were loaded onto rhenium filaments, and isotope analyses were

processed using multi-collector TRITON TIMS (Thermal Ionization Mass Spectrometry) in static mode. The findings show Sm/Nd uncertainties and $^{143}Nd/^{144}Nd$ ratios of better than 0.1% (2σ standard error) and 0.0015% (1σ), respectively, aligning with repeated analyses of the international rock standard BHVO-1 (Basalt Hawaiian-USGS; Gladney and Roelandts, 1987). The reference material yielded an estimated average Nd concentration of 25.87 ppm and a measured Sm concentration of 6.38 ppm. The decay constant (λ) was $6.54x10^{-12}$, and the $^{143}Nd/^{144}Nd$ ratios were normalized to $^{146}Nd/^{144}Nd = 0.7219$. TDM values were estimated using DePaolo's (1981) model.

## 4 RESULTS

### 4.1 Field observations and petrography

The Bonfim mafic and ultramafic complex is a highly metasomatized and deformed tectonostratigraphic zone located in the north-central portion of the Seridó Belt. Based on previous studies and 1:100,000-scale geological mapping, four major chronostratigraphic divisions were recognized: (i) the Paleo- (Carvalho, 1990; Santiago, 2017; Velásquez Ruiz et al., 2019; Santos et al., 2020; Côrrea et al., 2021) to Mesoarchean basement (this study); (ii) Paleoproterozoic gneissic to migmatitic units associated with the Caicó Complex (Jardim de Sá, 1994); (iii) Neoproterozoic metasedimentary sequences and granitic magmatism; (iv) in addition to Lower Cretaceous mafic dikes (Fig. 2).

The Archean basement consists of granitic to tonalitic gneisses along with supracrustal rocks, including mafic and ultramafic intrusions, metacarbonates, banded iron formations (not represented at the map scale), and metapelites. All units were metamorphosed under amphibolite facies conditions and subsequently deformed into a system of synclinal and anticlinal folds. The resulting fold architecture displays complex geometries related to the emplacement and evolution of dominantly dextral, SSW–NNE–trending transpressional shear zones, developed during the syn- to late-Brasiliano Orogeny (~650–540 Ma). In general, the foliations formed during this event show dips ranging from 20° to 75°, mainly towards the ENE. Poorly studied gneiss and

migmatites crop out to the NE and S of the study area. The alternation between quartz-feldspathic bands and bands rich in biotite, chlorite, and, rarely, hornblende controls the composition of these units. Typically, the lithological gradient ranges from syenogranites to tonalites. Slightly deformed areas exhibit a still-preserved porphyritic texture. In the more migmatized fractions, the neosomes vary in thickness from 1 to 5 cm, with garnet as the associated mineral phase.

The mafic and ultramafic bodies that constitute the focus of this study comprise serpentinite, pyroxenite, tremolitite, hornblendite, chloritite, anthophyllite chloritite, and talc schist (Fig. 3a-b). These rocks are strongly foliated, with moderate to steep dips (40–90°) toward the NW, and display a dominantly lenticular geometry. In situ, the mafic and ultramafic bodies display hues ranging from light to dark green, typically with medium- to coarse-grained textures and variable degrees of serpentinization. In some outcrops, the contact between the intrusive bodies and the migmatitic gneisses is distinctly defined by steeply dipping shear zones or well-defined magnetite-rich layers, commonly referred to as magnetitites. Intrusions are associated with Archean metasedimentary rocks along tectonic contacts, indicating the juxtaposition of coeval units during subsequent deformation events, or as allochthonous blocks embedded within the Neoproterozoic metasedimentary rocks of the Seridó Group.

During the geological mapping, 17 ultramafic bodies were sampled. The most representative petrographic occurrences, along with those with the best exposure conditions, are shown in Figure 2. Notable bodies include: (i) Body PFE-15, located about 250 m north of BR-304; (ii) Body PFE-18, near the São Tomé mine; (iii) Body PFE-28, within the boundaries of the Oiticica mine; and (iv) Body PFE-29, close to the Rio dos Ventos Farm. Additionally, smaller occurrences are also depicted in Figure 2. The main lithologies identified in the study area are described in detail below.

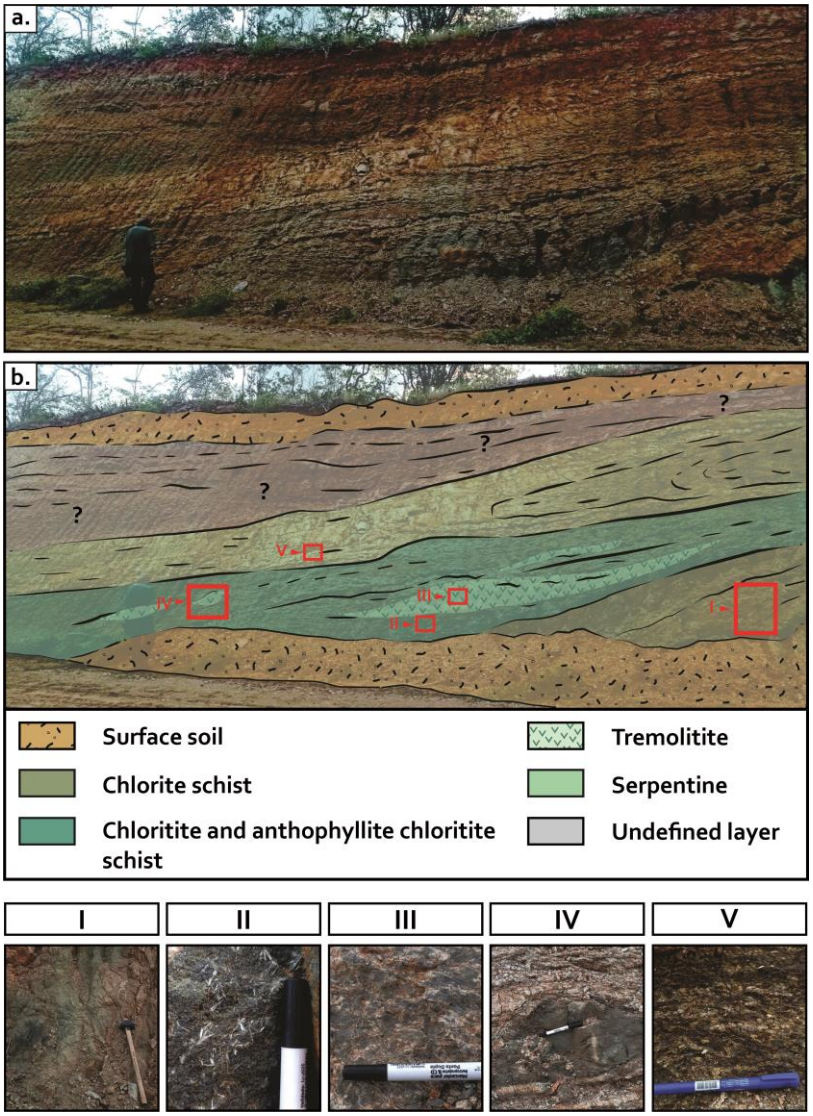



Figure 3 – a. Field photograph illustrating lithological characteristics and field relationships of the PFE-29 outcrop, Bonfim Mafic–Ultramafic Complex, Borborema Province. b. Distinct petrographic facies were identified and systematically characterized, revealing compositionally and texturally distinct protolith-derived assemblages and reflecting variable degrees of progressive metasomatic alteration. I – chlorite schist; II – Anthophyllite-chlorite schist; III-IV – tremolitite; V – serpentinite.

### *4.1.1 Serpentinite*

The serpentinites are greenish, often massive, rocks that are highly fractured and show pervasive metasomatic alteration, removing igneous and metamorphic assemblages (Fig. 4a-c), except for rare sites that preserve relic cores of olivine and less common chromite crystals (Fig. 5a). Bonfim serpentinites are relatively oxide-rich, commonly containing chromite and magnetite (Fig. 5b).

Chromite occurs as granular crystals or as cores surrounded by Al-rich altered spinel (Fig. 5c). Magnetite grains are associated with the reticular network of serpentine veinlets or occur within serpentine pseudomorphs. In certain minor areas, radial fibrous clusters of tremolite indicate an earlier phase of alteration among at least three stages. These aggregates replace totally or almost completely the igneous vestiges. Serpentine veinlets were formed during a second step of alteration (Fig. 5d). They break the main olivine crystals into uneven residual fragments, and the serpentine-group minerals are usually aligned perpendicular to the veinlet walls (Fig. 5e). Magnetite grains in these veins indicate simultaneous formation with serpentine. Later, through supergene weathering, the igneous remnants have weathered to randomly oriented saponite, serpentine-group phases, and iron oxyhydroxides.

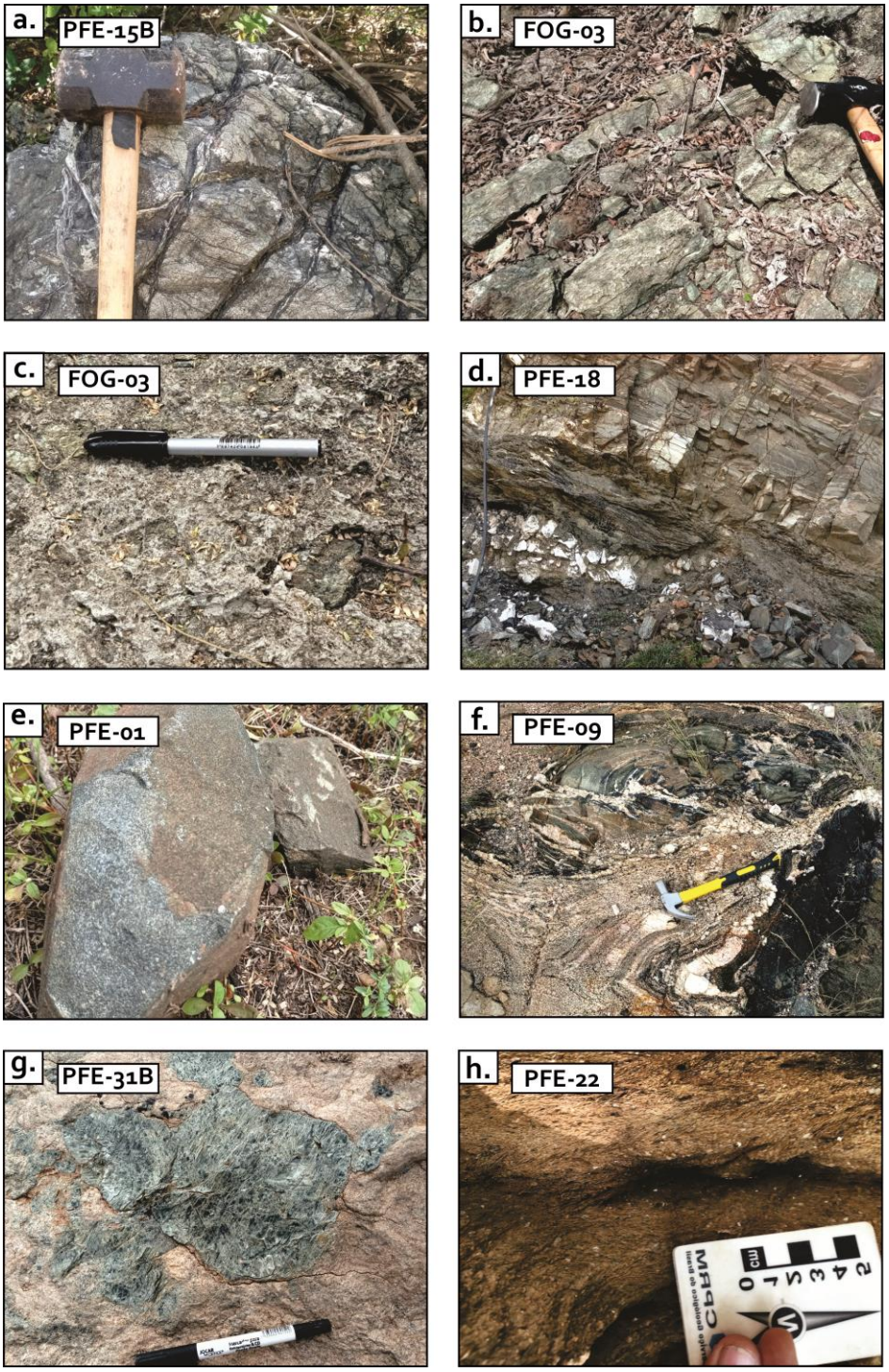



Figure 4 – Field photographs illustrating lithological characteristics and field relationships of the Bonfim Mafic–Ultramafic Complex, Borborema Province. a. Serpentinite outcrop displaying a greenish coloration, with a well-developed network of serpentine veins. b-c. Serpentinite outcrop characterized by a massive to weakly foliated structure, greenish coloration. d. Tremolitite intruded by pegmatite. e. Amphibolite fragment showing macroscopic textural features. f. Amphibolite outcrop crosscut by granodioritic to tonalitic leucosome. g. Chloritite outcrop dominantly composed of chlorite, displaying a massive structure and a characteristic greenish coloration. h. Chloritite outcrop composed dominantly of chlorite, with well-developed schistosity.

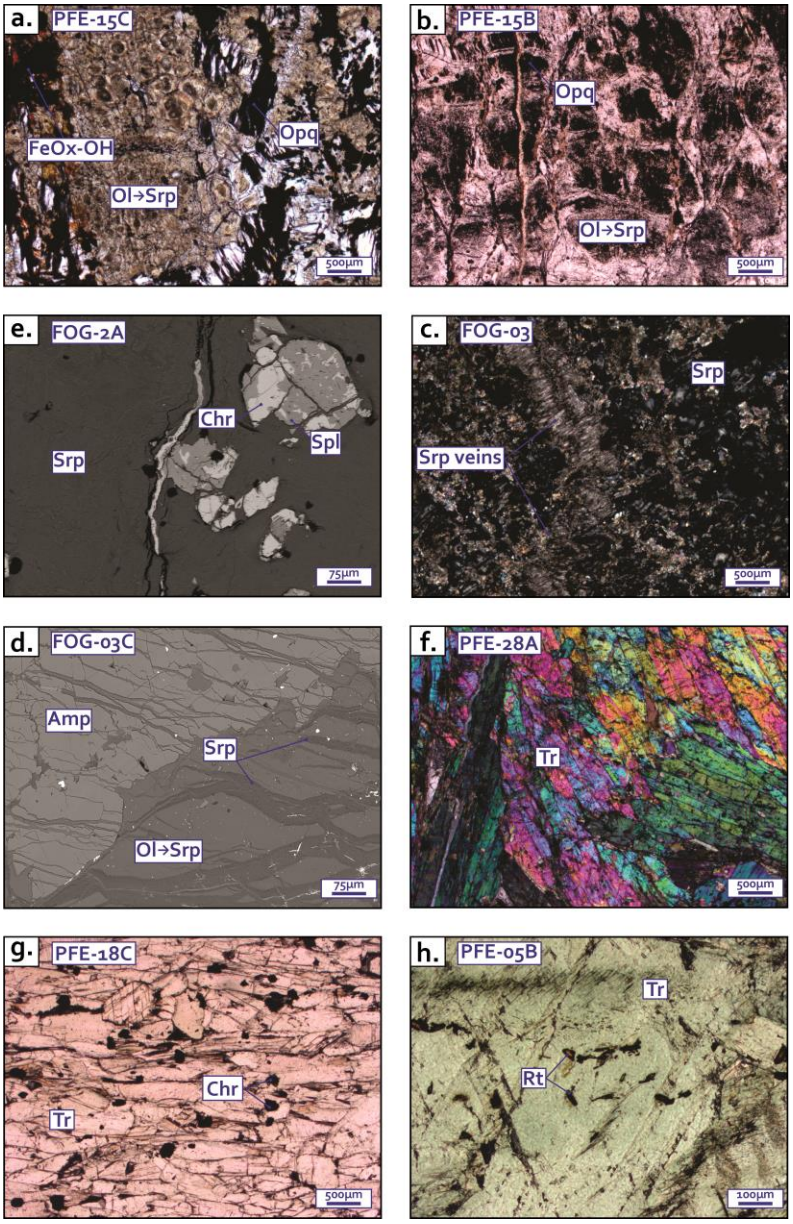



Figure 5 – Photomicrographs showing the representative mineralogy of typical rocks from the Bonfim Mafic–Ultramafic Complex. a. Serpentinite displaying relict olivine pseudomorphs replaced by serpentine, along with the formation of iron hydroxides derived from the destabilization of opaque phases, under plane-polarized light (PPL). b. Serpentinite showing opaque grains associated with the reticular network of serpentine veinlets or occurring within serpentine pseudomorphs (PPL). c. Chromite partially replaced by spinel (SEM backscatter electron - BSE). d. Serpentine veinlets under cross-polarized light (XPL). e. BSE image illustrating the textural relationships among amphibole crystals, serpentine-replaced olivine pseudomorphs, and associated serpentine veins. f. Tremolitite showing grains aligned along two distinct foliation directions (XPL). g. Subhedral magnetite grains enclosed within tremolite crystals (PPL). h. Aggregate of rutile included within a tremolite crystal (PPL). Amp – amphibole; Chr – chromite; FeOx-OH - iron hydroxides; Ol – olivine; Opq – opaque mineral; Spl – spinel; Rt – rutile; Srp – serpentine; and Tr – Tremolite.

### *4.1.2 Tremolitite*

Tremolitites (Fig. 4d) are medium-grained, massive to slightly foliated rocks with a green coloration. They are composed mainly of elongate prisms of tremolite, plus chromite and magnetite. The different facies of tremolitites show tremolite grains randomly oriented or aligned in two distinct foliation directions (Fig. 5f). In the foliated section, crystal sizes range from approximately 300 μm to 2 mm, while in the randomly oriented parts, they show sub-millimeter dimensions, typically between 90 and 500 μm. Amphibole crystals also contain medium to small chromite inclusions (Fig. 5g). Therefore, tremolite is interpreted as late-stage or coeval with chromite crystallization. Most magnetite grains are euhedral or subhedral (50 μm to ~1.5 mm) in tremolite crystals, occasionally forming irregular alignments. Other linear infillings of opaque minerals are described along tremolite cleavage planes. Accessory minerals consist of quartz, rutile, apatite, phlogopite, and zircon. Quartz appears as an interstitial mineral among amphibole grains. Rutile grains are prismatic, subhedral to euhedral, occurring as fine-grained aggregates (Fig. 5h) or larger isolated crystals. They are randomly enclosed within tremolite. Tabular phlogopite grains were described only in the sections related to the PFE-28 outcrop. They appear as unoriented aggregates ranging in size from 100 to 400 μm, in straight to irregular contact with the tremolite grains, or as single crystals within the voids and interstices between tremolite crystals. Zircon grains occur as isolated crystals within massive chromite, interpreted as coeval magmatic crystals. Subsequent alteration includes the peripheral replacement of tremolite by chlorite, with minor talc and iron oxyhydroxide formation.

### *4.1.3 Amphibolite*

Amphibolite bodies manifest as small lenses, found either within the mica schists of the Seridó Formation or associated with ultramafic lithologies from the study area (Fig. 4e). These amphibolites are medium-grained dark green rocks featuring well-developed foliation. They consist of bundles of hornblende, islands or residual crystals of plagioclase and quartz, and opaque minerals. Hornblende

appears as small prismatic grains (200 μm) or subidioblastic (500 μm to 1.5 mm), elongated, and plagioclase occurs without twinning linked to quartz grains (Fig. 6a). Incipient alteration processes cause irregularly distributed microcrystals of sericite in feldspar. Opaque minerals include magnetite and ilmenite. Zircon is enclosed within amphibole crystals (Fig. 6b).

### *4.1.4 Chlorite schists*

Chlorite schists are typically light gray, sometimes greenish, with noticeable laminar foliation and fine-grained (Fig. 4g-h). They appear as narrow, discontinuous layers associated with serpentinites, tremolitite, and talc schists. These rocks are more evident on the SW edge of the study area. Chlorite crystals show an irregular distribution pattern, often randomly oriented. In minor sections, they exist as elongated crystals or aligned clusters. This alignment appears parallel to the cleavage of tremolite residues, partially replaced by chlorite. Rutile is a common accessory mineral, occurring mainly as isolated prismatic grains disseminated within the chlorite matrix. In these rocks, magnetite occurs as isolated euhedral or subhedral crystals, ranging from 400 μm to 2 mm in size. Its partial oxidation is responsible for the influx of brownish oxyhydroxides of iron (Fig. 6c-d). Anthophyllite chloritite facies occurs along the PFE-29 outcrop, where anthophyllite crystals form fibrous to semi-acicular aggregates (Fig. 6e).

### *4.1.5 Talc schists*

Talc schists occur as minor units associated with tremolitite, serpentinite, and chlorite schist layers, commonly bordered by biotite schists. They have elongated NNE-SSW shapes, aligning with the host rocks' foliated structures. They are compact, greenish rocks with a fine to medium grain, occasionally exhibiting slight schistosity. Talc and magnetite grains completely replaced the original mineralogy, likely during the same alteration event. The talc areas show a micro-aggregated texture of unoriented particles of talc (Fig. 6g-h). Iron oxide transfer imparts a brownish hue to the talc, with tiny magnetite particles dispersed throughout the matrix. Later alteration produces a brownish rim of iron

oxyhydroxides.

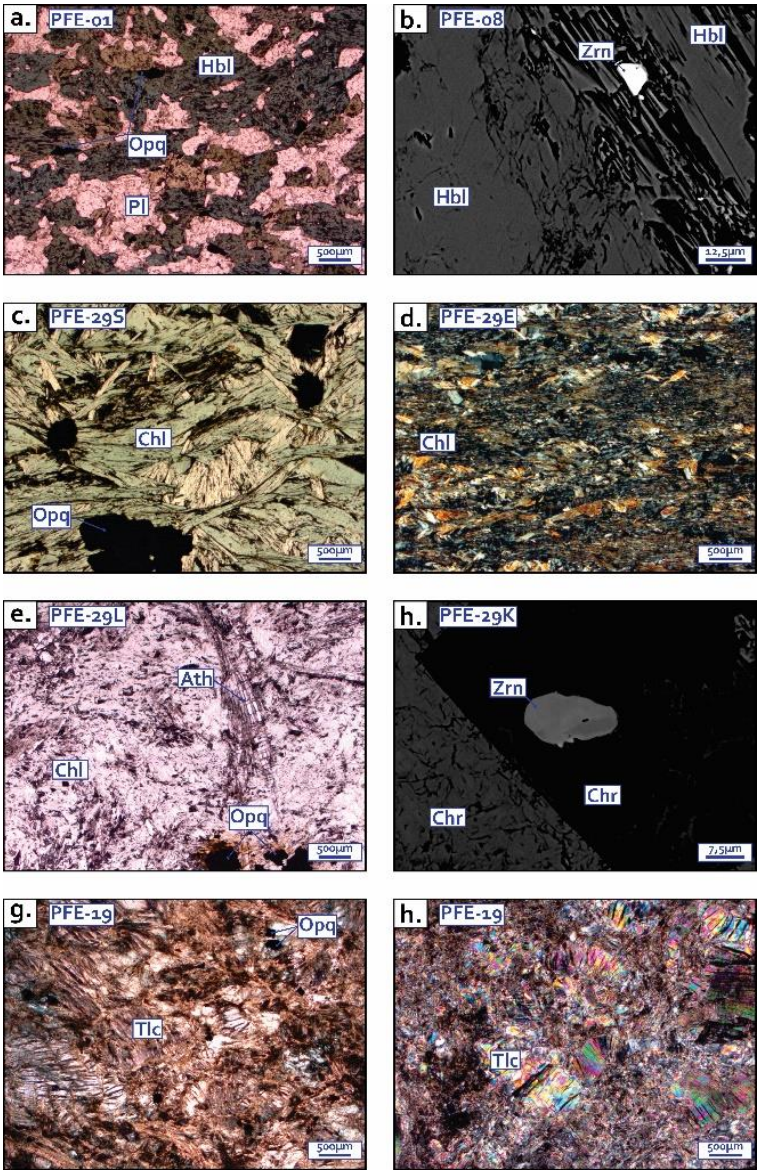



Figure 6 – Photomicrographs showing the representative mineralogy of typical rocks from the Bonfim Mafic–Ultramafic Complex. a. Amphibolite dominantly composed of large hornblende grains, with plagioclase and minor opaque minerals, PPL. b. BSE image illustrating zircon grain enclosed within hornblende. c. Chlorite schist displaying subhedral, isolated magnetite crystals within a randomly oriented chlorite matrix (PPL). d. Chlorite schist showing aligned submillimeter chlorite grains (XPL). e. Anthophyllite crystals in a chlorite matrix. Euhedral to subhedral magnetite grains and iron hydroxide formation in the lower part of the image (PPL). h. Zircon enclosed within a chromite crystal (BSE). g. Talc schist displaying a micro-aggregate texture characterized by randomly oriented talc grains, accompanied by the alteration of primary opaque mineral phases to iron oxides. This oxidative transformation imparts a pervasive brownish coloration to the talc-rich matrix (XPL). e. Very fine-grained aggregates of talc contrasting with larger talc crystals (XPL). Ath – anthophyllite; Chl – chlorite; Chr – chromite; Hbl – hornblende; Opq – opaque mineral; Pl – plagioclase; Tlc – talc; and Zr – Zircon.

## 4.2 U-Pb dating of zircon grains

### *4.2.1 Paleoarchean ultramafic rocks*

Two serpentinite samples from the PFE-15 body were dated, along with tremolitites from outcrops PFE-28 and PFE-18. Zircon in Paleoarchean intrusions appears as euhedral to subeuhedral crystals, ranging from 100 to 300 μm along the c-axis (Fig. 7a-f). Most crystal cores show concentric zoning with moderate to weak cathodoluminescence (CL), while some exhibit features from hydrothermal reactions. The peripheral zones display distinct oscillatory zoning. Figure 8a-f displays the age results for the Paleoarchean mafic and ultramafic rocks (Table 1, Appendix A). Individual analyses for these groups are linked to increased discordances, likely due to Pb loss.

Seven analyses for the PFE-15 sample reveals Th/U ratios of 0.44 to 1.35. The discordia diagram yields an upper intercept age of 3573 ± 62 Ma (MSWD of 1.1). The lower intercept age is 1319 ± 365 Ma (Fig. 8a). Six U-Pb isotopic analyses of the PFE-15B sample showed Th/U ratios of 0.02 to 0.47. On the discordia diagram, they yield an upper intercept age of 3525 ± 18 Ma (MSWD of 0.56). The lower intercept age was 2404 ± 532 Ma (Fig. 8b).

Twenty zircon U-Pb analyses on sample PFE-28A reveal Th/U ratios from 0.67 to 1.43. The concordia diagram indicates an upper intercept age of 3530 ± 28 Ma (MSWD of 0.82). The lower intercept age is 593 ± 59 Ma (Fig. 8c). Fifty-one U-Pb measurements for PFE-28 indicate Th/U ratios of 0.10 to 2.49 and the concordia diagram reveals an upper intercept age of 3500 ± 25 Ma (MSWD of 1.3). A lower intercept age of 559 ± 29 Ma is obtained (Fig. 8e). Two age groups are identified in PFE-28D samples. Eight analyses showed a Th/U ratio varying from 0.30 to 1.57. The U-Pb concordia diagram presents an upper intercept age of 3477 ± 59 Ma and MSWD = 3.1. The lower intercept age is 563 ± 48 Ma. Seven zircon U-Pb analyses on the PFE-28D sample reveal Th/U ratios from 0.08 to 1.73. On the concordia diagram, we determined an upper intercept age of 2274 ± 60 Ma (MSWD of 1.5). The lower intercept age is 262 ± 109 Ma (Fig. 8f).

Ten spots from the sample PFE-18C's analyses indicate Th/U ratios of 0.02 to 0.22. The discordia diagram gives an upper intercept age of 3528 ± 13 Ma with a MSWD of 1.6 and a lower intercept age of 521 ± 647 Ma (Fig. 8d).

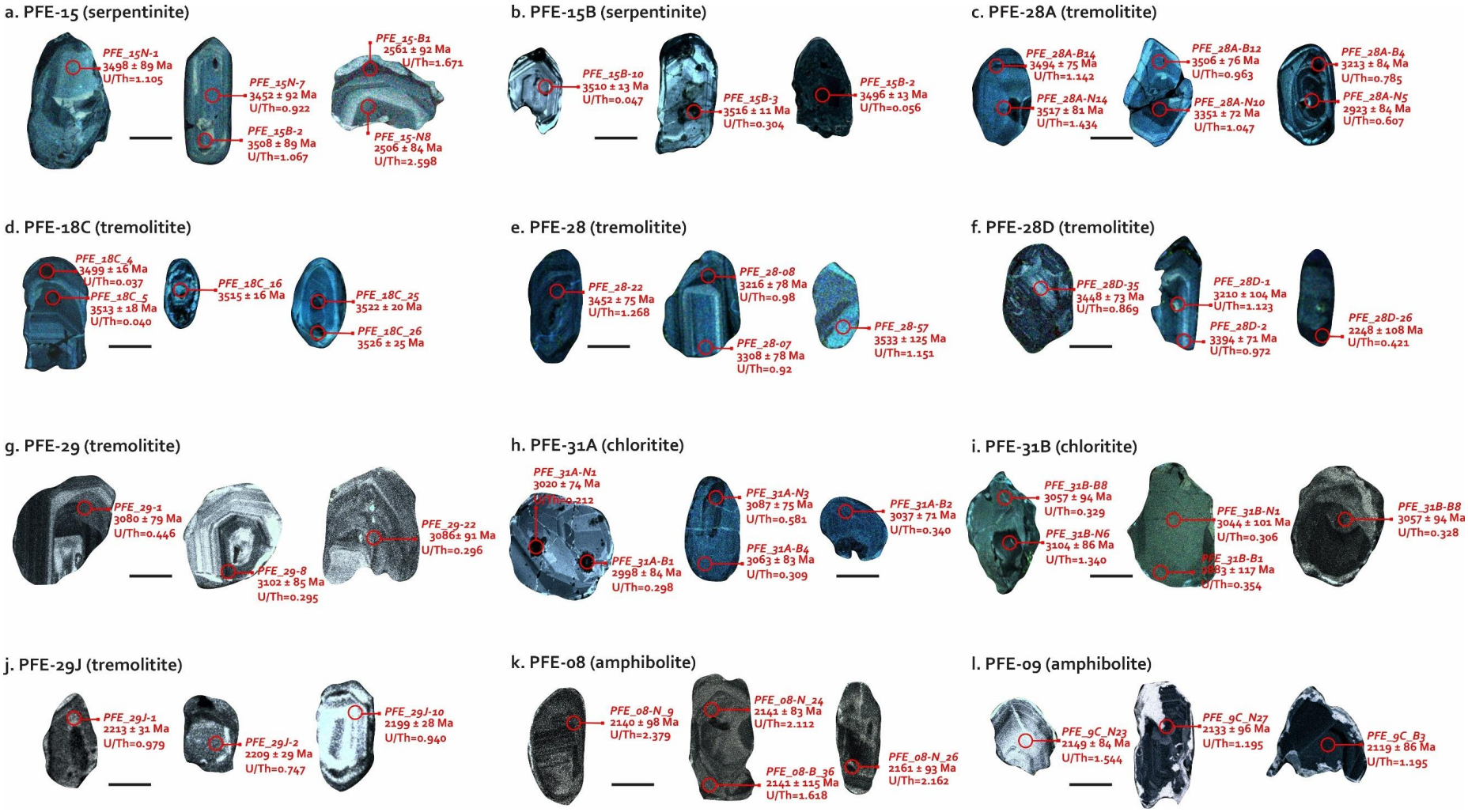



Figure 7 – Cathodoluminescence images of representative zircon grains. Scale bar = 100 µm.

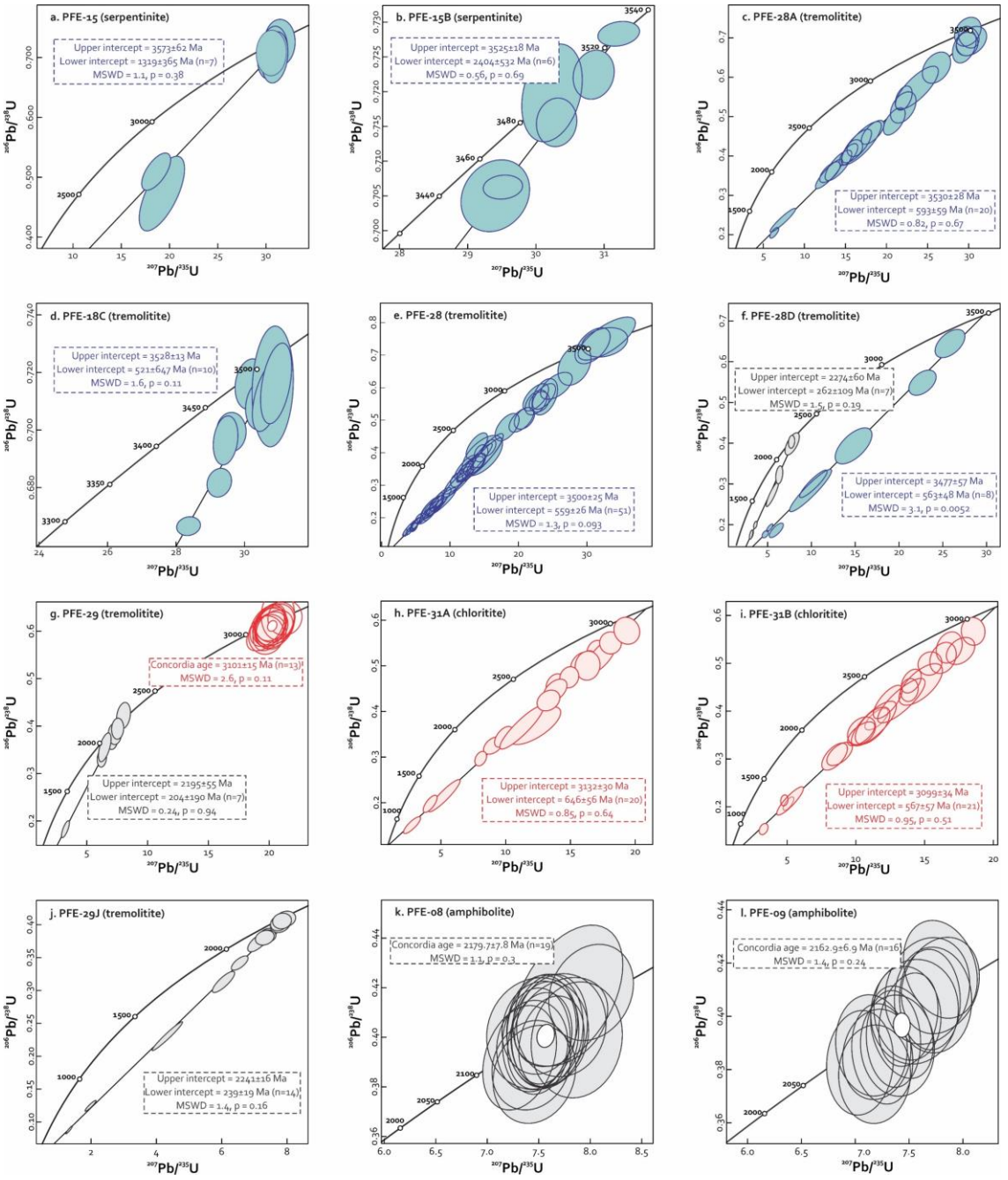



Figure 8 – U–Pb in zircon concordia diagrams.

### *4.2.2 Mesoarchean mafic and ultramafic association*

In the Mesoarchean intrusions, zircon occurs as subhedral to anhedral crystals, typically 100–250 µm long along the c-axis. Most crystalline cores exhibit incipient zoning with weak CL brightness. Internal features consistent with hydrothermal alteration are common, and the rims also display incipient oscillatory zoning (Fig. 7g-i). Figure 8g-i shows the age results for Mesoarchean

mafic and ultramafic rocks. Analyses indicate increased discordances, likely from Pb loss. Here, a tremolitite body (PFE-29) and two chloritite samples (PFE-31 and PFE-31B) were dated.

Sample PFE-29 reveals two distinct age populations (Fig. 8g). Thirteen analyses yield Th/U ratios ranging from 0.82 to 1.35. The Concordia diagram yields an age of 3101 ± 15 Ma, with an MSWD of 2.6. The second population comprises seven analyses, with Th/U ratios ranging from 0.44 to 2.59 and the Discordia diagram defines an upper intercept age of 2195 ± 22 Ma (MSWD = 0.24) and a lower intercept age of 204 ± 190 Ma.

Twelve U-Pb spots on PFE-31A show Th/U ratios between 0.12 and 1.51. The Discordia diagram yields an upper intercept age of 3132 ± 30 Ma with an MSWD of 0.85. The lower intercept age was 646 ± 56 Ma (Fig. 8h). Twenty-one analyses for the PFE-31B sample showed a Th/U ratio varying from 0.20 to 1.34. The lower intercept age was 646 ± 56 Ma. Twenty-one analyses for the PFE-31B sample showed a Th/U ratio from 0.20 to 1.34. The U-Pb concordia diagram presents an upper intercept age of 3099 ± 34 Ma and MSWD = 0.95 (Fig. 8i).

### *4.2.3 Rhyacian mafic rocks*

In the Rhyacian amphibolites, zircon occurs as subhedral to euhedral grains with lengths of 150–350 μm along the c-axis. CL imaging shows concentric oscillatory to sector zoning, with the rims characterized by narrow concentric oscillatory bands (Fig. 7j-l). Fourteen analyses for the PFE-29J sample have Th/U ratios of 0.16 to 1.45. The Concordia diagram shows an upper intercept age of 2241 ± 16 Ma with a MSWD of 1.4. Its lower intercept age is 239 ± 19 Ma (Fig. 8j). Nineteen analyses for the sample PFE-08 showed a Th/U ratio varying from 1.04 to 2.84. The U-Pb concordia diagram presents a linear array, yielding a concordia age of 2179.1 ± 7.8 Ma and MSWD = 1.1 (Fig. 8k). Performed sixteen zircon U-Pb analyses on sample PFE-09C uncovered Th/U ratios ranging from 0.57 to 2.52. The concordia diagram indicates a concordia age of 2162.9 ± 6.9 Ma and a mean square weighted deviation (MSWD) of 1.4 (Fig. 8l).

## 4.3 Major and trace elements

Seven analyzed samples show high LOI values, ranging from 6.52 to 21.90 (wt%), indicating complete or nearly complete serpentinization and higher levels of alteration. To compare the major oxide concentrations with data from various peridotites reported in the literature, we normalized all the analyzed values to a volatile-free basis (Table 2, Appendix A).

### *4.3.1 Paleoarchean ultramafic rocks*

Assessment of major and trace element distributions allows the distinction of two main geochemical types of Paleoarchean mafic–ultramafic intrusions, some of which correspond to the same intrusive body in the field. The first dataset is composed of serpentinite samples. Major oxides in this group vary within a narrow range (wt%), with $SiO_2$ (43.11-49.44), $Al_2O_3$ (1.09-2.58), $Fe_2O_3t$ (6.65-9.07), MgO (30.65-36.81), $TiO_2$ (0.01-0.06), CaO (0.03-4.23), $Na_2O$ (0.01-0.14), and $K_2O$ (0.01-0.04). Their LOI content varies from 12.00 to 21.90, and Mg# parameters are between 87.3 and 91.3. Cr concentrations range from 5430 to 10000 ppm. REE patterns are described by enrichment in LREE ($(La/Sm)_n$ = 0.86-4.61) related to HREE ($(Gd/Yb)_n$ = 0.25-2.10) and positive to negative Eu anomalies (Eu/Eu* = 0.43-1.47) and Ce anomalies between 0.45 and 1.45 (Fig. 09a). They display near-flat HFSE and slight LILE enrichment in the primitive mantle-normalized diagram (Fig. 9b).

The second lithochemical pattern observed is composed of tremolitites, mainly associated with the PFE-18 outcrop. The contents of major chemical components in these samples vary slightly (wt%): $SiO_2$ (52.49-55.62), $Al_2O_3$ (5.73-8.56), $TiO_2$ (0.12-0.71), CaO (9.13-11.28), $Na_2O$ (0.62-0.88), and $K_2O$ (0.04-0.10). Both MgO (11.28-19.99 wt%) and $Fe_2O_3t$ (7.26-14.35 wt%) exhibit wider variations. Values of the Mg# parameter range from 32.88% to 63.20%, and LOI values are between 0.97 and 2.22. Cr contents vary from 958 to 3200 ppm. REE patterns on the chondrite-normalized diagram show Eu anomalies of various intensities, ranging from 0.5 to 1.1, while Ce anomalies are between 1.1 and 1.2 (Fig. 9c). The total REE content in samples ranges from 25.99 to 70.65

ppm, with an average of about 43.10 ppm. They have a similar light REE content of $(La/Sm)_n$ = 0.79-1.42 when compared to the heavy REE concentration of $(Gd/Yb)_n$ = 0.81-1.06, exhibiting a relatively linear profile. These tremolitites are characterized by a nearly flat trace pattern in the primitive mantle-normalized diagram (Fig. 9d).

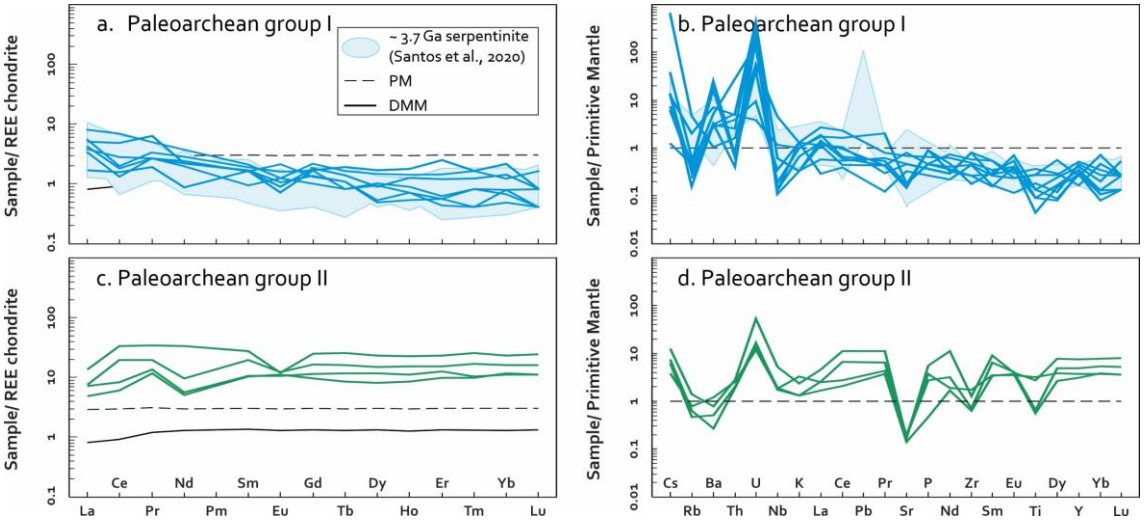



Figure 9 – Chondrite- and primitive mantle-normalized diagrams for Paleoarchean ultramafic intrusions. Normalization values from Anders and Grevesse (1989) and Sun and McDonough (1989), respectively.

### *4.3.2 Mesoarchean mafic- ultramafic association*

Mesoarchean mafic and ultramafic rocks show four distinct lithochemical signatures from a geochemical perspective. Group one includes PFE-05 and PFE-06 samples linked to tremolitite outcrops. Their major oxides are heterogeneously distributed, with (wt%): $SiO_2$ (52.50-54.64), $Al_2O_3$ (4.90-8.22), $Fe_2O_3t$ (2.65-15.58), MgO (12.35-19.84), $TiO_2$ (0.44-1.13), CaO (9.25-9.35), $Na_2O$ (0.75-0.89), and $K_2O$ (0.05-0.89). Results of Mg# parameters vary from 33% to 56%, and LOI values are between 1.24 and 2.06. The total REEs content in these rocks ranges from 183 to 277 ppm. The accumulation level of LREEs $(La/Sm)_n$ in these samples amounts to 0.80-1.75 and $(Gd/Yb)_n$ = 0.89-0.91. These show a heavy rare earth pattern that is drawn strictly parallel to one another, while LREEs exhibit some enrichment (Fig. 10a). Eu anomalies range from 0.50 to 1.02, and Ce anomalies are between 0.96 and 1.22. In the primitive

mantle–normalized diagram, the trace element distribution pattern is characterized by a generally flat trend with negative Nb, Sr, and Ti anomalies (Fig. 10b).

The second group consists of samples RDD-60, RDD-60-B, and RDE-18. Major oxides in this group vary within a narrow to moderate range (wt%), with $SiO_2$ (49.14-52.94), $Al_2O_3$ (5.85-9.14), $Fe_2O_3t$ (10.90-13.98), MgO (17.15-18.85), $TiO_2$ (0.46-0.96), CaO (5.85-7.85), $Na_2O$ (0.62-0.79), and $K_2O$ (0.06-4.04). LOI results are between 1.10 and 1.60. Mg# parameters range from 69.36% to 77.36%. The REE distribution is characterized by flat to slightly depleted LREE patterns relative to HREEs, with $(La/Sm)_n$ = 0.48-1.11 and near-flat $(Gd/Yb)_n$ = 1.01-1.09. Eu anomalies range from 1.31 to 1.44, whereas Ce anomalies range from 1.11 to 1.22 (Fig. 10c). The linear trend is also reproduced in the primitive mantle–normalized trace element diagram (Fig. 10d).

The third set includes six samples, mostly tremolitite, chloritite and talc schists. This set is characterized by significant variations in the content of its main oxides, measured in weight percent (wt%): $SiO_2$ (33.20-56.94), $Al_2O_3$ (1.68-19.58), $Fe_2O_3t$ (6.80-17.17), MgO (6.73-29.63), $TiO_2$ (0.07-1.97), CaO (0.07-9.97), $Na_2O$ (0.02-1.87), and $K_2O$ (0.01-0.84). The parameter Mg# varies in the range of 22.99-73.10%, and LOI values are between 0.65% and 11.90%. The total level of REE content (~81.87 ppm) fluctuates in the range of 53.23-137.2 ppm. The parameter $(La/Sm)_n$ is between 1.45 and 3.21, and the results of $(Gd/Yb)_n$ = 0.95-2.25, creating a downward slope pattern (Fig. 10e). Eu anomalies range from 0.35 to 1.02 and Ce anomalies are between 0.53 and 3.42. In the primitive mantle–normalized diagram, trace element patterns are marked by relative enrichment of selected LILEs over HFSEs, together with negative Nb, Sr, and Ti anomalies (Fig. 10f).

The final group consists of samples PFE-01 and STC-48, which are associated with Mesoarchean amphibolites. Their major chemical components vary in the following ranges (wt%): $SiO_2$ (53.23-53.53), $Al_2O_3$ (14.15-14.81), $Fe_2O_3t$ (12.51-13.58), MgO (5.67-6.60), $TiO_2$ (1.05 in both samples), CaO (9.46-10.15), $Na_2O$ (1.07-2.56), and $K_2O$ (0.27-0.37). Results of Mg# parameters vary from 24.78% to 20.65%, and LOI values are between 0.80 and 1.03. REE patterns on the chondrite-normalized diagram exhibit negative Eu anomalies,

with values between 0.69 and 0.74 (Fig. 10g). The total REE content in the samples ranges from 120.11 to 204.58 ppm. The parameter $(La/Sm)_n$ is between 2.65 and 2.85, and the results of $(Gd/Yb)_n$ = 1.48-1.53 (Fig. 10h).

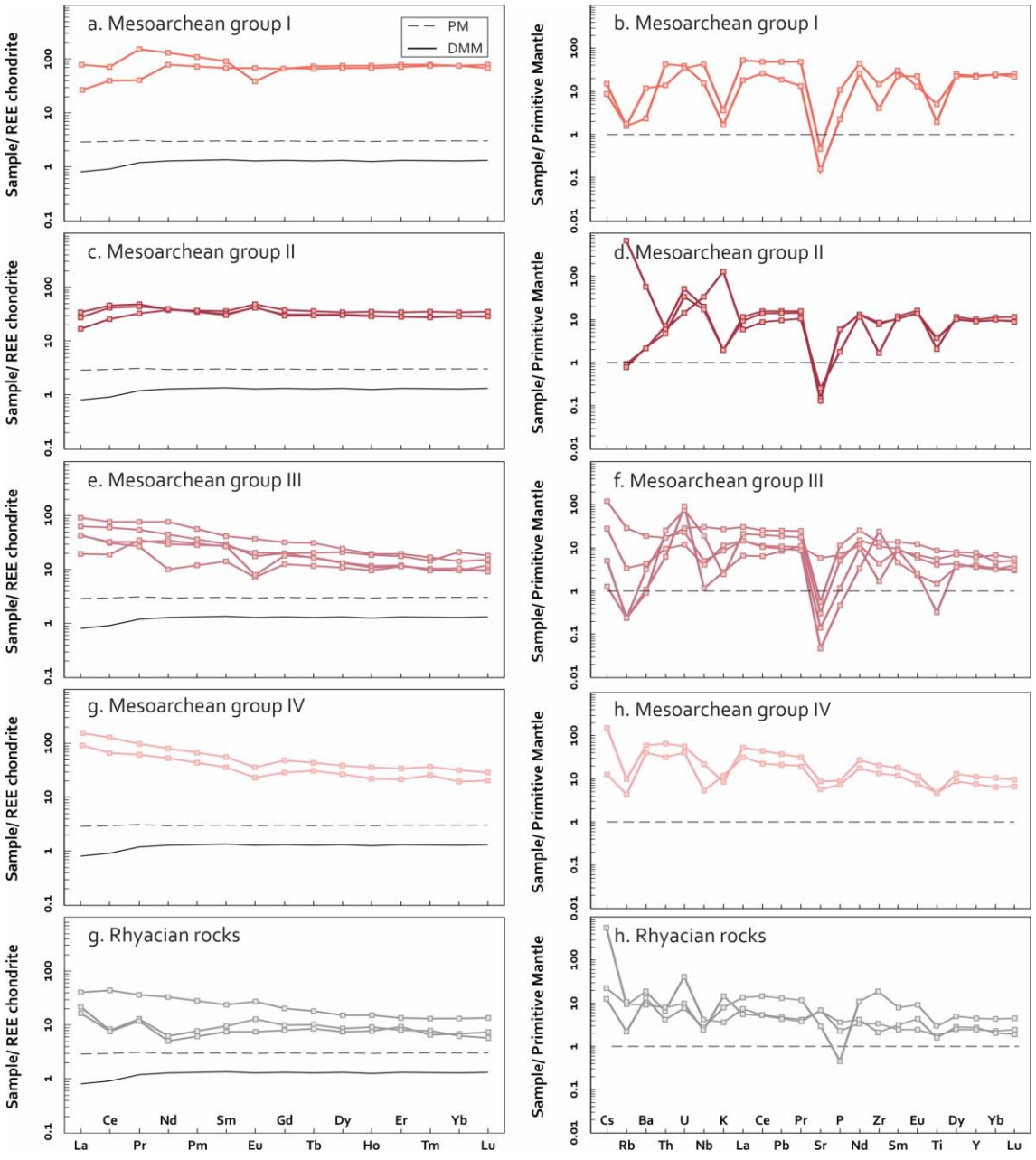



Figure 10 – Chondrite- and primitive mantle-normalized diagrams for Mesoarchean mafic–ultramafic intrusions. Normalization values from Anders and Grevesse (1989) and Sun and McDonough (1989), respectively.

### *4.3.3 Rhyacian mafic rocks*

Common amphibolites are the most widespread Rhyacian mafic rocks. Three (PFE-08, PFE-09A, and PFE-09B) samples were analyzed for whole-rock geochemistry. Their content of major chemical components vary in the following ranges (wt%): $SiO_2$ (49.24-52.21), $Al_2O_3$ (5.33-9.80), $Fe_2O_3t$ (11.33-19.63), MgO (8.54-12.61), $TiO_2$ (0.36-0.65), CaO (11.28-22.66), $Na_2O$ (0.64-2.01), and $K_2O$ (0.11-0.45). Values for Mg# parameters range from 27.64% to 40.47%, with low LOI results of 0.36 to 0.86. REE content in Rhyacian amphibolites ranges from 27.36 to 73.44 ppm, with an average of 44.02 ppm. These samples are characterized by a slight enrichment in LREEs ($(La/Sm)_n$ = 1.75-2.34) relative to HREEs ($(Gd/Yb)_n$ = 1.16-1.57). The Eu anomaly varies from slightly negative to positive (Eu/Eu* = 0.97-1.32; Fig. 10g). They are characterized by near-flat HFSE patterns and minor LILE enrichment in primitive mantle–normalized diagrams (Fig. 10h).

## 4.4 Nd isotopes

The Sm-Nd data for the Bonfim mafic-ultramafic rocks are plotted in Fig. 11 and summarized in Table 3 (Appendix A). In addition to the samples analyzed in this article, three mafic rock samples from Garcia et al. (2024) were included in constructing the isochron diagrams. The dataset comprises two distinct groups, represented by Paleoarchean and Mesoarchean intrusions. Their respective linear regressions produced different isochron ages. The first of twelve samples yields another linear regression pattern, with a slope corresponding to an age of 3615 ± 316 Ma. Analysis of the samples yielded $^{147}Sm/^{144}Nd$ ratios ranging from 0.1174 to 0.1837, $^{143}Nd/^{144}Nd$ ratios from 0.5108 to 0.5123, and εNd(t) values (calculated at the U–Pb age) between −2.55 and +1.11. The εNd(t) value calculated at the isochron age yields +0.3. Other Paleoarchean samples, mainly serpentinites and tremolitites, exhibited slightly anomalous $\varepsilon_{Nd}$ values. These results reflect disturbances in the Sm-Nd system by post-crystallization processes. For these, the $^{147}Sm/^{144}Nd$ ratios were between 0.1058 and 0.1958, and the $^{143}Nd/^{144}Nd$ ratios ranged from 0.5110 to 0.5123.

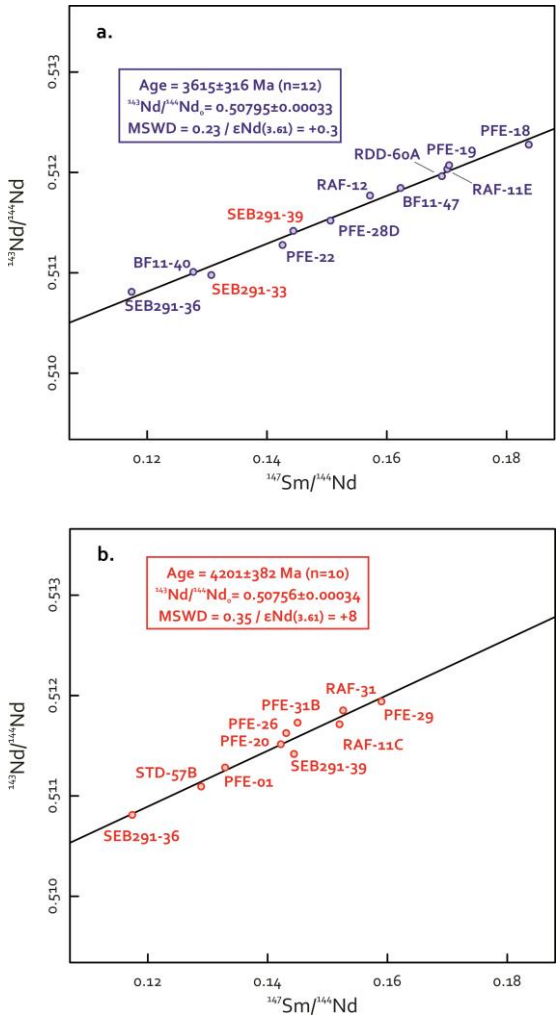



Figure 11 – Samples from the Bonfim Mafic–Ultramafic Complex defining a 4.20 Ga isochron (red circles) and a 3.61 Ga isochron (blue circles).

The oldest age was established based on the Mesoarchean samples. In the Sm-Nd diagram, these data yield an isochron with an age of 4201 ± 382 Ma (Fig. 11). Their $^{147}Sm/^{144}Nd$ and $^{143}Nd/^{144}Nd$ ratios range from 0.1174 to 0.1590 and from 0.5108 to 0.5121, respectively. The $\varepsilon_{Nd(t)}$ value (calculated at the U–Pb age) ranges from -3.89 to +3.02, indicating heterogeneities within the source region or mixing between mantle components and/or crustal contributions. The εNd(t) values calculated at the isochron ages are around +8.1. Although the age correlation is weak, four additional Mesoarchean samples were analyzed. They show $^{147}Sm/^{144}Nd$ ratios of 0.1239–0.1800 and $^{143}Nd/^{144}Nd$ ratios of 0.5112–0.5119, with $\varepsilon_{Nd(t)}$ values ranging from −6.82 to +2.63. The rocks are either strongly metasomatized or, when less altered, classified as amphibolites.

# 5 DISCUSSIONS

## 5.1 Geochemical effects of serpentinization

The PFE-19, PFE-15, and FOG-1-3 outcrops are composed exclusively of serpentinites. For these rocks, U-Pb dating of zircon grains indicates Paleoarchean ages between 3.57 62 Ma and 4.47 57 Ga. Geochemically, they are characterized by LOI values between 12.00 and 21.90 and MgO. Serpentinization, together with the superimposition of multiple later metasomatic processes, results in significant water incorporation into the system. Serpentine phases can contain more than 13 wt% $H_2O$ in their crystal structure, whereas talc typically contains ~4.7 wt% $H_2O$, and minerals such as chlorite may contain up to 14 wt% $H_2O$. All of this influences the high LOI values and the water balance of these samples. Major elements are generally the most susceptible to disturbance during hydration processes. Some studies suggest that slight variations in whole-rock Mg/Si ratios could reflect seawater–mantle interaction, differences in the degree of partial melting, modal mineralogy, and metasomatic processes, particularly those involving silica addition (Snow and Dick, 1995; Niu, 2004). In the $Al_2O_3/SiO_2$ versus $MgO/SiO_2$ diagram, the terrestrial array defines a magmatic depletion trend, extending from primitive mantle compositions in the lower right toward harzburgitic compositions in the upper left (Jagoutz et al., 1979; Hart and Zindler, 1986; Niu, 2004). In this diagram, the analyzed samples are characterized by low $Al_2O_3/SiO_2$ ratios, plotting slightly offset from the depleted mantle and below the terrestrial array. This distribution indicates that the protoliths likely experienced some degree of partial melting prior to serpentinization (e.g., Deschamps et al., 2013). On the other hand, the localized occurrence of talcified rocks suggests that lower $MgO/SiO_2$ ratios may be linked to silica enrichment.

Other elements, such as Na and especially Ca, can also show a depletion pattern resulting from serpentinization. In the Bonfim serpentinites, except for one sample, the Ca levels generally range from 0.03 to 2.96 wt%. These values are similar to those observed in abyssal peridotites and anhydrous ophiolites (Bodinier and Godard, 2003; Niu, 2004). However, according to Deschamps et

al., (2013), in this type of context, it is difficult to distinguish whether the low Ca contents reflect the composition of the protolith or are the result of later episodes. In the MgO versus $TiO_2$ diagram, the samples plot below the depleted mantle field, and their $TiO_2$ contents are consistent with values reported for mantle peridotites. However, the positive correlation between MgO and $TiO_2$ deviates from expected simple partial melting trends and may instead indicate metasomatic enrichment of Ti in a previously depleted mantle source or reflect control by modal variations of mineral phases (Johnson and Shimizu, 1990).

Studies suggest that while major elements are more susceptible to changes during hydration and serpentinization, trace elements and REEs generally remain more stable (e.g., Deschamps et al., 2012, 2013; Zhang et al., 2019; Zhang et al., 2024). This stability does not imply that their compositions are unaffected by hydrothermal processes; in fact, LREE enrichment is commonly observed. However, authors such as Deschamps et al. (2013) and Niu (2004) argue that elevated LREE concentrations likely reflect processes predating serpentinization, such as melt–rock interaction, whereas HREE generally remain reliable indicators of the primary composition of the rocks. This is supported by strong correlations observed between Yb and other relevant trace elements, indicating that they exhibit low mobility during the process of serpentinization (Fig. 12). According to Menzies et al. (1993) and O'Hanley (1996), the limited mobility of REEs during the hydration of peridotite can be attributed to the low abundance of clinopyroxene, which is the primary host for REEs. Clinopyroxene is more resistant to hydration compared to olivine and orthopyroxene.

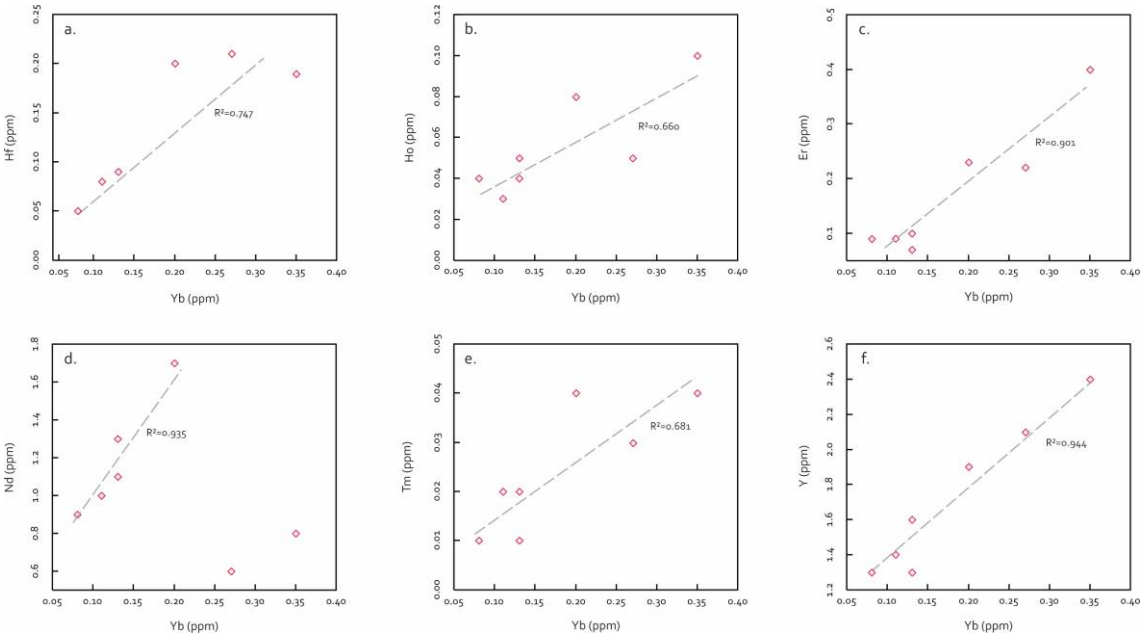



Figure 12 – Harker diagrams for Yb (ppm) and relevant trace elements (ppm).

## 5.1 Mantle dynamics and Paleoarchean petrogenetic evolution

Evidence for depleted mantle reservoirs in the Hadean eon is well established through Archean mantle-derived rocks. Simultaneously, recent studies reveal the presence of more enriched mantle components during the same eon (Morino et al., 2017; Garcia et al., 2023, 2024). These may represent initial reservoirs trapped deep in the mantle, which differentiated between 4.19 and 4.53 Ga (Boyet and Carlson, 2005; Rizo et al., 2011; O'Neil et al., 2016). In the Borborema Province, NE Brazil, traces of ancient enriched mantle reservoirs have been supported since Dantas et al. (2004). Specifically, in the São José do Campestre massif (see Dantas et al., 2013; Ribeiro et al., 2024) and later in the Bonfim mafic and ultramafic rock complex. In the latter case, Garcia et al. (2024) interpret negative $\mu^{142}$Nd values (~–10) as evidence that an enriched Hadean mantle significantly contributed to 3.5 Ga mafic magmatism in the Borborema Province, with mantle differentiation possibly occurring around 4.44 Ga. This coincides with evidence of depleted mantle sources in the North Atlantic and North China cratons (Morino et al., 2017; Liou et al., 2024).

The Paleoarchean samples identified in this study consist predominantly of serpentinites and tremolitites, with minor talc schists (not discussed here).

Geochemically, these rocks define two distinct groups. Serpentinites represent hydrated ultramafic rocks derived from mantle peridotites and record fluid–rock interaction processes that significantly modify their primary mineralogical and geochemical signatures. Although the main oxides and LREEs may have been affected by hydration, the incompatible elements and HREEs still show similarities to the protolith of these rocks, making them good indicators of their petrogenetic evolution. In chondrite-normalized REE diagrams, this pattern is characterized by slight LREE enrichment relative to HREE. The HREE segment indicates a highly refractory source, with concentrations lower than those estimated for the DMM (Depleted MORB Mantle; Workman and Hart, 2005) and the primitive mantle (PM), whereas the LREE pattern suggests subsequent refertilization or late-stage metasomatism. The HREE depletion relative to the DMM likely reflects a mantle source that is more strongly depleted than the average DMM composition. In such cases, element concentrations are primarily controlled by their partitioning behavior during partial melting, leading to progressively lower abundances of incompatible elements with increasing degrees of melt extraction.

In the MgO (wt%) versus $TiO_2$ (wt%) and Yb (ppm) versus La/Yb diagrams (Fig. 13a-b), these samples also show some depletion in relation to the DMM. In the Y (ppm) versus U (ppm) plot, these rocks plot predominantly within the field of abyssal peridotites (Fig. 13c). In the Gd/Yb versus Th (ppm) diagram, they fall within the field of serpentinized abyssal peridotites that have experienced melt–rock interaction (Fig. 13e). Dick and Bullen (1984) established that abyssal peridotites are residues of mantle melting associated with MORB generation. This type of lithology occurs mainly along slowly expanding domes (Deschamps et al., 2012, 2013), in which mantle peridotites are frequently exposed on the seabed, along normal faults, in oceanic core complexes, or along transform faults. Here, the geochemical affinity with abyssal peridotites, together with refractory HREE signatures and slight LREE enrichment, indicates a mantle source that underwent significant melt extraction, followed by localized refertilization and subsequent serpentinization. In these abyssal settings, serpentinization is primarily driven by hydrothermal circulation at mid-ocean ridges, although its intensity varies from site to site (Deschamps et al., 2013). In the Bonfim serpentinites, Fig. 13f shows

a magmatic depletion trend influenced by increased serpentinization in these samples. According to Deschamps et al. (2012), elements such as U tend to occur at higher concentrations in serpentitic minerals.

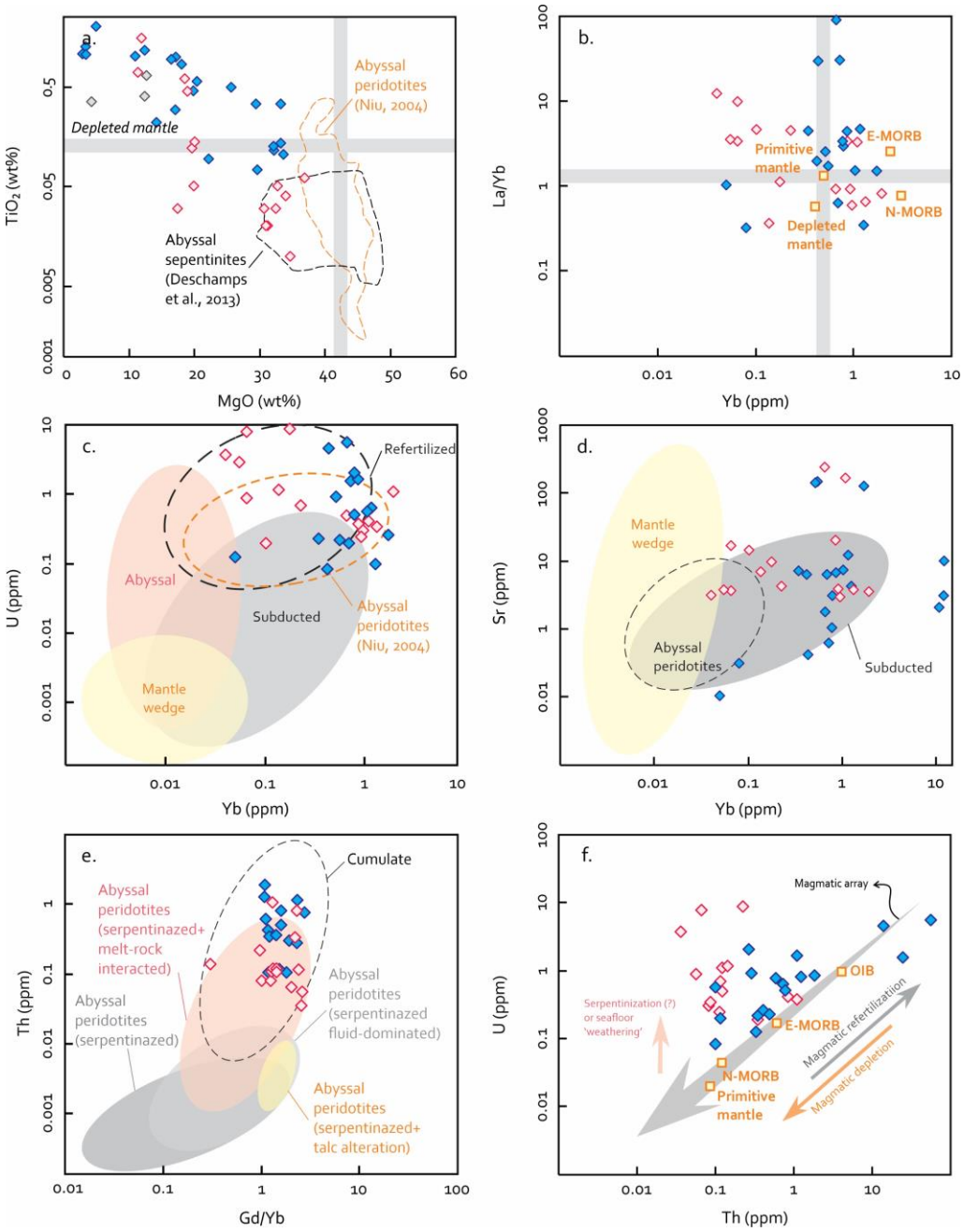



Figure 13 – a. MgO (wt%) versus $TiO_2$ (wt%) (after Deschamps et al., 2013). b. Plots of Yb versus La/Yb (after Deschamps et al., 2013). c-d. Yb (ppm) versus U (ppm) and Yb (ppm) versus Sr (ppm) after Deschamps et al., (2013). e. Gd/Yb versus Th (ppm) plot from (Zuo et al., 2022). f. Th (ppm) versus U (ppm) from Niu (2004). Paleoarchean samples – pink diamond. Mesoarchean samples – blue diamond.

The second group of Paleoarchean samples mainly concerns tremolitites and hornblendites stretched and oriented according to the regional SW-NE trend. With the exception of late quartz injections and opaque phases, these rocks are almost entirely monomineralic. The late quartz input is reflected in $SiO_2$ contents of 52.49 to 55.62 wt%, while low LOI values (0.97 to 2.22 wt%) indicate a reliable primary signature. Moderate to high concentrations of $Al_2O_3$ (5.73–8.56 wt%) and CaO (9.13–11.28 wt%), along with moderate MgO levels (11.28–19.99 wt%), do not align with typical mantle peridotites (Eggins et al., 1998). Chemically, the main distinction between this group and the first lies in the presence of an enrichment pattern that is absent in the latter. These samples plot above the depleted mantle (DMM) field in the MgO (wt%) versus $TiO_2$ (wt%) diagram (Fig. 13a), indicating Ti enrichment relative to depleted mantle compositions. In agreement, the Yb (ppm) versus La/Yb and Yb (ppm) versus U (ppm) diagrams show a coherent enrichment trend (Fig. 13b-c). In chondrite- and primitive mantle-normalized diagrams, this group of rocks is characterized by a systematic enrichment in REEs and other incompatible elements relative to the serpentinites of the previous group. In mantle-derived rocks, olivine and orthopyroxene play a negligible role in hosting REEs, whereas clinopyroxene represents the principal reservoir for these elements (Johnson et al., 1990). Although REE enrichment can, in some cases, be attributed to subsequent metasomatic processes, their $^{147}Sm/^{144}Nd$ ratios (0.1788–0.19958) are subchondritic and closely match the CHUR standard (Faure, 2005). In fact, the εNd(3.61 Ga) values for these samples are +0.3, indicating near-CHUR compositions with only a slight positive deviation. These values suggest limited disturbance of the Sm–Nd system, arguing against pervasive late-stage metasomatic overprinting. Rather, they indicate preservation of a mantle-derived signature with minimal differentiation, while also being inconsistent with highly depleted sources.

Clinopyroxene-dominated source is associate with (I) mantle metasomatism (Gao et al., 2004), (II) high-pressure cumulates (Fan et al., 2001; Xu, 2002; Downes, 2007), or (III) subsolidus differentiation through modal segregation of minerals in the upper mantle (Chen et al., 2001). Metasomatic overprinting complicates detailed petrographic characterization. Nevertheless, in

the Gd/Yb versus Th (ppm) diagram, the samples predominantly plot within the cumulate field, pointing to a likely cumulate origin and a prior stage of mineral accumulation. To date, the most suitable depleted analogues to the enriched Paleoarchean mantle sources identified in Borborema are those documented in the North Atlantic and North China cratons. However, our new data indicate that enriched and depleted sources coexist in the same space and time. As documented in other regions, the evolutionary history of this type of primitive mantle is interpreted to include at least two discrete differentiation stages. In these models, an initially enriched reservoir would have produced a more depleted reservoir following the process of differentiation. Unfortunately, the $^{147}Sm/^{144}Nd$ ratios for serpentinites are isotopically disturbed, making their accurate application unfeasible. However, their correspondence with the DMM indicates that these rocks are potentially the depleted analogue that had not yet been identified in the region.

### 5.2 Petrogenesis and geochemical evolution of Mesoarchean intrusions

In contrast to the reports on Paleoarchean types, there have been no documented cases of Mesoarchean (~3.1 Ga) mafic and ultramafic intrusions in the local literature. The spatial connections and repeated lithological features suggest possible theories of cogeneticity, indicating that these materials may have originated from the same mantle system. This may involve recurrent melting and episodic or reactivated magmatic activity over time. However, certain constraints must be considered. Based on petrography, MgO and CaO levels, as well as the contents of trace and incompatible elements, these samples were categorized into four distinct subgroups. Here, the pattern of rare earth elements REEs and LILEs is considerably higher than what is observed in Paleoarchean samples, suggesting that the sources may not be as depleted as the DMM identified previously. Or it may simply signify greater metasomatic contributions.

The first set corresponds to tremolitites, which contain trace amounts of opaque minerals, rutile, and rare aggregates of late quartz. These tremolitites exhibit low LOI values ranging from 1.24 to 2.06 wt% and $SiO_2$ content between 52.00 and 53.30 wt%. Similar to Paleoarchean tremolitites, they have elevated

CaO values between 9.02 and 9.12 wt%, MgO levels ranging from 12.05 to 19.35 wt%, and an Mg# value of 33 to 56. Figure 13a shows that most samples plot above the DMM field, and in the Yb (ppm) versus La/Yb diagram they cluster near the enriched mantle domain. The same enrichment pattern is also observed in the Yb (ppm) versus U (ppm) and Yb (ppm) versus Sr (ppm) diagrams (Fig. 13c-d), as well as in the dispersion of the samples along the magmatic refertilization trend shown in Fig. 13f. In the Gd/Yb versus Th (ppm) graph (Fig. 13e), they are mainly concentrated in the cumulative field. In comparison to Paleoarchean tremolitites, these rocks display a slight enrichment in LREEs, LILEs, Nb, Ta, and Zr. The $Al_2O_3$ contents (4.78–8.02 wt%), coupled with relatively elevated CaO values and LREE-enriched to slightly fractionated REE patterns, are consistent with a contribution from a clinopyroxene-rich source (Marchesi et al. 2013). Cr levels range from 984 to 1745 ppm. According to Le Roux et al. (2007), the association between elevated Cr contents and Al2O3 and moderate to high Fe2O3 is consistent with mantle refertilization, possibly related to the formation or addition of clinopyroxene and spinel (Marchesi et al. 2013). Notable negative anomalies for Sr and Eu show oscillations between positive and negative values, suggesting either the absence of plagioclase or the removal of this mineral phase during the primary crystallization of these rocks.

Overall, the data indicate an enriched precursor source. The $^{147}Sm/^{144}Nd$ ratios (0.1290–0.1800) reflect partial preservation of an initially subchondritic reservoir (Garcia et al., 2024), while also indicating disturbance of the Sm–Nd system. The $\varepsilon_{Nd(t)}$ values (−6.82 to +4.49) suggest a heterogeneous evolution, with the positive values pointing to the involvement of a relatively depleted mantle component, likely reflecting inheritance from a previously depleted mantle protolith preserved even after metasomatism, whereas the negative values indicate enrichment and/or crustal influence. In addition, the εNd(4.2 Ga) value of +8 indicates a markedly depleted mantle signature at earlier stages, reinforcing the interpretation that the source region experienced prior depletion events before subsequent enrichment and isotopic re-equilibration. Together, these features are consistent with a combination of source heterogeneity and subsequent processes such as metasomatism, selective crustal contamination, and mineral-controlled fractionation.

The second subgroup, composed of samples RDD-60, RDD-60-B, and RDE-18, differs from the tremolitites by its slightly higher CaO and REE contents. MgO contents range from 17.58 to 18.39 wt%, with aluminum ranging from 5.65 to 8.92 wt%. Cr is between 1895 and 3543 ppm, indicating lower levels of differentiation. The third group is mainly composed of hornblendites, tremolitites, and chloritites, reflecting variable degrees of alteration (LOI ranging from 0.65 to 11.90 wt%, with the highest values observed in the most altered chloritites). In the Yb (ppm) versus La/Yb diagram, these samples are dispersed across the enriched mantle fields, a pattern that is similarly observed in the Yb (ppm) versus U (ppm) and Yb (ppm) versus Sr (ppm) plots. Their high degree of alteration is further reflected in the Th (ppm) versus U (ppm) diagram.

The amphibolites are classified as basaltic andesites on the TAS diagram and display a tholeiitic affinity (supplementary figures S1-S2), with $SiO_2$ contents ranging from 52.00 to 53.20 wt%, MgO from 5.53 to 6.44 wt%, and $Fe_2O_3$ contents between 12.20 and 13.25 wt%. They display negative Nb–Ta and Ti anomalies on the primitive mantle–normalized spider diagram. The REE patterns and primitive mantle–normalized incompatible trace element patterns are characterized by LREE enrichment relative to HREE, with LILEs being markedly enriched compared to HFSE. Their HFSE depletion observed is consistent with derivation from mantle sources that may have experienced prior melt extraction. The variable enrichment in LILE and LREE suggests that an initially depleted mantle source was likely modified by slab-derived fluids and/or melts within the subduction mantle wedge. Together, these features are compatible with the evolution of a tholeiitic magmatic system. The εNd(t) values (−0.90 to +2.63) further support a relatively juvenile signature, although they may also reflect some degree of source heterogeneity or subsequent modification.

In the regional context, many metasomatic mineral phases are related to the circulation of hot fluids derived from Neoproterozoic pervasive magmatism, or may represent products of metamorphic re-equilibration after the subsurface exposure of these bodies. However, the occurrence of rocks with IAT affinity in the Archean Bonfim area reinforces the interpretation that part of this lithological association was influenced by early subduction-related processes. This is because oceanic crust formation, spreading, and subsequent convergence

commonly promote amphibole crystallization, including amphibole accumulations formed by replacement of precursor clinopyroxene grains. In hot subduction zones, amphibole fractionation occurs through the interaction between residual fluids and previously formed clinopyroxene grains (Smith, 2014). Under these conditions, the amphibole acts as an efficient reservoir for water and incompatible trace elements, facilitating their redistribution within the mantle wedge (Dvaison et al., 2007). While further studies are needed, establishing a Mesoarchean subduction zone may have been the precursor to the first enrichment and hydration of these rocks, consistent with the local development of serpentinites and chloritites and the occurrence of blackwalls in the regional context (Santiago et al., 2019).

### 5.4 Geodynamic implications

In classical ophiolite models (e.g., the Penrose type; Anonymous, 1972), when well preserved, the basal section is dominated by highly to extremely depleted residual peridotites, commonly harzburgite. These rocks are interpreted as fragments of depleted mantle that served as the source of the overlying mafic and ultramafic units (Kusky, 2004). They may also include layers of pyroxenite, dunite, wehrlite, and websterite, and locally contain chromite and olivine nodules. The interface between the most primitive peridotites and their melt-extraction products defines the petrological Moho. At higher structural levels, stratified gabbros are overlain by isotropic gabbros and swarms of mafic dikes. Owing to the distinctive nature of the Archean crust — characterized by greater thickness, different geodynamic regimes, higher mantle temperatures, and long-term preservation constraints — recognition of ophiolites in this time interval is generally restricted to dismembered slices or incomplete ophiolitic sections within greenstone belts, none of which preserves a complete sequence.

The Paleoarchean ultramafic intrusions of Bonfim comprise a diverse assemblage of rocks, including extremely depleted serpentinites associated with more enriched lithologies (e.g., tremolitites and chloritites), likely derived from clinopyroxenitic sources, as well as olivine websterites and gabbros. The latter two lithologies were described by Velásquez Ruiz et al. (2019) and Garcia et al.

(2024), and the geochemical affinity of the serpentinites with abyssal peridotite affinity, consistent with a mid-ocean ridge setting. Although relict MORB signatures are absent from the regional geological record, the REE patterns of the serpentinites are inconsistent with an arc-related setting. Zircon from these samples yields an age of 3.57 ± 62 Ga, within the range of 3.74 ± 12 to 3.52 ± 5 Ga reported for serpentinites in the region (Santos et al., 2020). Their REE abundances are also comparable to those of previously described serpentinites, as shown in chondrite-normalized patterns. Santos et al. (2020) interpreted the 3.74 ± 0.12 Ga value as the crystallization age of these rocks; however, subsequent sampling in the region has not reproduced this result. If this interpretation is correct, the lack of overlap between the ages does not preclude a genetic relationship between them. A plausible explanation proposed by Griffin et al. (2014) is that, between the Hadean and the Mesoarchean, periodic inversions of the asthenospheric mantle were relatively common. These mantle overturn events could fragment, recycling, and replenishing lithospheric layers at intervals of approximately 150–200 Ma. The time span of ~200 Ma proposed by Griffin et al. (2014) is consistent with the age range obtained here (~ 3.5 – 3.1 Ga), which can be interpreted as successive magmatic pulses separated by hundreds of millions of years.

Nevertheless, from ~3.53 ± 28 Ga (U–Pb zircon age) onward, lithological repetition is no longer observed, and the stratigraphy becomes progressively more differentiated, reflecting the crystallization of enriched melts. Accordingly, the emergence of more enriched lithologies from ~3.5 Ga in the Bonfim region may reflect a change in mantle conditions during the Archean. Here, although no doubt enriched mantle reservoirs already existed in the Hadean, these components appear to have found conditions favorable for crystallization only from ~3.5 Ga onwards, effectively remaining stored in a kind of hidden enriched mantle reservoir before that time. This shift likely reflects major changes in mantle dynamics, including decreased efficiency of melt extraction, secular mantle cooling, or similarly linked to the final stages of magma ocean solidification (Caro et al., 2005; Griffin et al., 2014). Together, the association of extensively depleted mantle sources, represented by serpentinites, with rocks derived from clinopyroxenitic sources and overlain by gabbroic units points to an ancient

oceanic crust. This may represent a dismembered ophiolitic sequence in which only the basal section has been preserved (Fig. 14).

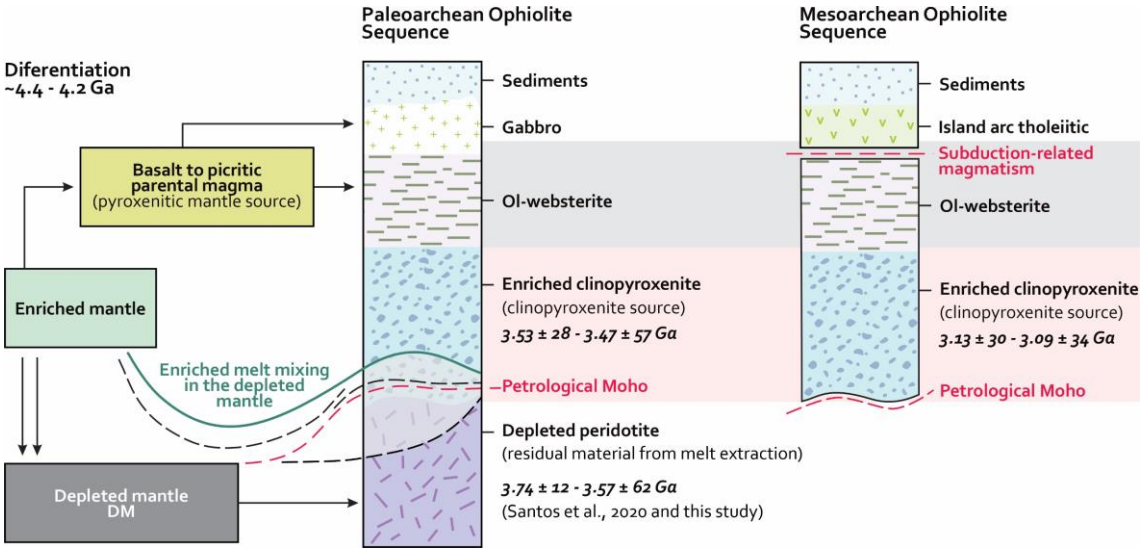



Figure 14 – Block diagram illustrating the mixing of enriched melts into a depleted mantle reservoir; and stratigraphic columns showing Paleo- and Mesoarchean ophiolite sequences preserved in the Bonfim area.

As observed in other parts of the world (e.g., Pedersen et al., 1991; Dilek et al., 1997; Furnes et al., 2012), mafic and ultramafic intrusions at ~3.1 Ga are interpreted as representing a second episode of oceanic crust formation. In contrast, the rocks described here are slightly enriched, show no clear evidence of preserved depleted peridotite signatures, and are dominated by tremolitites derived from clinopyroxenitic sources, as well as websterites and amphibolites with IAT affinities. However, the main difference lies in the fact that the island arc tholeiites display a typical subduction-related signature. The Sm–Nd isochron ages obtained for these lithologies point to Hadean source components, comparable to those described by Garcia et al. (2024). After exerting a significant influence on Paleoarchean mafic and ultramafic magmatism in the RGND, the same system was reactivated during the Mesoarchean, approximately 200 Ma later. It is possible that typical subduction-related lavas originated from the same pre-existing refractory peridotite residue, which, once progressively depleted, was refertilized through the direct influence of fluids released from the subducting plate. This influence is reflected in the enrichment of LREEs relative to HREEs,

as well as LILEs relative to HFSEs.

The metamorphic peaks in the Bonfim region have not been precisely dated. Nevertheless, high-grade metamorphic events at ~2.0 and ~0.6 Ga have been reported in the RGND (Dantas et al., 2004; Souza et al., 2016). Slightly earlier, the Rhyacian magmatism (2.24 ± 16 to 2.16 ± 6.9 Ga), represented by amphibolite bodies, is interpreted as another magmatic event that affected the northernmost sectors of the study area. These episodes were followed by at least three metasomatic events at 597 ± 5 Ma (phlogopite $^{40}Ar/^{39}Ar$ plateau ages; Velásquez Ruiz et al., 2019), 524 ± 2 Ma (molybdenite Re–Os; Hollanda et al., 2017), and 517 ± 6 Ma (phlogopite $^{40}Ar/^{39}Ar$ plateau ages; Velásquez Ruiz et al., 2019). All of which are associated with the emplacement of numerous Ediacaran plutons in the area.

## 6 CONCLUSIONS

Using an integrated dataset of whole-rock geochemistry, U–Pb zircon and rutile geochronology, and whole-rock Sm–Nd isotopic data from representative mafic and ultramafic intrusions of the Bonfim Complex (RGND, Borborema Province, Brazil), we draw the following conclusions regarding igneous protoliths, mantle sources, crystallization ages, petrogenesis, and Archean geodynamic setting:

1) Crystallization and petrogenetic evolution of mafic and ultramafic intrusions in the complex occur during two distinct episodes. The first episode is dated between 3.57 ± 30 and 3.47 ± 57 Ma (U-Pb in zircon). The second episode ranges from 3.09 ± 34 to 3.13 ± 30 Ma.
2) Paleoarchean serpentinites show depleted peridotite compositions and DMM-like HREE–HFSE patterns and are chemically consistent with Eoarchean intrusions previously described in the region (Santos et al., 2020).
3) The lithogeochemistry of Paleoarchean tremolitites and hornblendites resembles clinopyroxenite enriched mantle sources. The temporal and spatial relationships between Cr-spinel–rich clinopyroxenites and DMM-like peridotites indicate the coexistence of enriched and depleted sources

within the same mantle system.

4) Mesoarchean ultramafic protoliths are clinopyroxenites and are interpreted as being derived from enriched mantle sources. The associated amphibolites display an IAT-type geochemical affinity, suggesting that the system may have been influenced by subduction-related processes already during the Mesoarchean.
5) Sm–Nd isochron ages obtained for these episodes yield linear regressions of 4.20 ± 382 Ga and 3.61 ± 316 Ga, indicating that mantle differentiation processes were already active since the Hadean eon.
6) These intrusions are understood as a highly fragmented ophiolitic sequence. They exhibit a wide variety of stratigraphic, structural, and compositional features that reflect their development in an oceanic environment, especially within a mid-ocean ridge setting, until their subduction during the Mesoarchean era.

## Declaration of Generative AI and AI-assisted technologies in the writing process

The author(s) used Grammarly AI (v1.2.116.1536) to enhance language and readability. They reviewed and edited the content and take full responsibility for the publication.

## Declaration of competing interest

The authors declare that they have no known competing financial interests or personal relationships that could have appeared to influence the work reported in this paper.

## Acknowledgements

The authors would like to express their gratitude to the Coordenação de Aperfeiçoamento de Pessoal de Nível Superior (CAPES) and the Conselho Nacional de Desenvolvimento Científico e Tecnológico (CNPq - 444320/2020-2)

for their financial support. ELD and RAF are also grateful to CNPq for providing research fellowships. Additionally, the authors extend their thanks to the technical staff of the Laboratório de Estudos Geodinâmicos, Geocronológicos e Ambientais at the Universidade de Brasília for their assistance.

## References

Adame-Martínez, M.G., Solari, L.A., Ortega-Obregón, C. & Abdullin, F., 2020. U–Pb geochronology of rutile: deciphering the cooling history of the Oaxacan Complex granulites, southern Mexico. Revista Mexicana de Ciencias Geológicas, 37(2), 135–145. doi.org/10.22201/cgeo.20072902e.2020.2.1557.

Akbari, M., Ghorbani, M.R., Cousens, B.L., Graham, I.T., 2023. A robust discrimination scheme for ocean island basalts based on Ce/Rb, Tb/La, and Ba/Nb ratios. Chemical Geology 628, 121486. https://doi.org/10.1016/j.chemgeo.2023.121486.

Almeida, F.F.M., Hasui, Y., Brito Neves, B.B., Fuck, R.A., 1981. Brazilian structural provinces: an introduction. Earth Sci. Rev. 17, 1–29. doi.org/10.1016/0012-8252(81)9.

Alvim, P.F.T., Dantas, E.L., Fuck, R.A., Ferreira, A.C.D., 2026. A lost fragment of Siderian oceanic and juvenile arc crust preserved in the Borborema Province, northeast Brazil. Precambrian Research 433, 107979. doi.org/10.1016/j.precamres.2025.107979.

Anders, E., Grevesse, N., 1989. Abundances of the elements: meteoritic and solar. Geochimica et Cosmochimica Acta 53, 197–214. https://doi.org/10.1016/0016-7037(89)90286-X.

Anonymous, 1972. Definition of ophiolites. Geotimes 17, 24–25.

Archanjo, C.J., Hollanda, M.H.B.M., Rodrigues, S.W., Brito Neves, B.B., 2008. Fabrics of pre- and syntectonic granite plutons and chronology of shear zones in

the Eastern Borborema Province, NE Brazil. J. Struct. Geol. 30, 310–336. doi.org/10.1016/j.jsg.2007.11.011.

Arthaud, M. H., Caby, R., Fuck, R. A., Dantas, E. L., Parente, C. V., 2008. Geology of the northern Borborema Province, NE Brazil and its correlation with Nigeria, NW Africa. In: Pankhurst, R. J., Trouw, R. A. J., Brito Neves, B. B., De Wit, M. J. (Eds.), West Gondwama: Pre-Cenozoic Correlations Across the South Atlantic Region. Geological Society of London, Special Publications. 294, 49-67.

Bennett, V.C., Brandon, A.D., Nutman, A.P., 2007. Coupled 142Nd–143Nd isotopic evidence for Hadean mantle dynamics. Science 318 (5858), 1907–1910. doi.org/10.1126/science.1145928.

Bonatti, E., Michael, P.J., 1989. Mantle peridotites from continental rifts to ocean basins to subduction zones. Earth and Planetary Science Letters 91 (3–4), 297–311. doi.org/10.1016/0012-821X(89)90005-8.

Boyet, M., Carlson, R.W., 2005. $^{142}$Nd evidence for early (>4.53 Ga) global differentiation of the silicate Earth. Science 309 (5734), 576–581. doi.org/10.1126/science.1113634.

Brito Neves, B.B., Santos, E.J. dos, Van Schmus, W.R., 2000. Tectonic history of the Borborema Province, northeastern Brazil. In: Cordani, U., Milani, E.J., Thomaz Filho, A., Campos, D.A. (Eds.), Tectonic evolution of South America. 31st International Geological Congress, Rio de Janeiro, Brazil, pp. 151–182. repositorio.usp.br/directbitstream/82959a42-149a-48b4-8c64-b34fa2c6f949/1131015.pdf.

Caby, R., 1989. Precambrian terranes of Benin, Nigeria and northeast Brazil and the Late Proterozoic South Atlantic fit. Geological Society of America Special Paper 230, 145–158.

Caro, G., Bourdon, B., Birck, J.-L., Moorbath, S., 2003. 146Sm-142Nd evidence

from Isua metamorphosed sediments for early differentiation of the Earth's mantle. Nature 423, 428–432. doi.org/10.1038/nature01668.

Caro, G., Bourdon, B., Wood, B.J., Corgne, A., 2005. Trace-element fractionation in Hadean mantle generated by melt segregation from a magma ocean. Nature 436, 246–249. doi.org/10.1038/nature03827.

Carvalho, O.O. 1990. Geologia e petroquímica de uma sequência metavulcanossedimentar do Nordeste da Faixa Seridó, sudeste de Lajes/RN, Rio Grande do Norte. Master's Thesis, Universidade Federal do Rio Grande do Norte, Natal, 198 p.

Caxito, F.A., Uhlein, A., Dantas, E.L., Stevenson, R., Salgado, S.S., Dussin, I.A., Sial, A.N., 2016. A complete Wilson Cycle recorded within the Riacho do Pontal Orogen, NE Brazil: implications for the Neoproterozoic evolution of the Borborema Province at the heart of West Gondwana. Precambrian Research 282, 97–120. doi.org/10.1016/j.precamres.2016.07.001.

Chen, S., O'Reilly, S.Y., Zhou, X., Griffin, W.L., Zhang, G., Sun, M., Feng, J. & Zhang, M., 2001. Thermal and petrological structure of the lithosphere beneath Hannuoba, Sino-Korean Craton, China: evidence from xenoliths. Lithos, 56(4), 267–301. doi.org/10.1016/S0024-4937(00)00065-7.

Cordani, U.G., Nutman, A.P., Williams, S., 2004. The 3.4-3.5 São José do Campestre Massif, NE Brazil: remnants of the oldest crust in South America. Precambr. Res. 130,113–137. doi.org/10.1016/j.precamres.2003.11.002.

Corgne, A., Liebske, C., Wood, B.J., Rubie, D.C., Frost, D.J., 2005. Silicate perovskite–melt partitioning of trace elements and geochemical signature of a deep perovskitic reservoir. Geochimica et Cosmochimica Acta 69, 485–496. doi.org/10.1016/j.gca.2004.07.026.

Corsini, M., de Figueiredo, L.L., Caby, R., Fëraud, G., Ruffet, G., Vauchez, A.,

1998. Thermal history of the Pan-African/Brasiliano Borborema Province of northeast Brazil deduced from 40Ar/39Ar analysis. Tectonophysics 285, 103–117. doi.org/10.1016/S0040-1951(97)00192-3.

Curvo, E.A.C., Hadler Neto, J.C., Iunes, P.J., Guedes, S.O., Tello Sáenz, C.A., Paulo, S.R., Hackspacher, P.C., Palissari, R., Moreira, P.A.F.P., 2005. On epidote fission track dating. Radiat Meas 39, 641–645. doi.org/10.1016/j.radmeas.2004.06.016.

Dantas, E. L., Negrão, M. M., Bühn, B. M., 2008. 2.3 Ga continental crust generation in the Rio Grande do Norte terrane, ne - Brazil. In: VI South American Symposium on Isotope Geology, San Carlos de Bariloche.

Dantas, E.L., de Souza, Z.S., Wernick, E., Hackspacher, P.C., Martin, H., Xiaodong, D., Li, J.W., 2013. Crustal growth in the 3.4–2.7 Ga São José do Campestre Massif, Borborema Province, NE Brazil. Precambrian Research 227, 120–156. doi.org/10.1016/j.precamres.2012.08.006.

Dantas, E.L., Van Schmus, W.R., Hackspacher, P.C., Fetter, A.H., Brito Neves, B.B.B., Cordani, U.G., Nutman, A.P., Williams, I.S., 2004. The 3.4–3.5 Ga São José do Campestre massif, NE Brazil: remnants of the oldest crust in South America. Precambrian Res. 130, 113–137. doi.org/10.1016/j.precamres.2003.11.002.

Davidson, J., Turner, S., Handley, H., Macpherson, C. & Dosseto, A., 2007. Amphibole “sponge” in arc crust? Geology, 35(9), 787–790. doi.org/10.1130/G23637A.1.

Debaille, V., O’Neill, C., Brandon, A.D., Haenecour, P., Yin, Q.Z., Mattielli, N., Treiman, A.H., 2013. Stagnant-lid tectonics in early Earth revealed by 142Nd variations in late Archean rocks. Earth and Planetary Science Letters 373, 83–92. doi.org/10.1016/j.epsl.2013.04.016.

Deschamps, F., Godard, M., Guillot, S., Chauvel, C., Andreani, M., Hattori, K., Wunder, B., France, L., 2012, Behavior of fluid-mobile elements in serpentines from abyssal to subduction environments: Examples from Cuba and Dominican Republic Chemical Geology 312–313, 93–117, https://doi.org/10.1016/j.chemgeo.2012.04.009.

Deschamps, F., Godard, M., Guillot, S., Hattori, K., 2013, Geochemistry of subduction zone serpentinites: A review, Lithos 178, 96–127, http://dx.doi.org/10.1016/j.lithos.2013.05.019.

DePaolo, D. J., 1981. A neodymium and strontium isotopic study of the Mesozoic calcalkaline granitic batholiths of the Sierra Nevada and Peninsular ranges, California. Journal of Geophysical Research 86:10,470–10,488. doi.org/10.1029/JB086iB11p10.

Dick, H.J.B., Bullen, T., 1984. Chromian spinel as a petrogenetic indicator in abyssal and alpine-type peridotites and spatially associated lavas. Contributions to Mineralogy and Petrology 86, 54–76.

Dilek, Y., Coulton, A., & Hurst, S. D., 1997. Serpentinization and hydrothermal veining in peridotites at Site 920 in the MARK area (Leg 153). In J. A. Karson, M. Cannat, D. J. Miller & D. Elthon (Eds.), Proceedings of the Ocean Drilling Program, Scientific Results (Vol. 153, pp. 35–59). Ocean Drilling Program, College Station, TX. doi.org/10.2973/odp.proc.sr.153.004.1997.

Domingos, N.R.R., Medeiros, W.E., Oliveira, R.G., 2020. Geophysical evidence for doming during the Pan-African/Brasiliano orogeny in the Seridó belt, Borborema Province, Brazil. Precambrian Research 351, 105870. doi.org/10.1016/j.precamres.2020.105870.

Ebert, H., 1970. The Precambrian geology of the “Borborema” belt (States of Paraíba and Rio Grande do Norte) and the origin of its mineral provinces. Geologische Rundschau 59, 1294–1327.

Eggins, S.M., Rudnick, R.L. & McDonough, W.F., 1998. The composition of peridotites and their minerals: a laser-ablation ICP–MS study. Earth and Planetary Science Letters, 154(1–4), 53–71. doi.org/10.1016/S0012-821X(97)00195-7.

Faure, G., 2005. Isotopes: Principles and Applications. 3rd edition. John Wiley & Sons, Hoboken, NJ.

Fetter, A.H., Van Schmus, W.R., Santos, T.J.S., Arthaud, M.H., Nogueira Neto, J.A., 2003. Evidence for Neoproterozoic continental collision in the Borborema Province, NE Brazil: implications for the assembly of West Gondwana. Gondwana Research 6, 273–294. doi.org/10.1016/S1342-937X(05)70971-7.

Furnes, H., Dilek, Y., Pedersen, R.B., 2012. Structure, geochemistry, and tectonic evolution of trench-distal back-arc oceanic crust in the western Norwegian Caledonides: The Solund–Stavfjord ophiolite (Norway). Geological Society of America Bulletin 124, 1027–1047. doi.org/10.1130/B30561.1.

Ganade de Araújo, C.E., Weinberg, R.F., Cordani, U.G., 2014. Extruding the Borborema Province (NE Brazil): a two-stage Neoproterozoic collision process. Terra Nova 26, 157–168. doi.org/10.1111/ter.12084.

Gao, S., Rudnick, R.L., Yuan, H.L., Liu, X.M., Liu, Y.S., Xu, W.L., Ling, W.L., Ayers, J., Wang, X.C. & Wang, Q.H., 2004. Recycling lower continental crust in the North China craton. Nature, 432, 892–897. doi.org/10.1038/nature03162.

Garcia, V.B., O'Neil, J., Dantas, E.L., 2023. Rare evidence for the existence of a Hadean enriched mantle reservoir. Geochemical Perspect. Lett. 28, 1–6. doi.org/ 10.7185/geochemlet.2336.

Garcia, V.B., O'Neil, J., Dantas, E.L., Augustin, C.T., 2024. Composition and age constraints on a Hadean enriched mantle source revealed by the Paleoarchean São Tomé layered intrusion, NE Brazil. Earth and Planetary Science Letters 647,

119051. doi.org/10.1016/j.epsl.2024.119051.

Gioia, S.M.C.L., Pimentel, M.M., 2000. The Sm-Nd isotopic method in the geochronology laboratory of the University of Brasília. Anais da Academia Brasileira de Ciências 72(2), 219–245.

Griffin, W.L., Belousova, E.A., O'Neill, C., O'Reilly, S.Y., Malkovets, V., Pearson, N.J., Spetsius, S. & Wilde, S.A., 2014. The world turns over: Hadean–Archean crust–mantle evolution. Lithos, 189, 2–15. doi.org/10.1016/j.lithos.2013.08.018.

Hackspacher, P.C., Van Schmus, W.R., Dantas, E.L., 1990. Um embasamento transamazônico na Província Borborema. In: Congresso Brasileiro De Geologia, 36. Sociedade Brasileira de Geologia, Natal, pp. 2683–2696.

Harrison, T.M., Blichert-Toft, J., Müller, W., Albarède, F., Holden, P., Mojzsis, S.J., 2005. Heterogeneous Hadean hafnium: evidence of continental crust by 4.4–4.5 Ga. Science 310, 1947–1950. doi.org/10.1126/science.1117926.

Harrison, T.M., Schmitt, A.K., McCulloch, M.T., Lovera, O.M., 2008. Early (≥ 4.5 Ga) formation of terrestrial crust: Lu–Hf, $\delta^{18}O$, and Ti thermometry results for Hadean zircons. Earth and Planetary Science Letters 268, 476–486. doi.org/10.1016/j.epsl.2008.02.011.

Hollanda, M.H.B.M., Archanjo, C.J., Bautista, J.R., Souza, L.C., 2015. Detrital zircon ages and Nd isotope compositions of the Seridó and Lavras da Mangabeira basins (Borborema Province, NE Brazil): evidence for exhumation and recycling associated with a major shift in sedimentary provenance. Precambr. Res. 258, 186–207. doi.org/10.1016/j.precamres.2014.12.009.

Hollanda, M.H.B.M., Archanjo, C.J., Souza, L.C., Dunyi, L., Armstrong, L., 2011. Longlived Paleoproterozoic granitic magmatism in the Serido-Jaguaribe ´ domain, Borborema Province-NE Brazil. J. S. Am. Earth Sci. 32, 287–300. doi.org/10.1016/j.jsames.2011.02.008.

Hollanda, M.H.B.M., Souza Neto, J.A., Archanjo, C.J., Stein, H., Maia, A.C.S., 2017. Age of the granitic magmatism and the WMo mineralization in skarns of the Seridó belt (NE Brazil) based on zircon UPb (SHRIMP) and molybdenite ReOs dating. J. S. Am. Earth Sci. 79, 1–11. doi.org/10.1016/j.jsames.2017.07.011.

Hollocher, K., Robinson, P., Walsh, E., Roberts, D., 2012. Geochemistry of amphibolite-facies volcanics and gabbros of the Støren nappe in extensions west and southwest of Trondheim, Western Gneiss Region, Norway: a key to correlations and paleotectonic settings. American Journal of Science 312, 357–416. https://doi.org/10.2475/04.2012.01.

Jackson, S.E., Pearson, N.J., Griffin, W.L., Belousova, E.A., 2004. The application of laser ablation-inductively coupled plasma-mass spectrometry to in situ U–Pb zircon geochronology. Chem. Geol. 211 (1–2), 47–69. doi.org/10.1016/j.chemgeo.2004.06.017.

Jardim de Sá, E.F., 1994. A Faixa Seridó (Província Borborema, NE do Brasil) e o seu significado geodinâmico na cadeia Brasiliana/Pan Africana. Universidade de Brasília, Brasília, Thesis, p. 803.

Johnson, K. T. M., Dick, H. J. B. & Shimizu, N. (1990). Melting in the oceanic upper mantle: an ion microprobe study of diopside in abyssal peridotites. Journal of Geophysical Research 95, 2661–2678.

Kemp, A.I.S., Wilde, S.A., Hawkesworth, C.J., Coath, C.D., Nemchin, A., Pidgeon, R.T., Vervoort, J.D., DuFrane, S.A., 2010. Hadean crustal evolution revisited: New constraints from Pb-Hf isotope systematics of the Jack Hills zircons. Earth and Planetary Science Letters 296 (1-2), 45–56. doi.org/10.1016/j.epsl.2010.04.043.

Kusky, T.M. (Ed.), 2004. Precambrian ophiolites and related rocks. Developments in Precambrian Geology, Vol. 13. Elsevier, Amsterdam, 772 pp. ISBN: 978-0-444-50923-9.

Lesnov, F.P., 2010. Rare Earth Elements in Ultramafic and Mafic Rocks and Their Minerals: Main Types of Rocks. Rock-forming Minerals. CRC Press, London. ISBN 978-0415578905.

Liang, Y. & Elthon, D., 1990. Evidence from chromium abundances in mantle rocks for extraction of picrite and komatiite melts. Nature, 343, 551–553. doi.org/10.1038/343551a0.

Liou, P., Caro, G., Cui, X., Li, C., Peng, P., Guo, J., Zhai, M., 2024. Long-term isolation of Hadean mantle domains revealed from coupled 147-146Sm-143-142Nd systematics in the eastern North China Craton. Earth and Planetary Science Letters 638, 118761. doi.org/10.1016/j.epsl.2024.118761.

Liu, Y.S., Gao, S., Lee, C.T.A., Hu, S.H., Liu, X.M. & Yuan, H.L., 2005. Melt–peridotite interactions: links between garnet pyroxenite and high-Mg# signature of continental crust. Earth and Planetary Science Letters, 234(1–2), 39–57. doi.org/10.1016/j.epsl.2005.02.034.

Luvizotto, G.L., Zack, T., Meyer, H.P., Ludwig, T., Triebold, S., Kronz, A., Münker, C., Stockli, D.F., Prowatke, S., Klemme, S., Jacob, D.E., von Eynatten, H., 2009. Rutile crystals as potential trace element and isotope mineral standards for microanalysis. Chemical Geology 261 (3–4), 346–369. doi.org/10.1016/j.chemgeo.2008.04.012.

Maltese, A., Caro, G., Pandey, O.P., Upadhyay, D., Mezger, K., 2022. Direct evidence for crust–mantle differentiation in the late Hadean. Communications Earth & Environment 3, 15. doi.org/10.1038/s43247-022-00341-9.

Morino, P., Caro, G., Reisberg, L., Schumacher, A., 2017. Chemical stratification in the post-magma ocean Earth inferred from coupled 146,147Sm–142,143Nd systematics in ultramafic rocks of the Saglek block (3.25–3.9 Ga; northern Labrador, Canada). Earth Planet. Sci. Lett. 463, 136–150. doi.org/10.1016/j.epsl.2017.01.044.

Nascimento, M.A.L., Galindo, A.C., Medeiros, V.C., 2015. Ediacaran to Cambrian granitoid magmatism in the Seridó Belt, Borborema Province, NE Brazil: Tectonic implications for West Gondwana assembly. Journal of South American Earth Sciences 58, 161–180. doi.org/10.1016/j.jsames.2014.09.008.

Neves, S.P., 2015. Constraints from zircon geochronology on the tectonic evolution of the Borborema Province (NE Brazil): Widespread intracontinental Neoproterozoic reworking of a Paleoproterozoic accretionary orogen. Journal of South American Earth Sciences 58, 150–164. doi.org/10.1016/j.jsames.2014.08.004.

Nicolas, A., Prinzhofer, A., 1983. Cumulative or residual origin for the transition zone in ophiolites: structural evidence. Journal of Petrology 24 (2), 188–206. doi.org/10.1093/petrology/24.2.188.

Niu, Y., 2004. Bulk-rock major and trace element compositions of abyssal peridotites: implications for mantle melting, melt extraction and post-melting processes beneath mid-ocean ridges. Journal of Petrology 45(12), 2423–2458. https://doi.org/10.1093/petrology/egh068.

Niu, Y., Langmuir, C.H., Kinzler, R.J., 1997. The origin of abyssal peridotites: a new perspective. Earth and Planetary Science Letters 152 (1–4), 251–265. doi.org/10.1016/S0012-821X(97)00119-2.

O'Neil, J., Rizo, H., Boyet, M., Carlson, R.W., Rosing, M.T., 2016. Geochemistry and Nd isotopic characteristics of Earth's Hadean mantle and primitive crust. Earth and Planetary Science Letters 442, 194–205. doi.org/10.1016/j.epsl.2016.02.055.

Oliveira, R.G., Medeiros, W.E., 2018. Deep crustal framework of the Borborema Province, NE Brazil, derived from gravity and magnetic data. Precambrian Research 315, 45–65. doi.org/10.1016/j.precamres.2018.07.004.

Paton, C., Hellstrom, J., Paul, B., Woodhead, J., Hergt, J., 2011. Iolite: Freeware for the Visualisation and Processing of Mass Spectrometric Data. J. Anal. at. Spectrom. VL -IS -. doi.org/10.1039/C1JA10172B.

Pearce, J. A., 2008. Geochemical fingerprinting of oceanic basalts with applications to ophiolite classification and the search for Archean oceanic crust. Lithos. 100, 14–48. https://doi.org/10.1016/j.lithos.2007.06.016.

Pedersen, R. B., Furnes, H. & Dunning, G. R., 1991. A U/Pb age for the Sulitjelma Gabbro, North Norway; further evidence for the development of a Caledonian marginal basin in Ashgill–Llandovery time. Geological Magazine, 128(2), 141–153. doi.org/10.1017/S0016756800018331.

Petrus, J., Kamber, B.S., 2012. VizualAge: a novel approach to laser ablation ICP-MS UPb geochronology data reduction. Geostand. Geoanal. Res. 36 (3), 247–270. doi.org/10.1111/j.1751-908X.2012.00158.x.

Ribeiro, C.V.A., Dantas, E.L. & Fuck, R.A., 2025. Effects of high-temperature annealing and low-temperature metamictization on Archean zircon: constraints from U–Pb isotopes, trace elements and Raman dating. American Mineralogist, 110(8), 1291–1302. doi.org/10.2138/am-2024-9502.

Ribeiro, C.V.A., Dantas, E.L., Fuck, R.A., 2024. Paleoarchean sedimentation and Mesoarchean high-temperature metamorphism in northeastern Brazil: Tracing sources and depositional ages in polymetamorphic rocks. Lithos 478, 107641. doi.org/10.1016/j.lithos.2024.107641.

Rizo, H., Boyet, M., Blichert-Toft, J., Rosing, M., 2011. Combined Nd and Hf isotope evidence for deep-seated source of Isua lavas. Earth Planet. Sci. Lett. 312, 267–279. doi.org/10.1016/j.epsl.2011.10.014.

Roth, A.S.G., Bourdon, B., Mojzsis, S.J., Touboul, M., Sprung, P., Guitreau, M., BlichertToft, J., 2013. Inherited 142Nd anomalies in Eoarchean protoliths. Earth

Planet. Sci. Lett. 361, 50–57. doi.org/10.1016/j.epsl.2012.11.023.

Salim, J., 1979. Geologia e controle das mineralizações scheelitíferas da região da Serra do Feiticeiro e Bonfim, Lages-RN. M.Sc. dissertation, Universidade de Brasília, Brasília, Brazil, 106 pp.

Santiago, J.S., da Silva Souza, V., Dantas, E.L., de Oliveira, C.G., 2019. Ediacaran emerald mineralization in Northeastern Brazil: the case of the Fazenda Bonfim Deposit. Brazilian Journal of Geology 49 (4), e20190081. doi.org/10.1590/2317-4889201920190081.

Santos, F.G., Cavalcanti Neto, M.T.O., Ferreira, V.P., Bertotti, A.L., 2020. Eo to Paleoarchean metamafic-ultramafic rocks from the central portion of the Rio Grande do Norte Domain, Borborema Province, northeast Brazil: the oldest South American platform rocks. J. South Am. Earth Sci. 97, 102410. doi.org/10.1016/j.jsames.2019.102410.

Santos, L.C.M.L., Dantas, E.L., Santos, E.J., Santos, R.V., Lima, H.M., 2015. Early to late Paleoproterozoic magmatism in NE Brazil: the Alto Moxoto Terrane and its tectonic implications for the pre-West Gondwana assembly. J. S. Am. Earth Sci. 58, 188–209. doi.org/10.1016/j.jsames.2014.07.006.

Schneider, K.P., Hoffmann, J.E., Boyet, M., Münker, C., Kroner, ¨ A., 2018. Coexistence of enriched and modern-like 142Nd signatures in Archean igneous rocks of the eastern Kaapvaal Craton, southern Africa. Earth Planet. Sci. Lett. 487, 54–66. doi. org/10.1016/j.epsl.2018.01.022.

Sharkov, E.V. & Bogatikov, O.A., 1985. Ultramafic cumulates in crustal magmatic chambers. In: Precambrian Magmatism and Tectonics, Elsevier, Amsterdam, pp. 45–60.

Skuzovatov, S.Y., Rizvanova, N.G., Skublov, S.G. & Shatsky, V.S., 2023. U–Pb ID-TIMS age of rutile from the North Muya Block eclogites (northeastern

Transbaikal Area) as a tracer of the duration for exhumation of the continental lithosphere. Doklady Earth Sciences, 512(1), 810–818. doi.org/10.1134/S1028334X23601049.

Sláma, J., Košler, J., Condon, D. J., Crowley, J. L., Gerdes, A., Hanchar, J. M., Horstwood, M. S. A., Morris, G. A., Nasdala, L., Norberg, N., Schaltegger, U., Schoene, B., Tubrett, M. N., Whitehouse, M. J., 2008. Plešovice zircon — A new natural reference material for U–Pb and Hf isotopic microanalysis. Chemical Geology. 249(1–2), 1-35. dx.doi.org/10.1016/j.chemgeo.2007.11.005.

Snow, J.E., Dick, H.J.B., 1995. Pervasive magnesium loss by marine weathering of peridotite. Geochimica et Cosmochimica Acta 59, 4219–4235.

Smith, D.J., 2014. Clinopyroxene precursors to amphibole sponge in arc crust. Nature Communications, 5, 5329. doi.org/10.1038/ncomms5329.

Souza Neto, J.A., Legrand, J.M., Volfinger, M., Pascal, M.-L., Sonnet, P., 2008. W–Au skarns in the Neo-Proterozoic Seridó Mobile Belt, Borborema Province in northeastern Brazil: an overview with emphasis on the Bonfim deposit. Mineralium Deposita 43 (2), 185–205. doi.org/10.1007/s00126-007-0155-1.

Souza, Z.S., Kalsbeek, F., Deng, X.-D., Frei, R., Kokfelt, T.F., Dantas, E.L., Li, J.-W., Pimentel, M.M., Galindo, A.C., 2016. Generation of continental crust in the northern part of the Borborema Province, northeastern Brazil, from Archaean to Neoproterozoic. Precambrian Research 277, 1–18. doi.org/10.1016/j.precamres.2016.02.006.

Souza, Z.S., Martin, H., Peucat, J.J., Jardim de Sá, E.F., Macedo, M.H.F., 2007. CalcAlkaline Magmatism At the Archean-Proterozoic transition: the Caicó complex Basement (Ne Brasil). Jounal of Petrology. 48, 2149–2185. doi.org/10.1093/petrology/egm055.

Souza, Z.S., Vasconcelos, P.M., Nascimento, M.A.L., Silveira, F.V., Paiva, H.S.,

Dias, L.G. S., Thiede, D., Carmo, I.O., 2003. 40Ar/39Ar geochronology of Mesozoic and Cenozoic magmatism in NE Brazil. Available at: Isotope Geology South American Symposium 310–313. horizon.documentation.ird.fr/exl-doc/pleins_textes/divers17-05/010039206.pdf.

Sun, S. S., McDonough, W. F., 1989. Chemical and isotopic systematics of oceanic basalts: implications for mantle composition and processes. In Saunders, A. D., and Norry, M. J., eds. Magmatismin ocean basins. Geol. Soc. Lond. Spec. Publ. 42:313–345. http://dx.doi.org/10.1144/GSL.SP.1989.042.01.19.

Tomlinson, E.L., Kamber, B.S., 2021. Depth-dependent peridotite-melt interaction and the origin of variable silica in the cratonic mantle. Nature Communications 12, 1082. doi.org/10.1038/s41467-021-21343-9.

Van Schmus, W. R., Oliveira, E. P., Silva Filho, A. F., Toteu, S. F., Penaye, J., Guimarãaes, I. P., 2008. Proterozoic links between the Borborema Province, NE Brazil, and the Central African Fold Belt. In: Pankhurst R. J., Trouw R. A. J., Brito Neves B. B and De Wit M. J. (eds.) West Gondwana: Pre-Cenozoic correlations across the South Atlantic region. Geological Society, London, Special Publication. 294, 69-99. doi.org/10.1144/SP294.

Van Schmus, W.R., Brito Neves, B.B., Williams, I.S., Hackspacher, P.C., Fetter, A.H., Dantas, E.L., Babinski, M., 2003. The Seridó Group of NE Brazil, a late Neoproterozoic pre-to syn-collisional basin in West Gondwana: insights form SHRIMP U-Pb detrital zircon ages and Sm-Nd crustal residence (TDM) ages. Precambr. Res. 127, 287–327. doi.org/10.1016/S0301-9268(03)00197-9.

Van Schmus, W.R., Kozuch, M., Brito Neves, B.B., 2011. Precambrian history of the Zona Transversal of the Borborema Province, NE Brazil: insights from Sm–Ndand U–Pb geochronology. J. S. Am. Earth Sci. 31, 227–252. doi.org/10.1016/j.jsames.2011.02.010.

Velásquez Ruiz, F., Della Giustina, M.E.S., de Oliveira, C.G., Dantas, E.L.,

Hollanda, M.H. B., 2019. The 3.5 Ga São Tomé layered mafic-ultramafic intrusion, NE Brazil: insights into a Paleoarchean Fe-Ti-V oxide mineralization and its reworking during West Gondwana assembly. Precambrian Res 326, 462–478. doi.org/10.1016/j.precamres.2018.03.011.

Wiedenbeck, M., Priyanka, A., Corfu, F., Griffin, W., Meier, M., Oberli, F., von Quadt, A., Roddick, J.C., Spiegel, W., 2007. Three natural zircon standards for U-Th-Pb, Lu-Hf, trace element and REE analyses. Geostand. Newslett. 19 (1–23). doi.org/10.1111/j.1751-908X.1995.tb00147.x.

Workman, R.K., Hart, S.R., 2005. Major and trace element composition of the depleted MORB mantle (DMM). Earth and Planetary Science Letters 231, 53–72. doi.org/10.1016/j.epsl.2004.12.005.

Xu, Y.-G., 2002. Evidence for crustal components in the mantle and constraints on crustal recycling mechanisms: pyroxenite xenoliths from Hannuoba, North China. Chemical Geology, 182(2–4), 301–322. doi.org/10.1016/S0009-2541(01)00300-X.

Yang, J., Wang, C., Zhang, J. & Jin, Z., 2023. Genesis of Hawaiian lavas by crystallization of picritic magma in the deep mantle. Nature Communications, 14, 1382. doi.org/10.1038/s41467-023-37072-0.

Zhang, L., Wei-dong Sunb, W., Chen, R., 2019, Evolution of serpentinite from seafloor hydration to subduction zone metamorphism: Petrology and geochemistry of serpentinite from the ultrahigh pressure North Qaidam orogen in northern Tibet, Lithos 346–347, 105158, https://doi.org/10.1016/j.lithos.2019.105158.

Zhang, M., Zhao, J., Guo, J., Chen, X., Peng, X., 2024, Origin and multi-episodic melt/fluid interactions revealed by the subducted serpentinites in the North Qilian Belt, NW China: Implications for the compositional heterogeneity of the fossil oceanic mantle

Zuo, J., Williams, H.M., Yardley, B.W.D., 2022. Earth's earliest phaneritic ultramafic rocks: mantle slices or cumulates? Geochemistry, Geophysics, Geosystems 23(9), e2022GC010519. https://doi.org/10.1029/2022GC010519.

## Supplementary Information

### Supplementary Note 1

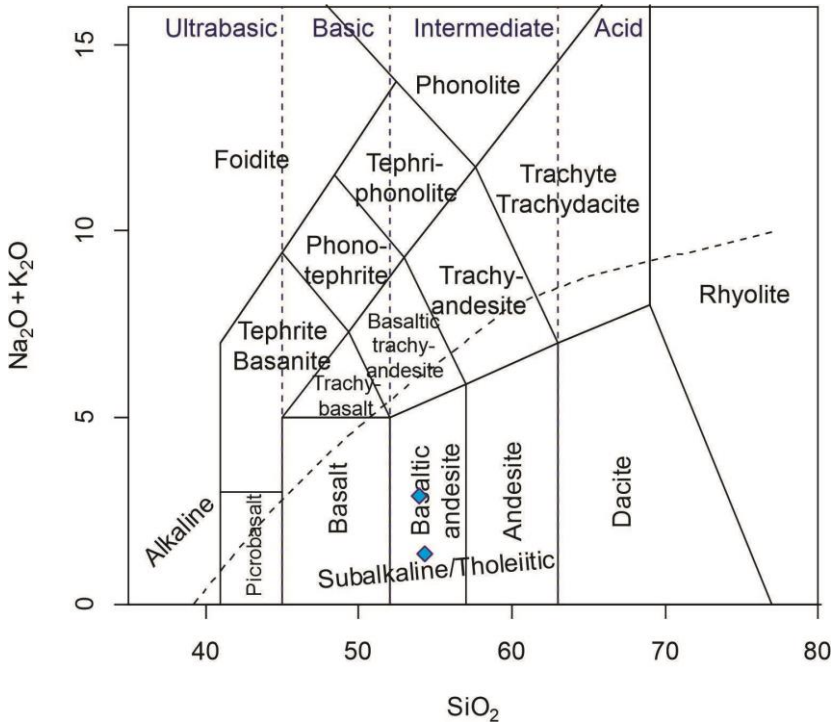



Fig. S1 – TAS ($Na_2O+K_2O$–$SiO_2$) diagram (Le Bas et al., 1986) showing the amphibolites (blue diamond).

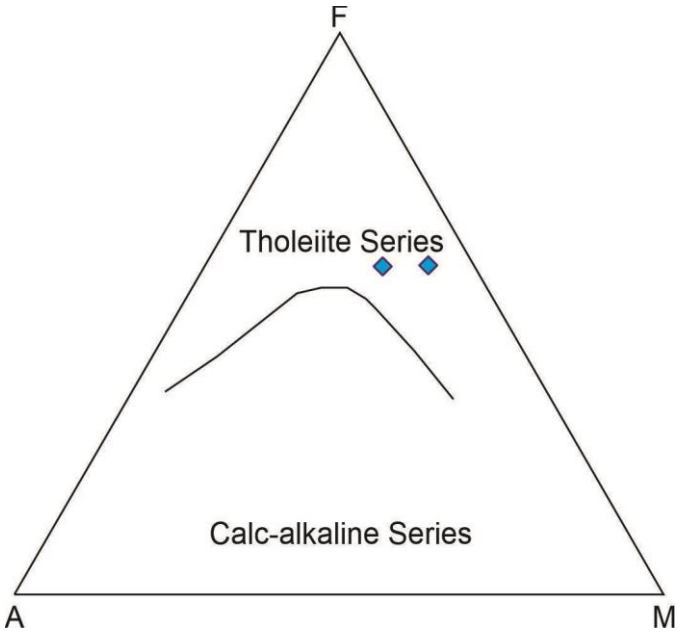



Fig. S2 – AFM (Na2O+K2O–MgO–FeOt) diagram (Irvine and Baragar, 1971) showing the amphibolites (blue diamond).

## References

Irvine, T. N. J., Baragar, W. R. A. F., 1971. A guide to the chemical classification of the common volcanic rocks. Canadian Journal of Earth Sciences. 8 (5), 523–548.https://ui.adsabs.harvard.edu/link_gateway/1971CaJES...8..523I/doi:10.1139/e71-055.

Le Bas, M. J., Le Maitre, R. W., Streckeisen, A., & Zanettin, B. (1986). A chemical classification of volcanic rocks based on the total alkali–silica diagram. Journal of Petrology, 27, 745–750. https://doi.org/10.1093/petrology/27.3.745.

# CAPÍTULO 5
# ARTIGO II

# 5 A LOST FRAGMENT OF SIDERIAN OCEANIC AND JUVENILE ARC CRUST PRESERVED IN THE BORBOREMA PROVINCE, NORTHEAST BRAZIL

Paula F.T. Alvim[1], Elton L. Dantas[1], Reinhardt A. Fuck[1], Alanielson C.D. Ferreira[1]

[1]Instituto de Geociências, Universidade de Brasília, Brasília, DF, Brazil, paulafreiretrindade@gmail.com, angicos63@gmail.com, reinhardt@unb.br, alanielson.ferreira@unb.br.

https://doi.org/10.1016/j.precamres.2025.107979

## ABSTRACT

The Tectono-Magmatic Lull (TML), or Siderian Quiet Interval, represents a pivotal stage in Earth's history between 2.36 and 2.23 Ga, marked by a global reduction in tectonic activity, magmatism, and crustal growth. It features a global decline in tectonic activity, magmatism, and crustal formation, creating a major gap in the geotectonic record worldwide. To investigate this interval, detailed field mapping, petrography, U–Pb zircon geochronology, whole-rock geochemistry, and Sm–Nd isotopic analyses were carried out on rocks from the Santa Luzia Sequence in the Lajes Block, Borborema Province (NE Brazil). The sequence, consisting of amphibolites, calc-silicate rocks, and hornblendites, yields U–Pb zircon ages ranging from 2.48 to 2.31 Ga, along with an older amphibolite dated at 3.14 Ga. Whole-rock geochemical patterns exhibit pronounced negative Nb, Ta, and Ti anomalies, indicating oceanic and arc-related affinities. Sm–Nd isotopic data reinforce this framework: juvenile lithotypes show positive $\varepsilon_{Nd(t)}$ values and Nd $T_{DM}$ ages of 2.36–2.12 Ga, whereas a subset of amphibolites preserves significantly older Nd $T_{DM}$ ages (3.97–2.62 Ga), revealing an Archean crustal substrate predating arc assembly. Coeval plutonic rocks document continued crustal reworking and juvenile addition from the Siderian into the Rhyacian. Spatial, geochemical, and isotopic relationships indicate that the calc-silicate rocks formed through metasomatic alteration of mafic precursors. Despite later

metasomatic and hydrothermal overprints that produced LREE enrichment and fluid-driven metamorphism, the primary magmatic signatures remain well preserved. Collectively, these results show that subduction-related magmatism persisted locally in Borborema, in contrast with the TML and tectonic shutdown theories.

**Keywords:** Tectono-Magmatic-Lull, Siderian, Santa Luzia Sequence, subduction, juvenile oceanic crust.

## 1 INTRODUCTION

Nearly three decades ago, Condie (1998) proposed that the global geological record shows episodic patterns. By analyzing U-Pb isotopic data from zircon grains globally, he connected distribution peaks to events of supercontinent formation occurring around 2.7, 1.9, and 1.2 Ga. In contrast, the intervals between these formations corresponded to significant decreases in crustal growth. This hypothesis is particularly relevant to the transition of the Archean and Proterozoic eons. Research indicates that over 50% of the Earth's current continental crust formed during the Archean eon, alongside the initial lithospheric amalgamation (Williams et al., 1991; Bleeker, 2003; Belousova et al., 2010; Dhuime et al., 2012). Following the Archean, the Early Paleoproterozoic represents a major lull in geotectonic evidence, the largest ever documented (Condie et al., 2009), possibly associated with the breakup of the first supercontinent (Strand and Köykkä, 2012).

Initially, this lacuna was estimated to last around 250 Ma, occurring between approximately 2.45 and 2.2 Ga (Condie et al., 2009; Condie and O'Nell, 2010). However, subsequent studies have narrowed this timeframe to approximately 2365 to 2235 Ma (Spencer et al., 2018; Condie et al., 2022). The Siderian Quiet Interval, also known as the Tectono-Magmatic Lull (TML), is marked by a global decrease in orogenic and magmatic activity (Condie et al., 2009; Condie and O'Nell, 2010; Pehrsson et al., 2014). This decline is primarily attributed to a complete and prolonged quiescence in plate tectonics – the shutdown hypothesis (O'Nell et al., 2007; Condie et al., 2009). However, the

concept of complete plate tectonic disconnection faced challenges in gaining acceptance, particularly among advocates of continuous crustal production over geological time (e.g., Partin et al., 2014; Pehrsson et al., 2014; Yang and Santosh, 2015). For these researches, the reduction in the geotectonic record is likely due to the destruction of the Earth's lithosphere through subduction, recycling, and metamorphic or orogenic reworking. This reduction may also result from biased geochronological data sampling or peripheral orogenies forming after creating the first supercratons (Pehrsson et al., 2014). In the latter case, while the cratonic interior remained stable, several orogenies around it would have been responsible for forming mainly island arcs, which are more difficult to preserve.

The theme's more recent actualization supports the thesis that there is no longer a shutdown but rather a tectonic slowdown (Spencer et al., 2018; Condie et al., 2022). Continental drift velocities before and after the TML resemble modern tectonic movement, but during the lull, drift slowed significantly, akin to conditions in low trench-effect regions (Forsyth and Uyeda, 1975; Spencer et al., 2018). Paleomagnetic evidence suggests a decoupling between slower-moving continental plates and faster oceanic plates during this timespan, with subduction likely occurring in external oceanic arcs while continental magmatism is temporarily halted (Spencer et al., 2018). Nevertheless, the main point is that all assumptions are based on the fact that rock segments dating from the beginning of the Paleoproterozoic, while not quantitatively significant, can be cataloged on all continents.

Inserted in this significant debate, we are presenting new field mapping, petrology, geochemistry and geochronological isotopic data of Siderian rocks from the Lajes Block in the northeast of the Borborema Province (BP), northeastern Brazil (Negrão et al., 2005; Dantas et al., 2008; Costa et al., 2021). The Santa Luzia Sequence (SLS), named by Dantas et al. (2008), is an Early Paleoproterozoic unit that includes E-MORB-like basalts, low-K tholeiitic volcanic rocks, metasomatic hydrothermal calc-silicate rocks (skarns) and a hornblendite. Furthermore, the new findings indicate that the Santa Luzia rocks may be remnants of ancient Siderian oceanic crust. Further detailed investigation was carried out to understand the origin and geodynamic context of these rocks and

their connection to global tectonics, which has been linked to a period of widespread tectonic slowing down.

## 2 GEOLOGICAL BACKGROUND

The Borborema Province covers an area of approximately 450,000 km² in the northeasternmost part of Brazil (Fig. 1a). It is a sizable Precambrian region formed from the convergence of the West Africa-São Luiz, Amazonian, and São Francisco-Congo cratons at c. 600 Ma (Almeida et al., 1981; Jardim de Sá, 1994; Trompette, 1994; Ganade et al., 2016). Throughout its evolutionary history, the superposition of distinct deformational, metamorphic, and magmatic episodes, coupled with a wide structural intricacy, has made this province a complex study system. The lithological framework of the BP primarily consists of extensive Paleoproterozoic gneiss-migmatite basement complexes (Brito Neves et al., 2000; Fetter et al., 2000; Souza et al., 2007, 2016; Dantas et al., 2008; Van Schmus et al., 2008; Santos et al., 2009; Santos et al., 2015, 2017), with minor Archean cores (e.g., Dantas et al., 2004; Arthaud et al., 2008; Ferreira et al., 2020). Neoproterozoic metasedimentary and metavolcanic sequences are present, forming major fold belts within it (Van Schmus et al., 2003; Hollanda et al., 2015).

The Brasiliano Orogeny (~640–550 Ma) transformed this framework into low- to high-grade metamorphic conditions, emplaced numerous granitic plutons, and developed large-scale shear zones (Vauchez et al., 1995; Archanjo et al., 2008; Neves et al., 2021). Researchers use these structures to divide the Borborema Province into northern, central, and southern sub-provinces. Litho-structural features then create informal geotectonic segments (Santos and Medeiros, 1999; Brito Neves et al., 2000; Neves, 2003; Van Schmus et al., 2011).

Located at the limit of the northern sub-province, the Rio Grande do Norte Domain (RGND) is one of these segments (Fig. 1b). The RGND, located at the northern sub-province limit, is bordered by the Portalegre Shear Zone to the west and the Patos Shear Zone to the south, with Phanerozoic sedimentary basins covering the north and east. The integration of field observations, whole-rock geochemical data, Nd isotopic signatures, U–Pb zircon ages and petrogenetic

constraints, with gamma-ray spectrometric measurements (K, Th, and U channels) enabled the subdivision of the RGND basement into three Archean massifs (São José do Campestre, Bonfim, and Campo Grande) and also three Paleoproterozoic crustal blocks. These blocks consist dominantly of high-grade migmatite–gneiss complexes, bounded or internally dissected by several shear zones that record local adjustments. The identified blocks are Antônio Martins, Caicó–São Vicente, and Lajes (Dantas et al., 2003).

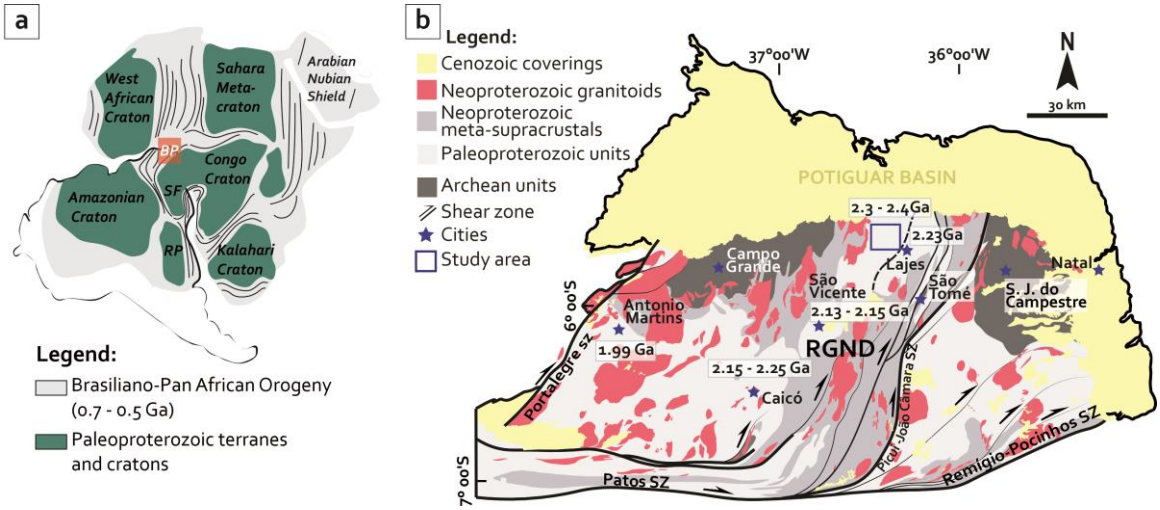



Figure 1 – Geological maps and lithological-structural relations. a. Localization of the Rio Grande do Norte domain (RGDN) in West Gondwana setting. b. Schematic and simplified map of RGND, showing its regional tectonism and geological framework (modified from Jardim de Sá, 1994; Medeiros et al., 2017). U–Pb zircon ages for the basement of each block are presented in the figure (Angelim, 2006 and references therein; Souza et al., 2007; Costa et al., 2018).

## 2.1 Lajes Block

The Lajes area, situated in northern RGND, covers approximately 2,270 km² and is bordered to the north by the Potiguar Basin's Phanerozoic cover and to the east and south by Neoproterozoic supracrustal rocks from the Seridó Group (Van Schmus et al., 2008, 2011). Dextral shear zones occur at the interface with metasedimentary rocks of the Seridó Group and nearby Brasiliano granitic intrusions (Fig. 2a-b).

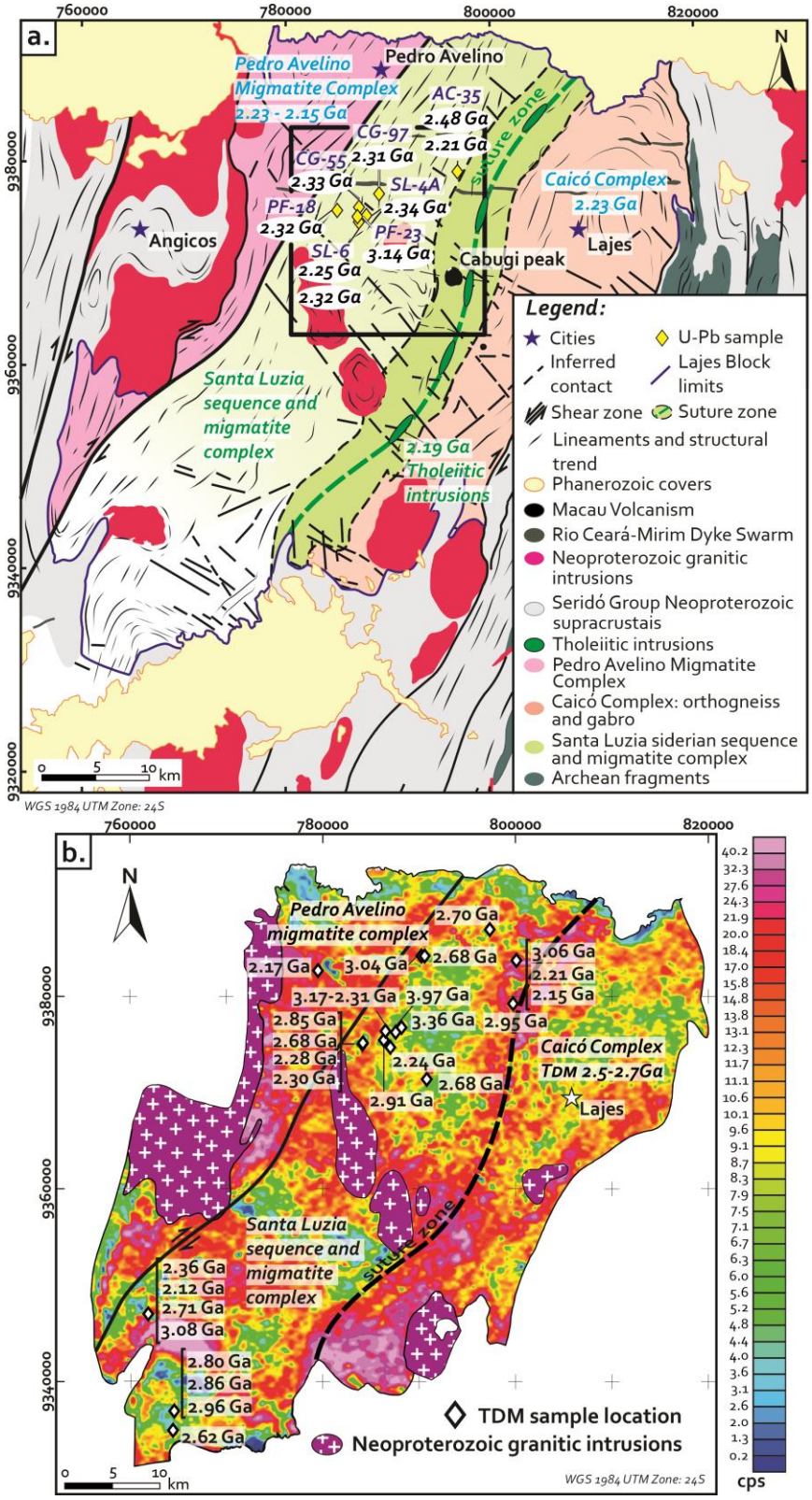



Figure 2 – Geological framework of the Lajes Block in the central part of the Rio Grande do Norte Domain. a. Study area delimited by a black rectangle and U-Pb sample localization in the Lajes Block setting. b. The Th map (modified from Danta et al., 2003) of the Lajes Block region showing the distribution of $T_{DM}$ and $\varepsilon_{Nd}$ values. Geochronological data for the Caicó and Pedro Avelino complexes are provided Souza et al. (2007) and Costa et al. (2018).

For a long time, the Lajes block basement was only identified as part of the Caicó Complex with a Rhyacian age (U–Pb zircon ages of 2.23-2.11 Ga; Hackspacher et al., 1990; Jardim de Sá, 1994; Souza et al., 2007, 2016; Hollanda et al., 2011). However, Dantas et al. (2008) and Costa et al. (2021) indicate that new findings also suggest the presence of Siderian fragments, which imply a new division among the into Paleoproterozoic units. These Paleoproterozoic rocks include granodioritic and tonalitic orthogneisses and migmatites (U–Pb zircon age of 2.45 ± 4.2 Ga; Costa et al., 2021), and the volcano-sedimentary rocks of the SLS (Negrão et al., 2005; Dantas et al., 2008). The Santa Luzia rocks comprise low-K tholeiitic amphibolites, calc-silicate rocks, and banded iron formations. Other plutonic rocks like gabbros, tonalites, and granodiorites dated at 2.31 ± 37 Ga (U-Pb zircon age), mark contemporaneous Siderian continental arc magmatism in the Lajes Block (Dantas et al., 2008).

Here, the Caicó Complex is considered exclusively as a plutonic unit in the eastern block area, consisting of granodiorite and granite orthogneisses, with U-Pb ages around 2.23 ± 7.3 Ga (U-Pb zircon age; Costa et al., 2018). On the western border of the Lajes Block, a high-K migmatitic granite gneiss dating from 2.23 to 2.15 Ga (U-Pb zircon ages) has been identified as a new unit, designated here as the Pedro Avelino Migmatite Complex. The Pedro Avelino Complex differs from the Caicó Complex by exhibiting a higher degree of Brasiliano migmatization. Mafic and ultramafic intrusions emplaced within the orthogneisses and migmatites, dated at 2.19 ± 9.8 Ga (U–Pb zircon age), are interpreted as representing the final stage of evolution of the West Lajes Block (Ferreira et al., 2019), while also expressing cogenetic relationships with the Caicó Complex rocks to the east of the Lajes Block. This boundary between the SLS and the Caicó Complex is further delineated by a linear feature identified as a Rhyacian suture zone in magnetotelluric data (Padilha et al., 2021). All this lithological arrangement shows subtle, straight structural features along a NNE-SSW trend, similar to large-scale dextral shear zones of the Brasiliano Orogeny, dipping at 55-80° west or east (Ferreira et al., 2019).

A key characteristic of the basement rocks from the Lages Block is the association of mafic rocks and calc-silicate rocks, including skarn occurrences and scheelite deposits (Lima et al., 1980; Salim, 1982; Corrêa et al., 2020, 2021;

Costa et al., 2022). Unlike most calc-silicate rocks in RGND, these are not part of the Seridó Group metasedimentary sequence (Souza Neto et al., 2008). Instead, they are genetically linked to amphibolites from the basement of the Lajes Block. The transformation of amphibolite into calc-silicate rocks correlates with the Brasiliano Orogeny, dated between 570 and 540 Ma (Souza Neto, 2008; Hollanda et al., 2017; Lucas et al., 2024). This indicates that the Brasiliano Orogeny played a crucial role in reshaping and aligning tectonic units along major tectonic contacts.

## 3 ANALYTICAL TECHNIQUES

Field mapping and structural interpretations divided the mapping area into thirteen lithostructural units at a scale of 1:100.000 (Fig. 3). Thirty-three samples from the Santa Luzia Sequence were analyzed by whole-rock geochemistry, including five hornblendites, eleven amphibolites, and eighteen calc-silicate rocks. Seven hornblendites, twelve amphibolites, and eleven calc-silicate rocks were selected for Sm-Nd isotope acquisitions. The geochronology of U-Pb zircon grains was performed on three amphibolites, three calc-silicate rocks, one hornblendite and one granitic leucosome.

### 3.1 LA-ICP-MS zircon U-Pb dating

Nine samples weighing approximately 15-20 kg each were collected for zircon U-Pb dating. Zircon grain separation was conducted using gravimetric and magnetic methodologies, followed by hand-selection under a binocular microscope. The selected zircon grains were mounted in epoxy resin and then polished to expose internal features. U-Pb data were obtained at the Laboratório de Estudos Geodinâmicos, Geocronológicos e Ambientais, Universidade de Brasília, Brazil. Cathodoluminescence (CL) and secondary electron (SE) imaging guided the selection of areas for in situ U-Pb dating. Isotope masses were measured using a Thermo Finnigan Element XR high-resolution single-collector sector field ICP-MS coupled to a 193 nm Iridia Excimer (ArF) laser ablation system. The laser system is equipped with a Cobalt dual-volume chamber. The

mass spectrometer was tuned to improve U and Pb sensitivity while minimizing oxide production before every analytical session. Each acquisition comprised 10 seconds of background measurement followed by 20 seconds of ablation. $^{202}$Hg, $^{204}$Pb, $^{206\text{-}208}$Pb, $^{232}$Th, and $^{238}$U masses were measured, and each one was estimated using the triple detection mode (SEM+Faraday) by sweeping the electrostatic sector on each mass. Each sweep lasted 82 milliseconds, resulting in over 800 scans for ablation. Laser parameters included a spot size of 25 μm, frequency of 20 Hz, and fluence of 2.0 J/cm². The additional laser parameters can be found in Supplementary Table 01. Raw data were processed using Iolite 4.0 (Paton et al., 2011) for time-resolved signal analysis, and individual signal inspection was conducted using VizualAge (Petrus and Kamber, 2012). Data correction included blank subtraction, LIEF correction using an exponential plus linear model, and normalization by GJ-1 zircon grain (Jackson et al., 2004). Plešovice zircon (Sláma et al., 2008) and 91500 zircon (Wiedenbeck et al., 2007) were utilized for quality control. The excessive variance in the primary calibrant was carried over to each analytical point. Systematic uncertainty of approximately 1% is propagated on each final age. The common lead correction was not applied. Ages are quoted at 2 sigma (2σ).

### 3.2 Whole-rock major and trace element analyses

Major and trace element analyses of whole-rock samples were conducted using X-ray fluorescence (XRF) spectrometry and inductively coupled plasma-mass spectrometry (ICP-MS) at ACME Analytical Laboratories Ltd, Vancouver, Canada. Before analysis, samples were crushed and powdered to 200-mesh using a vibratory grind mill at the Laboratório de Estudos Geodinâmicos, Geocronológicos e Ambientais, Universidade de Brasília, Brazil. Major oxides and minor element concentrations were determined using X-ray fluorescence on fusion disks created with lithium tetraborate. Trace element abundances were estimated by melting a 0.2 g subsample with lithium metaborate/tetraborate, followed by digestion in diluted nitric acid and ICP-MS analyses. The percentage loss on ignition (LOI) is calculated by finding the difference in weight after heating the sample to 1000°C for approximately 150 minutes. Base metal and precious

metal quantities were determined by digesting a 0.5 g subsample in Aqua Regia and later analyzing it using ICP-MS.

### 3.3 Whole-rock Nd isotope analyses

Sm-Nd isotope analyses of whole rock were also conducted at the Laboratório de Estudos Geodinâmicos, Geocronológicos e Ambientais, Universidade de Brasília, Brazil, following the analytical techniques outlined by Gioia and Pimentel (2000). The rock samples were crushed and ground into a powder of 200-mesh using a vibratory grind mill. 50 mg of whole-rock subsample were combined with $^{149}Sm$-$^{150}Nd$ spike solution and dissolved in Savillex beakers. Sm and Nd extractions followed conventional cation exchange chromatography techniques inside Teflon columns with LN-Spec resin (HDEHP – diethylhexyl phosphoric acid supported on PTFE powder). Sm and Nd fractions were loaded onto rhenium evaporation filaments, and isotope analyses were processed on a multi-collector TRITON TIMS in static mode. The results indicate Sm/Nd uncertainties and $^{143}Nd/^{144}Nd$ ratios better than 0.1% (2σ standard error) and 0.0015% (1σ), respectively, consistent with repeated analyses of the international rock standard BHVO-1. The decay constant used was (λ) $6.54x10^{-12}$, and the $^{143}Nd/^{144}Nd$ ratios were normalized to $^{146}Nd/^{144}Nd = 0.7219$. $T_{DM}$ values were estimated using the DePaolo (1981) model.

## 4 RESULTS

### 4.1 Geology of the studied area

The study area is covered by geological mapping at a 1:100,000 scale, which reveals a 10 km long by 5 km wide sequence near the Santa Luzia farm, in the municipality of Angicos, Rio Grande do Norte (RN), northeastern Brazil. The main focus of this research is the geological unit represented by the SLS rocks (Fig. 3). Banded amphibolites are dark gray, moderately to strongly foliated, display fine- to medium-grained textures, cropping out along a NE-trending direction. Typically, the amphibolites occur as discontinuous layers or

boudinaged lenses (20–100 meters wide and 50–4000 meters long) within Siderian gabbros, tonalites, diorites, and granodiorites. They are also observed as enclaves and xenoliths within Rhyacian gneissic complexes (Fig. 4).

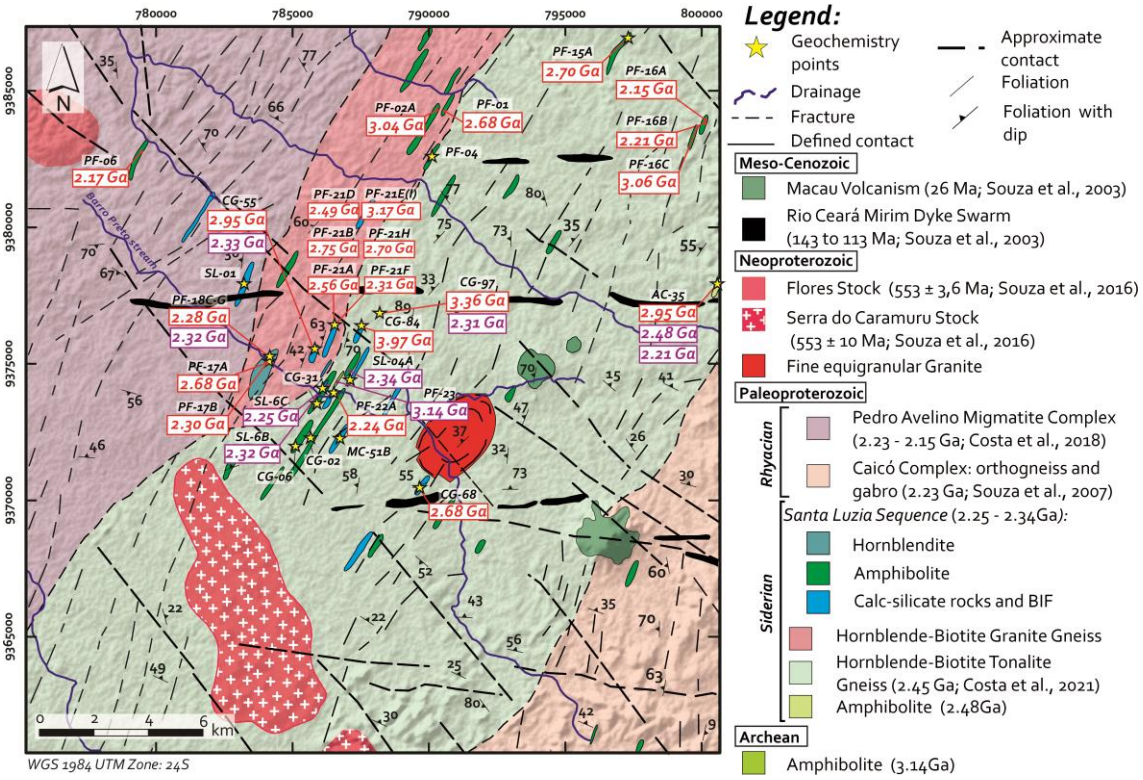



Figure 3 – Geological sketch of the Santa Luzia Sequence, in the Lajes Block region, showing the location of the U-Pb (purple square) studied samples and Sm-Nd $T_{DM}$ modal ages (red square).

The field relationships between the plutonic and amphibolitic rocks clearly indicate that more evolved lithotypes, such as tonalite, granodiorite, and diorite, occur as autoliths within more primitive rocks like amphibolite and gabbro, suggesting magma mixing and a cogenetic origin for both rock types. In the Lajes Block, hydrothermal alteration of Fe-rich amphibolites resulted in a progressive and transitional enrichment in $SiO_2$ and FeO, ultimately producing rocks compositionally and texturally analogous to banded iron formations (BIFs). These BIF layers display typical compositional banding with quartz-rich and magnetite-rich bands and include grunerite as a common accessory phase.

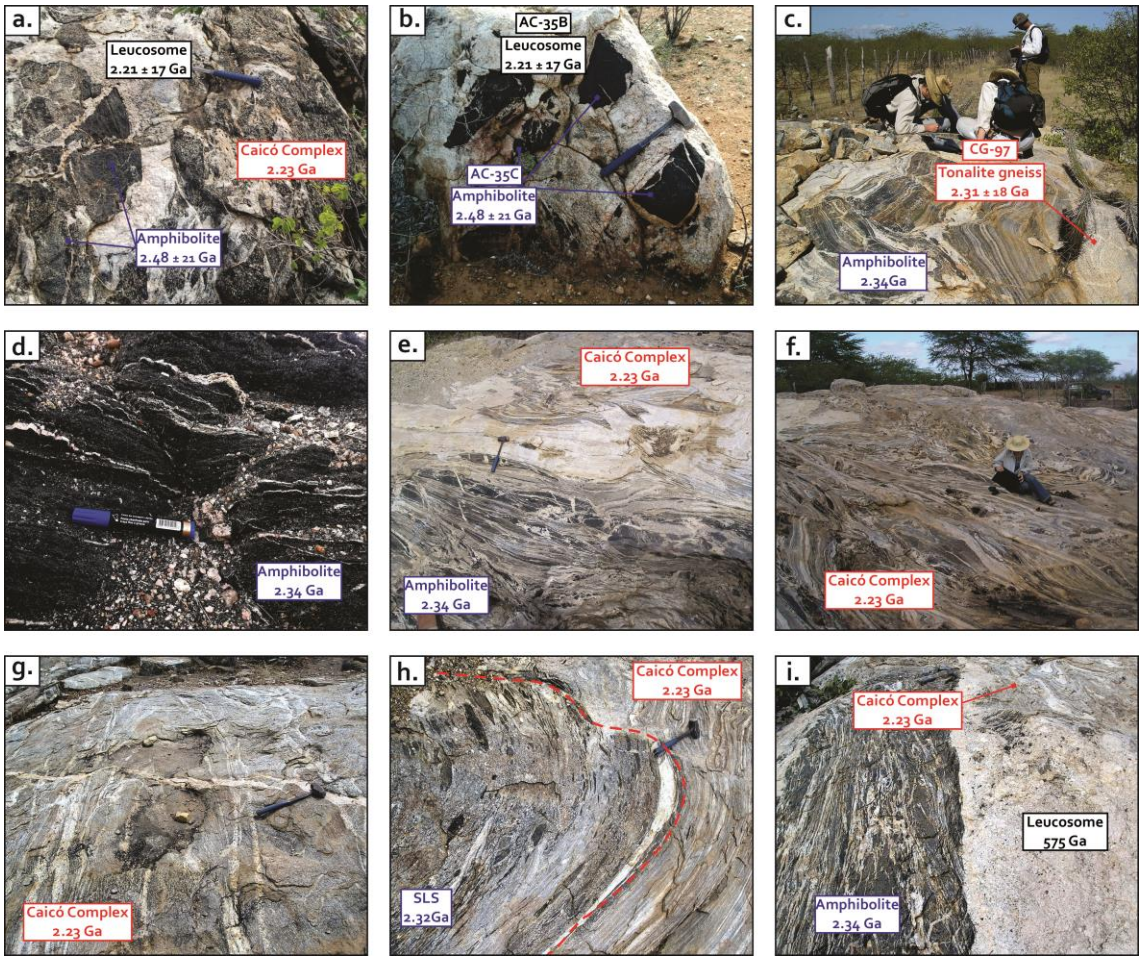



Figure 4 – Field photographs illustrating lithological characteristics and field relationships in the Santa Luzia Sequence, Lajes Block, Borborema Province. a. Amphibolite outcrop (2.48 Ga) intersected by 2.21 Ga granodioritic to tonalitic leucosome. b. Outcrop dated in this article, with granodioritic to tonalitic leucosome (2.21 Ga) with amphibolite xenoliths (2.48 Ga). c. Amphibolite fragments found as xenoliths within granodioritic and granitic orthogneisses. d. Banded amphibolite. e. Intense migmatization affecting the rocks of the Santa Luzia Sequence causes the amphibolites to be boudinaged and stretched along the main foliation of the rock, and aligned with the intrusive orthogneisses. f. Intense deformation orienting enclaves and xenoliths of amphibolites, diorites and tonalites. g. Granodioritic orthogneisses of the Caicó Complex with incipient migmatization. h-i. Intense Brasiliano deformation paralleling the layers and orienting boudins of amphibolites and more primitive rocks. SLS – Santa Luzia Sequence. The zircon U–Pb dated samples are shown in the photographs.

A similar process results in rocks such as skarns, here referred to as calc-silicate rocks. These are formed through the alteration of the amplibolite protolith (Fig. 5a-b), characterized by increased silicification and the addition of Ca-rich minerals like garnet and epidote in varying proportions (Fig. 5c-g). However,

despite extensive alteration of these rocks, which can be observed at various scales, some sites still retain features of the protolith. Calc-silicate rocks show a faint green tint and medium to coarse and banded texture. They typically form layers measuring between 1 and 1.5 meters thick. These layers are found within or next to amphibolite lenses, along concordant and gradational contacts, or enclosed in gneisses. In many cases, a gradual transition between the two lithotypes can be clearly observed in situ.

Although not being the main focus of this research, the plutonic rocks of Siderian age are present in the mapped area, interleaved with the SLS sequence. Hornblende-biotite tonalite gneiss, occupying the central mapped area, was dated by Dantas et al. (2008) and Costa et al. (2021) between 2.31 ± 37 Ga and 2.45 ± 4.2 Ga (U-Pb zircon ages), and extends southward along more than 50 km. These gneisses display a characteristic bluish-gray hue and fine-grained texture. They contain quartz, plagioclase, biotite, hornblende, minor K-feldspar, and accessory minerals such as titanite, zircon, and magnetite. The metatonalites underwent partial melting, resulting in a granodiorite to granite metatexite, with leucosome crosscutting amphibolite layers of SLS. To the northwest, the basement gradually becomes more felsic, marked by the transition from hornblende-biotite tonalite gneiss to hornblende-biotite granite gneiss.

The southeasternmost region contains orthogneiss, such as hornblende granodiorite gneiss from the Caicó Complex, while the western area is characterized by migmatites from the Pedro Avelino Complex. A suture zone to the east and a dextral shear zone to the west surround the Siderian fragments (see Ferreira et al., 2019; Padilha et al., 2021). Hornblende gneiss is gray to green with fine to medium grain size and noticeable banding due to alternating light quartz-feldspathic and dark mafic bands, primarily composed of biotite and/or hornblende. Gabbroic facies are rare and generally subconcordant with the regional Neoproterozoic structures. They show irregular circular shapes, are dark green to black, with medium grain size, and are made of iron-magnesian minerals and plagioclase. The western migmatite of the Pedro Avelino Complex consists of light-colored, foliated, coarse-grained rocks with pinkish K-feldspar (microcline) and quartz-feldspar aggregates within a gray matrix of quartz, plagioclase, biotite, and/or hornblende.

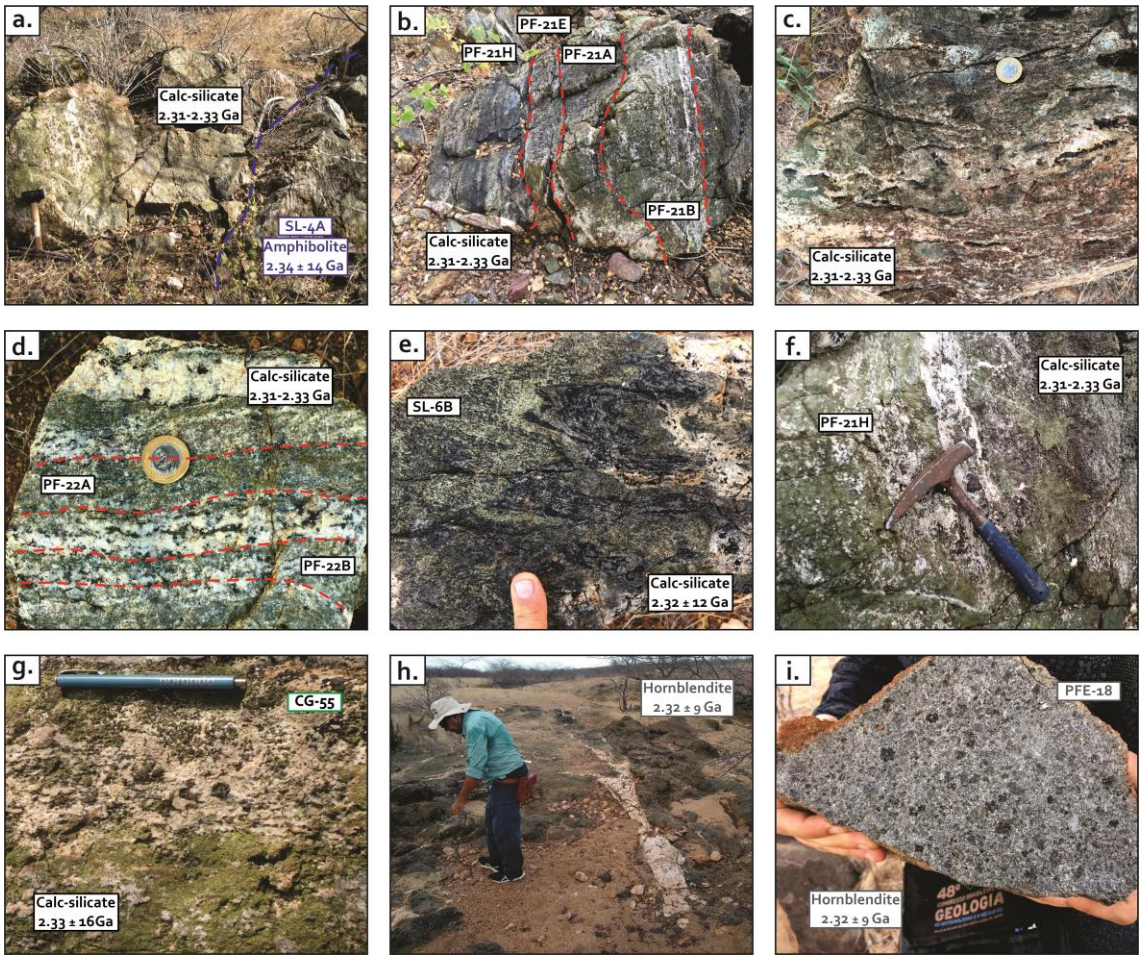



Figure 5 – Field photographs illustrating lithological characteristics and field relationships in the Santa Luzia Sequence, Lajes Block, Borborema Province. a. Dated outcrop of calc-silicate rocks in contact with amphibolite. b. Different facies analyzed from the progressive transition from amphibolite to calc-silicate rock. c. Calc-silicate rock with layers richer in garnets and layers richer in epidote. d. Banded calc-silicate rock with outlined facies domains, displaying green epidote–hornblende layers alternating with white plagioclase-rich bands with minor quartz and opaques. e. Transitional amphibolite to calc-silicate rock. f. Garnet-bearing calc-silicate rock with extensive epidotization. g. Banded calc-silicate rock, with green bands composed mainly of epidote and hornblende, and white bands consisting primarily of plagioclase, minor quartz and opaque minerals. h. Aplite dike cutting the hornblende. Granodioritic orthogneisses of the Caicó Complex with incipient migmatization. i. Dated coarse-grained hornblendite. The zircon U–Pb dated samples are shown in the photographs.

In shear zones, gneiss mylonites show retrometamorphic minerals including muscovite, chlorite, and epidote. The foliation in hornblende-biotite tonalite and granite gneiss generally dips at moderate to steep angles, mostly dipping toward W or NW. Neoproterozoic granite bodies like the Serra do

Caramuru (553 ± 10 Ma) and Flores stocks (553 ± 3.6 Ma) intrude these rocks (U-Pb zircon age, Souza et al., 2016). East-west Mesozoic basaltic dikes from the Rio Ceará Mirim swarm (with Ar/Ar ages ranging from 145 to 110 Ma, and a plateau age of 132.2 ± 1 Ma; Souza et al., 2003) cut through all rock types. The final event, Macau volcanism (with Ar/Ar age of 24.06 ± 0.8 Ma; Souza et al., 2003), represented by the alkaline Cabugi peak, took place southeast of the study area.

## 4.2 Petrography

Figures 6 and 7 show photomicrographs of typical mineral assemblages, and Table 1 presents the mineralogical paragenesis of selected rock types. Based on mineralogy and texture, the rocks are categorized into four groups: amphibolite, garnet-bearing calc-silicate rock, allanite-bearing calc-silicate rock, and diopside hornblendite. Below is a brief petrographic description of the analyzed rocks.

### *4.2.1 Amphibolite*

Mineralogically, the majority of amphibolite samples from the Santa Luzia Sequence are dominated by amphibole (50-75% vol.) and plagioclase (andesine) (15-35% vol.; Fig. 6a). Both minerals occur as sub-idioblastic to idioblastic crystals. Amphibole is dominantly hornblende. In length, these grains range from 0.5 to 4 mm and are usually oriented, while andesine ranges from 0.5 to 2 mm. The boundaries between these two mineral phases are clearly defined, ranging from straight to curved. Quartz content varies from trace to 15% by volume, with higher modal concentrations typically associated with veins. Accessory minerals include titanite, augite, biotite, zircon, apatite, and opaque minerals (Fig. 6b). Augite is a subhedral, rare, and primary mineral that occurs in curved contact with hornblende, indicating the uralitization process. Epidotization of hornblende and sericitization/kaolinization of andesine are subsequent mineral alterations (see Table 1).

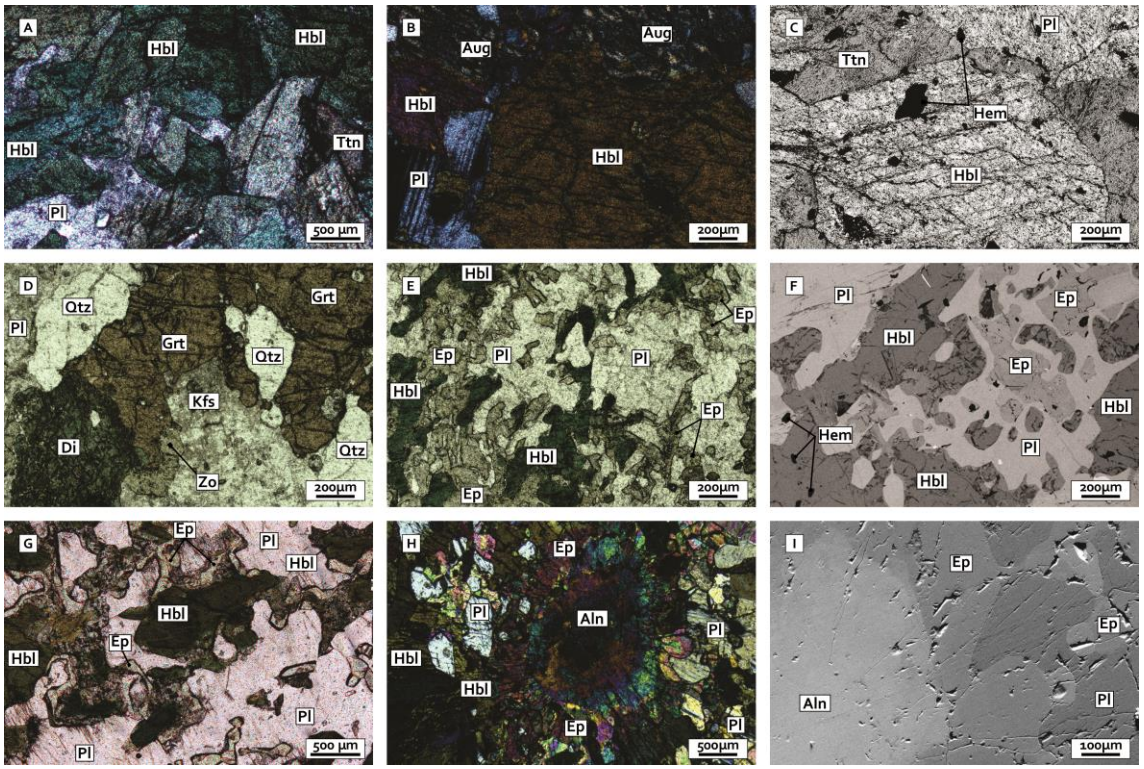



Figure 6 – Photomicrographs showing representative mineralogy of typical rocks of the Santa Luzia Sequence. a. Amphibolite dominantly composed of large grains of hornblende with minor andesine and titanite under plane-polarized light (PPL). b. Augite relict crystal in contact with hornblende under PPL. c. SEM backscatter electron (BSE) image illustrating the petrographic characteristics of amphibolite. Hornblende contains hematite inclusions. d. Photomicrograph of garnet-bearing calc-silicate rock composed of diopside, andradite, andesine, quartz, K-feldspart, and zoisite under PPL. e. Hornblende replaced by epidote in garnet-bearing calc-silicate gneiss under PPL. f. BSE image illustrating epidotization in garnet-bearing calc-silicate rock; hornblende contains small hematite inclusions. g. Hornblende replaced by epidote in epidote-rich calc-silicate rock under PPL. h. Epidote corona around allanite crystal in epidote-rich calc-silicate rock under cross-polarized light (XPL). i. BSE image illustrating epidote corona around allanite crystal in epidote-bearing calc-silicate rock. Grt garnet, Aln allanite, Aug augite, Ep epidote, Hbl hornblende, Hem hematite, Kfs K-feldspar, Pl plagioclase, Qtz quartz and Ttn titanite.

### *4.2.2 Garnet-bearing calc-silicate rock*

Garnet-bearing calc-silicate rocks comprise 35-55% plagioclase (andesine), 10-30% epidote, 5-25% hornblende, 3-5% garnet, 5% quartz, and 3% diopside. Plagioclase exhibits sub-idioblastic to xenoblastic grain habits, measuring 0.2 to 0.6 mm in length. Epidote is the main later alteration phase. It displays xenoblastic grains and varying sizes. Some epidote grains enclose

andesine and hornblende crystals, replacing them. Garnet appears as xenoblastic grains, with a brownish-red color, and lengths ranging from 1 to 4 mm. Quartz grains are xenoblastic, and make curved boundaries with garnet and diopside. Diopside grains are xenoblastic with green color and are approximately 0.5 to 1 mm in length. They are usually observed in curved to slightly diffuse contacts with garnet and andesine. Typical minor and accessory phases in these rocks include hematite, reddish-brown biotite, zircon, apatite, zoisite, K-feldspar, and titanite. Figures 6d-e show diffuse and curved contact relationships between garnet, quartz, zoisite, and diopside. The contact between garnet and K-feldspar is linear to straight. Hematite is found as small inclusions in hornblende and plagioclase (Fig. 6f).

### *4.2.3 Epidote-rich calc-silicate rock*

This unit is quite similar to the unit of garnet-bearing calc-silicate rock. The main petrographic differences are: (1) greater epidotization (25-40% vol.) of plagioclase (30-50% vol.) and hornblende (20-30% vol.); (2) formation of allanite (2% vol.); (3) absence of garnet and diopside; and (4) greater modal concentration of hematite (1-2% vol.) and titanite (trace-2% vol.). Quartz, zircon, apatite, and zoisite are minor accessory phases. Epidote occurs as a later alteration phase, replacing hornblende and plagioclase (Fig. 6g), or as coronas around allanite crystals (Fig. 6h-i). The saussuritization of plagioclase is primarily characterized by the formation of zoisite (Fig. 7a). Hematite occurs in idioblastic to sub-idioblastic grains, ranging from 1 to 4 mm in length or as tiny xenoblastic crystals. In the latter case, it is common to observe these small hematite grains in contact or forming symplectites with titanite and epidote (Fig. 7b-c).

### *4.2.4 Hornblendite*

In thin sections, hornblende displays coarse-grained foliated textures (Fig. 7d). Hornblende ranges from 60 to 75%, diopside from 30 to 40% vol., and opaque (hematite) from 2 to 4%. Minor olivine and zircon are also present, while quartz represents a later metamorphic phase. Hornblende is characterized by

anhedral to euhedral crystals, and some samples display poikilitic grains enclosing diopside crystals. It can also be found within grains of olivine and diopside. Grain boundaries can vary from straight to curved, especially between hornblende and diopside (Fig. 7e).

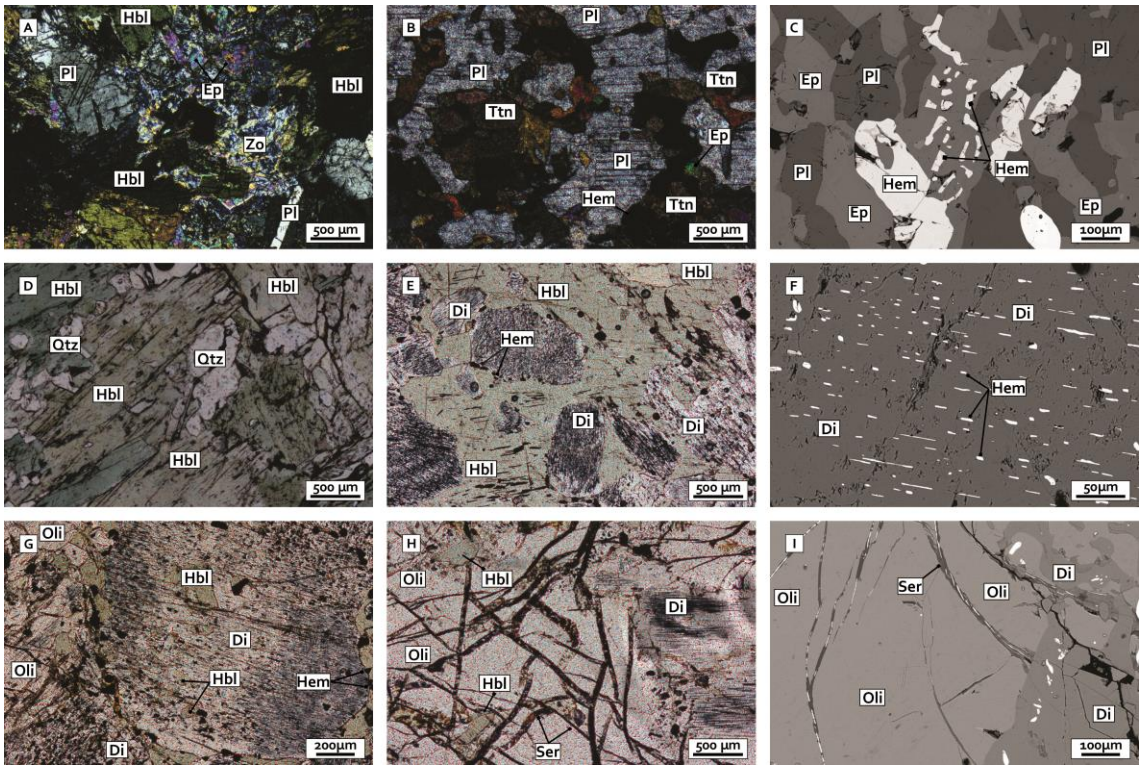
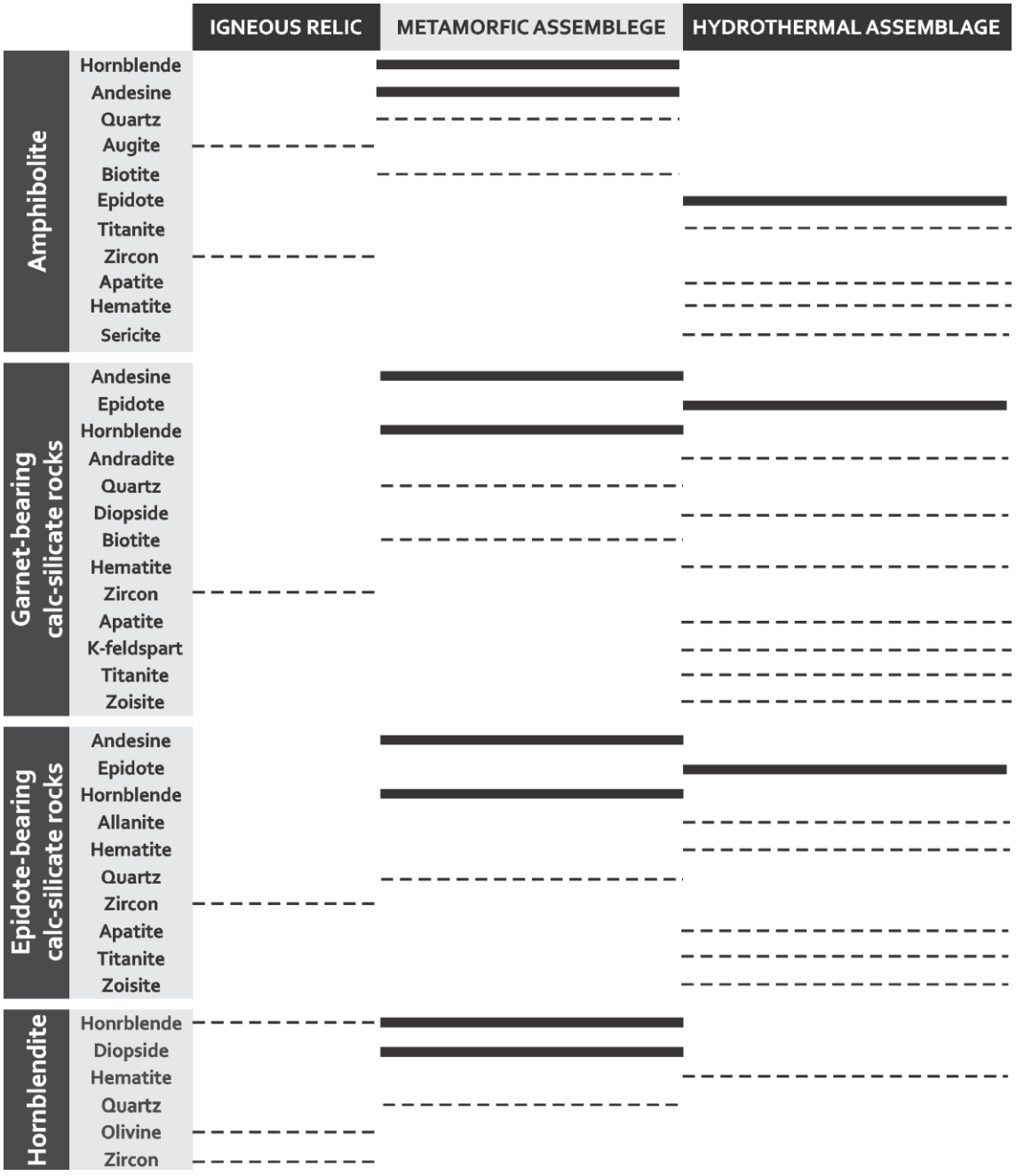



Figure 7 – Photomicrographs showing representative mineralogy of typical rocks of the Santa Luzia Sequence. a. Zoisite in epidote-rich calc-silicate rock under cross-polarized light (XPL). b. Titanite in in epidote-rich calc-silicate rock under XPL. c. BSE (backscatter electron) image illustrates an intergrowth of symplectitic hematite and epidote in epidote-rich calc-silicate rock. d. Hornblende in hornblendite from the Santa Luzia Sequence under plane-polarized light (PPL). e. Grains of hornblende enclosing diopside crystals in hornblendite under PPL. f. BSE image illustrates diopside grain containing numerous oriented hematite inclusions. g. Relicts of hornblende in diopside and olivine crystals in hornblendite under PPL. h. Cracks in olivine are partly filled with serpentine under PPL. i. BSE image illustrating cracks in olivine are partly filled with serpentine. Di diopside, Ep epidote, Hbl hornblende, Hem hematite, Kfs K-feldspar, Oli olivine, Pl plagioclase, Qtz quartz, Ser serpentine, Ttn titanite and Zo zoisite.

The diopside grains exhibit sub-euhedral to anhedral crystals and measure between 0.5 and 2 mm in length. Diopside is variably replaced by hornblende. Its boundaries with olivine are diffuse or curved. No reaction rims are observed. Hematite is located in the center of hornblende and diopside crystals as

numerous, oriented, and tiny inclusions or as chains of small grains along hornblende-diopside and diopside-olivine grain boundaries (Fig. 7f-g). Olivine grains are anhedral, with 2 to 4 mm lengths. Many olivine grains exhibit serpentinized fractures (Fig. 7h-i).

Table 1 – Modal concentration and mineralogical composition of samples from the Santa Luzia sequence. Higher modal concentrations are shown with a continuous line, while minor or trace phases are shown with a dashed line.



## 4.3 U-Pb dating

Nine samples from the study area were selected for LA-ICP-MS zircon U-Pb dating. The samples include amphibolite (PF-23, AC-35C, SL-4A, and SL-6C), garnet-bearing calc-silicate rock (CG-55 and SL-6B), hornblendite (PF-18), tonalitic orthogneiss (CG-97), and granitic leucosome (AC-35B). Cathodoluminescence images of representative zircon grains are presented alongside the U-Pb zircon ages (Fig. 8). Table 2 (Appendix B) lists isotope masses, ratios, and sample location.

### *4.3.1 Amphibolite*

The zircon grains in amphibolites are mainly subhedral to euhedral, appearing colorless or slightly yellowish under the microscope. They are prismatic, measuring 200 to 450 μm along the c axis, with a length-to-width ratio of 2:1 to 3:1. Cathodoluminescence imaging shows that most zircon grains have concentric zoning with local resorption and homogeneous cores. Inherited nuclei were seen only in sample PF-23, but they were not dated (Fig. 8a). The oldest zircon ages obtained in amphibolites came from the PF-23 sample, which yielded an upper intercept age of 3149 ± 18 Ma on the concordia diagram, and a mean square weighted deviation (MSWD) of 1.1 (Fig. 8b). Twenty-three zircon U-Pb analyses yielded Th/U ratios ranging from 0.69 to 1.86, which we interpret as igneous and define an Archean crystallization age for the protolith of the amphibolite. The lower intercept age is 668 ± 48 Ma and is attributed to the loss of common Pb.

Sample AC-35C is a xenolith of banded amphibolite within granitic leucosome, representing an ancient Siderian volcanism event at 2488 ± 21 Ma, with an MSWD of 1.2. The lower intercept age is 920 ± 445 Ma (Fig. 8d), without a clear geological meaning. Thirteen U-Pb zircon age measurements yielded Th/U ratios ranging from 0.15 to 0.52.

The two main mafic events were documented in two separate amphibolite samples. Sixteen U-Pb analyses were conducted on sample SL-4A, yielding an upper intercept age of 2348 ± 14 Ma with an MSWD of 1.3, as indicated by the

discordia diagram. The lower intercept is measured at 433 ± 156 Ma (Fig. 8f). Zircon crystals show Th/U ratios between 0.24 and 0.58, with a texture typical of magmatic crystallization. The youngest amphibolite (SL-6C) has an upper intercept age of 2250 ± 14 Ma (MSWD 1.5) and a lower intercept age of 357 ± 131 Ma (Fig. 8h), based on nineteen zircon U-Pb analyses with Th/U ratios of 0.26 to 0.54.

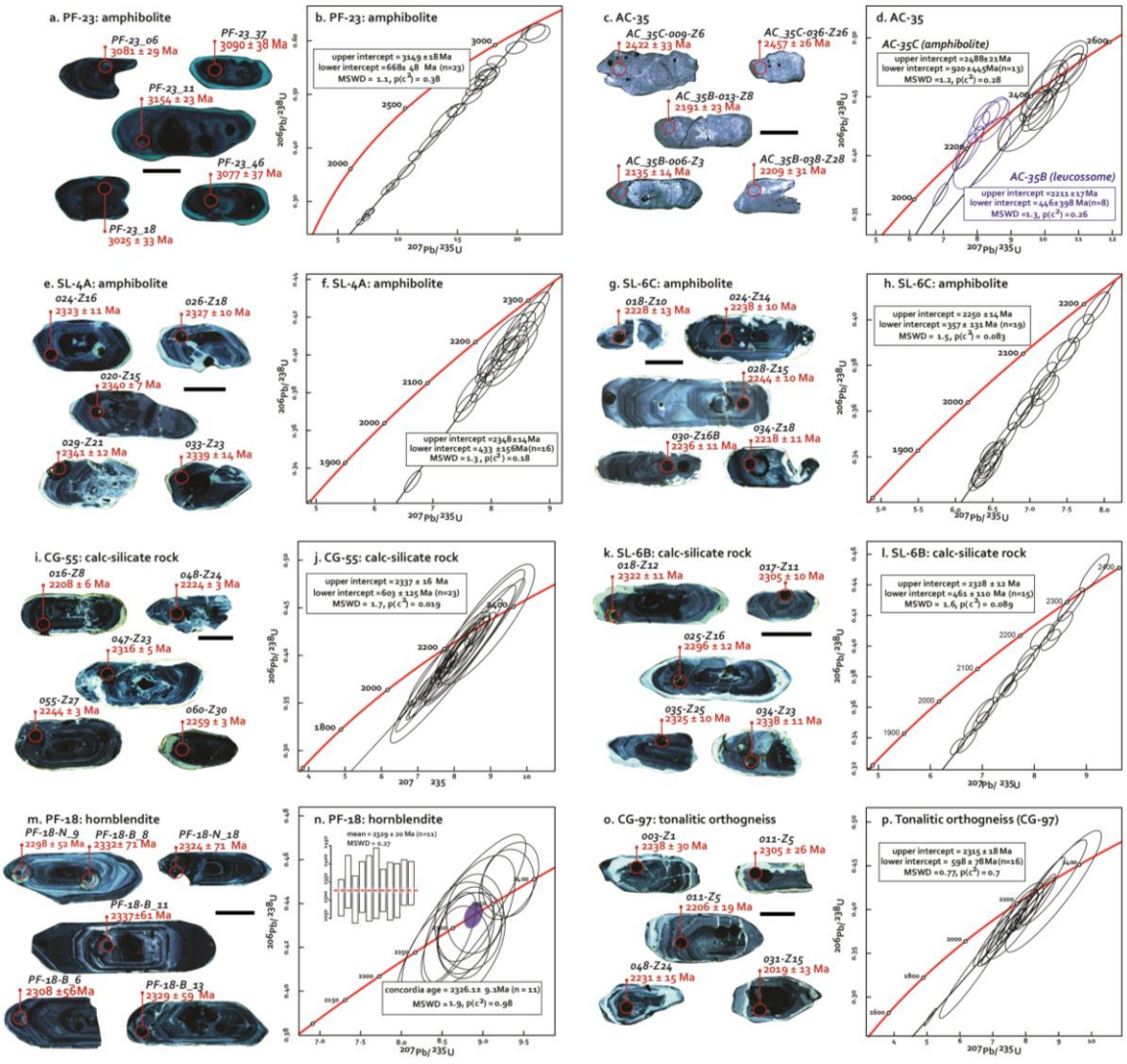



Figure 8 – Cathodoluminescence images of representative zircon grains and U-Pb Concordia diagrams. Scale bar = 100 μm.

### *4.3.2 Garnet-bearing calc-silicate rock*

The two calc-silicate rock samples (CG-55 and SL-6B, Figs. 8i-8k) provide Siderian ages, with upper intercept ages of 2328 ± 12 (MSWD 1.7) and 2337 ± 16 Ma (MSWD 1.6), respectively, indicating the major magmatic event in the Lajes Block. Th/U ratios range from 0.15 to 0.68. All zircon grains are uniform, euhedral to subhedral, measuring 120 to 450 µm in length, with a length-to-width ratio of 1:1 to 1:2. Under an optical microscope, they appear transparent, sometimes with brown shades. Most grains exhibit faint zoning in the core, being covered by a thin, clear layer at the rims. Minor convoluted bands, dissolution textures, or inclusion-rich areas from rims to cores, along with unmeasured inherited components, are described as causing discordance in most of discordia diagrams (Fig. 8h-l). The lower intercept in all ages is around 600 Ma, representing a common Pb loss due to the overprinting of the Brasiliano deformational and metamorphic event, as well described in the Borborema Province.

### *4.3.3 Hornblendite*

A small subcircular body in the Barro Preto creek of hornblendite displays zircon grains with subhedral to euhedral habits, which are colorless or brownish under the microscope, with sizes ranging from 250 to 470 µm and a length-to-width ratio of 2:1 to 4:1 (Fig. 8m). Most zircon grains exhibit well-developed oscillatory zoning. Rare, unzoned features resembling metamorphic bands are shown in detail. Eleven analyses reveal a Th/U ratio ranging from 0.49 to 1.6. The U-Pb concordia diagram presents a linear array, yielding a concordia age of 2326.1 ± 9.1 Ma and MSWD=1.9, with 97% concordance (Fig. 8n).

### *4.3.4 Tonalitic orthogneiss*

The zircon grains from the tonalitic orthogneiss display consistent morphologies. Most grains are euhedral to subhedral, measuring between 170 and 400 µm in length, with length-to-width ratios ranging from approximately 2:1 to 3:1. Under optical microscopy, they appear transparent to brown in color. Cathodoluminescence images reveal magmatic zoning, some hydrothermal

overgrowths, and the presence of inherited cores (Fig. 8o). For sample CG-97, sixteen U–Pb analyses yield an upper intercept age of 2315 ± 18 Ma, with an MSWD of 0.77 (Fig. 8p). The lower intercept age was estimated at 598 ± 78 Ma.

### *4.3.5 Granitic leucosome*

Zircon grains from the granitic leucosome are subhedral to euhedral, colorless or slightly yellowish under the microscope. Their sizes range from 250 to 500 µm, with a length-to-width ratio of 2:1 to 3:1. Cathodoluminescence imaging reveals that most zircon grains display concentric zoning, with some areas showing resorption (Fig. 8c). Eight analyses from the AC-35B sample reveal a Th/U ratio between 0.14 and 0.30 and with an upper intercept age of 2211 ± 17 Ma (MSWD 1.3). The lower intercept age was estimated at 446 ± 398 Ma, also indicating a common Pb loss during the Brasiliano events (Fig. 8d).

## 4.4 Whole-rock geochemistry

### *4.4.1 Amphibolite*

The amphibolites of the Santa Luzia Sequence have moderately variable $SiO_2$ (48.77-53.80 wt%), $Fe_2O_3t$ (9.17-12.40 wt%), and CaO (9.58-13.35 wt%) contents. They exhibit significant variations in $Al_2O_3$ (5.28-15.11 wt%), MgO (5.26-16.25 wt%), $Na_2O$ (0.76-3.62 wt%), and $TiO_2$ (0.31-1.17 wt%) contents, with Mg# ranging from 22 to 47 (Table 3; Appendix B). The $K_2O$ content, ranging from 0.48 to 1.21 wt%, is relatively low to intermediate. The low concentrations of $K_2O$ and $TiO_2$ in some samples denote similarity with MORB compositions. The rocks show tholeiitic affinity on the AFM diagram (Fig. 9a) and are classified as low-K tholeiites. The Santa Luzia amphibolites are located within the basalt and basaltic-andesite fields on the Nb/Y vs. Zr/Ti plot (Pearce, 1996; Fig. 9b). Field relationships, petrography, and geochronological inferences suggest a possible genetic connection between the amphibolites and the calc-silicate types. Figures 9c and 10 clearly show the geochemical interrelationships among these groups, likely originating from the same magmatic source.

On chondrite- and primitive mantle-normalized trace elements diagrams, the amphibolites exhibit the following characteristics: (1) slightly to moderately enriched LREE ($(La/Yb)_N$=1.97-12.85; $(La/Sm)_N$=1.14-3.29) and depleted HREE patterns ($(Gd/Yb)_N$=1.34-2.94); (2) negative to positive Eu and Ce-anomalies (Eu/Eu*=0.74-1.14; Ce/Ce*= 0.77-1.12); (3) negative Nb (Nb/Nb*=0.14-0.98) and Ta (Ta/Ta*=0.23-0.66) anomalies, except for one sample (Ta/Ta*=2.28); (4) large negative Ti-anomaly (Ti/Ti*=0.34-0.80; Fig. 11a-b).

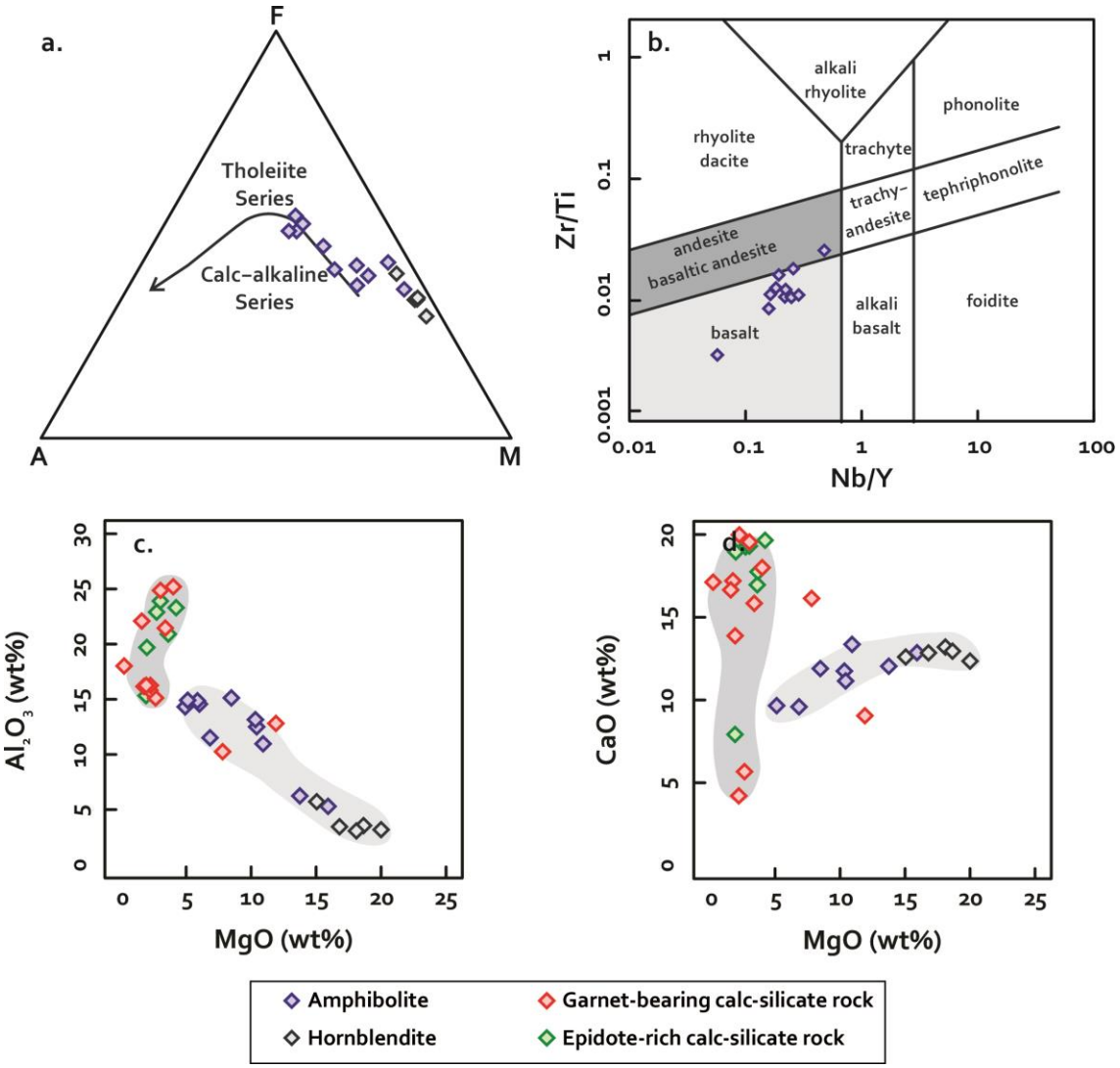



Figure 9 – a. AFM ($Na_2O$+K2O–MgO–FeOt) diagram (Irvine and Baragar, 1971) showing that the amphibolites (blue diamond) and hornblendite (gray diamond) plot along the tholeiite trend. b. Zr/Ti vs. Nb/Y diagram (Pearce, 1996). c. Harker diagrams for MgO (wt%) vs. $Al_2O_3$ (wt%). d. Harker diagrams for MgO (wt%) vs. CaO.

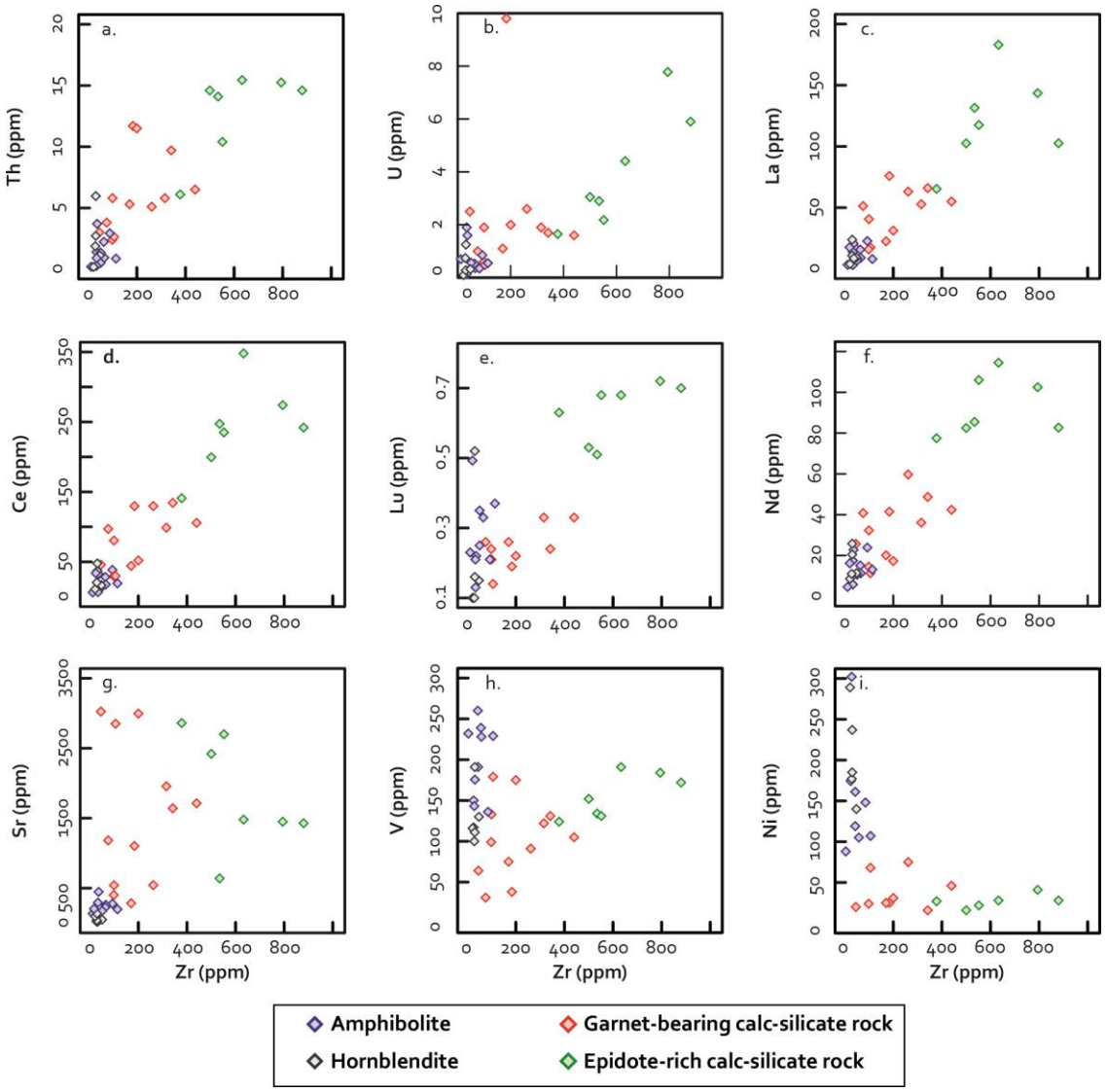



Figure 10 – Harker diagrams for Zr (ppm) and relevant trace elements (ppm).

### *4.4.2 Garnet-bearing calc-silicate rock*

Garnet-bearing calc-silicate samples exhibit significant variations in the content of major oxide elements: $SiO_2$ (39.17-64.06 wt%), $Fe_2O_3t$ (3.20-14.54 wt%), MgO (0.23-11.91 wt%), $Na_2O$ (0.30-4.16 wt%), $K_2O$ (0.13-1.73 wt%), $TiO_2$ (0.36-1.18 wt%). Their Mg# ranges from 1 to 44. Chemically, as a group, the garnet-bearing calc-silicate rocks represent considerable additions of Ca and Al and losses of Mg relative to low-K tholeiitic amphibolites (Fig. 9c-d). However, their distinguishing feature is a significant enrichment in LILEs and LREEs (Fig. 11c-d). The contents of HFSEs and HREEs are very similar to those measured for low-K tholeiitic rocks. Their positive correlation with Zr indicates that these

elements remain immobile during late alteration processes (Fig. 10a-g, Fig. 11c-d) and preserve well the protolith signature. V and Ni do not show a clear correlation with Zr (Fig. 10h–i).

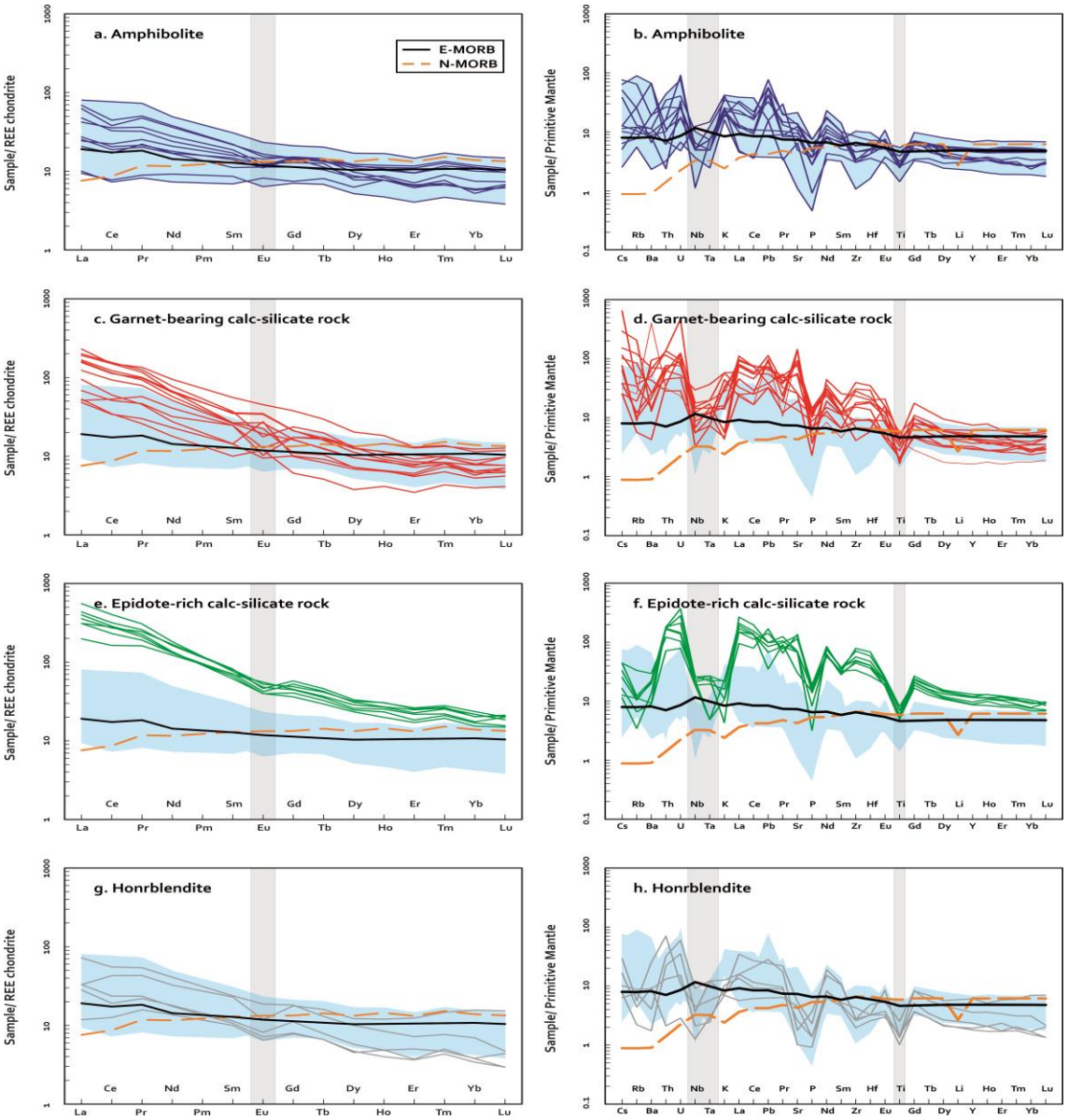



Figure 11 – Chondrite- and primitive mantle-normalized diagrams for hornblendite, amphibolites and calc-silicate gneisses. Normalization values from Sun and McDonough (1989). a-b. The blue lines represent amphibolites from the Santa Luzia Sequence. c-d. Garnet-bearing calc-silicate rock. e-f. Epidote-rich calc-silicate rocks. g-h Hornblendite. The blue shade is REEs and trace elements normalized contents of low-K tholeiitic rocks overlapped to garnet-bearing calc-silicate and epidote-rich calc-silicate. Gray bands highlight the Eu, Nb, and Ti anomalies.

On the chondrite-normalized trace elements diagram, these samples show significant enrichment in LREEs $(La/Yb)_N$=4.47-46.93; $(La/Sm)_N$=2.18-9.07) compared to HREEs ($(Gd/Yb)_N$=1.46-3.79), with positive to negative Eu anomalies (Eu/Eu*=0.49-1.52), as depicted in Fig. 11c. Their Ce anomalies range from Ce/Ce* = 0.99 to 1.08. The trace element distribution patterns in the primitive mantle-normalized diagram exhibit high enrichment in LILEs, with negative anomalies in Nb (Nb/Nb*=0.06-0.66), Ta (Ta/Ta*=0.13-0.85), Ti (Ti/Ti*=0.16-0.78, except for one positive sample with Ti/Ti*=1.25; Fig. 11d).

### *4.4.3 Epidote-rich calc-silicate rock*

Epidote-rich calc-silicate rocks also have significant variations in some of their major oxides element contents: $SiO_2$ (37.00-58.22 wt%), $Al_2O_3$ (15.33-23.90 wt%), CaO (7.92-18.95 wt%), and $Na_2O$ (0.40-3.59). A moderate range is observed in $Fe_2O_3$t (9.72-15.30 wt%), MgO (1.92-4.23 wt%), $K_2O$ (0.13-0.69 wt%), and $TiO_2$ (1.07-1.76 wt%) contents. Their Mg# is between 8 and 19. Concentrations of CaO and $Al_2O_3$ in these rocks are significantly higher than those observed in the low-K tholeiitic amphibolites (Fig. 9c-d). In comparison to garnet-bearing calc-silicate rocks, the concentrations of LILEs, LREEs, and HREEs are notably higher and more pronounced in these samples, supporting a higher level of alteration (Fig. 10a-g; Fig. 11e-f). V content shows a positive correlation with Zr, while Ni displays no clear relationship (Fig. 10h–i).

This group exhibits the highest concentrations of REEs and trace elements compared to the other studied units and positive correlations with Zr. They have higher ratios of $(La/Yb)_N$, ranging from 9.78 to 34.18, and $(La/Sm)_N$, ranging from 2.93 to 7.60, compared to HREEs with $(Gd/Yb)_N$ values between 2.30 and 2.65. Allanite-bearing calc-silicate rocks exhibit moderate to slightly negative Eu-anomalies (Eu/Eu* = 0.67-0.98) and positive Ce-anomalies (Ce/Ce* = 1.01-1.21, see Fig. 11e). On the primitive mantle-normalized spider diagram, these samples exhibit significant enrichment in LILEs and negative anomalies for Nb (Nb/Nb* = 0.10-0.23), Ta (Ta/Ta* = 0.04-0.18), and Ti (Ti/Ti* = 0.21-0.36; Fig. 11f).

### *4.4.4 Hornblendites*

The hornblendites are characterized by a moderate range of $SiO_2$ (49.30–55.20 wt%), $Fe_2O_3t$ (8.99–12.20 wt%), and MgO (15.05–20.0 wt%) contents, and Mg# (43.48-55.66). They display a restricted interval of $Al_2O_3$ (3.07-5.72 wt%), CaO (12.35-13.20 wt%), $Na_2O$ (0.62-0.76 wt%), $K_2O$ (0.21-0.38 wt%), and $TiO_2$ (0.22-0.55 wt%). These rocks exhibit subparallel to flat distribution patterns of REEs, with slight enrichment in LREEs ($(La/Yb)_N$=2.27-11.16; $(La/Sm)_N$=1.24-3.26) relative to HREEs ($(Gd/Yb)_N$=1.18-3.01). Negative Eu anomalies (Eu/Eu*=0.58-0.90) and negative to positive Ce anomalies (Ce/Ce*=0.85-1.25) are conspicuous (Fig. 11g). On a primitive mantle-normalized spider diagram, they are characterized by enrichment in LILEs and negative anomalies of Nb (Nb/Nb*=0.09-0.41) and Ti (Ti/Ti*=0.18-0.41; Fig. 11h). The Ta content is below detectable limits in most of the samples.

## 4.5. Sm-Nd isotope

Sm-Nd isotopic data from amphibolites, garnet-bearing calc-silicate, epidot-rich calc-silicate, and hornblendite are provided in Table 4 (Appendix B). The analyzed amphibolites exhibit $^{147}Sm/^{144}Sm$ ratios ranging from 0.0911 to 0.1696 and the $^{143}Nd/^{144}Nd$ ratios range from 0.5112 to 0.5123, allowing to distinguish some different groups. The main isotopic signature of a group of five samples of amphibolite displays positive $\varepsilon_{Nd(t)}$ values, considering the crystallization age of 2.35 Ga, ranging from +2.04 to +3.09. They also exhibit younger $T_{DM}$ model ages of 2.36 to 2.12 Ga, supporting a Paleoproterozoic juvenile source for the Siderian Santa Luzia Sequence. Also, a group of seven amphibolites, including the 2.48 Ga sample, display positive and negative $\varepsilon_{Nd(t)}$ values of -3.41 to +2.35 and $T_{DM}$ model ages between 2.62 and 3.06 Ga, suggesting an Archean oceanic crust as source to this mafic magmatism.

Garnet-bearing calc-silicate rocks have $^{147}Sm/^{144}Sm$ ratios ranging from 0.777 to 0.1381, and their $^{143}Nd/^{144}Nd$ ratios range from 0.5108 to 0.5115 (mean=0.5111), with dominantly Archean $T_{DM}$ model ages (between 2.67 and 3.97 Ga; Fig. 12a). All $\varepsilon_{Nd(t)}$ values are negative, ranging from -11.25 to -1.02. On

the other hand, epidote-rich calc-silicate rocks show $^{147}Sm/^{144}Sm$ between 0.0937 and 0.1432 and $^{143}Nd/^{144}Nd$ ratios range from 0.5111 to 0.5117. They display negative to positive $\varepsilon_{Nd(t)}$ values (-3.44 to +2.02) and $T_{DM}$ model ages between 2.24 and 3.17 Ga.

The hornblendites show an average $^{147}Sm/^{144}Sm$ ratio of 0.1269, ranging between 0.0876 and 0.1425. Four samples show slightly negative to positive $\varepsilon_{Nd(t)}$ values, ranging from -1.01 to +0.73, with older $T_{DM}$ model ages between 2.92 and 2.68 Ga. Three samples show positive $\varepsilon_{Nd(t)}$ between +1.03 and +2.69, and younger Paleoproterozoic $T_{DM}$ model ages (2.28 to 2.30 Ga).

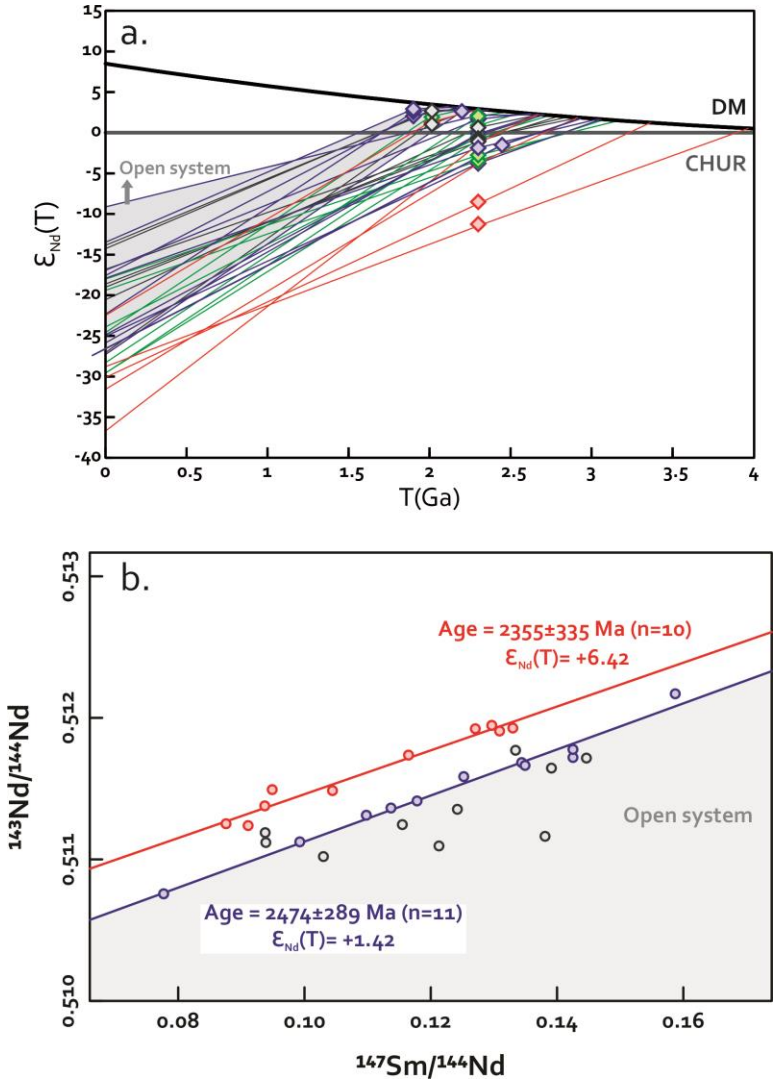



Figure 12 – a. Sm-Nd isotopes diagrams. – blue diamond, garnet-bearing calc-silicate rock – red diamond, epidote-rich calc-silicate rock – green diamond, hornblendite – gray diamond. b. Samples from the Santa Luzia Sequence defining a 2.47 Ga isochron (blue circles), a 2.35 Ga isochron (red circles), and outlier samples (gray circles).

Sm-Nd isochrons, encompassing all analyzed samples, effectively identify the main mafic event at 2.355 Ga and the oldest at 2.474 Ga, aligning with ages from U-Pb dating (Fig. 12b). An isochron age of 2.35 Ga, which includes amphibolites, calc-silicate rocks, and hornblendites, suggests these rocks are cogenetic. Their $\varepsilon_{Nd(t)}$ values, ranging from +3.44 to +2.02, confirm the juvenile signature of the oceanic crust in the Lages Block. Furthermore, the isotopic Sm-Nd system is partially open, leading $T_{DM}$ model ages to appear younger than the igneous crystallization event. This is observed in the studied rocks, which have $T_{DM}$ model ages of 2.2 and 2.1 Ga.

# 5 DISCUSSIONS

## 5.1 Tectonic significance of mafic magmatism of the Archean to Paleoproterozoic transition

U-Pb zircon geochronology and whole-rock Sm-Nd isotopic data provide robust constraints for discussing the origin and sources of the protoliths of the amphibolites. These lithological remnants occur as dismembered tectonic fragments, juxtaposed through subsequent orogenic processes. When integrated with petrographic and geochemical evidence, they enable the reconstruction of key aspects of mantle dynamics and the tectonic environments that governed the generation of this magmatism. Previous studies reported Paleoproterozoic magmatic ages around 2.15 Ga, which were initially interpreted as representing a single magmatic episode (Ferreira and Albuquerque, 1969; Jardim de Sá, 1994; Hackspacher et al., 1990; Van Schmus et al., 1995). However, since the works of Negrão et al. (2005), Souza et al. (2007), Dantas et al. (2008), Ferreira et al. (2019), Costa et al. (2021), and even our new integrated dataset combining petrography, geochemistry, and isotopic analyses, this framework has been continually refined. The results reveal a complex magmatic evolution, beginning with the formation of a Mesoarchean crust at 3.14 Ga, followed by the development of a Siderian oceanic arc between 2.4 and 2.3 Ga, a mafic magmatic event at 2.25 Ga, calc-alkaline magmatism at 2.23 Ga, and a subsequent tholeiitic pulse at 2.19 Ga (Souza et al., 2007; Ferreira et al., 2019).

These rock assemblages were later overprinted by Proterozoic deformation and high-grade metamorphic events. This confirms that several magmatic events took place in the northwest of the Lajes Block, which began during the transition from the Neoarchean to the early Paleoproterozoic and extended into the Rhyacian, passing through the Siderian and the TML.

Intra-oceanic systems' arc-forearc crust mainly comprises MORB-like igneous rocks (gabbro, forearc basalts), boninite/high-Mg andesite/intermediate, felsic plutons and dikes (diorite, tonalite-trondhjemite-granodiorite – TTG), and younger volcanic (island arc basalts – IAB, island arc tholeiitic basalts – IAT, basalt-andesite-dacite-rhyolite – BADR) and submarine sedimentary/volcaniclastic rocks (Whattam and Stern, 2011; Stern et al., 2012; Huang et al., 2022). In these sites, forearc basalts or boninite suites serve as initial subduction indicators, while TTG, IAB, IAT, and ADRs signify subsequent arc maturation. The spatial coexistence of MORB-like basalts, tonalitic gneisses, and low-K tholeiitic rocks indicates their formation in a primitive intraoceanic arc setting, likely representing an early-stage arc system. Whattam and Stern (2011) and Zhong et al. (2021) argue that this kind of magmatic progression is expressed by a chemo-stratigraphic variation.

Here, this chemical fluctuation is best expressed in Figure 13a, along with the MORB-IAT trend. Geochemical data for 2.45 ± 4.2 Ga tonalitic gneiss are missing. However, their spatial and temporal association with MORB-like basalts and low-K tholeiitic rocks from the Santa Luzia Sequence suggests that they formed during an intermediate stage related to subduction maturation. Petrographically, the protoliths of the studied amphibolites and related rocks from the SLS include basalts and gabbros that have been metamorphosed into massive and finely banded amphibolites. These rocks preserve mineralogical and textural features typical of mafic igneous protoliths and are interpreted as remnants of juvenile crust formed in oceanic arc settings during the Archean to Paleoproterozoic. They were likely accreted during the early stages of convergent tectonism, representing fragments of oceanic terranes incorporated during the initial phases of crustal amalgamation (Polat et al., 2012).

The 3.14 ± 18 Ga old amphibolite (PF-23) indicates Mesoarchean crust formation in the Lajes block. It may point to the existence of an even older oceanic

crust within the boundaries of the Lajes Block. This scenario aligns with a geodynamic evolution where segments of oceanic crust were accreted to the RGND, then expanded, and later subducted, leading to the formation of magmatic arcs and oceanic island arc complexes between approximately 2.4 and 2.3 Ga. This time frame marks the main tectono-magmatic event documented in the region.

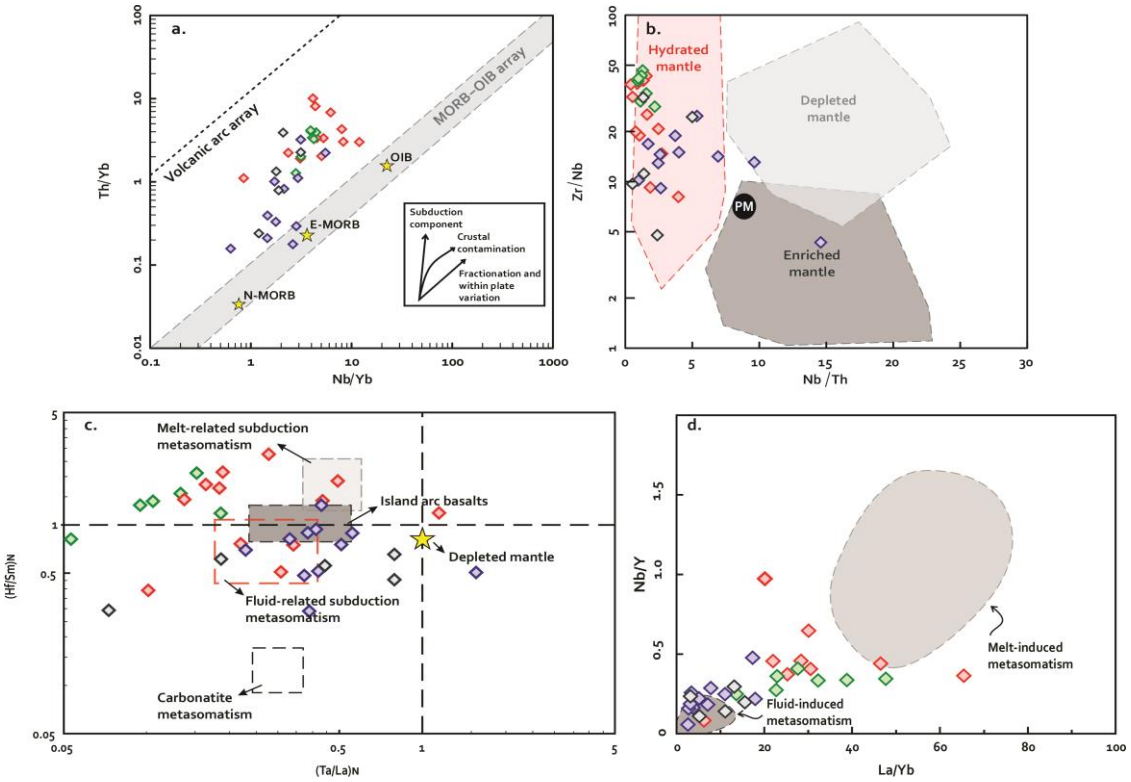



Figure 13 – a. Variation diagram of Th/Yb vs Nb/Yb after Pearce (2008). b. Zr/Nb vs. Nb/Th plot reflecting mantle hydration (after Condie, 2015). c. $(Hf/Sm)_N$ vs $(Ta/La)_N$ (after La Flèche et al., 1998) diagram for identification of subduction-related characteristics. d. Nb/Y vs. La/Yb (after Hoffer et al., 2008). Amphibolite – blue diamond, garnet-bearing calc-silicate rock – red diamond, epidote-rich calc-silicate rock – green diamond, hornblendite – gray diamond.

Boninite and high-Mg andesite are undocumented, but the low-K tholeiitic rocks recorded in the SLS likely originated from a depleted mantle source that was re-fertilized by subduction-related fluids and hydrous magmatism, with minor contributions of Archean crustal remnants. Their distribution of REEs, LILEs, and HFSEs, including negative anomalies of Nb-Ta and Ti, indicates that they are part of a Siderian juvenile oceanic island arc system, with minor layers of reworked

old Archean fragments. The major magmatic event recorded in the Lajes Block is of Siderian age and is characterized by formation of juvenile oceanic and continental crust growth, evidenced by zircon crystallization ages around 2.48 to 2.32 Ga and $T_{DM}$ model ages of 2.36 to 2.12 Ga and positive $\varepsilon_{Nd}(t)$ values varying between +1.20 and + 2.15.

The discrepancy observed between the crystallization ages and the $T_{DM}$ model ages can be explained by the distinct isotopic behavior of the U–Pb system in zircon and the Sm–Nd system in whole rock, which record different geological domains. Zircon grains, owing to their magmatic preservation and high resistance to post-crystallization processes, reliably constrain the crystallization ages of the protoliths. In contrast, the whole-rock Sm–Nd system is more prone to isotopic disturbance, since Nd may be partially mobilized during metamorphic or hydrothermal overprinting. Consequently, some Sm–Nd model ages appear younger than the corresponding U–Pb zircon ages. These younger values likely reflect partial isotopic resetting during subsequent thermal events, whereas the U–Pb system in zircon remained closed.

Continuous plate convergence led to the accretion of abundant Rhyacian Caicó Complex rocks. The rock formations were created by widespread granitic, alkali-granitic, and gabbroic magmatism dating back to 2.23 Ga and associated with magmatic arc processes. This was quickly followed by late-to post-collisional tholeiitic magmatism at 2.19 Ga (Ferreira et al., 2019), which has been structurally, geophysically (Padilha et al., 2019, 2021) and geochemically interpreted as the final stage of SLS arc collision. Ediacaran granitoids (~553 Ma; Souza et al., 2016) related to the Brasiliano Orogeny (Nascimento et al., 2015) intruded the basement and provided fluids to the late metasomatic alterations (Corrêa et al., 2020, 2021).

An old metamorphic event recorded by granitic leucosome indicates higher-grade episodes and melting in RGND around 2.21 to 2.0 Ga (Ferreira et al., 2020, 2023). This event was the first of three responsible for the chemical heterogeneities in the protholiths and disturbance of the Sm-Nd isotopic system of SLS rocks, along with other domains of BP (Ferreira et al., 2023). A pre-Brasiliano tectono-metamorphic event, during a Paleoproterozoic orogeny (~2.2–1.9 Ga; Boniface and Schenk, 2019), was responsible for the formation of

migmatites associated with low-angle structures (thrust-type tectonics) and limited magmatic activity (Jardim de Sá, 1994; Dantas et al., 2004; Souza et al., 2007). A similar situation is recorded in Africa (Aidoo et al., 2021). The third metamorphic event at 600 Ma (Brasiliano Orogeny) was more widespread, recorded in most lower intercepts of dated amphibolite lenses and calc-silicate rocks, and is responsible for the enrichment in LREE.

### 5.2 Constraints on the composition of the source

In Precambrian settings, mafic and ultramafic assemblages often indicate two different geotectonic environments. The first represents ancient oceanic lithosphere accreted onto continents during the closure of ocean basins and consequently undergoes subduction, accretion, and collision processes. The second refers to the roots of ancient island arcs (Ganguly et al., 2022). Only slices containing the geochemical signature of ancient oceanic crust and mantle sections are preserved in these environments. Here, we document a rare and well-preserved Siderian association of low-K tholeiitic amphibolites, garnet-bearing calc-silicate rocks, epidote-rich calc-silicate rocks, and hornblendite. Their chemical, petrographic, structural, temporal, and spatial relations strongly indicate a petrogenetic link. It is as if they were derived from a common precursor in a shared environment and in a short period of time but underwent different levels of differentiation, crustal contamination, and metasomatic alterations.

The studied amphibolite samples consist of basalts and basaltic andesite with tholeiitic affinity. Their low-K ($K_2O$ = 0.48-1.21 wt%) contents classify these samples as low-K tholeiites. The REE patterns and the primitive mantle-normalized incompatible trace element patterns indicate a petrogenetic evolution involving multiple stages. These stages range from MORB to enriched melt compositions and have a larger slab component. Samples AC-35C and PF-14B fit in the MORB-OIB diagonal on the Nb/Yb vs. Th/Yb plot (Fig. 13a). Nine samples of amphibolite spread in an enrichment trend on the Nb/Yb vs. Th/Yb diagram characterized by a magmatic succession, showing transitional features of MORB and arc affinity geochemical traits. In addition, their negative anomalies of Nb-Ta and Ti are also consistent with the geochemical features of typical lavas

related to supra subduction zones in island arc settings. Their concentrations of Ni (88-175 ppm) and V (117-260 ppm) also indicate an island-arc signature (Winter, 2010).

The late metasomatic events altered the original mineral composition and disturbed the distribution of major and minor chemical elements in the calc-silicate rocks. However, their original island arc signature appears preserved and well expressed through the Nb-Ta and Ti negative anomalies and on the Nb/Yb vs. Th/Yb plot (Fig. 13a). In this diagram, the scattering of samples shows that both calc-silicate rock types follow the same trend as low-K tholeiitic amphibolites, supporting a common precursor, with the primary differentiation between them marked by a substantial enrichment in LREEs and LILEs. This enrichment is reflected in the reduced quartz modal proportion and in the increased content of garnet, epidote, and allanite, along with notable textural changes. In the epidote-rich calc-silicate rocks, the increase in LREEs and LILEs is even more expressive and also expressed in HREEs and HFSEs contents (see Corrêa et al., 2021). This suggests that the late hydrothermal alteration was more pervasive in this unit than in the garnet-bearing calc-silicate one.

However, two other pathways must be considered. First, this behavior may also be due to interactions with an old crust. $\varepsilon_{Nd(t)}$ values in these rocks range from positive to negative, indicating a juvenile magmatic source but also suggesting a recycled Archean slab (model ages between 3.97 and 2.12 Ga). Second, petrogenetic models involving low-K tholeiitic basalts are often associated to basaltic andesite depleted mantle. In subduction systems, the origin of enriched components (LREEs and LILEs) is often attributed to the metasomatism of the mantle source region by hydrous fluids or melts (Pearce, 1982; Zhong et al., 2021). Plots of the samples studied on Nb/Th vs. Zr/Nb (Fig. 13b), Nb/T vs. Zr/Nb, $(Ta/La)_N$ vs. $(Hf/Sm)_N$, and La/Yb vs. Nb/Y diagrams show significant input from a hydrated arc mantle and fluid-induced metasomatism (Fig. 13b-d). In this sense, the transition from a depleted mantle source to a LREE-LILE-enriched metasomatized one occurs through the input of fluid components related to subduction and hydrous arc magmatism — a typical result of subduction evolution and chemo-stratigraphic maturation.

The parallel field relationship, age and even geochemical trends between the low-K tholeiitic amphibolites and the hornblendite body corroborate the hydrous magmatic origin. The hornblendite is a small, less-exposed metamorphic body, making it difficult to determine its primary mineralogy. Its geochemical characteristics (Table 3) indicate a mantle-derived, igneous origin (MgO = 15.05 – 18.65 wt%, Ni = 140 – 289 ppm, Mg# = 43.47 – 55.66), probably a residual, hydrous melt phase derived from the low-K tholeiitic mantle source. The described amphibole inclusions in olivine and clinopyroxene are consistent with an igneous relict phase, suggesting water in the magmatic source (Pilet et al., 2008; Polat et al., 2012). Experiments show that the stability field of amphibole occurs at 8 kbar at shallower to intermediate depths, consistent with primitive magmas found in subduction zones (Rapp and Watson, 1995; Fischer and Marty, 2005; Wallace, 2005). In addition to the negative anomalies of Nb-Ta and Ti, there is also a characteristic island arc feature. Many studies have demonstrated that amphibole functions like a sponge in these environments, filtering water that enters the crust from mantle-derived magmas (Davidson et al., 2007; Larocque and Canil, 2009; Aizawa et al., 2021). It may even be a fertile source for melts and fluids (Davidson et al., 2007). Hydrous minerals and enriched incompatible elements suggest that metasomatism occurs in the lithospheric mantle (Pilet et al., 2008; Smith, 2014).

Although Archean slab-derived components influenced the trace element content and pattern in the units of the Santa Luzia Sequence, the re-fertilization of the mantle source is probably the main reason for the increase in LILES, REEs, and $H_2O$ in the low-K tholeiitic amphibolites and hornblendite. The process was aided by adding $H_2O$ and trace elements from the amphibole. The incompatible elements and REEs enrichment is significantly higher in the calc-silicate types, indicating that late alteration events and epidotization were stronger and limited to them.

### 5.3 Hydrothermal and Metasomatic alteration of Mafic Rocks.

U-Pb geochronological data indicate that the garnet-bearing and epidote-rich calc-silicate rocks from the Santa Luzia Sequence are of Siderian age. The

metasomatic alteration events in the Santa Luzia Sequence are interpreted as a strong and complex event that spread throughout most of the Rio Grande do Norte Domain (Corrêa et al., 2020). Its various processes led to numerous metasomatic rocks with distinct mineralogical assemblages. In our study area, the calc-silicate units form through prolonged metasomatic reactions of low-K tholeiitic rocks associated with the formation of an island arc. The process of transformation of mafic rocks into calc-silicate rocks is a phenomenon that has been extensively documented at various geological sites worldwide. Even though the term “skarn” is commonly used to refer to this type of rock, in alignment with the suggestions put forth by Gillis and Banerjee (2000), Ordóñez-Calderón et al. (2008), and Gilgen et al. (2016), among others, this study employs the term "calc-silicate rock" to refer to these altered lithologies.

Chemically, the garnet-bearing calc-silicate rocks can be distinguished from the low-K tholeiitic rocks due to their higher $Al_2O_3$ (10.25-25.20 wt%) and CaO (4.21-19.98 wt%) contents and lower MgO. LILEs (Pb, Rb, Cs, Sr, Ba) and LREEs (La, Ce, Pr, Nd, Sm) were also variably enriched, confirming their large mobility. In contrast, some HREE concentration levels, such as Tb, Dy, Ho, Er, Tm, Yb, and Lu, are comparable to those of the low-K tholeiitic amphibolites, indicating their relative immobile behavior. These variations can be easily associated with diopside, garnet and epidote group mineral formation. The epidote-rich calc-silicate rocks are also associated with low-K tholeiitic rocks and display higher concentrations of $Al_2O_3$ (15.33-23.90 wt%), CaO (7.92-18.95 wt%), and $TiO_2$ (1.07-1.76 wt%). However, its main chemical distinguishing feature is the elevated concentrations of LREEs and LILEs (Fig. 14). In this context, both HREEs and HFSEs are also remobilized and concentrated. The increase in CaO, $TiO_2$, REEs, and trace elements is linked to the crystallization of apatite, epidote, zoisite, allanite, and titanite.

In the literature about the region, metasomatic fluids are believed to originate from hydrothermal migrations from the borders or cupolas of late Neoproterozoic igneous intrusions, younger than 575 Ma (Corrêa et al., 2020). The development of numerous shear zones during this period would have facilitated their rise. Corrêa et al. (2020, and references therein) argue that both studied calc-silicate rocks formed at the same crustal level under similar

temperature conditions. They estimated formation depth was between 10 and 15 km, at 400-580°C and 2-4 kbar. In this model, the key differences between garnet-bearing calc-silicate rocks and epidote-rich calc-silicate rocks are attributed to variations in the composition of the protolith and/or to the influence of multiple processes occurring within the system. These factors result in the formation of distinct mineral assemblages. Despite the studied calc-silicate rock types being associated with altered mafic rocks and spatially closer, the garnet-bearing calc-silicate ones show relatively older $T_{DM}$ model ages range (3.97 to 2.31 Ga), indicating an evolutionary history marked by Archean contributions. The positive to negative Eu anomalies (Eu/Eu*=0.49-1.52) may reflect (1) inheritance from a volcanic protolith and/or (2) mineralogical control. In the latter case, hydrothermal processes can redistribute REEs, with Eu being incorporated into or depleted by the crystallization of specific minerals, such as garnet and epidote. In addition to the limitations imposed by the composition of the protolith and the influences of the Archean slab, the dynamics of the magmatic-hydrothermal system itself may contribute to the diversity of mineralogical sets.

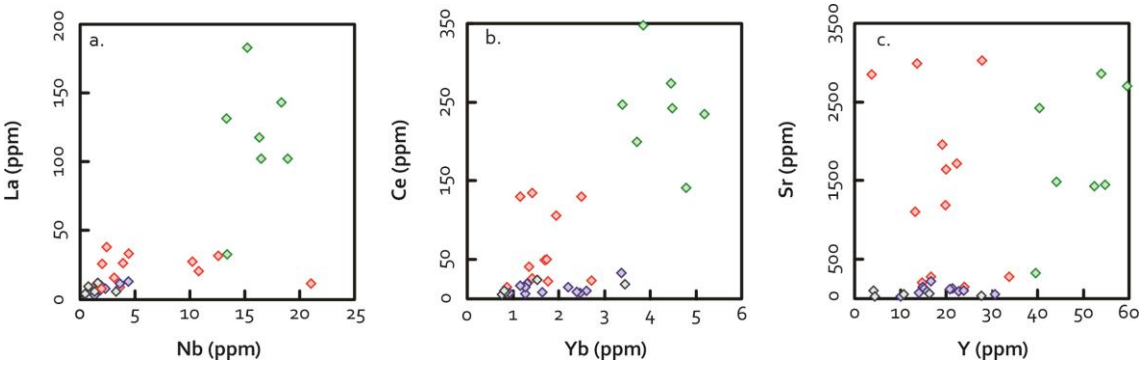



Figure 14 – a. Variation diagram of Nb (ppm) vs La (ppm). b. Yb (ppm) vs. Ce (ppm). c. Y (ppm) vs. Sr (ppm). Amphibolite – blue diamond, garnet-bearing calc-silicate rock – red diamond, epidote-rich calc-silicate rock – green diamond, hornblendite – gray diamond.

Hydrothermal fluids function as an active and constantly evolving system, which leads to the formation of distinct chemical signatures in a particular type of hydrothermal zoning during a young thermal and metamorphic Brasiliano event, around 600 Ma, that promoted the strong mobility record of some elements. Corrêa et al. (2021) suggest that higher concentrations of immobile elements are linked to hotter and deeper geological changes. Conversely, the presence of

alkalis, water, $CO_2$, and an increase in other more mobile elements is associated with lower temperatures in shallower regions. In this sense, higher input of HREEs, HFSEs, and even $Al_2O_3$ in the epidote-rich calc-silicate rocks predicts early hotter and deeper alteration, while garnet-bearing calc-silicate rocks are related to slightly lower temperatures.

### 5.5 Implication for plate tectonics in the early Paleoproterozoic

The last 30 years have seen much speculation about the plate tectonic regime at the start of the Paleoproterozoic era. The noticeable yet significant gap in zircon age spectra observed in magmatic activity, plate subduction, continental collision-related events, crustal growth, and apparent polar wander during the Early Paleoproterozoic era has led to interpretations of a complete shutdown or at least a period of significantly reduced tectonic activity. This hiatus is particularly notable between approximately 2365 and 2235 Ma (Condie et al., 2009; Condie and O'Nell, 2010; Spencer et al., 2018). While the scarce Siderian record is undeniable, some researchers have increasingly demonstrated that the tectonic shutdown or slowdown theory may have been a premature generalization. This is particularly evident when examining geological sites such as Laurentia, North China, India, northwest Africa, and, in our case, South America (Fetter et al., 2000; Gasquet et al., 2003; Santos et al., 2009; Wang et al., 2010; Kumar et al., 2012; Costa et al., 2021), especially the Borborema Province (see Neves, 2021).

Our research has reconstructed what appears to be ancient oceanic arc settings of Siderian age. The exposed fragment contains 2.48 Ga MORB-like basalts, 2.34 Ga old low-K tholeiitic rocks, 2.33 to 2.32 Ga old garnet-bearing calc-silicate rocks, epidote-rich calc-silicate rocks, and 2.32 Ga old hornblendite. These data, together with the 2.45 Ga tonalitic gneiss (Costa et al., 2021), suggest active plate subduction regime during the slowdown period in the Lajes Block region, Borborema Province. During this time window of record attenuation, other BP examples are represented in Fig. 15a and include: (i-ii) 2.30-2.35 Ga granodiorite gneiss of the Ceará Central Domain related to an island arc setting (Fetter et al., 2000; Santos et al., 2009); (iii) this study; (iv) 2.40 Ga supracrustal sequences interpreted as a period of magmatic insertion (Hollanda et al., 2011);

(v) slightly older 2.44 Ga orthogneisses and migmatites related to subduction settings in the Alto Moxotó Terrane (Santos et al., 2015); and (vi-viii) evidence of juvenile segments of 2.35-2.48 Ga is reported for tonalite-granodiorite gneiss links with the Neoarchean Granjeiro Complex (Pitarello et al., 2019; Archanjo et al., 2021).

On the other side of the Atlantic, northwest Africa, the initial Paleoproterozoic episodes of crustal growth are interpreted as starting around 2.3 Ga in the Paleoproterozoic Birimian-Eburnean orogeny (Gasquet et al., 2003; Aidoo et al., 2021). In the Paleoproterozoic Birimian terrane, slightly older rocks dating back to about 2.3 Ga (e.g. Taylor et al., 1992; Gasquet et al., 2003) have been identified as marking the early or initial stage of the Birimian-Eburnean Orogeny. These rocks are also interpreted as forming in a juvenile island arc (Aidoo et al., 2021). The theory of the development of multiple subduction zones in island arcs and intra-oceanic settings during the Siderian is supported by Pehrsson et al. (2014) and Spencer et al. (2018) and was initially proposed for West Gondwana by Bertrand and Jardim de Sá (1990). These systems are more challenging to preserve, explaining the scarce geological record. The convergence that began with the establishment of island arcs seems to have progressed, being responsible for the emplacement of abundant Rhyacian rocks, as well as the amalgamation of diverse juvenile and reworked Archean-Paleoproterozoic fragments (Fig. 15b).

Specifically, the tonalite gneisses and granodiorites forming the Granjeiro Complex, the 2.40 Ga lithotypes identified by Hollanda et al. (2011), and the rocks of the Santa Luzia Sequence seem to be aligned along shear zones (Fig. 15a). This setup implies that these units originally constituted a single block, which was then broken apart and reassembled during the Neoproterozoic. Hollanda et al. (2011) briefly theorized this earlier by establishing a correlation between the 2.40 Ga tonalites and the rocks of the Santa Luzia Sequence, which were previously described in Dantas et al. (2008). Nevertheless, the geological processes responsible for forming these rock sequences remain not entirely understood.

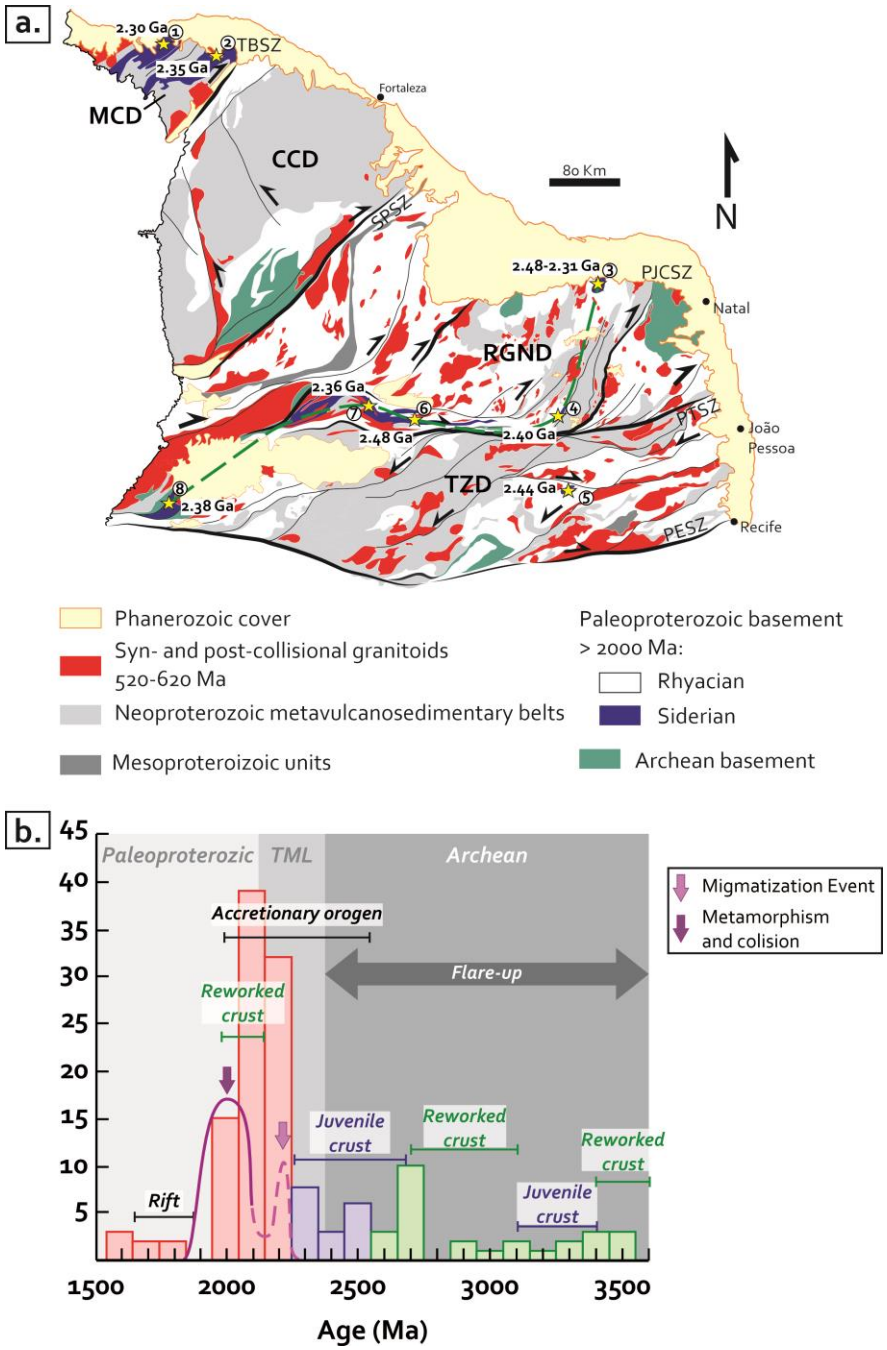



Figure 15 – a. Compilation of magmatic ages for the Siderian time interval in the MCD (Médio Coreaú Domain), CCD (Ceará Central Domains), RGND (Rio Grande do Norte Domain), and TZD (Traversal Zone Domain) settings. Yellow stars denote: 1-2. granodiorite gneiss of the Ceará Central Domain related to an island arc setting (Fetter et al., 2000; Santos et al., 2008); 3. this study; 4. supracrustal sequences interpreted as a period of magmatic insertion (Hollanda et al., 2011); 5. orthogneisses and migmatites related to subduction settings in the Alto Moxotó Terrane (Santos et al., 2015); and 6-8. tonalite-granodiorite gneiss links with the Neoarchean Granjeiro Complex (Pitarello et al., 2019; Archanjo et al., 2021). b. Histogram of Proterozoic U-Pb zircon ages of igneous and metaigneous rocks from the Borborema Province. Data have been filtered and from Neve et al (2021).

In the South American Platform, coeval 2.36 to 2.33 Ga island arc events are also recognized in the high-Al Lagoa Dourada TTG suite (Seixas et al., 2012), the orthogneiss of the Resende Suite (Teixeira et al., 2015) in the Mineiro Belt. TTG and sanukitoid suites dated between ~2.44 and ~2.07 Ga, along with enderbitic granulites (~2.44 Ga), are described within the Minas–Bahia Orogen, whereas the juvenile Cassiterita Orthogneiss (2.47–2.41 Ga) occurs in the Mineiro Belt (Barbosa et al., 2016, 2019; Bruno et al., 2021; Araújo, 2021). The 2.36 Ga Três Palmeiras greenstone belt with island-arc geochemical affinities and associated 2.34 Ga tonalite were documented in the Bacajá domain, Amazonian Craton (Vasquez et al., 2008; Macambira et al., 2009). In the eastern part of the Amazonian Craton, gabbroic rocks of the Île de Cayenne Complex, dated between 2.26 and 2.20 Ga, are also associated with early oceanic magmatic events (Delor et al., 2003). Rare magmatism related to constructive and passive continental margins is attributed to Vila Nova Group rocks at 2.27 Ga, Guyana Shield (McReath and Faraco, 2006). In the western border of the São Francisco Craton, events from the Early Paleoproterozoic are also documented (Fuck et al., 2014; Pontes et al., 2024). A juvenile magmatic contribution during the Siderian–Orosirian window is reported by Cruz et al. (2016) in the Gavião Paleoplate. The Natividade-Cavalcanti domain contains 2.37 and 2.35 Ga old granite gneisses, which played a significant role in forming the continental crust in the Tocantins Province (Fuck et al., 2014). Also in the Tocantins Province, 2.26-2.0 Ga arc magmatism is reported in the Cavalcante-Natividade Block (Saboia et al., 2025a), as well as 2.47 Ga to 2.28 Ga and 2.26-2.18 Ga arc rocks in the Almas-Conceição do Tocantins Domain (Saboia et al., 2020a, b, 2025b). In the southern part of the South American Platform, Luís Alves Craton, the work of Basei et al. (1998) documented enderbitic gneisses with a U-Pb crystallization age of 2.35 Ga. In the São Luís Craton, the age of 2.24 Ga is reported for arc-related calc-alkaline metapyroclastic rocks (Klein et al., 2009). Lastly, metamorphic zircon (2.36 Ga) and monazite (2.36–2.34 Ga) ages have been identified in the Santa Maria Chico (TTG, São Gabriel Block) and Santa Catarina granulite complexes of the Rio de La Plata Craton (Tickyj et al., 2004; Hartmann et al., 2008).

## 6 CONCLUSIONS

The Santa Luzia Sequence in the Lajes Block, Borborema Province, reveals well-preserved fragments of Siderian oceanic crust dating from 2.48 to 2.32 Ga. The geochemical analysis of amphibolites and calc-silicate rocks, including negative Nb, Ta, and Ti anomalies, strongly supports a subduction-related setting. These anomalies, along with REE patterns indicating enrichment of LREE, point to a young oceanic island arc setting during the Siderian. Sm-Nd isotope analysis of amphibolites, calc silicate rocks and hornblendite shows $\varepsilon_{Nd(t)}$ values ranging from -3.41 to +3.09, with $T_{DM}$ model ages between 2.2 to 3.97 and anorther group between 2.62 and 3.9 Ga suggesting a primarily juvenile magmatic origin for the majority of magmatic events, although some interaction with older crustal material is indicated by the slight negative $\varepsilon_{Nd(t)}$ values in some samples.

Metasomatic processes extensively altered the amphibolites, partly converting them into garnet-bearing and epidote-rich calc-silicate. These processes are linked to Neoproterozoic events (younger than 575 Ma), likely driven by fluid migration from late-stage Neoproterozoic intrusions. The metasomatic fluids, rich in LILEs and REEs, were crucial in forming complex mineral assemblages of epidote, garnet, and allanite.

The presence of low-K tholeiitic rocks, metasomatized calc-silicate assemblages, and hornblendite suggests that the region experienced active subduction during the global tectonic slowdown of the TML, between 2.36 and 2.23 Ga. This study demonstrates, together with similar results in the South American Platform and elsewhere, that the formation of oceanic and island arcs during the TML contributed to the incremental growth of crustal material, which would later be involved in the agglutination of Rhyacian continental masses. These findings challenge the previously accepted concept of a global tectonic shutdown during the Tectono-Magmatic Lull and show that tectonic and magmatic activity persisted in certain regions.

## ACKNOWLEDGEMENTS

The authors thank the Coordenação de Aperfeiçoamento de Pessoal de Nível Superior (CAPES) and Conselho Nacional de Desenvolvimento Científico e Tecnológico (CNPq - 444320/2020-2) for their financial support. ELD and RAF thank CNPq for research fellowships. The authors express gratitude to Mariana Negrão for her pioneering work on the Santa Luzia Sequence in 2005, to colleague Carlos Vinícius for his support in the field, and to the technical staff of the Laboratório de Estudos Geodinâmicos, Geocronológicos e Ambientais, Universidade de Brasília.

## Declaration of generative AI and AI-assisted technologies in the writing process

During the preparation of this work, the author(s) used Grammarly AI (v1.2.116.1536) to improve language and readability. After using this tool/service, the author(s) reviewed and edited the content as needed and take(s) full responsibility for the content of the publication.

## Role of the funding source

The Conselho Nacional de Desenvolvimento Científico e Tecnológico (CNPq) and the/Coordenação de Aperfeiçoamento de Pessoal de Nível Superior (CAPES) were responsible for the financial support for this study.

## REFERENCES

Aidoo, F., Nude, P. M., Sun, F. Y., Liang, T., Zhang, S. B., 2021. Paleoproterozoic TTG-like metagranites from the Dahomeyide Belt, Ghana: Constraints on the evolution of the Birimian-Eburnean Orogeny. Precambrian Research 353 (2021) 106024. https://doi.org/10.1016/j.precamres.2020.106024.

Aizawa, M., Shinjo, R., Okamura, S., Takahashi, T., Fujibayashi, N., 2021. Geochemical evidence for “cryptic amphibole fractionation” and lower crust melting for the generation of island arc tholeiitic rocks from northern Fossa

Magna, central Japan. Lithos 386–387, 106028. https://doi.org/10.1016/j.lithos.2021.106028.

Almeida, F. F. M., Hasui, Y., Brito Neves, B. B., Fuck, R. A., 1981. Brazilian structural provinces: An introduction. Earth-Science Reviews, 17, 1-29. https://doi.org/10.1016/0012-8252(81)90003-9.

Angelim, L. A. A. (Ed.), 2006. Geologia e recursos minerais do Estado do Rio Grande do Norte: texto explicativo dos mapas geológico e de recursos minerais do Estado do Rio Grande do Norte. CPRM–Serviço Geológico do Brasil, FAPERN, Recife, 119 pp. Available at: https://rigeo.sgb.gov.br/handle/doc/10234

Araújo, C. E. G., Heilbron, M., Cutts, K., Almeida, J. C. H., Lana, C., Cordani, U. G., Valeriano, C. M. 2021. Siderian to Rhyacian evolution of the Juiz de Fora Complex: Arc fingerprints and correlations within the Minas–Bahia Orogen and the Western Central Africa Belt. Precambrian Research 359, 106118. https://doi.org/10.1016/j.precamres.2021.106118.

Archanjo, C. J., Hollanda, M. H. B. M., Rodrigues, S. W., Brito Neves, B. B., 2008. Fabrics of pre- and syntectonic granite plutons and chronology of shear zones in the Eastern Borborema Province, NE Brazil. Journal of Structural Geology 30, 310–336. http://dx.doi.org/10.1016/j.jsg.2007.11.011.

Archanjo, C. J., Hollanda, M. H. B. M., Viegas, L. G. F., 2021. Late Ediacaran lateral-escape tectonics as recorded by the Patos shear zone (Borborema Province, NE Brazil). Brazilian Journal of Geology. 51(2): e20200132. https://doi.org/10.1590/2317-4889202120200132.

Arthaud, M. H., Caby, R., Fuck, R. A., Dantas, E. L., Parente, C. V., 2008. Geology of the northern Borborema Province, NE Brazil and its correlation with Nigeria, NW Africa. In: Pankhurst, R. J., Trouw, R. A. J., Brito Neves, B. B., De Wit, M. J. (Eds.), West Gondwama: Pre-Cenozoic Correlations Across the South Atlantic Region. Geological Society of London, Special Publications. 294, 49-67.

Barbosa, N., Teixeira, W., Ávila, C. A., Montecinos, P. M., Bongiolo, E. M., Vasconcelos, F. F., 2019. U–Pb geochronology and coupled Hf–Nd–Sr isotopic–chemical constraints of the Cassiterita Orthogneiss (2.47–2.41 Ga) in the Mineiro Belt, São Francisco Craton: Geodynamic fingerprints beyond the Archean–Paleoproterozoic Transition. Precambrian Research 326, 399–416. https://doi.org/10.1016/j.precamres.2018.01.017.

Basei, M. A. S., MacReath, L., Siga Júnior, O., 1998. The Santa Catarina Granulite Complex of Southern Brazil: a review. Gondwana Research 1(3-4), 383–391. https://doi.org/10.1016/S1342-937X(05)70854-6.

Belousova, E. A., Kostitsyn, Y. A., Griffin, W. L., Begg, G. C., O'Reilly, S. Y., Pearson, N. J., 2010. The growth of the continental crust: Constraints from zircon Hf-isotope data. Lithos. 119(3), 457-466. https://doi.org/10.1016/j.lithos.2010.07.024.

Bertrand, J. M., Jardim de Sá, E. F., 1990. Where are the Eburnian-Transamazonian collisional belts? Can. J. Earth Sci. 27, 1382-1393. http://dx.doi.org/10.1139/e90-148.

Bleeker, W., 2003. The late Archean record: a puzzle in ca. 35 pieces. Lithos. 71(2–4), 99-134. https://doi.org/10.1016/j.lithos.2003.07.003.

Boniface, N., Schenk, V., 2019. Pillow lava basalts with back-arc MORB affinity from the Usagaran Belt, Tanzania: relics of Orosirian ophiolites. Journal of the Geological Society. 176 (5): 1007–1021. https://doi.org/10.1144/jgs2018-205.

Brito Neves, B. B., Dos Santos, E. J., Van Schmus, W. R., 2000. Tectonic history of the Borborema Province, Northeastern Brazil. In: Cordani, U., Milani, E. J., Thomaz Filho, A., Campos, D. A., (Eds.). Tectonic evolution of South America. 31st International Geological Congress, Rio de Janeiro, Brazil. 151–182. https://repositorio.usp.br/directbitstream/82959a42-149a-48b4-8c64-b34fa2c6f949/1131015.pdf.

Bruno, H., Teixeira, W., Ávila, C. A., Noce, C. M., Tassinari, C. C. G., Lana, C. 2021. Evidence for a complex accretionary history preceding the amalgamation of Columbia: The Rhyacian Minas–Bahia Orogen, southern São Francisco Paleocontinent, Brazil. Gondwana Research 92, 149–171. https://doi.org/10.1016/j.gr.2020.12.019.

Caxito, F. A., Uhlein, A., Dantas, E. L., Stevenson, R., Salgado, S. S., Dussin, I. A., Sial, A. N., 2016. A complete Wilson cycle recorded within the Riacho do Pontal orogen, NE Brazil: implications for the Neoproterozoic evolution of the Borborema province at the heart of West Gondwana. Precambrian Research 282, 97–120. http://dx.doi.org/10.1016/j.precamres.2016.07.001.

Condie, K. C., 1998. Episodic continental growth and supercontinents: A mantle avalanche connection? Earth and Planetary Science Letters. 163, 97-108. https://doi.org/10.1016/S0012-821X(98)00178-2.

Condie, K., 2015. Changing tectonic settings through time: Indiscriminateuse of geochemical discriminant diagrams. Precambrian Research. 266, 587–591. https://doi.org/10.1016/j.precamres.2015.05.004.

Condie, K., O'Neill, C., 2010. The Archean-Proterozoic boundary: 500 my of tectonic transition in Earth history. American Journal of Science. 310(9), 775-790. https://doi.org/10.2475/09.2010.01.

Condie, K. C., O'Neill, C., Aster, R. C., 2009. Evidence and implications for a widespread magmatic shutdown for 250 My on Earth. Earth and Planetary Science Letters. 282, 294-298. http://dx.doi.org/10.1016/j.epsl.2009.03.033.

Condie, K., Pisarevsky, S. A., Puetz, S. J., Spencer, C. J. Spencer, Teixeira, W., Faleiros, F. M., 2022. A reappraisal of the global tectono-magmatic lull at ~ 2.3 Ga. Precambrian Research. 376, 106690. http://dx.doi.org/10.1016/j.precamres.2022.106690.

Corrêa, R. S., Oliveira, C. G., Dantas, E. L., Botelho, N. F., 2020. Hydrothermal footprint related to regionalscale shear zonecontrolled scheelite mineralization, Seridó Wskarn system, northeastern Brazil. Journal of South American Earth Sciences. v. 103, art. 102755. https://doi.org/10.1016/j.jsames.2020.102755.

Corrêa, R. S., Oliveira, C. G., Dantas, E. L., Della Giustina, M. E. S., Hollanda, M. H. B. M., 2021. The root zones of the Seridó Wskarn system, northeastern Brazil: Constraints on the metallogenesis of a large Ediacaran tungsten Province. Ore Geology Reviews. https://doi.org/10.1016/j.oregeorev.2020.103884.

Costa, A. P., Dantas, A. R., 2018. Geology and mineral resources of the Lajes sheet (SB.24-X-D-VI), Rio Grande do Norte State, Brazil. Scale 1:100,000. Geological Survey of Brazil (CPRM), Recife, 163 p. ISBN 978-85-7499-253-2.

Costa, A. P., Cavalcante, R., Dantas, A. R., Rodrigues, J. B., Cunha, A. L. C., Lages, G. A., Alcântara, V. C., Lima, R. B., Spisila, A. L., 2021. Fragments of juvenile Siderian continental crust in the Rio Piranhas-Seridó Domain, Borborema Province, Northeastern Brazil, as deduced by zircon U-Pb and whole-rock Sm-Nd systematics. Journal of the Geological Survey of Brazil. 4(3), 223-237. http://dx.doi.org/10.29396/jgsb.2021.v4.n3.3.

Cruz, S. C. P., Barbosa, J. S. F., Santos-Pinto, M., Peucat, J. J., Paquette, J. L., Souza, J. S., Martins, V. S., Chemale Jr., F., Carneiro, M. A. 2016. The Siderian–Orosirian magmatism in the Gavião Paleoplate, Brazil: U–Pb geochronology, geochemistry and tectonic implications. Journal of South American Earth Sciences 69, 43–79. https://ui.adsabs.harvard.edu/link_gateway/2016JSAES..69...43P/doi:10.1016/j.jsames.2016.02.007.

Dantas, E. L., Negrão, M. M., Bühn, B. M., 2008. 2.3 Ga continental crust generation in the Rio Grande do Norte terrane, ne - Brazil. In: VI South American Symposium on Isotope Geology, San Carlos de Bariloche.

Dantas, E. L., Silva, A. M., Almeida, T., and Moraes, R. A. V., 2003. Old geophysical data applied to modern geological mapping problems: a case-study in the Seridó Belt, NE Brazil. Revista Brasileira de Geociências. 33(2-Suplemento):65-72.

Dantas, E. L., Van Schmus, W. R., Hackspacher, P. C., Fetter, A. H., Neves, B. B. B., Cordani, U. G., Nutman, A. P., Williams, S., 2004. The 3.4-3.5 São José do Campestre Massif, NE Brazil: remnants of the oldest crust in South America. Precambrian Research 130, 113-137. http://dx.doi.org/10.1016/j.precamres.2003.11.002.

Davidson, J., Turner, S., Handley, H., Macpherson, C., Dosseto, A., 2007. Amphibole "sponge" in arc crust?. Geology. 35 (9): 787–790. https://doi.org/10.1130/g23637a.1.

Delor, C., Lahondère, D., Egal, E., Lafon, J.-M., Cocherie, A., Gurrot, C., Rossi, P., Truffert, C., Théveniaut, H., Phillips, D., Avelar, V. G. de., 2003. Transamazonian crustal growth and reworking as revealed bu the 1:500.000-scale geological map of French Guiana. In: Rossi, P., Lafon, H. M., Vasquez, M. L. Spécial Bouclier guyanais. Geologie de la France. Orléans, BRGM/SGF, p. 5-57.

DePaolo, D. J., 1981. A neodymium and strontium isotopic study of the Mesozoic calc-alkaline granitic batholiths of the Sierra Nevada and Peninsular ranges, California. Journal of Geophysical Research 86:10,470–10,488. http://dx.doi.org/10.1029/JB086iB11p10470.

Dhuime, B., Hawkesworth, C. J., Cawood, P. A., Storey, C. D., 2012. A change in the geodynamics of continental growth 3 billion years ago. Science. 335, 1334-1336. https://doi.org/10.1126/science.1216066.

Ferreira, A. C. D., Dantas, E. L., Fuck, R. A., Nedel, I. M., 2020. Arc accretion and crustal reworking from late Archean to Neoproterozoic in Northeast Brazil. Sci. Rep. 10, 7855. https://doi.org/10.1038/s41598-020-64688-9.

Ferreira, A. D. C., Filho, C. F. F., Dantas, E. L., Souza, V. D. S., 2019. Paleoproterozoic mafic-ultramafic magmatism in the Northern Borborema Province, Northeast Brazil: Tectonic setting and potential for deposits. The Journal of Geology. 127(5), 483-504. http://dx.doi.org/10.1086/704256.

Ferreira, A. C. D., Stevens, G., Dantas, E. L., Fuck, R. A., Santos, T. J. S., Leandro, M. V. S., 2023. Heterogeneous Archean oceanic protoliths in Neoproterozoic retrogressed eclogites from Northeast Brazil: petrological, geochemical and Sr–Nd–Pb–Hf isotopic constraints. Lithos. v. 438, art. 107370. https://doi.org/10.1016/j.lithos.2023.107370.

Fetter, A. H., Van Schmus, W. R., Santos, T. J. S., Nogueira Neto, J. A., Arthaud, M. H., 2000. U-Pb and Sm-Nd Geochronological constraints on the crustal evolution and basement architecture of Ceará state, NW Borborema Province, NE Brazil: implications for the existence of the paleoproterozoic supercontinent Atlantica. Revista Brasileira de Geociência. 30(1), 102-106. Available at: chrome-extension://efaidnbmnnnibpcajpcglclefindmkaj/https://ppegeo.igc.usp.br/portal/wp-content/uploads/tainacan-items/15906/42716/10928-13141-1-SM.pdf.

Ferreira, J. A. M., Albuquerque, J. P. T., 1969. Sinopse da geologia da folha Seridó. Série Geologia Regional, 18. SUDENE, Recife, 47 p.

Fischer, T. P., Marty, B., 2005. Volatile abundances in the sub-arc mantle: insights from volcanic and hydrothermal gas discharges. Journal of Volcanology and Geothermal Research. 140(1–3), 205-216. https://doi.org/10.1016/j.jvolgeores.2004.07.022.

Forsyth, D., Uyeda, S., 1975. On the relative importance of the driving forces of plate motion. Geophys. J. Int. 43, 163-200. http://dx.doi.org/10.1111/j.1365-246X.1975.tb00631.x.

Fuck, R. A., Dantas, E. L., Pimentel, M. M., Botelho, N. F., Armstrong, R., Laux, J. H., Junges, S. L., Soares, J., E., Praxedes, I. F., 2014. Paleoproterozoic crust-formation and reworking events in the Tocantins Province, central Brazil: A contribution for Atlantica supercontinent reconstruction. Precambrian Research. 244, 53–74. http://dx.doi.org/10.1016/j.precamres.2013.12.003.

Ganade, C. E., Cordani, U. G., Agnossoumounde, Y., Caby, R., Basei, M. A. S., Weinberg, R. F., Sato, K., 2016. Tightening-up NE Brazil and NW Africa connections: New U-Pb/Lu–Hf zircon data of a complete plate tectonic cycle in the Dahomey belt of the West Gondwana Orogen in Togo and Benin. Precambrian Research 276, 24–42. https://doi.org/10.1016/j.precamres.2016.01.032.

Ganguly, S., Verencar, A., Santosh, M., Saha, A., Li, S., Arolkar, N., 2022. Relics of 2.6–2.5 Ga oceanic crust from the ultramafic-mafic complex of Goa, western India: Magmatic response to a progressive subduction system. Lithos. 430–431, 106855. https://doi.org/10.1016/j.lithos.2022.106855.

Gasquet, D., Barbey, P., Adou, M., Paquette, L., 2003. Structure, Sr–Nd isotope geochemistry and zircon U–Pb geochronology of the granitoids of the Dabakala area (Côte d'Ivoire): evidence for a 2.3 Ga crustal growth event in the Palaeoproterozoic of West Africa? Precambrian Research. 127, 329–354. https://doi.org/10.1016/S0301-9268(03)00209-2.

Gilgen, S. A., Diamond, L. W., Mercolli, I., 2016. Sub-seafloor epidosite alteration: Timing, depth and stratigraphic distribution in the Semail ophiolite, Oman. Lithos. 260, 191–210. http://dx.doi.org/10.1016/j.lithos.2016.05.014.

Gillis, K. M., Banerjee, N. R., 2000. Hydrothermal alteration patterns in supra-subduction zone ophiolites. Geological Society of America Special Papers. 349, 283–298. http://dx.doi.org/10.1130/0-8137-2349-3.283.

Hackspacher, P., Dantas, E. L., Godoy, A. M., Oliveira, M. A. F., Fetter, A., Van Schmus, W. R., 1999. Considerations about the evolution of the Ribeira Belt in the São Paulo State - Brazil, from U/Pb geochronology in metavolcanic rocks of the São Roque Group In: IGRM South American Symposium on Isotope Geology 2, Villa Carlos Paz, Actas. 310-313.

Hackspacher, P. C., Van Schmus, W. R., Dantas, E. L., 1990. Um embasamento transamazônico na Província Borborema. In: Congresso Brasileiro de Geologia, 36. Sociedade Brasileira de Geologia, Natal. p. 2683–2696.

Hartmann, L. A., Liu, D., Wang, Y., Massonne, H. -J., Santos, J. O. S., 2008. Protolith age of Santa Maria Chico granulites dated on zircons from an associated amphibolite-facies granodiorite in southernmost Brazil. Anais da Academia Brasileira de Ciências. 80, 543–551. https://doi.org/10.1590/S0001-37652008000300014.

Hoffer, G., Eissen, J.-P., Beate, B., Bourdon, E., Fornari, M., Cotten, J., 2008. Geochemical and petrological constraints on rear-arc magma genesis processes in Ecuador: The Puyo cones and Mera lavas volcanic formations. Journal of Volcanology and Geothermal Research. 176(1), 107–118. https://doi.org/10.1016/j.jvolgeores.2008.05.023.

Hollanda, M. H. B. M., Archanjo, C. J., Bautista, J. R., Souza, L. C., 2015. Detrital zircon ages and Nd isotope compositions of the Seridó and Lavras da Mangabeira basins (Borborema Province, NE Brazil): Evidence for exhumation and recycling associated with a major shift in sedimentary provenance. Precambrian Research. 258, 186-207. https://doi.org/10.1016/j.precamres.2014.12.009.

Hollanda, M. H. B. M., Archanjo, C. J., Souza, L. C., Dunyi, L., Armstrong, L., 2011. Long-lived Paleoproterozoic granitic magmatism in the Seridó-Jaguaribe domain, Borborema Province-NE Brazil. Journal of South American Earth Sciences. 32, 287-300. https://doi.org/10.1016/j.jsames.2011.02.008.

Hollanda, M. H. B. M., Souza Neto, J. A., Archanjo, C. J., Stein, H., Maia, A. C. S., 2017. Age of the granitic magmatism and the WMo mineralization in skarns of the Seridó belt (NE Brazil) based on zircon UPb (SHRIMP) and molybdenite ReOs dating. Journal of South American Earth Sciences. 79, 1–11. https://doi.org/10.1016/j.jsames.2017.07.011.

Huang, M., Xu, T., Lü, Q., Lin, J., Bai, Z., Deng, Y., Zhang, Y., Badal, J., 2022. Crustal structure along the Wanzai–Yongchun profile in the Cathaysia Block, Southeast China, constrained by a joint active and passivesource seismic experiment. Geophysical Journal International. 231(1), 384–393. https://doi.org/10.1093/gji/ggac198.

Irvine, T. N. J., Baragar, W. R. A. F., 1971. A guide to the chemical classification of the common volcanic rocks. Canadian Journal of Earth Sciences. 8 (5), 523–548. https://ui.adsabs.harvard.edu/link_gateway/1971CaJES...8..523I/doi:10.1139/e71-055.

Jackson, S. E., Pearson, N. J., Griffin, W. L., Belousova, E. A., 2004. The application of laser ablation-inductively coupled plasma-mass spectrometry to in situ U–Pb zircon geochronology. Chemical Geology. 211(1-2), 47-69. https://doi.org/10.1016/j.chemgeo.2004.06.017.

Jardim de Sá, E. F., 1994. A Faixa Seridó (Província Borborema, NE do Brasil) e o seu significado geodinâmico na cadeia Brasiliana/Pan Africana. Thesis, Universidade de Brasília, Brasília. 803 p.

Klein, E. L., Luzardo, R., Moura, C. A. V., Lobato, D. C., Brito, R. S. C., Armstrong, R., 2009. Geochronology, Nd isotopes and reconnaissance geochemistry of volcanic and metavolcanic rocks of the São Luís Craton, northern Brazil: implications for tectonic setting and crustal evolution. Journal of South American Earth Sciences. 27, 129–145. https://doi.org/10.1016/j.jsames.2008.07.001.

Kumar, A., Hamilton, M. A., Halls, H. C., 2012. A Paleoproterozoic giant radiating dyke swarm in the Dharwar Craton, southern India. Geochemistry, Geophysics, Geosystems. v. 13, artigo GGG2011. https://doi.org/10.1029/2011GC003926.

La Flèche, M. R., Camire, G., Jenner, G. A., 1998. Geochemistry of post-Acadian, Carboniferous continental intraplate basalts from the Maritimes Basin, Magdalen islands, Quebec, Canada. Chemical Geology. 148, 115–136. https://doi.org/10.1016/S0009-2541(98)00002-3.

Larocque, J., Canil, D., 2010. The role of amphibole in the evolution of arc magmas and crust: the case from the Jurassic Bonanza arc section, Vancouver Island, Canada. Contributions to Mineralogy and Petrology 159, 475–492. http://dx.doi.org/10.1007/s00410-009-0436-z.

Lima, E. A. M., Wanderley, A. A., Vieira, Â. T., Medina, A. I. M., Barbosa, A. J., Vasconcelos, A. M., Amaral, C. A., Sato, E. Y., Silva, E. H. R., Leite, J. F., Moraes, J. F. S., Ribeiro, J. A.; Nesi, J. R., Angelim, L. A. A., Calheiros, M. E. V., 1980. Projeto Scheelita do Seridó: relatório final. Brasília: CPRM. Relatório técnico. https://rigeo.sgb.gov.br/handle/doc/9240.

Lucas, D., Hollanda, M. H. B. M., Souza Neto, J. A., Souza, L., 2024. Unraveling the evolution of the Bodó W-skarn district in the Seridó Mineral Province (NEBrazil): constraints from C–O stable isotopes, thermodynamic modeling, and geochronology. Mineralium Deposita, 60(1), 1–22. https://doi.org/10.1007/s00126-024-01300-4.

Macambira, M. J. B., Vasquez, M. L., da Silva, D. C. C., Galarza, M. A., Barros, C. E. de M., Camelo, J. de F., 2009. Crustal growth of the central-eastern Paleoproterozoic domain, SW Amazonian craton: Juvenile accretion vs. reworking. Journal of South American Earth Sciences 27, 235–246. http://dx.doi.org/10.1016/j.jsames.2009.02.001.

McReath, I., Faraco, M. T. L., 2006. Paleoproterozoic Greenstone-Granite Belts in Northern Brazil and the Former Guyana Shield - West African Craton Province. Geologia USP Série Científica 5(2), 49–63. http://dx.doi.org/10.5327/S1519-874X2006000100004.

Nascimento, M. A. L., Galindo, A. C., Medeiros, V. C., 2015. Ediacaran to Cambrian magmatic suites in the Rio Grande do Norte domain, extreme Northeastern Borborema Province (NE of Brazil): Current knowledge. Journal of South American Earth Sciences. 58, 281-299. http://dx.doi.org/10.1016/j.jsames.2014.09.008.

Negrão, M. N., Dantas, E. L., Souza, A. L. S., Rosado, T. M. S., 2005. Evidências de Fontes Crustais Arqueanas na Região do Cabugi RN. In: XXI Simpósio de Geologia do Nordeste, Recife. p. 89.

Neves, S. P., 2003. Proterozoic history of the Borborema Province (NE Brazil): correlations with neighboring cratons and Pan-African belts and implications for the evolution of Western Gondwana. Tectonics. 22, 1031. https://doi.org/10.1029/2001TC001352.

Neves, S. P., 2021. Comparative geological evolution of the Borborema Province and São Francisco Craton (eastern Brazil): Decratonization and crustal reworking during West Gondwana assembly and implications for paleogeographic reconstructions. *Precambrian Research,* 355, 106119. https://doi.org/10.1016/j.precamres.2021.106119.

Neves, S. P., Tommasi, A., Vauchez, A., Carrino, T. A., 2021. The Borborema strike-slip shear zone system (NE Brazil): Large-scale intracontinental strain localization in a heterogeneous plate. Lithosphere, Article ID 6407232. https://doi.org/10.2113/2021/6407232.

O'Neill, C., Lenardic, A., Moresi, L., Torsvik, T. H., Lee, C.-T. A., 2007. Episodic Precambrian subduction. Earth and Planetary Science Letters. 262, 552-562. https://doi.org/10.1016/j.epsl.2007.04.056.

Oliveira, R. G., Medeiros, W. E., 2018. Deep crustal framework of the Borborema Province, NE Brazil, derived from gravity and magnetic data. Precambrian Research 315, 45–65. https://doi.org/10.1016/j.precamres.2018.07.004.

Ordóñez-Calderón, J. C., Polat, A., Fryer, B. J., Gagnon, J. E., Raith, J. G., Appel, P. W. U., 2008. Evidence for HFSE and REE mobility during calc silicate metasomatism, Mesoarchean (~3075Ma) Ivisaartoq greenstone belt, southern West Greenland. Precambrian Research. 161 (3–4), 317-340. https://doi.org/10.1016/j.precamres.2007.09.004.

Padilha, A. L., Santos-Matos, A. C. L., Batista, J. C., Vitorello, I., Pádua, M. B., Fuck, R. A., 2021. Magnetotelluric evidence for a Rhyacian suture zone hidden underneath the Seridó belt, Borborema Province, Northeastern Brazil. Precambrian Research. 365, 106413. https://doi.org/10.1016/j.precamres.2021.106413.

Padilha, A. L., Vitorello, I., Pádua, M., Fuck, R. A., 2019. Magnetotelluric images of Paleoproterozoic accretion and Mesoproterozoic to Neoproterozoic reworking processes in the northern São Francisco Craton, central eastern Brazil. Precambrian Research 333, 105416. http://dx.doi.org/10.1016/j.precamres.2019.105416.

Partin, C., Bekker, A., Sylvester, P., Wodicka, N., Stern, R., Chacko, T., 2014. Filling in the juvenile magmatic gap: Evidence for uninterrupted Paleoproterozoic

plate tectonics. Earth and Planetary Science Letters. 388. 123-133. https://doi.org/10.1016/j.epsl.2013.11.041.

Paton, C., Hellstrom, J., Paul, B., Woodhead, J., Hergt, J., 2011. Iolite: Freeware for the Visualisation and Processing of Mass Spectrometric Data. J. Anal. At. Spectrom. VL - IS -. http://dx.doi.org/10.1039/C1JA10172B.

Pearce, J., 1982. Trace Element Characteristics of Lavas from Destructive Plate Boundaries. In: Andesites: Orogenic Andesites and Related Rocks, John Wiley and Sons, pp.525-548. Available at: https://www.researchgate.net/publication/304749002_Trace_Element_Characteristics_of_Lavas_from_Destructive_Plate_Boundaries.

Pearce, J.A. (1996). A user's guide to basalt discrimination diagrams. In: Wyman, D.A. (Ed.), Trace Element Geochemistry of Volcanic Rocks: Applications for Massive Sulphide Exploration. Geological Association of Canada, Short Course Notes, 12, 79–113. Available at: https://www.researchgate.net/publication/238170061_A_User%27s_Guide_to_Basalt_Discrimination_Diagrams.

Pearce, J. A., 2008. Geochemical fingerprinting of oceanic basalts with applications to ophiolite classification and the search for Archean oceanic crust. Lithos. 100, 14–48. https://doi.org/10.1016/j.lithos.2007.06.016.

Pehrsson, S., Buchan, K., Eglington, B., Berman, R., Rainbird, R., 2014. Did plate tectonics shutdown in the Paleoproterozoic? A view from the Siderian geologic record. Gondwana Research. 26. https://doi.org/10.1016/j.gr.2014.06.001.

Petrus, J., 2012. VizualAge: A novel approach to laser ablation ICP-MS U-Pb geochronology data reduction. Geostandards and Geoanalytical Research. 36(3), 247–270. http://dx.doi.org/10.1111/j.1751-908X.2012.00158.x.

Pilet, S., Baker, M. B., Stolper, E. M., 2008. Metasomatized Lithosphere and the Origin of Alkaline Lavas. Science. 320, 916-919. http://dx.doi.org/10.1126/science.1156563.

Pitarello, M. Z., Dos Santos, T. J. S., Ancelmi, M. F., 2019. Syn-to postdepositional processes related to high grade metamorphic BIFs: Geochemical and geochronological evidences from a Paleo to Neoarchean (3.5–2.6 Ga) terrane in NE Brazil. Journal of South American Earth Sciences. v. 96, p. 102312. https://doi.org/10.1016/j.jsames.2019.102312.

Polat, A., Fryer, B. J., Samson, I. M., Weisener, C., Appel, P. W. U., Frei, R., Windley, B. F., 2012. Geochemistry of ultramafic rocks and hornblendite veins in the Fiskenæsset layered anorthosite complex, SW Greenland: Evidence for hydrous upper mantle in the Archean. Precambrian Research. 214–215, 124–153. https://doi.org/10.1016/j.precamres.2011.11.013.

Pontes, J. C., Oliveira, E. P., Cruz, S. C. P., Santos, T. J. S., Silva, J. R. C. 2024. Evidence of Siderian juvenile-like contribution to the continental arc magmatism in the Western Guanambi–Correntina Block, São Francisco Craton (Brazil). Journal of South American Earth Sciences 137, 104841. https://doi.org/10.1016/j.jsames.2024.104841.

Rapp, R. P., Watson, E. B., 1995. Dehydration Melting of Metabasalt at 8–32 kbar: Implications for Continental Growth and Crust-Mantle Recycling. Journal of Petrology. 36(4), 891–931. https://doi.org/10.1093/petrology/36.4.891.

Saboia, A.M., Fuck, R.A., Dantas, E.L., Oliveira, C.G., Corrêa, R.T., Rodrigues, J.B., Scandolara, J.E., Costa, F.G., Cuadros, F.A., Uchigasaki, K. 2025. Paleoproterozoic (2.26-2.0 Ga) arc magmatism and geotectonic evolution of the Cavalcante-Natividade Block, Central Brazil. Journal of South American Earth Sciences 153, 105350. https://doi.org/10.1016/j.jsames.2025.105350.

Saboia, A.M., Fuck, R.A., Dantas, E.L., Oliveira, C.G., Corrêa, R.T., Scandolara, J.E., Costa, F.G., Rodrigues, J.B. Geotectonic evolution from the 2.47 Ga to 2.28 Ga Almas-Conceição do Tocantins Domain in Central Brazil, using isotopic (Sm-Nd) and whole-rock geochemical data: Insights into early Earth's geodynamical styles. Journal of the Geological Society, accepted 2025b. https://doi.org/10.1144/jgs2024-175.

Saboia, A. M., Oliveira, C. G., Dantas, E. L., Cordeiro, P., Scandolara, J. E., Rodrigues, J., Sousa, I. M. C. 2020a. The Siderian crust (2.47-2.3 Ga) of the Goiás massif and its role as a building block of the São Francisco paleocontinent. Precambrian Research 350, 105901. https://doi.org/10.1016/j.precamres.2020.105901.

Saboia, A. M., Oliveira, C. G., Dantas, E. L., Scandolara, J. E., Rodrigues, J., Cordeiro, P., Sousa, I. M. C. 2020b. The 2.26 to 2.18 Ga arc-related magmatism of the Almas-Conceição do Tocantins domain: An early stage of the São Francisco paleocontinent assembly in central Brazil. Journal of South American Earth Sciences 104, 102757. https://doi.org/10.1016/j.jsames.2020.102757.

Salim, J., 1982. Mineralização polifásica de tungstênio e molibidênio na região do Seridó, NE do Brasil. Cong. Lati. Am. Geol., Argentina. 2:529-543.

Santos, E. J., Medeiros, V. C., 1999. Constraints from granitic plutonism on Proterozoic crustal growth of the Transverse Zone, Borborema Province, NE-Brazil. Revista Brasileira de Geociências 29, 73–84. https://doi.org/10.25249/0375-7536.1999297384.

Santos, L. C. M. L., Dantas, E. L., Cawood, P. A., Santos, E. J., Fuck, R. A., 2017. Neoarchean crustal growth and Paleoproterozoic reworking in the Borborema Province, NE Brazil: insights from geochemical and isotopic data of TTG and metagranitic rocks of the Alto Moxotó Terrane. Journal of South American Earth Sciences 79, 342–363. https://doi.org/10.1016/j.jsames.2017.08.013.

Santos, L. C. M. L., Dantas, E. L., Santos, E. J., Santos, R. V., Lima, H. M., 2015. Early to late Paleoproterozoic magmatism in NE Brazil: the Alto Moxoto Terrane and its tectonic implications for the pre-West Gondwana assembly. Journal of South American Earth Sciences 58, 188–209. http://dx.doi.org/10.1016/j.jsames.2014.07.006.

Santos, T. J. S., Fetter, A. H., Hackspacher, P. C., VanSchmus, W. R., Nogueira Neto, J. A., 2008. Neoproterozoic tectonic and magmatic episodes in the NW sector of the Borborema Province, NE Brazil, during assembly of Western Gondwana. Journal of South American Earth Sciences, 25(3), 271–284. https://doi.org/10.1016/j.jsames.2007.05.006.

Santos, T., Fetter, A., Van Schmus, W., Hackspacher, P., 2009. Evidence for 2.35 to 2.30 Ga juvenile crustal growth in the northwest Borborema Province, NE Brazil. Geological Society, London, Special Publications. 323. 271-281. https://doi.org/10.1144/SP323.13.

Seixas, L. A. R., David, J., Stevenson, R., 2012. Geochemistry, Nd isotopes and U–Pb geochronology of a 2350 Ma TTG suite, Minas Gerais, Brazil: Implications for the crustal evolution of the southern São Francisco craton. Precambrian Research 196–197, 61–80. https://doi.org/10.1016/j.precamres.2011.11.002.

Sláma, J., Košler, J., Condon, D. J., Crowley, J. L., Gerdes, A., Hanchar, J. M., Horstwood, M. S. A., Morris, G. A., Nasdala, L., Norberg, N., Schaltegger, U., Schoene, B., Tubrett, M. N., Whitehouse, M. J., 2008. Plešovice zircon — A new natural reference material for U–Pb and Hf isotopic microanalysis. Chemical Geology. 249(1–2), 1-35. http://dx.doi.org/10.1016/j.chemgeo.2007.11.005.

Smith, D., 2014. Clinopyroxene precursors to amphibole sponge in arc crust. Nat Commun. 5, 4329. https://doi.org/10.1038/ncomms5329.

Souza Neto, J. A., Legrand, J. M., Volfinger, Pascal, M. L., Sonnet, P., 2008. W–Au skarns in the Neo-Proterozoic Seridó Mobile Belt, Borborema Province in

northeastern Brazil: an overview with emphasis on the Bonfim deposit. Miner Deposita. 43, 185–205. https://doi.org/10.1007/s00126-007-0155-1.

Souza, Z. S., Kalsbeek, F., Deng, X.-D., Frei, R., Kokfelt, T. F., Dantas, E.L., Li, J.-W., Pimentel, M. M., Galindo, A. C. 2016. Generation of continental crust in the northern part of the Borborema Province, northeastern Brazil, from Archaean to Neoproterozoic. Journal of South American Earth Sciences, 68, 68-96. https://doi.org/10.1016/j.jsames.2015.10.006.

Souza, Z. S., Martin, H., Peucat, J. J., Jardim de Sá, E. F., Macedo, M. H. F., 2007. Calc-Alkaline Magmatism At The Archean-Proterozoic Transition: The Caicó Complex Basement (Ne Brasil). Jounal of Petrology. 48, 2149-2185. http://dx.doi.org/10.1093/petrology/egm055.

Souza, Z. S., Vasconcelos, P. M., Nascimento, M. A. L., Silveira, F. V., Paiva, H. S., Dias, L. G. S., Thiede, D. & Carmo, I. O. 2003. $^{40}Ar/^{39}Ar$ geochronology of Mesozoic and Cenozoic magmatism in NE Brazil. Isotope Geology South American Symposium, 310-313. Available at: https://horizon.documentation.ird.fr/exl-doc/pleins_textes/divers17-05/010039206.pdf.

Spencer, C., Murphy, J., Kirkland, C., Liu, Y., Mitchell, R., 2018. A Palaeoproterozoic tectono-magmatic lull as a potential trigger for the supercontinent cycle. Nature Geoscience. 11, 97–101. https://doi.org/10.1038/s41561-017-0051-y.

Stern, R. J., Reagan, M., Ishizuka, O., Ohara, Y., Whattam, S., 2012. To understand subduction initiation, study forearc crust: To understand forearc crust, study ophiolites. Lithosphere. 4(6), 469–483. https://doi.org/10.1130/L183.1.

Strand, K., Köykkä, J., 2012. Early Paleoproterozoic rift volcanism in the eastern Fennoscandian Shield related to the breakup of the Kenorland supercontinent.

Precambrian Research. 214–215, 95-105. https://doi.org/10.1016/j.precamres.2012.02.011.

Sun, S. S., McDonough, W. F., 1989. Chemical and isotopic systematics of oceanic basalts: implications for mantle composition and processes. In Saunders, A. D., and Norry, M. J., eds. Magmatismin ocean basins. Geol. Soc. Lond. Spec. Publ. 42:313–345. http://dx.doi.org/10.1144/GSL.SP.1989.042.01.19.

Taylor, N. P., Moorbath, S., Leube, A., Hirdes, W., 1992. Early Proterozoic crustal evolution in the Birimian of Ghana: constraints from geochronology and isotope geochemistry. Precambr. Res. 56, 97–111. http://dx.doi.org/10.1016/0301-9268(92)90086-4.

Teixeira, W., Ávila, C. A., Dussinc, I. A., Corrêa Neto, A. V., Bongiolo, E. M., Santos, J. O., Barbosa, N. S., 2015. A juvenile accretion episode (2.35–2.32 Ga) in the Mineiro belt and its role to the Minas accretionary orogeny: Zircon U–Pb–Hf and geochemical evidences. Precambrian Research. 256, 148–169. http://dx.doi.org/10.1016/j.precamres.2014.11.009.

Tickyj, H., Hartmann, L. A., Vasconcellos, M. A. Z., Philipp, R. P., Remus, M. V. D., 2004. Electron microprobe dating of monazite substantiates ages of major geological events in the southern Brazilian shield. Journal of South American Earth Sciences. 16:699–713. http://dx.doi.org/10.1016/j.jsames.2004.01.001.

Trompette, R., 1994. Geology of Western Gondwana (2000-500): Pan-African-Brasiliano Aggregation of South America and Africa. Balkema, Rotterdam, 350 p. http://www.jstor.org/stable/41146557.

Van Schmus, W. R., Brito Neves, B. B., Hackspacher, P., Babinski, M. 1995. U/Pb and Sm/Nd geochronologic studies of the eastern Borborema Province, northeastern Brazil: initial conclusions. Journal of South American Earth Sciences. 8(3–4), 267–288. https://doi.org/10.1016/0895-9811(95)00013-6.

Van Schmus, W. R., Brito Neves, B. B., Williams, I. S., Hackspacher, P. C., Fetter, A. H., Dantas, E. L., Babinski, M., 2003. The Seridó Group of NE Brazil, a late Neoproterozoic pre-to syn-collisional basin in West Gondwana: insights form SHRIMP U-Pb detrital zircon ages and Sm-Nd crustal residence (TDM) ages. Precambrian Research 127, 287-327. https://doi.org/10.1016/S0301-9268(03)00197-9.

Van Schmus, W. R., Kozuch, M., Brito Neves, B. B., 2011. Precambrian history of the Zona Transversal of the Borborema Province, NE Brazil: insights from Sm–Ndand U–Pb geochronology. J. S. Am. Earth Sci. 31, 227-252. https://doi.org/10.1016/j.jsames.2011.02.010.

Van Schmus, W. R., Oliveira, E. P., Silva Filho, A. F., Toteu, S. F., Penaye, J., Guimarães, I. P., 2008. Proterozoic links between the Borborema Province, NE Brazil, and the Central African Fold Belt. In: Pankhurst R. J., Trouw R. A. J., Brito Neves B. B and De Wit M. J. (eds.) West Gondwana: Pre-Cenozoic correlations across the South Atlantic region. Geological Society, London, Special Publication. 294, 69-99. http://dx.doi.org/10.1144/SP294.5.

Vasquez, M. L., Macambira, M. J. B., Armstrong, R. A., 2008. Zircon geochronology of granitoids from the western Bacajá domain, southeastern Amazonian craton, Brazil: Neoarchean to Orosirian evolution. Precambrian Research 161, 279–302. http://dx.doi.org/10.1016/j.precamres.2007.09.001.

Vauchez, A., Neves, S. P., Caby, R., Corsini, M., Egydio-Silva, M., Arthaud, M., Amaro, V. 1995. The Borborema shear zone system, NE Brazil. Journal of South American Earth Sciences, 8(3–4), 247–266. https://doi.org/10.1016/0895-9811(95)00012-5.

Wallace, P. J., 2005. Volatiles in subduction zone magmas: concentrations and fluxes based on melt inclusion and volcanic gas data. Journal of Volcanology and Geothermal Research. 140(1–3), 217-240. http://dx.doi.org/10.1016/j.jvolgeores.2004.07.023.

Whattam, S. A., Stern, R. J., 2011. The “subduction initiation rule”: a key for linking ophiolites, intra-oceanic arcs, and subduction initiation. Contributions to Mineralogy and Petrology. 162, 1031–1045. https://doi.org/10.1007/s00410-011-0638-z.

Wiedenbeck, M., Priyanka, A., Corfu, F., Griffin, W., Meier, M., Oberli, F., von Quadt, A., Roddick, J. C., Spiegel, W., 2007. Three natural zircon standards for U-Th-Pb, Lu-Hf, trace element and REE analyses. Geostandards Newsletter. 19(1-23). http://dx.doi.org/10.1111/j.1751-908X.1995.tb00147.x.

Williams, H., Hoffman, P. F., Lewry, J. F., Monger, J. W. H., Rivers, T., 1991. Anatomy of North America: thematic geologic portrayals of the continent. Tectonophysics. 187 (1-3), 117-134. https://doi.org/10.1016/0040-1951(91)90416-P.

Winter, J. D. N., 2010. Principles of Igneous and Metamorphic Petrology, 2º edition, illustrated, Prentice Hall.

Yang, Q.-Y., Santosh, M., 2015. Paleoproterozoic arc magmatism in the North China Craton: No Siderian global plate tectonic shutdown. Gondwana Research. 28(1), 82.105. https://doi.org/10.1016/j.gr.2014.08.005.

Zhong, Y., Kusky, T., L., Wang, Polat, A., Liu, X., Luan, Z., Wang, C., Wang, J., Deng, H., Peng, Y., 2021. Alpine-style nappes thrust over ancient North China continental margin demonstrate large Archean horizontal plate motions. Nature Communications. 12:6172. https://doi.org/10.1038/s41467-021-26474-7.

# CAPÍTULO 6
# CONSIDERAÇÕES FINAIS

## CONSIDERAÇÕES FINAIS

A história evolutiva do Núcleo Arqueano Bonfim inicia-se com a diferenciação de magmas ricos em MgO entre o Hadeano (4201 ± 382 Ma; idade isocrônica Sm–Nd) e o Eoarqueano (3615 ± 316 Ma; idade isocrônica Sm–Nd). Os produtos gerados por esses magmas correspondem a resíduos ultramáficos que gradam composicionalmente de peridotitos depletados a olivina-websteritos. Eles apresentam assinaturas geoquímicas compatíveis com reservatórios mantélicos tanto depletados – similares ao DMM – quanto enriquecidos. Essas rochas ocorrem em dois pulsos magmáticos distintos. O primeiro apresenta idades de cristalização entre 3,57 ± 0,62 e 3,48 ± 0,57 Ga (U-Pb em zircão), enquanto o segundo varia de 3,10 ± 0,15 a 3,09 ± 0,34 Ga (U-Pb em zircão). Tectonicamente, são interpretadas como possíveis ofiolitos desmembrados que remontam oceanos primitivos. Para o conjunto de dados do Mesoarqueano, componentes associados a processos de subducção também são descritos em toleítos de arco e evidenciados pelo enriquecimento em elementos incompatíveis em talco-xistos, clorita-xistos e tremolititos. Um terceiro evento magmático, de idade riaciana (2,24 ± 0,16 – 2,16 ± 0,09 Ga), é também identificado nas unidades do Núcleo Arqueano Bonfim, estando melhor caracterizado a norte da área. A ausência de dados entre o Orosiriano e o Criogeniano indica um período de prolongada estabilidade tectônica. Essa quiescência foi interrompida por ciclos metasomáticos ocorridos entre 596 ± 5 Ma e 517 ± 5 Ma ($^{40}Ar/^{39}Ar$ em flogopita) e pela ativação de zonas de cisalhamento neoproterozoicas, associadas à orogenia Brasiliana/Pan-Africana e à amalgamação da porção ocidental da Gondwana.

A noroeste de Bonfim, a evolução da sequência Santa Luzia, situada no Bloco Lajes, é caracterizada por magmatismo juvenil (ƐNd(t) entre 0,73 – 2,69) toleítico de arco. Além de apresentar menor grau de retrabalhamento de fragmentos crustais arqueanos (TDM entre 2,56 e 3.97 Ga) e perturbação moderada do sistema isotópico Sm–Nd durante o Riaciano (TDM entre 2.28 – 2.12). A sequência é composta por anfibolitos, rochas calcissilicáticas e hornblenditos, apresentando idades de cristalização predominantemente siderianas, entre 2,48 ± 0,21 e 2,32 ± 0,91 Ga (U–Pb em zircão). Uma amostra

de anfibolito apresenta idade de 3,14 ± 0,18 Ga (U–Pb em zircão), evidenciando a influência de segmentos crustais mais antigos, retrabalhados durante eventos geológicos subsequentes. Os padrões geoquímicos de rocha total apresentam anomalias negativas marcantes em Nb, Ta e Ti, refletindo afinidades típicas de ambientes oceânicos e de arcos vulcânicos. As relações espaciais, geoquímicas e isotópicas sugerem que as rochas calcissilicáticas se originaram principalmente por alteração metasomática de precursores máficos. Embora tenham sofrido sobreposições metasomáticas e hidrotermais posteriores, resultando em enriquecimento em elementos de terras raras leves (LREE) e metamorfismo induzido por fluidos, as assinaturas magmáticas primárias permanecem preservadas, o que ressalta a resiliência da composição original dessas rochas. De maneira mais ampla, a sequência Santa Luzia se contrapõe as teorias de uma relativa paralisação tectônica logo após o início do Paleoproterozoico.

A comparação entre os conjuntos de dados de Bonfim e Santa Luzia indica que esses domínios registram diferentes níveis de preservação da assinatura magmática original e distintos graus de overprints metamórficos e metassomáticos. Em ambas as áreas esses episódios tardios modificaram a mineralogia primária. Todavia, o padrão de distribuição dos ETR pesados e de alguns elementos traço imóveis ainda resguarda o sinal geoquímico original. Do ponto de vista dos proxies isotópicos, o sistema Sm–Nd atua principalmente como traçador da fonte mantélica e dos processos de diferenciação manto–crosta. Embora conserve assinaturas juvenis a condríticas e, em menor proporção, evidências de retrabalhamento crustal, nas rochas mais alteradas o sistema Sm–Nd perde parcialmente sua robustez como indicador de fonte, exibindo perturbações isotópicas. Na Sequência Santa Luzia, por exemplo, esse comportamento reflete a atuação de eventos tectono-metamórficos riacianos a neoproterozoicos, que promoveram o reequilíbrio parcial do sistema. Como mencionado, o sinal de retrabalhamento crustal sugerido por esse método aponta para a participação de crostas mesoarqueanas, cronologicamente comparáveis às reconhecidas em Bonfim.

Por outro lado, as idades U–Pb em zircão constituem a ferramenta geocronológica mais robusta do conjunto, registrando diretamente eventos de

cristalização magmática. Mesmo sob intensa sobreposição metassomática e metamórfica, esse sistema preserva, em grande medida, o registro dos principais pulsos magmáticos e permite discriminar diferentes populações de zircão. Em termos tectônicos, a integração desses dados indica que Bonfim registra predominantemente um domínio de afinidade oceânica, com forte preservação de assinaturas mantélicas. Já Lajes, a partir da combinação entre Sm–Nd (fonte) e U–Pb (tempo de cristalização), revela a evolução de um sistema de arco insular, envolvendo refertilização mantélica, sobreposição tectono-metamórfica significativa e herança crustal mesoarqueana. Em conjunto, essas abordagens fornecem um quadro complementar para a evolução do DRGN, abrangendo diferentes estágios de diferenciação mantélica, reciclagem crustal e reequilíbrio tectono-metamórfico.

## REFERÊNCIAS

Almeida, F.F.M., Hasui, Y., Brito Neves, B.B., Fuck, R.A. 1981. Brazilian structural provinces: an introduction. Earth Science Reviews, **17,** 1–29. https://doi.org/10.1016/0012-8252(81)90003-9.

Angelim, L.A.A. (Ed.) 2006. Geologia e recursos minerais do Estado do Rio Grande do Norte: texto explicativo dos mapas geológico e de recursos minerais do Estado do Rio Grande do Norte. CPRM–Serviço Geológico do Brasil, FAPERN, Recife, 119.

Anonymous 1972. Penrose Field Conference on ophiolites: ophiolite definition and Penrose-type stratigraphy. Geotimes, **17,** 24–25.

Arthaud, M.H., Caby, R., Fuck, R.A., Dantas, E.L., Parente, C.V. 2008. Geology of the northern Borborema Province, NE Brazil and its correlation with Nigeria, NW Africa. *In:* Pankhurst, R.J., Trouw, R.A.J., Brito Neves, B.B., De Wit, M.J. (Eds.). West Gondwana: Pre-Cenozoic correlations across the South Atlantic region. London: Geological Society, Special Publications, **294,** 49–67.

Ashwal, L.D. 1993. Archean crustal evolution in Greenland: Evidence from isotopic studies. Precambrian Research, **61,** 1–28.

Belousova, E. A., Kostitsyn, Y. A., Griffin, W. L., Begg, G. C., O'Reilly, S. Y. Pearson, N. J. 2010. The growth of the continental crust: Constraints from zircon Hf-isotope data. Lithos, **119(3),** 457-466. https://doi.org/10.1016/j.lithos.2010.07.024.

Bendaoud, A., Ouzegane, K., Godard, G., Li´egeois, J. P., Kienast, J. R., Bruguier, O., Drareni, A. 2008. Geochronology and metamorphic PTX evolution of the Eburnean granulite-facies metapelites of Tidjenouine (Central Hoggar, Algeria): witness of the LATEA metacratonic evolution. Geological Society, London, Special Publication, **297(1),** 111-146. https://doi.org/10.1144/SP297.6.

Bennett, V.C., BRANDON, A.D., NUTMAN, A.P. 2007. Coupled $^{142}Nd$–$^{143}Nd$ isotopic evidence for Hadean mantle dynamics. Earth and Planetary Science Letters, **261,** 689–702. https://doi.org/10.1126/science.1145928.

Berman, R.G., Pehrsson, S., Davis, W.J., Ryan, J.J., Qui, H., Ashton, K.E. 2013. The Arrowsmith orogeny: Geochronological and thermobarometric constraints on its extent and tectonic setting in the Rae craton, with implications for pre-Nuna supercontinent reconstruction. Precambrian Research, **232,** 44-69. https://doi.org/10.1016/j.precamres.2012.10.015.

Bleeker, W. 2003. The late Archean record: a puzzle in ca. 35 pieces. Lithos, **71(2–4),** 99-134. https://doi.org/10.1016/j.lithos.2003.07.003.

Bleeker, W., Ernst, R.E. 2006. Short-lived mantle generated magmatic events and their dyke swarms: the key unlocking Earth's paleogeographic record back to 2.6 Ga. *In:* Dyke Swarms—Time Markers of Crustal Evolution, ed. E Hanski, S Mertanen, T Rämö, J Vuollo, pp. 3–26. London: Taylor & Francis Bradley DC. 2008. Passive margins through Earth history. Earth-Sci., **91,** 1–26.

Blichert-Toft, J., Puchtel, I.S. 2010. Lu–Hf and Sm–Nd isotope systematics of Archean komatiites: Evidence for depleted mantle sources through time. Journal of Petrology, **51(12):** 2473–2493. https://doi.org/10.1016/j.epsl.2010.07.012.

Block, S., Ganne, J., Baratoux, L., Zeh, A., Parra-Avila, L. A., Jessell, M., Ailleres, Siebenaller, L. L. 2015. Petrological and geochronological constraints on lower crust exhumation during Paleoproterozoic (Eburnean) orogeny, NW Ghana, West African Craton. Geol., **33(5),** 463-494. https://doi.org/10.1111/jmg.12129.

Bowring, S.A., Housh, T.M. 1995. The oldest zircons from the Acasta gneiss complex, northwestern Canada. Earth and Planetary Science Letters, **136,** 15–26.

Bowring, S.A., Nemchin, A.A., Paterson, J.B., Baker, J., Silver, L.T. 1990. U–Pb geochronology of the Acasta gneiss complex, northwestern Canada: Evidence for >4.0 Ga continental crust. Geochimica et Cosmochimica Acta, **54,** 3161–3171.

Boyet, M., Carlson, R.W. 2005. $^{142}$Nd evidence for early (~4.53 Ga) global differentiation of the silicate Earth. Science, **309,** 576–581. https://doi.org/10.1126/science.1113634.

Bradley, D. C. 2008. Passive margins through earth history. Earth Sci. Rev., **91,** 1-26. https://doi.org/10.1016/j.earscirev.2008.08.001.

Brito Neves, B.B. 1975. Regionalização geotectônica do Pré-Cambriano nordestino. Thesis, Instituto de Geociências, Universidade de São Paulo, 198.

Brito Neves, B.B., Santos, E.J., Van Schmus, W.R. 2000. Tectonic history of the Borborema Province, Northeastern Brazil. *In:* Cordani, U., Milani, E.J., Thomaz Filho, A., Campos, D.A. (Eds.). Tectonic evolution of South America. 31st International Geological Congress, Rio de Janeiro, Brazil, 151–182.

Brown, M., Johnson, T. 2019. Global age, temperature and pressure data for secular change in metamorphism. EarthChem Libr. https://doi.org/10.1594/IEDA/111316.

Brown, M., Johnson, T., Gardiner, N.J. 2020. Plate tectonics and the Archean Earth. Annual Review of Earth and Planetary Sciences, **48,** 291–320. https://doi.org/10.1146/annurev-earth-081619-052705.

Brown, M., Johnson, T., J. Spencer, C.J. 2022. Secular changes in metamorphism and metamorphic cooling rates track the evolving plate-tectonic regime on Earth. Journal of the Geological Society. 179 (2022) jgs2022-050. https://doi.org/10.1144/jgs2022-050.

Campbell, I.H., Griffiths, R.W. 1993. The evolution of the mantle's chemical structure. Earth and Planetary Science Letters, **117,** 123–135. https://doi.org/10.1016/0024-4937(93)90047-G.

Capitanio, F.A., Nebel, O., Cawood, P.A., Weinberg, R.F., Clos, F. 2019. Lithosphere differentiation in the early Earth controls Archean tectonics. Earth and Planetary Science Letters, **525,** 115755. https://doi.org/10.1016/j.epsl.2019.115755.

Caro, G., Bourdon, B., Birck, J.L., Moorbath, S. 2006. High-precision $^{142}Nd/^{144}Nd$ measurements in terrestrial rocks: constraints on the early differentiation of the Earth's mantle. Geochimica et Cosmochimica Acta, **70,** 164–191. https://doi.org/10.1016/j.gca.2005.08.015.

Caro, G., Bourdon, B., Wood, B.J., Corgne, A. 2005. Trace-element fractionation in Hadean mantle generated by melt segregation from a magma ocean. Nature, **436,** 246–249. https://doi.org/10.1038/nature03827.

Carvalho, O.O. 1990. Geologia e petroquímica de uma sequência metavulcanossedimentar do Nordeste da Faixa Seridó, sudeste de Lajes/RN, Rio Grande do Norte. Master's Thesis, Universidade Federal do Rio Grande do Norte, Natal, 198.

Cawood, P. A., Hawkesworth, C. J., Pisarevsky, S. A., Dhuime, B., Capitanio, F. C. & Nebel, O. 2018. Geological archive of the onset of plate tectonics. Philos. Trans. R. Soc. A., **376,** 20170405. https://doi.org/10.1098/rsta.2017.0405.

Cawood, P.A., Hawkesworth, C.J., Dhuime, B. 2013Thecontinental record and the generation of continental crust. Geol. Soc. Am. Bull., **125,** 14–32. (doi:10.1130/b30722.1).

Cawood, P.A., Hawkesworth, C.J., Pisarevsky, S.A., Dhuime, B., Capitanio, F.C., Nebel, O. 2018. Geological archive of the onset of plate tectonics. Philosophical

Transactions of the Royal Society A, **376,** 20170405. https://doi.org/10.1098/rsta.2017.0405.

Cawood, P.A., Kroener, A., Collins, W.J., Kusky, T.M., Mooney, W.D., Windley, B.F. 2009. Accretionary orogens through Earth history. *In:* Cawood, P.A., Kroner, A. (Eds.), Earth Accretionary Systems in Space and Time. Geological Society Special Publications., **318,** 1-36. https://doi.org/10.1144/SP318.1.

Christensen, U.R. 1985. Thermal evolution models for the Earth. Journal of Geophysical Research, **90,** B4, 2995–3007. https://doi.org/10.1029/JB090iB04p02995.

Cohen, K.M., Finney, S.C., Gibbard, P.L., Fan, J.-X. 2013 (updated). The ICS International Chronostratigraphic Chart. Episodes, **36,** 199–204. Available at: http://www.stratigraphy.org/ICSchart/ChronostratChart2021-10.pdf.

Coleman, R.G. 1971. Plate tectonic emplacement of upper mantle peridotites along continental edges. Journal of Geophysical Research, **76,** 1212–1222. https://doi.org/10.1029/JB076i005p01212.

Condie, K., O'Neill, C. 2010. The Archean-Proterozoic boundary: 500 My of tectonic transition in Earth history. American Journal of Science, **310,** 775–790. https://doi.org/10.2475/09.2010.01.

Condie, K., Pisarevsky, S.A., Puetz, S.J., Spencer, C.J., Teixeira, W., Faleiros, F.M. 2022. A reappraisal of the global tectono-magmatic lull at ~2.3 Ga. Precambrian Research, **376,** 106690. https://doi.org/10.1016/j.precamres.2022.106690.

Condie, K.C. 1981. Archean Greenstone Belts. Amsterdam: Elsevier. 434.

Condie, K.C. 1994. The Archean crustal evolution. Developments in Precambrian Geology, Elsevier, Amsterdam, 528 pp.

Condie, K.C. 1998. Episodic continental growth and supercontinents: A mantle avalanche connection? Earth and Planetary Science Letters, **163,** 97–108. https://doi.org/10.1016/S0012-821X(98)00178-2.

Condie, K.C., O'Neill, C., Aster, R.C. 2009. Evidence and implications for a widespread magmatic shutdown for 250 My on Earth. Earth and Planetary Science Letters, **282,** 294–298. https://doi.org/10.1016/j.epsl.2009.03.033.

Corrêa, R.S., Oliveira, C.G., Dantas, E.L., Botelho, N.F. 2020. Hydrothermal footprint related to regional-scale shear zone-controlled scheelite mineralization, Seridó W-skarn system, northeastern Brazil. Journal of South American Earth Sciences, **103,** art. 102755. https://doi.org/10.1016/j.jsames.2020.102755.

Corrêa, R.S., Oliveira, C.G., Dantas, E.L., Della Giustina, M.E.S., Hollanda, M.H.B.M. 2021. The root zones of the Seridó W-skarn system, northeastern Brazil: constraints on the metallogenesis of a large Ediacaran tungsten province. Ore Geology Reviews. https://doi.org/10.1016/j.oregeorev.2020.103884.

Costa, A.P., Cavalcante, R., Dantas, A.R., Rodrigues, J.B., Cunha, A.L.C., Lages, G.A., Alcântara, V.C., Lima, R.B., Spisila, A.L. 2022. Fragments of juvenile Siderian continental crust in the Rio Piranhas-Seridó Domain, Borborema Province, Northeastern Brazil, as deduced by zircon U-Pb and whole-rock Sm-Nd systematics. Journal of the Geological Survey of Brazil, **4, n. 3,** 223–237.

Costa, A.P., Dantas, A.R. 2018. Geology and mineral resources of the Lajes sheet (SB.24-X-D-VI), Rio Grande do Norte State, Brazil. Scale 1:100, 000. Geological Survey of Brazil (CPRM), Recife, 163 ISBN 978-85-7499-253-2.

Dantas, E.L., Negrão, M.M., Bühn, B.M. 2008. 2.3 Ga continental crust generation in the Rio Grande do Norte terrane, NE-Brazil. *In:* VI South American Symposium on Isotope Geology, San Carlos de Bariloche.

Dantas, E.L., Silva, A.M., Almeida, T., Moraes, R.A.V. 2003. Old geophysical data applied to modern geological mapping problems: a case-study in the Seridó Belt, NE Brazil. Revista Brasileira de Geociências, **33, n. 2 (Supl.),** 65–72.

Dantas, E.L., Van Schmus, W.R., Hackspacher, P.C., Fetter, A.H., Neves, B.B.B., Cordani, U.G., Nutman, A.P., Williams, S. 2004. The 3.4–3.5 São José do Campestre Massif, NE Brazil: remnants of the oldest crust in South America. Precambrian Research, **130,** 113–137. https://doi.org/10.1016/j.precamres.2003.11.002.

Debaille, V., O'Neill, C., Brandon, A.D., Haenecour, P., Yin, Q.Z., Mattielli, N., Treiman, A.H. 2013. Stagnant-lid tectonics in early Earth revealed by 142Nd variations in late Archean rocks. Earth and Planetary Science Letters, **373,** 83–92. https://doi.org/10.1016/j.epsl.2013.04.016.

DePaolo, D. J., 1981. A neodymium and strontium isotopic study of the Mesozoic calcalkaline granitic batholiths of the Sierra Nevada and Peninsular ranges, California. Journal of Geophysical Research 86:10,470–10,488. doi.org/10.1029/JB086iB11p10.

Dewey, J.F., Hempton, M.R., Kidd, W.S.F., Saroglu, F., Sengor, A.M.C. 1986. Shortening of continental lithosphere: The neotectonics of Eastern Anatolia—a young collision zone. *In:* Coward, M.P. & Ries, A.C. (eds) Collision Tectonics. Geological Society, London, Special Publications, **19,** 3–36.

Dhuime, B., Hawkesworth, C.J., Cawood, P.A., Storey, C.D. 2012. A change in the geodynamics of continental growth 3 billion years ago. Science, **335,** 1334–1336. https://doi.org/10.1126/science.1216066.

Dilek, Y., Furnes, H. 2011. Ophiolite genesis and global tectonics: geochemical and tectonic fingerprinting of ancient oceanic lithosphere. Geol. Soc. Am. Bull., **123 (3/4),** 387–411. doi: 10.1130/B30446.1.

Ebert, H. 1970. The Precambrian geology of the “Borborema” belt (States of Paraíba and Rio Grande do Norte) and the origin of its mineral provinces. Geologische Rundschau, **59,** 1294–1327.

Elkins-Tanton, L.T. 2008. Linked magma ocean solidification and atmospheric growth for Earth and Mars. Earth and Planetary Science Letters, **271,** 181–191. https://doi.org/10.1016/j.epsl.2008.03.062.

Ernst, R.E, Bleeker, W., Söderlund, U., Kerr, A.C. 2013. Large igneous provinces and supercontinents: toward completing the plate tectonic revolution. Lithos, **174,** 1-14. https://doi.org/10.1016/j.lithos.2013.02.017.

Ferreira, A.C.D., Dantas, E.L., Fuck, R.A., Nedel, I.M. 2020. Arc accretion and crustal reworking from late Archean to Neoproterozoic in Northeast Brazil. Scientific Reports, **10,** 7855. https://doi.org/10.1038/s41598-020-64688-9.

Ferreira, A.D.C., Filho, C.F.F., Dantas, E.L., Souza, V.D.S. 2019. Paleoproterozoic mafic-ultramafic magmatism in the Northern Borborema Province, Northeast Brazil: tectonic setting and potential for deposits. The Journal of Geology, **127, n. 5,** 483–504. http://dx.doi.org/10.1086/704256.

Fetter, A.H., Van Schmus, W.R., Santos, T.J.S., Nogueira Neto, J.A., Arthaud, M.H. 2000. U-Pb and Sm-Nd geochronological constraints on the crustal evolution and basement architecture of Ceará state, NW Borborema Province, NE Brazil: Implications for the existence of the Paleoproterozoic supercontinent Atlantica. Revista Brasileira de Geociências, **30,** 102–106.

Forsyth, D., Uyeda, S. 1975. On the relative importance of the driving forces of plate motion. Geophys. J. Int., **43,** 163-200.

François, C., Philippot, P., Rey, P., Rubatto, D. 2014. Burial and exhumation during Archean sagduction in the East Pilbara Granite-Greenstone Terrane.

Earth Planet. Sci. Lett., **396,** 235–251. https://doi.org/10.1016/j.epsl.2014.04.025.

Friend, C., Nutman, A.P. 2019. Tectono-stratigraphic terranes in Archaean gneiss complexes as evidence for plate tectonics: The Nuuk region, southern West Greenland. Gondwana Research. 72.

Furnes, H., de Wit, M., Staudigel, H., Rosing, M., Muehlenbachs, K. 2007. A vestige of Earth's oldest ophiolite. Science, **315, n. 5819,** 1704–1707. https://doi.org/10.1126/science.1139170.

Furnes, H., Dilek, Y. 2022. Archean versus Phanerozoic oceanic crust formation and tectonics: Ophiolites through time. Geosystems and Geoenvironment, **1, n. 1,** art. 100004. https://doi.org/10.1016/j.geogeo.2021.09.004.

Ganne, J., Andrade, V., Weinberg, R., Vidal, O., Dubacq, B., Kagambega, N., Naba, S., Baratoux, L., Jessell, M., Allibon, J. 2012. Modern-style plate subduction preserved in the Palaeoproterozoic West African craton. Nat. Geosci., **5,** 60-65. https://doi.org/10.1038/ngeo1321.

Garcia, V.B., O'Neil, J., Dantas, E.L. 2023. Rare evidence for the existence of a Hadean enriched mantle reservoir. Geochemical Perspectives Letters, **28,** 1–6. https://doi.org/10.7185/geochemlet.2336.

Garcia, V.B., O'Neil, J., Dantas, E.L., Augustin, C.T. 2024. Composition and age constraints on a Hadean enriched mantle source revealed by the Paleoarchean São Tomé layered intrusion, NE Brazil. Earth and Planetary Science Letters, **647,** 119051. https://doi.org/10.1016/j.epsl.2024.119051.

Gibson, S.A. 2002. Major element heterogeneity in Archean to Recent mantle plume starting-heads. Earth and Planetary Science Letters, **195,** 59–74. https://doi.org/10.1016/S0012-821X(01)00566-0.

Gibson, S.A., Thompson, R.N., Dickin, A.P. 2000. Ferropicrites: geochemical evidence for Fe-rich streaks in upwelling mantle plumes. Earth and Planetary Science Letters, **174,** 355–374. https://doi.org/10.1016/S0012-821X(99)00274-5.

Gioia, S.M.C.L., Pimentel, M.M., 2000. The Sm-Nd isotopic method in the geochronology laboratory of the University of Brasília. Anais da Academia Brasileira de Ciências, **72(2),** 219–245.

Hackspacher, P.C., Van Schmus, W.R., Dantas, E.L. 1990. Um embasamento transamazônico na Província Borborema. In: Congresso Brasileiro de Geologia, 36. Sociedade Brasileira de Geologia, Natal, 2683–2696.

Halla, J. 2005. Late Archean high-Mg granitoids (sanukitoids) in the southern Karelian domain, eastern Finland: Pb and Nd isotopic constraints on crust–mantle interactions. Lithos, **79,** 161–178. https://doi.org/10.1016/j.lithos.2004.05.007.

Harrison, T.M. 2009. The Hasdean crust: Evidence from >4 Ga zircons. Annu. Rev. Earth Planet. Sci., **37,** 479–505. https://doi.org/10.1146/annurev.earth.031208.100151.

Harrison, T.M. 2020. Hadean Earth, Springer, ebook. https://dx.doi.org/10.1007/978-3 -030-46687-9, 291 pp.

Heilimo, E., Halla, J., Hölttä, P. 2010. Discrimination and origin of the sanukitoid series: geochemical constraints from the Neoarchean western Karelian Province (Finland). Lithos, **115,** 27–39. https://doi.org/10.1016/j.lithos.2009.11.001.

Heilimo, E., Halla, J., Huhma, H. 2011. Single-grain zircon U–Pb age constraints of the western and eastern sanukitoid zones in the Finnish part of the Karelian Province. Lithos, **121,** 87–99. https://doi.org/10.1016/j.lithos.2010.10.006.

Henderson, D.R., Long, L.E., Barton Jr., J.M. 2000. Isotopic ages and chemical and isotopic composition of the Archaean Turfloop Batholith, Pietersburg granite–

greenstone terrane, Kaapvaal Craton, South Africa. South African Journal of Geology, **103 (1),** 38–46.

Herzberg, C., Condie, K., Korenaga, J. 2010. Thermal history of the Earth and its petrological expression. Earth and Planetary Science Letters, **292,** 79–88. https://doi.org/10.1016/j.epsl.2010.01.022.

Hickman, A. H. 2004. Two contrasting granite-greenstone terranes in the Pilbara Craton, Australia: evidence for vertical and horizontal tectonic regimes prior to 2900 Ma. Precambrian Res., **131,** 153–172. https://doi.org/10.1016/j.precamres.2003.12.009.

Hodel, F.J. 2017. Serpentinites néoprotérozoïques : une fenêtre sur la lithosphère océanique associée à la dislocation de Rodinia. Tese de Doutorado, Université Toulouse III – Paul Sabatier, Toulouse, 395 .

Holder, R.M., Viete, D.R., Brown, M., Johnson, T.E. 2019. Metamorphism and the evolution of plate tectonics. Nature, **572,** 378-81. https://doi.org/10.1038/s41586-019-1462-2.

Hollanda, M.H.B.M., Archanjo, C.J., Bautista, J.R., Souza, L.C. 2015. Detrital zircon ages and Nd isotope compositions of the Seridó and Lavras da Mangabeira basins (Borborema Province, NE Brazil): evidence for exhumation and recycling associated with a major shift in sedimentary provenance. Precambrian Research, **258,** 186–207. https://doi.org/10.1016/j.precamres.2014.12.009.

Hollanda, M.H.B.M., Archanjo, C.J., Souza, L.C., Dunyi, L., Armstrong, L. 2011. Long-lived Paleoproterozoic granitic magmatism in the Seridó-Jaguaribe domain, Borborema Province, NE Brazil. Journal of South American Earth Sciences, **32,** 287–300. https://doi.org/10.1016/j.jsames.2011.02.008.

Hollanda, M.H.B.M., Souza Neto, J.A., Archanjo, C.J., Stein, H., Maia, A.C.S. 2017. Age of the granitic magmatism and the W-Mo mineralization in skarns of the Seridó belt (NE Brazil) based on zircon U-Pb (SHRIMP) and molybdenite Re-Os dating. Journal of South American Earth Sciences, **79,** 1–11. https://doi.org/10.1016/j.jsames.2017.07.011.

Jackson, S.E., Pearson, N.J., Griffin, W.L., Belousova, E.A., 2004. The application of laser ablation-inductively coupled plasma-mass spectrometry to in situ U–Pb zircon geochronology. Chem. Geol., **211 (1–2),** 47–69. doi.org/10.1016/j.chemgeo.2004.06.017.

Jahn, B.M., Glikson, A.Y., Peucat, J.-J., Hickman, A.H. 1981. REE geochemistry and isotopic data of Archaean silicic volcanics and granitoids from the Pilbara Block, western Australia: implications for the early crustal evolution. Geochimica et Cosmochimica Acta, **45,** 1633–1652.

Jahn, B.M., Gruau, G. and Glikson, A.Y. 1982. Komatiites of the Onverwacht Group, S. Africa: REE geochemistry, Sm/Nd age and mantle evolution. Contrib. Mineral. Pe- trol., **80,** 25-40.

Jardim de Sá, E.F. 1994. A Faixa Seridó (Província Borborema, NE do Brasil) e o seu significado geodinâmico na cadeia Brasiliana/Pan-Africana. Thesis, Universidade de Brasília, Brasília, 803.

Keller, B., Schoene, B. 2018. Plate tectonics and continental basaltic geochemistry throughout Earth history. Earth and Planetary Science Letters, **481,** 290–304. https://doi.org/10.1016/j.epsl.2017.10.031.

King, E.M., Valley, J.M., Davis, D.W., Edwards, G.R. 1998. Oxygen isotope ratios of Archean plutonic rocks from granite-greenstone belts of the Superior Province: indicator of magmatic source. Precambrian Research, **92,** 365–387.

Kusky, T.M. (Ed.). 2004. Precambrian ophiolites and related rocks. Developments in Precambrian Geology, 13. Amsterdam: Elsevier, 772 ISBN 978-0-444-50923-9.

Labrosse, S., Hernlund, J.W., Coltice, N. 2007. A crystallizing dense magma ocean at the base of the Earth's mantle. Nature, **450,** 866–869. https://doi.org/10.1038/nature06355.

Laurent, O., Martin, H., Moyen, J. F., Doucelance, R. 2014. The diversity and evolution of late-Archean granitoids: Evidence for the onset of "modern-style" plate tectonics between 3.0 and 2.5Ga. Lithos, **205,** 208-235. http://dx.doi.org/10.1016/j.lithos.2014.06.012.

Lenardic, A. 2018. The diversity of tectonic modes and thoughts about transitions between them. Philosophical Transactions of the Royal Society A: Mathematical, Physical and Engineering Sciences, **376,** 20170416. https://doi.org/10.1098/rsta.2017.0416.

Lesnov, F.P., 2010. Rare Earth Elements in Ultramafic and Mafic Rocks and Their Minerals: Main Types of Rocks. Rock-forming Minerals. CRC Press, London. ISBN 978-0415578905.

Lima, E.A.M., Wanderley, A.A., Vieira, Â.T., Medina, A.I.M., Barbosa, A.J., Vasconcelos, A.M., Amaral, C.A., Sato, E.Y., Silva, E.H.R., Leite, J.F., Moraes, J.F.S., Ribeiro, J.A., Nesi, J.R., Angelim, L.A.A., Calheiros, M.E.V. 1980. Projeto Scheelita do Seridó: relatório final. Brasília: CPRM. Relatório técnico. https://rigeo.sgb.gov.br/handle/doc/9240.

Liu, S., Bao, H., Sun, G., Wang, W., Fu, J., Gao, L., Guo, R., Hu, Y. 2022. Archean crust-mantle geodynamic regimes: A review. Geoscience Frontiers, **13,** 100063. https://doi.org/10.1016/j.geogeo.2022.100063.

Lobach-Zhuchenko, S.B., Rollinson, H., Chekulaev, V.P., Savatenkov, V.M., Kovalenko, A.V., Martin, H., Guseva, N.S., Arestova, N.A. 2008. Petrology of a Late Archaean, Highly Potassic, Sanukitoid Pluton from the Baltic Shield: insights into Late Archaean Mantle Metasomatism. Journal of Petrology, **49 (3),** 393–420. https://doi.org/10.1093/petrology/egm084.

Lucas, D., Hollanda, M.H.B.M., Souza Neto, J.A., Souza, L. 2024. Unraveling the evolution of the Bodó W-skarn district in the Seridó Mineral Province (NE Brazil): constraints from C–O stable isotopes, thermodynamic modeling, and geochronology. Mineralium Deposita, **60, n. 1,** 1–22. https://doi.org/10.1007/s00126-024-01300-4.

Macambira, M. J. B., Vasquez, M. L., Silva, D. C. C., Galarza, M. A., Barros, C. E. M., Camelo, J. F. 2009. Crustal growth of the central-eastern Paleoproterozoic domain, SW Amazonian craton: Juvenile accretion vs. reworking. Journal of South American Earth Sciences, **27(4),** 235–246. https://doi.org/10.1016/j.jsames.2009.02.001.

Macgregor, A. 1951. Some milestones in the Precambrian of Southern Rhodesia. Proceedings of the Geological Society of South Africa, **54,** 27–71.

Maltese, A., Caro, G., Pandey, O.P., Upadhyay, D., Mezger, K. 2022. Direct evidence for crust–mantle differentiation in the late Hadean. Communications Earth & Environment, **3,** 15. https://doi.org/10.1038/s43247-022-00341-9.

Manikyamba, C., Ray, J., Ganguly, S., Singh, M.R., Santosh, M., Saha, A., Satyanarayanan, M. 2015. Boninitic metavolcanic rocks and island arc tholeiites from the Older Metamorphic Group (OMG) of Singhbhum Craton, eastern India: geochemical evidence for archean subduction processes. Precambrian Research, **271,** 138–159.

Martin, H., Moyen, J.-F. 2002. Secular changes in tonalite-trondhjemite-granodiorite composition as markers of the progressive cooling of Earth. Geology,

**30, n. 4,** 319–322. https://doi.org/10.1130/0091-7613(2002)030<0319:SCITTG>2.0.CO, 2.

Martin, H., Pinti, D. L. 2014. Archean Eon. *In:* Harff, J., Mescolotti, L., Petersen, S., Thiede, J. (eds.). Encyclopedia of Marine Geosciences. Dordrecht: Springer, 61–66.

Martínez, J.C., Massonne, H.-J., Frisicale, M.C., Dristas, J.A. 2017. Trans-Amazonian U-Th-Pb monazite ages and P-T-d exhumation paths of garnet-bearing leucogranite and migmatitic country rock of the southeastern Tandilia belt, Rio de la Plata craton in Argentina. Lithos, **274–275,** 328–348. https://doi.org/10.1016/j.lithos.2017.01.007.

Medeiros, V.C., Cavalcante, R., Cunha, A.L.C., Dantas, A.R., Costa, A.P., Brito, A.A., Rodrigues, J.B., Silva, M.A. 2017. O furo estratigráfico de Riacho Fechado (Currais Novos/RN), Domínio Rio Piranhas-Seridó (Província Borborema, NE Brasil): procedimentos e resultados. Estudos Geológicos, **27, n. 3,** 3–44. https://doi.org/10.18190/1980-8208/estudosgeologicos.v27n3p1-40.

Moorbath, S., Hawkesworth, C.J., Zhang, Z., Vernon, R.H. 1973. The early Archaean of Greenland: crustal evolution and isotopic evidence. Contributions to Mineralogy and Petrology, **39,** 207–229.

Moorbath, S., Taylor, P.N., Goodwin, R. 1981. Origin of granitic magma by crustal remobilisation: Rb–Sr and Pb/Pb geochronology and isotope geochemistry of the late Archaean Qôrqut granite complex of southern West Greenland. Geochim. Cosmochim. Acta, **45,** 1051–1060.

Morino, P., Caro, G., Reisberg, L., Schumacher, A. 2017. Chemical stratification in the post-magma ocean Earth inferred from coupled 146, 147Sm–142, 143Nd systematics in ultramafic rocks of the Saglek block (3.25–3.9 Ga, northern Labrador, Canada). Earth and Planetary Science Letters, **463,** 136–150. https://doi.org/10.1016/j.epsl.2017.01.044.

Moyen, J. F., Van Hunen, J. 2012. Short-term episodicity of Archaean plate tectonics. Geology, **40 (5),** 451–454. https://doi.org/10.1130/G322894.1.

Moyen, J.F. 2011. The composite Archaean grey gneisses: petrological significance, and evidence for a non-unique tectonic setting for Archaean crustal growth. Lithos, **123 (1–4),** 21–36. https://doi.org/10.1016/j.lithos.2010.09.015.

Murphy, D., Rizo, H., O'Neil, J., Hepple, R., Wiemer, D., Kemp, A., Vervoort, J. 2021. Combined Sm–Nd, Lu–Hf, and 142Nd study of Paleoarchean basalts from the East Pilbara Terrane, Western Australia. Chemical Geology, **578,** 120301. https://doi.org/10.1016/j.chemgeo.2021.120301.

Murphy, D.T., Brandon, A.D., Debaille, V., Burgess, R., Ballentine, C. 2010. In search of a hidden long-term isolated sub-chondritic Nd-142/Nd-144 reservoir in the deep mantle: Implications for the Nd isotope systematics of the Earth. Geochimica et Cosmochimica Acta, **74,** 738–750. https://doi.org/10.1016/j.gca.2009.10.005.

Negrão, M.N., Dantas, E.L., Souza, A.L.S., Rosado, T.M.S. 2005. Evidências de fontes crustais arqueanas na região do Cabugi RN. *In:* XXI Simpósio de Geologia do Nordeste, Recife, 89.

Neves, S.P., Tommasi, A., Vauchez, A., Carrino, T.A. 2021. The Borborema strike-slip shear zone system (NE Brazil): large-scale intracontinental strain localization in a heterogeneous plate. Lithosphere, Article ID 6407232. https://doi.org/10.2113/2021/6407232.

O'Neil, J., Carlson, R.W., Paquette, J.L., Francis, D. 2012. Formation age and metamorphic history of the Nuvvuagittuq Greenstone Belt. Precambrian Research, **220–221,** 23–44. https://doi.org/10.1016/j.precamres.2012.07.009.

O'Neill, C., Lenardic, A., Moresi, L., Torsvik, T. H., Lee, C.-T. A. 2007. Episodic Precambrian subduction. Earth and Planetary Science Letters, **262,** 552-562. https://doi.org/10.1016/j.epsl.2007.04.056.

Padilha, A.L., Santos-Matos, A.C.L., Batista, J.C., Vitorello, I., Pádua, M.B., Fuck, R.A. 2021. Magnetotelluric evidence for a Rhyacian suture zone hidden underneath the Seridó belt, Borborema Province, Northeastern Brazil. Precambrian Research, **365,** art. 106413. https://doi.org/10.1016/j.precamres.2021.106413.

Partin, C., Bekker, A., Sylvester, P., Wodicka, N., Stern, R., Chacko, T. 2014. Filling in the juvenile magmatic gap: Evidence for uninterrupted Paleoproterozoic plate tectonics. Earth and Planetary Science Letters, **388,** 123–133. https://doi.org/10.1016/j.epsl.2013.11.041.

Paton, C., Hellstrom, J., Paul, B., Woodhead, J., Hergt, J., 2011. Iolite: Freeware for the Visualisation and Processing of Mass Spectrometric Data. J. Anal. at. Spectrom. VL -IS -. doi.org/10.1039/C1JA10172B.

Pearce, J.A., Lippard, S.J., Roberts, S. 1984. Characteristics and tectonic significance of supra-subduction zone ophiolites. Geological Society, London, Special Publications, **16,** 77–94. https://doi.org/10.1144/GSL.SP.1984.016.01.06.

Pehrsson, S., Berman, R., Eglington, B., Rainbird, R. 2013. Two Neoarchean supercontinents revisited: the Rae family of cratons and their implications for alternate preNuna configurations. Precambrian Research, **232,** 27-43. https://doi.org/10.1016/j.precamres.2013.02.005.

Pehrsson, S., Buchan, K., Eglington, B., Berman, R., Rainbird, R. 2014. Did plate tectonics shutdown in the Paleoproterozoic? A view from the Siderian geologic record. Gondwana Research, **26,** 1–12. https://doi.org/10.1016/j.gr.2014.06.001.

Percival, J.A., Skulski, T., Sanborn-Barrie, M., Stott, G.M., Leclair, A.D., Corkery, M.T., Boily, M. 2012. Geology and tectonic evolution of the Superior province, Canada. *In:* Tectonic styles in Canada: the LITHOPROBE perspective (eds JA Percival. FA Cook, RM Clowes). Vancouver, Canada: Geological Association of Canada. 321–378.

Petrus, J., Kamber, B.S., 2012. VizualAge: a novel approach to laser ablation ICP-MS UPb geochronology data reduction. Geostand. Geoanal. Res., **36 (3),** 247–270. doi.org/10.1111/j.1751-908X.2012.00158.x.

Polat, A., Fraser, K.J., Ludwig, K.R. 2010. Archaean crustal evolution and geochemistry of Greenland shield rocks. Precambrian Research, **178,** 57–82.

Polat, A., Frei, R., Scherstén, A., Appel, P.W.U. 2010. New age (ca. 2970 Ma), mantle source composition and geodynamic constraints on the Archean Fiskenæsset anorthosite complex, SW Greenland. Chemical Geology, **276,** 91–104. https://doi.org/10.1016/j.chemgeo.2010.06.016.

Polat, A., Kerrich, R. 2006. Reading the geochemical fingerprints of Archean hot subduction volcanic rocks: Evidence for accretion and crustal recycling in a mobile tectonic regime. Geophys Monogr Ser., **164,** 189–213. https://doi.org/10.1029/164GM13.

Ribeiro, C.V.A., Dantas, E.L., Fuck, R.A. 2024. Paleoarchean sedimentation and Mesoarchean high-temperature metamorphism in northeastern Brazil: Tracing sources and depositional ages in polymetamorphic rocks. Lithos, **478,** 107641. https://doi.org/10.1016/j.lithos.2024.107641.

Rizo, H., Boyet, M., Blichert-Toft, J., Rosing, M. 2011. Combined Nd and Hf isotope evidence for deep-seated source of Isua lavas. Earth and Planetary Science Letters, **312,** 267–279. https://doi.org/10.1016/j.epsl.2011.10.014.

Rizo, H., Boyet, M., Blichert-Toft, J., Rosing, M.T. 2013. Early mantle dynamics inferred from Nd variations in Archean rocks from southwest Greenland. Earth and Planetary Science Letters, **377–378,** 324–335. https://doi.org/10.1016/j.epsl.2013.07.012.

Robin, C.M.I., Bailey, R.C. 2009. Simultaneous generation of Archean crust and subcratonic roots by vertical tectonics. Geology, **37,** 523–526. https://doi.org/ 10.1130/G25519A.1.

Roth, A.S.G., Bourdon, B., Mojzsis, S.J., Touboul, M., Sprung, P., Guitreau, M., Blichert-Toft, J. 2013. Inherited Nd anomalies in Eoarchean protoliths. Earth and Planetary Science Letters, **361,** 50–57. https://doi.org/10.1016/j.epsl.2012.11.023.

Salim, J. 1979. Geologia e controle das mineralizações scheelitíferas da região da Serra do Feiticeiro e Bonfim, Lages-RN. Master's Thesis, Universidade de Brasília, Brasília, 106.

Salim, J. 1982. Mineralização polifásica de tungstênio e molibdênio na região do Seridó, NE do Brasil. Congreso Latinoamericano de Geología, Argentina, 2, 529–543.

Santos, F.G., Cavalcanti Neto, M.T.O., Ferreira, V.P., Bertotti, A.L. 2020. Eo to Paleoarchean metamafic-ultramafic rocks from the central portion of the Rio Grande do Norte Domain, Borborema Province, northeast Brazil: the oldest South American platform rocks. Journal of South American Earth Sciences, **97,** 102410. https://doi.org/10.1016/j.jsames.2019.102410.

Santos, L.C.M.L., Dantas, E.L., Cawood, P.A., Santos, E.J., Fuck, R.A. 2017. Neoarchean crustal growth and Paleoproterozoic reworking in the Borborema Province, NE Brazil: insights from geochemical and isotopic data of TTG and metagranitic rocks of the Alto Moxotó Terrane. Journal of South American Earth Sciences, **79,** 342–363. https://doi.org/10.1016/j.jsames.2017.08.013.

Santos, L.C.M.L., Dantas, E.L., Santos, E.J., Santos, R.V., Lima, H.M. 2015. Early to late Paleoproterozoic magmatism in NE Brazil: the Alto Moxoto Terrane and its tectonic implications for the pre-West Gondwana assembly. Journal of South American Earth Sciences, **58,** 188–209. https://doi.org/10.1016/j.jsames.2014.07.006.

Santos, T., Fetter, A., Van Schmus, W., Hackspacher, P. 2009. Evidence for 2.35 to 2.30 Ga juvenile crustal growth in the northwest Borborema Province, NE Brazil. London: Geological Society, Special Publications, **323,** 271–281. https://doi.org/10.1144/SP323.13.

Santosh, M., Arai, T., Maruyama, S. 2017. Hadean Earth and primordial continents: The cradle of prebiotic life. Geoscience Frontiers, **8,** 309–327. https://doi.org/10.1016/j.gsf.2016.07.005.

Seixas, L.A.R., David, J., Stevenson, R. 2012. Geochemistry, Nd isotopes and U–Pb geochronology of a 2350Ma TTG suite, Minas Gerais, Brazil: Implications for the crustal evolution of the southern São Francisco craton. Precambrian Research, **196–197,** 61–80. https://doi.org/10.1016/j.precamres.2011.11.002.

Singh, M.R., Manikyamba, C., Ganguly, S., Ray, Santosh, J.M., Singh, T.D., Kumar, B.C. 2017. Paleoproterozoic arc basalt-boninite-high magnesian andesite-Nb enriched basalt association from the Malangtoli volcanic suite, Singhbhum Craton, eastern India: Geochemical record for subduction initiation to arc maturation continuum. Journal of Asian Earth Sciences, **134,** 191–206.

Sláma, J., Košler, J., Condon, D. J., Crowley, J. L., Gerdes, A., Hanchar, J. M., Horstwood, M. S. A., Morris, G. A., Nasdala, L., Norberg, N., Schaltegger, U., Schoene, B., Tubrett, M. N., Whitehouse, M. J., 2008. Plešovice zircon — A new natural reference material for U–Pb and Hf isotopic microanalysis. Chemical Geology, **249(1–2),** 1-35. dx.doi.org/10.1016/j.chemgeo.2007.11.005.

Smithies, R. H., Van Kranendonk, M. J., Champion, D. C. 2007. The Mesoarchean emergence of modern-style subduction. Gondwana Res., **11,** 50–68. https://doi.org/10.1016/j.gr.2006.02.001.

Smithies, R.H. 2000. The Archaean tonalite–trondhjemite–granodiorite (TTG) series is not an analogue of Cenozoic adakite. Earth and Planetary Science Letters, **182,** 115–125. https://doi.org/10.1016/S0012-821X(00)00236-3.

Smithies, R.H., Champion, D.C., Van Kranendonk, M.J. 2005. Modern-style subduction processes in the Mesoarchean: geochemical evidence from the 3.12 Ga Whundo intra-oceanic arc. Earth Planet. Sci. Lett., **231,** 221–237. doi:10.1016/j.epsl.2004.12.026.

Souza Neto, J.A., Legrand, J.M., Volfinger, P., Sonnet, P., M.L. 2008. W–Au skarns in the Neo-Proterozoic Seridó Mobile Belt, Borborema Province in northeastern Brazil: an overview with emphasis on the Bonfim deposit. Mineralium Deposita, **43,** 185–205. https://doi.org/10.1007/s00126-007-0155-1.

Souza, Z.S., Kalsbeek, F., Deng, X.-D., Frei, R., Kokfelt, T.F., Dantas, E.L., Li, J.-W., Pimentel, M.M., Galindo, A.C. 2016. Generation of continental crust in the northern part of the Borborema Province, northeastern Brazil, from Archaean to Neoproterozoic. Journal of South American Earth Sciences, **68,** 68–96. https://doi.org/10.1016/j.jsames.2015.10.006.

Souza, Z.S., Martin, H., Peucat, J.J., Jardim de Sá, E.F., Macedo, M.H.F. 2007. Calc-alkaline magmatism at the Archean-Proterozoic transition: The Caicó Complex basement (NE Brazil). Journal of Petrology, **48,** 2149–2185. https://doi.org/10.1093/petrology/egm055.

Souza, Z.S., Vasconcelos, P.M., Nascimento, M.A.L., Silveira, F.V., Paiva, H.S., Dias, L.G.S., Thiede, D., Carmo, I.O. 2003. $^{40}Ar/^{39}Ar$ geochronology of Mesozoic and Cenozoic magmatism in NE Brazil. Isotope Geology South American

Symposium, 310–313. https://horizon.documentation.ird.fr/exl-doc/pleins_textes/divers17-05/010039206.pdf.

Spencer, C., Murphy, J., Kirkland, C., Liu, Y., Mitchell, R. 2018. A Palaeoproterozoic tectono-magmatic lull as a potential trigger for the supercontinent cycle. Nature Geoscience, **11,** 1–7. https://doi.org/10.1038/s41561-017-0051-y.

Stern, R.J., Scholl, D.W. 2010. Yin and yang of continental crust creation and destruction by plate tectonic processes. International Geology Review, **52 (1),** 1–31.

Thébaud, N., Rey, P.F. 2013. Archean gravity-driven tectonics on hot and flooded continents: Controls on long-lived mineralized hydrothermal systems away from continental margins. Precambr. Res., **229,** 93–104. https://doi.org/10.1016/j. precamres.2012.03.001.

Tonks, W.B., Melosh, H.J. 1993. Magma ocean formation due to giant impacts. Journal of Geophysical Research, **98,** 5319–5333. https://doi.org/10.1029/92JE02726.

Touboul, M., Puchtel, I.S., Walker, R.J. 2012. $^{182}$W evidence for long-term preservation of early mantle differentiation products. Science, **335,** 1065–1069. https://doi.org/10.1126/science.1216351.

Trompette, R. 1994. Geology of Western Gondwana (2000–500): Pan-African-Brasiliano Aggregation of South America and Africa. Rotterdam: Balkema, 350.

Turner, S., Wilde, S., W¨orner, G., Schaefer, B., Lai, Y.J. 2020. An andesitic source for Jack Hills zircon supports onset of plate tectonics in the Hadean. Nat. Commun., **11,** 1241. https://doi.org/10.1038/s41467-020-14857-1.

Ulrich, M., Picard, C., Guillot, S., Chauvel, C., Cluzel, D., Meffre, S. 2010. Multiple melting stages and refertilization as indicators for ridge to subduction formation:

The New Caledonia ophiolite. Lithos, **115,** 223–236. https://doi.org/10.1016/j.lithos.2009.12.011.

Uysal, I., Ersoy, E.Y., Dilek, Y., Escayola, M., Sarıfakıoğlu, E., Saka, S., and Hirata, T. 2015, Depletion and refertilization of the Tethyan oceanic upper mantle as revealed by the early Jurassic Refahiye ophiolite, NE Anatolia—Turkey: Gondwana Research, **27,** 594–611.

Van Keken, P., Hacker, B.R., Syracuse, E.M., Abers, G.A. 2011. Subduction factory: 4. Depth-dependent flux of H2Ofrom subducting slabs worldwide. Journal of Geophysical Research. 116(B01401), 1–15. https://doi.org/10.1029/2010JB007922.

Van Kranendonk, Martin and Contributors, Altermann, Wladyslaw and Beard, Brian and Hoffman, Paul and Johnson, Clark and Kasting, James and Melezhik, Victor and Nutman, Allen and Papineau, Dominic and Pirajno, Franco. 2012. A Chronostratigraphic Division of the Precambrian. The Geologic Time Scale 2012. 1, 299-392.

Van Schmus, W.R., Brito Neves, B.B., Williams, I.S., Hackspacher, P.C., Fetter, A.H., Dantas, E.L., Babinski, M. 2003. The Seridó Group of NE Brazil, a late Neoproterozoic pre- to syn-collisional basin in West Gondwana: insights from SHRIMP U-Pb detrital zircon ages and Sm-Nd crustal residence (TDM) ages. Precambrian Research, **127,** 287–327. https://doi.org/10.1016/S0301-9268(03)00197-9.

Van Schmus, W.R., Oliveira, E.P., Silva Filho, A.F., Toteu, S.F., Penaye, J., Guimarães, I.P. 2008. Proterozoic links between the Borborema Province, NE Brazil, and the Central African Fold Belt. *In:* Pankhurst, R.J., Trouw, R.A.J., Brito Neves, B.B., De Wit, M.J. (Eds.). West Gondwana: Pre-Cenozoic correlations across the South Atlantic region. London: Geological Society, Special Publication, **294,** 69–99. https://doi.org/10.1144/SP294.

Van Thienen, P., Van den Berg, A.P., Vlaar, N.J. 2004. Continental growth and crustal thickness in the Archean: A geodynamical model. Earth and Planetary Science Letters, **223,** 43–55.

Vasquez, M.L., Macambira, M.J.B., Armstrong, R.A. 2008. Zircon geochronology of granitoids from the western Bacajá domain, southeastern Amazonian craton, Brazil: Neoarchean to Orosirian evolution. Precambrian Research, **161(3–4),** 279–302. https://doi.org/10.1016/j.precamres.2007.09.001.

Velásquez Ruiz, F., Della Giustina, M.E.S., De Oliveira, C.G., Dantas, E.L., Hollanda, M.H.B. 2019. The 3.5 Ga São Tomé layered mafic-ultramafic intrusion, NE Brazil: insights into a Paleoarchean Fe-Ti-V oxide mineralization and its reworking during West Gondwana assembly. Precambrian Research, **326,** 462–478. https://doi.org/10.1016/j.precamres.2018.03.011.

Wang, C., Song, S., Wei, C., Su, L., Allen, M.B., Niu, Y., Li, X.-H., Dong, J. 2022. Palaeoarchaean deep mantle heterogeneity recorded by enriched plume remnants. Earth and Planetary Science Letters, **587,** 117585. https://doi.org/10.1016/j.epsl.2022.117585.

Wasilewski, B., O'Neil, J., Rizo, H. 2022. Archean crustal evolution of the Saglek-Hebron Complex, Northern Labrador, revealed from coupled 147−146Sm–143−142Nd systematics. Earth and Planetary Science Letters, **594,** 117735. https://doi.org/10.1016/j.epsl.2022.117735.

Wiedenbeck, M., Priyanka, A., Corfu, F., Griffin, W., Meier, M., Oberli, F., von Quadt, A., Roddick, J.C., Spiegel, W., 2007. Three natural zircon standards for U-Th-Pb, Lu-Hf, trace element and REE analyses. Geostand. Newslett., **19** (1–23). doi.org/10.1111/j.1751-908X.1995.tb00147.x.

Williams, H., Hoffman, P. F., Lewry, J. F., Monger, J. W. H., Rivers, T. 1991. Anatomy of North America: thematic geologic portrayals of the continent. Tectonophysics, **187 (1-3),** 117-134.

Windley, B. F., Kusky, T. M., Polat, A. 2021. Onset of plate tectonics by the Eoarchean. Precambrian Research, **352,** 105980. https://doi.org/10.1016/j.precamres.2020.105980.

Xie, L., Walter, M., Katsura, T., Xu, F., Wang, J., Fei, Y. 2024. Crystallization of a hydrous magma ocean in the shallow lower mantle. Earth and Planetary Science Letters, **633,** 118651. https://doi.org/10.1016/j.epsl.2024.118651.

Yang, Q.-Y., Santosh, M. 2015. Paleoproterozoic arc magmatism in the North China Craton: No Siderian global plate tectonic shutdown. Gondwana Research, **28,** 82–105. https://doi.org/10.1016/j.gr.2014.08.005.

# APÊNDICE A

**Table 1.** U-Pb in zircon grains data of rocks in the Bonfim area, northeastern of Borborema province.

| | | | | Data for Tera-Wasserburg plot (b) | | | | | | Data for Wetherill plot (b) | | | | | | | Dates | | | | | | | | |
|---|---|---|---|---|---|---|---|---|---|---|---|---|---|---|---|---|---|---|---|---|---|---|---|---|---|
| Identifier | Th/U | $^{206}Pb/^{204}Pb$ | 1s% | $^{238}U/^{206}Pb$ | 1s% | $^{207}Pb/^{206}Pb$ | 1s% | $^{208}Pb/^{206}Pb$ | 1s% | $^{207}Pb/^{235}U$ | 1s% | $^{206}Pb/^{238}U$ | 1s% | Rho | $^{208}Pb/^{232}Th$ | 1s% | $^{207}Pb/^{206}Pb$ | 2s (abs) | $^{206}Pb/^{238}U$ | 2s (abs) | $^{207}Pb/^{235}U$ | 2s (abs) | $^{208}Pb/^{232}Th$ | 2s (abs) | Concordance (%) |
| *PFE-15* | | | | | | | | | | | | | | | | | | | | | | | | | |
| PFE-15-N_1 | 1.105 | -437.356 | -74.863 | 1.426 | 2.014 | 0.311 | 2.906 | 0.157 | 2.911 | 30.472 | 1.821 | 0.698 | 2.013 | -0.108 | 0.190 | 2.136 | 3498 | 89 | 3402 | 107 | 3495 | 36 | 3506 | 138 | 97 |
| PFE-15-N_3 | 1.350 | 1163.210 | 78.802 | 1.377 | 2.195 | 0.312 | 2.805 | 0.211 | 3.300 | 31.409 | 2.058 | 0.725 | 2.218 | -0.027 | 0.190 | 2.272 | 3503 | 86 | 3503 | 120 | 3523 | 42 | 3505 | 147 | 100 |
| PFE-15-N_4 | 1.340 | 743.944 | 82.271 | 1.378 | 2.240 | 0.271 | 2.591 | 0.428 | 9.404 | 19.212 | 5.006 | 0.473 | 5.361 | 0.658 | 0.111 | 6.257 | 3272 | 82 | 2431 | 228 | 2972 | 103 | 2101 | 250 | 74 |
| PFE-15-N_5 | 0.444 | -2194.457 | -53.902 | 1.980 | 2.587 | 0.259 | 2.606 | 0.108 | 7.978 | 18.613 | 3.254 | 0.509 | 2.478 | 0.636 | 0.162 | 3.744 | 3210 | 85 | 2643 | 108 | 3000 | 61 | 3015 | 209 | 82 |
| PFE-15-N_9 | 0.821 | -2537.111 | -63.613 | 1.409 | 2.266 | 0.312 | 2.769 | 0.121 | 3.742 | 30.876 | 1.846 | 0.714 | 2.151 | 0.061 | 0.189 | 3.270 | 3492 | 87 | 3458 | 116 | 3506 | 36 | 3492 | 210 | 99 |
| PFE-15-B_2 | 1.067 | -564.320 | -101.715 | 1.419 | 2.259 | 0.315 | 2.870 | 0.161 | 2.738 | 30.918 | 1.765 | 0.700 | 2.506 | 0.205 | 0.198 | 2.330 | 3508 | 89 | 3435 | 121 | 3509 | 35 | 3636 | 155 | 98 |
| PFE-15-B_4 | 0.942 | -9482.205 | -66.547 | 1.410 | 2.172 | 0.308 | 3.114 | 0.138 | 3.356 | 30.552 | 2.118 | 0.708 | 2.183 | -0.025 | 0.198 | 2.946 | 3474 | 97 | 3439 | 116 | 3507 | 38 | 3646 | 195 | 99 |
| *PFE-15B* | | | | | | | | | | | | | | | | | | | | | | | | | |
| PFE-15B_2 | 0.056 | 344.950 | 103.979 | 1.396 | 0.187 | 0.306 | 0.406 | 0.155 | 0.425 | 30.304 | 0.355 | 0.716 | 0.179 | 0.065 | 3.313 | 64.964 | 3496 | 13 | 3481 | 10 | 3496 | 7 | 43451 | 5338 | 100 |
| PFE-15B_3 | 0.304 | 196.017 | 318.039 | 1.372 | 0.138 | 0.309 | 0.360 | 0.191 | 0.365 | 31.214 | 0.360 | 0.728 | 0.137 | 0.200 | 1.138 | 277.667 | 3516 | 11 | 3527 | 7 | 3525 | 7 | 62529 | 5686 | 100 |
| PFE-15B_4 | 0.018 | 1888.276 | 108.831 | 1.414 | 0.124 | 0.302 | 0.414 | 0.214 | 0.481 | 29.516 | 0.392 | 0.706 | 0.125 | 0.111 | 14.724 | 46.404 | 3479 | 13 | 3444 | 7 | 3470 | 8 | 65672 | 5052 | 99 |
| PFE-15B_7 | -0.474 | -99.592 | -457.977 | 1.390 | 0.447 | 0.304 | 0.642 | 0.161 | 0.662 | 30.236 | 0.604 | 0.720 | 0.443 | 0.273 | -1.959 | -80.704 | 3486 | 20 | 3495 | 24 | 3493 | 12 | 37780 | 6314 | 100 |
| PFE-15B_10 | -0.047 | -14.606 | -1785.102 | 1.383 | 0.160 | 0.308 | 0.418 | 0.159 | 0.432 | 30.847 | 0.407 | 0.722 | 0.160 | 0.132 | -6.075 | -44.873 | 3510 | 13 | 3505 | 9 | 3513 | 8 | 44854 | 3963 | 100 |
| PFE-15B_12 | 0.212 | -94.745 | -488.991 | 1.417 | 0.318 | 0.301 | 0.720 | 0.162 | 0.659 | 29.405 | 0.708 | 0.705 | 0.319 | 0.179 | 0.907 | 625.507 | 3473 | 22 | 3439 | 17 | 3466 | 14 | 50667 | 8369 | 99 |
| *PFE-28A* | | | | | | | | | | | | | | | | | | | | | | | | | |
| PFE-28A-N_2 | 0.901 | 45406.144 | 34.342 | 2.552 | 2.859 | 0.273 | 2.305 | 0.193 | 2.519 | 15.375 | 2.979 | 0.404 | 2.819 | 0.666 | 0.145 | 2.727 | 3293 | 73 | 2174 | 104 | 2815 | 56 | 2722 | 139 | 66.0 |
| PFE-28A-N_3 | 0.759 | 10442.489 | 55.775 | 1.845 | 4.452 | 0.294 | 2.942 | 0.180 | 4.922 | 23.701 | 4.462 | 0.573 | 3.939 | 0.771 | 0.181 | 2.433 | 3401 | 94 | 2887 | 189 | 3200 | 100 | 3349 | 150 | 84.9 |
| PFE-28A-N_4 | 1.026 | 2282.620 | 107.395 | 2.882 | 5.193 | 0.268 | 3.213 | 0.223 | 2.836 | 14.150 | 4.715 | 0.376 | 4.193 | 0.760 | 0.124 | 2.683 | 3249 | 103 | 2038 | 149 | 2704 | 105 | 2361 | 120 | 62.7 |
| PFE-28A-N_5 | 0.607 | 2217.914 | 40.882 | 4.950 | 2.626 | 0.217 | 2.492 | 0.193 | 3.885 | 6.334 | 3.512 | 0.205 | 2.731 | 0.720 | 0.107 | 3.530 | 2923 | 84 | 1197 | 59 | 1996 | 61 | 2051 | 137 | 41.0 |
| PFE-28A-N_9 | 0.881 | -4932.826 | -46.069 | 1.473 | 2.610 | 0.308 | 2.756 | 0.143 | 2.630 | 29.473 | 1.973 | 0.678 | 2.482 | 0.374 | 0.184 | 2.065 | 3471 | 86 | 3316 | 133 | 3458 | 42 | 3415 | 130 | 95.5 |
| PFE-28A-N_10 | 1.047 | -241341.399 | -182.303 | 2.233 | 2.692 | 0.283 | 2.304 | 0.192 | 2.805 | 18.317 | 3.056 | 0.460 | 2.696 | 0.674 | 0.137 | 2.700 | 3351 | 72 | 2426 | 108 | 2979 | 60 | 2592 | 131 | 72.4 |
| PFE-28A-N_11 | 0.730 | 595.639 | 206.764 | 4.578 | 4.491 | 0.203 | 3.632 | 0.152 | 3.317 | 7.374 | 8.582 | 0.237 | 5.207 | 0.942 | 0.081 | 3.322 | 2784 | 129 | 1355 | 124 | 2036 | 135 | 1567 | 100 | 48.7 |
| PFE-28A-N_13 | 0.970 | 1993.903 | 81.117 | 1.412 | 1.527 | 0.308 | 2.570 | 0.151 | 2.476 | 30.008 | 1.686 | 0.702 | 1.635 | -0.197 | 0.181 | 2.013 | 3474 | 80 | 3419 | 87 | 3479 | 33 | 3363 | 125 | 98.4 |
| PFE-28A-N_14 | 1.434 | 2549.487 | 92.349 | 1.455 | 2.235 | 0.315 | 2.661 | 0.273 | 11.162 | 30.331 | 2.549 | 0.692 | 2.204 | 0.344 | 0.162 | 5.665 | 3517 | 81 | 3377 | 116 | 3483 | 49 | 3000 | 317 | 96.0 |
| PFE-28A-N_15 | 0.735 | -26832.696 | -69.562 | 2.446 | 3.985 | 0.275 | 3.231 | 0.177 | 2.921 | 16.373 | 4.504 | 0.425 | 4.127 | 0.749 | 0.182 | 3.217 | 3301 | 104 | 2268 | 155 | 2867 | 84 | 3376 | 200 | 68.7 |
| PFE-28A-N_16 | 1.006 | 2033.705 | 64.377 | 1.618 | 2.492 | 0.301 | 3.017 | 0.191 | 4.991 | 26.085 | 2.724 | 0.624 | 2.635 | 0.350 | 0.180 | 3.707 | 3441 | 96 | 3114 | 129 | 3334 | 57 | 3325 | 228 | 90.5 |
| PFE-28A-B_1 | 0.895 | 1617.240 | 77.643 | 1.851 | 2.189 | 0.291 | 2.247 | 0.169 | 2.354 | 22.089 | 1.929 | 0.547 | 2.265 | 0.412 | 0.173 | 2.421 | 3395 | 69 | 2801 | 102 | 3177 | 38 | 3220 | 144 | 82.5 |
| PFE-28A-B_3 | 0.742 | 994.946 | 42.613 | 1.914 | 2.787 | 0.304 | 3.161 | 0.169 | 3.273 | 22.038 | 2.899 | 0.523 | 3.114 | 0.414 | 0.181 | 2.596 | 3459 | 97 | 2700 | 137 | 3170 | 60 | 3358 | 160 | 78.1 |
| PFE-28A-B_4 | 0.785 | 1743.109 | 46.385 | 2.801 | 2.683 | 0.260 | 2.734 | 0.167 | 2.610 | 13.110 | 3.874 | 0.359 | 3.043 | 0.673 | 0.123 | 3.243 | 3213 | 84 | 1965 | 103 | 2654 | 70 | 2364 | 154 | 61.2 |
| PFE-28A-B_5 | 0.762 | -21892.006 | -143.381 | 2.355 | 1.864 | 0.275 | 2.842 | 0.148 | 3.193 | 16.145 | 2.407 | 0.420 | 2.106 | 0.212 | 0.141 | 3.290 | 3307 | 88 | 2255 | 80 | 2875 | 47 | 2663 | 164 | 68.2 |
| PFE-28A-B_8 | 0.603 | -211.375 | -414.287 | 3.137 | 4.798 | 0.257 | 2.739 | 0.220 | 6.736 | 12.997 | 5.159 | 0.354 | 4.330 | 0.870 | 0.137 | 5.757 | 3187 | 86 | 1931 | 145 | 2601 | 106 | 2562 | 275 | 60.6 |
| PFE-28A-B_10 | 0.710 | -40212.838 | -74.988 | 2.576 | 5.537 | 0.276 | 3.274 | 0.160 | 2.894 | 16.927 | 5.853 | 0.433 | 5.202 | 0.805 | 0.145 | 3.565 | 3302 | 101 | 2283 | 202 | 2854 | 126 | 2728 | 183 | 69.2 |
| PFE-28A-B_12 | 0.963 | -169.448 | -349.116 | 1.462 | 1.775 | 0.313 | 2.437 | 0.162 | 2.619 | 29.814 | 1.769 | 0.685 | 1.755 | 0.067 | 0.194 | 2.459 | 3506 | 76 | 3352 | 92 | 3472 | 35 | 3581 | 161 | 95.6 |
| PFE-28A-B_13 | 0.624 | 2887.547 | 70.193 | 1.401 | 2.134 | 0.300 | 2.616 | 0.106 | 3.255 | 29.893 | 2.200 | 0.716 | 2.073 | 0.270 | 0.206 | 2.608 | 3441 | 81 | 3469 | 112 | 3473 | 44 | 3779 | 180 | 100.8 |
| PFE-28A-B_14 | 1.142 | -65.886 | -315.337 | 2.111 | 2.973 | 0.310 | 2.404 | 0.257 | 6.035 | 20.948 | 2.586 | 0.488 | 2.881 | 0.583 | 0.165 | 3.737 | 3494 | 75 | 2546 | 121 | 3120 | 49 | 3077 | 214 | 72.9 |
| *PFE-18C* | | | | | | | | | | | | | | | | | | | | | | | | | |
| PFE-18C_3 | 0.040 | 0.000 | 78.349 | 1.391 | 0.218 | 0.309 | 0.592 | 7414209.976 | 0.674 | 30.799 | 0.557 | 0.717 | 0.219 | 0.010 | -4.895 | -149.260 | 3513 | 18 | 3483 | 12 | 3511 | 11 | 62565 | 5023 | 99.2 |
| PFE-18C_4 | -0.038 | 0.000 | -48.810 | 1.496 | 0.223 | 0.306 | 0.532 | 11722047.406 | 0.596 | 28.365 | 0.455 | 0.667 | 0.223 | -0.116 | 8.398 | 88.152 | 3499 | 16 | 3292 | 12 | 3431 | 9 | 71266 | 4993 | 94.1 |
| PFE-18C_5 | -0.218 | 0.000 | 108.434 | 1.395 | 0.484 | 0.303 | 0.712 | 10705008.516 | 0.798 | 30.167 | 0.644 | 0.716 | 0.477 | 0.156 | -0.794 | -384.848 | 3482 | 23 | 3479 | 26 | 3492 | 12 | 50172 | 4159 | 99.9 |
| PFE-18C_10 | 0.022 | 0.000 | -102.969 | 1.463 | 0.270 | 0.309 | 0.555 | 11269599.114 | 0.907 | 29.262 | 0.550 | 0.682 | 0.268 | 0.137 | -15.083 | -64.024 | 3512 | 17 | 3350 | 14 | 3461 | 11 | 76399 | 5419 | 95.4 |
| PFE-18C_15 | 0.050 | 0.000 | -72.803 | 1.427 | 0.349 | 0.305 | 0.701 | 11690287.714 | 0.673 | 29.611 | 0.621 | 0.699 | 0.352 | -0.020 | -27.271 | -139.739 | 3493 | 23 | 3417 | 19 | 3472 | 12 | 108933 | 6228 | 97.8 |
| PFE-18C_16 | 0.029 | 0.000 | 87.328 | 1.411 | 0.532 | 0.310 | 0.753 | 15041378.855 | 0.853 | 30.476 | 0.614 | 0.709 | 0.530 | 0.174 | -539.543 | -167.791 | 3516 | 23 | 3452 | 28 | 3500 | 12 | 156649 | 9161 | 98.2 |
| PFE-18C_23 | 0.092 | 0.000 | -58.177 | 1.436 | 0.513 | 0.304 | 0.601 | 7263998.740 | 0.929 | 29.447 | 0.476 | 0.696 | 0.509 | 0.198 | 2.565 | 77.694 | 3485 | 19 | 3405 | 27 | 3467 | 9 | 49922 | 3636 | 97.7 |
| PFE-18C_24 | 0.023 | 0.000 | 85.088 | 1.417 | 1.177 | 0.314 | 1.336 | 18387999.038 | 1.333 | 30.824 | 0.787 | 0.715 | 1.165 | 0.118 | 25.924 | 38.400 | 3526 | 42 | 3469 | 63 | 3510 | 15 | 56879 | 6714 | 98.4 |
| PFE-18C_25 | -0.107 | 0.000 | 101.551 | 1.405 | 0.676 | 0.311 | 0.631 | 12589680.644 | 0.681 | 30.679 | 0.611 | 0.712 | 0.683 | 0.520 | -2.986 | -177.879 | 3522 | 20 | 3463 | 36 | 3508 | 12 | 57062 | 5956 | 98.3 |
| PFE-18C_26 | 0.022 | 0.000 | 124.017 | 1.392 | 0.755 | 0.312 | 0.807 | 11110882.990 | 0.997 | 30.921 | 0.617 | 0.716 | 0.831 | 0.411 | 10.841 | 46.444 | 3526 | 25 | 3480 | 45 | 3516 | 12 | 61542 | 8946 | 98.7 |

| | | | | | | | | | | | | | | | | | | | | | | | | | |
|---|---|---|---|---|---|---|---|---|---|---|---|---|---|---|---|---|---|---|---|---|---|---|---|---|---|
| *PFE-28* | | | | | | | | | | | | | | | | | | | | | | | | | |
| PFE-28_1.FIN2 | 1.585 | -592.351 | -72.220 | 3.068 | 5.483 | 0.275 | 2.692 | 0.300 | 3.443 | 15.159 | 6.615 | 0.391 | 5.767 | 0.908 | 0.121 | 4.038 | 3294 | 86 | 2078 | 201 | 2710 | 128 | 2305 | 175 | 63.1 |
| PFE-28_3.FIN2 | 0.877 | -862.657 | -61.156 | 3.400 | 7.944 | 0.269 | 3.798 | 0.187 | 7.323 | 15.020 | 7.503 | 0.392 | 7.016 | 0.904 | 0.125 | 5.270 | 3274 | 116 | 2063 | 251 | 2628 | 185 | 2368 | 239 | 63.0 |
| PFE-28_4.FIN2 | 0.691 | -771.368 | -51.934 | 3.482 | 7.472 | 0.248 | 3.675 | 0.149 | 4.284 | 13.574 | 7.799 | 0.368 | 6.555 | 0.941 | 0.127 | 4.694 | 3111 | 133 | 1963 | 227 | 2507 | 190 | 2393 | 215 | 63.1 |
| PFE-28_5.FIN2 | 1.313 | -1126.288 | -59.306 | 1.830 | 2.641 | 0.298 | 3.181 | 0.230 | 3.392 | 22.595 | 2.888 | 0.554 | 2.780 | 0.461 | 0.163 | 1.899 | 3415 | 100 | 2860 | 115 | 3190 | 64 | 3048 | 107 | 83.7 |
| PFE-28_6.FIN2 | 0.807 | -426.198 | -85.318 | 3.081 | 4.576 | 0.250 | 3.117 | 0.159 | 6.877 | 12.251 | 5.168 | 0.357 | 4.067 | 0.819 | 0.097 | 4.772 | 3136 | 100 | 1947 | 138 | 2573 | 108 | 1863 | 170 | 62.1 |
| PFE-28_7.FIN2 | 0.915 | -1181.605 | -50.618 | 2.478 | 2.358 | 0.276 | 2.507 | 0.206 | 2.894 | 15.680 | 2.709 | 0.415 | 2.507 | 0.489 | 0.160 | 2.104 | 3308 | 78 | 2228 | 93 | 2842 | 53 | 2989 | 118 | 67.3 |
| PFE-28_8.FIN2 | 0.979 | -1019.720 | -50.852 | 3.132 | 3.264 | 0.261 | 2.535 | 0.215 | 3.196 | 12.268 | 3.975 | 0.339 | 3.256 | 0.473 | 0.113 | 2.477 | 3216 | 78 | 1868 | 105 | 2585 | 76 | 2158 | 101 | 58.1 |
| PFE-28_9.FIN2 | 0.229 | -566.539 | -59.903 | 6.568 | 3.092 | 0.181 | 3.370 | 0.135 | 12.478 | 4.041 | 4.859 | 0.160 | 3.169 | 0.713 | 0.125 | 6.046 | 2598 | 115 | 952 | 56 | 1602 | 78 | 2364 | 262 | 36.7 |
| PFE-28_10.FIN2 | 1.578 | -2422.578 | -33.598 | 1.826 | 2.341 | 0.303 | 2.671 | 0.271 | 2.207 | 23.035 | 2.616 | 0.556 | 2.281 | 0.283 | 0.162 | 1.747 | 3452 | 82 | 2840 | 106 | 3213 | 51 | 3039 | 98 | 82.3 |
| PFE-28_11.FIN2 | 1.132 | -1452.763 | -41.822 | 2.031 | 3.248 | 0.297 | 2.897 | 0.204 | 2.947 | 20.430 | 3.604 | 0.501 | 3.086 | 0.578 | 0.149 | 2.372 | 3411 | 91 | 2599 | 137 | 3104 | 68 | 2807 | 125 | 76.2 |
| PFE-28_12.FIN2 | 1.466 | -2141.400 | -39.017 | 1.518 | 3.515 | 0.307 | 4.222 | 0.221 | 5.707 | 28.187 | 3.496 | 0.669 | 3.849 | 0.326 | 0.193 | 3.954 | 3482 | 123 | 3293 | 195 | 3418 | 70 | 3557 | 258 | 94.6 |
| PFE-28_13.FIN2 | 0.297 | -2343.167 | -43.453 | 5.255 | 3.491 | 0.205 | 4.511 | 0.149 | 4.739 | 5.623 | 5.089 | 0.198 | 3.418 | 0.542 | 0.155 | 2.808 | 2796 | 145 | 1160 | 72 | 1880 | 97 | 2905 | 152 | 41.5 |
| PFE-28_14.FIN2 | 0.100 | -1135.752 | -34.841 | 6.892 | 4.213 | 0.160 | 3.895 | 0.046 | 6.932 | 3.886 | 8.534 | 0.165 | 5.243 | 0.912 | 0.107 | 4.968 | 2354 | 139 | 975 | 93 | 1497 | 117 | 2038 | 192 | 41.4 |
| PFE-28_15.FIN2 | 1.156 | 536.039 | 23.784 | 5.478 | 4.421 | 0.228 | 3.560 | 0.375 | 5.127 | 6.763 | 8.059 | 0.209 | 5.432 | 0.851 | 0.106 | 7.112 | 2967 | 110 | 1205 | 117 | 1982 | 127 | 2015 | 260 | 40.6 |
| PFE-28_19.FIN2 | 1.174 | -50.067 | -158.918 | 1.365 | 3.306 | 0.330 | 4.152 | 0.170 | 6.992 | 32.909 | 5.154 | 0.751 | 3.565 | 0.717 | 0.187 | 6.452 | 3583 | 121 | 3594 | 192 | 3578 | 88 | 3446 | 408 | 100.3 |
| PFE-28_20.FIN2 | 0.314 | -504.466 | -52.642 | 3.753 | 5.431 | 0.244 | 3.731 | 0.115 | 7.269 | 11.120 | 7.291 | 0.315 | 5.494 | 0.856 | 0.119 | 5.239 | 3073 | 121 | 1736 | 167 | 2398 | 142 | 2301 | 239 | 56.5 |
| PFE-28_21.FIN2 | 1.026 | -312.500 | -131.778 | 3.284 | 2.812 | 0.254 | 2.978 | 0.207 | 2.981 | 10.973 | 3.253 | 0.316 | 2.804 | 0.398 | 0.109 | 2.563 | 3163 | 94 | 1764 | 86 | 2510 | 57 | 2095 | 102 | 55.8 |
| PFE-28_22.FIN2 | 1.268 | -939.516 | -66.573 | 1.807 | 2.590 | 0.302 | 2.381 | 0.230 | 2.515 | 23.737 | 2.893 | 0.573 | 2.779 | 0.588 | 0.173 | 2.068 | 3452 | 75 | 2904 | 127 | 3238 | 57 | 3220 | 124 | 84.1 |
| PFE-28_23.FIN2 | 0.498 | 34.165 | 1121.698 | 6.706 | 2.810 | 0.165 | 3.121 | 0.107 | 2.756 | 3.507 | 3.833 | 0.154 | 2.839 | 0.461 | 0.055 | 2.388 | 2472 | 103 | 919 | 48 | 1506 | 59 | 1076 | 50 | 37.2 |
| PFE-28_24.FIN2 | 2.494 | -155.674 | -356.308 | 4.649 | 2.380 | 0.241 | 2.868 | 0.595 | 2.706 | 7.157 | 2.934 | 0.220 | 2.189 | 0.345 | 0.089 | 2.184 | 3081 | 93 | 1280 | 51 | 2114 | 53 | 1712 | 72 | 41.5 |
| PFE-28_25.FIN2 | 0.391 | -642.324 | -86.780 | 5.851 | 4.415 | 0.192 | 3.631 | 0.074 | 4.867 | 4.939 | 6.320 | 0.182 | 4.278 | 0.811 | 0.054 | 4.468 | 2699 | 128 | 1070 | 85 | 1748 | 109 | 1068 | 93 | 39.6 |
| PFE-28_26.FIN2 | 1.134 | -1106.078 | -40.372 | 2.738 | 2.543 | 0.277 | 2.511 | 0.201 | 2.827 | 14.239 | 2.677 | 0.376 | 2.382 | 0.390 | 0.114 | 3.377 | 3314 | 78 | 2049 | 84 | 2751 | 50 | 2168 | 140 | 61.8 |
| PFE-28_27.FIN2 | 0.296 | -1151.891 | -70.476 | 3.662 | 5.719 | 0.255 | 2.981 | 0.116 | 15.341 | 10.705 | 7.108 | 0.300 | 5.853 | 0.921 | 0.121 | 3.766 | 3189 | 100 | 1674 | 172 | 2434 | 137 | 2298 | 163 | 52.5 |
| PFE-28_28.FIN2 | 1.434 | -1827.264 | -73.781 | 1.792 | 3.937 | 0.304 | 3.735 | 0.219 | 3.531 | 23.847 | 3.222 | 0.572 | 4.012 | 0.405 | 0.154 | 2.708 | 3468 | 113 | 2904 | 187 | 3254 | 65 | 2893 | 145 | 83.7 |
| PFE-28_29.FIN2 | 0.915 | -353.905 | -120.528 | 6.373 | 5.160 | 0.185 | 4.588 | 0.205 | 4.289 | 5.080 | 7.524 | 0.183 | 4.811 | 0.901 | 0.073 | 6.551 | 2549 | 170 | 1070 | 95 | 1686 | 145 | 1418 | 180 | 42.0 |
| PFE-28_30.FIN2 | 0.229 | -2222.046 | -31.320 | 5.010 | 5.969 | 0.217 | 4.294 | 0.105 | 8.067 | 7.379 | 9.313 | 0.232 | 6.305 | 0.770 | 0.106 | 5.948 | 2878 | 155 | 1326 | 150 | 2029 | 163 | 2023 | 230 | 46.1 |
| PFE-28_31.FIN2 | 1.383 | -1647.237 | -46.369 | 1.679 | 2.912 | 0.304 | 3.055 | 0.223 | 4.097 | 25.550 | 3.740 | 0.606 | 2.821 | 0.553 | 0.177 | 2.968 | 3468 | 99 | 3043 | 138 | 3314 | 75 | 3296 | 180 | 87.8 |
| PFE-28_32.FIN2 | 1.317 | -1710.831 | -35.320 | 1.816 | 3.102 | 0.287 | 2.828 | 0.206 | 3.198 | 22.530 | 3.377 | 0.570 | 3.031 | 0.595 | 0.158 | 3.244 | 3370 | 87 | 2893 | 141 | 3186 | 67 | 2950 | 177 | 85.9 |
| PFE-28_34.FIN2 | 0.408 | -2675.097 | -36.274 | 5.666 | 2.786 | 0.193 | 3.662 | 0.124 | 4.513 | 4.795 | 4.320 | 0.180 | 3.017 | 0.463 | 0.084 | 3.010 | 2715 | 112 | 1063 | 59 | 1759 | 73 | 1631 | 94 | 39.2 |
| PFE-28_35.FIN2 | 0.973 | -2736.115 | -35.231 | 4.791 | 4.914 | 0.216 | 4.360 | 0.209 | 4.138 | 7.087 | 7.026 | 0.232 | 5.289 | 0.802 | 0.079 | 3.786 | 2878 | 139 | 1331 | 126 | 2039 | 131 | 1529 | 112 | 46.2 |
| PFE-28_36.FIN2 | 0.557 | -1305.296 | -62.186 | 5.239 | 6.067 | 0.212 | 4.809 | 0.209 | 4.779 | 7.385 | 7.847 | 0.226 | 5.179 | 0.880 | 0.130 | 5.487 | 2770 | 180 | 1322 | 131 | 1982 | 167 | 2447 | 251 | 47.7 |
| PFE-28_37.FIN2 | 0.588 | -317.366 | -129.068 | 6.051 | 3.025 | 0.202 | 2.999 | 0.216 | 10.201 | 4.752 | 4.315 | 0.171 | 3.219 | 0.568 | 0.090 | 2.656 | 2794 | 103 | 1013 | 60 | 1746 | 70 | 1736 | 88 | 36.3 |
| PFE-28_38.FIN2 | 0.576 | -62.688 | -787.628 | 3.151 | 4.964 | 0.254 | 3.622 | 0.191 | 6.717 | 13.087 | 6.574 | 0.354 | 4.993 | 0.790 | 0.118 | 3.556 | 3182 | 120 | 1931 | 166 | 2589 | 136 | 2245 | 151 | 60.7 |
| PFE-28_41.FIN2 | 0.683 | -1464.282 | -45.418 | 2.590 | 2.959 | 0.270 | 3.110 | 0.143 | 5.380 | 14.555 | 2.847 | 0.398 | 2.710 | 0.277 | 0.124 | 2.125 | 3261 | 101 | 2153 | 100 | 2773 | 53 | 2362 | 95 | 66.0 |
| PFE-28_42.FIN2 | 0.740 | -2695.878 | -31.214 | 2.098 | 3.317 | 0.283 | 3.637 | 0.154 | 3.976 | 18.346 | 3.878 | 0.479 | 3.648 | 0.558 | 0.154 | 3.610 | 3336 | 115 | 2505 | 155 | 2983 | 81 | 2886 | 194 | 75.1 |
| PFE-28_44.FIN2 | 0.528 | 295.698 | 9.183 | 5.040 | 4.393 | 0.236 | 3.068 | 0.344 | 4.441 | 7.012 | 4.844 | 0.213 | 4.060 | 0.752 | 0.163 | 8.824 | 3057 | 100 | 1237 | 91 | 2071 | 96 | 2992 | 468 | 40.5 |
| PFE-28_45.FIN2 | 1.128 | -1320.478 | -35.746 | 1.439 | 3.591 | 0.311 | 3.381 | 0.284 | 19.784 | 30.834 | 3.387 | 0.729 | 3.090 | 0.513 | 0.177 | 2.430 | 3475 | 106 | 3503 | 170 | 3487 | 72 | 3286 | 148 | 100.8 |
| PFE-28_46.FIN2 | 0.307 | -1059.526 | -41.567 | 2.553 | 3.772 | 0.241 | 3.216 | 0.059 | 5.725 | 13.924 | 4.631 | 0.421 | 3.882 | 0.651 | 0.116 | 4.271 | 3097 | 97 | 2243 | 145 | 2699 | 85 | 2209 | 178 | 72.4 |
| PFE-28_47.FIN2 | 0.813 | -2550.322 | -33.184 | 5.121 | 6.182 | 0.229 | 5.024 | 0.199 | 3.765 | 8.693 | 10.396 | 0.249 | 7.097 | 0.892 | 0.100 | 8.415 | 2919 | 163 | 1400 | 176 | 2082 | 182 | 1886 | 302 | 47.9 |
| PFE-28_48.FIN2 | 0.496 | -2905.641 | -23.810 | 2.969 | 3.437 | 0.256 | 2.606 | 0.124 | 4.149 | 12.194 | 4.106 | 0.344 | 3.477 | 0.742 | 0.132 | 2.822 | 3184 | 84 | 1893 | 117 | 2572 | 89 | 2492 | 131 | 59.4 |
| PFE-28_49.FIN2 | 0.886 | -2103.755 | -48.867 | 3.980 | 6.188 | 0.247 | 3.643 | 0.197 | 2.979 | 11.205 | 7.651 | 0.307 | 5.795 | 0.903 | 0.101 | 4.833 | 3098 | 117 | 1694 | 174 | 2382 | 160 | 1933 | 180 | 54.7 |
| PFE-28_50.FIN2 | 0.457 | -1603.896 | -59.809 | 4.747 | 6.021 | 0.216 | 4.694 | 0.224 | 7.023 | 7.666 | 7.617 | 0.239 | 4.958 | 0.842 | 0.107 | 3.417 | 2868 | 157 | 1368 | 124 | 2053 | 160 | 2056 | 133 | 47.7 |
| PFE-28_51.FIN2 | 1.458 | -1796.559 | -39.624 | 4.183 | 2.945 | 0.246 | 2.850 | 0.337 | 3.068 | 8.280 | 4.078 | 0.250 | 3.280 | 0.780 | 0.096 | 3.167 | 3107 | 93 | 1428 | 82 | 2253 | 72 | 1849 | 111 | 46.0 |
| PFE-28_52.FIN2 | 1.380 | -557.677 | -99.969 | 4.992 | 4.915 | 0.240 | 3.047 | 0.386 | 3.879 | 8.114 | 7.114 | 0.234 | 5.258 | 0.919 | 0.105 | 5.595 | 3066 | 97 | 1337 | 126 | 2127 | 126 | 1996 | 211 | 43.6 |
| PFE-28_53.FIN2 | 0.840 | 26.775 | 879.234 | 4.523 | 4.778 | 0.235 | 3.681 | 0.265 | 5.729 | 8.589 | 7.522 | 0.257 | 5.667 | 0.843 | 0.113 | 4.711 | 3015 | 118 | 1451 | 143 | 2181 | 123 | 2147 | 190 | 48.1 |
| PFE-28_54.FIN2 | 0.252 | -370.018 | -159.597 | 5.997 | 3.198 | 0.193 | 3.725 | 0.103 | 6.249 | 4.673 | 5.385 | 0.171 | 3.293 | 0.747 | 0.102 | 6.348 | 2708 | 129 | 1016 | 62 | 1719 | 94 | 1956 | 236 | 37.5 |
| PFE-28_55.FIN2 | 0.613 | -2685.137 | -38.284 | 4.310 | 3.529 | 0.232 | 2.534 | 0.191 | 4.326 | 7.966 | 5.289 | 0.252 | 4.246 | 0.891 | 0.110 | 4.064 | 3026 | 84 | 1434 | 107 | 2191 | 88 | 2095 | 161 | 47.4 |
| PFE-28_56.FIN2 | 1.264 | -3285.184 | -34.484 | 2.039 | 2.661 | 0.301 | 2.779 | 0.267 | 3.101 | 20.875 | 2.916 | 0.506 | 2.717 | 0.404 | 0.170 | 2.561 | 3433 | 87 | 2644 | 122 | 3112 | 56 | 3164 | 149 | 77.0 |
| PFE-28_57.FIN2 | 1.151 | -1658.208 | -54.507 | 1.363 | 2.637 | 0.318 | 4.131 | 0.291 | 33.962 | 32.616 | 4.239 | 0.739 | 2.527 | 0.255 | 0.223 | 4.954 | 3533 | 125 | 3562 | 139 | 3555 | 85 | 4056 | 361 | 100.8 |
| PFE-28_58.FIN2 | 0.563 | -1882.313 | -32.657 | 3.376 | 7.606 | 0.251 | 4.294 | 0.130 | 7.237 | 14.726 | 8.213 | 0.391 | 6.505 | 0.596 | 0.120 | 7.331 | 3090 | 143 | 2066 | 233 | 2616 | 189 | 2261 | 318 | 66.8 |
| PFE-28_59.FIN2 | 1.006 | -8965.024 | -31.479 | 2.865 | 3.542 | 0.271 | 3.372 | 0.246 | 3.806 | 13.465 | 4.440 | 0.360 | 3.202 | 0.662 | 0.134 | 2.851 | 3275 | 117 | 1975 | 110 | 2684 | 91 | 2541 | 137 | 60.3 |
| *PFE-28D* | | | | | | | | | | | | | | | | | | | | | | | | | |
| PFE-28D_1.FIN2 | 1.123 | 2840.645 | 39.874 | 2.995 | 7.591 | 0.261 | 2.965 | 0.212 | 3.809 | 14.815 | 5.825 | 0.393 | 4.616 | 0.616 | 0.122 | 5.201 | 3210 | 104 | 2111 | 176 | 2695 | 157 | 2308 | 231 | 65.8 |
| PFE-28D_2.FIN2 | 0.972 | 2685.644 | 35.420 | 1.568 | 2.170 | 0.289 | 2.301 | 0.161 | 3.345 | 25.826 | 2.698 | 0.645 | 2.230 | 0.508 | 0.191 | 2.871 | 3394 | 71 | 3200 | 112 | 3330 | 55 | 3518 | 184 | 94.3 |
| PFE-28D_5.FIN2 | 0.300 | 1768.833 | 49.036 | 5.729 | 3.709 | 0.225 | 2.952 | 0.142 | 10.932 | 5.995 | 5.534 | 0.186 | 3.907 | 0.739 | 0.121 | 3.594 | 2966 | 95 | 1093 | 79 | 1910 | 95 | 2298 | 154 | 36.9 |
| PFE-28D_7.FIN2 | 1.131 | 2953.036 | 37.096 | 3.711 | 4.181 | 0.237 | 2.815 | 0.234 | 3.379 | 10.232 | 6.293 | 0.300 | 4.561 | 0.901 | 0.103 | 3.347 | 3053 | 90 | 1673 | 132 | 2358 | 116 | 1971 | 124 | 54.8 |
| PFE-28D_14.FIN2 | 0.936 | -11640.554 | -36.248 | 5.657 | 2.178 | 0.192 | 2.702 | 0.204 | 4.532 | 4.739 | 3.185 | 0.177 | 2.122 | 0.481 | 0.064 | 2.240 | 2735 | 91 | 1049 | 41 | 1763 | 54 | 1253 | 54 | 38.3 |
| PFE-28D_16.FIN2 | 0.739 | -13197.773 | -24.338 | 4.787 | 6.820 | 0.225 | 4.339 | 0.188 | 2.542 | 9.906 | 9.925 | 0.284 | 7.478 | 0.928 | 0.113 | 5.177 | 2912 | 146 | 1563 | 207 | 2171 | 196 | 2192 | 228 | 53.7 |
| PFE-28D_17.FIN2 | 1.565 | -2570.652 | -51.998 | 5.273 | 1.995 | 0.198 | 1.850 | 0.333 | 2.485 | 5.238 | 2.847 | 0.192 | 2.037 | 0.759 | 0.073 | 2.175 | 2791 | 62 | 1133 | 42 | 1855 | 51 | 1417 | 59 | 40.6 |
| PFE-28D_35.FIN2 | 0.869 | -2421.190 | -28.428 | 1.865 | 2.311 | 0.301 | 2.364 | 0.162 | 1.994 | 22.686 | 2.781 | 0.549 | 2.310 | 0.456 | 0.179 | 1.886 | 3448 | 73 | 2809 | 105 | 3198 | 51 | 3328 | 116 | 81.5 |
| PFE-28D_38.FIN2 | 1.040 | -3494.267 | -39.261 | 2.498 | 1.633 | 0.139 | 1.855 | 0.170 | 2.382 | 7.733 | 1.890 | 0.403 | 1.607 | 0.166 | 0.114 | 1.778 | 2197 | 65 | 2182 | 60 | 2195 | 34 | 2187 | 74 | 99.3 |
| PFE-28D_3.FIN2 | 0.257 | 27380.695 | 33.624 | 4.335 | 8.013 | 0.142 | 2.614 | 0.057 | 2.703 | 5.538 | 5.221 | 0.275 | 4.506 | 0.894 | 0.117 | 15.244 | 2205 | 93 | 1546 | 129 | 1828 | 120 | 2114 | 574 | 70.1 |
| PFE-28D_6.FIN2 | 0.079 | 17050.322 | 41.635 | 5.761 | 2.455 | 0.130 | 2.467 | 0.028 | 2.344 | 3.152 | 2.874 | 0.176 | 2.437 | 0.556 | 0.109 | 2.140 | 2078 | 90 | 1043 | 47 | 1439 | 47 | 2093 | 85 | 50.2 |
| PFE-28D_20.FIN2 | 1.733 | -680.150 | -126.963 | 2.523 | 2.831 | 0.140 | 3.241 | 0.197 | 5.591 | 7.804 | 4.318 | 0.398 | 2.751 | 0.642 | 0.077 | 5.517 | 2218 | 112 | 2159 | 101 | 2200 | 78 | 1501 | 160 | 97.3 |
| PFE-28D_28.FIN2 | 1.254 | -1376.755 | -36.885 | 5.850 | 2.749 | 0.129 | 2.240 | 0.292 | 3.097 | 3.114 | 2.654 | 0.176 | 2.659 | 0.615 | 0.067 | 2.804 | 2046 | 79 | 1040 | 51 | 1427 | 40 | 1316 | 71 | 50.8 |
| PFE-28D_11.FIN2 | 0.375 | 83920.339 | 27.742 | 5.068 | 1.967 | 0.131 | 1.846 | 0.057 | 3.662 | 3.599 | 2.241 | 0.199 | 1.849 | 0.473 | 0.051 | 2.511 | 2093 | 63 | 1171 | 40 | 1544 | 35 | 1007 | 49 | 55.9 |
| PFE-28D_26.FIN2 | 0.421 | -2977.965 | -63.538 | 3.160 | 2.846 | 0.144 | 3.047 | 0.082 | 3.874 | 6.333 | 2.629 | 0.322 | 2.797 | 0.294 | 0.104 | 2.195 | 2248 | 108 | 1797 | 88 | 2016 | 49 | 2013 | 71 | 79.9 |

| | | | | | | | | | | | | | | | | | | | | | | | | | |
|---|---|---|---|---|---|---|---|---|---|---|---|---|---|---|---|---|---|---|---|---|---|---|---|---|---|
| *PFE-31A* | | | | | | | | | | | | | | | | | | | | | | | | | |
| PFE-31A-N_1 | 0.212 | -8923.042 | -41.517 | 1.874 | 1.782 | 0.230 | 2.331 | 0.035 | 2.476 | 16.962 | 1.728 | 0.531 | 1.851 | 0.168 | 0.142 | 1.793 | 3020 | 74 | 2739 | 83 | 2932 | 31 | 2678 | 90 | 90.7 |
| PFE-31A-N_2 | 0.480 | -1605.905 | -63.801 | 5.953 | 6.301 | 0.154 | 4.895 | 0.082 | 2.982 | 5.259 | 9.459 | 0.215 | 6.748 | 0.923 | 0.055 | 4.696 | 2246 | 170 | 1231 | 151 | 1655 | 174 | 1071 | 98 | 54.8 |
| PFE-31A-N_3 | 0.581 | 23266.479 | 34.829 | 1.966 | 3.071 | 0.239 | 2.291 | 0.140 | 7.989 | 17.378 | 2.704 | 0.521 | 2.865 | 0.690 | 0.142 | 2.964 | 3087 | 75 | 2685 | 128 | 2944 | 56 | 2683 | 150 | 87.0 |
| PFE-31A-N_6 | 1.507 | 4541.715 | 93.603 | 2.536 | 2.146 | 0.140 | 2.541 | 0.311 | 6.045 | 7.700 | 2.018 | 0.399 | 2.212 | 0.278 | 0.116 | 2.432 | 2191 | 88 | 2156 | 81 | 2193 | 39 | 2220 | 102 | 98.4 |
| PFE-31A-N_7 | 0.333 | 224.871 | 451.615 | 3.070 | 2.377 | 0.199 | 3.048 | 0.051 | 4.016 | 9.043 | 3.381 | 0.325 | 2.370 | 0.449 | 0.077 | 3.887 | 2775 | 103 | 1811 | 76 | 2322 | 59 | 1492 | 112 | 65.2 |
| PFE-31A-N_8 | 0.279 | 1323.113 | 114.992 | 2.975 | 2.647 | 0.205 | 2.682 | 0.044 | 2.527 | 9.842 | 2.933 | 0.344 | 2.701 | 0.535 | 0.088 | 2.436 | 2829 | 88 | 1899 | 88 | 2399 | 54 | 1699 | 79 | 67.1 |
| PFE-31A-N_9 | 0.438 | -723.251 | -126.490 | 2.316 | 1.970 | 0.142 | 2.713 | 0.096 | 6.527 | 8.499 | 1.850 | 0.434 | 1.880 | -0.025 | 0.127 | 2.177 | 2200 | 95 | 2318 | 74 | 2277 | 33 | 2419 | 99 | 105.4 |
| PFE-31A-N_10 | 0.116 | 1403.529 | 52.067 | 2.744 | 5.028 | 0.230 | 3.565 | 0.039 | 10.979 | 12.268 | 6.600 | 0.369 | 4.556 | 0.699 | 0.152 | 5.808 | 3033 | 116 | 2018 | 160 | 2603 | 115 | 2848 | 306 | 66.6 |
| PFE-31A-N_12 | 0.247 | 5978.207 | 41.625 | 2.002 | 1.890 | 0.229 | 2.295 | 0.039 | 2.633 | 15.979 | 1.710 | 0.501 | 1.926 | 0.189 | 0.131 | 2.177 | 3018 | 75 | 2612 | 82 | 2868 | 33 | 2482 | 102 | 86.5 |
| PFE-31A-B_1 | 0.298 | -3517.055 | -91.002 | 2.009 | 2.162 | 0.228 | 2.590 | 0.052 | 2.788 | 15.905 | 2.288 | 0.503 | 2.150 | 0.288 | 0.143 | 2.442 | 2998 | 84 | 2617 | 92 | 2857 | 44 | 2688 | 123 | 87.3 |
| PFE-31A-B_2 | 0.340 | 1209.162 | 100.900 | 1.968 | 1.787 | 0.232 | 2.220 | 0.056 | 2.280 | 16.406 | 1.473 | 0.509 | 1.859 | 0.133 | 0.141 | 2.380 | 3037 | 71 | 2647 | 80 | 2895 | 29 | 2656 | 118 | 87.1 |
| PFE-31A-B_3 | 0.291 | -49.649 | -2829.422 | 2.017 | 2.838 | 0.237 | 3.649 | 0.061 | 7.363 | 16.325 | 2.440 | 0.500 | 2.605 | 0.065 | 0.155 | 2.565 | 3059 | 115 | 2606 | 113 | 2886 | 47 | 2913 | 138 | 85.2 |
| PFE-31A-B_4 | 0.309 | 596.105 | 161.829 | 1.824 | 1.924 | 0.237 | 2.676 | 0.055 | 3.206 | 18.094 | 1.940 | 0.550 | 1.829 | 0.003 | 0.166 | 2.909 | 3063 | 86 | 2818 | 84 | 2985 | 37 | 3089 | 166 | 92.0 |
| PFE-31A-B_5 | 0.200 | 12910.729 | 56.835 | 2.167 | 2.060 | 0.219 | 2.787 | 0.030 | 2.892 | 13.865 | 2.205 | 0.458 | 2.217 | 0.208 | 0.112 | 2.733 | 2932 | 92 | 2421 | 91 | 2728 | 43 | 2146 | 111 | 82.5 |
| PFE-31A-B_6 | 0.337 | -3814.731 | -67.743 | 3.383 | 2.286 | 0.194 | 2.608 | 0.055 | 2.485 | 8.072 | 2.298 | 0.297 | 2.239 | 0.338 | 0.081 | 2.859 | 2737 | 87 | 1670 | 65 | 2227 | 40 | 1594 | 93 | 61.0 |
| PFE-31A-B_7 | 0.491 | 250.094 | 308.714 | 3.202 | 6.434 | 0.214 | 3.240 | 0.093 | 5.150 | 11.223 | 6.147 | 0.365 | 5.262 | 0.895 | 0.098 | 4.011 | 2882 | 115 | 1972 | 183 | 2439 | 138 | 1877 | 144 | 68.4 |
| PFE-31A-B_8 | 0.330 | 730.886 | 140.675 | 6.974 | 4.183 | 0.120 | 5.911 | 0.058 | 3.398 | 2.772 | 9.703 | 0.151 | 5.045 | 0.834 | 0.046 | 3.519 | 1820 | 191 | 922 | 93 | 1258 | 129 | 900 | 62 | 50.6 |
| PFE-31A-B_9 | 0.207 | 6020.320 | 69.208 | 2.621 | 2.773 | 0.139 | 2.802 | 0.047 | 6.027 | 7.345 | 2.755 | 0.379 | 2.604 | 0.587 | 0.118 | 2.582 | 2180 | 100 | 2066 | 91 | 2156 | 52 | 2248 | 109 | 94.8 |
| PFE-31A-B_10 | 0.447 | 2730.535 | 96.783 | 2.119 | 1.977 | 0.227 | 2.582 | 0.076 | 2.425 | 14.909 | 1.955 | 0.475 | 1.978 | 0.125 | 0.132 | 1.982 | 2992 | 82 | 2497 | 82 | 2800 | 36 | 2496 | 93 | 83.5 |
| PFE-31A-B_11 | 1.029 | 2355.071 | 85.593 | 1.732 | 2.081 | 0.242 | 3.150 | 0.186 | 3.477 | 19.351 | 2.126 | 0.577 | 2.106 | -0.093 | 0.160 | 2.085 | 3099 | 101 | 2929 | 99 | 3051 | 42 | 3000 | 116 | 94.5 |
| PFE-31A-B_12 | 0.314 | 1262.269 | 99.507 | 2.243 | 2.285 | 0.222 | 2.506 | 0.050 | 3.385 | 13.819 | 2.669 | 0.446 | 2.319 | 0.464 | 0.116 | 3.205 | 2966 | 80 | 2368 | 93 | 2720 | 52 | 2204 | 134 | 79.8 |
| PFE-31A-B_14 | 1.165 | 3211.966 | 67.028 | 2.372 | 2.364 | 0.226 | 2.993 | 0.235 | 2.938 | 13.300 | 2.686 | 0.424 | 2.220 | 0.256 | 0.134 | 2.402 | 2986 | 95 | 2272 | 86 | 2688 | 48 | 2541 | 114 | 76.1 |
| PFE-31A-B_15 | 0.263 | -1148.878 | -76.635 | 5.243 | 3.780 | 0.150 | 3.642 | 0.050 | 6.571 | 4.168 | 5.307 | 0.198 | 3.943 | 0.725 | 0.056 | 5.119 | 2294 | 129 | 1157 | 83 | 1636 | 86 | 1097 | 109 | 50.5 |
| *PFE-31B* | | | | | | | | | | | | | | | | | | | | | | | | | |
| PFE-31B-N_1 | 0.3063 | -707.8237 | -106.8287 | 1.9809 | 2.6600 | 0.2345 | 3.1850 | 0.0574 | 3.7654 | 16.3401 | 2.3611 | 0.5112 | 2.6431 | 0.2461 | 0.1477 | 3.0301 | 3044 | 101 | 2651 | 114 | 2897 | 52 | 2778 | 157 | 87 |
| PFE-31B-N_3 | 0.2854 | 1711.0238 | 71.6439 | 2.9242 | 2.9632 | 0.2101 | 2.9264 | 0.0463 | 2.8700 | 10.3815 | 3.8568 | 0.3526 | 2.8595 | 0.6346 | 0.0932 | 3.2440 | 2859 | 97 | 1937 | 96 | 2436 | 68 | 1820 | 120 | 68 |
| PFE-31B-N_4 | 0.3646 | 935.5326 | 164.5625 | 2.2721 | 2.0643 | 0.2263 | 2.6716 | 0.0655 | 4.1946 | 13.8882 | 1.8856 | 0.4442 | 2.1521 | 0.1341 | 0.1248 | 2.3737 | 2988 | 85 | 2361 | 85 | 2733 | 36 | 2373 | 106 | 79 |
| PFE-31B-N_5 | 0.3091 | 5560.2435 | 59.1074 | 2.8356 | 3.1233 | 0.2097 | 4.2382 | 0.0543 | 3.8481 | 10.4085 | 3.9699 | 0.3588 | 3.3036 | 0.3254 | 0.0976 | 4.2939 | 2849 | 132 | 1968 | 110 | 2449 | 73 | 1878 | 154 | 69 |
| PFE-31B-N_6 | 1.3403 | 1839.3769 | 105.2644 | 1.9034 | 2.1984 | 0.2436 | 2.7194 | 0.2401 | 2.4596 | 17.6177 | 2.3795 | 0.5257 | 2.1637 | 0.3630 | 0.1572 | 2.3160 | 3104 | 86 | 2732 | 91 | 2962 | 51 | 2945 | 127 | 88 |
| PFE-31B-N_7 | 0.3118 | 10578.2952 | 51.9958 | 4.7244 | 2.0871 | 0.1622 | 2.7874 | 0.0488 | 2.7528 | 4.7920 | 2.2642 | 0.2135 | 2.1870 | 0.1738 | 0.0547 | 1.9925 | 2432 | 99 | 1245 | 49 | 1773 | 39 | 1085 | 45 | 51 |
| PFE-31B-N_8 | 1.3191 | -40511.9715 | -56.5289 | 3.2880 | 4.0010 | 0.2029 | 3.5827 | 0.2858 | 3.5728 | 8.8194 | 4.2794 | 0.3106 | 3.1921 | 0.5692 | 0.1006 | 3.7090 | 2811 | 120 | 1738 | 99 | 2296 | 82 | 1934 | 136 | 62 |
| PFE-31B-N_10 | 1.0677 | -942.2722 | -212.7607 | 2.2353 | 4.3356 | 0.2317 | 3.5998 | 0.2050 | 3.0848 | 14.7153 | 4.4102 | 0.4558 | 3.8856 | 0.6584 | 0.1308 | 3.0467 | 3021 | 119 | 2404 | 161 | 2790 | 80 | 2481 | 143 | 80 |
| PFE-31B-N_11 | 0.3075 | -1664.5127 | -63.5832 | 2.4876 | 3.4385 | 0.2098 | 2.4696 | 0.0561 | 4.5967 | 12.3239 | 3.4921 | 0.4191 | 3.3500 | 0.7222 | 0.1199 | 3.3639 | 2870 | 78 | 2237 | 127 | 2592 | 74 | 2280 | 145 | 78 |
| PFE-31B-N_12 | 0.4002 | -1732.6779 | -52.0550 | 2.6459 | 5.8625 | 0.2227 | 3.0092 | 0.1000 | 8.2236 | 13.3073 | 5.2963 | 0.4219 | 4.5380 | 0.8219 | 0.1378 | 4.3887 | 2952 | 100 | 2236 | 178 | 2618 | 119 | 2593 | 215 | 76 |
| PFE-31B-B_1 | 0.3545 | -358.3804 | -225.3165 | 2.9277 | 5.0857 | 0.2140 | 3.7525 | 0.0655 | 5.0816 | 11.3112 | 5.9457 | 0.3741 | 5.1199 | 0.7693 | 0.0940 | 5.7946 | 2883 | 117 | 2023 | 176 | 2479 | 119 | 1857 | 223 | 70 |
| PFE-31B-B_2 | 0.2021 | -141.5217 | -465.8470 | 4.9815 | 2.8494 | 0.1759 | 2.3829 | 0.0501 | 6.1231 | 5.0986 | 3.1266 | 0.2067 | 2.8320 | 0.7174 | 0.0795 | 3.9384 | 2580 | 84 | 1207 | 62 | 1814 | 57 | 1542 | 117 | 47 |
| PFE-31B-B_4 | 0.2526 | 6474.3933 | 43.0374 | 2.6122 | 2.6773 | 0.2104 | 2.6014 | 0.0440 | 2.9999 | 11.5014 | 3.0407 | 0.3833 | 2.3588 | 0.6767 | 0.1115 | 3.9475 | 2872 | 85 | 2104 | 92 | 2543 | 55 | 2127 | 158 | 73 |
| PFE-31B-B_5 | 0.3535 | -392.3665 | -171.2272 | 5.3552 | 4.5029 | 0.1657 | 3.1534 | 0.0624 | 2.5430 | 5.2143 | 7.6367 | 0.2124 | 5.7115 | 0.8793 | 0.0606 | 5.3770 | 2473 | 118 | 1224 | 124 | 1754 | 116 | 1183 | 123 | 49 |
| PFE-31B-B_6 | 0.3838 | -216.8365 | -482.2765 | 2.8160 | 4.2083 | 0.2188 | 3.6681 | 0.0794 | 8.6986 | 11.2168 | 4.6317 | 0.3697 | 4.2607 | 0.6322 | 0.1006 | 3.9734 | 2932 | 118 | 2015 | 147 | 2513 | 84 | 1933 | 145 | 69 |
| PFE-31B-B_7 | 0.2365 | 327.8917 | 382.1266 | 2.1837 | 2.2365 | 0.2186 | 2.4974 | 0.0414 | 4.1165 | 14.0351 | 2.1113 | 0.4628 | 2.1855 | 0.4077 | 0.1287 | 2.8646 | 2938 | 79 | 2443 | 89 | 2741 | 40 | 2474 | 146 | 83 |
| PFE-31B-B_8 | 0.3288 | 2758.3234 | 45.8922 | 1.7672 | 2.0574 | 0.2357 | 2.9209 | 0.0502 | 3.1264 | 18.5317 | 1.9353 | 0.5667 | 2.0967 | -0.0376 | 0.1528 | 2.8189 | 3057 | 94 | 2886 | 97 | 3010 | 38 | 2868 | 150 | 94 |
| PFE-31B-B_9 | 0.5397 | 3696.0892 | 81.9903 | 6.5816 | 3.2853 | 0.1589 | 4.7416 | 0.1407 | 4.7944 | 3.2872 | 3.9543 | 0.1535 | 3.1027 | 0.3290 | 0.0604 | 6.7588 | 2388 | 150 | 919 | 53 | 1485 | 71 | 1181 | 153 | 38 |
| PFE-31B-B_10 | 0.2024 | 6095.6512 | 44.7858 | 2.0155 | 2.0584 | 0.2227 | 2.8730 | 0.0326 | 2.4308 | 15.3879 | 2.2670 | 0.4995 | 2.0142 | 0.0939 | 0.1336 | 2.3606 | 2955 | 95 | 2603 | 87 | 2827 | 43 | 2530 | 112 | 88 |
| PFE-31B-B_11 | 0.3034 | 217.1514 | 475.3888 | 3.4149 | 3.8657 | 0.1981 | 3.7815 | 0.0663 | 10.1979 | 8.4525 | 4.5301 | 0.3049 | 3.8117 | 0.6045 | 0.0794 | 3.6686 | 2744 | 124 | 1703 | 114 | 2232 | 95 | 1541 | 109 | 62 |
| PFE-31B-B_12 | 0.2884 | -1137.0840 | -56.9981 | 1.8913 | 2.4669 | 0.2273 | 2.8785 | 0.0509 | 6.1116 | 16.7928 | 2.3314 | 0.5332 | 2.4722 | 0.2208 | 0.1369 | 3.0579 | 3001 | 92 | 2745 | 110 | 2913 | 45 | 2588 | 150 | 91 |

| | | | | | | | | | | | | | | | | | | | | | | | | |
|---|---|---|---|---|---|---|---|---|---|---|---|---|---|---|---|---|---|---|---|---|---|---|---|---|
| *PFE-29* | | | | | | | | | | | | | | | | | | | | | | | | |
| PFE-29_1.FIN2 | 0.446 | 879.458 | 52.852 | 1.646 | 2.178 | 0.237 | 2.587 | 0.070 | 4.336 | 20.132 | 2.559 | 0.614 | 2.278 | 0.162 | 0.169 | 6.428 | 3080 | 79 | 3076 | 113 | 3087 | 49 | 3142 | 372 | 100 |
| PFE-29_2.FIN2 | 0.653 | 7899.547 | 20.881 | 3.067 | 2.276 | 0.138 | 2.708 | 0.106 | 2.309 | 6.236 | 2.488 | 0.332 | 2.263 | 0.152 | 0.098 | 6.357 | 2150 | 96 | 1845 | 73 | 2002 | 44 | 1890 | 229 | 86 |
| PFE-29_3.FIN2 | 0.224 | 7620.605 | 46.081 | 2.724 | 2.494 | 0.140 | 3.037 | 0.041 | 4.478 | 7.118 | 2.595 | 0.372 | 2.444 | 0.163 | 0.120 | 6.580 | 2186 | 106 | 2037 | 86 | 2121 | 45 | 2280 | 284 | 93 |
| PFE-29_8.FIN2 | 0.295 | 122.409 | 102.275 | 1.647 | 2.423 | 0.242 | 2.613 | 0.073 | 31.479 | 20.170 | 2.567 | 0.611 | 2.728 | 0.279 | 0.195 | 9.759 | 3102 | 85 | 3091 | 119 | 3092 | 51 | 3543 | 588 | 100 |
| PFE-29_9.FIN2 | 0.552 | 351.130 | 81.656 | 1.617 | 2.415 | 0.247 | 2.855 | 0.086 | 4.053 | 21.299 | 2.722 | 0.628 | 2.389 | 0.064 | 0.179 | 6.747 | 3133 | 90 | 3134 | 119 | 3143 | 53 | 3323 | 409 | 100 |
| PFE-29_10.FIN2 | 3.082 | 52.153 | 144.518 | 2.416 | 2.568 | 0.140 | 2.959 | 0.493 | 3.589 | 8.022 | 2.877 | 0.422 | 2.743 | 0.232 | 0.121 | 6.387 | 2174 | 101 | 2260 | 105 | 2221 | 52 | 2302 | 278 | 104 |
| PFE-29_11.FIN2 | 1.331 | 783.963 | 57.027 | 2.646 | 2.424 | 0.139 | 3.167 | 0.210 | 3.186 | 7.304 | 2.972 | 0.384 | 2.447 | 0.021 | 0.116 | 6.590 | 2170 | 110 | 2089 | 87 | 2140 | 52 | 2218 | 276 | 96 |
| PFE-29_12.FIN2 | 2.166 | -99.869 | -65.164 | 2.953 | 3.282 | 0.134 | 2.773 | 0.359 | 2.720 | 6.474 | 3.292 | 0.355 | 3.461 | 0.576 | 0.108 | 6.544 | 2104 | 97 | 1948 | 115 | 2026 | 61 | 2067 | 258 | 93 |
| PFE-29_13.FIN2 | 0.997 | 1253.369 | 29.600 | 2.546 | 2.604 | 0.138 | 3.141 | 0.161 | 3.519 | 7.535 | 2.721 | 0.394 | 2.275 | 0.055 | 0.121 | 6.486 | 2155 | 109 | 2140 | 83 | 2169 | 49 | 2309 | 284 | 99 |
| PFE-29_14.FIN2 | 0.368 | 153.452 | 89.273 | 1.651 | 2.336 | 0.241 | 2.676 | 0.064 | 5.135 | 20.212 | 2.651 | 0.613 | 2.400 | 0.083 | 0.175 | 6.979 | 3090 | 86 | 3071 | 118 | 3091 | 51 | 3249 | 415 | 99 |
| PFE-29_15.FIN2 | 0.380 | 84.106 | 86.685 | 1.711 | 3.663 | 0.246 | 2.987 | 0.068 | 8.623 | 20.025 | 2.759 | 0.608 | 3.328 | 0.375 | 0.185 | 8.377 | 3124 | 97 | 3044 | 163 | 3094 | 59 | 3397 | 520 | 97 |
| PFE-29_16.FIN2 | 0.526 | 567.124 | 59.558 | 1.718 | 2.834 | 0.244 | 3.555 | 0.154 | 44.263 | 19.757 | 3.005 | 0.592 | 2.800 | 0.074 | 0.187 | 7.882 | 3107 | 113 | 2988 | 134 | 3071 | 59 | 3450 | 498 | 96 |
| PFE-29_17.FIN2 | 0.355 | 135.232 | 157.561 | 1.692 | 2.667 | 0.243 | 4.135 | 0.057 | 4.866 | 19.736 | 3.268 | 0.600 | 2.823 | 0.510 | 0.183 | 7.244 | 3096 | 135 | 3020 | 135 | 3068 | 66 | 3379 | 451 | 98 |
| PFE-29_20.FIN2 | 0.417 | 342.794 | 64.065 | 1.650 | 2.640 | 0.249 | 3.645 | 0.093 | 34.694 | 20.434 | 3.308 | 0.611 | 3.132 | 0.284 | 0.170 | 8.971 | 3139 | 111 | 3062 | 151 | 3116 | 77 | 3150 | 510 | 98 |
| PFE-29_22.FIN2 | 0.296 | 556.453 | 40.583 | 1.684 | 3.042 | 0.240 | 2.890 | 0.047 | 5.654 | 19.835 | 2.906 | 0.611 | 2.913 | 0.387 | 0.176 | 7.648 | 3086 | 91 | 3062 | 143 | 3082 | 61 | 3251 | 457 | 99 |
| PFE-29_23.FIN2 | 0.640 | 596.227 | 60.296 | 1.704 | 2.497 | 0.246 | 2.797 | 0.095 | 3.501 | 20.125 | 2.593 | 0.598 | 2.474 | 0.030 | 0.164 | 6.464 | 3125 | 90 | 3014 | 119 | 3089 | 49 | 3060 | 368 | 96 |
| PFE-29_24.FIN2 | 0.332 | -15.787 | -2132.113 | 1.613 | 2.797 | 0.238 | 2.968 | 0.049 | 6.447 | 20.714 | 2.658 | 0.635 | 3.363 | 0.051 | 0.166 | 7.407 | 3068 | 96 | 3145 | 164 | 3116 | 52 | 3088 | 421 | 103 |
| PFE-29_26.FIN2 | 0.355 | 479.119 | 69.115 | 1.683 | 2.415 | 0.249 | 2.933 | 0.060 | 3.831 | 20.449 | 2.985 | 0.607 | 2.521 | 0.270 | 0.186 | 7.105 | 3136 | 92 | 3048 | 121 | 3110 | 53 | 3422 | 445 | 97 |
| PFE-29_28.FIN2 | 0.111 | 5776.585 | 36.312 | 5.891 | 3.459 | 0.132 | 2.621 | 0.035 | 2.804 | 3.241 | 4.061 | 0.183 | 4.005 | 0.748 | 0.102 | 6.418 | 2080 | 92 | 1075 | 78 | 1456 | 60 | 1964 | 240 | 52 |
| PFE-29_31.FIN2 | 0.494 | 829.337 | 26.751 | 1.670 | 3.316 | 0.244 | 3.364 | 0.083 | 4.059 | 20.385 | 3.488 | 0.614 | 3.092 | 0.326 | 0.182 | 6.912 | 3095 | 107 | 3070 | 154 | 3089 | 69 | 3367 | 423 | 99 |
| *PFE-29J* | | | | | | | | | | | | | | | | | | | | | | | | |
| PFE-29J_1.FIN2 | 0.98 | 217 | 141 | 2.65 | 1.4 | 0.13931 | 0.89 | 0.173 | 6.975 | 7.3395 | 1.6 | 0.37848 | 1.3 | 0.763 | 0.11 | 2.28 | 2213 | 31 | 2068 | 45 | 2150 | 30 | 2220 | 81 | 93 |
| PFE-29J_2.FIN2 | 0.75 | -1465 | -31 | 2.59 | 1.0 | 0.13899 | 0.83 | 0.114 | 3.633 | 7.4147 | 1.4 | 0.38520 | 1.0 | 0.208 | 0.11 | 1.30 | 2209 | 29 | 2100 | 36 | 2161 | 24 | 2067 | 51 | 95 |
| PFE-29J_3.FIN2 | 1.45 | 2341 | 49 | 3.17 | 1.7 | 0.13980 | 1.13 | 0.041 | 4.191 | 6.0553 | 2.3 | 0.31294 | 2.1 | 0.828 | 0.02 | 9.66 | 2215 | 39 | 1751 | 66 | 1981 | 39 | 328 | 63 | 79 |
| PFE-29J_5.FIN2 | 0.89 | 772 | 63 | 8.20 | 2.5 | 0.11320 | 1.25 | 0.115 | 2.071 | 1.9860 | 3.5 | 0.12460 | 2.7 | 0.932 | 0.03 | 3.13 | 1840 | 46 | 756 | 38 | 1099 | 42 | 609 | 37 | 41 |
| PFE-29J_6.FIN2 | 0.64 | 532 | 72 | 4.66 | 3.0 | 0.13630 | 1.18 | 0.118 | 4.505 | 4.3367 | 4.4 | 0.23054 | 3.9 | 0.970 | 0.07 | 4.63 | 2179 | 42 | 1327 | 91 | 1678 | 68 | 1408 | 124 | 61 |
| PFE-29J_7.FIN2 | 0.95 | 957 | 32 | 11.75 | 2.6 | 0.10861 | 1.02 | 0.143 | 1.779 | 1.3304 | 3.1 | 0.08796 | 2.8 | 0.945 | 0.02 | 2.39 | 1769 | 37 | 543 | 29 | 852 | 35 | 496 | 23 | 31 |
| PFE-29J_8.FIN2 | 1.02 | 441 | 152 | 2.45 | 1.2 | 0.14077 | 1.10 | 0.154 | 1.476 | 7.9522 | 1.6 | 0.40863 | 1.2 | 0.171 | 0.11 | 1.36 | 2230 | 38 | 2208 | 46 | 2228 | 26 | 2187 | 57 | 99 |
| PFE-29J_9.FIN2 | 0.82 | -362 | -200 | 2.49 | 1.4 | 0.13969 | 1.32 | 0.118 | 1.905 | 7.7971 | 1.6 | 0.40067 | 1.3 | 0.275 | 0.11 | 1.80 | 2219 | 45 | 2171 | 50 | 2207 | 29 | 2062 | 71 | 98 |
| PFE-29J_10.FIN2 | 0.94 | 5452 | 40 | 2.93 | 1.3 | 0.13815 | 0.83 | 0.033 | 1.471 | 6.5495 | 1.6 | 0.34164 | 1.3 | 0.692 | 0.02 | 5.44 | 2199 | 28 | 1893 | 42 | 2054 | 27 | 471 | 51 | 86 |
| PFE-29J_11.FIN2 | 0.55 | 1838 | 56 | 2.61 | 1.0 | 0.13910 | 0.92 | 0.084 | 1.265 | 7.4033 | 1.4 | 0.38280 | 1.0 | 0.093 | 0.11 | 1.43 | 2217 | 34 | 2089 | 37 | 2160 | 26 | 2097 | 57 | 94 |
| PFE-29J_12.FIN2 | 0.16 | 2185 | 72 | 2.69 | 1.5 | 0.13677 | 1.03 | 0.024 | 2.944 | 7.0899 | 1.7 | 0.37258 | 1.5 | 0.659 | 0.11 | 2.37 | 2182 | 36 | 2040 | 52 | 2120 | 32 | 2164 | 97 | 94 |
| PFE-29J_13.FIN2 | 0.56 | -1272 | -248 | 2.48 | 1.2 | 0.13824 | 1.06 | 0.086 | 1.445 | 7.7568 | 1.4 | 0.40260 | 1.2 | 0.201 | 0.12 | 1.38 | 2202 | 37 | 2181 | 46 | 2203 | 25 | 2340 | 61 | 99 |
| PFE-29J_14.FIN2 | 0.95 | 1183 | 77 | 2.46 | 1.2 | 0.13888 | 1.24 | 0.138 | 1.371 | 7.8456 | 1.5 | 0.40569 | 1.2 | 0.093 | 0.12 | 2.00 | 2208 | 42 | 2195 | 45 | 2212 | 27 | 2213 | 84 | 99 |
| PFE-29J_17.FIN2 | 0.39 | 4671 | 36 | 2.63 | 1.2 | 0.13865 | 1.32 | 0.062 | 3.991 | 7.3171 | 1.6 | 0.38028 | 1.2 | 0.230 | 0.11 | 1.96 | 2201 | 45 | 2077 | 44 | 2148 | 29 | 2026 | 76 | 94 |
| *PFE-08* | | | | | | | | | | | | | | | | | | | | | | | | |
| PFE-08-N_9 | 2.38 | 506 | 50 | 2.47 | 1.8 | 0.13732 | 2.80 | 0.430 | 4.169 | 7.6146 | 2.1 | 0.40423 | 1.8 | 0.066 | 0.12 | 5.32 | 2140 | 98 | 2183 | 67 | 2183 | 39 | 2215 | 222 | 102 |
| PFE-08-N_13 | 2.41 | 763 | 51 | 2.51 | 2.5 | 0.14332 | 3.52 | 0.502 | 3.680 | 7.8690 | 2.3 | 0.39895 | 2.4 | 0.092 | 0.13 | 5.22 | 2191 | 117 | 2155 | 86 | 2203 | 39 | 2404 | 236 | 98 |
| PFE-08-N_15 | 2.84 | 497 | 87 | 2.53 | 1.8 | 0.13792 | 2.30 | 0.514 | 2.783 | 7.6232 | 1.7 | 0.39818 | 1.9 | 0.213 | 0.12 | 5.10 | 2165 | 81 | 2155 | 70 | 2186 | 30 | 2211 | 214 | 100 |
| PFE-08-N_24 | 2.11 | 209 | 99 | 2.53 | 2.0 | 0.13613 | 2.37 | 0.377 | 2.657 | 7.5105 | 1.7 | 0.39854 | 2.0 | 0.211 | 0.12 | 5.05 | 2141 | 83 | 2155 | 75 | 2166 | 32 | 2219 | 212 | 101 |
| PFE-08-N_26 | 2.16 | 436 | 107 | 2.48 | 2.0 | 0.13856 | 2.66 | 0.420 | 3.396 | 7.7169 | 2.4 | 0.40623 | 1.8 | 0.292 | 0.12 | 5.20 | 2161 | 93 | 2192 | 68 | 2194 | 40 | 2349 | 229 | 101 |
| PFE-08-B_6 | 2.01 | 340 | 86 | 2.52 | 2.1 | 0.13748 | 2.93 | 0.388 | 2.963 | 7.4769 | 1.8 | 0.39846 | 2.2 | -0.068 | 0.12 | 5.25 | 2137 | 104 | 2154 | 83 | 2162 | 31 | 2357 | 232 | 101 |
| PFE-08-B_14 | 1.41 | -565 | -63 | 2.59 | 2.1 | 0.13523 | 2.94 | 0.309 | 4.694 | 7.3141 | 2.0 | 0.39174 | 2.2 | 0.279 | 0.12 | 5.08 | 2107 | 105 | 2123 | 78 | 2140 | 36 | 2340 | 224 | 101 |
| PFE-08-B_17 | 1.43 | 2408 | 58 | 2.37 | 1.8 | 0.13765 | 2.79 | 0.277 | 2.508 | 8.0080 | 2.1 | 0.41809 | 1.9 | 0.189 | 0.13 | 5.49 | 2147 | 95 | 2260 | 78 | 2221 | 37 | 2522 | 257 | 105 |
| PFE-08-B_18 | 1.12 | 1179 | 54 | 2.52 | 2.2 | 0.13628 | 2.48 | 0.215 | 2.876 | 7.5507 | 1.7 | 0.40178 | 2.1 | 0.136 | 0.12 | 5.10 | 2139 | 86 | 2170 | 76 | 2172 | 30 | 2368 | 241 | 101 |
| PFE-08-B_19 | 2.13 | 96 | 139 | 2.51 | 2.2 | 0.13756 | 2.80 | 0.403 | 2.713 | 7.4886 | 2.7 | 0.40142 | 2.3 | 0.062 | 0.12 | 5.22 | 2146 | 95 | 2167 | 85 | 2173 | 40 | 2332 | 229 | 101 |
| PFE-08-B_21 | 1.93 | 622 | 41 | 2.48 | 2.2 | 0.13513 | 2.70 | 0.362 | 3.813 | 7.5610 | 2.0 | 0.40284 | 2.3 | 0.101 | 0.12 | 5.24 | 2116 | 96 | 2189 | 90 | 2171 | 35 | 2297 | 227 | 103 |
| PFE-08-B_23 | 1.79 | -17842 | -71 | 2.42 | 2.6 | 0.13466 | 2.90 | 0.396 | 4.342 | 7.7827 | 2.8 | 0.41671 | 2.8 | 0.439 | 0.14 | 5.35 | 2112 | 107 | 2235 | 105 | 2189 | 53 | 2659 | 266 | 106 |
| PFE-08-B_27 | 1.63 | 801 | 85 | 2.50 | 2.2 | 0.13535 | 3.03 | 0.266 | 2.702 | 7.5382 | 1.9 | 0.40238 | 2.3 | -0.038 | 0.11 | 5.16 | 2127 | 105 | 2174 | 86 | 2171 | 34 | 2167 | 212 | 102 |
| PFE-08-B_30 | 1.35 | -3246 | -47 | 2.54 | 2.0 | 0.13660 | 2.99 | 0.242 | 2.438 | 7.4366 | 1.9 | 0.39647 | 1.9 | 0.077 | 0.12 | 5.21 | 2133 | 104 | 2148 | 70 | 2157 | 34 | 2232 | 219 | 101 |
| PFE-08-B_31 | 1.29 | -6293 | -65 | 2.60 | 2.0 | 0.13821 | 2.74 | 0.244 | 3.134 | 7.4268 | 2.1 | 0.38874 | 1.9 | 0.145 | 0.11 | 5.15 | 2155 | 96 | 2111 | 70 | 2153 | 37 | 2193 | 213 | 98 |
| PFE-08-B_32 | 1.76 | 9319 | 46 | 2.49 | 1.9 | 0.13382 | 2.64 | 0.314 | 4.792 | 7.5108 | 2.0 | 0.40387 | 1.9 | 0.109 | 0.11 | 5.08 | 2109 | 93 | 2182 | 72 | 2166 | 36 | 2170 | 209 | 103 |
| PFE-08-B_33 | 1.04 | 9397 | 58 | 2.61 | 2.0 | 0.13940 | 2.83 | 0.205 | 3.681 | 7.4577 | 2.2 | 0.38505 | 2.1 | 0.151 | 0.12 | 5.25 | 2175 | 100 | 2094 | 74 | 2158 | 39 | 2203 | 219 | 96 |
| PFE-08-B_34 | 2.09 | -603 | -92 | 2.47 | 2.1 | 0.13638 | 2.99 | 0.385 | 2.791 | 7.7197 | 2.3 | 0.40488 | 2.1 | -0.048 | 0.12 | 5.23 | 2153 | 109 | 2185 | 78 | 2188 | 40 | 2298 | 228 | 102 |
| PFE-08-B_3 | 1.62 | -79 | -279 | 2.52 | 2.5 | 0.13803 | 3.39 | 0.318 | 3.765 | 7.6011 | 2.0 | 0.40279 | 2.3 | -0.135 | 0.12 | 5.20 | 2141 | 115 | 2174 | 85 | 2176 | 37 | 2280 | 225 | 102 |

| *PFE-09* | | | | | | | | | | | | | | | | | | | | | | | | |
|---|---|---|---|---|---|---|---|---|---|---|---|---|---|---|---|---|---|---|---|---|---|---|---|---|
| PFE-9C-N_1 | 1.41 | -179 | -410 | 2.58 | 2.0 | 0.13691 | 2.75 | 0.236 | 2.687 | 7.3917 | 1.9 | 0.38897 | 2.0 | -0.049 | 0.12 | 2.55 | 2142 | 97 | 2113 | 71 | 2152 | 33 | 2267 | 108 | 99 |
| PFE-9C-N_6 | 0.57 | 1295 | 173 | 2.60 | 2.0 | 0.13567 | 2.67 | 0.087 | 2.326 | 7.2508 | 1.6 | 0.38588 | 2.0 | -0.151 | 0.11 | 2.20 | 2129 | 94 | 2098 | 73 | 2137 | 28 | 2039 | 92 | 99 |
| PFE-9C-N_8 | 1.05 | -1416 | -140 | 2.58 | -99.1 | 0.13743 | 2.58 | 0.201 | 2.578 | 7.1795 | 1.9 | 0.37824 | 2.0 | 0.023 | 0.13 | 2.04 | 2154 | 91 | 2063 | 69 | 2126 | 35 | 2413 | 93 | 96 |
| PFE-9C-N_11 | 1.58 | -12968 | -57 | 2.54 | 1.9 | 0.13643 | 2.72 | 0.241 | 2.346 | 7.4330 | 1.6 | 0.39403 | 1.8 | -0.289 | 0.11 | 1.90 | 2137 | 96 | 2137 | 66 | 2159 | 29 | 2090 | 75 | 100 |
| PFE-9C-N_18 | 0.82 | 6041 | 44 | 2.48 | 2.1 | 0.13764 | 2.80 | 0.149 | 2.708 | 7.7222 | 1.9 | 0.40609 | 2.0 | -0.011 | 0.13 | 1.98 | 2150 | 98 | 2191 | 76 | 2198 | 32 | 2429 | 90 | 102 |
| PFE-9C-N_20 | 2.52 | 5240 | 56 | 2.43 | 1.8 | 0.13584 | 2.34 | 0.445 | 3.204 | 7.7902 | 1.9 | 0.41157 | 1.8 | 0.189 | 0.13 | 2.50 | 2141 | 82 | 2217 | 69 | 2199 | 34 | 2419 | 114 | 104 |
| PFE-9C-N_23 | 1.54 | 4420 | 72 | 2.47 | 1.9 | 0.13659 | 2.40 | 0.237 | 2.395 | 7.6927 | 1.5 | 0.40628 | 1.9 | -0.027 | 0.11 | 1.83 | 2149 | 84 | 2192 | 71 | 2191 | 27 | 2101 | 73 | 102 |
| PFE-9C-N_27 | 1.20 | -1623 | -111 | 2.49 | 1.8 | 0.13613 | 2.72 | 0.188 | 3.539 | 7.4845 | 1.7 | 0.40116 | 1.8 | -0.103 | 0.11 | 1.96 | 2133 | 96 | 2170 | 65 | 2171 | 28 | 2104 | 78 | 102 |
| PFE-9C-B_1 | 0.87 | -683 | -173 | 2.51 | 1.9 | 0.13612 | 2.53 | 0.129 | 1.976 | 7.4931 | 1.5 | 0.39874 | 1.8 | 0.233 | 0.11 | 1.63 | 2139 | 89 | 2158 | 68 | 2167 | 26 | 2025 | 63 | 101 |
| PFE-9C-B_3 | 1.49 | 1899 | 56 | 2.60 | 1.8 | 0.13430 | 2.45 | 0.242 | 2.517 | 7.2001 | 1.8 | 0.38569 | 1.8 | 0.098 | 0.11 | 1.99 | 2119 | 86 | 2098 | 65 | 2129 | 32 | 2115 | 80 | 99 |
| PFE-9C-B_4 | 0.98 | 8386 | 49 | 2.63 | 2.0 | 0.13304 | 2.57 | 0.167 | 2.195 | 7.0438 | 1.8 | 0.38254 | 2.1 | 0.067 | 0.12 | 2.26 | 2097 | 91 | 2082 | 73 | 2116 | 30 | 2197 | 94 | 99 |
| PFE-9C-B_10 | 1.14 | 1404 | 187 | 2.40 | 1.9 | 0.13501 | 2.78 | 0.175 | 2.100 | 7.7906 | 1.8 | 0.41765 | 1.8 | -0.216 | 0.11 | 1.89 | 2116 | 98 | 2245 | 68 | 2200 | 31 | 2178 | 78 | 106 |
| PFE-9C-B_16 | 1.46 | 1775 | 88 | 2.51 | 2.1 | 0.13599 | 2.91 | 0.230 | 2.608 | 7.5507 | 2.2 | 0.40172 | 2.0 | 0.053 | 0.11 | 2.01 | 2127 | 99 | 2171 | 75 | 2169 | 38 | 2139 | 81 | 102 |
| PFE-9C-B_17 | 1.19 | 299 | 2410 | 2.56 | 1.9 | 0.13534 | 2.44 | 0.176 | 2.314 | 7.3545 | 1.4 | 0.39149 | 1.9 | -0.068 | 0.10 | 1.76 | 2133 | 85 | 2125 | 68 | 2151 | 25 | 1978 | 67 | 100 |
| PFE-9C-B_18 | 1.60 | -905 | -63 | 2.46 | 2.1 | 0.13489 | 2.71 | 0.267 | 2.498 | 7.6692 | 2.1 | 0.40953 | 2.0 | 0.144 | 0.12 | 2.59 | 2118 | 95 | 2206 | 77 | 2183 | 37 | 2303 | 112 | 104 |
| PFE-9C-B_19 | 1.06 | 23 | 5226 | 2.57 | 2.0 | 0.13336 | 2.88 | 0.161 | 2.492 | 7.1503 | 1.9 | 0.38906 | 2.0 | -0.073 | 0.11 | 2.13 | 2092 | 101 | 2113 | 73 | 2122 | 34 | 2045 | 83 | 101 |

**Table 2.** Whole-rock geochemistry data of rocks in the Bonfim area, northeastern of Borborema province. n.d. - not determined; <l.d. - below limit of detection.

| Sample | PFE-15 | PFE-19 | PFE-18 | PFE-18B | PFE-18C | PFE-18D | PFE-28 | PFE-28B | PFE-28A | PFE-28C |
|---|---|---|---|---|---|---|---|---|---|---|
| Zone | 24S | 24S | 24S | 24S | 24S | 24S | 24S | 24S | 24S | 24S |
| Easting (m) | 824176 | 819151 | 818510 | 818510 | 818510 | 818510 | 819299 | 819299 | 819299 | 819299 |
| Northing (m) | 9364410 | 9353535 | 9353356 | 9353356 | 9353356 | 9353356 | 9349431 | 9349431 | 9349431 | 9349431 |
| Lithology | serpentinite | serpentinite | tremolitite | tremolitite | tremolitite | tremolitite | tremolitite | tremolitite | tremolitite | serpentinite |
| SiO2 (wt%) | 44.32 | 48.63 | 55.62 | 54.31 | 54.56 | 52.49 | 40.29 | 33.20 | 54.65 | 48.86 |
| TiO2 (wt%) | 0.06 | 0.04 | 0.71 | 0.12 | 0.14 | 0.62 | 0.05 | 0.03 | 0.05 | 1.56 |
| Al2O3 (wt%) | 2.58 | 2.45 | 8.56 | 5.73 | 5.86 | 6.34 | 2.86 | 0.99 | 2.75 | 16.15 |
| Cr2O3 (wt%) | 1.16 | 0.81 | 0.14 | 0.48 | 0.39 | 0.23 | 4.66 | 0.14 | 0.23 | 0.03 |
| Fe2O3t (wt%) | 9.07 | 6.65 | 14.35 | 7.49 | 7.26 | 12.51 | 13.48 | 1.97 | 7.83 | 12.25 |
| MnO (wt%) | 0.12 | 0.09 | 0.15 | 0.14 | 0.13 | 0.27 | 0.14 | 0.06 | 0.27 | 0.26 |
| MgO (wt%) | 36.81 | 33.93 | 11.28 | 19.58 | 19.99 | 18.51 | 32.60 | 17.33 | 19.79 | 11.79 |
| CaO (wt%) | 0.37 | 0.13 | 9.13 | 11.28 | 10.97 | 9.35 | 0.09 | 25.32 | 13.58 | 2.20 |
| Na2O (wt%) | 0.04 | 0.14 | 0.88 | 0.66 | 0.67 | 0.62 | 0.03 | 0.15 | 0.29 | 1.89 |
| K2O (wt%) | 0.01 | 0.04 | 0.10 | 0.04 | 0.04 | 0.07 | 0.02 | 0.07 | 0.15 | 1.55 |
| P2O5 (wt%) | <l.d. | <l.d. | 0.08 | 0.01 | 0.06 | 0.12 | <l.d. | 0.06 | 0.06 | 0.24 |
| LOI | 13.75 | 15.30 | 0.97 | 1.92 | 2.22 | 1.48 | 12.15 | 33.80 | 3.33 | 9.38 |
| Total | 101.74 | 99.41 | 100.75 | 99.13 | 99.92 | 101.30 | 100.27 | 101.26 | 100.13 | 100.86 |
| Ba (ppm) | 43.10 | 14.80 | 16.70 | 1.90 | 3.60 | 11.00 | 19.10 | 496.00 | 21.50 | 412.00 |
| Cs (ppm) | 0.11 | 5.35 | 0.03 | 0.06 | 0.05 | 0.10 | 0.06 | 0.40 | 0.44 | 4.27 |
| Ga (ppm) | 3.40 | 6.50 | 14.30 | 10.10 | 10.20 | 10.20 | 3.40 | 2.30 | 6.30 | 19.40 |
| Hf (ppm) | 0.19 | 0.21 | 1.29 | 0.30 | 0.34 | 0.95 | 0.17 | 0.12 | 0.37 | 3.03 |
| Nb (ppm) | 0.87 | 6.53 | 2.60 | 2.72 | 2.48 | 7.42 | 0.30 | 0.68 | 0.90 | 11.05 |
| Rb (ppm) | 0.20 | 6.00 | 0.50 | 0.40 | 0.30 | 0.90 | 0.80 | 1.60 | 3.10 | 38.10 |

| | | | | | | | | | | |
|---|---|---|---|---|---|---|---|---|---|---|
| **Sr (ppm)** | 9.90 | 7.00 | 4.00 | 3.00 | 3.90 | 3.60 | 4.30 | 245.00 | 41.10 | 172.50 |
| **Ta (ppm)** | 0.20 | 4.70 | 0.20 | 0.50 | 0.50 | 0.50 | 0.10 | 0.10 | 0.10 | 0.60 |
| **Th (ppm)** | 0.44 | 0.28 | 0.22 | 0.16 | 0.17 | 0.24 | 0.23 | 0.24 | 2.14 | 1.66 |
| **U (ppm)** | 8.95 | 1.20 | 0.25 | 0.31 | 0.35 | 1.12 | 0.71 | 0.50 | 0.38 | 0.42 |
| **V (ppm)** | 51.00 | 33.00 | 202.00 | 96.00 | 104.00 | 169.00 | 57.00 | 14.00 | 56.00 | 217.00 |
| **W (ppm)** | 3.70 | 1.60 | 9.40 | 3.80 | 2.20 | 19.80 | 6.00 | 2.00 | 3.20 | 15.20 |
| **Y (ppm)** | 2.40 | 2.10 | 17.10 | 14.30 | 22.10 | 33.80 | 4.90 | 13.90 | 17.50 | 22.40 |
| **Zr (ppm)** | 9.00 | 5.00 | 39.00 | 7.00 | 8.00 | 29.00 | 9.00 | 5.00 | 9.00 | 107.00 |
| **La (ppm)** | 0.80 | 0.20 | 3.40 | 2.30 | 3.50 | 6.30 | 4.10 | 2.40 | 11.60 | 14.70 |
| **Ce (ppm)** | 1.90 | 0.70 | 9.90 | 7.30 | 11.90 | 20.20 | 3.60 | 4.50 | 27.30 | 33.90 |
| **Pr (ppm)** | 0.17 | 0.07 | 1.21 | 1.04 | 1.76 | 3.06 | 1.02 | 0.63 | 2.87 | 3.64 |
| **Nd (ppm)** | 0.80 | 0.60 | 5.10 | 4.60 | 8.70 | 15.00 | 4.50 | 3.70 | 11.40 | 17.50 |
| **Sm (ppm)** | 0.24 | 0.15 | 1.55 | 1.53 | 2.87 | 4.05 | 1.06 | 0.94 | 2.39 | 4.20 |
| **Eu (ppm)** | 0.04 | 0.02 | 0.59 | 0.62 | 0.69 | 0.67 | 0.18 | 0.25 | 0.62 | 1.34 |
| **Gd (ppm)** | 0.33 | 0.08 | 2.25 | 1.87 | 3.22 | 4.88 | 1.06 | 1.79 | 2.16 | 4.87 |
| **Tb (ppm)** | 0.07 | 0.04 | 0.42 | 0.31 | 0.59 | 0.92 | 0.17 | 0.30 | 0.41 | 0.76 |
| **Dy (ppm)** | 0.41 | 0.18 | 2.85 | 1.98 | 3.59 | 5.65 | 0.93 | 2.07 | 2.43 | 4.51 |
| **Ho (ppm)** | 0.10 | 0.05 | 0.62 | 0.47 | 0.85 | 1.25 | 0.16 | 0.52 | 0.45 | 0.90 |
| **Er (ppm)** | 0.40 | 0.22 | 2.01 | 1.56 | 2.44 | 3.66 | 0.45 | 1.51 | 1.88 | 2.66 |
| **Tm (ppm)** | 0.04 | 0.03 | 0.25 | 0.24 | 0.41 | 0.62 | 0.08 | 0.25 | 0.27 | 0.32 |
| **Yb (ppm)** | 0.35 | 0.27 | 1.82 | 1.90 | 2.62 | 3.80 | 0.45 | 1.29 | 1.70 | 2.17 |
| **Lu (ppm)** | 0.02 | 0.02 | 0.27 | 0.27 | 0.39 | 0.59 | 0.07 | 0.21 | 0.30 | 0.26 |
| **Mg-number** | 71.67 | 76.08 | 32.88 | 61.96 | 63.20 | 47.98 | 60.12 | 84.59 | 61.17 | 37.50 |
| **∑REE** | 5.67 | 2.63 | 32.24 | 25.99 | 43.53 | 70.65 | 17.83 | 20.36 | 65.78 | 91.73 |

**Table 2.** Continuation.

| Sample | PFE-05 | PFE-06 | RDD-60-A | RDD-60 | RDE-18 | PFE-07 | PFE-20 | PFE-25I | PFE-29 | PFE-31 |
|---|---|---|---|---|---|---|---|---|---|---|
| Zone | 24S | 24S | 24S | 24S | 24S | 24S | 24S | 24S | 24S | 24S |
| Easting (m) | 824521 | 824448 | 814011 | 814011 | 819176 | 823459 | 818709 | 817814 | 813559 | 814409 |
| Northing (m) | 9357119 | 9356836 | 9334380 | 9334380 | 9356254 | 9355178 | 9357397 | 9351521 | 9344283 | 9345106 |
| Lithology | hornblendite | hornblendite | ultramafic | ultramafic | ultramafic | hornblendite | tremolitite | chloritite | tremolitite | chloritite |
| SiO2 (wt%) | 54.64 | 52.50 | 51.98 | 52.94 | 49.14 | 52.08 | 56.94 | 50.58 | 55.66 | 51.73 |
| TiO2 (wt%) | 0.44 | 1.13 | 0.96 | 0.82 | 0.46 | 0.92 | 0.09 | 1.97 | 0.07 | 1.23 |
| Al2O3 (wt%) | 4.90 | 8.22 | 6.75 | 5.85 | 9.14 | 4.95 | 1.68 | 9.50 | 4.59 | 15.02 |
| Cr2O3 (wt%) | 0.25 | 0.14 | <l.d. | <l.d. | <l.d. | 0.17 | 0.25 | 0.16 | 0.20 | 0.03 |
| Fe2O3t (wt%) | 9.64 | 15.58 | 13.98 | 15.77 | 10.90 | 17.17 | 9.69 | 15.99 | 6.80 | 14.05 |
| MnO (wt%) | 0.09 | 0.30 | 0.29 | 0.19 | 0.16 | 0.38 | 0.23 | 0.21 | 0.15 | 0.17 |
| MgO (wt%) | 19.84 | 12.35 | 17.15 | 18.02 | 18.85 | 16.45 | 22.14 | 9.82 | 29.63 | 6.73 |
| CaO (wt%) | 9.35 | 9.25 | 7.85 | 5.85 | 6.52 | 7.99 | 9.30 | 9.97 | 1.76 | 9.46 |
| Na2O (wt%) | 0.75 | 0.89 | 0.72 | 0.62 | 0.79 | 0.55 | 0.09 | 0.95 | 0.07 | 1.87 |
| K2O (wt%) | 0.05 | 0.11 | 0.09 | 0.06 | 4.04 | 0.07 | 0.01 | 0.84 | <l.d. | 0.36 |
| P2O5 (wt%) | 0.05 | 0.25 | 0.02 | 0.12 | <l.d. | 0.11 | 0.01 | 0.26 | <l.d. | 0.15 |
| LOI | 2.06 | 1.24 | 2.30 | 1.40 | 1.60 | 0.65 | 2.61 | 2.46 | 6.52 | 1.87 |
| Total | 99.60 | 100.29 | 100.64 | 99.15 | 99.05 | 99.93 | 101.14 | 100.52 | 101.74 | 101.04 |
| Ba (ppm) | 16.70 | 83.40 | 22.00 | 15.00 | 284.00 | 6.40 | 38.60 | 132.00 | 7.60 | 61.60 |
| Cs (ppm) | 0.12 | 0.07 | <l.d. | <l.d. | 0.10 | 0.01 | 0.01 | 0.97 | 0.04 | 0.22 |
| Ga (ppm) | 16.80 | 20.30 | <l.d. | <l.d. | 19.30 | 11.20 | 2.70 | 17.60 | 5.40 | 18.30 |
| Hf (ppm) | 2.80 | 4.10 | 2.40 | 2.20 | 3.85 | 3.24 | 0.38 | 3.75 | 1.04 | 2.56 |
| Nb (ppm) | 11.35 | 30.60 | 21.70 | 14.30 | 7.65 | 13.85 | 0.35 | 22.20 | 1.64 | 5.74 |
| Rb (ppm) | 1.00 | 1.00 | 2.30 | 0.60 | 2.80 | 0.30 | <l.d. | 18.20 | 0.30 | 4.30 |
| Sr (ppm) | 3.00 | 9.70 | 5.30 | 2.80 | 122.00 | 13.00 | 6.10 | 23.60 | 3.00 | 123.00 |

| | | | | | | | | | | |
|---|---|---|---|---|---|---|---|---|---|---|
| **Ta (ppm)** | 1.30 | 2.00 | <l.d. | <l.d. | 0.60 | 0.90 | 0.10 | 1.30 | 0.10 | 0.40 |
| **Th (ppm)** | 3.65 | 1.17 | 0.90 | 0.60 | 2.74 | 2.18 | 0.20 | 1.46 | 0.53 | 0.81 |
| **U (ppm)** | 0.82 | 0.74 | 1.80 | 1.10 | 0.86 | 1.60 | 0.08 | 0.61 | 1.97 | 0.25 |
| **V (ppm)** | 204.00 | 178.00 | 179.00 | 206.00 | 229.00 | 107.00 | 62.00 | 282.00 | 55.00 | 312.00 |
| **W (ppm)** | 14.20 | 3.80 | <l.d. | <l.d. | 5.70 | 3.30 | 2.00 | 5.50 | 2.60 | 4.70 |
| **Y (ppm)** | 105.50 | 101.00 | 117.90 | 41.30 | 34.50 | 16.40 | 6.40 | 35.10 | 16.20 | 27.30 |
| **Zr (ppm)** | 92.00 | 166.00 | 94.30 | 94.00 | 152.00 | 121.00 | 11.00 | 152.00 | 38.00 | 98.00 |
| **La (ppm)** | 12.40 | 36.90 | 10.00 | 6.40 | 21.80 | 14.80 | 3.20 | 21.20 | 9.10 | 10.00 |
| **Ce (ppm)** | 47.40 | 87.30 | 42.90 | 24.90 | 39.80 | 36.10 | 25.00 | 46.00 | 11.50 | 19.90 |
| **Pr (ppm)** | 7.33 | 13.60 | 7.41 | 3.92 | 5.46 | 4.87 | 1.00 | 6.85 | 3.10 | 2.88 |
| **Nd (ppm)** | 35.60 | 59.90 | 37.10 | 18.20 | 24.30 | 20.40 | 4.20 | 34.50 | 13.30 | 15.50 |
| **Sm (ppm)** | 10.05 | 13.60 | 11.52 | 4.48 | 5.25 | 4.34 | 1.08 | 6.09 | 4.05 | 3.93 |
| **Eu (ppm)** | 3.81 | 2.19 | 2.39 | 2.41 | 1.31 | 0.99 | 0.32 | 2.07 | 0.44 | 1.16 |
| **Gd (ppm)** | 13.00 | 13.45 | 14.01 | 5.82 | 5.63 | 3.96 | 0.98 | 6.31 | 3.59 | 3.94 |
| **Tb (ppm)** | 2.66 | 2.41 | <l.d. | <l.d. | 1.13 | 0.60 | 0.20 | 1.12 | 0.62 | 0.74 |
| **Dy (ppm)** | 18.20 | 16.70 | 20.27 | 7.29 | 6.47 | 3.24 | 1.17 | 5.87 | 3.25 | 5.15 |
| **Ho (ppm)** | 4.22 | 3.79 | 4.51 | 1.59 | 1.23 | 0.61 | 0.21 | 1.09 | 0.65 | 1.03 |
| **Er (ppm)** | 12.60 | 11.40 | 13.33 | 4.45 | 3.46 | 1.87 | 0.74 | 3.09 | 1.92 | 2.83 |
| **Tm (ppm)** | 1.90 | 1.83 | 2.13 | 0.69 | 0.62 | 0.25 | 0.11 | 0.41 | 0.23 | 0.35 |
| **Yb (ppm)** | 12.15 | 12.20 | 14.34 | 4.75 | 3.15 | 1.72 | 0.84 | 2.32 | 1.58 | 3.42 |
| **Lu (ppm)** | 1.64 | 1.90 | 2.05 | 0.68 | 0.50 | 0.22 | 0.11 | 0.37 | 0.24 | 0.44 |
| **Mg-number** | 56.21 | 33.08 | 43.33 | 41.61 | 51.89 | 37.40 | 58.77 | 27.69 | 73.10 | 22.99 |
| **∑REE** | 182.96 | 277.17 | 86.68 | 91.54 | 79.63 | 93.97 | 39.16 | 137.29 | 53.57 | 71.27 |

**Table 2.** Continuation.

| Sample | PFE-31B | PFE-01 | STC-48 | PFE-08 | PFE-09A | PFE-09B |
|---|---|---|---|---|---|---|
| Zone | 24S | 24S | 24S | 24S | 24S | 24S |
| Easting (m) | 814409 | 825825 | 825659 | 827037 | 827197 | 827197 |
| Northing (m) | 9345106 | 9362116 | 9363267 | 9369460 | 9369860 | 9369860 |
| Lithology | chloritite | amphibolite | amphibolite | amphibolite | amphibolite | amphibolite |
| SiO2 (wt%) | 33.20 | 53.53 | 53.23 | 49.24 | 49.61 | 52.21 |
| TiO2 (wt%) | 0.33 | 1.05 | 1.05 | 0.65 | 0.36 | 0.40 |
| Al2O3 (wt%) | 19.58 | 14.15 | 14.81 | 5.79 | 5.33 | 9.80 |
| Cr2O3 (wt%) | 0.11 | 0.06 | 0.03 | 0.12 | 0.27 | 0.22 |
| Fe2O3t (wt%) | 10.87 | 12.51 | 13.58 | 19.63 | 13.94 | 11.33 |
| MnO (wt%) | 0.03 | 0.17 | 0.18 | 0.30 | 0.33 | 0.33 |
| MgO (wt%) | 29.42 | 6.60 | 5.67 | 12.61 | 8.54 | 12.35 |
| CaO (wt%) | 0.07 | 10.15 | 9.46 | 11.53 | 22.66 | 11.28 |
| Na2O (wt%) | 0.02 | 1.07 | 2.56 | 0.89 | 0.64 | 2.01 |
| K2O (wt%) | <l.d. | 0.27 | 0.37 | 0.25 | 0.11 | 0.45 |
| P2O5 (wt%) | 0.01 | 0.21 | 0.16 | 0.01 | 0.08 | 0.05 |
| LOI | 11.90 | 1.03 | 0.80 | 0.86 | 0.39 | 0.76 |
| Total | 100.16 | 101.57 | 99.20 | 0.86 | 0.39 | 0.76 |
| Ba (ppm) | 44.60 | 130.50 | 64.80 | 92.50 | 130.50 | 64.80 |
| Cs (ppm) | 0.04 | 4.49 | 0.18 | 0.10 | 4.49 | 0.18 |
| Ga (ppm) | 38.70 | 9.10 | 11.50 | 10.50 | 9.10 | 11.50 |
| Hf (ppm) | 8.15 | 0.77 | 1.12 | 3.68 | 0.77 | 1.12 |
| Nb (ppm) | 7.12 | 3.03 | 1.72 | 1.98 | 3.03 | 1.72 |
| Rb (ppm) | 0.30 | 5.90 | 6.10 | 1.40 | 5.90 | 6.10 |
| Sr (ppm) | 1.00 | 142.00 | 145.00 | 62.10 | 142.00 | 145.00 |

| | | | | | | |
|---|---|---|---|---|---|---|
| **Ta (ppm)** | 0.60 | 0.30 | 0.20 | 0.20 | 0.30 | 0.20 |
| **Th (ppm)** | 1.55 | 0.57 | 0.69 | 0.36 | 0.57 | 0.69 |
| **U (ppm)** | 0.49 | 0.88 | 0.21 | 0.16 | 0.88 | 0.21 |
| **V (ppm)** | 225.00 | 91.00 | 170.00 | 173.00 | 91.00 | 170.00 |
| **W (ppm)** | 1.80 | 12.40 | 3.20 | 2.30 | 12.40 | 3.20 |
| **Y (ppm)** | 18.50 | 12.30 | 11.20 | 20.70 | 12.30 | 11.20 |
| **Zr (ppm)** | 270.00 | 24.00 | 38.00 | 209.00 | 24.00 | 38.00 |
| **La (ppm)** | 10.30 | 5.10 | 3.90 | 9.50 | 5.10 | 3.90 |
| **Ce (ppm)** | 19.00 | 9.60 | 9.20 | 26.50 | 9.60 | 9.20 |
| **Pr (ppm)** | 2.41 | 1.16 | 1.06 | 3.24 | 1.16 | 1.06 |
| **Nd (ppm)** | 9.10 | 5.70 | 4.60 | 15.00 | 5.70 | 4.60 |
| **Sm (ppm)** | 2.07 | 1.41 | 1.11 | 3.51 | 1.41 | 1.11 |
| **Eu (ppm)** | 0.40 | 0.72 | 0.42 | 1.53 | 0.72 | 0.42 |
| **Gd (ppm)** | 2.46 | 1.96 | 1.57 | 4.00 | 1.96 | 1.57 |
| **Tb (ppm)** | 0.42 | 0.37 | 0.31 | 0.66 | 0.37 | 0.31 |
| **Dy (ppm)** | 2.64 | 2.09 | 1.82 | 3.69 | 2.09 | 1.82 |
| **Ho (ppm)** | 0.53 | 0.51 | 0.43 | 0.85 | 0.51 | 0.43 |
| **Er (ppm)** | 1.80 | 1.28 | 1.48 | 2.15 | 1.28 | 1.48 |
| **Tm (ppm)** | 0.25 | 0.19 | 0.16 | 0.32 | 0.19 | 0.16 |
| **Yb (ppm)** | 1.56 | 1.03 | 1.12 | 2.16 | 1.03 | 1.12 |
| **Lu (ppm)** | 0.29 | 0.14 | 0.18 | 0.33 | 0.14 | 0.18 |
| **Mg-number** | 62.80 | 24.76 | 20.65 | 28.60 | 27.64 | 40.47 |
| **∑REE** | 53.23 | 31.26 | 27.36 | 73.44 | 31.26 | 27.36 |

**Table 3.** Sm-Nd isotopic data of rocks in the Bonfim area, northeastern of Borborema province.

| Sample | UTM Zone | Easting (m) | Northing (m) | Lithology | Sm(ppm) | Nd(ppm) | Sm/Nd | $^{147}Sm/^{144}Nd$ | $^{143}Nd/^{144}Nd$ | $e_{Nd\ (0)}$ | $e_{Nd\ (t)}$ | $T_{DM\ (Ga)}$ |
|---|---|---|---|---|---|---|---|---|---|---|---|---|
| PFE-01 | 24S | 825825 | 9362116 | amphibolite | 8.151 | 37.083 | 0.220 | 0.1329 | 0.5113 | -26.43 | -1.84 | 3.49 |
| STC-48 | 24S | 825659 | 9363267 | amphibolite | 5.373 | 24.148 | 0.223 | 0.1345 | 0.5115 | -22.28 | 2.63 | 3.16 |
| SEB291-36 | 24S | | | amphibolite | 3.603 | 18.559 | 0.194 | 0.1174 | 0.5108 | -35.64 | -3.95 | 3.67 |
| BF11-47 | 24S | 814745 | 9349742 | amphibolite | 1.758 | 6.548 | 0.268 | 0.1623 | 0.5118 | -15.47 | 0.11 | 3.83 |
| PFE-05 | 24S | 824521 | 9357119 | hornblendite | 10.921 | 36.673 | 0.298 | 0.1800 | 0.5119 | -13.48 | -6.82 | 5.36 |
| PFE-06 | 24S | 824448 | 9356836 | hornblendite | 13.223 | 61.962 | 0.213 | 0.1290 | 0.5115 | -22.63 | 0.91 | 2.99 |
| PFE-07 | 24S | 823459 | 9355178 | hornblendite | 4.158 | 20.280 | 0.205 | 0.1239 | 0.5112 | -27.33 | 1.79 | 3.22 |
| PFE-08 | 24S | 827037 | 9369460 | amphibolite | 3.796 | 15.549 | 0.244 | 0.1476 | 0.5118 | -17.17 | -4.20 | 3.19 |
| PFE-09A | 24S | 827197 | 9369860 | amphibolite | 1.448 | 5.481 | 0.264 | 0.1597 | 0.5119 | -15.22 | -5.68 | 3.61 |
| PFE-15 | 24S | 824176 | 9364410 | serpentinite | 0.210 | 1.001 | 0.210 | 0.1267 | 0.5116 | -20.72 | 3.68 | 2.74 |
| PFE-15B | 24S | 824176 | 9364410 | serpentinite | 0.271 | 1.546 | 0.175 | 0.1058 | 0.5110 | -32.73 | 2.44 | 3.07 |
| PFE-18 | 24S | 818510 | 9353356 | tremolitite | 1.729 | 5.687 | 0.304 | 0.1837 | 0.5123 | -7.04 | -1.16 | 4.39 |
| PFE-18B | 24S | 818510 | 9353356 | tremolitite | 1.493 | 4.938 | 0.302 | 0.1828 | 0.5119 | -14.69 | -8.46 | 6.14 |
| PFE-18C | 24S | 818510 | 9353356 | tremolitite | 2.303 | 7.111 | 0.324 | 0.1958 | 0.5117 | -18.08 | -17.80 | 11.83 |
| PFE-19 | 24S | 819151 | 9353535 | serpentinite | 2.297 | 8.150 | 0.282 | 0.1704 | 0.5121 | -11.04 | 0.89 | 3.76 |
| PFE-20 | 24S | 818709 | 9357397 | tremolitite | 0.970 | 4.126 | 0.235 | 0.1422 | 0.5115 | -21.91 | -0.07 | 3.45 |
| PFE-22 | 24S | 817695 | 9358746 | chloritite | 1.661 | 7.040 | 0.236 | 0.1426 | 0.5113 | -26.55 | -2.10 | 3.98 |
| PFE-25I | 24S | 817814 | 9351521 | chloritite | 8.179 | 38.344 | 0.213 | 0.1289 | 0.5113 | -25.79 | 1.33 | 3.27 |
| PFE-25II | 24S | 817814 | 9351521 | chloritite | 2.925 | 13.716 | 0.213 | 0.1289 | 0.5111 | -30.12 | -3.02 | 3.66 |
| PFE-28 | 24S | 819299 | 9349431 | tremolitite | 0.830 | 3.524 | 0.236 | 0.1424 | 0.5111 | -29.12 | -4.60 | 4.24 |
| PFE-28A | 24S | 819299 | 9349431 | tremolitite | 1.921 | 10.135 | 0.190 | 0.1146 | 0.5119 | -14.71 | 22.63 | 1.94 |
| PFE-28B | 24S | 819299 | 9349431 | tremolitite | 1.042 | 3.426 | 0.304 | 0.1839 | 0.5114 | -23.80 | -18.13 | 8.63 |
| PFE-28C | 24S | 819299 | 9349431 | tremolitite | 4.069 | 16.353 | 0.249 | 0.1504 | 0.5123 | -7.24 | 13.83 | 2.12 |
| PFE-28D | 24S | 819299 | 9349431 | tremolitite | 9.800 | 39.333 | 0.249 | 0.1506 | 0.5115 | -21.81 | -0.96 | 3.90 |
| PFE-29 | 24S | 813559 | 9344283 | tremolitite | 3.616 | 13.744 | 0.263 | 0.1590 | 0.5119 | -13.60 | 1.50 | 3.35 |
| PFE-31 | 24S | 814409 | 9345106 | chloritite | 3.683 | 14.587 | 0.252 | 0.1526 | 0.5119 | -15.33 | 2.34 | 3.21 |
| PFE-31B | 24S | 814409 | 9345106 | chloritite | 1.539 | 6.416 | 0.240 | 0.1450 | 0.5117 | -17.71 | 3.02 | 3.13 |

| | | | | | | | | | | | | |
|---|---|---|---|---|---|---|---|---|---|---|---|---|
| SEB291-33 | 24S | | | ultramafic | 7.873 | 36.404 | 0.216 | 0.1307 | 0.5110 | -32.38 | -2.56 | 3.95 |
| SEB291-39 | 24S | | | ultramafic | 24.899 | 104.216 | 0.239 | 0.1444 | 0.5114 | -23.80 | -0.14 | 3.77 |
| RDD-60A | 24S | 814011 | 9334380 | ultramafic | 9.924 | 35.463 | 0.280 | 0.1692 | 0.5120 | -13.17 | -0.71 | 4.03 |
| RAF-11C* | 24S | 815344 | 9349502 | Mafic | 1.980 | 7.872 | 0.252 | 0.1520 | 0.5117 | -18.02 | -0.13 | 3.52 |
| RAF-11E* | 24S | 815344 | 9349502 | Mafic | 2.213 | 7.866 | 0.281 | 0.1701 | 0.5119 | -14.06 | -2.03 | 4.26 |
| RAF-12* | 24S | 815409 | 9349742 | Mafic | 1.759 | 6.763 | 0.260 | 0.1572 | 0.5118 | -16.78 | 1.11 | 3.67 |

*Values from Garcia et al. (2024).

**Table 4.** U-Pb in rutile grains data of rocks in the Bonfim area, northeastern of Borborema province.

| Spot | $f206$ (%) | U ($mg.g^{-1}$) | 2se | $^{206}Pb/^{204}Pb$ | $^{207}Pb/^{206}Pb$ | 2s | $^{207}Pb/^{235}U$ | 2s | $^{206}Pb/^{238}U$ | 2s | Rho | Idades (Ma)[1] $^{207}Pb/^{206}Pb$ | 2s | $^{206}Pb/^{238}U$ | 2s | $^{207}Pb/^{235}U$ | 2s | % conc[2] |
|---|---|---|---|---|---|---|---|---|---|---|---|---|---|---|---|---|---|---|
| ***PFE05B*** | | | | | | | | | | | | | | | | | | |
| Spot 127.FIN2 | 0.12 | 56.6 | 1.4 | 15529 | 0.0577 | 0.0018 | 0.674 | 0.055 | 0.0839 | 0.0051 | 0.39 | 527 | 70 | 520 | 31 | 523 | 33 | 99 |
| Spot 129.FIN2 | 0.12 | 61.6 | 0.9 | 15913 | 0.0588 | 0.0019 | 0.651 | 0.052 | 0.0803 | 0.0048 | 0.06 | 549 | 63 | 498 | 29 | 506 | 31 | 98 |
| Spot 130.FIN2 | 0.12 | 62.5 | 1.2 | 16011 | 0.0577 | 0.0017 | 0.632 | 0.051 | 0.0800 | 0.0048 | 0.11 | 519 | 68 | 496 | 29 | 498 | 31 | 99 |
| Spot 131.FIN2 | 0.13 | 57.3 | 0.8 | 14159 | 0.0587 | 0.0020 | 0.614 | 0.050 | 0.0763 | 0.0046 | 0.13 | 530 | 73 | 474 | 28 | 488 | 30 | 97 |
| Spot 135.FIN2 | 0.13 | 60.7 | 1.0 | 14370 | 0.0615 | 0.0027 | 0.659 | 0.057 | 0.0782 | 0.0048 | 0.09 | 611 | 97 | 485 | 29 | 513 | 34 | 94 |
| Spot 136.FIN2 | 0.13 | 55.3 | 1.8 | 14477 | 0.0575 | 0.0018 | 0.655 | 0.053 | 0.0831 | 0.0051 | 0.26 | 489 | 74 | 514 | 30 | 510 | 33 | 101 |
| Spot 139.FIN2 | 0.13 | 59.4 | 1.0 | 14293 | 0.0572 | 0.0019 | 0.595 | 0.048 | 0.0756 | 0.0046 | 0.20 | 501 | 75 | 470 | 28 | 476 | 32 | 99 |
| Spot 140.FIN2 | 0.16 | 47.6 | 1.3 | 11812 | 0.0562 | 0.0019 | 0.612 | 0.050 | 0.0791 | 0.0048 | 0.24 | 471 | 73 | 491 | 29 | 485 | 32 | 101 |
| Spot 142.FIN2 | 0.17 | 45.7 | 0.6 | 10763 | 0.0571 | 0.0020 | 0.587 | 0.048 | 0.0748 | 0.0045 | 0.23 | 489 | 76 | 465 | 28 | 469 | 31 | 99 |
| Spot 143.FIN2 | 0.13 | 55.9 | 0.8 | 13874 | 0.0573 | 0.0019 | 0.629 | 0.052 | 0.0795 | 0.0048 | 0.42 | 499 | 75 | 493 | 29 | 493 | 32 | 100 |
| Spot 147.FIN2 | 0.10 | 74.4 | 1.2 | 17977 | 0.0574 | 0.0019 | 0.640 | 0.052 | 0.0803 | 0.0049 | 0.35 | 520 | 70 | 498 | 29 | 501 | 32 | 99 |
| Spot 148.FIN2 | 0.11 | 66.3 | 1.0 | 16436 | 0.0585 | 0.0018 | 0.648 | 0.052 | 0.0800 | 0.0048 | 0.36 | 556 | 66 | 496 | 29 | 506 | 32 | 98 |
| Spot 149.FIN2 | 0.13 | 58.8 | 1.2 | 14337 | 0.0574 | 0.0018 | 0.630 | 0.051 | 0.0795 | 0.0048 | 0.23 | 493 | 70 | 494 | 28 | 496 | 32 | 100 |
| Spot 150.FIN2 | 0.12 | 61.9 | 1.4 | 15259 | 0.0562 | 0.0018 | 0.621 | 0.050 | 0.0798 | 0.0048 | 0.22 | 462 | 69 | 495 | 29 | 490 | 31 | 101 |
| Spot 157.FIN2 | 0.12 | 68.1 | 1.1 | 16240 | 0.0576 | 0.0018 | 0.622 | 0.050 | 0.0785 | 0.0047 | 0.18 | 503 | 73 | 487 | 28 | 491 | 32 | 99 |
| Spot 160.FIN2 | 0.13 | 63.5 | 0.9 | 13911 | 0.0591 | 0.0022 | 0.616 | 0.051 | 0.0752 | 0.0046 | 0.20 | 563 | 81 | 467 | 28 | 486 | 32 | 96 |
| ***PFE18*** | | | | | | | | | | | | | | | | | | |
| Spot 162.FIN2 | 0.06 | 125.9 | 2.2 | 29340 | 0.0565 | 0.0016 | 0.612 | 0.049 | 0.0779 | 0.0047 | 0.30 | 477 | 60 | 484 | 28 | 485 | 30 | 100 |
| Spot 167.FIN2 | 0.10 | 84.6 | 1.6 | 19111 | 0.0571 | 0.0018 | 0.617 | 0.050 | 0.0783 | 0.0047 | 0.23 | 490 | 68 | 486 | 28 | 489 | 30 | 99 |
| Spot 174.FIN2 | 0.07 | 123.2 | 1.6 | 27747 | 0.0571 | 0.0016 | 0.611 | 0.048 | 0.0777 | 0.0047 | 0.23 | 491 | 66 | 482 | 28 | 484 | 30 | 100 |
| Spot 175.FIN2 | 0.07 | 119.0 | 1.6 | 26989 | 0.0571 | 0.0016 | 0.626 | 0.050 | 0.0788 | 0.0047 | 0.26 | 509 | 59 | 489 | 28 | 493 | 31 | 99 |
| Spot 176.FIN2 | 0.12 | 67.7 | 1.6 | 16245 | 0.0593 | 0.0018 | 0.679 | 0.055 | 0.0830 | 0.0050 | 0.18 | 566 | 70 | 514 | 30 | 527 | 32 | 97 |
| Spot 178.FIN2 | 0.08 | 113.3 | 2.3 | 22763 | 0.0590 | 0.0018 | 0.605 | 0.049 | 0.0742 | 0.0045 | 0.20 | 567 | 73 | 461 | 27 | 482 | 30 | 96 |
| Spot 179.FIN2 | 0.28 | 29.9 | 0.5 | 6611 | 0.0568 | 0.0022 | 0.611 | 0.052 | 0.0778 | 0.0047 | 0.19 | 476 | 88 | 483 | 28 | 481 | 32 | 100 |
| Spot 180.FIN2 | 0.05 | 169.5 | 2.2 | 37600 | 0.0567 | 0.0016 | 0.609 | 0.048 | 0.0778 | 0.0047 | 0.36 | 479 | 61 | 483 | 28 | 482 | 31 | 100 |

| | | | | | | | | | | | | | | | | | | |
|---|---|---|---|---|---|---|---|---|---|---|---|---|---|---|---|---|---|---|
| Spot 181.FIN2 | 0.08 | 99.1 | 1.3 | 22100 | 0.0621 | 0.0023 | 0.700 | 0.058 | 0.0823 | 0.0050 | 0.32 | 654 | 82 | 509 | 30 | 537 | 34 | 95 |
| Spot 182.FIN2 | 0.13 | 65.8 | 0.8 | 14424 | 0.0585 | 0.0018 | 0.629 | 0.051 | 0.0772 | 0.0047 | 0.21 | 547 | 70 | 480 | 28 | 494 | 32 | 97 |
| Spot 183.FIN2 | 0.09 | 88.1 | 0.7 | 20272 | 0.0594 | 0.0017 | 0.679 | 0.055 | 0.0833 | 0.0050 | 0.35 | 573 | 66 | 516 | 30 | 525 | 33 | 98 |
| Spot 184.FIN2 | 0.04 | 186.1 | 2.2 | 42680 | 0.0571 | 0.0015 | 0.647 | 0.051 | 0.0818 | 0.0049 | 0.35 | 495 | 57 | 507 | 29 | 506 | 31 | 100 |
| Spot 186.FIN2 | 0.05 | 180.4 | 2.7 | 38094 | 0.0567 | 0.0016 | 0.605 | 0.048 | 0.0774 | 0.0047 | 0.33 | 470 | 62 | 481 | 28 | 480 | 31 | 100 |
| Spot 187.FIN2 | 0.18 | 42.1 | 1.2 | 10114 | 0.0549 | 0.0019 | 0.667 | 0.055 | 0.0869 | 0.0053 | 0.29 | 406 | 81 | 537 | 31 | 519 | 34 | 104 |
| Spot 189.FIN2 | 0.05 | 135.8 | 4.8 | 36405 | 0.0576 | 0.0016 | 0.775 | 0.061 | 0.0985 | 0.0059 | 0.43 | 499 | 60 | 606 | 35 | 582 | 35 | 104 |
| Spot 190.FIN2 | 0.06 | 125.6 | 3.9 | 29393 | 0.0595 | 0.0018 | 0.728 | 0.059 | 0.0885 | 0.0054 | 0.40 | 577 | 66 | 546 | 32 | 554 | 35 | 99 |
| Spot 191.FIN2 | 0.06 | 127.2 | 3.3 | 33328 | 0.0587 | 0.0017 | 0.778 | 0.062 | 0.0970 | 0.0059 | 0.49 | 553 | 64 | 597 | 35 | 584 | 35 | 102 |
| ***PFE20*** | | | | | | | | | | | | | | | | | | |
| Spot 193.FIN2 | 0.56 | 15.1 | 0.4 | 3337 | 0.0594 | 0.0037 | 0.684 | 0.066 | 0.0842 | 0.0053 | 0.14 | 495 | 143 | 521 | 31 | 521 | 39 | 100 |
| Spot 194.FIN2 | 0.43 | 17.4 | 0.4 | 4371 | 0.0589 | 0.0028 | 0.732 | 0.065 | 0.0917 | 0.0056 | 0.27 | 521 | 113 | 565 | 33 | 558 | 38 | 101 |
| Spot 196.FIN2 | 0.35 | 20.8 | 0.5 | 5417 | 0.0600 | 0.0028 | 0.788 | 0.068 | 0.0955 | 0.0059 | 0.26 | 553 | 102 | 588 | 35 | 592 | 38 | 99 |
| Spot 201.FIN2 | 0.35 | 20.9 | 0.6 | 5326 | 0.0561 | 0.0028 | 0.704 | 0.064 | 0.0907 | 0.0056 | 0.36 | 409 | 114 | 559 | 33 | 541 | 38 | 103 |
| Spot 206.FIN2 | 0.79 | 10.3 | 0.3 | 2360 | 0.0605 | 0.0037 | 0.729 | 0.069 | 0.0868 | 0.0054 | 0.11 | 576 | 139 | 537 | 31 | 553 | 41 | 97 |
| ***PFE31B*** | | | | | | | | | | | | | | | | | | |
| Spot 207.FIN2 | 0.12 | 72.8 | 1.0 | 15289 | 0.0614 | 0.0021 | 0.697 | 0.058 | 0.0827 | 0.0050 | 0.56 | 671 | 69 | 512 | 30 | 534 | 35 | 96 |
| Spot 208.FIN2 | 0.15 | 61.7 | 0.8 | 12647 | 0.0598 | 0.0020 | 0.658 | 0.053 | 0.0799 | 0.0048 | 0.13 | 580 | 75 | 496 | 29 | 513 | 32 | 97 |
| Spot 212.FIN2 | 0.11 | 77.9 | 2.0 | 16478 | 0.0571 | 0.0017 | 0.662 | 0.053 | 0.0841 | 0.0051 | 0.23 | 474 | 67 | 521 | 30 | 515 | 33 | 101 |
| Spot 213.FIN2 | 0.17 | 55.0 | 0.8 | 11331 | 0.0598 | 0.0020 | 0.655 | 0.054 | 0.0806 | 0.0049 | 0.28 | 584 | 70 | 500 | 29 | 515 | 33 | 97 |
| Spot 215.FIN2 | 0.13 | 63.9 | 2.2 | 13887 | 0.0582 | 0.0019 | 0.704 | 0.057 | 0.0874 | 0.0053 | 0.36 | 540 | 69 | 540 | 31 | 539 | 34 | 100 |

**Suplementary Table 1.** U-Pb in zircon (Reference Materials).

| | | | | Data for Tera-Wasserburg plot (b) | | | | | | Data for Wetherill plot (b) | | | | | | | | Dates | | | | | | | | | | |
|---|---|---|---|---|---|---|---|---|---|---|---|---|---|---|---|---|---|---|---|---|---|---|---|---|---|---|---|---|
| Identifier | Th/U | $^{206}Pb/^{204}Pb$ | 1s% | $^{238}U/^{206}Pb$ | 1s% | $^{207}Pb/^{206}Pb$ | 1s% | $^{208}Pb/^{206}Pb$ | 1s% | $^{207}Pb/^{235}U$ | 1s% | $^{206}Pb/^{238}U$ | 1s% | Rho | $^{208}Pb/^{232}Th$ | 1s% | $^{207}Pb/^{206}Pb$ | 2s (abs) | 2ssys (abs) | $^{206}Pb/^{238}U$ | 2s (abs) | 2ssys (abs) | $^{207}Pb/^{235}U$ | 2s (abs) | 2ssys (abs) | $^{208}Pb/^{232}Th$ | 2s (abs) | 2ssys (abs) | Concordance (%) |
| GJ1_6 | 0.0 | 163.800 | 214.791 | 10.23 | 1.8 | 0.05965 | 2.56 | 0.006 | 5.58 | 0.8095 | 1.7 | 0.0981 | 1.9 | 0.02 | 0.0306 | 4.08 | 535 | 111 | 111 | 603 | 22 | 22 | 601 | 15 | 17 | 609 | 49 | 134 | 113 |
| GJ1_7 | 0.0 | 1019.935 | 43.203 | 10.24 | 1.9 | 0.05910 | 2.60 | 0.010 | 25.69 | 0.7964 | 1.7 | 0.0980 | 1.9 | 0.01 | 0.0319 | 5.29 | 513 | 112 | 112 | 602 | 21 | 21 | 596 | 16 | 19 | 633 | 65 | 143 | 117 |
| GJ1_9 | 0.0 | 189.547 | 153.460 | 10.53 | 1.9 | 0.06032 | 2.59 | 0.008 | 10.18 | 0.7983 | 2.0 | 0.0954 | 1.9 | 0.10 | 0.0342 | 4.93 | 556 | 115 | 115 | 587 | 21 | 21 | 594 | 18 | 20 | 678 | 65 | 152 | 106 |
| GJ1_11 | 0.0 | 2042.573 | 36.660 | 10.33 | 1.7 | 0.05953 | 2.38 | 0.006 | 4.69 | 0.8012 | 1.7 | 0.0968 | 1.7 | 0.10 | 0.0299 | 5.01 | 538 | 103 | 103 | 595 | 19 | 19 | 596 | 16 | 18 | 595 | 59 | 135 | 111 |
| GJ1_12 | 0.0 | -30.711 | -1002.021 | 10.10 | 2.0 | 0.05952 | 2.94 | 0.006 | 5.09 | 0.8074 | 1.9 | 0.0987 | 1.9 | 0.04 | 0.0316 | 4.82 | 510 | 131 | 131 | 606 | 21 | 21 | 599 | 17 | 19 | 627 | 60 | 142 | 119 |
| GJ1_13 | 0.0 | 136.861 | 234.962 | 10.30 | 1.7 | 0.05929 | 2.58 | 0.009 | 20.46 | 0.8089 | 1.9 | 0.0971 | 1.7 | 0.12 | 0.0322 | 6.23 | 544 | 108 | 108 | 597 | 19 | 19 | 600 | 17 | 19 | 638 | 77 | 150 | 110 |
| GJ1_16 | 0.0 | 578.719 | 44.067 | 10.37 | 1.7 | 0.06027 | 2.59 | 0.006 | 5.60 | 0.8064 | 2.0 | 0.0965 | 1.7 | 0.02 | 0.0280 | 5.18 | 556 | 112 | 112 | 593 | 19 | 19 | 598 | 18 | 20 | 558 | 57 | 127 | 107 |
| GJ1_17 | 0.0 | -279.652 | -80.430 | 10.26 | 1.7 | 0.05905 | 2.63 | 0.006 | 5.90 | 0.7985 | 1.7 | 0.0976 | 1.7 | 0.26 | 0.0291 | 5.33 | 526 | 123 | 123 | 600 | 20 | 20 | 597 | 17 | 19 | 579 | 61 | 133 | 114 |
| GJ1_18 | 0.0 | -468.004 | -82.048 | 10.42 | 1.8 | 0.06093 | 3.05 | 0.008 | 5.68 | 0.8000 | 2.1 | 0.0954 | 1.6 | 0.14 | 0.0400 | 4.77 | 552 | 141 | 141 | 587 | 18 | 18 | 598 | 21 | 23 | 791 | 74 | 176 | 106 |
| GJ1_19 | 0.0 | -116.709 | -187.200 | 10.22 | 1.8 | 0.05946 | 2.53 | 0.005 | 5.93 | 0.8052 | 1.6 | 0.0981 | 1.8 | 0.13 | 0.0261 | 5.80 | 526 | 113 | 113 | 603 | 20 | 20 | 598 | 14 | 17 | 519 | 60 | 122 | 115 |
| GJ1_20 | 0.0 | -283.401 | -66.469 | 10.28 | 1.9 | 0.05997 | 2.63 | 0.008 | 8.15 | 0.8070 | 1.7 | 0.0977 | 1.9 | 0.02 | 0.0357 | 6.11 | 542 | 116 | 116 | 600 | 21 | 21 | 599 | 15 | 17 | 707 | 84 | 166 | 111 |
| GJ1_21 | 0.0 | -853.674 | -39.251 | 10.40 | 2.0 | 0.06059 | 3.00 | 0.007 | 8.90 | 0.8022 | 1.7 | 0.0968 | 2.0 | 0.32 | 0.0313 | 5.66 | 546 | 131 | 131 | 595 | 23 | 23 | 596 | 15 | 17 | 622 | 70 | 145 | 109 |
| GJ1_22 | 0.0 | -1820.244 | -47.089 | 10.22 | 1.7 | 0.06022 | 2.89 | 0.005 | 7.53 | 0.8124 | 1.9 | 0.0978 | 1.6 | 0.18 | 0.0248 | 6.50 | 565 | 135 | 135 | 601 | 19 | 19 | 602 | 18 | 20 | 495 | 64 | 120 | 106 |
| GJ1_23 | 0.0 | -494.568 | -83.431 | 10.37 | 1.6 | 0.06121 | 2.70 | 0.006 | 7.28 | 0.8144 | 1.8 | 0.0963 | 1.6 | 0.26 | 0.0314 | 6.96 | 582 | 120 | 120 | 592 | 18 | 18 | 603 | 17 | 19 | 623 | 85 | 153 | 102 |
| GJ1_25 | 0.0 | -534.775 | -99.089 | 10.26 | 1.7 | 0.05940 | 2.74 | 0.006 | 7.09 | 0.8025 | 2.2 | 0.0974 | 1.7 | 0.02 | 0.0284 | 6.99 | 518 | 119 | 119 | 599 | 19 | 19 | 596 | 19 | 21 | 563 | 78 | 139 | 116 |
| GJ1_27 | 0.0 | 6516.936 | 43.096 | 10.16 | 2.0 | 0.05887 | 2.40 | 0.006 | 9.22 | 0.8131 | 1.7 | 0.0992 | 2.0 | 0.10 | 0.0264 | 6.98 | 530 | 108 | 108 | 609 | 23 | 23 | 602 | 16 | 18 | 525 | 72 | 129 | 115 |
| GJ1_28 | 0.0 | 9168.406 | 57.871 | 10.39 | 1.7 | 0.05948 | 2.83 | 0.007 | 10.34 | 0.7902 | 2.1 | 0.0962 | 1.6 | 0.15 | 0.0294 | 6.47 | 514 | 126 | 126 | 592 | 19 | 19 | 589 | 18 | 20 | 584 | 75 | 141 | 115 |
| GJ1_1 | 0.0 | -14.211 | -2087.724 | 10.22 | 2.3 | 0.05979 | 2.98 | 0.006 | 5.01 | 0.8080 | 1.9 | 0.0980 | 2.3 | 0.06 | 0.0303 | 5.16 | 532 | 135 | 135 | 602 | 26 | 26 | 600 | 17 | 17 | 601 | 61 | 94 | 113 |
| GJ1_4 | 0.0 | -1791.017 | -96.593 | 10.35 | 2.2 | 0.06040 | 3.06 | 0.006 | 12.30 | 0.8066 | 1.8 | 0.0966 | 2.2 | 0.01 | 0.0297 | 5.90 | 559 | 134 | 134 | 594 | 25 | 25 | 599 | 17 | 17 | 590 | 69 | 98 | 106 |
| GJ1_8 | 0.0 | 256.648 | 138.148 | 10.13 | 2.0 | 0.05912 | 2.54 | 0.007 | 19.27 | 0.8147 | 1.9 | 0.0990 | 1.9 | 0.13 | 0.0324 | 10.93 | 536 | 118 | 118 | 608 | 23 | 23 | 603 | 17 | 17 | 638 | 130 | 149 | 113 |
| GJ1_9 | 0.0 | -508.455 | -47.493 | 10.41 | 1.9 | 0.06115 | 3.10 | 0.007 | 17.21 | 0.8068 | 2.2 | 0.0962 | 1.8 | 0.14 | 0.0303 | 5.62 | 587 | 146 | 146 | 591 | 21 | 21 | 603 | 21 | 21 | 602 | 67 | 97 | 101 |
| GJ1_20 | 0.0 | 75.697 | 275.095 | 10.46 | 1.9 | 0.05815 | 2.85 | 0.008 | 14.92 | 0.7730 | 1.9 | 0.0961 | 1.9 | 0.21 | 0.0348 | 7.23 | 462 | 129 | 129 | 591 | 21 | 21 | 580 | 16 | 16 | 689 | 96 | 125 | 128 |
| GJ1_1.FIN2 | 0.0 | 105.327 | 280.738 | 10.25 | 0.8 | 0.05984 | 1.60 | 0.005 | 9.12 | 0.8001 | 1.2 | 0.0975 | 0.8 | 0.09 | 0.0286 | 11.85 | 585 | 77 | 77 | 600 | 9 | 9 | 596 | 11 | 11 | 565 | 133 | 133 | 103 |
| GJ1_3.FIN2 | 0.0 | 367.013 | 113.999 | 10.32 | 0.8 | 0.06006 | 1.48 | 0.011 | 31.60 | 0.8063 | 1.3 | 0.0969 | 0.8 | 0.04 | 0.0420 | 15.71 | 583 | 65 | 65 | 596 | 9 | 9 | 599 | 12 | 12 | 814 | 236 | 236 | 102 |
| GJ1_4.FIN2 | 0.0 | -1951.759 | -25.178 | 10.24 | 0.8 | 0.06014 | 1.65 | 0.005 | 7.82 | 0.8132 | 1.5 | 0.0977 | 0.9 | 0.05 | 0.0292 | 11.14 | 595 | 70 | 70 | 601 | 10 | 10 | 603 | 14 | 14 | 578 | 127 | 127 | 101 |
| GJ1_5.FIN2 | 0.0 | -2879.367 | -19.879 | 10.30 | 0.8 | 0.05972 | 1.37 | 0.040 | 84.06 | 0.8067 | 1.1 | 0.0971 | 0.8 | 0.15 | 0.0342 | 12.38 | 574 | 60 | 60 | 597 | 9 | 9 | 600 | 10 | 10 | 674 | 163 | 163 | 104 |
| GJ1_9.FIN2 | 0.0 | -3750.506 | -21.625 | 10.09 | 0.8 | 0.06002 | 1.64 | 0.008 | 18.00 | 0.8198 | 1.4 | 0.0992 | 0.8 | 0.07 | 0.0377 | 11.18 | 577 | 71 | 71 | 609 | 10 | 10 | 607 | 13 | 13 | 742 | 163 | 163 | 106 |
| GJ1_10.FIN2 | 0.0 | -853.903 | -26.007 | 10.22 | 0.9 | 0.05992 | 1.51 | 0.007 | 24.08 | 0.8117 | 1.3 | 0.0980 | 0.9 | 0.07 | 0.0282 | 11.63 | 577 | 66 | 66 | 602 | 10 | 10 | 602 | 12 | 12 | 559 | 129 | 129 | 104 |
| GJ1_11.FIN2 | 0.0 | -1006.749 | -21.445 | 10.14 | 1.0 | 0.05983 | 1.58 | 0.006 | 10.47 | 0.8191 | 1.3 | 0.0990 | 1.1 | 0.19 | 0.0302 | 11.06 | 570 | 72 | 72 | 608 | 13 | 13 | 606 | 12 | 12 | 598 | 131 | 131 | 107 |
| GJ1_12.FIN2 | 0.0 | -437.203 | -41.518 | 10.09 | 1.0 | 0.05922 | 1.50 | 0.005 | 8.71 | 0.8131 | 1.3 | 0.0994 | 1.0 | 0.13 | 0.0298 | 12.21 | 552 | 66 | 66 | 610 | 12 | 12 | 603 | 11 | 11 | 588 | 141 | 141 | 111 |
| GJ1_13.FIN2 | 0.0 | -666.584 | -27.532 | 10.17 | 0.9 | 0.05913 | 1.54 | 0.005 | 8.60 | 0.8041 | 1.4 | 0.0982 | 1.0 | 0.06 | 0.0290 | 11.70 | 548 | 67 | 67 | 604 | 11 | 11 | 598 | 12 | 12 | 574 | 133 | 133 | 110 |
| GJ1_14.FIN2 | 0.0 | -531.261 | -39.925 | 10.28 | 0.9 | 0.06016 | 1.78 | 0.010 | 21.73 | 0.8046 | 1.5 | 0.0970 | 1.0 | 0.20 | 0.0388 | 15.93 | 582 | 78 | 78 | 597 | 11 | 11 | 598 | 14 | 14 | 757 | 222 | 222 | 102 |
| GJ1_16.FIN2 | 0.0 | 359.405 | 49.962 | 10.30 | 0.9 | 0.06015 | 1.69 | 0.006 | 9.28 | 0.8110 | 1.6 | 0.0973 | 0.9 | 0.46 | 0.0283 | 11.65 | 581 | 72 | 72 | 598 | 10 | 10 | 601 | 14 | 14 | 560 | 129 | 129 | 103 |
| GJ1_17.FIN2 | 0.0 | 229.291 | 92.255 | 10.17 | 1.0 | 0.05956 | 1.81 | 0.007 | 13.96 | 0.8105 | 1.4 | 0.0981 | 0.9 | 0.13 | 0.0347 | 11.41 | 559 | 78 | 78 | 603 | 10 | 10 | 602 | 13 | 13 | 685 | 154 | 154 | 108 |
| GJ1_18.FIN2 | 0.0 | 908.374 | 29.215 | 10.36 | 0.9 | 0.06044 | 1.65 | 0.027 | 79.38 | 0.8057 | 1.6 | 0.0966 | 0.8 | 0.13 | 0.0280 | 12.48 | 591 | 74 | 74 | 594 | 10 | 10 | 598 | 15 | 15 | 553 | 136 | 136 | 100 |
| GJ1_19.FIN2 | 0.0 | 468.122 | 48.237 | 10.27 | 0.8 | 0.06051 | 1.58 | 0.006 | 8.81 | 0.8116 | 1.2 | 0.0975 | 0.8 | 0.04 | 0.0278 | 11.64 | 597 | 68 | 68 | 599 | 9 | 9 | 602 | 11 | 11 | 550 | 127 | 127 | 100 |
| GJ1_2.FIN2 | 0.0 | -93.208 | -163.094 | 10.19 | 1.4 | 0.06012 | 1.78 | 0.006 | 9.95 | 0.8153 | 1.8 | 0.0985 | 1.3 | 0.00 | 0.0303 | 9.20 | 577 | 76 | 76 | 605 | 16 | 16 | 604 | 16 | 16 | 598 | 108 | 108 | 105 |
| GJ1_3.FIN2 | 0.0 | -88.531 | -203.999 | 10.17 | 1.1 | 0.05891 | 1.19 | 0.006 | 9.19 | 0.8004 | 1.6 | 0.0981 | 1.1 | 0.19 | 0.0306 | 8.51 | 549 | 52 | 52 | 603 | 13 | 13 | 596 | 15 | 15 | 605 | 101 | 101 | 110 |
| GJ1_6.FIN2 | 0.0 | 3864.025 | 42.411 | 10.08 | 1.2 | 0.05888 | 1.67 | 0.006 | 8.54 | 0.8107 | 2.0 | 0.0993 | 1.2 | 0.24 | 0.0313 | 8.26 | 538 | 72 | 72 | 610 | 14 | 14 | 601 | 18 | 18 | 619 | 100 | 100 | 113 |
| GJ1_9.FIN2 | 0.0 | -1249.491 | -27.268 | 10.32 | 1.3 | 0.06059 | 1.92 | 0.008 | 26.39 | 0.8097 | 2.1 | 0.0971 | 1.2 | 0.15 | 0.0328 | 10.79 | 591 | 81 | 81 | 597 | 14 | 14 | 600 | 19 | 19 | 644 | 134 | 134 | 101 |
| GJ1_13.FIN2 | 0.0 | -482.350 | -36.060 | 10.25 | 1.2 | 0.06081 | 1.52 | 0.018 | 64.28 | 0.8165 | 1.8 | 0.0978 | 1.2 | 0.26 | 0.0339 | 11.98 | 609 | 66 | 66 | 601 | 14 | 14 | 605 | 16 | 16 | 665 | 148 | 148 | 99 |
| GJ1_14.FIN2 | 0.0 | -987.174 | -24.124 | 10.26 | 1.1 | 0.06072 | 1.52 | 0.006 | 8.16 | 0.8174 | 1.8 | 0.0972 | 1.2 | 0.15 | 0.0302 | 8.24 | 609 | 67 | 67 | 598 | 13 | 13 | 605 | 17 | 17 | 597 | 97 | 97 | 98 |
| GJ1_15.FIN2 | 0.0 | -553.480 | -37.541 | 10.53 | 1.2 | 0.05940 | 1.71 | 0.007 | 11.40 | 0.7883 | 1.7 | 0.0951 | 1.2 | 0.00 | 0.0304 | 9.44 | 555 | 80 | 80 | 586 | 13 | 13 | 589 | 15 | 15 | 602 | 112 | 112 | 106 |
| GJ1_16.FIN2 | 0.0 | -1302.468 | -18.908 | 10.21 | 1.2 | 0.05926 | 1.66 | 0.006 | 10.22 | 0.8039 | 1.7 | 0.0978 | 1.1 | 0.23 | 0.0297 | 9.60 | 559 | 78 | 78 | 602 | 13 | 13 | 598 | 15 | 15 | 587 | 112 | 112 | 108 |
| GJ1_17.FIN2 | 0.0 | -1135.233 | -28.192 | 10.43 | 1.3 | 0.05968 | 1.74 | 0.008 | 17.76 | 0.7937 | 1.9 | 0.0961 | 1.2 | 0.04 | 0.0318 | 7.61 | 562 | 78 | 78 | 592 | 14 | 14 | 592 | 17 | 17 | 629 | 94 | 94 | 105 |
| GJ1_1.FIN2 | 0.0 | 613.742 | 91.944 | 10.22 | 1.6 | 0.05954 | 2.44 | 0.007 | 4.31 | 0.8077 | 1.6 | 0.0979 | 1.7 | 0.07 | 0.0319 | 8.60 | 530 | 105 | 105 | 601 | 19 | 19 | 599 | 15 | 15 | 634 | 107 | 107 | 113 |
| GJ1_2.FIN2 | 0.0 | 1723.589 | 42.155 | 10.04 | 1.7 | 0.05916 | 2.58 | 0.006 | 3.33 | 0.8040 | 1.5 | 0.0987 | 2.0 | 0.06 | 0.0309 | 8.42 | 509 | 112 | 112 | 606 | 23 | 23 | 598 | 14 | 14 | 615 | 102 | 102 | 119 |
| GJ1_4.FIN2 | 0.0 | -4635.290 | -50.774 | 10.42 | 1.8 | 0.06068 | 2.86 | 0.006 | 7.89 | 0.8008 | 2.2 | 0.0956 | 1.8 | 0.04 | 0.0294 | 9.17 | 548 | 126 | 126 | 588 | 21 | 21 | 594 | 19 | 19 | 584 | 106 | 106 | 107 |
| GJ1_5.FIN2 | 0.0 | -5325.331 | -44.559 | 10.22 | 1.7 | 0.05885 | 2.38 | 0.006 | 5.28 | 0.8029 | 1.8 | 0.0980 | 1.7 | 0.07 | 0.0278 | 9.13 | 505 | 107 | 107 | 602 | 20 | 20 | 596 | 16 | 16 | 552 | 99 | 99 | 119 |
| GJ1_6.FIN2 | 0.0 | 3176.150 | 48.954 | 10.27 | 1.7 | 0.05972 | 2.81 | 0.008 | 22.97 | 0.8130 | 1.8 | 0.0976 | 1.7 | 0.15 | 0.0314 | 8.96 | 550 | 115 | 115 | 600 | 20 | 20 | 602 | 16 | 16 | 624 | 110 | 110 | 109 |
| GJ1_7.FIN2 | 0.0 | 2507.354 | 44.789 | 10.27 | 1.8 | 0.05996 | 2.40 | 0.007 | 7.14 | 0.8110 | 1.7 | 0.0969 | 1.7 | 0.01 | 0.0303 | 8.93 | 544 | 109 | 109 | 596 | 19 | 19 | 601 | 15 | 15 | 602 | 106 | 106 | 110 |
| GJ1_8.FIN2 | 0.0 | -7645.481 | -45.577 | 10.41 | 2.1 | 0.06100 | 2.98 | 0.007 | 6.57 | 0.8181 | 1.7 | 0.0970 | 2.0 | 0.13 | 0.0297 | 9.50 | 582 | 124 | 124 | 596 | 23 | 23 | 605 | 15 | 15 | 590 | 110 | 110 | 102 |
| GJ1_12.FIN2 | 0.0 | 3585.910 | 70.342 | 10.31 | 1.9 | 0.06079 | 2.48 | 0.008 | 18.97 | 0.8194 | 1.6 | 0.0976 | 1.9 | 0.02 | 0.0311 | 10.39 | 573 | 108 | 108 | 600 | 22 | 22 | 606 | 14 | 14 | 617 | 124 | 124 | 105 |
| GJ1_13.FIN2 | 0.0 | 1525.643 | 93.603 | 10.31 | 1.7 | 0.06121 | 2.80 | 0.006 | 5.12 | 0.8121 | 1.5 | 0.0971 | 1.7 | 0.28 | 0.0288 | 8.90 | 575 | 117 | 117 | 597 | 19 | 19 | 602 | 14 | 14 | 573 | 101 | 101 | 104 |
| GJ1_15.FIN2 | 0.0 | -405.974 | -85.699 | 10.26 | 1.6 | 0.05973 | 2.58 | 0.006 | 5.73 | 0.8189 | 2.1 | 0.0973 | 1.6 | 0.41 | 0.0295 | 9.49 | 552 | 117 | 117 | 598 | 18 | 18 | 605 | 19 | 19 | 586 | 109 | 109 | 108 |
| GJ1_16.FIN2 | 0.0 | 1575.721 | 50.326 | 10.17 | 1.7 | 0.05984 | 2.63 | 0.010 | 31.71 | 0.8178 | 2.1 | 0.0983 | 1.6 | 0.08 | 0.0317 | 9.86 | 532 | 114 | 114 | 604 | 19 | 19 | 604 | 19 | 19 | 628 | 121 | 121 | 114 |
| GJ1_17.FIN2 | 0.0 | 1574.158 | 46.165 | 10.32 | 1.7 | 0.06054 | 2.31 | 0.007 | 5.01 | 0.8170 | 1.7 | 0.0969 | 1.6 | 0.05 | 0.0319 | 9.17 | 587 | 106 | 106 | 596 | 19 | 19 | 604 | 15 | 15 | 634 | 114 | 114 | 102 |
| GJ1_18.FIN2 | 0.0 | -155.143 | -131.722 | 10.16 | 1.5 | 0.05931 | 2.63 | 0.009 | 21.37 | 0.8111 | 1.9 | 0.0982 | 1.5 | 0.29 | 0.0336 | 10.34 | 530 | 127 | 127 | 604 | 17 | 17 | 601 | 17 | 17 | 664 | 133 | 133 | 114 |
| GJ1_20.FIN2 | 0.0 | 690.489 | 83.195 | 10.13 | 1.8 | 0.05927 | 2.36 | 0.007 | 4.47 | 0.8145 | 1.7 | 0.0992 | 1.8 | 0.10 | 0.0325 | 8.90 | 522 | 105 | 105 | 609 | 21 | 21 | 603 | 16 | 16 | 644 | 113 | 113 | 117 |
| GJ1_22.FIN2 | 0.0 | 449.692 | 113.391 | 10.58 | 1.6 | 0.06076 | 2.51 | 0.007 | 7.00 | 0.7979 | 2.0 | 0.0945 | 1.6 | 0.02 | 0.0276 | 9.01 | 568 | 113 | 113 | 581 | 18 | 18 | 593 | 18 | 18 | 549 | 97 | 97 | 102 |
| GJ1_23.FIN2 | 0.0 | -56.732 | -496.617 | 10.24 | 2.0 | 0.05929 | 2.85 | 0.007 | 6.43 | 0.8036 | 1.8 | 0.0984 | 1.9 | 0.20 | 0.0297 | 9.41 | 498 | 126 | 126 | 604 | 22 | 22 | 597 | 16 | 16 | 591 | 109 | 109 | 121 |

| | | | | | | | | | | | | | | | | | | | | | | | | | | | | |
|---|---|---|---|---|---|---|---|---|---|---|---|---|---|---|---|---|---|---|---|---|---|---|---|---|---|---|---|---|
| GJ1_24.FIN2 | 0.0 | 120.179 | 342.813 | 10.40 | 1.7 | 0.05971 | 2.82 | 0.012 | 44.58 | 0.7943 | 1.9 | 0.0963 | 1.7 | 0.20 | 0.0311 | 9.24 | 518 | 121 | 121 | 592 | 19 | 19 | 591 | 17 | 17 | 618 | 112 | 112 | 114 |
| GJ1_25.FIN2 | 0.0 | -408.716 | -40.918 | 10.44 | 1.8 | 0.05981 | 2.87 | 0.008 | 10.96 | 0.7915 | 1.8 | 0.0962 | 1.8 | 0.23 | 0.0320 | 10.34 | 516 | 127 | 127 | 591 | 20 | 20 | 590 | 16 | 16 | 635 | 128 | 128 | 115 |
| GJ1_26.FIN2 | 0.0 | 43.876 | 634.273 | 10.18 | 1.9 | 0.05963 | 2.57 | 0.007 | 6.38 | 0.8027 | 1.5 | 0.0983 | 1.9 | 0.05 | 0.0301 | 9.47 | 526 | 113 | 113 | 604 | 22 | 22 | 599 | 14 | 14 | 598 | 111 | 111 | 115 |
| GJ1_27.FIN2 | 0.0 | 1293.339 | 59.257 | 10.30 | 2.0 | 0.05962 | 2.94 | 0.007 | 8.63 | 0.8042 | 1.9 | 0.0978 | 1.9 | 0.17 | 0.0302 | 10.02 | 532 | 134 | 134 | 601 | 22 | 22 | 597 | 18 | 18 | 579 | 100 | 100 | 113 |
| GJ1_33.FIN2 | 0.0 | 4150.478 | 38.788 | 10.28 | 1.7 | 0.05949 | 2.63 | 0.011 | 32.45 | 0.8039 | 1.9 | 0.0973 | 1.6 | 0.18 | 0.0330 | 9.94 | 520 | 113 | 113 | 598 | 19 | 19 | 597 | 17 | 17 | 654 | 127 | 127 | 115 |
| GJ1_2 | 0.0 | 904.725 | 54.358 | 10.02 | 1.8 | 0.05946 | 2.77 | 0.007 | 3.60 | 0.8145 | 1.6 | 0.0994 | 2.0 | 0.14 | 0.0321 | 3.72 | 518 | 121 | 121 | 610 | 23 | 23 | 603 | 15 | 15 | 637 | 47 | 256 | 118 |
| GJ1_4 | 0.0 | -8892.056 | -49.058 | 10.43 | 1.9 | 0.06133 | 3.17 | 0.007 | 8.36 | 0.8070 | 2.4 | 0.0954 | 2.0 | 0.09 | 0.0306 | 4.90 | 563 | 141 | 141 | 587 | 22 | 22 | 598 | 21 | 21 | 609 | 59 | 248 | 104 |
| GJ1_5 | 0.0 | 6318.018 | 54.886 | 10.23 | 1.8 | 0.05900 | 2.45 | 0.006 | 5.64 | 0.8047 | 1.7 | 0.0979 | 1.8 | 0.07 | 0.0287 | 5.28 | 513 | 109 | 109 | 602 | 21 | 21 | 598 | 16 | 16 | 570 | 59 | 233 | 117 |
| GJ1_7 | 0.0 | 188.679 | 203.686 | 10.20 | 1.9 | 0.06001 | 2.51 | 0.005 | 10.65 | 0.8186 | 1.8 | 0.0975 | 1.8 | 0.06 | 0.0219 | 7.04 | 547 | 113 | 113 | 599 | 21 | 21 | 605 | 16 | 16 | 437 | 61 | 184 | 109 |
| GJ1_8 | 0.0 | -1543.197 | -46.610 | 10.52 | 2.3 | 0.06091 | 3.20 | 0.006 | 7.45 | 0.8101 | 1.8 | 0.0962 | 2.2 | 0.11 | 0.0295 | 6.22 | 580 | 132 | 132 | 591 | 25 | 25 | 601 | 16 | 16 | 586 | 71 | 241 | 102 |
| GJ1_9 | 0.0 | -611.537 | -63.972 | 10.29 | 1.9 | 0.06043 | 2.84 | 0.015 | 38.04 | 0.8075 | 1.6 | 0.0975 | 1.9 | 0.19 | 0.0470 | 24.02 | 572 | 127 | 127 | 599 | 21 | 21 | 600 | 14 | 14 | 714 | 149 | 194 | 105 |
| GJ1_13 | 0.0 | -825.214 | -44.732 | 10.28 | 1.8 | 0.06081 | 3.01 | 0.009 | 4.28 | 0.8081 | 1.6 | 0.0974 | 1.8 | 0.32 | 0.0431 | 4.21 | 558 | 126 | 126 | 599 | 20 | 20 | 600 | 14 | 14 | 852 | 70 | 340 | 107 |
| GJ1_14 | 0.0 | -1179.705 | -34.470 | 10.18 | 1.6 | 0.05999 | 2.40 | 0.012 | 44.70 | 0.8172 | 1.8 | 0.0981 | 1.6 | 0.05 | 0.0329 | 21.84 | 555 | 101 | 101 | 603 | 18 | 18 | 609 | 18 | 18 | 631 | 240 | 325 | 109 |
| GJ1_15 | 0.0 | -433.259 | -97.777 | 10.35 | 1.7 | 0.06091 | 2.88 | 0.006 | 5.78 | 0.8171 | 2.1 | 0.0966 | 1.7 | 0.21 | 0.0277 | 5.53 | 587 | 131 | 131 | 594 | 19 | 19 | 608 | 20 | 20 | 551 | 60 | 226 | 101 |
| GJ1_16 | 0.0 | -299.745 | -73.043 | 10.27 | 1.7 | 0.06086 | 2.73 | 0.009 | 35.67 | 0.8235 | 2.1 | 0.0974 | 1.7 | 0.01 | 0.0305 | 6.66 | 571 | 117 | 117 | 599 | 19 | 19 | 607 | 19 | 19 | 604 | 79 | 251 | 105 |
| GJ1_17 | 0.0 | -143.947 | -202.514 | 10.21 | 1.7 | 0.05906 | 2.37 | 0.006 | 6.15 | 0.8066 | 1.8 | 0.0978 | 1.6 | 0.08 | 0.0272 | 6.11 | 538 | 109 | 109 | 601 | 19 | 19 | 599 | 17 | 17 | 541 | 65 | 224 | 112 |
| GJ1_18 | 0.0 | -2169.600 | -64.333 | 10.14 | 1.6 | 0.05883 | 2.83 | 0.009 | 23.30 | 0.8052 | 1.9 | 0.0984 | 1.6 | 0.36 | 0.0349 | 7.70 | 512 | 136 | 136 | 605 | 19 | 19 | 598 | 17 | 17 | 690 | 103 | 287 | 118 |
| GJ1_19 | 0.0 | -2252.520 | -54.833 | 10.03 | 1.9 | 0.05928 | 2.99 | 0.006 | 6.15 | 0.8166 | 1.8 | 0.1001 | 1.9 | 0.27 | 0.0283 | 5.78 | 499 | 132 | 132 | 614 | 22 | 22 | 604 | 16 | 16 | 562 | 64 | 232 | 123 |
| GJ1_20 | 0.0 | -1049.932 | -46.266 | 10.22 | 1.9 | 0.06004 | 2.39 | 0.007 | 4.72 | 0.8189 | 1.7 | 0.0983 | 1.9 | 0.17 | 0.0356 | 4.77 | 555 | 105 | 105 | 604 | 22 | 22 | 606 | 16 | 16 | 705 | 66 | 286 | 109 |
| GJ1_21 | 0.0 | -8184.150 | -43.560 | 9.96 | 1.8 | 0.05733 | 2.46 | 0.005 | 6.31 | 0.8025 | 1.9 | 0.1006 | 1.8 | 0.18 | 0.0241 | 5.72 | 450 | 110 | 110 | 618 | 22 | 22 | 596 | 18 | 18 | 480 | 54 | 198 | 137 |
| GJ1_22 | 0.0 | -359.954 | -73.506 | 10.51 | 1.6 | 0.06107 | 2.57 | 0.007 | 8.06 | 0.8077 | 2.0 | 0.0951 | 1.6 | 0.00 | 0.0269 | 4.80 | 583 | 116 | 116 | 585 | 18 | 18 | 599 | 18 | 18 | 536 | 51 | 218 | 100 |
| GJ1_23 | 0.0 | -186.659 | -146.456 | 10.32 | 2.1 | 0.05996 | 3.08 | 0.007 | 6.76 | 0.8067 | 1.9 | 0.0978 | 2.1 | 0.21 | 0.0330 | 5.74 | 519 | 137 | 137 | 601 | 24 | 24 | 599 | 17 | 17 | 655 | 74 | 267 | 116 |
| GJ1_24 | 0.0 | -511.400 | -52.712 | 10.46 | 1.8 | 0.06022 | 3.03 | 0.013 | 47.98 | 0.7958 | 2.0 | 0.0958 | 1.8 | 0.26 | 0.0329 | 5.08 | 534 | 130 | 130 | 589 | 20 | 20 | 592 | 18 | 18 | 652 | 65 | 265 | 110 |
| GJ1_25 | 0.0 | -185.040 | -80.234 | 10.51 | 1.9 | 0.06021 | 3.14 | 0.008 | 12.19 | 0.7906 | 1.9 | 0.0956 | 1.9 | 0.30 | 0.0333 | 7.59 | 525 | 139 | 139 | 588 | 22 | 22 | 589 | 17 | 17 | 659 | 97 | 275 | 112 |
| GJ1_26 | 0.0 | 361.058 | 79.381 | 10.05 | 2.0 | 0.05935 | 2.74 | 0.006 | 7.44 | 0.8075 | 1.5 | 0.0995 | 2.1 | 0.06 | 0.0306 | 6.45 | 516 | 119 | 119 | 611 | 24 | 24 | 603 | 15 | 15 | 607 | 77 | 252 | 118 |
| Plesovice_1 | 0.3 | 1455.518 | 35.971 | 18.19 | 1.9 | 0.05363 | 2.74 | 0.047 | 2.58 | 0.4090 | 1.6 | 0.0552 | 1.9 | 0.18 | 0.0177 | 2.21 | 287 | 124 | 124 | 346 | 13 | 13 | 347 | 10 | 11 | 355 | 16 | 75 | 121 |
| Plesovice_2 | 0.2 | 524.156 | 118.178 | 17.82 | 1.8 | 0.05265 | 2.39 | 0.044 | 2.73 | 0.4113 | 1.7 | 0.0562 | 1.8 | 0.08 | 0.0182 | 2.31 | 260 | 110 | 110 | 353 | 12 | 12 | 349 | 10 | 12 | 364 | 17 | 77 | 135 |
| Plesovice_3 | 0.3 | 1841.549 | 43.653 | 18.25 | 1.9 | 0.05309 | 2.54 | 0.050 | 2.35 | 0.4046 | 1.6 | 0.0551 | 2.0 | 0.02 | 0.0182 | 1.89 | 272 | 116 | 116 | 346 | 13 | 13 | 344 | 9 | 11 | 364 | 14 | 76 | 127 |
| Plesovice_4 | 0.3 | 5506.366 | 54.037 | 18.09 | 1.8 | 0.05324 | 2.36 | 0.049 | 2.66 | 0.4096 | 1.6 | 0.0554 | 1.8 | 0.08 | 0.0177 | 2.13 | 287 | 107 | 107 | 348 | 12 | 12 | 348 | 10 | 11 | 355 | 15 | 75 | 121 |
| Plesovice_5 | 0.3 | -60910.304 | -163.989 | 18.19 | 1.9 | 0.05419 | 2.90 | 0.050 | 2.39 | 0.4121 | 1.8 | 0.0552 | 1.8 | 0.28 | 0.0183 | 2.34 | 301 | 132 | 132 | 346 | 12 | 12 | 350 | 11 | 12 | 367 | 17 | 77 | 115 |
| Plesovice_6 | 0.2 | 2159.225 | 46.532 | 18.62 | 1.9 | 0.05365 | 2.57 | 0.049 | 2.87 | 0.4003 | 1.7 | 0.0540 | 2.0 | 0.06 | 0.0180 | 2.40 | 292 | 122 | 122 | 339 | 13 | 13 | 341 | 10 | 11 | 361 | 17 | 76 | 116 |
| Plesovice_7 | 0.2 | 4188.948 | 47.096 | 17.60 | 2.4 | 0.05331 | 3.48 | 0.045 | 2.92 | 0.4182 | 2.3 | 0.0569 | 2.4 | 0.08 | 0.0173 | 2.54 | 279 | 162 | 162 | 357 | 17 | 17 | 354 | 14 | 15 | 346 | 17 | 73 | 128 |
| Plesovice_8 | 0.2 | 303.563 | 156.208 | 18.01 | 1.7 | 0.05318 | 2.85 | 0.049 | 2.97 | 0.4094 | 2.2 | 0.0555 | 1.6 | 0.13 | 0.0184 | 2.41 | 258 | 133 | 133 | 348 | 11 | 11 | 347 | 13 | 14 | 369 | 18 | 78 | 135 |
| Plesovice_9 | 0.3 | 1603.108 | 55.121 | 18.40 | 1.5 | 0.05333 | 2.50 | 0.050 | 2.87 | 0.4020 | 1.9 | 0.0542 | 1.5 | 0.06 | 0.0180 | 2.61 | 283 | 118 | 118 | 340 | 10 | 10 | 342 | 11 | 12 | 361 | 19 | 77 | 120 |
| Plesovice_10 | 0.2 | 597.813 | 56.723 | 18.45 | 1.9 | 0.05438 | 2.87 | 0.034 | 8.44 | 0.4056 | 2.0 | 0.0544 | 1.9 | 0.16 | 0.0178 | 2.76 | 310 | 133 | 133 | 341 | 13 | 13 | 345 | 12 | 13 | 357 | 19 | 76 | 110 |
| Plesovice_11 | 0.3 | -451.815 | -78.332 | 18.49 | 2.0 | 0.05251 | 2.86 | 0.049 | 2.91 | 0.3945 | 2.0 | 0.0545 | 2.1 | 0.01 | 0.0175 | 2.34 | 229 | 136 | 136 | 342 | 14 | 14 | 337 | 11 | 13 | 351 | 16 | 74 | 150 |
| Plesovice_12 | 0.3 | -206.868 | -162.363 | 18.06 | 2.1 | 0.05377 | 2.62 | 0.051 | 2.78 | 0.4101 | 1.8 | 0.0559 | 2.1 | 0.23 | 0.0181 | 2.08 | 295 | 125 | 125 | 350 | 14 | 14 | 348 | 11 | 12 | 363 | 15 | 76 | 119 |
| Plesovice_13 | 0.3 | 356.778 | 126.386 | 18.28 | 1.8 | 0.05262 | 2.30 | 0.048 | 2.93 | 0.4043 | 1.7 | 0.0548 | 1.7 | 0.01 | 0.0175 | 2.27 | 282 | 114 | 114 | 344 | 12 | 12 | 344 | 10 | 11 | 350 | 16 | 74 | 122 |
| Plesovice_14 | 0.2 | 6367.900 | 50.189 | 18.32 | 2.2 | 0.05441 | 3.03 | 0.048 | 2.63 | 0.4107 | 1.9 | 0.0552 | 2.3 | 0.19 | 0.0175 | 2.12 | 298 | 147 | 147 | 346 | 15 | 15 | 348 | 11 | 12 | 351 | 15 | 74 | 116 |
| Plesovice_15 | 0.2 | 2759.577 | 56.947 | 18.63 | 1.8 | 0.05351 | 2.89 | 0.050 | 3.10 | 0.3968 | 1.9 | 0.0534 | 1.7 | 0.24 | 0.0183 | 2.92 | 271 | 135 | 135 | 335 | 11 | 11 | 338 | 11 | 12 | 366 | 21 | 78 | 124 |
| Plesovice_16 | 0.2 | -801.882 | -58.098 | 18.83 | 1.9 | 0.05347 | 2.63 | 0.049 | 3.55 | 0.3898 | 1.7 | 0.0526 | 1.8 | 0.00 | 0.0170 | 2.84 | 297 | 123 | 123 | 331 | 12 | 12 | 336 | 11 | 12 | 341 | 19 | 73 | 111 |
| Plesovice_17 | 0.2 | -1600.434 | -39.307 | 18.36 | 1.9 | 0.05340 | 2.80 | 0.043 | 3.69 | 0.4030 | 1.9 | 0.0547 | 1.9 | 0.12 | 0.0179 | 2.37 | 271 | 131 | 131 | 343 | 13 | 13 | 343 | 11 | 12 | 359 | 17 | 76 | 127 |
| Plesovice_18 | 0.3 | 197.579 | 180.383 | 18.06 | 1.8 | 0.05242 | 2.54 | 0.050 | 3.64 | 0.4062 | 1.8 | 0.0555 | 1.8 | 0.07 | 0.0178 | 2.81 | 263 | 121 | 121 | 348 | 12 | 12 | 345 | 11 | 12 | 356 | 20 | 76 | 132 |
| Plesovice_19 | 0.3 | 779.260 | 50.671 | 18.20 | 2.0 | 0.05335 | 2.34 | 0.047 | 3.30 | 0.4080 | 1.7 | 0.0553 | 2.0 | 0.18 | 0.0166 | 2.74 | 293 | 106 | 106 | 347 | 13 | 13 | 347 | 10 | 11 | 332 | 18 | 71 | 118 |
| Plesovice_20 | 0.2 | -166.412 | -159.001 | 18.17 | 2.0 | 0.05417 | 2.89 | 0.042 | 4.02 | 0.4133 | 1.9 | 0.0553 | 1.9 | 0.24 | 0.0188 | 2.77 | 300 | 132 | 132 | 347 | 13 | 13 | 350 | 11 | 12 | 375 | 21 | 80 | 116 |
| Plesovice_21 | 0.2 | -259.564 | -79.889 | 18.26 | 1.8 | 0.05365 | 3.01 | 0.033 | 3.78 | 0.4025 | 2.3 | 0.0548 | 1.7 | 0.06 | 0.0179 | 3.22 | 270 | 143 | 143 | 344 | 11 | 11 | 342 | 13 | 14 | 359 | 23 | 77 | 128 |
| Plesovice_22 | 0.2 | -429.327 | -48.361 | 18.07 | 1.9 | 0.05419 | 2.98 | 0.043 | 4.28 | 0.4139 | 2.0 | 0.0551 | 1.7 | 0.20 | 0.0193 | 2.94 | 294 | 139 | 139 | 346 | 11 | 11 | 351 | 12 | 13 | 387 | 23 | 83 | 118 |
| Plesovice_23 | 0.2 | -111.564 | -200.224 | 17.45 | 2.0 | 0.05257 | 3.10 | 0.045 | 2.47 | 0.4115 | 1.9 | 0.0577 | 2.0 | 0.20 | 0.0184 | 2.31 | 219 | 145 | 145 | 361 | 14 | 14 | 349 | 11 | 13 | 369 | 17 | 78 | 165 |
| Plesovice_24 | 0.2 | 771.727 | 71.364 | 17.89 | 2.1 | 0.05279 | 2.85 | 0.050 | 2.82 | 0.4093 | 2.0 | 0.0564 | 2.1 | 0.01 | 0.0184 | 2.35 | 244 | 132 | 132 | 353 | 14 | 14 | 347 | 12 | 13 | 369 | 17 | 78 | 145 |
| Plesovice_25 | 0.2 | 2010.460 | 54.750 | 18.12 | 2.6 | 0.05741 | 4.93 | 0.047 | 4.09 | 0.4222 | 3.3 | 0.0552 | 2.5 | 0.07 | 0.0184 | 4.05 | 410 | 212 | 212 | 346 | 17 | 17 | 356 | 19 | 20 | 368 | 30 | 81 | 84 |
| Plesovice_26 | 0.2 | -355.435 | -137.256 | 17.85 | 1.8 | 0.05351 | 2.95 | 0.047 | 3.08 | 0.4136 | 2.1 | 0.0562 | 1.8 | 0.21 | 0.0184 | 2.47 | 266 | 139 | 139 | 352 | 13 | 13 | 350 | 12 | 13 | 368 | 18 | 78 | 132 |
| Plesovice_27 | 0.2 | -1633.428 | -47.641 | 17.54 | 1.9 | 0.05395 | 2.76 | 0.049 | 3.47 | 0.4259 | 2.0 | 0.0573 | 2.0 | 0.02 | 0.0190 | 2.69 | 300 | 125 | 125 | 359 | 14 | 14 | 359 | 12 | 13 | 379 | 20 | 81 | 120 |
| Plesovice_28 | 0.2 | 1908.692 | 60.582 | 17.84 | 1.9 | 0.05471 | 2.48 | 0.047 | 2.92 | 0.4224 | 1.7 | 0.0564 | 2.0 | 0.20 | 0.0185 | 2.52 | 344 | 113 | 113 | 353 | 14 | 14 | 357 | 10 | 12 | 371 | 19 | 78 | 103 |
| Plesovice_30 | 0.2 | 567.489 | 72.482 | 18.14 | 2.2 | 0.05500 | 3.10 | 0.043 | 3.64 | 0.4186 | 2.0 | 0.0556 | 2.0 | 0.15 | 0.0181 | 2.88 | 325 | 141 | 141 | 348 | 14 | 14 | 354 | 12 | 13 | 363 | 21 | 77 | 107 |
| Plesovice_31 | 0.2 | 922.870 | 65.011 | 17.64 | 2.0 | 0.05384 | 2.92 | 0.048 | 3.12 | 0.4215 | 1.9 | 0.0571 | 2.0 | 0.09 | 0.0178 | 2.28 | 283 | 136 | 136 | 358 | 14 | 14 | 356 | 12 | 13 | 356 | 16 | 75 | 126 |
| Plesovice_32 | 0.2 | 1292.884 | 56.540 | 17.52 | 1.7 | 0.05353 | 3.09 | 0.046 | 3.04 | 0.4209 | 2.3 | 0.0571 | 1.7 | 0.21 | 0.0180 | 2.61 | 263 | 142 | 142 | 358 | 12 | 12 | 355 | 14 | 15 | 361 | 19 | 77 | 136 |
| Plesovice_1 | 0.2 | -20.994 | -935.573 | 18.03 | 2.0 | 0.05099 | 2.78 | 0.030 | 3.75 | 0.3945 | 1.9 | 0.0552 | 1.9 | 0.05 | 0.0177 | 3.64 | 182 | 129 | 129 | 346 | 13 | 13 | 337 | 11 | 11 | 354 | 25 | 49 | 190 |
| Plesovice_2 | 0.2 | 851.667 | 57.839 | 18.23 | 1.7 | 0.05371 | 3.13 | 0.031 | 5.07 | 0.4076 | 2.4 | 0.0546 | 1.8 | 0.23 | 0.0174 | 2.85 | 285 | 154 | 154 | 343 | 12 | 12 | 346 | 14 | 14 | 348 | 20 | 46 | 120 |
| Plesovice_3 | 0.2 | -607.243 | -63.485 | 18.59 | 1.9 | 0.05309 | 3.04 | 0.027 | 3.81 | 0.3935 | 1.9 | 0.0533 | 1.8 | 0.40 | 0.0163 | 3.19 | 240 | 149 | 149 | 335 | 12 | 12 | 336 | 11 | 11 | 327 | 21 | 44 | 139 |
| Plesovice_4 | 0.2 | -527.564 | -41.735 | 18.53 | 2.5 | 0.05486 | 3.84 | 0.037 | 14.28 | 0.4032 | 2.3 | 0.0538 | 2.3 | 0.15 | 0.0198 | 8.59 | 302 | 170 | 170 | 341 | 17 | 17 | 346 | 15 | 15 | 394 | 66 | 81 | 113 |
| Plesovice_5 | 0.2 | 168.534 | 83.922 | 18.58 | 1.7 | 0.05339 | 2.78 | 0.034 | 5.83 | 0.3987 | 1.9 | 0.0536 | 1.8 | 0.17 | 0.0174 | 2.96 | 272 | 130 | 130 | 336 | 12 | 12 | 340 | 11 | 11 | 349 | 20 | 46 | 124 |
| Plesovice_6 | 0.2 | -523.101 | -75.859 | 18.62 | 1.9 | 0.05431 | 2.81 | 0.030 | 2.56 | 0.4062 | 1.5 | 0.0538 | 1.9 | 0.07 | 0.0170 | 2.25 | 340 | 121 | 121 | 337 | 13 | 13 | 346 | 9 | 9 | 342 | 15 | 43 | 99 |
| Plesovice_7 | 0.2 | -165.292 | -153.512 | 18.35 | 1.7 | 0.05451 | 3.02 | 0.033 | 11.17 | 0.4103 | 2.0 | 0.0543 | 1.6 | 0.07 | 0.0167 | 2.85 | 304 | 142 | 142 | 340 | 11 | 11 | 348 | 12 | 12 | 334 | 19 | 44 | 112 |
| Plesovice_8 | 0.2 | 373.860 | 78.697 | 18.16 | 1.8 | 0.05428 | 3.27 | 0.030 | 3.06 | 0.4089 | 2.2 | 0.0551 | 1.8 | 0.13 | 0.0166 | 2.68 | 321 | 151 | 151 | 345 | 12 | 12 | 347 | 13 | 13 | 333 | 18 | 43 | 108 |
| Plesovice_9 | 0.2 | 1967.138 | 52.155 | 18.81 | 1.9 | 0.05634 | 4.93 | 0.030 | 3.41 | 0.4162 | 3.7 | 0.0529 | 1.8 | 0.23 | 0.0166 | 3.17 | 343 | 176 | 176 | 332 | 12 | 12 | 351 | 21 | 21 | 333 | 21 | 45 | 97 |
| Plesovice_10 | 0.2 | -1804.116 | -170.878 | 18.16 | 2.0 | 0.05308 | 2.90 | 0.035 | 11.18 | 0.4050 | 1.8 | 0.0548 | 1.9 | 0.07 | 0.0175 | 4.59 | 253 | 133 | 133 | 344 | 13 | 13 | 344 | 10 | 10 | 351 | 32 | 52 | 136 |
| Plesovice_11 | 0.2 | -363.489 | -61.082 | 18.28 | 2.5 | 0.05081 | 3.66 | 0.029 | 3.90 | 0.3948 | 2.2 | 0.0549 | 2.4 | 0.09 | 0.0163 | 2.60 | 238 | 173 | 173 | 345 | 16 | 16 | 337 | 12 | 12 | 327 | 17 | 42 | 145 |
| Plesovice_12 | 0.2 | -148.979 | -109.252 | 17.87 | 2.3 | 0.05288 | 4.17 | 0.060 | 41.94 | 0.4086 | 3.1 | 0.0554 | 2.1 | 0.16 | 0.0224 | 17.31 | 252 | 199 | 199 | 347 | 14 | 14 | 346 | 18 | 18 | 442 | 145 | 153 | 138 |
| Plesovice_13 | 0.2 | -15.041 | -1097.381 | 18.30 | 2.4 | 0.05400 | 4.19 | 0.029 | 3.42 | 0.4118 | 3.7 | 0.0548 | 2.5 | 0.07 | 0.0169 | 2.97 | 324 | 206 | 206 | 344 | 17 | 17 | 348 | 21 | 21 | 339 | 20 | 45 | 106 |

| | | | | | | | | | | | | | | | | | | | | | | | | | | | | | |
|---|---|---|---|---|---|---|---|---|---|---|---|---|---|---|---|---|---|---|---|---|---|---|---|---|---|---|---|---|---|
| Plesovice_14 | 0.1 | -387.232 | -100.269 | 18.55 | 2.5 | 0.05346 | 3.57 | 0.031 | 13.58 | 0.4033 | 2.7 | 0.0543 | 2.3 | 0.07 | 0.0162 | 5.23 | 273 | 160 | 160 | 341 | 15 | 15 | 343 | 15 | 15 | 325 | 34 | 51 | 125 |
| Plesovice_15 | 0.2 | 40.829 | 293.186 | 18.44 | 2.5 | 0.05455 | 4.62 | 0.059 | 36.10 | 0.4089 | 3.6 | 0.0547 | 2.6 | 0.06 | 0.0242 | 25.33 | 267 | 196 | 196 | 343 | 17 | 17 | 346 | 21 | 21 | 371 | 106 | 109 | 129 |
| Plesovice_16 | 0.2 | 274.177 | 52.565 | 18.69 | 2.0 | 0.05397 | 2.89 | 0.028 | 4.64 | 0.4071 | 2.9 | 0.0534 | 1.9 | 0.09 | 0.0157 | 3.57 | 290 | 137 | 137 | 335 | 12 | 12 | 345 | 17 | 17 | 316 | 22 | 44 | 116 |
| Plesovice_17 | 0.2 | -38.339 | -303.935 | 18.90 | 1.7 | 0.05378 | 2.77 | 0.031 | 6.76 | 0.4030 | 2.8 | 0.0530 | 1.7 | 0.03 | 0.0169 | 3.72 | 369 | 130 | 130 | 333 | 11 | 11 | 342 | 16 | 16 | 339 | 25 | 47 | 90 |
| Plesovice_18 | 0.2 | 44.238 | 490.016 | 18.75 | 2.4 | 0.05152 | 3.22 | 0.029 | 2.89 | 0.3808 | 2.0 | 0.0544 | 2.5 | 0.09 | 0.0166 | 2.62 | 161 | 154 | 154 | 341 | 17 | 17 | 327 | 11 | 11 | 333 | 17 | 43 | 212 |
| Plesovice_19 | 0.2 | -52.864 | -417.505 | 19.17 | 2.2 | 0.05174 | 4.09 | 0.029 | 5.16 | 0.3709 | 3.0 | 0.0523 | 2.2 | 0.59 | 0.0165 | 5.01 | 175 | 193 | 193 | 328 | 14 | 14 | 319 | 16 | 16 | 331 | 33 | 51 | 187 |
| Plesovice_20 | 0.2 | -42.181 | -459.911 | 18.63 | 2.1 | 0.05237 | 2.99 | 0.031 | 10.05 | 0.3885 | 1.8 | 0.0542 | 2.0 | 0.04 | 0.0170 | 4.24 | 213 | 146 | 146 | 340 | 13 | 13 | 333 | 10 | 10 | 339 | 28 | 49 | 159 |
| Plesovice_1 | 0.2 | -20.994 | -935.573 | 18.03 | 2.0 | 0.05099 | 2.78 | 0.030 | 3.75 | 0.3945 | 1.9 | 0.0552 | 1.9 | 0.05 | 0.0177 | 3.64 | 182 | 129 | 129 | 346 | 13 | 13 | 337 | 11 | 11 | 354 | 25 | 49 | 190 |
| Plesovice_2 | 0.2 | 851.667 | 57.839 | 18.23 | 1.7 | 0.05371 | 3.13 | 0.031 | 5.07 | 0.4076 | 2.4 | 0.0546 | 1.8 | 0.23 | 0.0174 | 2.85 | 285 | 154 | 154 | 343 | 12 | 12 | 346 | 14 | 14 | 348 | 20 | 46 | 120 |
| Plesovice_3 | 0.2 | -607.243 | -63.485 | 18.59 | 1.9 | 0.05309 | 3.04 | 0.027 | 3.81 | 0.3935 | 1.9 | 0.0533 | 1.8 | 0.40 | 0.0163 | 3.19 | 240 | 149 | 149 | 335 | 12 | 12 | 336 | 11 | 11 | 327 | 21 | 44 | 139 |
| Plesovice_4 | 0.2 | -527.564 | -41.735 | 18.53 | 2.5 | 0.05486 | 3.84 | 0.037 | 14.28 | 0.4032 | 2.3 | 0.0538 | 2.3 | 0.15 | 0.0198 | 8.59 | 302 | 170 | 170 | 341 | 17 | 17 | 346 | 15 | 15 | 394 | 66 | 81 | 113 |
| Plesovice_5 | 0.2 | 168.534 | 83.922 | 18.58 | 1.7 | 0.05339 | 2.78 | 0.034 | 5.83 | 0.3987 | 1.9 | 0.0536 | 1.8 | 0.17 | 0.0174 | 2.96 | 272 | 130 | 130 | 336 | 12 | 12 | 340 | 11 | 11 | 349 | 20 | 46 | 124 |
| Plesovice_6 | 0.2 | -523.101 | -75.859 | 18.62 | 1.9 | 0.05431 | 2.81 | 0.030 | 2.56 | 0.4062 | 1.5 | 0.0538 | 1.9 | 0.07 | 0.0170 | 2.25 | 340 | 121 | 121 | 337 | 13 | 13 | 346 | 9 | 9 | 342 | 15 | 43 | 99 |
| Plesovice_7 | 0.2 | -165.292 | -153.512 | 18.35 | 1.7 | 0.05451 | 3.02 | 0.033 | 11.17 | 0.4103 | 2.0 | 0.0543 | 1.6 | 0.07 | 0.0167 | 2.85 | 304 | 142 | 142 | 340 | 11 | 11 | 348 | 12 | 12 | 334 | 19 | 44 | 112 |
| Plesovice_8 | 0.2 | 373.860 | 78.697 | 18.16 | 1.8 | 0.05428 | 3.27 | 0.030 | 3.06 | 0.4089 | 2.2 | 0.0551 | 1.8 | 0.13 | 0.0166 | 2.68 | 321 | 151 | 151 | 345 | 12 | 12 | 347 | 13 | 13 | 333 | 18 | 43 | 108 |
| Plesovice_9 | 0.2 | 1967.138 | 52.155 | 18.81 | 1.9 | 0.05634 | 4.93 | 0.030 | 3.41 | 0.4162 | 3.7 | 0.0529 | 1.8 | 0.23 | 0.0166 | 3.17 | 343 | 176 | 176 | 332 | 12 | 12 | 351 | 21 | 21 | 333 | 21 | 45 | 97 |
| Plesovice_10 | 0.2 | -1804.116 | -170.878 | 18.16 | 2.0 | 0.05308 | 2.90 | 0.035 | 11.18 | 0.4050 | 1.8 | 0.0548 | 1.9 | 0.07 | 0.0175 | 4.59 | 253 | 133 | 133 | 344 | 13 | 13 | 344 | 10 | 10 | 351 | 32 | 52 | 136 |
| Plesovice_11 | 0.2 | -363.489 | -61.082 | 18.28 | 2.5 | 0.05081 | 3.66 | 0.029 | 3.90 | 0.3948 | 2.2 | 0.0549 | 2.4 | 0.09 | 0.0163 | 2.60 | 238 | 173 | 173 | 345 | 16 | 16 | 337 | 12 | 12 | 327 | 17 | 42 | 145 |
| Plesovice_12 | 0.2 | -148.979 | -109.252 | 17.87 | 2.3 | 0.05288 | 4.17 | 0.060 | 41.94 | 0.4086 | 3.1 | 0.0554 | 2.1 | 0.16 | 0.0224 | 17.31 | 252 | 199 | 199 | 347 | 14 | 14 | 346 | 18 | 18 | 442 | 145 | 153 | 138 |
| Plesovice_13 | 0.2 | -15.041 | -1097.381 | 18.30 | 2.4 | 0.05400 | 4.19 | 0.029 | 3.42 | 0.4118 | 3.7 | 0.0548 | 2.5 | 0.07 | 0.0169 | 2.97 | 324 | 206 | 206 | 344 | 17 | 17 | 348 | 21 | 21 | 339 | 20 | 45 | 106 |
| Plesovice_14 | 0.1 | -387.232 | -100.269 | 18.35 | 2.4 | 0.05346 | 3.57 | 0.031 | 13.58 | 0.4033 | 2.7 | 0.0543 | 2.3 | 0.07 | 0.0162 | 5.23 | 273 | 160 | 160 | 341 | 15 | 15 | 343 | 15 | 15 | 325 | 34 | 51 | 125 |
| Plesovice_15 | 0.2 | 40.829 | 293.186 | 18.44 | 2.5 | 0.05455 | 4.62 | 0.059 | 36.10 | 0.4089 | 3.6 | 0.0547 | 2.6 | 0.06 | 0.0242 | 25.33 | 267 | 196 | 196 | 343 | 17 | 17 | 346 | 21 | 21 | 371 | 106 | 109 | 129 |
| Plesovice_16 | 0.2 | 274.177 | 52.565 | 18.69 | 2.0 | 0.05397 | 2.89 | 0.028 | 4.64 | 0.4071 | 2.9 | 0.0534 | 1.9 | 0.09 | 0.0157 | 3.57 | 290 | 137 | 137 | 335 | 12 | 12 | 345 | 17 | 17 | 316 | 22 | 44 | 116 |
| Plesovice_17 | 0.2 | -38.339 | -303.935 | 18.90 | 1.7 | 0.05378 | 2.77 | 0.031 | 6.76 | 0.4030 | 2.8 | 0.0530 | 1.7 | 0.03 | 0.0169 | 3.72 | 369 | 130 | 130 | 333 | 11 | 11 | 342 | 16 | 16 | 339 | 25 | 47 | 90 |
| Plesovice_18 | 0.2 | 44.238 | 490.016 | 18.75 | 2.4 | 0.05152 | 3.22 | 0.029 | 2.89 | 0.3808 | 2.0 | 0.0544 | 2.5 | 0.09 | 0.0166 | 2.62 | 161 | 154 | 154 | 341 | 17 | 17 | 327 | 11 | 11 | 333 | 17 | 43 | 212 |
| Plesovice_19 | 0.2 | -52.864 | -417.505 | 19.17 | 2.2 | 0.05174 | 4.09 | 0.029 | 5.16 | 0.3709 | 3.0 | 0.0523 | 2.2 | 0.59 | 0.0165 | 5.01 | 175 | 193 | 193 | 328 | 14 | 14 | 319 | 16 | 16 | 331 | 33 | 51 | 187 |
| Plesovice_20 | 0.2 | -42.181 | -459.911 | 18.63 | 2.1 | 0.05237 | 2.99 | 0.031 | 10.05 | 0.3885 | 1.8 | 0.0542 | 2.0 | 0.04 | 0.0170 | 4.24 | 213 | 146 | 146 | 340 | 13 | 13 | 333 | 10 | 10 | 339 | 28 | 49 | 159 |
| Plesovice_1 | 0.2 | -109.030 | -487.971 | 17.99 | 1.4 | 0.05370 | 2.09 | 0.039 | 2.25 | 0.4118 | 1.9 | 0.0559 | 1.4 | 0.17 | 0.0175 | 1.96 | 310 | 98 | 98 | 350 | 10 | 10 | 349 | 11 | 11 | 351 | 14 | 14 | 113 |
| Plesovice_1 | 0.2 | -259.890 | -215.158 | 17.90 | 1.4 | 0.05356 | 1.88 | 0.041 | 3.96 | 0.4144 | 1.8 | 0.0562 | 1.4 | 0.26 | 0.0177 | 2.24 | 313 | 88 | 88 | 352 | 10 | 10 | 352 | 11 | 11 | 355 | 16 | 16 | 112 |
| 91500_19.FIN2 | 0.5 | 66.414 | 82.234 | 5.62 | 1.8 | 0.07444 | 3.99 | 0.084 | 4.69 | 1.8057 | 3.1 | 0.1771 | 1.7 | 0.24 | 0.0533 | 9.15 | 949 | 165 | 165 | 1050 | 34 | 34 | 1038 | 39 | 39 | 1046 | 186 | 186 | 111 |
| 91500_1.FIN2 | 0.5 | -37.546 | -130.508 | 5.69 | 1.8 | 0.07827 | 3.69 | 0.093 | 4.03 | 1.8903 | 3.3 | 0.1775 | 1.8 | 0.07 | 0.0589 | 3.89 | 1087 | 143 | 143 | 1052 | 35 | 35 | 1067 | 44 | 44 | 1154 | 87 | 87 | 97 |
| 91500_2.FIN2 | 0.5 | 29.895 | 158.336 | 5.55 | 1.9 | 0.07687 | 3.07 | 0.088 | 4.18 | 1.9054 | 3.0 | 0.1822 | 2.0 | 0.21 | 0.0564 | 3.86 | 1042 | 117 | 117 | 1077 | 39 | 39 | 1073 | 38 | 38 | 1106 | 83 | 83 | 103 |
| 91500_3.FIN2 | 0.5 | 61.615 | 104.064 | 5.46 | 1.9 | 0.07620 | 3.27 | 0.623 | 59.81 | 1.9105 | 3.1 | 0.1847 | 2.1 | 0.05 | 0.0574 | 4.81 | 1013 | 143 | 143 | 1091 | 41 | 41 | 1075 | 40 | 40 | 1124 | 105 | 105 | 108 |
| 91500_4.FIN2 | 0.5 | 74.519 | 79.193 | 5.61 | 1.6 | 0.07490 | 3.33 | 0.092 | 3.99 | 1.8363 | 3.2 | 0.1794 | 1.5 | 0.01 | 0.0565 | 3.78 | 971 | 136 | 136 | 1063 | 30 | 30 | 1046 | 43 | 43 | 1109 | 82 | 82 | 109 |
| 91500_5.FIN2 | 0.5 | 9234.360 | 33.886 | 5.44 | 1.5 | 0.07527 | 3.43 | 0.089 | 4.37 | 1.9255 | 3.3 | 0.1841 | 1.7 | 0.02 | 0.0529 | 3.92 | 1037 | 150 | 150 | 1088 | 35 | 35 | 1086 | 49 | 49 | 1040 | 79 | 79 | 105 |
| 91500_6.FIN2 | 0.5 | -9023.557 | -26.014 | 5.53 | 2.2 | 0.07378 | 3.29 | 0.091 | 4.24 | 1.8496 | 3.6 | 0.1809 | 2.2 | 0.05 | 0.0576 | 4.12 | 953 | 124 | 124 | 1080 | 39 | 39 | 1049 | 43 | 43 | 1129 | 90 | 90 | 113 |
| 91500_7.FIN2 | 0.5 | -358.514 | -26.482 | 5.77 | 2.7 | 0.07394 | 2.84 | 0.082 | 4.73 | 1.7786 | 3.3 | 0.1778 | 2.3 | 0.35 | 0.0489 | 4.02 | 985 | 108 | 108 | 1053 | 45 | 45 | 1027 | 42 | 42 | 962 | 75 | 75 | 107 |
| 91500_8.FIN2 | 0.5 | -454.188 | -19.784 | 5.56 | 2.2 | 0.07418 | 3.24 | 0.092 | 5.69 | 1.8372 | 2.9 | 0.1788 | 1.9 | 0.02 | 0.0547 | 4.91 | 977 | 136 | 136 | 1059 | 38 | 38 | 1049 | 38 | 38 | 1072 | 102 | 102 | 108 |
| 91500_9.FIN2 | 0.5 | -54.319 | -112.272 | 5.51 | 2.1 | 0.07689 | 3.83 | 0.117 | 13.55 | 1.9316 | 4.8 | 0.1779 | 2.1 | 0.02 | 0.0568 | 3.80 | 1006 | 125 | 125 | 1064 | 47 | 47 | 1073 | 53 | 53 | 1115 | 82 | 82 | 106 |
| 91500_10.FIN2 | 0.5 | -171.702 | -42.714 | 5.52 | 1.9 | 0.07166 | 2.93 | 0.085 | 4.15 | 1.8246 | 3.0 | 0.1836 | 1.9 | 0.11 | 0.0525 | 4.13 | 948 | 133 | 133 | 1085 | 37 | 37 | 1045 | 38 | 38 | 1031 | 83 | 83 | 115 |
| 91500_11.FIN2 | 0.5 | -214.787 | -25.144 | 5.65 | 2.2 | 0.07463 | 3.39 | 0.108 | 13.09 | 1.7848 | 3.0 | 0.1792 | 2.1 | 0.41 | 0.0580 | 6.12 | 961 | 147 | 147 | 1061 | 42 | 42 | 1031 | 39 | 39 | 1133 | 132 | 132 | 110 |
| 91500_12.FIN2 | 0.5 | -88.458 | -52.254 | 5.54 | 2.0 | 0.07433 | 3.32 | 0.090 | 4.98 | 1.8861 | 3.0 | 0.1842 | 2.1 | 0.03 | 0.0530 | 4.41 | 1013 | 142 | 142 | 1088 | 41 | 41 | 1066 | 38 | 38 | 1041 | 89 | 89 | 107 |
| 91500_13.FIN2 | 0.5 | -152.447 | -34.174 | 5.44 | 1.9 | 0.07874 | 3.17 | 0.116 | 16.46 | 1.9935 | 2.9 | 0.1843 | 1.9 | 0.01 | 0.0565 | 3.99 | 1078 | 130 | 130 | 1089 | 38 | 38 | 1103 | 39 | 39 | 1107 | 85 | 85 | 101 |
| 91500_14.FIN2 | 0.5 | -250.309 | -40.469 | 5.52 | 3.1 | 0.07297 | 3.56 | 0.131 | 23.45 | 1.8438 | 3.7 | 0.1786 | 2.6 | 0.35 | 0.0490 | 5.02 | 1004 | 146 | 146 | 1057 | 52 | 52 | 1060 | 52 | 52 | 965 | 94 | 94 | 105 |
| 91500_15.FIN2 | 0.5 | -370.277 | -23.590 | 5.49 | 1.8 | 0.07626 | 3.30 | 0.123 | 27.24 | 1.9102 | 3.1 | 0.1848 | 1.8 | 0.03 | 0.0512 | 3.98 | 1026 | 150 | 150 | 1092 | 36 | 36 | 1072 | 42 | 42 | 1006 | 78 | 78 | 106 |
| 91500_16.FIN2 | 0.5 | -317.131 | -27.194 | 5.64 | 2.4 | 0.07802 | 3.70 | 0.099 | 4.17 | 1.9140 | 3.7 | 0.1801 | 2.1 | 0.27 | 0.0541 | 3.69 | 1030 | 150 | 150 | 1066 | 42 | 42 | 1070 | 47 | 47 | 1063 | 76 | 76 | 103 |
| 91500_17.FIN2 | 0.5 | -607.150 | -24.122 | 5.65 | 1.8 | 0.07663 | 2.93 | 0.102 | 10.21 | 1.8723 | 3.0 | 0.1783 | 1.7 | 0.31 | 0.0491 | 4.39 | 1044 | 109 | 109 | 1056 | 34 | 34 | 1061 | 38 | 38 | 966 | 83 | 83 | 101 |
| 91500_18.FIN2 | 0.5 | -687.925 | -29.095 | 5.63 | 2.2 | 0.07742 | 4.07 | 0.099 | 7.77 | 1.9690 | 3.5 | 0.1807 | 2.2 | 0.01 | 0.0494 | 3.52 | 1096 | 160 | 160 | 1069 | 44 | 44 | 1094 | 45 | 45 | 974 | 67 | 67 | 98 |
| 91500_19.FIN2 | 0.5 | -743.108 | -23.367 | 5.65 | 2.5 | 0.07668 | 3.11 | 0.091 | 4.14 | 1.9205 | 2.9 | 0.1795 | 2.1 | 0.34 | 0.0528 | 3.85 | 1062 | 118 | 118 | 1063 | 41 | 41 | 1088 | 34 | 34 | 1038 | 78 | 78 | 100 |
| 91500_1.FIN2 | 0.6 | 17.855 | 842.072 | 5.62 | 1.9 | 0.07494 | 2.85 | 0.113 | 4.35 | 1.8438 | 1.7 | 0.1791 | 1.9 | 0.23 | 0.0541 | 7.98 | 999 | 114 | 114 | 1060 | 37 | 37 | 1057 | 22 | 22 | 1065 | 165 | 165 | 106 |
| 91500_2.FIN2 | 0.6 | 92.670 | 177.338 | 5.62 | 2.0 | 0.07560 | 2.69 | 0.111 | 3.14 | 1.8630 | 1.6 | 0.1791 | 1.9 | 0.15 | 0.0541 | 8.07 | 1022 | 109 | 109 | 1061 | 37 | 37 | 1064 | 21 | 21 | 1064 | 168 | 168 | 104 |
| 91500_3.FIN2 | 0.6 | 212.523 | 83.611 | 5.66 | 1.7 | 0.07387 | 2.46 | 0.110 | 2.39 | 1.8095 | 1.6 | 0.1770 | 1.7 | 0.13 | 0.0539 | 8.04 | 983 | 105 | 105 | 1049 | 33 | 33 | 1045 | 22 | 22 | 1061 | 166 | 166 | 107 |
| 91500_4.FIN2 | 0.6 | -1552.144 | -50.080 | 5.60 | 1.8 | 0.07543 | 2.77 | 0.108 | 2.73 | 1.8546 | 2.4 | 0.1793 | 1.8 | 0.24 | 0.0521 | 8.05 | 1016 | 111 | 111 | 1062 | 36 | 36 | 1065 | 28 | 28 | 1026 | 161 | 161 | 105 |
| 91500_5.FIN2 | 0.6 | -723.767 | -69.602 | 5.50 | 1.8 | 0.07425 | 2.74 | 0.111 | 5.36 | 1.8788 | 2.2 | 0.1809 | 1.7 | 0.13 | 0.0529 | 8.03 | 984 | 112 | 112 | 1071 | 34 | 34 | 1067 | 29 | 29 | 1041 | 163 | 163 | 109 |
| 91500_6.FIN2 | 0.6 | 91.521 | 152.488 | 5.70 | 1.9 | 0.07436 | 2.64 | 0.108 | 2.86 | 1.8160 | 2.0 | 0.1764 | 1.9 | 0.03 | 0.0530 | 8.12 | 991 | 108 | 108 | 1046 | 37 | 37 | 1046 | 26 | 26 | 1044 | 165 | 165 | 106 |
| 91500_7.FIN2 | 0.6 | 93.219 | 112.713 | 5.55 | 1.7 | 0.07656 | 2.67 | 0.112 | 4.59 | 1.9109 | 2.3 | 0.1794 | 1.8 | 0.03 | 0.0537 | 8.00 | 1050 | 107 | 107 | 1062 | 36 | 36 | 1078 | 30 | 30 | 1056 | 165 | 165 | 101 |
| 91500_8.FIN2 | 0.6 | 888.583 | 93.996 | 5.59 | 1.8 | 0.07773 | 2.97 | 0.121 | 6.64 | 1.9337 | 2.3 | 0.1796 | 1.8 | 0.30 | 0.0551 | 8.07 | 1065 | 120 | 120 | 1063 | 35 | 35 | 1086 | 29 | 29 | 1084 | 170 | 170 | 100 |
| 91500_9.FIN2 | 0.6 | 1502.953 | 62.141 | 5.69 | 1.8 | 0.07798 | 3.29 | 0.113 | 2.94 | 1.8952 | 2.5 | 0.1764 | 1.8 | 0.12 | 0.0560 | 8.25 | 1059 | 129 | 129 | 1046 | 35 | 35 | 1071 | 32 | 32 | 1099 | 176 | 176 | 99 |
| 91500_10.FIN2 | 0.6 | 352.372 | 43.830 | 5.71 | 2.2 | 0.07752 | 2.99 | 0.111 | 3.04 | 1.8784 | 2.5 | 0.1760 | 2.1 | 0.24 | 0.0541 | 8.13 | 1060 | 120 | 120 | 1043 | 40 | 40 | 1065 | 33 | 33 | 1063 | 168 | 168 | 98 |
| 91500_11.FIN2 | 0.6 | 156.572 | 100.985 | 5.51 | 1.9 | 0.07601 | 3.01 | 0.107 | 3.38 | 1.8898 | 2.0 | 0.1828 | 1.9 | 0.04 | 0.0536 | 8.18 | 1018 | 124 | 124 | 1080 | 38 | 38 | 1072 | 27 | 27 | 1055 | 168 | 168 | 106 |
| 91500_12.FIN2 | 0.6 | 2017.142 | 48.221 | 5.44 | 2.3 | 0.07450 | 2.83 | 0.109 | 3.50 | 1.8918 | 1.8 | 0.1855 | 2.3 | 0.05 | 0.0526 | 8.19 | 998 | 127 | 127 | 1094 | 46 | 46 | 1079 | 26 | 26 | 1048 | 181 | 181 | 110 |
| 91500_13.FIN2 | 0.6 | 1228.662 | 54.208 | 5.60 | 1.7 | 0.07492 | 2.52 | 0.109 | 2.98 | 1.8609 | 2.1 | 0.1789 | 1.7 | 0.11 | 0.0520 | 8.00 | 1010 | 105 | 105 | 1060 | 34 | 34 | 1061 | 28 | 28 | 1024 | 160 | 160 | 105 |
| 91500_14.FIN2 | 0.6 | -551.284 | -45.845 | 5.52 | 2.0 | 0.07342 | 3.47 | 0.108 | 3.10 | 1.8281 | 2.7 | 0.1797 | 2.1 | 0.08 | 0.0525 | 8.07 | 956 | 131 | 131 | 1063 | 41 | 41 | 1046 | 34 | 34 | 1034 | 163 | 163 | 111 |
| 91500_15.FIN2 | 0.6 | -714.628 | -48.085 | 5.54 | 2.0 | 0.07705 | 3.38 | 0.106 | 2.60 | 1.8901 | 3.3 | 0.1782 | 1.7 | 0.26 | 0.0527 | 8.04 | 1040 | 123 | 123 | 1066 | 39 | 39 | 1078 | 34 | 34 | 1037 | 162 | 162 | 103 |
| 91500_16.FIN2 | 0.6 | 786.039 | 36.927 | 5.75 | 1.9 | 0.07648 | 2.64 | 0.107 | 3.26 | 1.8341 | 1.9 | 0.1740 | 2.0 | 0.09 | 0.0509 | 8.20 | 1048 | 107 | 107 | 1032 | 38 | 38 | 1053 | 25 | 25 | 1002 | 160 | 160 | 98 |
| 91500_17.FIN2 | 0.6 | 873.624 | 35.604 | 5.45 | 1.7 | 0.07568 | 3.02 | 0.110 | 3.31 | 1.8921 | 1.9 | 0.1829 | 1.8 | 0.19 | 0.0534 | 8.17 | 1013 | 119 | 119 | 1081 | 36 | 36 | 1073 | 26 | 26 | 1049 | 167 | 167 | 107 |
| 91500_18.FIN2 | 0.6 | 25.110 | 371.072 | 5.72 | 1.9 | 0.07473 | 3.21 | 0.104 | 2.79 | 1.8417 | 2.7 | 0.1760 | 1.9 | 0.09 | 0.0506 | 7.98 | 1013 | 113 | 113 | 1043 | 37 | 37 | 1043 | 22 | 22 | 997 | 155 | 155 | 103 |
| 91500_19.FIN2 | 0.5 | 68.842 | 174.061 | 5.77 | 2.9 | 0.07602 | 3.08 | 0.122 | 10.21 | 1.8773 | 3.5 | 0.1719 | 2.7 | 0.18 | 0.0541 | 8.05 | 1111 | 133 | 133 | 1019 | 52 | 52 | 1071 | 40 | 40 | 1064 | 167 | 167 | 92 |
| 91500_20.FIN2 | 0.6 | -1226.025 | -76.680 | 5.50 | 2.1 | 0.07560 | 3.01 | 0.124 | 13.07 | 1.9151 | 2.4 | 0.1820 | 1.9 | 0.11 | 0.0542 | 8.14 | 1008 | 123 | 123 | 1076 | 37 | 37 | 1079 | 31 | 31 | 1066 | 169 | 169 | 107 |

| | | | | | | | | | | | | | | | | | | | | | | | | | | | | | |
|---|---|---|---|---|---|---|---|---|---|---|---|---|---|---|---|---|---|---|---|---|---|---|---|---|---|---|---|---|---|
| 91500_21.FIN2 | 0.6 | -649.724 | -46.862 | 5.65 | 1.8 | 0.07472 | 2.68 | 0.115 | 2.93 | 1.7990 | 2.1 | 0.1778 | 1.9 | 0.21 | 0.0555 | 8.11 | 998 | 111 | 111 | 1053 | 36 | 36 | 1049 | 23 | 23 | 1091 | 172 | 172 | 106 |
| 91500_22.FIN2 | 0.6 | 192.915 | 66.354 | 5.69 | 2.3 | 0.07277 | 2.89 | 0.108 | 4.81 | 1.7580 | 1.8 | 0.1783 | 2.2 | 0.34 | 0.0498 | 8.11 | 936 | 118 | 118 | 1056 | 43 | 43 | 1032 | 25 | 25 | 982 | 155 | 155 | 113 |
| 91500_23.FIN2 | 0.6 | 171.690 | 75.579 | 5.78 | 1.9 | 0.07414 | 2.24 | 0.128 | 13.20 | 1.8216 | 1.6 | 0.1741 | 1.9 | 0.17 | 0.0529 | 8.90 | 1019 | 97 | 97 | 1033 | 37 | 37 | 1050 | 21 | 21 | 1038 | 176 | 176 | 101 |
| 91500_29.FIN2 | 0.6 | -295.747 | -71.342 | 5.57 | 2.1 | 0.07494 | 3.07 | 0.104 | 3.19 | 1.8646 | 2.1 | 0.1815 | 2.1 | 0.09 | 0.0490 | 8.12 | 985 | 127 | 127 | 1073 | 42 | 42 | 1063 | 27 | 27 | 965 | 153 | 153 | 109 |
| 91500_30.FIN2 | 0.6 | 200.139 | 56.422 | 5.46 | 2.2 | 0.07341 | 3.26 | 0.105 | 3.43 | 1.8412 | 2.1 | 0.1792 | 2.2 | 0.22 | 0.0502 | 8.25 | 965 | 129 | 129 | 1060 | 45 | 45 | 1060 | 30 | 30 | 988 | 159 | 159 | 110 |
| 91500_31.FIN2 | 0.6 | 411.136 | 42.153 | 5.37 | 1.7 | 0.07344 | 2.74 | 0.111 | 2.88 | 1.8994 | 2.1 | 0.1867 | 1.8 | 0.03 | 0.0522 | 8.10 | 961 | 112 | 112 | 1102 | 36 | 36 | 1075 | 28 | 28 | 1027 | 162 | 162 | 115 |
| 91500_32.FIN2 | 0.6 | 718.776 | 49.681 | 5.56 | 1.9 | 0.07513 | 2.83 | 0.109 | 3.27 | 1.8591 | 2.0 | 0.1796 | 2.0 | 0.02 | 0.0514 | 8.13 | 1004 | 115 | 115 | 1063 | 39 | 39 | 1066 | 25 | 25 | 1011 | 160 | 160 | 106 |
| 91500_34.FIN2 | 0.6 | 597.068 | 48.945 | 5.57 | 1.8 | 0.07492 | 2.60 | 0.111 | 3.11 | 1.8670 | 1.8 | 0.1805 | 1.9 | 0.00 | 0.0526 | 8.24 | 1008 | 107 | 107 | 1068 | 37 | 37 | 1065 | 24 | 24 | 1035 | 166 | 166 | 106 |
| 91500_13.FIN2 | 0.6 | 1228.662 | 54.208 | 5.60 | 1.7 | 0.07492 | 2.52 | 0.109 | 2.98 | 1.8609 | 2.1 | 0.1789 | 1.7 | 0.11 | 0.0520 | 8.00 | 1010 | 105 | 105 | 1060 | 34 | 34 | 1061 | 28 | 28 | 1024 | 160 | 160 | 105 |
| 91500_14.FIN2 | 0.6 | -551.284 | -45.845 | 5.52 | 2.0 | 0.07342 | 3.47 | 0.108 | 3.10 | 1.8281 | 2.7 | 0.1797 | 2.1 | 0.08 | 0.0525 | 8.07 | 956 | 131 | 131 | 1063 | 41 | 41 | 1046 | 34 | 34 | 1034 | 163 | 163 | 111 |
| 91500_15.FIN2 | 0.6 | -714.628 | -48.085 | 5.54 | 2.0 | 0.07705 | 3.38 | 0.106 | 2.60 | 1.8901 | 3.3 | 0.1782 | 1.7 | 0.26 | 0.0527 | 8.04 | 1040 | 123 | 123 | 1066 | 39 | 39 | 1078 | 34 | 34 | 1037 | 162 | 162 | 103 |
| 91500_16.FIN2 | 0.6 | 786.039 | 36.927 | 5.75 | 1.9 | 0.07648 | 2.64 | 0.107 | 3.26 | 1.8341 | 1.9 | 0.1740 | 2.0 | 0.09 | 0.0509 | 8.20 | 1048 | 107 | 107 | 1032 | 38 | 38 | 1053 | 25 | 25 | 1002 | 160 | 160 | 98 |
| 91500_17.FIN2 | 0.6 | 873.624 | 35.604 | 5.45 | 1.7 | 0.07568 | 3.02 | 0.110 | 3.31 | 1.8921 | 1.9 | 0.1829 | 1.8 | 0.19 | 0.0534 | 8.17 | 1013 | 119 | 119 | 1081 | 36 | 36 | 1073 | 26 | 26 | 1049 | 167 | 167 | 107 |
| 91500_18.FIN2 | 0.6 | 25.110 | 371.072 | 5.72 | 1.9 | 0.07473 | 3.21 | 0.104 | 2.79 | 1.8417 | 2.7 | 0.1760 | 1.9 | 0.09 | 0.0506 | 7.98 | 1013 | 113 | 113 | 1043 | 37 | 37 | 1043 | 22 | 22 | 997 | 155 | 155 | 103 |
| 91500_19.FIN2 | 0.5 | 68.842 | 174.061 | 5.77 | 2.9 | 0.07602 | 3.08 | 0.122 | 10.21 | 1.8773 | 3.5 | 0.1719 | 2.7 | 0.18 | 0.0541 | 8.05 | 1111 | 133 | 133 | 1019 | 52 | 52 | 1071 | 40 | 40 | 1064 | 167 | 167 | 92 |
| 91500_20.FIN2 | 0.6 | -1226.025 | -76.680 | 5.50 | 2.1 | 0.07560 | 3.01 | 0.124 | 13.07 | 1.9151 | 2.4 | 0.1820 | 1.9 | 0.11 | 0.0542 | 8.14 | 1008 | 123 | 123 | 1076 | 37 | 37 | 1079 | 31 | 31 | 1066 | 169 | 169 | 107 |
| 91500_22.FIN2 | 0.6 | 192.915 | 66.354 | 5.69 | 2.3 | 0.07277 | 2.89 | 0.108 | 4.81 | 1.7580 | 1.8 | 0.1783 | 2.2 | 0.34 | 0.0498 | 8.11 | 936 | 118 | 118 | 1056 | 43 | 43 | 1032 | 25 | 25 | 982 | 155 | 155 | 113 |
| 91500_23.FIN2 | 0.6 | 171.690 | 75.579 | 5.78 | 1.9 | 0.07414 | 2.24 | 0.128 | 13.20 | 1.8216 | 1.6 | 0.1741 | 1.9 | 0.17 | 0.0529 | 8.90 | 1019 | 97 | 97 | 1033 | 37 | 37 | 1050 | 21 | 21 | 1038 | 176 | 176 | 101 |
| 91500_24.FIN2 | 0.6 | 106.155 | 110.886 | 5.57 | 1.8 | 0.07455 | 3.25 | 0.107 | 2.98 | 1.8592 | 2.7 | 0.1804 | 1.9 | 0.13 | 0.0504 | 8.13 | 975 | 124 | 124 | 1067 | 37 | 37 | 1058 | 31 | 31 | 993 | 157 | 157 | 110 |
| 91500_27.FIN2 | 0.6 | 617.615 | 56.027 | 5.66 | 1.8 | 0.07442 | 2.80 | 0.109 | 3.09 | 1.8306 | 2.0 | 0.1770 | 1.7 | 0.11 | 0.0513 | 8.14 | 985 | 115 | 115 | 1049 | 33 | 33 | 1051 | 26 | 26 | 1010 | 160 | 160 | 107 |
| 91500_28.FIN2 | 0.5 | -664.260 | -59.367 | 5.59 | 1.8 | 0.07483 | 2.66 | 0.108 | 2.99 | 1.8424 | 2.4 | 0.1772 | 2.1 | 0.17 | 0.0520 | 8.15 | 1001 | 111 | 111 | 1057 | 38 | 38 | 1060 | 29 | 29 | 1024 | 162 | 162 | 106 |
| 91500_29.FIN2 | 0.6 | -295.747 | -71.342 | 5.57 | 2.1 | 0.07494 | 3.07 | 0.104 | 3.19 | 1.8646 | 2.1 | 0.1815 | 2.1 | 0.09 | 0.0490 | 8.12 | 985 | 127 | 127 | 1073 | 42 | 42 | 1063 | 27 | 27 | 965 | 153 | 153 | 109 |
| 91500_30.FIN2 | 0.6 | 200.139 | 56.422 | 5.46 | 2.2 | 0.07341 | 3.26 | 0.105 | 3.43 | 1.8412 | 2.1 | 0.1792 | 2.2 | 0.22 | 0.0502 | 8.25 | 965 | 129 | 129 | 1060 | 45 | 45 | 1060 | 30 | 30 | 988 | 159 | 159 | 110 |
| 91500_31.FIN2 | 0.6 | 411.136 | 42.153 | 5.37 | 1.7 | 0.07344 | 2.74 | 0.111 | 2.88 | 1.8994 | 2.1 | 0.1867 | 1.8 | 0.03 | 0.0522 | 8.10 | 961 | 112 | 112 | 1102 | 36 | 36 | 1075 | 28 | 28 | 1027 | 162 | 162 | 115 |
| 91500_32.FIN2 | 0.6 | 718.776 | 49.681 | 5.56 | 1.9 | 0.07513 | 2.83 | 0.109 | 3.27 | 1.8591 | 2.0 | 0.1796 | 2.0 | 0.02 | 0.0514 | 8.13 | 1004 | 115 | 115 | 1063 | 39 | 39 | 1066 | 25 | 25 | 1011 | 160 | 160 | 106 |
| 91500_33.FIN2 | 0.6 | 296.636 | 79.730 | 5.68 | 1.8 | 0.07547 | 2.87 | 0.112 | 3.78 | 1.8209 | 2.0 | 0.1755 | 2.1 | 0.05 | 0.0517 | 8.11 | 1011 | 116 | 116 | 1048 | 37 | 37 | 1048 | 26 | 26 | 1018 | 161 | 161 | 104 |
| 91500_34.FIN2 | 0.6 | 597.068 | 48.945 | 5.57 | 1.8 | 0.07492 | 2.60 | 0.111 | 3.11 | 1.8670 | 1.8 | 0.1805 | 1.9 | 0.00 | 0.0526 | 8.24 | 1008 | 107 | 107 | 1068 | 37 | 37 | 1065 | 24 | 24 | 1035 | 166 | 166 | 106 |
| 91500_3.FIN2 | 0.6 | 212.523 | 83.611 | 5.66 | 1.7 | 0.07387 | 2.46 | 0.110 | 2.39 | 1.8095 | 1.6 | 0.1770 | 1.7 | 0.13 | 0.0539 | 8.04 | 983 | 105 | 105 | 1049 | 33 | 33 | 1045 | 22 | 22 | 1061 | 166 | 166 | 107 |
| 91500_4.FIN2 | 0.6 | -1552.144 | -50.080 | 5.60 | 1.8 | 0.07543 | 2.77 | 0.108 | 2.73 | 1.8546 | 2.4 | 0.1793 | 1.8 | 0.24 | 0.0521 | 8.05 | 1016 | 111 | 111 | 1062 | 36 | 36 | 1065 | 28 | 28 | 1026 | 161 | 161 | 105 |
| 91500_5.FIN2 | 0.6 | -723.767 | -69.602 | 5.50 | 1.8 | 0.07425 | 2.74 | 0.111 | 5.36 | 1.8788 | 2.2 | 0.1809 | 1.7 | 0.13 | 0.0529 | 8.03 | 984 | 112 | 112 | 1071 | 34 | 34 | 1067 | 29 | 29 | 1041 | 163 | 163 | 109 |
| 91500_6.FIN2 | 0.6 | 91.521 | 152.488 | 5.70 | 1.9 | 0.07436 | 2.64 | 0.108 | 2.86 | 1.8160 | 2.0 | 0.1764 | 1.9 | 0.03 | 0.0530 | 8.12 | 991 | 108 | 108 | 1046 | 37 | 37 | 1046 | 26 | 26 | 1044 | 165 | 165 | 106 |
| 91500_7.FIN2 | 0.6 | 93.219 | 112.713 | 5.55 | 1.7 | 0.07656 | 2.67 | 0.112 | 4.59 | 1.9109 | 2.3 | 0.1794 | 1.8 | 0.03 | 0.0537 | 8.00 | 1050 | 107 | 107 | 1062 | 36 | 36 | 1078 | 30 | 30 | 1056 | 165 | 165 | 101 |
| 91500_8.FIN2 | 0.6 | 888.583 | 93.996 | 5.59 | 1.8 | 0.07773 | 2.97 | 0.121 | 6.64 | 1.9337 | 2.3 | 0.1796 | 1.8 | 0.30 | 0.0551 | 8.07 | 1065 | 120 | 120 | 1063 | 35 | 35 | 1086 | 29 | 29 | 1084 | 170 | 170 | 100 |
| 91500_9.FIN2 | 0.6 | 1502.953 | 62.141 | 5.69 | 1.8 | 0.07798 | 3.29 | 0.113 | 2.94 | 1.8952 | 2.5 | 0.1764 | 1.8 | 0.12 | 0.0560 | 8.25 | 1059 | 129 | 129 | 1046 | 35 | 35 | 1071 | 32 | 32 | 1099 | 176 | 176 | 99 |
| 91500_10.FIN2 | 0.6 | 352.372 | 43.830 | 5.71 | 2.2 | 0.07752 | 2.99 | 0.111 | 3.04 | 1.8784 | 2.5 | 0.1760 | 2.1 | 0.24 | 0.0541 | 8.13 | 1060 | 120 | 120 | 1043 | 40 | 40 | 1065 | 33 | 33 | 1063 | 168 | 168 | 98 |
| 91500_11.FIN2 | 0.6 | 156.572 | 100.985 | 5.51 | 1.9 | 0.07601 | 3.01 | 0.107 | 3.38 | 1.8898 | 2.0 | 0.1828 | 1.9 | 0.04 | 0.0536 | 8.18 | 1018 | 124 | 124 | 1080 | 38 | 38 | 1072 | 27 | 27 | 1055 | 168 | 168 | 106 |
| 91500_12.FIN2 | 0.6 | 2017.142 | 48.221 | 5.44 | 2.3 | 0.07450 | 2.83 | 0.109 | 3.50 | 1.8918 | 1.8 | 0.1855 | 2.3 | 0.05 | 0.0526 | 8.19 | 998 | 127 | 127 | 1094 | 46 | 46 | 1079 | 26 | 26 | 1048 | 181 | 181 | 110 |

**Suplementary Table 2.** Reference standards for whole-rock geochemical analysis.

| | | Standard | | | | | | | | | | | | | | | | | | | |
|---|---|---|---|---|---|---|---|---|---|---|---|---|---|---|---|---|---|---|---|---|---|
| | Description | BXMG-5 | BXMG-5 | OREAS 24b | OREAS 24b | OREAS 24b | SY-4 | SY-5 | NCSDC71301 | OREAS 146 | SY-5 | OREAS 146 | OREAS 460 | SY-4 | OREAS 460 | BCS-348 | BXMG-5 | OREAS 24b | SY-4 | SY-5 | NCSDC71301 | OREAS 146 | OREAS 460 |
| SiO2 | % | | | 66.8 | 67.1 | | 50.5 | 49.3 | 54.8 | | 49.6 | 20.1 | 49.4 | 48.8 | | | | 67.1 | 50.9 | 49.3 | 54.6 | 20.1 | |
| Al2O3 | % | | | 15 | 15.1 | | 20.6 | 13.95 | 17.7 | | 14.05 | 2.96 | 12.5 | 20.1 | | | | 15.1 | 20.9 | 13.95 | 17.65 | 2.96 | |
| Fe2O3 | % | | | 6.34 | 6.43 | | 6.2 | 10.4 | 7.24 | | 10.35 | 28 | 26.1 | 6 | | | | 6.43 | 6.25 | 10.4 | 7.3 | 28 | |
| CaO | % | | | 1.5 | 1.48 | | 8.04 | 6.94 | 1.38 | | 7.09 | 17.1 | 0.99 | 7.88 | | | | 1.48 | 7.95 | 6.94 | 1.36 | 17.1 | |
| MgO | % | | | 2.74 | 2.68 | | 0.54 | 3.12 | 0.64 | | 3.24 | 6.68 | 1.22 | 0.51 | | | | 2.68 | 0.53 | 3.12 | 0.62 | 6.68 | |
| Na2O | % | | | 1.14 | 1.11 | | 7.24 | 3.98 | 7.25 | | 4.16 | 0.29 | 0.18 | 6.94 | | | | 1.11 | 7.17 | 3.98 | 7.01 | 0.29 | |
| K2O | % | | | 3.33 | 3.4 | | 1.68 | 4.1 | 7.46 | | 4.04 | 1.26 | 1.46 | 1.58 | | | | 3.4 | 1.68 | 4.1 | 7.28 | 1.26 | |
| Cr2O3 | % | | | 0.02 | 0.022 | | 0.002 | 0.022 | <0.002 | | 0.023 | 0.026 | 0.052 | 0.002 | | | | 0.022 | 0.002 | 0.022 | 0.002 | 0.026 | |
| TiO2 | % | | | 0.78 | 0.79 | | 0.29 | 1.72 | 0.47 | | 1.72 | 1.37 | 1.87 | 0.27 | | | | 0.79 | 0.29 | 1.72 | 0.46 | 1.37 | |
| MnO | % | | | 0.06 | 0.06 | | 0.11 | 0.13 | 0.12 | | 0.12 | 2.42 | 0.05 | 0.1 | | | | 0.06 | 0.11 | 0.13 | 0.12 | 2.42 | |
| P2O5 | % | | | 0.15 | 0.16 | | 0.13 | 2 | 0.01 | | 1.96 | 0.53 | 0.43 | 0.12 | | | | 0.16 | 0.13 | 2 | 0.01 | 0.53 | |
| SrO | % | | | <0.01 | <0.01 | | 0.13 | 0.34 | 0.14 | | 0.34 | 0.35 | 0.02 | 0.12 | | | | <0.01 | 0.12 | 0.34 | 0.13 | 0.35 | |
| BaO | % | | | 0.08 | 0.08 | | 0.04 | 0.71 | 0.03 | | 0.71 | 1.47 | 0.09 | 0.04 | | | | 0.08 | 0.04 | 0.71 | 0.03 | 1.47 | |
| LOI | % | 26.7 | 26.4 | | | | | | | | | | | | 2.63 | 11.55 | 26.7 | | | | | | 2.63 |
| Total | % | | | | | | 100.06 | | 97.24 | | | | | | | | | | 100.63 | | 96.57 | | |
| Ba | ppm | | | 739 | 771 | 749 | | 6340 | | >10000 | 6460 | | 782 | | | | | 771 | | 6340 | | >10000 | |
| Ce | ppm | | | 81.9 | 94 | 90.7 | | 485 | | 4780 | 453 | | 1775 | | | | | 94 | | 485 | | 4850 | |
| Cr | ppm | | | 152 | 161 | 159 | | 158 | | 189 | 166 | | 383 | | | | | 161 | | 158 | | 177 | |
| Cs | ppm | | | 10.85 | 11.15 | 11.3 | | 0.57 | | 0.62 | 0.67 | | 3.59 | | | | | 11.15 | | 0.57 | | 0.5 | |
| Dy | ppm | | | 6.25 | 6.37 | 6.08 | | 11.4 | | 244 | 11.4 | | 20.1 | | | | | 6.37 | | 11.4 | | 222 | |
| Er | ppm | | | 3.73 | 3.56 | 3.78 | | 5.6 | | 92 | 4.96 | | 5.85 | | | | | 3.56 | | 5.6 | | 84 | |
| Eu | ppm | | | 1.4 | 1.29 | 1.47 | | 7.45 | | 135.5 | 7.54 | | 21.6 | | | | | 1.29 | | 7.45 | | 117.5 | |
| Ga | ppm | | | 22.1 | 21.7 | 21.4 | | 20.2 | | 9.9 | 21.7 | | 26.2 | | | | | 21.7 | | 20.2 | | 3 | |
| Gd | ppm | | | 5.96 | 6.83 | 6.54 | | 20.5 | | 364 | 20.3 | | 50.5 | | | | | 6.83 | | 20.5 | | 325 | |
| Hf | ppm | | | 6.49 | 6.42 | 6.35 | | 16.55 | | 4.42 | 16 | | 11.1 | | | | | 6.42 | | 16.55 | | 3.94 | |
| Ho | ppm | | | 1.19 | 1.26 | 1.27 | | 2.09 | | 40.2 | 1.98 | | 2.92 | | | | | 1.26 | | 2.09 | | 35.4 | |
| La | ppm | | | 45.2 | 47.3 | 46.8 | | 236 | | 2560 | 239 | | 1320 | | | | | 47.3 | | 236 | | 2540 | |

| | | | | | | | | | | | | | |
|---|---|---|---|---|---|---|---|---|---|---|---|---|---|
| **Lu** | ppm | | 0.46 | 0.57 | 0.48 | 0.64 | 6.73 | 0.71 | 0.57 | | 0.57 | 0.64 | 6.29 |
| **Nb** | ppm | | 17 | 18.05 | 16.4 | 23.2 | 417 | 23.2 | 703 | | 18.05 | 23.2 | 389 |
| **Nd** | ppm | | 39.6 | 40.3 | 37.6 | 209 | 2140 | 215 | 832 | | 40.3 | 209 | 2300 |
| **Pr** | ppm | | 10.1 | 10.8 | 11 | 54.6 | 579 | 55.1 | 232 | | 10.8 | 54.6 | 563 |
| **Rb** | ppm | | 169.5 | 163.5 | 162.5 | 78.8 | 29 | 77 | 65.6 | | 163.5 | 78.8 | 26.7 |
| **Sc** | ppm | | 17 | 18.5 | 19.1 | 12.8 | 21.8 | 15.5 | 31.1 | | 18.5 | 12.8 | 18.4 |
| **Sm** | ppm | | 7.26 | 7.44 | 7.81 | 31.7 | 454 | 31.4 | 103 | | 7.44 | 31.7 | 471 |
| **Sn** | ppm | | 4.6 | 5.3 | 4.9 | 3.3 | 48.6 | 3.1 | 16.1 | | 5.3 | 3.3 | 44.4 |
| **Sr** | ppm | | 127.5 | 124 | 117 | 3060 | 3090 | 3120 | 296 | | 124 | 3060 | 3000 |
| **Ta** | ppm | | 1.4 | 1.5 | 1.4 | 1 | 4.4 | 1 | 13.2 | | 1.5 | 1 | 4 |
| **Tb** | ppm | | 0.89 | 1.02 | 1.06 | 2.42 | 49.2 | 2.33 | 5.22 | | 1.02 | 2.42 | 44.2 |
| **Th** | ppm | | 16.2 | 17.35 | 17.7 | 25.4 | 909 | 24.2 | 111 | | 17.35 | 25.4 | 901 |
| **Ti** | % | | 0.52 | 0.53 | 0.53 | 1.1 | 0.95 | 1.16 | 1.2 | | 0.53 | 1.1 | 0.87 |
| **Tm** | ppm | | 0.49 | 0.49 | 0.52 | 0.71 | 10.75 | 0.69 | 0.71 | | 0.49 | 0.71 | 9.79 |
| **U** | ppm | | 3.19 | 3.36 | 3.52 | 5.43 | 2.84 | 5.05 | 3.92 | | 3.36 | 5.43 | 2.46 |
| **V** | ppm | | 123 | 119 | 120 | 138 | 163 | 153 | 268 | | 119 | 138 | 144 |
| **W** | ppm | | 4.8 | 5.1 | 4.9 | 1.6 | 30.8 | 0.5 | 5.1 | | 5.1 | 1.6 | 27.1 |
| **Y** | ppm | | 34.7 | 34.6 | 32.3 | 56.6 | 934 | 59.5 | 58.9 | | 34.6 | 56.6 | 900 |
| **Yb** | ppm | | 3.63 | 3.5 | 3.44 | 4.73 | 54.3 | 4.79 | 3.69 | | 3.5 | 4.73 | 50 |
| **Zr** | ppm | | 227 | 231 | 242 | 802 | 244 | 831 | 446 | | 231 | 802 | 231 |

**Suplementary Table 3.** U-Pb in rutile (Reference Materials).

| Spot | $f206$ (%) | U (µg.g$^{-1}$) | 2se | $^{206}Pb/^{204}Pb$ | $^{207}Pb/^{206}Pb$ | 2s | $^{207}Pb/^{235}U$ | 2s | $^{206}Pb/^{238}U$ | 2s | Rho | Idades (Ma)[1] $^{207}Pb/^{206}Pb$ | 2s | $^{206}Pb/^{238}U$ | 2s | $^{207}Pb/^{235}U$ | 2s | % conc[2] |
|---|---|---|---|---|---|---|---|---|---|---|---|---|---|---|---|---|---|---|
| ***R19*** | | | | | | | | | | | | | | | | | | |
| R19-2.FIN2 | 0.44 | 24.2 | 0.2 | 4245 | 0.0618 | 0.0048 | 0.640 | 0.064 | 0.0774 | 0.0048 | 0.10 | 561 | 156 | 481 | 28 | 500 | 41 | 96 |
| R19-5.FIN2 | 0.45 | 21.1 | 0.6 | 4167 | 0.0584 | 0.0029 | 0.671 | 0.059 | 0.0843 | 0.0052 | 0.10 | 510 | 114 | 521 | 31 | 524 | 37 | 99 |
| R19-6.FIN2 | 0.43 | 22.9 | 0.4 | 4355 | 0.0603 | 0.0032 | 0.678 | 0.062 | 0.0824 | 0.0050 | 0.24 | 560 | 123 | 511 | 30 | 526 | 39 | 97 |
| R19-7.FIN2 | 0.48 | 18.7 | 0.4 | 3869 | 0.0540 | 0.0028 | 0.627 | 0.056 | 0.0841 | 0.0052 | 0.21 | 388 | 119 | 520 | 31 | 495 | 33 | 105 |
| R19-8.FIN2 | 0.42 | 25.6 | 0.3 | 4422 | 0.0537 | 0.0039 | 0.593 | 0.063 | 0.0797 | 0.0050 | 0.30 | 311 | 167 | 494 | 30 | 473 | 38 | 104 |
| R19-10.FIN2 | 0.46 | 22.5 | 0.3 | 4088 | 0.0569 | 0.0035 | 0.622 | 0.059 | 0.0801 | 0.0049 | 0.11 | 445 | 144 | 497 | 29 | 492 | 38 | 101 |
| ***R10*** | | | | | | | | | | | | | | | | | | |
| R10-1.FIN2 | 0.05 | 51.8 | 0.8 | 36742 | 0.0750 | 0.0020 | 1.892 | 0.149 | 0.1821 | 0.0109 | 0.22 | 1064 | 54 | 1078 | 60 | 1079 | 51 | 100 |
| R10-2.FIN2 | 0.05 | 50.5 | 0.8 | 34946 | 0.0747 | 0.0020 | 1.842 | 0.145 | 0.1795 | 0.0108 | 0.37 | 1056 | 52 | 1064 | 59 | 1062 | 51 | 100 |
| R10-3.FIN2 | 0.05 | 55.2 | 0.6 | 39844 | 0.0760 | 0.0020 | 1.977 | 0.156 | 0.1893 | 0.0114 | 0.52 | 1090 | 51 | 1117 | 62 | 1106 | 54 | 101 |
| R10-4.FIN2 | 0.05 | 52.6 | 0.9 | 38312 | 0.0767 | 0.0020 | 2.017 | 0.159 | 0.1897 | 0.0114 | 0.36 | 1102 | 53 | 1120 | 62 | 1119 | 54 | 100 |
| R10-5.FIN2 | 0.05 | 49.6 | 0.5 | 35190 | 0.0774 | 0.0021 | 1.991 | 0.158 | 0.1872 | 0.0113 | 0.43 | 1123 | 54 | 1106 | 61 | 1112 | 53 | 99 |
| R10-6.FIN2 | 0.06 | 45.5 | 0.8 | 32832 | 0.0753 | 0.0020 | 1.976 | 0.155 | 0.1912 | 0.0115 | 0.19 | 1071 | 55 | 1127 | 62 | 1107 | 54 | 102 |
| R10-7.FIN2 | 0.06 | 45.6 | 0.7 | 31603 | 0.0770 | 0.0020 | 1.999 | 0.158 | 0.1878 | 0.0113 | 0.46 | 1116 | 53 | 1109 | 61 | 1114 | 53 | 100 |
| R10-8.FIN2 | 0.06 | 49.9 | 0.7 | 32998 | 0.0746 | 0.0020 | 1.836 | 0.145 | 0.1785 | 0.0107 | 0.33 | 1063 | 54 | 1059 | 59 | 1058 | 52 | 100 |
| R10-9.FIN2 | 0.07 | 39.0 | 0.6 | 25504 | 0.0755 | 0.0021 | 1.886 | 0.149 | 0.1814 | 0.0109 | 0.22 | 1071 | 56 | 1074 | 60 | 1075 | 52 | 100 |
| R10-10.FIN2 | 0.07 | 39.9 | 0.6 | 25964 | 0.0763 | 0.0021 | 1.906 | 0.151 | 0.1801 | 0.0108 | 0.33 | 1102 | 54 | 1067 | 59 | 1084 | 54 | 98 |
| R10-11.FIN2 | 0.07 | 45.3 | 0.6 | 28533 | 0.0744 | 0.0019 | 1.853 | 0.146 | 0.1808 | 0.0109 | 0.23 | 1050 | 53 | 1071 | 59 | 1064 | 51 | 101 |
| R10-12.FIN2 | 0.07 | 42.2 | 0.8 | 27241 | 0.0752 | 0.0020 | 1.886 | 0.149 | 0.1823 | 0.0110 | 0.30 | 1066 | 53 | 1079 | 60 | 1077 | 55 | 100 |
| R10-14.FIN2 | 0.07 | 41.7 | 0.6 | 27436 | 0.0775 | 0.0021 | 2.076 | 0.165 | 0.1952 | 0.0118 | 0.49 | 1129 | 54 | 1150 | 64 | 1142 | 56 | 101 |

| | | | | | | | | | | | | | | | | | | |
|---|---|---|---|---|---|---|---|---|---|---|---|---|---|---|---|---|---|---|
| R10-15.FIN2 | 0.08 | 35.8 | 0.7 | 22613 | 0.0773 | 0.0021 | 1.985 | 0.158 | 0.1874 | 0.0113 | 0.40 | 1133 | 52 | 1107 | 61 | 1113 | 52 | 99 |
| R10-16.FIN2 | 0.08 | 37.8 | 0.6 | 23324 | 0.0760 | 0.0021 | 1.940 | 0.153 | 0.1852 | 0.0112 | 0.26 | 1089 | 57 | 1095 | 61 | 1093 | 52 | 100 |
| R10-17.FIN2 | 0.06 | 49.6 | 0.9 | 29936 | 0.0755 | 0.0020 | 1.915 | 0.151 | 0.1833 | 0.0110 | 0.38 | 1088 | 52 | 1085 | 60 | 1085 | 51 | 100 |
| R10-18.FIN2 | 0.08 | 39.4 | 0.5 | 22765 | 0.0764 | 0.0022 | 1.852 | 0.147 | 0.1763 | 0.0106 | 0.22 | 1109 | 56 | 1047 | 59 | 1064 | 52 | 98 |
| R10-19.FIN2 | 0.08 | 41.0 | 0.6 | 23844 | 0.0743 | 0.0021 | 1.862 | 0.147 | 0.1829 | 0.0110 | 0.15 | 1055 | 59 | 1083 | 60 | 1068 | 53 | 101 |
| R10-21.FIN2 | 0.07 | 43.1 | 0.5 | 26295 | 0.0783 | 0.0021 | 2.136 | 0.169 | 0.1977 | 0.0119 | 0.25 | 1148 | 52 | 1163 | 64 | 1160 | 55 | 100 |
| R10-23.FIN2 | 0.08 | 42.0 | 0.6 | 23587 | 0.0754 | 0.0020 | 1.934 | 0.153 | 0.1853 | 0.0111 | 0.23 | 1078 | 56 | 1096 | 61 | 1092 | 53 | 100 |
| R10-24.FIN2 | 0.08 | 41.3 | 0.6 | 23616 | 0.0763 | 0.0020 | 1.997 | 0.158 | 0.1906 | 0.0115 | 0.32 | 1099 | 53 | 1125 | 63 | 1115 | 53 | 101 |
| R10-25.FIN2 | 0.09 | 39.1 | 0.6 | 20703 | 0.0759 | 0.0022 | 1.875 | 0.150 | 0.1792 | 0.0108 | 0.24 | 1080 | 58 | 1062 | 59 | 1071 | 52 | 99 |
| R10-26.FIN2 | 0.07 | 45.4 | 0.4 | 25700 | 0.0763 | 0.0021 | 2.044 | 0.163 | 0.1936 | 0.0117 | 0.43 | 1100 | 56 | 1141 | 63 | 1126 | 54 | 101 |
| R10-27.FIN2 | 0.08 | 42.5 | 0.6 | 22522 | 0.0748 | 0.0021 | 1.915 | 0.152 | 0.1849 | 0.0111 | 0.23 | 1065 | 56 | 1093 | 60 | 1084 | 52 | 101 |
| R10-28.FIN2 | 0.08 | 43.7 | 0.8 | 23233 | 0.0752 | 0.0021 | 1.936 | 0.153 | 0.1871 | 0.0113 | 0.30 | 1075 | 56 | 1106 | 61 | 1093 | 52 | 101 |
| R10-29.FIN2 | 0.10 | 37.6 | 0.6 | 18932 | 0.0745 | 0.0022 | 1.857 | 0.149 | 0.1796 | 0.0108 | 0.16 | 1043 | 61 | 1066 | 60 | 1067 | 53 | 100 |
| R10-30.FIN2 | 0.09 | 43.6 | 0.7 | 21982 | 0.0747 | 0.0021 | 1.867 | 0.148 | 0.1807 | 0.0109 | 0.21 | 1075 | 56 | 1070 | 59 | 1068 | 53 | 100 |
| R10-31.FIN2 | 0.09 | 44.2 | 0.7 | 21456 | 0.0754 | 0.0021 | 1.869 | 0.148 | 0.1794 | 0.0108 | 0.32 | 1076 | 55 | 1063 | 59 | 1070 | 52 | 99 |
| R10-32.FIN2 | 0.08 | 45.8 | 0.8 | 23143 | 0.0768 | 0.0021 | 1.984 | 0.157 | 0.1874 | 0.0113 | 0.20 | 1114 | 57 | 1107 | 61 | 1109 | 55 | 100 |
| R10-33.FIN2 | 0.09 | 41.9 | 0.7 | 21045 | 0.0766 | 0.0021 | 2.069 | 0.164 | 0.1960 | 0.0118 | 0.26 | 1106 | 55 | 1154 | 63 | 1137 | 53 | 101 |
| R10-34.FIN2 | 0.10 | 40.7 | 0.7 | 19022 | 0.0755 | 0.0022 | 1.894 | 0.150 | 0.1827 | 0.0110 | 0.33 | 1068 | 56 | 1083 | 59 | 1079 | 52 | 100 |
| R10-35.FIN2 | 0.08 | 49.3 | 0.9 | 23401 | 0.0756 | 0.0021 | 1.993 | 0.158 | 0.1902 | 0.0114 | 0.25 | 1082 | 55 | 1122 | 62 | 1113 | 55 | 101 |
| R10-36.FIN2 | 0.10 | 42.0 | 0.7 | 19447 | 0.0748 | 0.0022 | 1.934 | 0.154 | 0.1869 | 0.0112 | 0.24 | 1057 | 58 | 1104 | 61 | 1095 | 52 | 101 |
| R10-52.FIN2 | 0.09 | 48.6 | 0.9 | 21210 | 0.0749 | 0.0022 | 1.859 | 0.148 | 0.1792 | 0.0108 | 0.14 | 1069 | 59 | 1063 | 59 | 1069 | 53 | 99 |
| R10-53.FIN2 | 0.08 | 52.1 | 0.6 | 22208 | 0.0758 | 0.0021 | 1.891 | 0.150 | 0.1821 | 0.0109 | 0.27 | 1090 | 57 | 1078 | 60 | 1080 | 51 | 100 |
| R10-54.FIN2 | 0.09 | 50.8 | 0.7 | 21328 | 0.0763 | 0.0021 | 1.899 | 0.150 | 0.1808 | 0.0109 | 0.28 | 1099 | 55 | 1071 | 59 | 1080 | 53 | 99 |
| R10-55.FIN2 | 0.09 | 48.7 | 0.7 | 20914 | 0.0766 | 0.0021 | 1.927 | 0.153 | 0.1830 | 0.0110 | 0.27 | 1096 | 56 | 1083 | 60 | 1092 | 52 | 99 |

# APÊNDICE B

**Table 1.** U-Pb in zircon grains data of rocks in the Santa Luzia sequence, northeastern of Borborema province.

| PF-23 | Th/U | Isotopic ratio | | | | | | rho | Age (Ma) | | | | | | Conc (%) |
|---|---|---|---|---|---|---|---|---|---|---|---|---|---|---|---|
| | | $^{207}Pb/^{206}Pb$ | 1% | $^{207}Pb/^{235}U$ | 1% | $^{206}Pb/^{238}U$ | 1% | | $^{207}Pb/^{206}Pb$ | 2s(abs) | $^{207}Pb/^{235}U$ | 2s(abs) | $^{206}Pb/^{238}U$ | 2s(abs) | |
| ***36°24'44.51" W / 5°39'21.09" S*** | | | | | | | | | | | | | | | |
| PF_23-5 | 0.698 | 0.252 | 1.637 | 21.344 | 1.888 | 0.617 | 0.973 | 0.406 | 3183.514 | 34.038 | 3147.120 | 17.689 | 3089.970 | 42.631 | 97 |
| PF_23-6 | 0.926 | 0.236 | 1.516 | 18.262 | 1.776 | 0.561 | 0.827 | 0.132 | 3080.731 | 29.450 | 3001.417 | 13.010 | 2867.127 | 32.406 | 93 |
| PF_23-8 | 1.546 | 0.189 | 1.477 | 6.864 | 1.859 | 0.262 | 0.858 | 0.433 | 2720.453 | 28.518 | 2088.620 | 15.392 | 1497.999 | 19.752 | 55 |
| PF_23-10 | 1.373 | 0.197 | 1.478 | 7.700 | 1.934 | 0.281 | 0.920 | 0.534 | 2793.488 | 28.866 | 2189.142 | 18.048 | 1594.081 | 22.850 | 57 |
| PF_23-11 | 0.980 | 0.247 | 1.392 | 19.915 | 1.756 | 0.587 | 0.765 | 0.304 | 3154.463 | 23.250 | 3088.137 | 12.572 | 2975.691 | 29.552 | 94 |
| PF_23-12 | 1.310 | 0.231 | 1.485 | 17.383 | 1.985 | 0.542 | 1.058 | 0.519 | 3044.710 | 28.266 | 2953.254 | 21.684 | 2791.430 | 43.745 | 92 |
| PF_23-13 | 1.266 | 0.204 | 1.551 | 9.169 | 2.387 | 0.323 | 1.419 | 0.748 | 2844.851 | 33.138 | 2335.923 | 31.209 | 1800.197 | 42.165 | 63 |
| PF_23-15 | 1.294 | 0.216 | 1.507 | 11.452 | 1.924 | 0.385 | 0.972 | 0.523 | 2936.281 | 29.353 | 2552.744 | 18.673 | 2095.092 | 31.073 | 71 |
| PF_23-18 | 1.248 | 0.228 | 1.560 | 14.845 | 1.957 | 0.470 | 1.077 | 0.524 | 3025.397 | 33.009 | 2798.556 | 19.977 | 2492.155 | 39.003 | 82 |
| PF_23-20 | 1.576 | 0.193 | 1.631 | 7.536 | 2.347 | 0.278 | 1.320 | 0.724 | 2753.852 | 38.293 | 2162.335 | 30.638 | 1581.788 | 35.758 | 57 |
| PF_23-21 | 1.392 | 0.219 | 1.860 | 10.723 | 2.704 | 0.356 | 1.670 | 0.772 | 2945.477 | 45.854 | 2481.252 | 39.835 | 1956.794 | 54.058 | 66 |
| PF_23-25 | 1.090 | 0.230 | 1.553 | 14.998 | 2.049 | 0.471 | 1.120 | 0.664 | 3036.474 | 32.268 | 2805.227 | 23.816 | 2480.356 | 43.347 | 82 |
| PF_23-26 | 1.228 | 0.236 | 1.586 | 16.226 | 2.058 | 0.497 | 1.227 | 0.637 | 3075.997 | 34.214 | 2882.218 | 23.895 | 2596.908 | 48.672 | 84 |
| PF_23-27 | 1.453 | 0.206 | 1.570 | 9.597 | 2.317 | 0.331 | 1.423 | 0.717 | 2864.844 | 33.296 | 2375.947 | 30.472 | 1835.515 | 42.925 | 64 |
| PF_23-28 | 1.124 | 0.221 | 1.989 | 13.864 | 3.385 | 0.448 | 2.619 | 0.836 | 2957.019 | 51.855 | 2673.158 | 66.033 | 2358.343 | 105.233 | 80 |
| PF_23-29 | 1.327 | 0.232 | 1.651 | 16.664 | 2.025 | 0.521 | 1.099 | 0.478 | 3045.745 | 36.674 | 2915.623 | 21.855 | 2704.555 | 43.574 | 89 |
| PF_23-34 | 1.867 | 0.196 | 1.512 | 7.340 | 1.859 | 0.270 | 0.872 | 0.367 | 2778.829 | 30.297 | 2148.325 | 15.215 | 1541.274 | 20.592 | 55 |
| PF_23-37 | 1.226 | 0.237 | 1.701 | 17.493 | 2.355 | 0.530 | 1.628 | 0.737 | 3090.495 | 38.084 | 2952.427 | 32.851 | 2748.315 | 73.880 | 89 |
| PF_23-38 | 1.405 | 0.232 | 1.521 | 16.493 | 1.981 | 0.512 | 1.078 | 0.669 | 3062.752 | 30.923 | 2897.587 | 23.108 | 2657.859 | 43.262 | 87 |
| PF_23-43 | 0.391 | 0.257 | 1.702 | 21.723 | 1.940 | 0.613 | 1.072 | 0.308 | 3211.421 | 39.585 | 3170.660 | 19.354 | 3074.916 | 47.917 | 96 |
| PF_23-44 | 0.915 | 0.235 | 1.543 | 17.506 | 1.820 | 0.537 | 0.840 | 0.284 | 3078.811 | 31.550 | 2957.587 | 14.953 | 2767.200 | 32.454 | 90 |
| PF_23-45 | 1.093 | 0.217 | 1.652 | 12.639 | 3.012 | 0.412 | 2.127 | 0.902 | 2944.797 | 36.614 | 2591.405 | 54.389 | 2199.679 | 79.662 | 75 |
| PF_23-46 | 0.878 | 0.236 | 1.631 | 17.367 | 2.060 | 0.531 | 1.213 | 0.515 | 3077.330 | 37.179 | 2947.533 | 24.108 | 2735.733 | 50.680 | 89 |

**Table 1.** Continuation.

| AC-35C | Th/U | Isotopic ratio | | | | | | rho | Age (Ma) | | | | | | Conc (%) |
|---|---|---|---|---|---|---|---|---|---|---|---|---|---|---|---|
| | | $^{207}Pb/^{206}Pb$ | 0.010 | $^{207}Pb/^{235}U$ | 0.010 | $^{206}Pb/^{238}U$ | 0.010 | | $^{207}Pb/^{206}Pb$ | 1s | $^{207}Pb/^{235}U$ | 1s | $^{206}Pb/^{238}U$ | 1s | |
| ***36°16'12.57" W / 5°42'41.22" S*** | | | | | | | | | | | | | | | |
| 005-Z2 | 0.391 | 0.166 | 1.543 | 10.118 | 2.444 | 0.442 | 1.895 | 0.771 | 2470.864 | 26.808 | 2445.597 | 22.580 | 2358.393 | 37.419 | 96 |
| 006-Z3 | 0.295 | 0.156 | 1.072 | 9.030 | 1.861 | 0.420 | 1.521 | 0.812 | 2362.069 | 18.824 | 2341.075 | 17.009 | 2262.056 | 29.018 | 97 |
| 009-Z6 | 0.391 | 0.161 | 1.869 | 10.584 | 2.623 | 0.476 | 1.841 | 0.697 | 2421.550 | 32.621 | 2487.330 | 24.335 | 2508.777 | 38.257 | 101 |
| 010-Z7 | 0.234 | 0.158 | 1.161 | 9.689 | 1.827 | 0.444 | 1.411 | 0.764 | 2389.533 | 20.335 | 2405.642 | 16.814 | 2367.598 | 27.949 | 98 |
| 013-Z8 | 0.191 | 0.159 | 2.655 | 9.444 | 3.587 | 0.429 | 2.412 | 0.669 | 2401.776 | 46.448 | 2382.076 | 32.935 | 2303.280 | 46.711 | 97 |
| 024-Z16 | 0.516 | 0.163 | 0.907 | 10.777 | 1.386 | 0.481 | 1.048 | 0.741 | 2433.845 | 15.814 | 2504.108 | 12.878 | 2531.345 | 21.941 | 101 |
| 025-Z17 | 0.200 | 0.159 | 1.632 | 10.031 | 2.336 | 0.458 | 1.672 | 0.709 | 2395.713 | 28.561 | 2437.683 | 21.571 | 2429.940 | 33.848 | 100 |
| 030-Z22 | 0.418 | 0.163 | 0.734 | 10.250 | 1.260 | 0.457 | 1.025 | 0.799 | 2435.878 | 12.792 | 2457.619 | 11.658 | 2425.715 | 20.711 | 99 |
| 033-Z23 | 0.197 | 0.164 | 0.946 | 10.706 | 1.468 | 0.474 | 1.122 | 0.751 | 2446.912 | 16.481 | 2497.971 | 13.631 | 2501.504 | 23.260 | 100 |
| 034-Z24 | 0.216 | 0.159 | 1.771 | 9.992 | 2.784 | 0.457 | 2.149 | 0.768 | 2392.704 | 31.005 | 2434.077 | 25.700 | 2425.616 | 43.438 | 100 |
| 036-Z26 | 0.347 | 0.165 | 1.518 | 10.690 | 2.094 | 0.470 | 1.442 | 0.680 | 2457.296 | 26.408 | 2496.588 | 19.444 | 2485.729 | 29.749 | 100 |
| 037-Z27 | 0.041 | 0.161 | 1.150 | 9.788 | 1.832 | 0.441 | 1.426 | 0.771 | 2418.176 | 20.089 | 2415.006 | 16.881 | 2354.389 | 28.133 | 97 |
| 039-Z29 | 0.280 | 0.162 | 1.276 | 9.840 | 2.126 | 0.439 | 1.700 | 0.795 | 2432.427 | 22.245 | 2419.923 | 19.592 | 2348.347 | 33.463 | 97 |
| **AC-35B** | Th/U | Isotopic ratio | | | | | | rho | Age (Ma) | | | | | | Conc (%) |
| | | $^{207}Pb/^{206}Pb$ | 0.010 | $^{207}Pb/^{235}U$ | 0.010 | $^{206}Pb/^{238}U$ | 0.010 | | $^{207}Pb/^{206}Pb$ | 1s | $^{207}Pb/^{235}U$ | 1s | $^{206}Pb/^{238}U$ | 1s | |
| ***36°16'12.57" W / 5°42'41.22" S*** | | | | | | | | | | | | | | | |
| 006-Z3 | 0.218 | 0.137 | 0.768 | 6.919 | 1.330 | 0.367 | 1.086 | 0.805 | 2135.474 | 13.823 | 2101.108 | 11.797 | 2016.258 | 18.795 | 96 |
| 008-Z5 | 0.195 | 0.137 | 1.102 | 7.639 | 1.930 | 0.403 | 1.584 | 0.816 | 2145.267 | 19.812 | 2189.448 | 17.326 | 2183.519 | 29.341 | 100 |
| 013-Z8 | 0.202 | 0.141 | 1.305 | 8.523 | 1.700 | 0.438 | 1.090 | 0.625 | 2191.368 | 23.343 | 2288.383 | 15.450 | 2341.977 | 21.399 | 102 |
| 015-Z10 | 0.146 | 0.138 | 1.039 | 8.048 | 1.663 | 0.424 | 1.298 | 0.771 | 2149.229 | 18.679 | 2236.381 | 15.015 | 2277.501 | 24.896 | 102 |
| 016-Z11 | 0.154 | 0.139 | 1.228 | 7.784 | 2.165 | 0.407 | 1.782 | 0.819 | 2159.623 | 22.050 | 2206.344 | 19.477 | 2203.181 | 33.261 | 100 |
| 027-Z19 | 0.119 | 0.147 | 2.966 | 8.146 | 4.277 | 0.402 | 3.082 | 0.719 | 2263.686 | 52.635 | 2247.354 | 38.679 | 2176.206 | 56.921 | 97 |
| 038-Z28 | 0.173 | 0.143 | 1.725 | 8.445 | 2.443 | 0.430 | 1.730 | 0.702 | 2208.900 | 30.791 | 2280.003 | 22.177 | 2304.293 | 33.517 | 101 |
| 039-Z29 | 0.306 | 0.138 | 1.519 | 8.278 | 1.900 | 0.434 | 1.141 | 0.586 | 2157.738 | 27.271 | 2261.941 | 17.211 | 2322.735 | 22.256 | 103 |

**Table 1.** Continuation.

| CG-55 | Th/U | Isotopic ratio | | | | | | rho | Age (Ma) | | | | | | Conc (%) |
|---|---|---|---|---|---|---|---|---|---|---|---|---|---|---|---|
| | | $^{207}Pb/^{206}Pb$ | 2σ | $^{207}Pb/^{235}U$ | 2σ | $^{206}Pb/^{238}U$ | 2σ | | $^{207}Pb/^{206}Pb$ | 2σ | $^{207}Pb/^{235}U$ | 2σ | $^{206}Pb/^{238}U$ | 2σ | |
| ***36°24'54.70" W / 5°38'37.93" S*** | | | | | | | | | | | | | | | |
| 003 Z-1 | 0.625 | 0.124 | 0.012 | 7.596 | 0.689 | 0.376 | 0.034 | 0.972 | 2015.968 | 8.195 | 2184.442 | 78.332 | 2059.733 | 33.233 | 108 |
| 004 Z-2 | 0.609 | 0.121 | 0.006 | 7.316 | 0.359 | 0.367 | 0.018 | 0.967 | 1970.463 | 3.616 | 2150.765 | 42.884 | 2015.825 | 26.954 | 109 |
| 008 Z-4 | 0.616 | 0.124 | 0.006 | 7.569 | 0.377 | 0.377 | 0.019 | 0.969 | 2018.894 | 2.833 | 2181.221 | 43.671 | 2061.014 | 25.773 | 108 |
| 012 Z-6 | 0.655 | 0.132 | 0.013 | 8.183 | 0.783 | 0.399 | 0.038 | 0.959 | 2127.920 | 4.752 | 2251.461 | 83.092 | 2162.327 | 27.058 | 106 |
| 015 Z-7 | 0.648 | 0.133 | 0.026 | 8.091 | 1.510 | 0.399 | 0.074 | 0.957 | 2134.661 | 14.041 | 2241.238 | 156.065 | 2164.283 | 56.472 | 105 |
| 016 Z-8 | 0.672 | 0.138 | 0.019 | 8.565 | 1.126 | 0.414 | 0.054 | 0.969 | 2207.913 | 5.914 | 2292.884 | 113.006 | 2232.741 | 43.231 | 104 |
| 020 Z-10 | 0.537 | 0.113 | 0.003 | 6.671 | 0.164 | 0.343 | 0.008 | 0.958 | 1848.786 | 4.189 | 2068.842 | 21.479 | 1899.776 | 12.182 | 112 |
| 023 Z-11 | 0.536 | 0.113 | 0.003 | 6.902 | 0.179 | 0.343 | 0.009 | 0.911 | 1846.819 | 3.994 | 2098.887 | 22.734 | 1906.335 | 9.991 | 114 |
| 027 Z-13 | 0.638 | 0.134 | 0.006 | 8.114 | 0.424 | 0.402 | 0.021 | 0.953 | 2153.333 | 4.009 | 2243.836 | 46.166 | 2178.678 | 15.357 | 104 |
| 028 Z-14 | 0.580 | 0.121 | 0.003 | 7.173 | 0.188 | 0.365 | 0.010 | 0.881 | 1964.351 | 3.713 | 2133.189 | 23.107 | 2006.360 | 7.965 | 109 |
| 031 Z-15 | 0.581 | 0.124 | 0.008 | 7.306 | 0.465 | 0.376 | 0.024 | 0.908 | 2020.722 | 3.516 | 2149.561 | 55.268 | 2053.447 | 9.945 | 106 |
| 035 Z-17 | 0.628 | 0.135 | 0.010 | 8.087 | 0.507 | 0.404 | 0.025 | 0.964 | 2170.248 | 8.736 | 2240.829 | 55.115 | 2190.186 | 24.844 | 103 |
| 036 Z-18 | 0.633 | 0.137 | 0.010 | 8.224 | 0.627 | 0.408 | 0.031 | 0.862 | 2183.834 | 6.166 | 2255.948 | 66.733 | 2204.312 | 14.495 | 103 |
| 039 Z-19 | 0.609 | 0.129 | 0.003 | 7.812 | 0.222 | 0.389 | 0.011 | 0.894 | 2080.944 | 3.931 | 2209.557 | 25.259 | 2115.494 | 8.433 | 106 |
| 043 Z-21 | 0.666 | 0.144 | 0.005 | 8.623 | 0.271 | 0.425 | 0.013 | 0.877 | 2278.844 | 2.702 | 2298.992 | 28.219 | 2284.896 | 6.041 | 101 |
| 044 Z-22 | 0.611 | 0.130 | 0.006 | 8.042 | 0.399 | 0.390 | 0.019 | 0.950 | 2091.590 | 3.743 | 2235.733 | 43.807 | 2131.413 | 16.998 | 107 |
| 047 Z-23 | 0.682 | 0.147 | 0.017 | 8.911 | 1.065 | 0.433 | 0.052 | 0.855 | 2316.161 | 4.609 | 2328.957 | 103.596 | 2320.236 | 10.545 | 101 |
| 048 Z-24 | 0.653 | 0.140 | 0.008 | 8.422 | 0.451 | 0.415 | 0.022 | 0.925 | 2224.397 | 3.455 | 2277.574 | 47.444 | 2240.106 | 11.938 | 102 |
| 051 Z-25 | 0.558 | 0.119 | 0.009 | 7.237 | 0.692 | 0.362 | 0.035 | 0.967 | 1942.193 | 7.105 | 2141.092 | 81.872 | 1991.556 | 34.852 | 110 |
| 052 Z-26 | 0.634 | 0.138 | 0.017 | 8.427 | 1.037 | 0.412 | 0.051 | 0.951 | 2201.058 | 2.088 | 2278.051 | 106.006 | 2223.318 | 13.187 | 103 |
| 055 Z-27 | 0.648 | 0.141 | 0.011 | 8.522 | 0.652 | 0.419 | 0.032 | 0.945 | 2244.122 | 2.990 | 2288.258 | 67.285 | 2257.106 | 14.984 | 102 |
| 056 Z-28 | 0.639 | 0.139 | 0.007 | 8.282 | 0.431 | 0.413 | 0.021 | 0.932 | 2211.281 | 4.185 | 2262.344 | 46.072 | 2225.883 | 11.645 | 102 |
| 060 Z-30 | 0.659 | 0.143 | 0.004 | 8.634 | 0.227 | 0.423 | 0.011 | 0.921 | 2259.113 | 2.915 | 2300.193 | 23.596 | 2271.333 | 9.520 | 102 |

**Table 1.** Continuation.

| SL-4A | Th/U | Isotopic ratio | | | | | | rho | Age (Ma) | | | | | | Conc (%) |
|---|---|---|---|---|---|---|---|---|---|---|---|---|---|---|---|
| | | $^{207}Pb/^{206}Pb$ | 0.010 | $^{207}Pb/^{235}U$ | 0.010 | $^{206}Pb/^{238}U$ | 0.010 | | $^{207}Pb/^{206}Pb$ | 1s | $^{207}Pb/^{235}U$ | 1s | $^{206}Pb/^{238}U$ | 1s | |
| ***36°24'30.81" W / 5°39'3.46" S*** | | | | | | | | | | | | | | | |
| 004-Z01 | 0.371 | 0.145 | 0.517 | 6.654 | 0.873 | 0.333 | 0.704 | 0.774 | 2287.580 | 8.891 | 2066.495 | 7.708 | 1852.160 | 11.332 | 81 |
| 005-Z02 | 0.586 | 0.148 | 0.704 | 7.558 | 1.082 | 0.372 | 0.822 | 0.734 | 2317.367 | 12.070 | 2179.883 | 9.706 | 2036.833 | 14.362 | 88 |
| 016-Z11 | 0.491 | 0.149 | 0.574 | 7.848 | 1.038 | 0.383 | 0.865 | 0.816 | 2331.962 | 9.821 | 2213.683 | 9.349 | 2088.185 | 15.435 | 90 |
| 020-Z15 | 0.424 | 0.150 | 0.435 | 8.292 | 0.934 | 0.402 | 0.826 | 0.870 | 2340.379 | 7.438 | 2263.404 | 8.459 | 2179.219 | 15.276 | 93 |
| 024-Z16 | 0.584 | 0.148 | 0.653 | 7.966 | 1.035 | 0.390 | 0.803 | 0.750 | 2322.892 | 11.194 | 2227.235 | 9.337 | 2124.712 | 14.534 | 91 |
| 025-Z17 | 0.249 | 0.146 | 0.419 | 7.888 | 0.819 | 0.392 | 0.704 | 0.834 | 2300.994 | 7.206 | 2218.345 | 7.382 | 2129.968 | 12.764 | 93 |
| 026-Z18 | 0.404 | 0.148 | 0.577 | 8.237 | 0.892 | 0.403 | 0.680 | 0.723 | 2326.835 | 9.884 | 2257.435 | 8.074 | 2181.661 | 12.584 | 94 |
| 027-Z19 | 0.410 | 0.149 | 0.846 | 8.355 | 1.266 | 0.406 | 0.941 | 0.724 | 2337.401 | 14.485 | 2270.272 | 11.479 | 2196.504 | 17.522 | 94 |
| 028-Z20 | 0.434 | 0.151 | 1.196 | 8.267 | 1.836 | 0.397 | 1.393 | 0.751 | 2356.395 | 20.422 | 2260.748 | 16.632 | 2156.573 | 25.541 | 92 |
| 029-Z21 | 0.434 | 0.150 | 0.709 | 8.729 | 1.227 | 0.423 | 1.001 | 0.802 | 2341.107 | 12.133 | 2310.064 | 11.178 | 2275.114 | 19.194 | 97 |
| 033-Z23 | 0.503 | 0.149 | 0.804 | 8.475 | 1.352 | 0.412 | 1.087 | 0.792 | 2338.688 | 13.757 | 2283.254 | 12.276 | 2221.853 | 20.422 | 95 |
| 034-Z24 | 0.494 | 0.150 | 1.437 | 8.397 | 1.923 | 0.405 | 1.279 | 0.653 | 2351.465 | 24.551 | 2274.876 | 17.452 | 2190.652 | 23.753 | 93 |
| 035-Z25 | 0.363 | 0.147 | 1.311 | 8.193 | 2.132 | 0.405 | 1.681 | 0.783 | 2306.375 | 22.504 | 2252.595 | 19.290 | 2193.871 | 31.260 | 95 |
| 036-Z26 | 0.467 | 0.150 | 1.143 | 8.559 | 1.712 | 0.415 | 1.274 | 0.734 | 2340.781 | 19.552 | 2292.212 | 15.563 | 2238.132 | 24.098 | 96 |
| 038-Z28 | 0.442 | 0.146 | 0.784 | 7.654 | 1.373 | 0.380 | 1.127 | 0.810 | 2300.692 | 13.468 | 2191.199 | 12.327 | 2076.137 | 20.001 | 90 |
| 039-Z29 | 0.532 | 0.149 | 1.132 | 8.132 | 1.639 | 0.397 | 1.186 | 0.711 | 2329.156 | 19.393 | 2245.765 | 14.822 | 2155.417 | 21.722 | 93 |

**Table 1.** Continuation.

| SL-6C | Th/U | Isotopic ratio | | | | | | rho | Age (Ma) | | | | | | Conc (%) |
|---|---|---|---|---|---|---|---|---|---|---|---|---|---|---|---|
| | | $^{207}Pb/^{206}Pb$ | 0.010 | $^{207}Pb/^{235}U$ | 0.010 | $^{206}Pb/^{238}U$ | 0.010 | | $^{207}Pb/^{206}Pb$ | 1s | $^{207}Pb/^{235}U$ | 1s | $^{206}Pb/^{238}U$ | 1s | |
| ***36°24'56.12" W / 5°39'24.50" S*** | | | | | | | | | | | | | | | |
| 004-Z01 | 0.310 | 0.139 | 0.584 | 6.875 | 1.012 | 0.359 | 0.827 | 0.796 | 2213.114 | 10.129 | 2095.459 | 8.975 | 1977.788 | 14.086 | 89 |
| 006-Z03 | 0.291 | 0.139 | 0.525 | 6.667 | 0.976 | 0.348 | 0.823 | 0.824 | 2215.134 | 9.101 | 2068.228 | 8.617 | 1924.017 | 13.687 | 87 |
| 010-Z05 | 0.366 | 0.138 | 0.622 | 6.479 | 1.047 | 0.340 | 0.842 | 0.783 | 2204.187 | 10.805 | 2042.999 | 9.209 | 1887.197 | 13.773 | 86 |
| 016-Z08 | 0.458 | 0.141 | 0.492 | 7.196 | 0.808 | 0.371 | 0.640 | 0.751 | 2237.406 | 8.514 | 2136.016 | 7.200 | 2032.232 | 11.162 | 91 |
| 018-Z10 | 0.474 | 0.140 | 0.769 | 7.423 | 1.076 | 0.384 | 0.753 | 0.665 | 2227.788 | 13.309 | 2163.791 | 9.626 | 2096.981 | 13.473 | 94 |
| 022-Z12 | 0.362 | 0.137 | 0.443 | 6.441 | 0.693 | 0.342 | 0.533 | 0.698 | 2185.571 | 7.707 | 2037.907 | 6.090 | 1895.264 | 8.748 | 87 |
| 024-Z14 | 0.523 | 0.141 | 0.589 | 7.518 | 0.799 | 0.387 | 0.540 | 0.598 | 2237.881 | 10.186 | 2175.111 | 7.160 | 2109.200 | 9.713 | 94 |
| 028-Z15 | 0.320 | 0.141 | 0.565 | 7.894 | 0.909 | 0.405 | 0.712 | 0.750 | 2243.894 | 9.773 | 2218.983 | 8.196 | 2192.101 | 13.237 | 98 |
| 030-Z16B | 0.393 | 0.141 | 0.621 | 7.687 | 0.894 | 0.396 | 0.643 | 0.671 | 2236.260 | 10.742 | 2195.060 | 8.030 | 2151.226 | 11.756 | 96 |
| 033-Z17 | 0.421 | 0.138 | 0.681 | 6.435 | 1.314 | 0.337 | 1.124 | 0.846 | 2207.918 | 11.812 | 2037.103 | 11.548 | 1872.757 | 18.268 | 85 |
| 034-Z18 | 0.282 | 0.139 | 0.629 | 7.180 | 1.022 | 0.374 | 0.806 | 0.763 | 2218.413 | 10.904 | 2134.031 | 9.112 | 2047.517 | 14.138 | 92 |
| 035-Z19 | 0.269 | 0.139 | 0.612 | 6.976 | 0.915 | 0.364 | 0.681 | 0.703 | 2214.849 | 10.611 | 2108.320 | 8.130 | 2000.887 | 11.712 | 90 |
| 036-Z20 | 0.443 | 0.141 | 0.737 | 7.207 | 1.041 | 0.369 | 0.736 | 0.671 | 2245.551 | 12.736 | 2137.340 | 9.286 | 2026.615 | 12.797 | 90 |
| 040-Z22 | 0.445 | 0.139 | 0.859 | 6.422 | 1.302 | 0.335 | 0.978 | 0.734 | 2216.622 | 14.897 | 2035.244 | 11.439 | 1861.193 | 15.814 | 84 |
| 041-Z23 | 0.373 | 0.142 | 0.592 | 7.028 | 0.924 | 0.359 | 0.710 | 0.733 | 2250.363 | 10.221 | 2115.035 | 8.218 | 1978.695 | 12.102 | 88 |
| 042-Z24 | 0.303 | 0.140 | 0.552 | 6.386 | 0.877 | 0.332 | 0.681 | 0.739 | 2223.606 | 9.561 | 2030.312 | 7.698 | 1845.657 | 10.937 | 83 |
| 046-Z25 | 0.382 | 0.139 | 0.514 | 6.434 | 0.829 | 0.336 | 0.650 | 0.743 | 2210.774 | 8.917 | 2036.910 | 7.284 | 1869.726 | 10.553 | 85 |
| 047-Z26 | 0.542 | 0.138 | 0.617 | 6.326 | 0.946 | 0.331 | 0.717 | 0.723 | 2208.373 | 10.702 | 2021.995 | 8.293 | 1844.543 | 11.505 | 84 |
| 048-Z27 | 0.326 | 0.139 | 0.553 | 6.501 | 1.102 | 0.340 | 0.953 | 0.853 | 2211.112 | 9.592 | 2045.985 | 9.699 | 1886.222 | 15.590 | 85 |

**Table 1.** Continuation.

| PF-18 | Th/U | Isotopic ratio | | | | | | rho | Age (Ma) | | | | | | Conc (%) |
|---|---|---|---|---|---|---|---|---|---|---|---|---|---|---|---|
| | | $^{207}Pb/^{206}Pb$ | 0.010 | $^{207}Pb/^{235}U$ | 0.010 | $^{206}Pb/^{238}U$ | 0.010 | | $^{207}Pb/^{206}Pb$ | 2σ | $^{207}Pb/^{235}U$ | 2σ | $^{206}Pb/^{238}U$ | 2σ | |
| ***36°36'36.99" W / 5°59'38.49" S*** | | | | | | | | | | | | | | | |
| PF-18-N_9.FIN2 | 1.613 | 0.146 | 1.476 | 8.579 | 1.616 | 0.424 | 2.017 | 0.681 | 2297.723 | 51.688 | 2293.296 | 29.358 | 2279.023 | 77.719 | 99 |
| PF-18-N_14.FIN2 | 0.869 | 0.150 | 2.139 | 8.758 | 1.459 | 0.422 | 1.649 | 0.032 | 2331.966 | 73.253 | 2310.609 | 27.281 | 2268.385 | 62.729 | 97 |
| PF-18-N_15.FIN2 | 0.491 | 0.146 | 2.153 | 8.736 | 3.733 | 0.433 | 3.584 | 0.859 | 2285.620 | 75.339 | 2291.161 | 68.652 | 2307.715 | 139.463 | 101 |
| PF-18-N_18.FIN2 | 1.318 | 0.150 | 2.062 | 8.797 | 1.625 | 0.428 | 1.871 | 0.300 | 2324.341 | 71.244 | 2311.283 | 30.392 | 2289.619 | 72.095 | 99 |
| PF-18-N_21.FIN2 | 1.237 | 0.149 | 2.595 | 8.821 | 1.874 | 0.430 | 1.867 | 0.005 | 2316.644 | 87.909 | 2315.063 | 34.672 | 2301.591 | 71.835 | 99 |
| PF-18-B_5.FIN2 | 0.573 | 0.150 | 2.903 | 8.639 | 3.047 | 0.417 | 2.674 | 0.490 | 2320.771 | 98.705 | 2305.846 | 48.800 | 2242.925 | 101.681 | 97 |
| PF-18-B_6.FIN2 | 1.288 | 0.148 | 1.626 | 8.781 | 1.586 | 0.429 | 1.521 | 0.381 | 2308.353 | 56.072 | 2312.140 | 29.716 | 2300.188 | 58.626 | 100 |
| PF-18-B_7.FIN2 | 0.683 | 0.149 | 2.358 | 8.833 | 2.640 | 0.432 | 2.823 | 0.620 | 2313.818 | 80.412 | 2311.065 | 52.793 | 2308.995 | 110.535 | 100 |
| PF-18-B_8.FIN2 | 1.291 | 0.148 | 2.070 | 8.900 | 1.630 | 0.435 | 1.654 | 0.101 | 2310.123 | 70.879 | 2324.461 | 29.599 | 2326.727 | 64.368 | 101 |
| PF-18-B_11.FIN2 | 1.176 | 0.151 | 1.773 | 9.309 | 1.354 | 0.449 | 1.397 | 0.096 | 2336.743 | 60.618 | 2365.995 | 24.841 | 2389.742 | 55.727 | 102 |
| PF-18-B_13.FIN2 | 1.158 | 0.150 | 1.735 | 9.319 | 1.618 | 0.450 | 1.596 | 0.375 | 2329.255 | 59.385 | 2364.263 | 30.426 | 2392.401 | 63.287 | 103 |

| CG-97 | Th/U | Isotopic ratio | | | | | | rho | Age (Ma) | | | | | | Conc (%) |
|---|---|---|---|---|---|---|---|---|---|---|---|---|---|---|---|
| | | $^{207}Pb/^{206}Pb$ | 2σ | $^{207}Pb/^{235}U$ | 2σ | $^{206}Pb/^{238}U$ | 2σ | | $^{207}Pb/^{206}Pb$ | 2σ | $^{207}Pb/^{235}U$ | 2σ | $^{206}Pb/^{238}U$ | 2σ | |
| ***36°23'54.49" W / 5°37'54.72" S*** | | | | | | | | | | | | | | | |
| 003 Z-1 | 0.647 | 0.141 | 0.034 | 8.360 | 0.682 | 0.418 | 0.034 | 0.956 | 2238.429 | 29.539 | 2270.879 | 14.019 | 2247.802 | 154.789 | 101 |
| 004 Z-2 | 0.504 | 0.107 | 0.041 | 6.352 | 0.797 | 0.326 | 0.041 | 0.956 | 1752.767 | 40.517 | 2025.667 | 22.244 | 1813.197 | 198.317 | 116 |
| 008 Z-4 | 0.610 | 0.127 | 0.027 | 7.505 | 0.535 | 0.383 | 0.027 | 0.962 | 2060.630 | 22.874 | 2173.553 | 11.415 | 2090.455 | 127.262 | 105 |
| 011 Z-5 | 0.152 | 0.146 | 0.040 | 8.851 | 0.819 | 0.431 | 0.040 | 0.919 | 2304.753 | 25.630 | 2322.774 | 11.972 | 2310.342 | 179.699 | 101 |
| 015 Z-7 | 0.645 | 0.138 | 0.023 | 8.339 | 0.458 | 0.413 | 0.023 | 0.953 | 2205.733 | 18.642 | 2268.620 | 8.947 | 2223.926 | 103.277 | 103 |
| 016 Z-8 | 0.585 | 0.123 | 0.032 | 7.306 | 0.621 | 0.374 | 0.032 | 0.942 | 2002.604 | 68.237 | 2149.492 | 34.267 | 2039.946 | 148.623 | 107 |
| 019 Z-9 | 0.605 | 0.128 | 0.036 | 7.672 | 0.708 | 0.387 | 0.036 | 0.852 | 2073.454 | 11.420 | 2193.295 | 5.695 | 2105.503 | 165.694 | 106 |
| 020 Z-10 | 0.623 | 0.132 | 0.021 | 7.866 | 0.411 | 0.398 | 0.021 | 0.810 | 2126.564 | 12.022 | 2215.844 | 5.904 | 2150.914 | 95.459 | 104 |
| 023 Z-11 | 0.429 | 0.094 | 0.008 | 5.095 | 0.152 | 0.277 | 0.008 | 0.968 | 1511.059 | 27.357 | 1835.341 | 16.516 | 1571.382 | 41.541 | 121 |
| 028 Z-14 | 0.631 | 0.136 | 0.024 | 8.291 | 0.497 | 0.407 | 0.024 | 0.929 | 2174.819 | 9.830 | 2263.319 | 4.767 | 2200.320 | 111.755 | 104 |
| 031 Z-15 | 0.152 | 0.124 | 0.015 | 7.458 | 0.288 | 0.377 | 0.015 | 0.908 | 2019.371 | 13.252 | 2167.974 | 6.712 | 2057.897 | 68.123 | 107 |
| 035 Z-17 | 0.618 | 0.134 | 0.015 | 8.041 | 0.291 | 0.401 | 0.015 | 0.908 | 2154.777 | 11.063 | 2235.587 | 5.392 | 2177.755 | 66.821 | 104 |
| 039 Z-19 | 0.598 | 0.128 | 0.012 | 7.735 | 0.240 | 0.387 | 0.012 | 0.866 | 2070.693 | 6.214 | 2200.639 | 3.106 | 2105.579 | 55.683 | 106 |
| 047 Z-23 | 0.570 | 0.120 | 0.023 | 6.952 | 0.445 | 0.364 | 0.023 | 0.948 | 1953.985 | 36.992 | 2105.260 | 18.992 | 1990.944 | 109.538 | 108 |
| 048 Z-24 | 0.656 | 0.140 | 0.057 | 8.841 | 1.193 | 0.421 | 0.057 | 0.915 | 2231.312 | 14.875 | 2321.691 | 7.097 | 2258.321 | 257.018 | 104 |
| 051 Z-25 | 0.571 | 0.122 | 0.027 | 7.305 | 0.525 | 0.369 | 0.027 | 0.956 | 1979.037 | 12.411 | 2149.362 | 6.366 | 2022.353 | 124.748 | 109 |

**Table 2.** Whole-rock geochemistry data of rocks in the Santa Luzia sequence, northeastern of Borborema province. n.d. - not determined; <l.d. - below limit of detection.

| Sample | AC-35C | PF04 | PF9C | PF11 | PF12 | PF14B | PF14C | PF15A | CG-6 | CG-2 | CG-31 |
|---|---|---|---|---|---|---|---|---|---|---|---|
| Longitude (W) | 36°16'12.57" | 36°22'52.29" | 36°38'6.48" | 36°36'21.95" | 36°36'41.92" | 36°20'46.57" | 36°20'46.57" | 36°18'58.38" | 36°25'31.92" | 36°25'19.35" | 36°24'47.91" |
| Latitude (S) | 5°42'41.22" | 5°34'48.28" | 5°54'9.57" | 5°58'7.11" | 6° 0'45.49" | 5°31'15.41" | 5°31'15.41" | 5°32'21.54" | 5°40'34.77" | 5°40'21.50" | 5°39'23.52" |
| Lithology | Amphibolite | Amphibolite | Amphibolite | Amphibolite | Amphibolite | Amphibolite | Amphibolite | Amphibolite | Amphibolite | Amphibolite | Amphibolite |
| SiO2 (wt%) | 49.92 | 49.20 | 50.60 | 53.20 | 53.80 | 51.90 | 51.80 | 51.10 | 49.27 | 48.77 | 48.88 |
| TiO2 (wt%) | 0.59 | 0.99 | 0.60 | 0.69 | 0.84 | 0.31 | 0.98 | 1.17 | 0.53 | 0.57 | 0.56 |
| Al2O3 (wt%) | 6.90 | 14.85 | 10.95 | 11.50 | 14.90 | 5.28 | 14.55 | 14.30 | 12.49 | 13.14 | 15.11 |
| Cr2O3 (wt%) | 0.23 | 0.03 | 0.14 | 0.09 | 0.05 | 0.20 | 0.04 | 0.04 | n.d. | n.d. | n.d. |
| Fe2O3t (wt%) | 12.56 | 12.35 | 10.05 | 10.30 | 11.30 | 11.20 | 12.40 | 11.90 | 11.05 | 9.17 | 9.72 |
| MnO (wt%) | 0.27 | 0.18 | 0.22 | 0.16 | 0.18 | 0.17 | 0.18 | 0.17 | 0.17 | 0.15 | 0.16 |
| MgO (wt%) | 13.63 | 6.20 | 11.25 | 7.17 | 5.45 | 16.25 | 6.35 | 5.26 | 10.76 | 10.66 | 8.81 |
| CaO (wt%) | 11.89 | 10.65 | 13.35 | 9.58 | 9.65 | 12.85 | 9.71 | 10.55 | 11.14 | 11.74 | 11.89 |
| Na2O (wt%) | 0.97 | 3.13 | 1.81 | 2.54 | 3.62 | 0.76 | 3.23 | 3.05 | 2.04 | 2.06 | 2.79 |
| K2O (wt%) | 1.26 | 0.67 | 0.56 | 0.68 | 0.75 | 0.48 | 1.21 | 0.59 | 0.69 | 1.03 | 0.77 |
| P2O5 (wt%) | 0.08 | 0.08 | 0.16 | 0.06 | 0.06 | 0.01 | 0.10 | 0.14 | 0.11 | 0.16 | 0.02 |
| LOI | 1.30 | 0.88 | 1.21 | 0.57 | 0.75 | 1.19 | 1.02 | 0.62 | 1.60 | 2.40 | 1.20 |
| Total | 99.60 | 99.24 | 100.94 | 96.57 | 101.39 | 100.60 | 101.64 | 98.92 | 99.85 | 99.85 | 99.91 |
| Ba (ppm) | 463.00 | 79.30 | 79.10 | 67.80 | 134.50 | 16.10 | 464.00 | 60.90 | 45.70 | 129.30 | 57.20 |
| Co (ppm) | 54.30 | 48.00 | 43.00 | 50.00 | 45.00 | 57.00 | 41.00 | 43.00 | 75.50 | 93.40 | 86.60 |
| Cs (ppm) | 0.50 | 0.04 | 0.30 | 0.08 | 0.05 | 0.02 | 0.10 | 0.09 | 0.40 | 0.60 | 0.10 |
| Cu (ppm) | 1.40 | 60.00 | 3.00 | 65.00 | 39.00 | 7.00 | 84.00 | 67.00 | 9.10 | n.d. | 5.00 |
| Ga (ppm) | 10.10 | 15.80 | 10.40 | 14.00 | 16.20 | 8.50 | 15.00 | 15.20 | 17.30 | 13.30 | 16.40 |
| Hf (ppm) | 1.30 | 1.60 | 2.20 | 1.50 | 2.00 | 1.10 | 1.80 | 3.00 | 1.30 | 1.60 | 0.50 |
| Nb (ppm) | 8.80 | 3.60 | 7.20 | 3.50 | 3.80 | 2.60 | 3.50 | 4.60 | 3.70 | 3.60 | 0.80 |
| Ni (ppm) | 298.00 | 119.00 | 148.00 | 161.00 | 110.00 | 175.00 | 105.00 | 107.00 | 110.00 | n.d. | 88.00 |
| Pb (ppm) | 1.10 | <l.d. | 4.00 | 3.00 | 3.00 | <l.d. | 4.00 | <l.d. | 2.30 | 5.40 | 1.10 |
| Rb (ppm) | 56.60 | 7.60 | 8.20 | 5.80 | 4.90 | 3.50 | 16.70 | 7.60 | 15.90 | 40.80 | 6.60 |
| Sc (ppm) | 52.00 | 36.00 | 39.00 | 30.00 | 38.00 | 34.00 | 31.00 | 28.00 | 35.00 | 35.00 | 49.00 |
| Sr (ppm) | 103.20 | 174.50 | 278.00 | 175.00 | 225.00 | 23.10 | 260.00 | 197.50 | 292.60 | 446.40 | 135.90 |
| Ta (ppm) | 0.60 | 0.20 | 0.30 | 0.20 | 0.30 | 0.10 | 0.20 | 0.20 | 0.30 | 0.50 | 0.30 |
| Th (ppm) | 0.60 | 0.52 | 2.93 | 1.35 | 2.23 | 0.27 | 0.94 | 0.86 | 1.40 | 3.70 | 0.20 |

| | | | | | | | | | | | |
|---|---|---|---|---|---|---|---|---|---|---|---|
| **U (ppm)** | 0.10 | 0.37 | 0.85 | 0.56 | 0.53 | 0.14 | 0.36 | 0.55 | 1.90 | 1.60 | 0.70 |
| **V (ppm)** | 178.00 | 260.00 | 136.00 | 192.00 | 239.00 | 117.00 | 228.00 | 229.00 | 150.00 | 143.00 | 232.00 |
| **Y (ppm)** | 30.70 | 22.70 | 15.10 | 15.80 | 20.80 | 10.10 | 21.40 | 23.80 | 14.90 | 16.50 | 14.00 |
| **Zn (ppm)** | 30.00 | 107.00 | 104.00 | 96.00 | 113.00 | 134.00 | 111.00 | 80.00 | 25.00 | 20.00 | 34.00 |
| **Zr (ppm)** | 38.50 | 51.00 | 93.00 | 51.00 | 64.00 | 34.00 | 66.00 | 114.00 | 33.80 | 36.60 | 12.00 |
| **La (ppm)** | 26.40 | 6.80 | 22.70 | 8.40 | 15.70 | 3.10 | 9.00 | 8.00 | 13.90 | 20.60 | 3.30 |
| **Ce (ppm)** | 66.80 | 14.70 | 38.50 | 16.30 | 28.30 | 6.70 | 17.70 | 19.20 | 30.80 | 32.90 | 6.30 |
| **Pr (ppm)** | 8.16 | 2.47 | 5.63 | 2.27 | 3.60 | 1.00 | 2.40 | 2.83 | 4.06 | 5.31 | 0.92 |
| **Nd (ppm)** | 31.00 | 10.70 | 23.90 | 10.60 | 15.10 | 5.80 | 11.30 | 13.10 | 17.50 | 22.80 | 4.60 |
| **Sm (ppm)** | 6.23 | 3.00 | 4.46 | 2.26 | 3.46 | 1.75 | 2.85 | 3.23 | 3.80 | 4.40 | 1.40 |
| **Eu (ppm)** | 1.78 | 0.92 | 1.18 | 0.87 | 0.89 | 0.49 | 0.85 | 1.10 | 0.96 | 1.27 | 0.63 |
| **Gd (ppm)** | 5.80 | 4.11 | 4.02 | 3.12 | 3.95 | 1.94 | 3.91 | 4.20 | 3.56 | 4.06 | 2.05 |
| **Tb (ppm)** | 0.95 | 0.68 | 0.53 | 0.49 | 0.62 | 0.32 | 0.63 | 0.68 | 0.59 | 0.65 | 0.38 |
| **Dy (ppm)** | 5.80 | 3.96 | 3.00 | 2.86 | 3.77 | 1.78 | 4.04 | 4.19 | 2.67 | 3.34 | 2.15 |
| **Ho (ppm)** | 1.17 | 0.78 | 0.54 | 0.61 | 0.72 | 0.33 | 0.75 | 0.83 | 0.54 | 0.58 | 0.54 |
| **Er (ppm)** | 3.28 | 2.47 | 1.46 | 1.60 | 2.13 | 0.91 | 2.15 | 2.62 | 1.51 | 1.46 | 1.39 |
| **Tm (ppm)** | 0.51 | 0.38 | 0.20 | 0.27 | 0.33 | 0.14 | 0.35 | 0.40 | 0.21 | 0.23 | 0.21 |
| **Yb (ppm)** | 3.37 | 2.47 | 1.31 | 1.64 | 2.21 | 0.92 | 2.39 | 2.60 | 1.26 | 1.15 | 1.27 |
| **Lu (ppm)** | 0.50 | 0.35 | 0.21 | 0.25 | 0.33 | 0.13 | 0.33 | 0.37 | 0.21 | 0.22 | 0.23 |
| **Mg-number** | 37.84 | 23.84 | 41.11 | 30.27 | 23.12 | 47.50 | 24.20 | 21.61 | 37.78 | 42.02 | 36.11 |
| **∑REE** | 161.75 | 53.79 | 107.64 | 51.54 | 81.11 | 25.31 | 58.65 | 63.35 | 81.57 | 98.97 | 25.37 |

**Table 2.** Continuation.

| **Sample** | **CG-55** | **CG-68** | **MC-51B** | **SL-1** | **SL-3C** | **SL-6B** | **SL-6D** | **SL-6F** | **SL-6G** | **PF21F** | **CG-84** |
|---|---|---|---|---|---|---|---|---|---|---|---|
| **Longitude (W)** | **36°24'54.70"** | **36°22'28.15"** | **36°24'39.50"** | **36°26'36.04"** | **36°24'47.95"** | **36°24'56.12"** | **36°24'56.12"** | **36°24'56.12"** | **36°24'56.12"** | **36°24'48.90"** | **36°24'15.23"** |
| **Latitude (S)** | **5°38'37.93"** | **5°40'51.70"** | **5°40'21.62"** | **5°37'20.40"** | **5°38'8.66"** | **5°39'24.50"** | **5°39'24.50"** | **5°39'24.50"** | **5°39'24.50"** | **5°38'8.18"** | **5°38'12.28"** |
| **Lithology** | **Garnet-bearing calc-silicate** | **Garnet-bearing calc-silicate** | **Garnet-bearing calc-silicate** | **Garnet-bearing calc-silicate** | **Garnet-bearing calc-silicate** | **Garnet-bearing calc-silicate** | **Garnet-bearing calc-silicate** | **Garnet-bearing calc-silicate** | **Garnet-bearing calc-silicate** | **Garnet-bearing calc-silicate** | **Garnet-bearing calc-silicate** |
| **SiO2 (wt%)** | 51.31 | 49.55 | 39.17 | 48.68 | 47.74 | 44.79 | 46.22 | 39.17 | 48.34 | 41.50 | 64.06 |
| **TiO2 (wt%)** | 0.71 | 0.40 | 0.42 | 0.90 | 0.95 | 1.18 | 0.97 | 0.82 | 0.36 | 0.86 | 0.60 |
| **Al2O3 (wt%)** | 16.16 | 16.18 | 16.26 | 12.81 | 22.09 | 21.45 | 10.25 | 24.87 | 18.02 | 25.20 | 15.81 |
| **Cr2O3 (wt%)** | n.d. | n.d. | n.d. | 0.09 | 0.00 | 0.03 | 0.00 | 0.01 | 0.00 | 0.04 | n.d. |

| | | | | | | | | | | | |
|---|---|---|---|---|---|---|---|---|---|---|---|
| **Fe2O3t (wt%)** | 7.03 | 3.20 | 13.43 | 9.48 | 7.37 | 9.26 | 14.54 | 8.01 | 10.52 | 8.36 | 5.40 |
| **MnO (wt%)** | 0.07 | 0.10 | 0.16 | 0.14 | 0.10 | 0.11 | 0.12 | 0.12 | 0.05 | 0.30 | 0.08 |
| **MgO (wt%)** | 1.76 | 1.93 | 2.25 | 11.91 | 1.59 | 3.40 | 7.81 | 3.03 | 0.23 | 4.01 | 2.21 |
| **CaO (wt%)** | 17.20 | 13.88 | 19.98 | 9.05 | 16.65 | 15.84 | 16.14 | 19.55 | 17.12 | 18.05 | 4.21 |
| **Na2O (wt%)** | 1.12 | 3.44 | 0.30 | 2.36 | 1.98 | 1.92 | 1.44 | 0.57 | 1.75 | 0.77 | 4.16 |
| **K2O (wt%)** | 0.17 | 0.42 | 0.14 | 1.73 | 0.13 | 0.48 | 0.83 | 0.45 | 0.99 | 0.90 | 1.72 |
| **P2O5 (wt%)** | 0.22 | 0.13 | 0.08 | 0.27 | 0.25 | 0.31 | 0.05 | 0.14 | 0.28 | 0.10 | 0.19 |
| **LOI** | 1.30 | 2.80 | 1.40 | 2.10 | 0.80 | 0.80 | 1.30 | 2.70 | 2.10 | <l.d. | 1.50 |
| **Total** | 97.05 | 92.03 | 93.59 | 99.52 | 99.65 | 99.57 | 99.67 | 99.44 | 99.76 | 100.73 | |
| **Ba (ppm)** | 655.70 | 352.30 | 29.70 | 489.00 | 150.00 | 178.00 | 102.00 | 467.00 | 184.00 | 2800.00 | 89.40 |
| **Co (ppm)** | 67.50 | 63.10 | 63.80 | 60.60 | 28.30 | 51.20 | 26.40 | 29.80 | 23.30 | 26.00 | 120.00 |
| **Cs (ppm)** | 0.60 | 5.10 | 0.20 | 1.20 | 0.50 | 0.30 | 0.30 | 0.20 | 0.80 | 0.25 | 2.30 |
| **Cu (ppm)** | 0.70 | 0.60 | 0.20 | 65.10 | 1.50 | 0.30 | 1.70 | 0.30 | 1.30 | 3.00 | 2.70 |
| **Ga (ppm)** | 36.20 | 27.30 | 36.10 | 15.30 | 33.00 | 30.60 | 16.50 | 38.30 | 15.30 | 39.20 | 21.50 |
| **Hf (ppm)** | 9.00 | 5.50 | 1.80 | 2.80 | 6.80 | 10.70 | 6.10 | 5.70 | 2.00 | 2.70 | 4.20 |
| **Nb (ppm)** | 8.80 | 4.80 | 2.30 | 10.80 | 7.80 | 10.20 | 12.60 | 6.20 | 4.00 | 7.20 | 21.00 |
| **Ni (ppm)** | 16.00 | 25.00 | 20.00 | n.d. | <l.d. | 46.00 | 75.00 | 31.00 | <l.d. | 68.00 | 26.00 |
| **Pb (ppm)** | 4.60 | 5.20 | 6.90 | 6.20 | 3.90 | 5.00 | 2.70 | 2.70 | 8.00 | 7.00 | 2.30 |
| **Rb (ppm)** | 5.60 | 23.20 | 3.60 | 76.40 | 6.30 | 7.70 | 21.70 | 12.10 | 53.10 | 15.90 | 130.00 |
| **Sc (ppm)** | 13.00 | 4.00 | 9.00 | 23.00 | 10.00 | 17.00 | 17.00 | 14.00 | 5.00 | 7.00 | 13.00 |
| **Sr (ppm)** | 1641.40 | 1103.20 | 3024.80 | 541.00 | 1956.10 | 1712.20 | 542.70 | 2995.20 | 1182.60 | 2850.00 | 284.50 |
| **Ta (ppm)** | 0.70 | 0.60 | 0.30 | 0.80 | 0.50 | 0.60 | 0.80 | 0.50 | 0.30 | 0.50 | 1.50 |
| **Th (ppm)** | 9.70 | 11.70 | 3.00 | 5.80 | 5.80 | 6.50 | 5.10 | 11.50 | 3.80 | 2.64 | 5.30 |
| **U (ppm)** | 1.70 | 9.80 | 2.50 | 1.90 | 1.90 | 1.60 | 2.60 | 2.00 | 1.00 | 0.49 | 1.10 |
| **V (ppm)** | 131.00 | 38.00 | 64.00 | 133.00 | 122.00 | 105.00 | 91.00 | 175.00 | 31.00 | 179.00 | 75.00 |
| **Y (ppm)** | 20.00 | 13.20 | 27.80 | 16.70 | 19.20 | 22.30 | 33.80 | 13.60 | 19.80 | 7.40 | 24.00 |
| **Zn (ppm)** | 3.00 | 8.00 | 9.00 | 35.00 | 8.00 | 23.00 | 15.00 | 14.00 | 7.00 | 52.00 | 70.00 |
| **Zr (ppm)** | 341.70 | 183.80 | 45.90 | 99.70 | 315.30 | 439.70 | 261.30 | 200.00 | 75.70 | 106.00 | 170.20 |
| **La (ppm)** | 66.00 | 75.90 | 16.90 | 40.60 | 52.80 | 55.00 | 63.10 | 31.20 | 51.30 | 17.50 | 22.50 |
| **Ce (ppm)** | 134.30 | 129.60 | 45.90 | 80.50 | 98.80 | 105.70 | 129.70 | 51.90 | 97.00 | 29.90 | 44.20 |
| **Pr (ppm)** | 14.03 | 13.09 | 6.41 | 8.86 | 10.41 | 11.23 | 15.07 | 5.09 | 10.95 | 2.90 | 5.21 |
| **Nd (ppm)** | 48.70 | 41.50 | 25.70 | 32.30 | 36.10 | 42.40 | 59.70 | 17.30 | 40.80 | 11.30 | 20.10 |
| **Sm (ppm)** | 7.50 | 5.40 | 5.00 | 5.28 | 5.38 | 7.09 | 11.31 | 2.92 | 7.24 | 2.03 | 5.00 |
| **Eu (ppm)** | 1.36 | 1.73 | 0.98 | 1.49 | 2.04 | 2.62 | 3.48 | 2.11 | 2.68 | 0.92 | 0.79 |
| **Gd (ppm)** | 6.51 | 3.03 | 4.78 | 4.45 | 4.52 | 5.80 | 10.44 | 2.73 | 5.86 | 1.68 | 4.79 |
| **Tb (ppm)** | 0.93 | 0.49 | 0.81 | 0.59 | 0.58 | 0.80 | 1.39 | 0.39 | 0.75 | 0.24 | 0.77 |

| | | | | | | | | | | | |
|---|---|---|---|---|---|---|---|---|---|---|---|
| **Dy (ppm)** | 4.41 | 2.46 | 4.59 | 3.28 | 3.29 | 4.29 | 6.97 | 2.35 | 3.84 | 1.29 | 4.38 |
| **Ho (ppm)** | 0.69 | 0.46 | 1.01 | 0.61 | 0.59 | 0.80 | 1.28 | 0.45 | 0.64 | 0.29 | 0.79 |
| **Er (ppm)** | 1.91 | 1.24 | 2.86 | 1.62 | 1.71 | 2.07 | 2.94 | 1.29 | 1.78 | 0.78 | 2.33 |
| **Tm (ppm)** | 0.25 | 0.19 | 0.40 | 0.24 | 0.29 | 0.30 | 0.41 | 0.22 | 0.25 | 0.13 | 0.29 |
| **Yb (ppm)** | 1.42 | 1.16 | 2.71 | 1.35 | 1.73 | 1.94 | 2.50 | 1.42 | 1.70 | 0.87 | 1.76 |
| **Lu (ppm)** | 0.24 | 0.19 | 0.43 | 0.21 | 0.33 | 0.33 | 0.40 | 0.22 | 0.26 | 0.14 | 0.26 |
| **Mg-number** | 13.50 | 27.33 | 9.46 | 43.93 | 11.86 | 18.63 | 25.09 | 19.08 | 1.34 | 23.02 | 20.33 |
| **∑REE** | 288.25 | 276.44 | 118.48 | 181.38 | 218.57 | 240.37 | 308.69 | 119.59 | 225.05 | 69.97 | 113.17 |

**Table 2.** Continuation.

| **Sample** | **PF21A** | **PF21B** | **PF21H** | **PF22A** | **PF22B** | **SL-4B** | **SL-4C** |
|---|---|---|---|---|---|---|---|
| **Longitude (W)** | **36°24'48.90"** | **36°24'48.90"** | **36°24'48.90"** | **36°24'32.25"** | **36°24'32.25"** | **36°24'30.81"** | **36°24'30.81"** |
| **Latitude (S)** | **5°38'8.18"** | **5°38'8.18"** | **5°38'8.18"** | **5°39'3.02"** | **5°39'3.02"** | **5°39'3.46"** | **5°39'3.46"** |
| **Lithology** | **Epidote-rich calc-silicate** | **Epidote-rich calc-silicate** | **Epidote-rich calc-silicate** | **Epidote-rich calc-silicate** | **Epidote-rich calc-silicate** | **Epidote-rich calc-silicate** | **Epidote-rich calc-silicate** |
| **SiO2 (wt%)** | 37.20 | 37.00 | 41.20 | 38.20 | 40.90 | 58.22 | 39.68 |
| **TiO2 (wt%)** | 1.26 | 1.18 | 1.07 | 1.51 | 1.13 | 1.09 | 1.76 |
| **Al2O3 (wt%)** | 23.90 | 23.30 | 22.90 | 20.90 | 19.70 | 15.33 | 20.91 |
| **Cr2O3 (wt%)** | 0.02 | 0.05 | 0.03 | 0.04 | 0.02 | 0.01 | 0.01 |
| **Fe2O3t (wt%)** | 10.50 | 11.25 | 10.15 | 15.30 | 14.60 | 9.72 | 13.99 |
| **MnO (wt%)** | 0.15 | 0.17 | 0.11 | 0.22 | 0.09 | 0.08 | 0.08 |
| **MgO (wt%)** | 3.02 | 4.23 | 2.73 | 3.69 | 1.98 | 1.92 | 3.63 |
| **CaO (wt%)** | 19.30 | 19.65 | 19.25 | 17.75 | 18.95 | 7.92 | 16.96 |
| **Na2O (wt%)** | 0.40 | 0.81 | 0.71 | 0.78 | 0.86 | 3.59 | 0.66 |
| **K2O (wt%)** | 0.69 | 0.32 | 0.33 | 0.65 | 0.13 | 0.48 | 0.68 |
| **P2O5 (wt%)** | 0.41 | 0.30 | 0.38 | 0.07 | 0.35 | 0.32 | 0.18 |
| **LOI** | 1.16 | 1.16 | <l.d. | 1.23 | 0.65 | 1.00 | 1.00 |
| **Total** | 98.34 | 99.77 | 99.15 | 100.54 | 99.53 | 99.68 | 99.54 |
| **Ba (ppm)** | 206.00 | 62.50 | 95.10 | 155.50 | 64.80 | 140.00 | 152.00 |
| **Co (ppm)** | 20.00 | 27.00 | 18.00 | 20.00 | 10.00 | 48.60 | 38.00 |
| **Cs (ppm)** | 0.35 | 0.13 | 0.09 | 0.35 | 0.26 | 0.10 | 0.20 |
| **Cu (ppm)** | <l.d. | 3.00 | 1.00 | 4.00 | 3.00 | 1.90 | 0.30 |
| **Ga (ppm)** | 30.70 | 28.30 | 39.70 | 47.70 | 44.40 | 22.80 | 41.00 |

| | | | | | | | |
|---|---|---|---|---|---|---|---|
| **Hf (ppm)** | 12.50 | 8.30 | 11.20 | 18.10 | 14.60 | 12.40 | 21.10 |
| **Nb (ppm)** | 16.30 | 13.40 | 16.50 | 18.30 | 15.20 | 13.30 | 18.90 |
| **Ni (ppm)** | 22.00 | 27.00 | 16.00 | 41.00 | 28.00 | <l.d. | 28.00 |
| **Pb (ppm)** | 6.00 | 12.00 | 10.00 | 7.00 | 7.00 | 2.50 | 4.80 |
| **Rb (ppm)** | 21.20 | 4.20 | 2.20 | 7.80 | 7.20 | 7.10 | 6.60 |
| **Sc (ppm)** | 14.00 | 14.00 | 11.00 | 22.00 | 17.00 | 15.00 | 21.00 |
| **Sr (ppm)** | 2700.00 | 2860.00 | 2420.00 | 1450.00 | 1480.00 | 639.50 | 1428.00 |
| **Ta (ppm)** | 0.20 | 0.20 | 1.10 | 1.10 | 1.00 | 0.80 | 0.90 |
| **Th (ppm)** | 10.40 | 6.10 | 14.60 | 15.25 | 15.45 | 14.10 | 14.60 |
| **U (ppm)** | 2.18 | 1.65 | 3.05 | 7.78 | 4.41 | 2.90 | 5.90 |
| **V (ppm)** | 131.00 | 124.00 | 152.00 | 184.00 | 191.00 | 134.00 | 172.00 |
| **Y (ppm)** | 59.50 | 53.90 | 40.40 | 54.80 | 44.10 | 39.50 | 52.40 |
| **Zn (ppm)** | 66.00 | 89.00 | 71.00 | 31.00 | 48.00 | 27.00 | 8.00 |
| **Zr (ppm)** | 552.00 | 378.00 | 500.00 | 794.00 | 633.00 | 534.40 | 880.00 |
| **La (ppm)** | 117.50 | 65.30 | 102.50 | 143.50 | 183.00 | 131.50 | 102.60 |
| **Ce (ppm)** | 235.00 | 141.00 | 199.50 | 274.00 | 348.00 | 247.30 | 241.90 |
| **Pr (ppm)** | 27.30 | 18.05 | 21.30 | 28.90 | 34.30 | 25.20 | 23.51 |
| **Nd (ppm)** | 106.00 | 77.50 | 82.50 | 102.50 | 114.50 | 85.50 | 82.70 |
| **Sm (ppm)** | 16.60 | 14.40 | 13.40 | 16.30 | 15.55 | 12.48 | 14.18 |
| **Eu (ppm)** | 3.56 | 3.25 | 3.06 | 4.04 | 3.69 | 3.07 | 4.28 |
| **Gd (ppm)** | 15.90 | 14.50 | 11.20 | 13.45 | 12.30 | 10.00 | 12.45 |
| **Tb (ppm)** | 2.16 | 2.00 | 1.53 | 1.95 | 1.67 | 1.38 | 1.73 |
| **Dy (ppm)** | 11.40 | 10.60 | 8.43 | 10.90 | 8.85 | 8.01 | 9.81 |
| **Ho (ppm)** | 2.12 | 1.89 | 1.63 | 2.14 | 1.77 | 1.39 | 1.87 |
| **Er (ppm)** | 5.89 | 5.57 | 4.14 | 5.73 | 4.89 | 3.85 | 5.09 |
| **Tm (ppm)** | 0.84 | 0.78 | 0.63 | 0.80 | 0.66 | 0.58 | 0.76 |
| **Yb (ppm)** | 5.18 | 4.79 | 3.71 | 4.45 | 3.84 | 3.39 | 4.48 |
| **Lu (ppm)** | 0.68 | 0.63 | 0.53 | 0.72 | 0.68 | 0.51 | 0.70 |
| **Mg-number** | 15.21 | 18.99 | 14.36 | 13.07 | 7.80 | 10.97 | 13.93 |
| **∑REE** | 550.13 | 360.26 | 454.06 | 609.38 | 733.70 | 534.16 | 506.06 |

**Table 3.** Continuation.

| Sample | PF13A | PF17A | PF18A | PF18C | PF18G |
|---|---|---|---|---|---|
| Longitude (W) | 36°36'36.99" | 36°26'10.00" | 36°15'39.60" | 36°15'39.60" | 36°15'39.60" |
| Latitude (S) | 5°59'38.49" | 5°38'43.00" | 5°23'3.48" | 5°23'3.48" | 5°23'3.48" |
| Lithology | Honrblendite | Honrblendite | Honrblendite | Honrblendite | Honrblendite |
| SiO2 (wt%) | 51.90 | 49.30 | 51.90 | 50.40 | 55.20 |
| TiO2 (wt%) | 0.55 | 0.30 | 0.29 | 0.32 | 0.22 |
| Al2O3 (wt%) | 5.72 | 3.55 | 3.45 | 3.18 | 3.07 |
| Cr2O3 (wt%) | 0.12 | 0.19 | 0.16 | 0.17 | 0.19 |
| Fe2O3t (wt%) | 12.20 | 11.20 | 10.15 | 12.20 | 8.99 |
| MnO (wt%) | 0.24 | 0.18 | 0.21 | 0.18 | 0.18 |
| MgO (wt%) | 15.05 | 18.65 | 16.80 | 20.00 | 18.10 |
| CaO (wt%) | 12.60 | 12.95 | 12.85 | 12.35 | 13.20 |
| Na2O (wt%) | 0.76 | 0.67 | 0.64 | 0.64 | 0.62 |
| K2O (wt%) | 0.38 | 0.22 | 0.31 | 0.21 | 0.22 |
| P2O5 (wt%) | 0.08 | 0.05 | 0.03 | 0.03 | 0.02 |
| LOI | 1.16 | 1.11 | 1.75 | 0.87 | 1.98 |
| Total | 100.76 | 98.39 | 98.55 | 100.56 | 101.99 |
| Ba (ppm) | 28.30 | 176.00 | 62.40 | 65.50 | 12.20 |
| Co (ppm) | 65.00 | 79.00 | 68.00 | 95.00 | 56.00 |
| Cs (ppm) | 0.05 | 0.23 | 0.08 | 0.13 | 0.06 |
| Cu (ppm) | 27.00 | 51.00 | 115.00 | 36.00 | 14.00 |
| Ga (ppm) | 11.30 | 5.00 | 4.80 | 4.60 | 4.20 |
| Hf (ppm) | 1.50 | 1.00 | 1.00 | 0.80 | 1.00 |
| Nb (ppm) | 6.50 | 3.20 | 1.50 | 0.90 | 2.60 |
| Ni (ppm) | 185.00 | 237.00 | 140.00 | 289.00 | 177.00 |
| Pb (ppm) | 2.00 | <l.d. | <l.d. | <l.d. | <l.d. |
| Rb (ppm) | 4.80 | 3.60 | 5.60 | 2.80 | 1.40 |
| Sc (ppm) | 51.00 | 41.00 | 43.00 | 36.00 | 36.00 |
| Sr (ppm) | 37.50 | 115.50 | 55.10 | 96.20 | 21.30 |
| Ta (ppm) | 0.50 | 0.10 | 0.10 | 0.10 | 0.50 |
| Th (ppm) | 2.72 | 5.97 | 1.12 | 0.18 | 1.88 |
| U (ppm) | 1.25 | 0.23 | 0.32 | 0.06 | 0.74 |
| V (ppm) | 191.00 | 111.00 | 130.00 | 116.00 | 100.00 |

| | | | | | |
|---|---|---|---|---|---|
| **Y (ppm)** | 27.70 | 16.20 | 10.70 | 8.20 | 8.80 |
| **Zn (ppm)** | n.d. | n.d. | n.d. | n.d. | n.d. |
| **Zr (ppm)** | 31.00 | 31.00 | 48.00 | 22.00 | 29.00 |
| **La (ppm)** | 10.90 | 23.80 | 9.30 | 3.90 | 10.90 |
| **Ce (ppm)** | 37.10 | 47.70 | 16.50 | 10.90 | 20.40 |
| **Pr (ppm)** | 4.83 | 6.05 | 2.45 | 1.77 | 2.63 |
| **Nd (ppm)** | 20.50 | 25.80 | 11.30 | 8.60 | 11.00 |
| **Sm (ppm)** | 4.66 | 4.82 | 2.31 | 2.03 | 2.16 |
| **Eu (ppm)** | 0.91 | 1.44 | 0.63 | 0.50 | 0.55 |
| **Gd (ppm)** | 4.89 | 5.00 | 3.06 | 2.15 | 2.21 |
| **Tb (ppm)** | 0.75 | 0.61 | 0.37 | 0.31 | 0.31 |
| **Dy (ppm)** | 4.17 | 3.43 | 1.97 | 1.61 | 1.55 |
| **Ho (ppm)** | 0.84 | 0.59 | 0.34 | 0.28 | 0.34 |
| **Er (ppm)** | 2.79 | 1.62 | 1.13 | 0.82 | 0.84 |
| **Tm (ppm)** | 0.44 | 0.23 | 0.14 | 0.13 | 0.15 |
| **Yb (ppm)** | 3.44 | 1.53 | 0.84 | 0.75 | 0.83 |
| **Lu (ppm)** | 0.52 | 0.16 | 0.15 | 0.10 | 0.10 |
| **Mg-number** | 43.48 | 50.94 | 50.79 | 50.55 | 55.66 |
| **∑REE** | 96.74 | 122.78 | 50.49 | 33.85 | 53.97 |

**Table 4.** Sm-Nd isotopic data of rocks in the Santa Luzia sequence, northeastern of Borborema province.

| Sample | AC-35C | PF-01 | PF-09B | PF-09D | PF-16A | PF-16B | PF-02A | PF-06 | PF-09C | PF-12 | PF-15A | PF-16C |
|---|---|---|---|---|---|---|---|---|---|---|---|---|
| Region | Lages block | Lages block | Lages block | Lages block | Lages block | Lages block | Lages block | Lages block | Lages block | Lages block | Lages block | Lages block |
| Data source | this study | this study | this study | this study | this study | this study | this study | this study | this study | this study | this study | this study |
| Lithology | Amphibolite | Amphibolite | Amphibolite | Amphibolite | Amphibolite | Amphibolite | Amphibolite | Amphibolite | Amphibolite | Amphibolite | Amphibolite | Amphibolite |
| Longitude (W) | 36°16'12.57" | 36°22'37.62" | 36°38'6.48" | 36°38'6.48" | 36°17'28.62" | 36°17'28.62" | 36°18'58.38" | 36°28'38.37" | 36°38'6.48" | 36°36'41.92" | 36°18'58.38" | 36°15'39.60" |
| Latitude (S) | 5°42'41.22 | 5°33'53.26" | 5°54'9.57" | 5°54'9.57" | 5°34'6.15" | 5°34'6.15" | 5°32'21.54" | 5°34'43.32" | 5°54'9.57" | 6° 0'45.49" | 5°32'21.54" | 5°23'3.48" |
| Sm(ppm) | 7.813 | 5.815 | 12.832 | 2.135 | 10.260 | 8.847 | 2.455 | 3.570 | 4.964 | 3.455 | 3.527 | 2.648 |
| Nd(ppm) | 39.934 | 32.015 | 85.167 | 13.598 | 48.814 | 45.916 | 10.414 | 16.643 | 26.392 | 15.585 | 13.432 | 12.828 |
| Sm/Nd | 0.196 | 0.182 | 0.151 | 0.157 | 0.210 | 0.193 | 0.236 | 0.214 | 0.188 | 0.222 | 0.263 | 0.206 |
| $^{147}Sm/^{144}Nd$ | 0.11830 | 0.10979 | 0.09108 | 0.09489 | 0.12706 | 0.11647 | 0.14252 | 0.12966 | 0.11370 | 0.13399 | 0.15872 | 0.12478 |
| $^{143}Nd/^{144}Nd$ | 0.511484 | 0.511312 | 0.511239 | 0.511493 | 0.511923 | 0.511737 | 0.511720 | 0.511947 | 0.511363 | 0.511770 | 0.512170 | 0.511353 |
| ± 2s | 11 | 14 | 18 | 12 | 12 | 10 | 6 | 11 | 5 | 7 | 8 | 6 |
| $e_{Nd\ (0)}$ | -22.50 | -25.87 | -27.29 | -22.34 | -13.95 | -17.58 | -17.91 | -13.48 | -24.87 | -16.93 | -9.13 | -25.07 |
| $e_{Nd\ (t)}$ | 1.73 | -0.14 | 2.62 | 2.55 | 3.09 | 2.04 | -1.86 | 2.92 | -0.30 | 1.66 | 2.15 | -3.79 |
| $T_{DM\ (Ga)}$ | 2.65 | 2.68 | 2.36 | 2.12 | 2.15 | 2.21 | 3.04 | 2.17 | 2.71 | 2.62 | 2.70 | 3.06 |

**Table 4.** Continuation.

| Sample | CG-55 | CG 68 | CG 84 | PF-21F | PF-09A | PF-21A | PF-21B | PF-21D | PF-21E(I) | PF-21H | PF-22A |
|---|---|---|---|---|---|---|---|---|---|---|---|
| Region | Lages block | Lages block | Lages block | Lages block | Lages block | Lages block | Lages block | Lages block | Lages block | Lages block | Lages block |
| Data source | this study | this study | this study | this study | this study | this study | this study | this study | this study | this study | this study |
| Lithology | Garnet-bearing calc-silicat gneiss | Garnet-bearing calc-silicat gneiss | Garnet-bearing calc-silicat gneiss | Garnet-bearing calc-silicat gneiss | Epidote-bearing calc-silicat gneiss | Epidote-bearing calc-silicat gneiss | Epidote-bearing calc-silicat gneiss | Epidote-bearing calc-silicat gneiss | Epidote-bearing calc-silicat gneiss | Epidote-bearing calc-silicat gneiss | Epidote-bearing calc-silicat gneiss |
| Longitude (W) | 36°24'54.70" | 36°22'28.15" | 36°24'15.23" | 36°24'48.90" | 36°38'6.48" | 36°24'48.90" | 36°24'48.90" | 36°24'48.90" | 36°24'48.90" | 36°24'48.90" | 36°24'32.25" |
| Latitude (S) | 5°38'37.93" | 5°40'51.70" | 5°38'12.28" | 5°38'8.18" | 5°54'9.57" | 5°38'8.18" | 5°38'8.18" | 5°38'8.18" | 5°38'8.18" | 5°38'8.18" | 5°39'3.02" |
| Sm(ppm) | 7.591 | 5.324 | 4.576 | 1.735 | 8.287 | 16.679 | 15.483 | 0.498 | 11.536 | 16.599 | 15.707 |
| Nd(ppm) | 44.565 | 41.411 | 20.035 | 10.045 | 35.863 | 107.527 | 79.435 | 3.190 | 48.021 | 100.519 | 101.318 |
| Sm/Nd | 0.170 | 0.129 | 0.228 | 0.173 | 0.231 | 0.155 | 0.195 | 0.156 | 0.240 | 0.165 | 0.155 |
| $^{147}Sm/^{144}Nd$ | 0.10300 | 0.07770 | 0.13810 | 0.10444 | 0.13968 | 0.09377 | 0.11783 | 0.09434 | 0.14521 | 0.09982 | 0.09371 |
| $^{143}Nd/^{144}Nd$ | 0.511020 | 0.510757 | 0.511163 | 0.511486 | 0.511644 | 0.511122 | 0.511413 | 0.511188 | 0.511715 | 0.511123 | 0.511378 |
| ± 2s | 6 | 6 | 8 | 8 | 6 | 14 | 4 | 14 | 13 | 11 | 18 |
| $e_{Nd\ (0)}$ | -31.56 | -36.69 | -28.77 | -22.47 | -19.39 | -29.57 | -23.90 | -28.29 | -18.00 | -29.55 | -24.58 |

| | | | | | | | | | | | |
|---|---|---|---|---|---|---|---|---|---|---|---|
| $e_{Nd\ (t)}$ | -3.48 | -1.02 | -11.25 | 1.27 | -3.44 | 0.90 | -0.54 | 2.03 | -2.76 | -0.88 | 1.92 |
| $T_{DM\ (Ga)}$ | 2.91 | 2.67 | 3.97 | 2.31 | 3.08 | 2.56 | 2.75 | 2.49 | 3.17 | 2.70 | 2.24 |

**4.** Continuation.

| **Sample** | **PF-13A** | **PF-13C** | **PF-13D** | **PF-17A** | **PF-17B** | **PF-18C** | **PF-18G** |
|---|---|---|---|---|---|---|---|
| **Region** | **Lages block** | **Lages block** | **Lages block** | **Lages block** | **Lages block** | **Lages block** | **Lages block** |
| **Data source** | **this study** | **this study** | **this study** | **this study** | **this study** | **this study** | **this study** |
| **Lithology** | **Hornblendite** | **Hornblendite** | **Hornblendite** | **Hornblendite** | **Hornblendite** | **Hornblendite** | **Hornblendite** |
| **Longitude (W)** | **36°36'36.99"** | **36°36'36.99"** | **36°36'36.99"** | **36°26'10.00"** | **36°26'10.00"** | **36°15'39.60"** | **36°15'39.60"** |
| **Latitude (S)** | **5°59'38.49"** | **5°59'38.49"** | **5°59'38.49"** | **5°38'43.00"** | **5°38'43.00"** | **5°23'3.48"** | **5°23'3.48"** |
| **Sm(ppm)** | 4.952 | 4.231 | 3.084 | 3.187 | 0.142 | 2.203 | 2.242 |
| **Nd(ppm)** | 22.272 | 19.231 | 14.243 | 14.280 | 0.978 | 9.344 | 10.822 |
| **Sm/Nd** | 0.222 | 0.220 | 0.217 | 0.223 | 0.145 | 0.236 | 0.207 |
| **$^{147}Sm/^{144}Nd$** | 0.13449 | 0.13309 | 0.13099 | 0.13493 | 0.08764 | 0.14262 | 0.12531 |
| **$^{143}Nd/^{144}Nd$** | 0.511684 | 0.511928 | 0.511907 | 0.511664 | 0.511252 | 0.511777 | 0.511585 |
| **± 2s** | 14 | 18 | 6 | 9 | 14 | 18 | 16 |
| $e_{Nd\ (0)}$ | -18.61 | -19.00 | -16.80 | -20.54 | -13.85 | -14.26 | -27.04 |
| $e_{Nd\ (t)}$ | -1.01 | -0.62 | -0.67 | 0.73 | 2.56 | 2.69 | 1.03 |
| $T_{DM\ (Ga)}$ | 2.80 | 2.86 | 2.92 | 2.68 | 2.30 | 2.28 | 2.28 |

**Suplementary Table 1.** U-Pb in zircon (Reference Materials).

| | | | | Data for Tera-Wasserburg plot | | | | | | Data for Wetherill plot | | | | | | | | Dates | | | | | | | | | | |
|---|---|---|---|---|---|---|---|---|---|---|---|---|---|---|---|---|---|---|---|---|---|---|---|---|---|---|---|---|
| Identifier | Th/U | $^{206}Pb/^{204}Pb$ | 1s% | $^{238}U/^{206}Pb$ | 1s% | $^{207}Pb/^{206}Pb$ | 1s% | $^{208}Pb/^{206}Pb$ | 1s% | $^{207}Pb/^{235}U$ | 1s% | $^{206}Pb/^{238}U$ | 1s% | Rho | $^{208}Pb/^{232}Th$ | 1s% | $^{207}Pb/^{206}Pb$ | 2s (abs) | 2ssys (abs) | $^{206}Pb/^{238}U$ | 2s (abs) | 2ssys (abs) | $^{207}Pb/^{235}U$ | 2s (abs) | 2ssys (abs) | $^{208}Pb/^{232}Th$ | 2s (abs) | 2ssys (abs) | % conc |
| GJ1-1.FIN2 | 0.033 | -3866.062 | -2.564 | 10.458 | 0.974 | 0.060 | 1.431 | 0.014 | 44.398 | 0.801 | 1.296 | 0.097 | 0.947 | 0.283 | 0.048 | 18.098 | 561.819 | 57.418 | 62.229 | 593.848 | 7.727 | 10.756 | 595.647 | 10.856 | 11.457 | 795.448 | 156.504 | 186.552 | 105.701 |
| GJ1-2.FIN2 | 0.033 | -3114.536 | -2.814 | 10.205 | 0.923 | 0.060 | 1.534 | 0.011 | 69.594 | 0.822 | 1.388 | 0.098 | 0.919 | 0.134 | 0.031 | 15.705 | 561.969 | 63.441 | 67.991 | 603.820 | 7.381 | 10.589 | 606.718 | 12.355 | 12.945 | 585.573 | 135.947 | 174.543 | 107.447 |
| GJ1-3.FIN2 | 0.033 | -2990.268 | -4.053 | 10.174 | 0.988 | 0.059 | 1.891 | 0.004 | 28.430 | 0.803 | 1.537 | 0.099 | 0.967 | -0.094 | 0.023 | 16.058 | 500.438 | 73.007 | 76.327 | 607.662 | 8.196 | 11.203 | 594.984 | 13.282 | 13.791 | 456.176 | 115.154 | 145.807 | 121.426 |
| GJ1-4.FIN2 | 0.033 | -3465.142 | -3.778 | 10.341 | 1.094 | 0.060 | 2.024 | 0.005 | 22.462 | 0.809 | 1.640 | 0.097 | 1.102 | -0.009 | 0.032 | 16.691 | 562.270 | 83.314 | 86.590 | 599.329 | 10.100 | 12.604 | 599.369 | 14.281 | 14.758 | 614.622 | 162.964 | 201.862 | 106.591 |
| GJ1-5.FIN2 | 0.033 | -2826.416 | -3.229 | 10.302 | 0.902 | 0.061 | 1.420 | 0.004 | 11.192 | 0.823 | 1.282 | 0.098 | 0.930 | 0.153 | 0.033 | 14.051 | 597.262 | 57.979 | 62.916 | 600.650 | 7.527 | 10.668 | 607.909 | 11.289 | 11.928 | 611.988 | 120.318 | 168.710 | 100.567 |
| GJ1-6.FIN2 | 0.033 | -2555.904 | -3.128 | 10.375 | 0.935 | 0.061 | 1.478 | 0.004 | 10.571 | 0.815 | 1.335 | 0.097 | 0.923 | 0.130 | 0.029 | 13.971 | 570.254 | 60.781 | 65.511 | 597.038 | 7.377 | 10.536 | 601.984 | 11.525 | 12.123 | 563.248 | 110.645 | 156.014 | 104.697 |
| GJ1-7.FIN2 | 0.035 | -3724.306 | -4.767 | 10.359 | 0.989 | 0.060 | 1.694 | 0.013 | 42.520 | 0.820 | 1.346 | 0.098 | 0.985 | 0.443 | 0.038 | 18.253 | 581.034 | 62.014 | 65.588 | 599.918 | 8.377 | 11.272 | 604.825 | 11.557 | 12.147 | 630.851 | 116.605 | 138.502 | 103.250 |
| GJ1-8.FIN2 | 0.032 | -2282.678 | -3.145 | 10.264 | 0.931 | 0.060 | 1.427 | 0.004 | 9.434 | 0.824 | 1.288 | 0.098 | 0.933 | 0.081 | 0.034 | 13.384 | 577.344 | 60.169 | 65.242 | 603.308 | 7.609 | 10.750 | 607.283 | 11.098 | 11.720 | 663.760 | 119.273 | 176.173 | 104.497 |
| GJ1-9.FIN2 | 0.033 | -3284.045 | -3.431 | 10.211 | 0.945 | 0.060 | 1.514 | 0.004 | 9.507 | 0.824 | 1.270 | 0.099 | 0.941 | 0.088 | 0.033 | 13.382 | 567.656 | 64.571 | 69.337 | 606.379 | 7.780 | 10.902 | 608.397 | 11.212 | 11.859 | 639.585 | 115.171 | 170.143 | 106.822 |
| GJ1-10.FIN2 | 0.032 | -3918.740 | -2.866 | 10.259 | 0.907 | 0.058 | 1.506 | 0.028 | 83.536 | 0.793 | 1.312 | 0.098 | 0.947 | 0.030 | 0.047 | 25.848 | 500.347 | 62.546 | 67.215 | 602.869 | 7.818 | 10.892 | 590.751 | 11.421 | 12.036 | 689.757 | 155.654 | 168.358 | 120.490 |
| GJ1-11.FIN2 | 0.033 | -2580.326 | -3.101 | 10.294 | 0.954 | 0.061 | 1.395 | 0.006 | 34.389 | 0.828 | 1.229 | 0.098 | 0.946 | 0.261 | 0.037 | 14.482 | 621.808 | 55.407 | 60.326 | 601.825 | 7.808 | 10.884 | 613.583 | 11.260 | 11.959 | 703.639 | 141.705 | 193.301 | 96.786 |
| GJ1-12.FIN2 | 0.033 | -2317.326 | -3.114 | 10.274 | 0.933 | 0.060 | 1.478 | 0.004 | 11.402 | 0.814 | 1.311 | 0.098 | 0.954 | 0.119 | 0.029 | 14.685 | 555.631 | 57.541 | 62.023 | 602.952 | 7.932 | 10.975 | 602.554 | 11.113 | 11.712 | 576.287 | 123.960 | 167.132 | 108.517 |
| GJ1-13.FIN2 | 0.033 | -4178.591 | -2.887 | 10.366 | 0.985 | 0.060 | 1.369 | 0.004 | 11.097 | 0.815 | 1.260 | 0.097 | 0.948 | 0.169 | 0.032 | 13.925 | 595.526 | 53.159 | 58.079 | 598.076 | 7.786 | 10.832 | 602.536 | 10.887 | 11.526 | 622.615 | 120.878 | 171.006 | 100.428 |
| GJ1-14.FIN2 | 0.034 | -3501.988 | -2.720 | 10.220 | 0.865 | 0.061 | 1.491 | 0.004 | 12.389 | 0.827 | 1.329 | 0.098 | 0.883 | 0.116 | 0.031 | 14.030 | 581.233 | 59.388 | 63.924 | 604.748 | 6.784 | 10.194 | 608.585 | 11.515 | 12.118 | 608.193 | 119.740 | 168.145 | 104.046 |
| GJ1-15.FIN2 | 0.034 | -3565.758 | -3.074 | 10.299 | 0.871 | 0.061 | 1.472 | 0.003 | 9.049 | 0.821 | 1.286 | 0.097 | 0.918 | 0.071 | 0.026 | 13.499 | 602.512 | 57.726 | 62.261 | 597.606 | 7.302 | 10.487 | 605.514 | 11.052 | 11.673 | 499.381 | 91.576 | 133.929 | 99.186 |
| GJ1-16.FIN2 | 0.034 | -2569.814 | -2.593 | 10.245 | 0.870 | 0.059 | 1.565 | 0.004 | 14.865 | 0.806 | 1.509 | 0.098 | 1.054 | 0.787 | 0.032 | 13.156 | 533.053 | 64.644 | 69.078 | 601.869 | 9.504 | 12.178 | 595.935 | 13.140 | 13.665 | 626.405 | 107.756 | 162.551 | 112.910 |
| GJ1-17.FIN2 | 0.033 | -2920.588 | -2.430 | 10.366 | 1.009 | 0.061 | 1.479 | 0.004 | 10.984 | 0.818 | 1.423 | 0.097 | 0.944 | 0.243 | 0.033 | 13.668 | 633.566 | 59.500 | 64.125 | 596.946 | 7.710 | 10.766 | 607.415 | 12.758 | 13.336 | 644.912 | 120.763 | 174.186 | 94.220 |
| GJ1-18.FIN2 | 0.033 | -4069.211 | -6.580 | 10.256 | 0.876 | 0.060 | 1.678 | 0.005 | 15.310 | 0.809 | 1.420 | 0.099 | 1.077 | 0.670 | 0.031 | 15.626 | 513.666 | 70.670 | 74.830 | 607.842 | 9.741 | 12.316 | 598.091 | 12.204 | 12.758 | 597.753 | 141.359 | 182.093 | 118.334 |
| GJ1-19.FIN2 | 0.032 | -5357.045 | -2.252 | 10.326 | 0.917 | 0.060 | 1.538 | 0.005 | 17.447 | 0.813 | 1.295 | 0.098 | 0.964 | 0.024 | 0.033 | 14.693 | 564.391 | 63.103 | 67.600 | 600.089 | 8.037 | 11.017 | 601.021 | 11.235 | 11.858 | 626.561 | 132.370 | 178.393 | 106.325 |
| GJ1-20.FIN2 | 0.034 | -2343.976 | -3.969 | 10.289 | 0.881 | 0.060 | 1.465 | 0.003 | 9.584 | 0.812 | 1.305 | 0.098 | 1.028 | 0.072 | 0.027 | 13.826 | 567.835 | 61.983 | 66.909 | 599.968 | 9.088 | 11.840 | 601.803 | 11.610 | 12.242 | 534.162 | 102.296 | 145.769 | 105.659 |
| GJ1-21.FIN2 | 0.033 | -5215.501 | -2.241 | 10.176 | 0.914 | 0.059 | 1.542 | 0.010 | 39.622 | 0.812 | 1.377 | 0.099 | 0.923 | 0.019 | 0.036 | 16.173 | 519.513 | 60.782 | 65.091 | 608.074 | 7.497 | 10.710 | 600.089 | 11.643 | 12.208 | 676.345 | 156.525 | 197.348 | 117.047 |
| GJ1-22.FIN2 | 0.033 | -2808.591 | -2.469 | 10.316 | 0.898 | 0.061 | 1.468 | 0.005 | 18.276 | 0.819 | 1.482 | 0.097 | 0.886 | 0.093 | 0.031 | 13.952 | 575.360 | 59.850 | 64.582 | 598.851 | 6.771 | 10.133 | 606.056 | 12.216 | 12.723 | 603.155 | 117.689 | 166.178 | 104.083 |
| GJ1-23.FIN2 | 0.032 | -2282.643 | -2.934 | 10.244 | 0.978 | 0.059 | 1.447 | 0.005 | 16.069 | 0.811 | 1.366 | 0.098 | 0.922 | 0.335 | 0.033 | 14.301 | 539.862 | 56.339 | 60.937 | 605.424 | 7.656 | 10.950 | 599.609 | 11.797 | 12.379 | 633.422 | 129.205 | 178.210 | 112.144 |
| GJ1-24.FIN2 | 0.033 | -3478.314 | -3.480 | 10.239 | 1.452 | 0.060 | 1.940 | 0.006 | 31.014 | 0.826 | 1.930 | 0.098 | 1.237 | 0.189 | 0.033 | 17.855 | 577.660 | 80.398 | 83.860 | 603.730 | 12.079 | 14.275 | 608.173 | 17.620 | 18.040 | 634.986 | 186.038 | 223.050 | 104.513 |
| GJ1-25.FIN2 | 0.034 | -4166.078 | -2.596 | 10.358 | 0.879 | 0.060 | 1.461 | 0.005 | 14.034 | 0.807 | 1.364 | 0.097 | 0.893 | 0.082 | 0.032 | 13.916 | 569.731 | 60.348 | 65.170 | 595.796 | 6.868 | 10.174 | 600.034 | 12.254 | 12.861 | 622.448 | 120.428 | 170.483 | 104.575 |
| GJ1-26.FIN2 | 0.032 | -2558.826 | -3.178 | 10.247 | 0.903 | 0.060 | 1.434 | 0.004 | 11.829 | 0.816 | 1.336 | 0.098 | 0.919 | 0.080 | 0.030 | 15.156 | 565.755 | 58.257 | 63.112 | 602.236 | 7.359 | 10.565 | 602.657 | 11.622 | 12.225 | 580.155 | 132.195 | 173.940 | 106.448 |
| GJ1-27.FIN2 | 0.034 | -2129.864 | -3.235 | 10.315 | 0.915 | 0.060 | 1.513 | 0.003 | 13.091 | 0.812 | 1.404 | 0.098 | 0.953 | 0.215 | 0.026 | 14.526 | 554.825 | 63.062 | 67.719 | 600.439 | 7.879 | 10.913 | 599.951 | 12.113 | 12.677 | 509.466 | 108.208 | 147.223 | 108.221 |
| GJ1-28.FIN2 | 0.032 | -4196.231 | -2.341 | 10.217 | 0.919 | 0.059 | 1.547 | 0.006 | 34.622 | 0.808 | 1.426 | 0.099 | 0.925 | 0.154 | 0.036 | 16.224 | 523.379 | 65.210 | 69.798 | 606.600 | 7.504 | 10.698 | 598.733 | 12.664 | 13.234 | 632.036 | 138.595 | 174.419 | 115.901 |
| GJ1-29.FIN2 | 0.034 | -3186.221 | -2.879 | 10.280 | 0.979 | 0.060 | 1.582 | 0.027 | 79.937 | 0.810 | 1.349 | 0.097 | 1.026 | 0.223 | 0.050 | 19.506 | 570.583 | 60.755 | 64.824 | 595.988 | 9.033 | 11.789 | 599.090 | 11.513 | 12.097 | 886.047 | 251.681 | 291.589 | 104.453 |
| GJ1-30.FIN2 | 0.033 | -3524.238 | -3.117 | 10.189 | 0.966 | 0.060 | 1.470 | 0.004 | 14.080 | 0.821 | 1.277 | 0.099 | 0.938 | 0.024 | 0.030 | 13.904 | 539.074 | 60.924 | 65.728 | 607.764 | 7.741 | 10.879 | 605.461 | 11.228 | 11.869 | 589.484 | 114.325 | 161.983 | 112.742 |
| GJ1-31.FIN2 | 0.033 | -2822.912 | -3.266 | 10.369 | 0.928 | 0.060 | 1.591 | 0.005 | 9.348 | 0.815 | 1.415 | 0.097 | 1.047 | 0.007 | 0.034 | 13.271 | 559.717 | 61.617 | 65.690 | 597.119 | 9.256 | 11.912 | 601.436 | 12.344 | 12.910 | 673.822 | 119.298 | 178.016 | 106.682 |
| GJ1-32.FIN2 | 0.033 | -6353.135 | 44.222 | 10.438 | 0.884 | 0.060 | 1.741 | 0.004 | 9.762 | 0.811 | 1.486 | 0.097 | 1.053 | -0.022 | 0.030 | 13.849 | 552.215 | 67.499 | 71.165 | 596.506 | 9.275 | 11.893 | 598.684 | 12.788 | 13.315 | 586.088 | 112.839 | 160.526 | 108.021 |
| GJ1-34.FIN2 | 0.033 | -2982.227 | -2.763 | 10.310 | 0.961 | 0.060 | 1.457 | 0.003 | 16.005 | 0.817 | 1.351 | 0.098 | 0.952 | 0.119 | 0.025 | 15.515 | 564.871 | 60.771 | 65.656 | 601.192 | 7.877 | 10.918 | 602.845 | 11.651 | 12.239 | 480.796 | 114.601 | 148.325 | 106.430 |
| GJ1-35.FIN2 | 0.033 | -2684.597 | -3.407 | 10.178 | 0.927 | 0.059 | 1.456 | 0.004 | 13.476 | 0.818 | 1.332 | 0.099 | 0.944 | 0.163 | 0.032 | 14.303 | 534.387 | 57.823 | 62.479 | 608.303 | 7.848 | 10.959 | 603.675 | 11.510 | 12.110 | 612.041 | 124.740 | 172.035 | 113.832 |
| GJ1-37.FIN2 | 0.033 | -2609.060 | -5.115 | 10.310 | 0.891 | 0.061 | 1.618 | 0.004 | 11.973 | 0.829 | 1.459 | 0.098 | 1.180 | 0.085 | 0.031 | 14.158 | 605.269 | 65.091 | 69.237 | 599.835 | 11.152 | 13.447 | 611.058 | 12.592 | 13.131 | 579.563 | 115.255 | 160.454 | 99.102 |
| GJ1-38.FIN2 | 0.033 | -3105.318 | -3.048 | 10.343 | 1.649 | 0.061 | 1.757 | 0.041 | 86.664 | 0.824 | 1.700 | 0.098 | 1.010 | 0.184 | 0.043 | 15.108 | 569.124 | 68.076 | 71.702 | 600.927 | 8.784 | 11.593 | 608.115 | 13.545 | 13.966 | 766.802 | 155.064 | 204.504 | 105.588 |
| GJ1-39.FIN2 | 0.033 | -3825.662 | -3.771 | 10.252 | 1.052 | 0.059 | 1.352 | 0.004 | 16.257 | 0.805 | 1.276 | 0.098 | 0.927 | 0.185 | 0.031 | 14.711 | 550.055 | 59.960 | 65.677 | 602.428 | 7.484 | 10.643 | 597.853 | 11.207 | 11.848 | 568.986 | 116.489 | 156.832 | 109.521 |
| GJ1-40.FIN2 | 0.033 | -2967.699 | -3.482 | 10.405 | 0.894 | 0.061 | 1.420 | 0.011 | 36.749 | 0.816 | 1.335 | 0.097 | 0.912 | 0.698 | 0.044 | 16.379 | 617.229 | 55.393 | 60.112 | 595.773 | 7.157 | 10.358 | 602.480 | 11.498 | 12.095 | 813.498 | 196.774 | 246.280 | 96.524 |
| GJ1-42.FIN2 | 0.033 | -2399.508 | -2.850 | 10.154 | 0.986 | 0.060 | 1.612 | 0.005 | 14.949 | 0.815 | 1.385 | 0.099 | 0.965 | 0.039 | 0.031 | 14.195 | 544.750 | 65.412 | 69.614 | 607.376 | 8.165 | 11.179 | 601.770 | 11.859 | 12.427 | 591.917 | 119.263 | 165.629 | 111.496 |
| GJ1-44.FIN2 | 0.033 | -6696.021 | -2.987 | 10.365 | 0.878 | 0.061 | 1.649 | 0.005 | 24.919 | 0.815 | 1.475 | 0.097 | 1.018 | 0.317 | 0.028 | 15.626 | 584.779 | 65.340 | 69.333 | 597.647 | 8.825 | 11.578 | 601.092 | 12.771 | 13.306 | 528.463 | 124.735 | 160.678 | 102.200 |
| GJ1-45.FIN2 | 0.034 | -4870.254 | -3.309 | 10.370 | 0.906 | 0.059 | 1.468 | 0.005 | 11.449 | 0.797 | 1.343 | 0.097 | 0.903 | 0.101 | 0.037 | 13.668 | 531.473 | 59.894 | 64.633 | 595.939 | 7.019 | 10.273 | 591.996 | 11.553 | 12.144 | 717.098 | 132.713 | 191.426 | 112.130 |
| GJ1-46.FIN2 | 0.033 | 10548.932 | -2.688 | 10.114 | 0.933 | 0.061 | 1.527 | 0.004 | 10.235 | 0.839 | 1.331 | 0.100 | 0.940 | -0.029 | 0.030 | 14.083 | 580.772 | 63.964 | 68.593 | 611.921 | 7.827 | 10.978 | 615.336 | 11.759 | 12.374 | 583.521 | 116.595 | 163.140 | 105.363 |
| GJ1-47.FIN2 | 0.032 | -3691.293 | -3.409 | 10.279 | 0.985 | 0.061 | 1.769 | 0.017 | 56.786 | 0.825 | 1.449 | 0.098 | 1.063 | 0.025 | 0.034 | 19.709 | 561.809 | 70.964 | 74.688 | 604.086 | 9.584 | 12.216 | 606.637 | 12.609 | 13.158 | 569.839 | 133.127 | 153.699 | 107.525 |
| GJ1-48.FIN2 | 0.033 | -2674.936 | -2.818 | 10.442 | 0.964 | 0.061 | 1.413 | 0.005 | 8.559 | 0.814 | 1.263 | 0.097 | 0.980 | 0.082 | 0.032 | 13.142 | 596.592 | 58.178 | 63.188 | 594.246 | 8.239 | 11.129 | 601.959 | 10.926 | 11.565 | 628.629 | 108.605 | 164.054 | 99.607 |

| | | | | | | | | | | | | | | | | | | | | | | | | | | | | |
|---|---|---|---|---|---|---|---|---|---|---|---|---|---|---|---|---|---|---|---|---|---|---|---|---|---|---|---|---|
| GJ1-49.FIN2 | 0.034 | -2311.916 | -2.885 | 10.273 | 0.954 | 0.060 | 1.477 | 0.003 | 9.980 | 0.809 | 1.278 | 0.098 | 0.949 | -0.008 | 0.025 | 14.038 | 554.494 | 58.553 | 63.119 | 603.981 | 7.870 | 10.938 | 600.381 | 10.771 | 11.385 | 487.538 | 96.858 | 135.939 | 108.925 |
| GJ1-50.FIN2 | 0.033 | -6015.807 | -2.744 | 10.269 | 1.019 | 0.058 | 1.525 | 0.004 | 8.888 | 0.794 | 1.344 | 0.098 | 0.970 | 0.080 | 0.029 | 13.510 | 487.932 | 63.729 | 68.356 | 602.874 | 8.184 | 11.157 | 589.851 | 11.601 | 12.194 | 567.505 | 103.869 | 151.764 | 123.557 |
| GJ1-51.FIN2 | 0.034 | -4179.795 | -3.025 | 10.290 | 0.936 | 0.061 | 1.499 | 0.004 | 12.231 | 0.827 | 1.228 | 0.098 | 0.962 | -0.025 | 0.030 | 13.714 | 586.999 | 62.272 | 66.972 | 602.177 | 8.055 | 11.056 | 611.590 | 10.604 | 11.263 | 579.157 | 109.892 | 157.935 | 102.586 |
| GJ1-52.FIN2 | 0.032 | -11981.575 | -2.491 | 10.303 | 0.960 | 0.061 | 1.783 | 0.004 | 13.707 | 0.835 | 1.582 | 0.098 | 0.975 | -0.006 | 0.031 | 14.042 | 584.604 | 73.443 | 77.230 | 601.815 | 8.250 | 11.192 | 612.095 | 13.867 | 14.368 | 610.602 | 120.994 | 169.768 | 102.944 |
| GJ1-53.FIN2 | 0.033 | -2457.424 | -2.691 | 10.198 | 0.931 | 0.061 | 1.446 | 0.009 | 56.156 | 0.827 | 1.325 | 0.099 | 0.915 | 0.131 | 0.032 | 15.700 | 579.661 | 61.155 | 66.153 | 607.645 | 7.521 | 10.837 | 609.723 | 11.863 | 12.488 | 613.791 | 141.738 | 182.015 | 104.828 |
| GJ1-54.FIN2 | 0.033 | -6543.159 | -3.141 | 10.474 | 0.922 | 0.061 | 1.528 | 0.004 | 11.521 | 0.804 | 1.500 | 0.096 | 0.905 | 0.203 | 0.029 | 14.516 | 581.973 | 62.962 | 67.513 | 592.055 | 7.010 | 10.236 | 594.886 | 12.995 | 13.520 | 562.712 | 118.711 | 161.607 | 101.732 |
| GJ1-55.FIN2 | 0.033 | -3715.123 | -2.851 | 10.199 | 0.899 | 0.058 | 1.392 | 0.004 | 14.674 | 0.789 | 1.336 | 0.098 | 0.912 | 0.226 | 0.032 | 14.046 | 501.247 | 55.481 | 60.426 | 604.313 | 7.285 | 10.537 | 588.605 | 11.554 | 12.152 | 608.866 | 120.338 | 168.795 | 120.562 |
| GJ1-56.FIN2 | 0.034 | -2207.146 | -3.447 | 10.283 | 0.858 | 0.060 | 1.588 | 0.007 | 42.044 | 0.812 | 1.388 | 0.098 | 1.040 | 0.764 | 0.037 | 16.664 | 551.215 | 60.668 | 64.697 | 604.361 | 9.199 | 11.895 | 600.206 | 11.959 | 12.530 | 648.782 | 134.555 | 166.816 | 109.642 |
| GJ1-58.FIN2 | 0.033 | -2353.440 | -2.942 | 10.350 | 0.956 | 0.061 | 1.599 | 0.004 | 12.036 | 0.817 | 1.417 | 0.098 | 1.008 | 0.162 | 0.024 | 15.190 | 608.115 | 68.520 | 72.999 | 599.447 | 8.712 | 11.515 | 605.882 | 12.932 | 13.522 | 469.811 | 107.655 | 141.416 | 98.575 |
| GJ1-59.FIN2 | 0.032 | -2164.484 | -3.165 | 10.367 | 0.903 | 0.061 | 1.575 | 0.005 | 24.210 | 0.815 | 1.416 | 0.097 | 0.933 | 0.140 | 0.034 | 14.794 | 574.375 | 64.310 | 68.656 | 597.229 | 7.531 | 10.640 | 601.321 | 12.275 | 12.836 | 656.409 | 142.313 | 190.739 | 103.979 |
| GJ1-60.FIN2 | 0.033 | -2106.293 | -2.578 | 10.153 | 1.064 | 0.061 | 1.772 | 0.006 | 25.679 | 0.833 | 1.467 | 0.099 | 0.993 | -0.027 | 0.035 | 14.620 | 593.434 | 66.996 | 70.497 | 610.041 | 8.913 | 11.915 | 611.209 | 12.946 | 13.495 | 666.323 | 141.436 | 191.397 | 102.799 |
| 91500-3.FIN2 | 1.124 | -602.772 | -3.543 | 5.698 | 1.833 | 0.074 | 2.697 | 0.111 | 5.037 | 1.814 | 2.614 | 0.179 | 1.499 | 0.255 | 0.052 | 10.568 | 966.022 | 113.645 | 116.099 | 1059.959 | 26.450 | 29.449 | 1048.028 | 35.845 | 36.303 | 1013.236 | 75.507 | 208.474 | 109.724 |
| 91500-4.FIN2 | 1.093 | -1120.344 | -3.817 | 5.765 | 1.187 | 0.073 | 2.349 | 0.109 | 4.207 | 1.785 | 2.242 | 0.176 | 1.221 | -0.045 | 0.053 | 10.347 | 902.210 | 94.122 | 96.828 | 1045.100 | 19.820 | 23.545 | 1020.397 | 28.087 | 28.578 | 1046.864 | 64.721 | 211.366 | 115.838 |
| 91500-5.FIN2 | 1.078 | -741.867 | -3.017 | 5.800 | 1.099 | 0.073 | 2.297 | 0.113 | 5.316 | 1.761 | 2.057 | 0.174 | 1.220 | 0.014 | 0.053 | 10.326 | 928.053 | 91.921 | 94.691 | 1030.918 | 19.504 | 23.174 | 1018.290 | 25.236 | 25.763 | 1047.573 | 63.275 | 210.843 | 111.084 |
| 91500-7.FIN2 | 0.975 | -863.917 | -3.544 | 5.744 | 1.424 | 0.077 | 2.659 | 0.112 | 4.221 | 1.851 | 2.545 | 0.176 | 1.409 | 0.169 | 0.056 | 10.431 | 1069.497 | 112.415 | 114.915 | 1044.299 | 23.983 | 27.132 | 1061.638 | 36.139 | 36.627 | 1089.537 | 72.596 | 220.675 | 97.644 |
| 91500-8.FIN2 | 1.050 | -1210.192 | -2.933 | 5.648 | 1.168 | 0.073 | 2.115 | 0.126 | 10.112 | 1.806 | 1.967 | 0.180 | 1.177 | 0.056 | 0.056 | 10.276 | 936.321 | 89.913 | 93.136 | 1064.184 | 19.139 | 23.099 | 1031.913 | 25.248 | 25.826 | 1101.708 | 62.644 | 219.955 | 113.656 |
| 91500-9.FIN2 | 1.033 | -662.723 | -3.357 | 5.800 | 1.189 | 0.077 | 2.766 | 0.110 | 5.372 | 1.847 | 2.410 | 0.175 | 1.261 | -0.044 | 0.052 | 10.338 | 975.813 | 95.764 | 97.726 | 1036.870 | 20.626 | 24.190 | 1040.356 | 29.348 | 29.791 | 1011.834 | 61.829 | 203.589 | 106.257 |
| 91500-10.FIN2 | 1.072 | -749.359 | -3.316 | 5.707 | 1.248 | 0.078 | 2.381 | 0.116 | 3.264 | 1.903 | 2.221 | 0.178 | 1.149 | -0.006 | 0.054 | 10.239 | 1055.664 | 92.629 | 95.218 | 1052.485 | 18.267 | 22.303 | 1061.803 | 28.573 | 29.083 | 1065.038 | 58.112 | 212.788 | 99.699 |
| 91500-13.FIN2 | 1.066 | -1612.594 | -2.978 | 5.754 | 1.762 | 0.077 | 2.286 | 0.115 | 3.690 | 1.902 | 2.251 | 0.178 | 1.252 | 0.055 | 0.053 | 10.324 | 1032.968 | 86.772 | 89.413 | 1055.449 | 19.657 | 23.121 | 1065.053 | 28.329 | 28.821 | 1042.159 | 62.661 | 209.300 | 102.176 |
| 91500-14.FIN2 | 1.071 | -1015.902 | -2.673 | 5.666 | 1.259 | 0.077 | 2.386 | 0.114 | 3.621 | 1.879 | 2.353 | 0.178 | 1.151 | 0.056 | 0.053 | 10.301 | 968.276 | 100.037 | 102.823 | 1056.088 | 18.462 | 22.518 | 1047.173 | 29.574 | 30.043 | 1035.016 | 60.760 | 207.652 | 109.069 |
| 91500-15.FIN2 | 1.128 | -870.904 | -4.249 | 5.817 | 1.842 | 0.079 | 3.758 | 0.108 | 4.904 | 1.894 | 3.820 | 0.174 | 1.736 | 0.021 | 0.046 | 10.816 | 1021.980 | 140.751 | 142.292 | 1030.998 | 30.956 | 33.462 | 1047.249 | 47.513 | 47.795 | 896.826 | 78.477 | 189.961 | 100.882 |
| 91500-16.FIN2 | 1.091 | -926.823 | -3.345 | 5.759 | 1.213 | 0.075 | 2.423 | 0.106 | 3.004 | 1.811 | 2.440 | 0.177 | 1.114 | 0.103 | 0.049 | 10.327 | 930.498 | 101.136 | 103.864 | 1047.855 | 17.429 | 21.618 | 1024.227 | 32.395 | 32.872 | 961.990 | 58.301 | 194.150 | 112.612 |
| 91500-18.FIN2 | 1.130 | -749.998 | -3.245 | 5.786 | 1.592 | 0.074 | 3.716 | 0.104 | 5.057 | 1.775 | 3.373 | 0.176 | 1.478 | -0.010 | 0.046 | 10.912 | 845.709 | 148.295 | 149.956 | 1041.900 | 25.425 | 28.406 | 1010.511 | 42.864 | 43.191 | 894.702 | 82.269 | 191.160 | 123.198 |
| 91500-19.FIN2 | 1.080 | -927.719 | -2.689 | 5.557 | 1.123 | 0.078 | 2.423 | 0.112 | 3.856 | 1.941 | 2.345 | 0.181 | 1.132 | 0.173 | 0.052 | 10.315 | 1019.278 | 93.213 | 95.726 | 1075.723 | 18.614 | 22.890 | 1071.490 | 27.139 | 27.572 | 1016.427 | 60.625 | 204.111 | 105.538 |
| 91500-21.FIN2 | 1.074 | -1105.064 | -2.644 | 5.695 | 1.219 | 0.077 | 2.481 | 0.112 | 3.692 | 1.858 | 2.242 | 0.178 | 1.175 | 0.112 | 0.050 | 10.304 | 1009.064 | 100.268 | 102.842 | 1055.577 | 18.965 | 22.908 | 1059.645 | 30.774 | 31.313 | 983.636 | 57.999 | 197.587 | 104.610 |
| 91500-22.FIN2 | 1.066 | -1375.322 | -2.581 | 5.713 | 1.158 | 0.072 | 2.189 | 0.111 | 3.372 | 1.752 | 1.951 | 0.178 | 1.216 | 0.017 | 0.050 | 10.349 | 906.835 | 88.821 | 91.783 | 1051.883 | 19.841 | 23.609 | 1013.484 | 24.447 | 25.017 | 982.789 | 60.833 | 198.372 | 115.995 |
| 91500-25.FIN2 | 1.060 | -757.126 | -3.230 | 5.829 | 1.121 | 0.076 | 2.246 | 0.108 | 4.124 | 1.798 | 2.077 | 0.174 | 1.148 | 0.019 | 0.047 | 10.439 | 974.214 | 94.710 | 97.702 | 1033.601 | 17.917 | 21.881 | 1030.036 | 27.171 | 27.728 | 922.405 | 62.368 | 188.300 | 106.096 |
| 91500-26.FIN2 | 1.061 | -1223.802 | -3.637 | 5.888 | 2.095 | 0.077 | 3.405 | 0.124 | 5.209 | 1.845 | 3.521 | 0.173 | 1.309 | -0.167 | 0.052 | 10.568 | 880.414 | 107.737 | 109.180 | 1029.445 | 21.794 | 25.227 | 1019.660 | 31.508 | 31.729 | 1008.877 | 74.970 | 206.957 | 116.927 |
| 91500-27.FIN2 | 1.030 | -780.536 | -4.642 | 5.941 | 3.485 | 0.075 | 2.681 | 0.125 | 12.302 | 1.803 | 2.847 | 0.177 | 1.762 | 0.163 | 0.047 | 10.403 | 933.774 | 97.688 | 99.823 | 1046.681 | 28.211 | 30.421 | 1016.967 | 34.387 | 34.757 | 933.082 | 60.645 | 188.477 | 112.091 |
| PLES-1.FIN2 | 0.267 | -3720.565 | -2.802 | 18.951 | 0.966 | 0.056 | 1.740 | 0.031 | 4.390 | 0.408 | 1.546 | 0.053 | 0.972 | 0.061 | 0.018 | 10.477 | 361.441 | 74.132 | 78.161 | 334.167 | 4.658 | 6.335 | 345.602 | 8.730 | 9.061 | 356.753 | 25.228 | 74.030 | 92.454 |
| PLES-2.FIN2 | 0.281 | -2230.116 | -2.675 | 18.736 | 0.913 | 0.053 | 1.515 | 0.031 | 3.808 | 0.396 | 1.445 | 0.054 | 0.913 | 0.120 | 0.018 | 10.352 | 274.846 | 69.657 | 74.790 | 337.752 | 4.152 | 6.003 | 336.874 | 7.975 | 8.324 | 354.628 | 22.404 | 72.825 | 122.888 |
| PLES-3.FIN2 | 0.268 | -1652.122 | -2.473 | 19.046 | 0.945 | 0.055 | 1.791 | 0.031 | 5.158 | 0.402 | 1.577 | 0.053 | 0.995 | 0.039 | 0.017 | 10.589 | 324.373 | 77.200 | 81.145 | 332.016 | 4.825 | 6.440 | 341.289 | 8.779 | 9.098 | 349.304 | 26.881 | 73.262 | 102.356 |
| PLES-4.FIN2 | 0.268 | -2230.484 | -3.861 | 19.589 | 1.053 | 0.054 | 2.380 | 0.030 | 5.448 | 0.391 | 2.199 | 0.052 | 1.033 | 0.019 | 0.018 | 10.922 | 292.190 | 91.007 | 93.553 | 323.754 | 5.026 | 6.526 | 332.615 | 11.881 | 12.097 | 352.915 | 32.968 | 76.305 | 110.803 |
| PLES-5.FIN2 | 0.253 | -1686.906 | -15.706 | 19.301 | 1.021 | 0.054 | 1.950 | 0.032 | 15.955 | 0.387 | 1.829 | 0.052 | 1.060 | 0.366 | 0.017 | 11.902 | 271.775 | 89.178 | 92.974 | 329.034 | 5.324 | 6.798 | 330.852 | 10.258 | 10.531 | 331.484 | 42.553 | 75.802 | 121.069 |
| PLES-6.FIN2 | 0.275 | -2285.970 | -2.721 | 18.881 | 0.882 | 0.054 | 1.658 | 0.030 | 6.774 | 0.401 | 1.484 | 0.053 | 0.874 | -0.002 | 0.016 | 10.451 | 343.094 | 64.791 | 68.706 | 334.808 | 3.742 | 5.701 | 340.443 | 8.192 | 8.531 | 315.327 | 21.842 | 65.340 | 97.585 |
| PLES-7.FIN2 | 0.252 | -1244.987 | -4.170 | 19.044 | 1.182 | 0.056 | 3.217 | 0.029 | 6.768 | 0.413 | 2.739 | 0.053 | 1.299 | 0.033 | 0.018 | 11.285 | 374.407 | 121.677 | 123.505 | 331.945 | 7.235 | 8.396 | 348.162 | 15.566 | 15.747 | 350.644 | 38.331 | 78.534 | 88.659 |
| PLES-8.FIN2 | 0.253 | -2031.230 | -3.384 | 18.596 | 0.962 | 0.054 | 1.982 | 0.027 | 4.938 | 0.406 | 1.718 | 0.054 | 1.009 | 0.016 | 0.016 | 10.869 | 291.242 | 93.135 | 96.967 | 340.059 | 5.064 | 6.686 | 343.555 | 9.667 | 9.961 | 320.913 | 29.250 | 69.175 | 116.762 |
| PLES-9.FIN2 | 0.259 | -1214.397 | -3.060 | 18.864 | 1.030 | 0.054 | 1.891 | 0.031 | 6.530 | 0.396 | 1.733 | 0.054 | 1.031 | 0.449 | 0.017 | 10.873 | 246.164 | 84.011 | 87.829 | 336.994 | 5.206 | 6.768 | 336.543 | 9.496 | 9.780 | 337.176 | 30.732 | 72.554 | 136.898 |
| PLES-10.FIN2 | 0.272 | -1595.146 | -2.934 | 19.071 | 1.025 | 0.054 | 1.960 | 0.028 | 4.063 | 0.396 | 1.658 | 0.053 | 1.000 | -0.040 | 0.015 | 10.548 | 286.973 | 80.986 | 84.396 | 333.137 | 4.887 | 6.497 | 336.688 | 9.095 | 9.392 | 307.892 | 23.082 | 64.513 | 116.087 |
| PLES-11.FIN2 | 0.277 | -2573.377 | -2.987 | 18.784 | 0.867 | 0.054 | 2.349 | 0.033 | 13.763 | 0.402 | 2.206 | 0.053 | 0.987 | 0.048 | 0.016 | 10.991 | 279.360 | 110.163 | 113.331 | 334.548 | 4.799 | 6.447 | 340.397 | 12.614 | 12.842 | 314.688 | 30.449 | 68.620 | 119.755 |
| PLES-12.FIN2 | 0.270 | -1963.620 | -2.957 | 18.736 | 0.937 | 0.055 | 1.966 | 0.030 | 4.028 | 0.402 | 1.938 | 0.054 | 0.944 | 0.040 | 0.017 | 10.524 | 304.241 | 78.382 | 81.662 | 337.180 | 4.441 | 6.203 | 340.233 | 10.833 | 11.089 | 331.790 | 24.372 | 69.207 | 110.826 |
| PLES-13.FIN2 | 0.262 | -3092.831 | -2.904 | 19.082 | 0.962 | 0.052 | 1.973 | 0.026 | 4.453 | 0.382 | 1.826 | 0.053 | 0.976 | 0.162 | 0.015 | 10.764 | 162.231 | 94.052 | 97.957 | 332.489 | 4.662 | 6.320 | 325.764 | 9.891 | 10.155 | 296.676 | 25.543 | 63.358 | 204.948 |
| PLES-14.FIN2 | 0.271 | -1917.482 | -2.822 | 19.241 | 1.013 | 0.056 | 2.253 | 0.030 | 5.369 | 0.410 | 2.183 | 0.052 | 0.974 | 0.020 | 0.016 | 10.735 | 322.536 | 81.423 | 83.979 | 329.466 | 4.604 | 6.255 | 345.327 | 11.712 | 11.928 | 319.633 | 27.064 | 68.065 | 102.149 |
| PLES-15.FIN2 | 0.258 | -1894.365 | -2.639 | 18.977 | 0.967 | 0.054 | 2.177 | 0.028 | 5.920 | 0.396 | 1.897 | 0.053 | 1.019 | -0.026 | 0.016 | 10.843 | 240.293 | 93.809 | 96.975 | 333.989 | 5.053 | 6.627 | 336.007 | 10.417 | 10.674 | 315.297 | 28.329 | 67.753 | 138.993 |

| | | | | | | | | | | | | | | | | | | | | | | | | | | | | | | |
|---|---|---|---|---|---|---|---|---|---|---|---|---|---|---|---|---|---|---|---|---|---|---|---|---|---|---|---|---|---|---|
| PLES-16.FIN2 | 0.265 | -2292.171 | -2.462 | 18.955 | 1.060 | 0.056 | 2.432 | 0.031 | 10.780 | 0.413 | 2.468 | 0.053 | 0.933 | 0.102 | 0.016 | 10.966 | 307.767 | 91.289 | 93.731 | 333.208 | 4.291 | 6.062 | 343.178 | 11.202 | 11.364 | 322.560 | 30.663 | 69.761 | 108.266 |
| PLES-17.FIN2 | 0.262 | -1638.381 | -2.726 | 19.096 | 1.040 | 0.054 | 2.032 | 0.046 | 39.575 | 0.392 | 1.884 | 0.053 | 1.035 | 0.326 | 0.016 | 11.130 | 235.062 | 92.030 | 95.620 | 332.556 | 5.175 | 6.711 | 332.994 | 10.269 | 10.526 | 324.741 | 33.134 | 71.164 | 141.476 |
| PLES-18.FIN2 | 0.263 | -1579.065 | -2.679 | 18.735 | 0.990 | 0.051 | 2.072 | 0.066 | 58.208 | 0.382 | 1.832 | 0.054 | 1.053 | -0.090 | 0.016 | 11.802 | 169.657 | 98.557 | 102.247 | 337.377 | 5.396 | 6.921 | 326.603 | 10.044 | 10.311 | 320.880 | 40.523 | 73.564 | 198.858 |
| PLES-19.FIN2 | 0.285 | -2718.054 | -3.038 | 18.967 | 0.987 | 0.056 | 3.071 | 0.034 | 12.289 | 0.414 | 3.184 | 0.053 | 1.040 | 0.314 | 0.016 | 10.423 | 328.317 | 81.243 | 82.586 | 334.812 | 5.239 | 6.772 | 341.371 | 10.703 | 10.795 | 323.368 | 21.856 | 66.860 | 101.978 |
| PLES-20.FIN2 | 0.266 | -1321.089 | -2.833 | 18.880 | 0.959 | 0.056 | 2.138 | 0.030 | 4.198 | 0.413 | 1.900 | 0.053 | 0.998 | -0.047 | 0.016 | 10.610 | 355.294 | 93.652 | 96.934 | 335.593 | 4.897 | 6.521 | 347.897 | 10.713 | 10.977 | 327.550 | 25.603 | 68.886 | 94.455 |
| PLES-21.FIN2 | 0.254 | -1644.507 | -2.372 | 19.175 | 0.945 | 0.055 | 2.440 | 0.026 | 5.326 | 0.396 | 2.369 | 0.053 | 0.944 | 0.077 | 0.015 | 10.724 | 249.366 | 90.501 | 92.906 | 330.160 | 4.348 | 6.075 | 331.536 | 10.258 | 10.419 | 291.817 | 24.601 | 62.204 | 132.399 |
| PLES-22.FIN2 | 0.258 | -2925.635 | -2.867 | 19.059 | 0.989 | 0.054 | 2.064 | 0.031 | 16.885 | 0.400 | 1.882 | 0.053 | 1.010 | -0.006 | 0.015 | 10.914 | 287.155 | 89.695 | 93.079 | 332.555 | 4.963 | 6.549 | 337.347 | 10.019 | 10.271 | 303.399 | 28.255 | 65.595 | 115.810 |
| PLES-23.FIN2 | 0.259 | -1810.192 | -2.430 | 19.057 | 0.985 | 0.054 | 2.111 | 0.030 | 7.288 | 0.398 | 2.031 | 0.053 | 0.981 | 0.066 | 0.016 | 10.854 | 261.675 | 91.593 | 94.890 | 332.488 | 4.705 | 6.352 | 337.159 | 11.227 | 11.468 | 327.970 | 29.611 | 70.480 | 127.061 |
| PLES-24.FIN2 | 0.252 | -4797.428 | -2.418 | 19.075 | 0.981 | 0.053 | 1.915 | 0.028 | 4.485 | 0.396 | 1.853 | 0.053 | 0.990 | 0.157 | 0.016 | 10.733 | 273.071 | 89.520 | 93.480 | 331.198 | 4.778 | 6.401 | 337.409 | 10.534 | 10.807 | 312.197 | 26.436 | 66.549 | 121.286 |
| PLES-25.FIN2 | 0.271 | -2264.820 | -2.534 | 19.005 | 0.963 | 0.052 | 1.700 | 0.030 | 4.246 | 0.378 | 1.662 | 0.053 | 0.986 | 0.062 | 0.016 | 10.614 | 192.448 | 78.572 | 83.065 | 333.653 | 4.762 | 6.404 | 323.905 | 8.894 | 9.183 | 322.477 | 25.311 | 67.928 | 173.374 |
| PLES-26.FIN2 | 0.258 | -2431.204 | -2.193 | 19.271 | 1.018 | 0.052 | 2.526 | 0.026 | 4.753 | 0.374 | 2.299 | 0.052 | 1.023 | 0.239 | 0.015 | 10.908 | 160.725 | 102.957 | 105.503 | 329.483 | 5.021 | 6.567 | 319.709 | 12.017 | 12.217 | 295.307 | 27.458 | 63.900 | 204.998 |
| PLES-27.FIN2 | 0.259 | -1356.459 | -2.410 | 19.161 | 1.027 | 0.054 | 2.140 | 0.027 | 4.310 | 0.385 | 1.930 | 0.053 | 0.999 | -0.004 | 0.015 | 10.749 | 220.741 | 95.664 | 99.008 | 331.595 | 4.851 | 6.457 | 326.032 | 9.927 | 10.164 | 309.590 | 26.463 | 66.104 | 150.219 |

**Suplementary Table 2.** Reference standards for whole-rock geochemical analysis.

| | Description | GBM908-10 | GBM908-10 | MRGeo08 | NCSDC71301 | OREAS 24b | SY-4 | SY-4 | OREAS 460 | GRE-3 | OREAS 602 | EMOG-17 | GRE-3 | OREAS 460 | OREAS 146 | OREAS 602 | BXMG-5 | OREAS 146 | GRE-3 | BXMG-5 |
|---|---|---|---|---|---|---|---|---|---|---|---|---|---|---|---|---|---|---|---|---|
| SiO2 | % | | | | 54.70 | | 48.70 | 50.40 | | 3.11 | | | 3.10 | 49.80 | | | | 20.30 | 3.23 | |
| Al2O3 | % | | | | 17.45 | | 20.40 | 20.10 | | 0.92 | | | 0.89 | 12.60 | | | | 2.98 | 0.89 | |
| Fe2O3 | % | | | | 7.40 | | 6.14 | 5.98 | | 51.00 | | | 50.20 | 26.90 | | | | 28.60 | 51.40 | |
| CaO | % | | | | 1.40 | | 8.10 | 7.80 | | 16.75 | | | 18.15 | 1.03 | | | | 17.10 | 18.50 | |
| MgO | % | | | | 0.62 | | 0.50 | 0.50 | | 0.18 | | | 0.17 | 1.27 | | | | 6.92 | 0.16 | |
| Na2O | % | | | | 6.94 | | 7.11 | 6.88 | | 0.10 | | | 0.12 | 0.20 | | | | 0.36 | 0.04 | |
| K2O | % | | | | 7.44 | | 1.63 | 1.58 | | 0.02 | | | <0.01 | 1.50 | | | | 1.26 | <0.01 | |
| Cr2O3 | % | | | | 0.00 | | 0.00 | 0.00 | | 0.01 | | | 0.01 | 0.05 | | | | 0.03 | 0.01 | |
| TiO2 | % | | | | 0.45 | | 0.28 | 0.27 | | 1.54 | | | 1.54 | 1.93 | | | | 1.39 | 1.55 | |
| MnO | % | | | | 0.12 | | 0.11 | 0.10 | | 1.61 | | | 1.58 | 0.05 | | | | 2.36 | 1.66 | |
| P2O5 | % | | | | 0.02 | | 0.13 | 0.13 | | 14.50 | | | 14.80 | 0.44 | | | | 0.54 | 15.00 | |
| SrO | % | | | | 0.14 | | 0.14 | 0.13 | | 0.22 | | | 0.24 | 0.03 | | | | 0.38 | 0.24 | |
| BaO | % | | | | 0.03 | | 0.04 | 0.04 | | 0.78 | | | 0.76 | 0.09 | | | | 1.46 | 0.77 | |
| LOI | % | | | | | | | | | | | | | | | | 25.90 | | | |
| Total | % | | | | 96.71 | | 97.84 | 98.47 | | 94.70 | | | 95.52 | 100.97 | | | | 93.03 | 97.41 | |
| Ba | ppm | | | | 242 | 733 | 313 | | 826 | | | | 7290 | 795 | >10000 | | | >10000 | 6990 | |
| Ce | ppm | | | | 271 | 90 | 114 | | 1825 | | | | 4100 | 1865 | 4690 | | | 4640 | 4240 | |
| Cr | ppm | | | | <10 | 140 | 10 | | 390 | | | | 50 | 380 | 190 | | | 180 | 60 | |
| Cs | ppm | | | | 2 | 10 | 1 | | 4 | | | | 0 | 3 | 1 | | | 1 | 0 | |
| Dy | ppm | | | | 5 | 6 | 19 | | 20 | | | | 91 | 19 | 225 | | | 229 | 95 | |
| Er | ppm | | | | 3 | 3 | 15 | | 6 | | | | 27 | 6 | 82 | | | 83 | 28 | |
| Eu | ppm | | | | 2 | 1 | 2 | | 22 | | | | 69 | 21 | 123 | | | 122 | 77 | |
| Ga | ppm | | | | 39 | 21 | 30 | | 35 | | | | 43 | 29 | 31 | | | 31 | 46 | |
| Gd | ppm | | | | 7 | 6 | 16 | | 48 | | | | 185 | 45 | 363 | | | 365 | 202 | |
| Hf | ppm | | | | 39 | 6 | 12 | | 12 | | | | 19 | 12 | 4 | | | 4 | 21 | |
| Ho | ppm | | | | 1 | 1 | 4 | | 3 | | | | 13 | 3 | 37 | | | 38 | 13 | |
| La | ppm | | | | 163 | 44 | 53 | | 1290 | | | | 2150 | 1340 | 2530 | | | 2520 | 2150 | |
| Lu | ppm | | | | 0 | 1 | 2 | | 1 | | | | 2 | 1 | 7 | | | 7 | 2 | |
| Nb | ppm | | | | 73 | 15 | 13 | | 699 | | | | >2500 | 654 | 395 | | | 388 | >2500 | |
| Nd | ppm | | | | 68 | 38 | 58 | | 823 | | | | 1805 | 835 | 2270 | | | 2250 | 1935 | |
| Pr | ppm | | | | 23 | 10 | 14 | | 252 | | | | 486 | 237 | 567 | | | 561 | 493 | |
| Rb | ppm | | | | 133 | 161 | 54 | | 72 | | | | 1 | 74 | 26 | | | 26 | 1 | |
| Sm | ppm | | | | 9 | 7 | 12 | | 105 | | | | 266 | 102 | 449 | | | 441 | 272 | |
| Sn | ppm | | | | 7 | 4 | 8 | | 16 | | | | 44 | 17 | 45 | | | 45 | 46 | |
| Sr | ppm | | | | 1430 | 121 | 1230 | | 307 | | | | 2050 | 294 | 3150 | | | 3160 | 2260 | |
| Ta | ppm | | | | 2 | 1 | 1 | | 14 | | | | 166 | 12 | 4 | | | 4 | 172 | |
| Tb | ppm | | | | 1 | 1 | 3 | | 5 | | | | 21 | 4 | 47 | | | 48 | 22 | |
| Th | ppm | | | | 85 | 16 | 2 | | 117 | | | | 119 | 110 | 899 | | | 897 | 114 | |
| Tm | ppm | | | | 0 | 1 | 2 | | 1 | | | | 3 | 1 | 10 | | | 10 | 3 | |
| U | ppm | | | | 17 | 3 | 1 | | 4 | | | | 113 | 4 | 3 | | | 3 | 110 | |
| V | ppm | | | | 210 | 114 | 10 | | 251 | | | | 1170 | 233 | 165 | | | 154 | 1220 | |
| W | ppm | | | | 3 | 6 | 2 | | 7 | | | | 4 | 5 | 29 | | | 29 | 3 | |
| Y | ppm | | | | 26 | 32 | 122 | | 58 | | | | 297 | 59 | 926 | | | 931 | 336 | |
| Yb | ppm | | | | 3 | 3 | 16 | | 4 | | | | 14 | 4 | 51 | | | 51 | 16 | |
| Zr | ppm | | | | 1645 | 222 | 656 | | 465 | | | | 953 | 471 | 233 | | | 236 | 1065 | |
| Ag | ppm | 3 | 3.2 | 4.4 | | | | | | | >100 | 70 | | | | >100 | | | | 27 |

| | | | | | | | | | | |
|---|---|---|---|---|---|---|---|---|---|---|
| As | ppm | 58 | 52 | 31 | | | 696 | 599 | | 664 |
| Cd | ppm | 1.6 | 1.7 | 2.2 | | | 26 | 21 | | 25 |
| Co | ppm | 26 | 28 | 20 | | | 11 | 777 | | 10 |
| Cu | ppm | 3580 | 3480 | 622 | | | 5280 | 8390 | | 4960 |
| Li | ppm | 10 | 10 | 40 | | | 20 | 30 | | 20 |
| Mo | ppm | 61 | 62 | 14 | | | 5 | 1110 | | 4 |
| Ni | ppm | 2190 | 2250 | 692 | | | 66 | 7620 | | 57 |
| Pb | ppm | 2080 | 2040 | 1090 | | | 1090 | 7470 | | 1025 |
| Sc | ppm | 17 | 18 | 12 | | | 5 | 8 | | 4 |
| Tl | ppm | <10 | <10 | <10 | | | <10 | <10 | | <10 |
| Zn | ppm | 1085 | 1090 | 825 | | | 4580 | 7600 | | 4070 |

**Suplementary Table 2.** Continuation.

| | Description | BXMG-5 | OREAS 24b | OREAS 24b | OREAS 24b | SY-4 | SY-5 | NCSDC71301 | OREAS 146 | SY-5 | OREAS 146 | OREAS 460 | SY-4 | OREAS 460 | BCS-348 |
|---|---|---|---|---|---|---|---|---|---|---|---|---|---|---|---|
| SiO2 | % | | 3.63 | 3.50 | 3.44 | | 4.73 | | 54.30 | 4.79 | | 3.69 | | | |
| Al2O3 | % | | 227.00 | 231.00 | 242.00 | | 802.00 | | 244.00 | 831.00 | | 446.00 | | | |
| Fe2O3 | % | | 66.80 | 67.10 | | 50.50 | 49.30 | 54.80 | | 49.60 | 20.10 | 49.40 | 48.80 | | |
| CaO | % | | 15.00 | 15.10 | | 20.60 | 13.95 | 17.70 | | 14.05 | 2.96 | 12.50 | 20.10 | | |
| MgO | % | | 6.34 | 6.43 | | 6.20 | 10.40 | 7.24 | | 10.35 | 28.00 | 26.10 | 6.00 | | |
| Na2O | % | | 1.50 | 1.48 | | 8.04 | 6.94 | 1.38 | | 7.09 | 17.10 | 0.99 | 7.88 | | |
| K2O | % | | 2.74 | 2.68 | | 0.54 | 3.12 | 0.64 | | 3.24 | 6.68 | 1.22 | 0.51 | | |
| Cr2O3 | % | | 1.14 | 1.11 | | 7.24 | 3.98 | 7.25 | | 4.16 | 0.29 | 0.18 | 6.94 | | |
| TiO2 | % | | 3.33 | 3.40 | | 1.68 | 4.10 | 7.46 | | 4.04 | 1.26 | 1.46 | 1.58 | | |
| MnO | % | | 0.02 | 0.02 | | 0.00 | 0.02 | <0.002 | | 0.02 | 0.03 | 0.05 | 0.00 | | |
| P2O5 | % | | 0.78 | 0.79 | | 0.29 | 1.72 | 0.47 | | 1.72 | 1.37 | 1.87 | 0.27 | | |
| SrO | % | | 0.06 | 0.06 | | 0.11 | 0.13 | 0.12 | | 0.12 | 2.42 | 0.05 | 0.10 | | |
| BaO | % | | 0.15 | 0.16 | | 0.13 | 2.00 | 0.01 | | 1.96 | 0.53 | 0.43 | 0.12 | | |
| LOI | % | | <0.01 | <0.01 | | 0.13 | 0.34 | 0.14 | | 0.34 | 0.35 | 0.02 | 0.12 | | |
| Total | % | | 0.08 | 0.08 | | 0.04 | 0.71 | 0.03 | | 0.71 | 1.47 | 0.09 | 0.04 | | |
| Ba | ppm | | 739 | 771 | 749 | | 6340 | | >10000 | 6460 | | 782 | | | |
| Ce | ppm | | 82 | 94 | 91 | | 485 | | 4780 | 453 | | 1775 | | | |
| Cr | ppm | | 152 | 161 | 159 | | 158 | | 189 | 166 | | 383 | | | |
| Cs | ppm | | 11 | 11 | 11 | | 1 | | 1 | 1 | | 4 | | | |
| Dy | ppm | | 6 | 6 | 6 | | 11 | | 244 | 11 | | 20 | | | |
| Er | ppm | | 4 | 4 | 4 | | 6 | | 92 | 5 | | 6 | | | |
| Eu | ppm | | 1 | 1 | 1 | | 7 | | 136 | 8 | | 22 | | | |
| Ga | ppm | | 22 | 22 | 21 | | 20 | | 10 | 22 | | 26 | | | |
| Gd | ppm | | 6 | 7 | 7 | | 21 | | 364 | 20 | | 51 | | | |
| Hf | ppm | | 6 | 6 | 6 | | 17 | | 4 | 16 | | 11 | | | |
| Ho | ppm | | 1 | 1 | 1 | | 2 | | 40 | 2 | | 3 | | | |
| La | ppm | | 45 | 47 | 47 | | 236 | | 2560 | 239 | | 1320 | | | |
| Lu | ppm | | 0 | 1 | 0 | | 1 | | 7 | 1 | | 1 | | | |
| Nb | ppm | | 17 | 18 | 16 | | 23 | | 417 | 23 | | 703 | | | |
| Nd | ppm | | 40 | 40 | 38 | | 209 | | 2140 | 215 | | 832 | | | |
| Pr | ppm | | 10 | 11 | 11 | | 55 | | 579 | 55 | | 232 | | | |
| Rb | ppm | | 170 | 164 | 163 | | 79 | | 29 | 77 | | 66 | | | |

| | | |